**Charles University, Faculty of Mathematics and Physics**
**Astronomical Institute**

Habilitation Thesis

# Per asteroides ad astra

**Miroslav Brož**

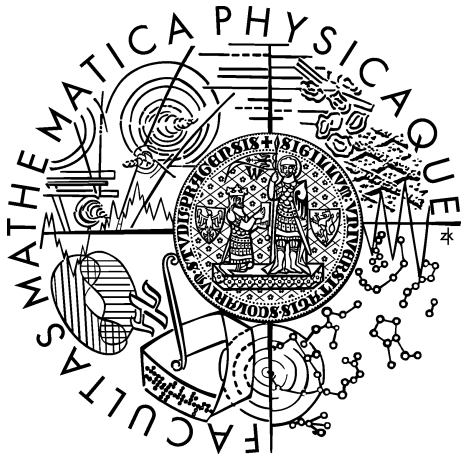


Prague, 2015

## Acknowledgements

I have to heartily thank to my friendly coworkers Alessandro Morbidelli, David Nesvorný, Bill Bottke, David Vokrouhlický (i.e. my former Ph. D. supervisor), Petr Harmanec, Josef Hanuš, Josef Ďurech, David Čapek, Pavel Mayer, Martin Šolc, and many other colleagues and students I had a pleasure to discuss and solve scientific problems with. Last — but not least — I am really grateful to my wife Míša and sons Rostík and Víťa, simply for their existence and curiosity.

In the course of time, my work was supported by the Grant Agency of the Czech Republic (grants no. 205/08/P196, 205/08/0064, 13-01308S), the Research Programme MSM0021620860 of the Czech Ministry of Education and by the Observatory and Planetarium in Hradec Králové.

Brož, Miroslav

Per asteroides ad astra

(asteroids, stars, celestial mechanics, thermal effects, collisions)

## Contents

# 1 Introduction

Asteroids (formerly, star-like bodies) and stars (i.e. real ones) are clearly closely related from an etymologist point of view. Coined by William Herschel in 1802, both objects exhibit the same point-like appearance on the sky, the only notable difference being the proper motion and the paralax.

Well, everybody knows there are a couple of additional differences. Nevertheless, we found this particular combination of subjects very fruitful. The quest for understanding both the central body and the small stuff bound to it by gravity is definitely logical. As a profound example, we may recall the age of the Sun that was actually inferred from radiometric ages of meteorites — or calcium–aluminium inclusions in ordinary chondrites, to be more specific — which pile up at $t = (4.559 \pm 0.004)$ Gyr and no one is older (Jacobsen and Wasserburg 1980; Tilton 1988; Guenther 1989).

There are also a number of similarities from a physicist point of view. You know, there are many useful papers which treat both as abstract point masses (e.g. Poincaré 1892). In 'advanced' applications, all the objects are spheres and no more than that (Eddington 1931). However, state-of-the-art models (Flock et al. 2013, Morbidelli et al. 2014, Bitsch et al. 2014) aspiring to capture all of the relevant physics are, in plain words, horribly complicated. Let us summarize it in four words: turbulence, chaos, irreversibility and $t = 0$.

In more words, radiative magneto–hydrodynamical (RMHD) equations exhibit several inherent instabilities which manifest themselves as turbulence (Figure 1) or collapse. Even in simple $N$-body problems, deterministic chaos can drive the overall evolution. The processes like mutual collisions are often thermodynamically irreversible, so no one can integrate the equations backward in time. And finally, we cannot measure the initial conditions, regardless of fantastic advances in instrumentation and observations (Parker et al. 2008, Mainzer et al. 2011, Schenk et al. 2012, Marchis et al. 2014).

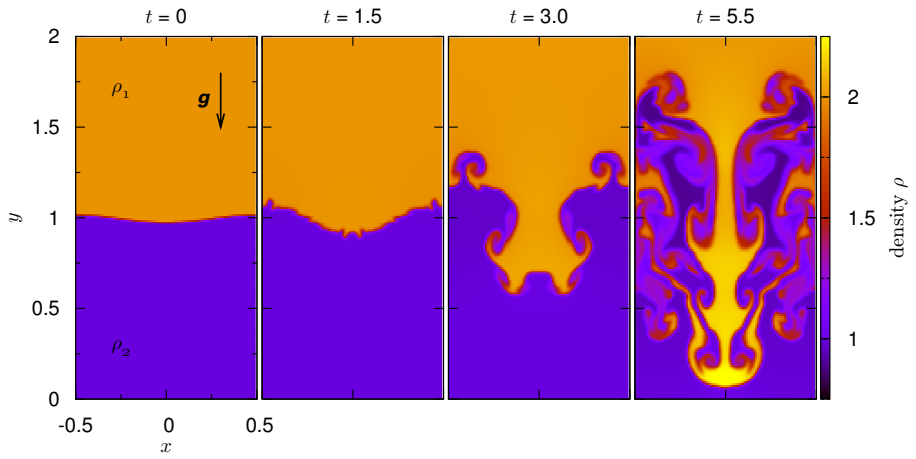


**Figure 1**: An evolution of the Rayleigh–Taylor instability from a small initial perturbation of the boundary. Since there appear mutual motions of the fluid, the Kelvin–Helmholtz instability occurs inevitably too. Initial conditions: $\rho_1 = 2$, $\rho_2 = 1$, $\Phi = y$, or $\mathbf{g} = -\nabla\Phi = (0, -1)$, respectively, $P(y)$ corresponds to a hydrostatic equilibrium, $\mathbf{v}_1 = \mathbf{v}_2 = (0, 0)$. Boundary conditions: periodic on the left and right, $\frac{\partial \rho}{\partial t} = 0$, $\frac{\partial \mathbf{v}}{\partial t} = \mathbf{0}$, $\frac{\partial P}{\partial t} = 0$ up and down. The state equation corresponds to ideal gas. A computation by the Pluto code (Mignone et al. 2007) in two dimensions, on a mesh with $100 \times 200$ points. The integration by a linearized Roe Riemann solver was controlled by the Courant-Friedrichs-Lewy condition, $C = 0.4$.

In order to stay on the safe side, we are going to discuss a sort of 'intermediate' models — it means neither pure point masses nor full RMHD — of asteroids and stars. In this thesis, we present nine research papers on the former subject and three on the latter, and also two relevant textbooks. Apart from that, I am glad to state that years of teaching resulted in nine bachelor theses and three diploma theses (and counting).

## 1.1 Contents and structure of the thesis

Briefly speaking, the papers selected for this thesis mostly deal with asteroid families, gravitational resonances and mutual relations between them, which are strongly enhanced by non-gravitational forces. The term families essentially means a similarity of orbits, strongly indicating a common origin. The term resonance is closely related to commensurable orbital or secular frequencies present in the system.

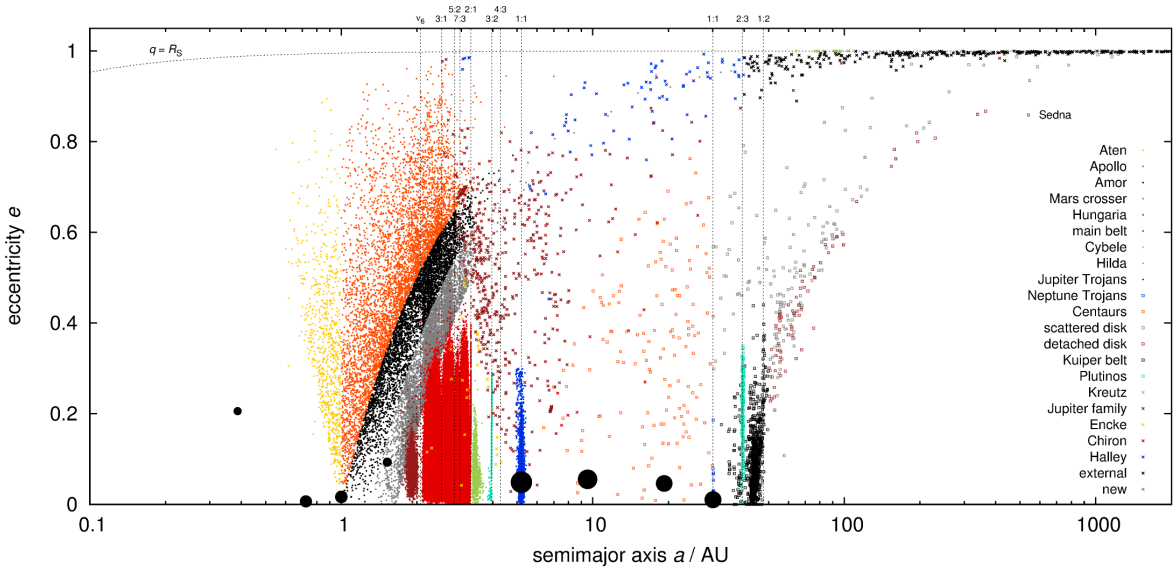


**Figure 2**: The observed state of the Solar System displayed on a plot semimajor axis $a$ vs eccentricity $e$. Symbols and colour discriminate various types and populations of small bodies: asteroids are shown as circles, trans-neptunian objects as squares and comets as crosses. There are more than $5 \cdot 10^5$ objects plotted, which might be either Aten, Apollo, Amor, Mars crosser, Hungaria, main belt, Cybele, Hilda, Jupiter Trojan, Centaur, Neptune Trojan, scattered disk, detached disk, Kuiper belt, Plutino, Kruetz, Jupiter family, Encke, Chiron, Halley, external, or new comet. Data were downloaded from the Minor Planet Center, AstOrb and AstDyS catalogues. Vertical lines denote major mean-motion resonances with Jupiter or Neptune and the $\nu_6$ secular resonance. The dotted line (close to the top) corresponds to a perihelion distance $q$ equal to the radius $R_\odot$ of the Sun.

In Section 2.1, we study populations of asteroids located in the mean-motion resonances with Jupiter, namely 2:1, 3:2 and 4:3 (see Figure 2), which seem to be quite diverse and consequently interesting. We identified one already known (Schubart) and one entirely new family (Hilda). And more importantly, we realized there is a clear fingerprint of non-gravitational forces and torques visible in their eccentricity distributions.

In Section 2.2 we focus on our new discovery, the Hilda family located in the 3:2 resonance. We constructed a rather complex model of its long-term orbital and spin evolution and it turned out, this is (likely) the oldest asteroid family in the Solar System, dating back to the Late Heavy Bombardment, approximately 3.85 billion years ago.

We then pay a close attention to the 1:1 resonance with Jupiter, i.e. the famous Trojan region, in Section 2.3. We reexamined previous family identifications and come up with a surprising conclusion, that there is actually only one family (and one new) which is definitely an important number for collisional models.

In Section 2.4, we try to understand the Eos family which is surrounded by a distinct halo. We explain its existence by the presence of 7:3, 9:4 and $z_1$ resonances which scatter asteroids in both eccentricity and inclination. We were also able to *exclude* a possibility that such halos are created during the migration of planets.

A complex study of the Late Heavy Bombardment is presented in Section 2.5. We attempt to combine various types of models — for the planetary migration, collisions between comets and asteroids, orbital evolution of asteroid families — in order to answer the question, how the bombardment affected the main asteroid belt. As a pre-requisite, we had to prepare an up-to-date list of asteroid families, including their physical properties. By the way, this is the work I am mostly proud of.

In Section 2.6, we construct a new collisional model of the main belt, split into six parts along major resonances, in order to use new observational data from WISE and the new family identification. As a major result, we conclude that an assumption of monolithic structure is better that a rubble-pile one.

In a series of two papers (Sections 2.7 and 2.8), we use our orbital and spin evolution model to match the observed distribution of spin pole latitudes for both large and small asteroids. A similar analysis is presented in Section 2.9 for individual families, which was only possible thanks to significantly increasing number of available and derived spin and shape models of asteroids.

Moving towards astrophysics, in Section 3.1 we interpret observations of the multiple star V505 Sagittarii for which multiple datasets exist: light-time effect measurements, speckle interferometry and radial

velocities. We heavily build up on known methods from the Solar System dynamics here. Section 3.2 is also devoted to an individual object, V2368 Ophiuichi this time, for which we compute and interpret stellar evolution tracks. Finally, the Section 3.3 touches a bit interstellar medium as we try to independently estimate the distance to $\varepsilon$ Aurigae, an eclipsing binary with the longest known orbital period.

Regarding the two textbooks, the one presented in Section 4.1 is based on the course 'Fyzika malých těles sluneční soustavy' (Physics of the small Solar System bodies, denoted NAST020) which was held at the Astronomical Institute from 2005 to 2014, with a two-year interval.

Similarly, 'Stavba a vývoj hvězd' (Structure and evolution of stars) in Section 4.2 reflects a basic course called Astrophysics II (NAST014). This course was first led together with Petr Harmanec, starting from 2008. We subsequently added several new chapters, namely 2.2 Stellar spectra, 14.3 Hydrodynamics of simple waves, and most importantly, 15 Gravitational collapse of protostars 16 Explosive stadia in evolution of stars. To prepare (a lot of) illustrations, we used an up-to-date stellar evolution code called MesaStar (Paxton et al. 2011) quite extensively.

Individual papers are reprinted in Appendix A. Abstracts of bachelor and diploma theses are included as Appendix B.

## 1.2 Behind the scenes

Let me also add some 'behind-the-scenes' information, because the papers alone are much more boring than real life. It would be a shame to loose the thrill of discovery, wouldn't be?

In 2008, we prepared an update of resonant population, a usual work. At the same time we thought that the Yarkovsky effect cannot be efficient at all in resonances. While I was finalising a presentation for the DDA meeting in Boulder, I decided to process one more numerical integration which was started about a month ago. At about midnight, I was astonished to realise, that there is a clear and systematic Yarkovsky drift in *eccentricity*, not in semimajor axis, as usually! Of course, this allowed an age determination of asteroid families, so I quickly rewrote the whole presentation, which was scheduled in the morning. This was a 'last-night' discovery.

Another story is related to a strange orbit of the V505 Sgr triple star. This was an idea of Dr. Mayer, who suggested we should try a 4th-body which would perturb the system in order to explain all the observational data. We submitted the resulting 10-page long paper to A&A and a few days later, I was really surprised by a rejection. Both the referee and editor thought that the speckle measurements are wrong and that the light-time effect is *not* related to the orbital motion. It was a sad experience for me, but today I better understand the reasons: a wrong title and one completely wrong conclusion. Well, we resubmitted a rewritten paper to AJ without any problems. Moreover, in 2013, we succeeded with an ESO proposal for follow-up spectroscopic observations.

Back in 2011, there were several papers discussing Trojan families and we thus were really motivated to study their orbital evolution. Soon, we found out that something is wrong: it was surprisingly difficult to identify the families using new orbital data, except the Eurybates which was clear beyond doubt. Moreover, our orbital evolution models provided only very poor fits. It took a few weeks until we understood that *no* other families exist! In other words, we experienced a sort of 'paradigm shift' which is a worthwhile experience, in any case.

Regarding the 2013 paper about the Eos family halo, it is fair to admit, that I was initially disappointed by the conclusion, because a possibility that halos originate from perturbations by planetary migration seems much more attractive. Regardless of my disappointment, it popped up during our discussions in Nice there should be *many* more families created in the main belt during the migration and the associated Late Heavy Bombardment — more than 100 with a minimum 100-km parent body size! The very fact that we observe only 20 of them was indeed a perfect motivation for us to work hard on our next paper and prepare new models, much more complex than we used ever before.

Being on the other side, as a referee of about 16 papers (mostly for the Icarus journal, and individual ones for Celestial Mechanics, Planetary and Space Science, Monthly Notices, and Nature) I enjoyed discussions and scientific debates which occasionally were quite emotional, or at least not emotionless. That was a minor note, but worth to mention.[1]

[1]Something I want to remember myself: when I was writing these words, the Rosetta/Philae had landed on 67P! Jean–Jacques Dordain (director general of ESA) commented on this as follows: *The biggest problem of a success is that it looks easy, and especially for us who are not doing anything.*

# 2 Physics of small Solar System bodies

## 2.1 Asteroid families in the first order resonances with Jupiter

Gravitational resonances are particular parts of the phase space where a body is under a strong influence of another distant body and exhibits a particular type of motion, characterized by *librations* of a given critical angle (see Figure 3). In the case of an asteroid and Jupiter, the critical angle of a mean-motion resonance is defined as:

$$\sigma \equiv (p+q)\lambda' - p\lambda - \varpi\,, \tag{1}$$

where $\lambda'$ denotes the true longitude of Jupiter, $\lambda$ and $\varpi$ are the true longitude and the longitude of the pericentre of the asteroid, and $p$ and $q$ are small integer numbers.

As explained in our paper Brož and Vokrouhlický (2008), we studied the distribution of asteroids captured in the 2:1, 3:2 and 4:3 mean-motion resonance with Jupiter. In order to recognize fine details, it is necessary to compute suitable *resonant elements* $a_\mathrm{r}$, $e_\mathrm{r}$, $\sin I_\mathrm{r}$ (Roig et al. 2002), instead of osculating ones. More specifically, we use the following (approximate) condition:

$$|\sigma| < 5^\circ \quad \wedge \quad \frac{\Delta\sigma}{\Delta t} < 0 \quad \wedge \quad |\varpi - \varpi'| < 5^\circ\,, \tag{2}$$

when we register the osculating elements and then we perform an averaging over 10 Myr to suppress long-period oscillations and obtain quasi-integrals of motion. Resonant semimajor axis then essentially corresponds to the (average) libration *amplitude*.

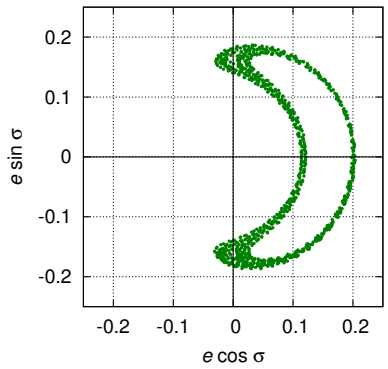


**Figure 3**: A typical trajectory of an asteroid located inside the 2:1 mean-motion resonance with Jupiter on a polar plot eccentricity $e$ vs the critical angle $\sigma$, as defined by Eq. (1). The angle $\sigma$ exhibits librations in this case, not circulations about the origin.

We identified 274 asteroids in the 2:1 resonance, 1197 in 3:2 — including two asteroid families, Schubart and Hilda — and only 3 in 4:3. Current statistics (as of 2014) are higher by approximately 50 % but we see no qualitative differences yet. More importantly, we realised that the Yarkovsky effect (actually, any sort of energy dissipation) causes a systematic drift in *eccentricity* when objects are captured in 1$^\mathrm{st}$ order resonances. While this is a standard part of celestial mechanics (Murray and Dermott 1999), it seems to be the first use in this context. Of course, this enabled us to determine dynamical ages of the families. Using our 'standard' dynamical model (Brož 2006), we derived $t_\mathrm{age} = (1.7 \pm 0.7)$ Gyr for Schubart and $\gtrsim 4$ Gyr for Hilda. The latter result motivated us to perform also simulations which include the *planetary migration*, as the age might correspond to late dynamical instabilities of our planetary system and the late heavy bombardment (LHB), dated back to $\simeq 3.85$ Gyr (Gomes et al. 2005, Morbidelli et al. 2005, Tsiganis et al. 2005). It turned out that the whole 3:2 resonance with Jupiter is unstable when Jupiter and Saturn cross their mutual 2:1 resonance and so the correspondence of the age/LHB is not a mere coincidence.

We were also curious why there are no families observed in the 2:1 resonance with Jupiter. In order to address this question, we prepared a model of a synthetic family, assuming an isotropic disruption (see Figure 4). In this case, however, we must account for the terrestrial planets too, as they partially break the protection mechanism of the resonance (Skoulidou et al. 2014). It seems that any family will be dispersed in less then 0.5 Gyr, so that the initial concentration of bodies is not recognisable anymore.

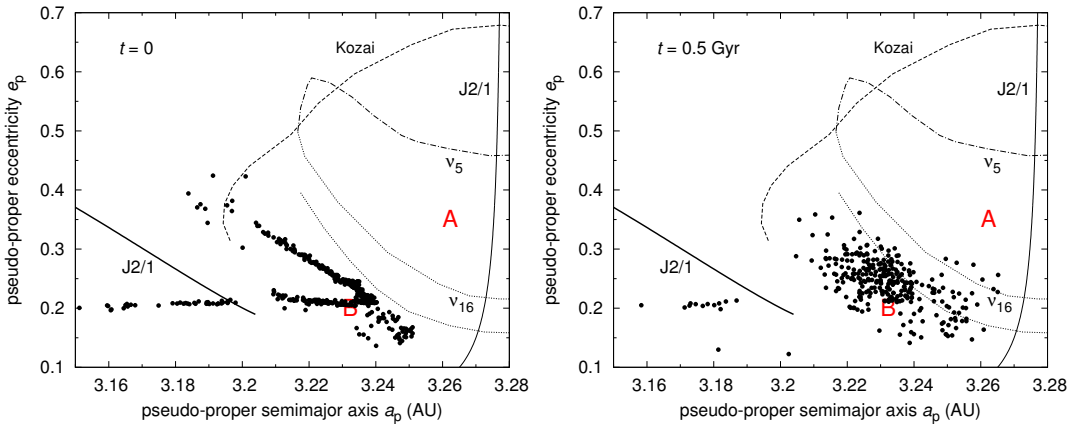


**Figure 4**: Long-term orbital evolution of a synthetic family created in the J2/1 resonance, the resonant semimajor axis $a_{\rm r}$ vs the eccentricity $e_{\rm r}$. Left: initial conditions at $t = 0$ (after a 10 Myr of averaging). We assumed an isotropic velocity field, which would create a regular 'ellipse' in the space of osculating elements, however, due to the very definition of the pseudo-proper elements, bodies which fall on the right-hand side of the libration centre are displayed on the left. Right: an evolved family at $t = 0.5$ Gyr, as computed by a modified SWIFT symplectic integrator (Levison and Duncan 1994). Our model included gravitational perturbations by both giant and terrestrial planets, the Yarkovsky and YORP thermal effects and spin axis reorientations by non-disruptive collisions. A detailed description of all parameters is included in Brož and Vokrouhlický (2008). The letters A and B denote two stable island, where the chaotic diffusion is slow. Note there are no fragments located in the island A.

## 2.2 Did the Hilda collisional family form during the late heavy bombardment?

In Brož et al. (2011), we focused our attention on the Hilda group — which is a name used for the whole population in the 3:2 mean-motion resonance with Jupiter — and the Hilda family in particular, which is a part of it, significantly concentrated between the resonant inclination $\sin I_{\rm r} = 0.14$ and 0.17. The family is spectrally homogeneous (C-type; see Figure 5) and its size-frequency distribution is steeper than that of background which are both indications that it is indeed of collisional origin. And moreover, we have numerical model capable to explain its overall structure. Before we proceed, let us *schematically* describe its basic ingredients.

We use a symplectic integration scheme (Levison and Duncan 1994), denoted as kick–drift–kick, where the 'kick' (actually, a perturbation) is performed as:

$$\dot{\mathbf{r}}_{n+1} = \dot{\mathbf{r}}_n + \ddot{\mathbf{r}}\frac{\Delta t}{2}\,, \tag{3}$$

and the 'drift' corresponds to an analytical solution of the two-body problem (the Sun–asteroid), which involves a numerical solution of the transcendent Kepler equation:

$$M = E - e\sin E\,, \tag{4}$$

$$\mathbf{r}_{n+1} = p(E)\mathbf{r}_n + q(E)\dot{\mathbf{r}}_n\,, \tag{5}$$

$$\dot{\mathbf{r}}_{n+1} = \dot{p}(E)\mathbf{r}_n + \dot{q}(E)\dot{\mathbf{r}}_n\,; \tag{6}$$

we account for gravitational perturbations by planets, expressed in the heliocentric frame:

$$\ddot{\mathbf{r}}_j = \sum_i \left[-\frac{Gm_i}{r_i^3}\mathbf{r}_i - \frac{Gm_i}{r_{ji}^3}\mathbf{r}_{ji}\right]\,, \tag{7}$$

possibly, the planetary migration, in an analytical way (Malhotra 1995), and also eccentricity damping (Morbidelli et al. 2010):

$$\dot{\mathbf{r}}_{n+1} = \dot{\mathbf{r}}_n\left[1 + \frac{\Delta v}{\dot{r}}\frac{\Delta t}{\tau_{\rm mig}}\exp\left(-\frac{t-t_0}{\tau_{\rm mig}}\right)\right]\,, \tag{8}$$

the Yarkovsky thermal effect (Vokrouhlický 1998, Vokrouhlický and Farinella 1999):

$$f_X(\zeta) + {\rm i}f_Y(\zeta) = -\frac{8}{3\sqrt{3\pi}}\,\Phi\,t'_{1-1}(R';\zeta)\,, \tag{9}$$

$$f_Z(\zeta) = -\frac{4}{3}\sqrt{\frac{2}{3\pi}}\,\Phi\,t'_{10}(R';\zeta)\,, \tag{10}$$

$$\Phi \equiv \frac{(1-A)\mathcal{E}_\star \pi R^2}{m_j c_{\rm vac}}\,, \tag{11}$$

the YORP effect (Čapek and Vokrouhlický 2004):

$$\dot{\omega} = c f_k(\gamma)\,, \tag{12}$$

$$\dot{\gamma} = \frac{c g_k(\gamma)}{\omega}\,, \tag{13}$$

$$c \equiv c_{\rm YORP}\left(\frac{a}{a_0}\right)^{-2}\left(\frac{R}{R_0}\right)^{-2}\left(\frac{\rho}{\rho_0}\right)^{-1}, \tag{14}$$

mass shedding beyond the critical angular frequency (Pravec and Harris 2000):

$$\omega_{\rm crit} = \sqrt{\frac{4}{3}\pi G\rho}\,, \tag{15}$$

and random collisional reorientations with the time scale (Farinella et al. 1998):

$$\tau_{\rm reor} = B\left(\frac{\omega}{\omega_0}\right)^{\beta_1}\left(\frac{R}{R_0}\right)^{\beta_2}. \tag{16}$$

The notation is as usual: the index $i$ corresponds to planets, $j$ to test particles (i.e. asteroids with negligible masses), $t$ time (independent variable), $\Delta t$ the time step, $\mathbf{r}_j$ position vector(s) (for all test particles), $\dot{\mathbf{r}}$ the velocity, $\ddot{\mathbf{r}}$ the acceleration, $M$ the mean anomaly, $E$ the eccentric anomaly, $e$ the eccentricity, $p(E)$, $q(E)$ functions of orbital elements, $G$ the gravitational constant, $m_i$ planetary mass(es), $m_j$ mass(es) of 'mass-less' particles, $\Delta v = \sqrt{GM/a_{\rm ini}} - \sqrt{GM/a_{\rm fin}}$ a measure of the total change of the semimajor axis, $\tau_{\rm mig}$ the migration time scale, $e_{\rm damp}$ eccentricity damping parameter(s), $(f_X, f_Y, f_Z)$ the Yarkovsky acceleration vector expressed in the body-centric frame (that is the place where $\gamma$ is hidden), $t'$ dipole coefficients $R'$ a radius scaled by the seasonal thermal wave penetration depth $l_{\rm s} \equiv \sqrt{K/(\rho_{\rm surf} C \omega_{\rm rev})}$, $K$ the thermal conductivity, $C$ the specific heat capacity, $\rho_{\rm surf}$ the density (of surface layers), $\omega_{\rm rev}$ orbital angular frequency, $\zeta \equiv \exp(\mathrm{i}\omega(t-t_0))$ a complex phase of rotation, $A$ the Bond albedo, $\mathcal{E}_\star$ subsolar insolation, $R$ the radius, $c_{\rm vac}$ the speed of light, $\omega$ the angular frequency of rotation, $\gamma$ the obliquity, $f_k(\gamma)$, $g_k(\gamma)$ parametric functions describing the YORP torques (computed numerically), $c_{\rm YORP}$ the scaling parameter, $a$ the semimajor axis, $\rho$ the bulk density, and finally, $B$, $\beta_1$, $\beta_2$ the normalisation and exponents describing the reorientations.

So, using the model above, we verified that a synthetic family, which is assumed to be initially isotropic, evolves naturally towards the observed state — with a size-dependent extension in the resonant eccentricity $e_{\rm r}$ values (i.e. the result of the thermal acceleration) and the central depletion of $e_{\rm r}$ for small bodies (i.e. the consequence of the thermal torque). We then constructed a simple stationary collisional model to estimate the number of disruption events during the last 4 Gyr. The result $n_{\rm events} = 0.004$ is clearly too small and we treat it as an independent evidence that the LHB is responsible for the origin of the Hilda family. Indeed, a non-stationary model of the LHB produces $n_{\rm events}$ up to 0.2 which is of the right order.

Last, but not least, we ran an extensive set of about $10^3$ planetary-migration simulations. The synthetic family is often dispersed too much, because of the secondary resonances between the libration frequency $f_{3:2}$ of an asteroid in the 3:2 resonance with Jupiter and the frequency $f_{1\mathrm{J}-2\mathrm{S}}$ of the critical argument of Jupiter–Saturn 1:2 resonance (similar as in Kortenkamp et al. 2004). Consequently, the family must have been created during the later migration phase. Nevertheless, if the planetary migration was *not* smooth but rather violent, involving close encounter between giant planets (Morbidelli et al. 2010), these conclusions may change.

Finally, let us note there is a disagreement with Grav et al. (2012) who classified the Hilda family as D-type. However, their conclusion was based on 11 measurements of the infrared albedo $p_{\rm IR}$ and they probably picked up the scattered D-types only (cf. Figure 5).

## 2.3 Eurybates — the only asteroid family among Trojans?

Trojans of Jupiter, captured in the 1:1 mean-motion resonance, is a very important group of asteroids which has been used many times to address the early orbital evolution of planets (Marzari and Scholl

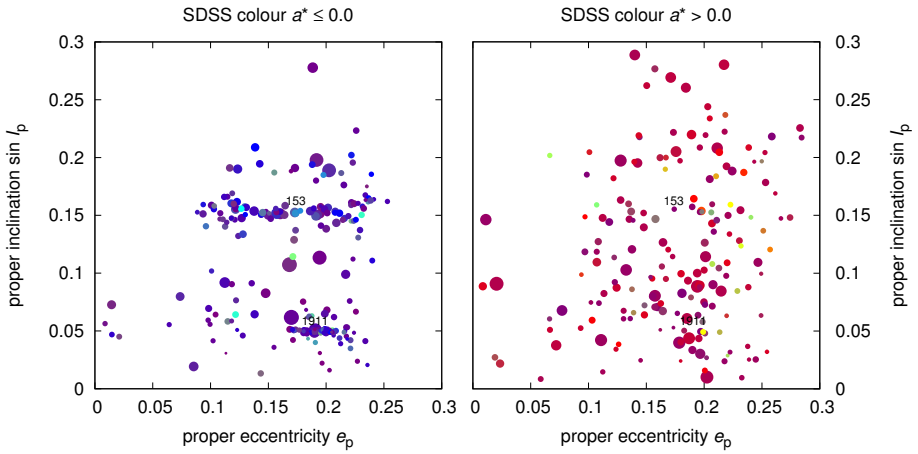


**Figure 5**: A subset of asteroids located in the 3:2 mean-motion resonance with Jupiter for which colour indices were measured by the Sloan Digital Sky Survey (ADR4 catalogue; Parker et al. 2008). The plots show the proper eccentricity $e_\mathrm{p}$ vs the proper inclination $\sin I_\mathrm{p}$, taken from the AstDyS catalogue (Knežević and Milani 2003). Sizes of symbols are inversely proportional to the absolute magnitude $H$. Left: asteroids with the index $a^* = 0.89(g-r) + 0.45(r-i) - 0.57 \le 0$ (i.e. mostly corresponding to C-type reflectance spectra; Ivezić et al. 2001). Right: those with $a^* > 0$ (i.e. D-type). There are two families clearly visible: associated with (153) Hilda and (1911) Schubart; both of them are C-type.

1998, Morbidelli et al. 2005, Levison et al. 2009, Nesvorný et al. 2013). It was also extensively studied by means of spectroscopy and broad-band photometry, both visual and infrared (Fornasier et al. 2007, Roig et al. 2008, Emery et al. 2011, Grav et al. 2011). There also exist Trojans of Mars (Christou et al. 2013) and Neptune (Sheppard and Trujillo 2010), but the former are not very numerous and the latter are much more difficult to observe because of their darkness and distance.

As the interpretation of data and simulations often depends on the observed number of collisional families, we chose this topic for our study Brož and Rozehnal (2011). We computed suitable resonant elements by means of Milani (1993). We then used the hierarchical clustering algorithm (Zappalá et al. 1994), the slope of size-frequency distributions, and colour data (Parker et al. 2008), to conclude there is only *one* reliable family identified previously, namely around the asteroid (3548) Eurybates. At the same time, we reported a discovery of two small clusters associated with (4709) Ennomos and (9799) 1996 RJ.

We also performed several numerical simulations of synthetic families. As before, we assumed a simple isotropic disruption (Farinella et al. 1994) and computed orbital evolution of fragments over 4 Gyr, which is controlled by the chaotic diffusion, the Yarkovsky drift being inefficient in the $0^{\mathrm{th}}$ resonance. It turned out that it would be indeed impossible to explain extended groups like Aneas or 1988 $\mathrm{RG}_{10}$, which span the whole range of stable semimajor axis. Moreover, given the intrinsic probability of Trojan–Trojan collisions (Dell'Oro et al. 1998), the total number of collisional families should be indeed low (about one). This essentially confirms our previous conclusion.

Since the numbers of objects in orbital catalogues steadily increase, we continue monitoring of the Trojan families (Rozehnal and Brož 2014). It seems, there are three more, composed of mostly small objects and thus not visible in previous data: (624) Hektor, (20961) Arkesilaos, and (247341) 2001 $\mathrm{UV}_{209}$. The Hektor family is particularly interesting, because (624) Hektor has a satellite (Marchis et al. 2014). Its association with the family, created by a cratering event, is a topic worth of a separate study. A preliminary model of the orbital evolution of the Hektor family (Figure 6) shows that we can exclude at least some of the initial geometries, namely those having the true anomaly $f_\mathrm{imp} \simeq 0°$.

## 2.4 The Eos family halo

The Eos family is a very prominent group, one of the three mentioned already by Hirayama (1918). When colour data for almost $10^5$ asteroids became available (Ivezić et al. 2001, Parker et al. 2008), it occurred as even more prominent, because of its unique colour corresponding to the K taxonomic type and a distinct halo dispersed both in eccentricity and inclination (see Figure 7, left). Morbidelli et al. (2010) suggested that it could have been created during the giant-planet migration, by purely gravitational perturbations.

In Brož and Morbidelli (2013), we tried to assess the contribution of the classical long-term orbital evolution to the creation of this halo. Using an $N$-body model, we found out that orbits interacting with

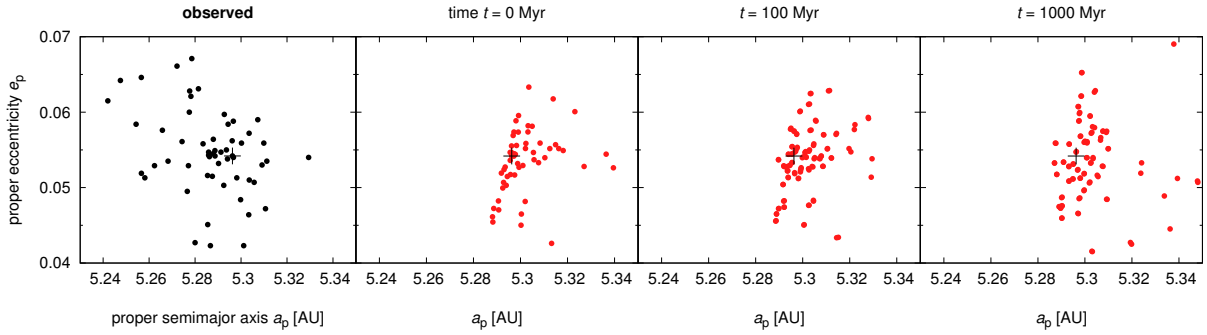


**Figure 6**: The observed Hektor family located in the 1:1 resonance with Jupiter (i.e. the Trojan region, namely the L4 cloud) and a comparison with an $N$-body model of a long-term evolution. The initial conditions ($t = 0$) correspond to an isotropic velocity field with the peak at about the escape velocity, $v_{\rm esc} = 70\,{\rm m/s}$. The true anomaly of the break-up was $f_{\rm imp} = 0^\circ$ and the argument of perihelion $\omega_{\rm imp} = 30^\circ$. We used the Swift integrator (Levison and Duncan 1994), modified according to Laskar and Robutel (2001), with the time step $\Delta t = 91.3\,{\rm day}$. The Yarkovsky/YORP effects were also included, but they are not effective in the $0^{\rm th}$-order resonance. The situation at $t = 1\,{\rm Gyr}$ indicates that the shape of the synthetic family remains incompatible with the observed family.

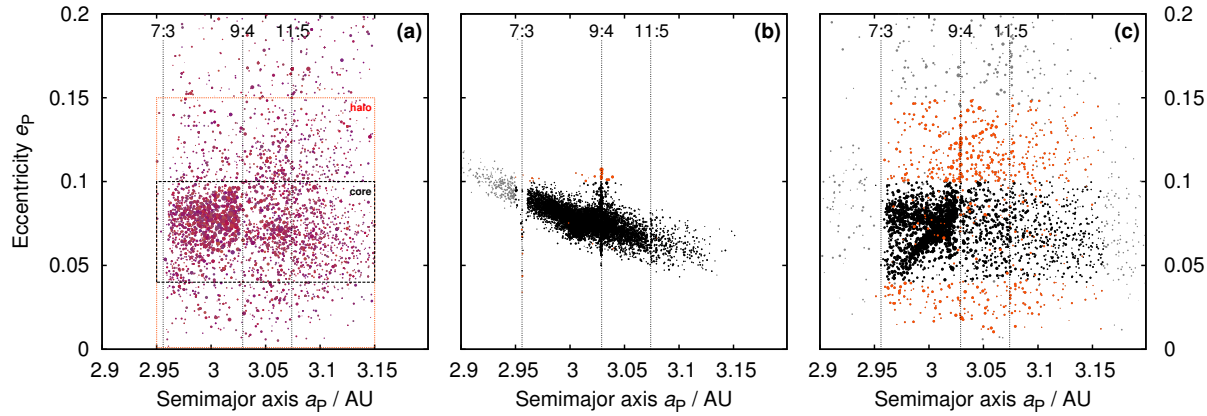


**Figure 7**: A comparison of the observed Eos family and an $N$-body model of a synthetic family. All the plots show the proper semimajor axis $a_{\rm p}$ vs the proper eccentricity $e_{\rm p}$. Left: The observed asteroids with Eos-like colours, i.e. $a^* \in (0.0, 0.1)\,{\rm mag}$, $i - z \in (-0.03, 0.08)\,{\rm mag}$, according to the Sloan Digital Sky Survey data (Parker et al. 2008). The sizes of symbols are inversely proportional to the absolute magnitude $H$. We can discern the *core* of the family approximately as a 'box' in the space of proper elements, $a_{\rm p} \in (2.95, 3.16)\,{\rm AU}$, $e_{\rm p} \in (0.04, 0.10)$, and $\sin I_{\rm p} \in (0.15, 0.20)$, while the surrounding *halo* is more extended in terms of $e_{\rm p} \in (0.00, 0.15)$, and $\sin I_{\rm p} \in (0.12, 0.24)$. Middle: The initial conditions of the $N$-body model, with 6545 test particles and assuming an isotropic velocity field with an ejection velocity $v_{\rm ej} = 93\,{\rm m/s}$ for $D = 5\,{\rm km}$ bodies and a $1/D$ scaling. The geometry of the collisional disruption was controlled by the true anomaly $f = 150^\circ$ and the argument of perihelion $\omega = 30^\circ$. Initially, majority of asteroids (denoted by black colour) is located within the core and only a few are in the halo (see orange colour). Right: The synthetic family after 1.7 Gyr, evolved due to the Yarkovsky semimajor-axis drift and interactions with various resonances, namely the 7/3, 9/4 and 11/5 mean-motion resonances with Jupiter, a three-body resonance $3{\rm J} - 2{\rm S} - 1$ and a $z_1 \equiv g - g_6 + s - s_6$ secular resonance. The assumed thermal parameters correspond to regolith-covered basaltic asteroids, with the bulk density $\rho = 2\,500\,{\rm kg\,m^{-3}}$ and the surface thermal conductivity $K = 0.001\,{\rm W\,m^{-1}\,K^{-1}}$. The probable age of the Eos family was derived from the observed ratio of the halo/core populations as $t_{\rm age} = 1.5$ to $1.9\,{\rm Gyr}$. Adapted from Brož and Morbidelli (2013).

the 9:4, 7:3 and resonances are scattered into the surroundings and the number of objects in the halo thus increases with time (Figure 7, right). This may actually serve as an independent age estimate, which is $t_{\rm age} = 1.5$ to 1.9 Gyr, and consequently *no* migration is needed to explain the halo.

According to Carruba et al. (2013), who analysed families in the multi-domain space of proper orbital elements, colours and albedos, halos are quite common. While we might think that all of them may be created by a similar mechanism, this has not been actually computed yet, in a systematic way.

## 2.5 Constraining the cometary flux through the asteroid belt during the late heavy bombardment

The late heavy bombardment (LHB) as a concept was introduced after Apollo and Luna missions delivered lunar samples and their radiometric (U–Pb, Rb–Sr) ages were too 'young' — 4.1 to 3.8 billion years (Tera et al. 1974, Ryder et al. 2000). The stratigraphy of the lunar surface also strongly indicates that a number of large basins, e.g. Imbrium, Crisium and Orientale, were created during this cataclysm. At the same time, it is not likely that these may be created by leftover planetesimals (Bottke et al. 2007). Furthermore, there are many signs of intense bombardment throughout the Solar System — ranging from terrestrial planets (Mercury), shock ages of meteorites, to basins on icy moons of giant planets (Marchi et al. 2013, Cohen et al. 2000, Kring and Swindle 2008 Charnoz et al. 2009). In Brož et al. (2013), we studied the LHB in the context of the Nice model (Gomes et al. 2005, Morbidelli et al. 2012), in which one assumes that (at least a part of) the bombardment was caused by a sudden dynamical dispersal of a by then massive trans-neptunian disk of comets.

As a (substantial) preparatory work, we had to estimate basic physical properties, most importantly the parent-body sizes $D_{\rm PB}$, for all known large asteroid families, because this is the major observational constraint for all collisional models. There are a few awaited problems, thought: the method to determine $D_{\rm PB}$ (Durda et al. 2007) involves a somewhat dangerous extrapolation, the value of $D_{\rm PB}$ may sometimes depend on individual membership, and family lists are not always consistent (cf. Parker et al. 2008, Nesvorný 2010, Masiero et al. 2013, Carruba et al. 2013). Nevertheless, the resulting production function of asteroid families (Figure 8) does not depend much on individual cases, it is rather a statistical characterisation of the whole main asteroid belt. It is also reassuring that the dynamical ages of families (well, mostly the upper-limits derived by means of Nesvorný et al. 2005) are spanned across the whole interval of 4 Gyr and not beyond that (Figure 9).

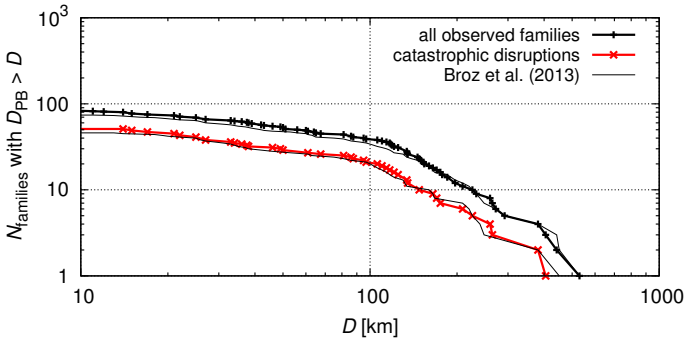


**Figure 8**: A production function (i.e. the cumulative number $N(>D)$ of families with parent-body size $D_{\rm PB}$ larger than $D$) for all observed main-belt families (thin gray) and families corresponding to catastrophic disruptions (thick black), i.e. with largest remnant/parent body mass ratio lower than 0.5. Adapted from Brož et al. (2013) and updated according to Nesvorný et al. (submitted).

Our collisional model is based on the Boulder code (Morbidelli et al. 2009). We shall briefly describe its features as follows. The number of collisions is given by:

$$n_{ij} \quad = \quad p_{\rm i}(t) f_{\rm g} \frac{(D_i + d_j)^2}{4} n_i n_j \Delta t \,, \tag{17}$$

the size of the largest remnant (Benz and Asphaug 1999):

$$M_{\rm LR} \quad = \quad \left[ -\frac{1}{2} \left( \frac{Q}{Q^\star_D} - 1 \right) + \frac{1}{2} \right] M_{\rm tot} \quad \text{for } Q < Q^\star_D \,, \tag{18}$$

$$M_{\rm LR} \quad = \quad \left[ -0.35 \left( \frac{Q}{Q^\star_D} - 1 \right) + \frac{1}{2} \right] M_{\rm tot} \quad \text{for } Q > Q^\star_D \,, \tag{19}$$

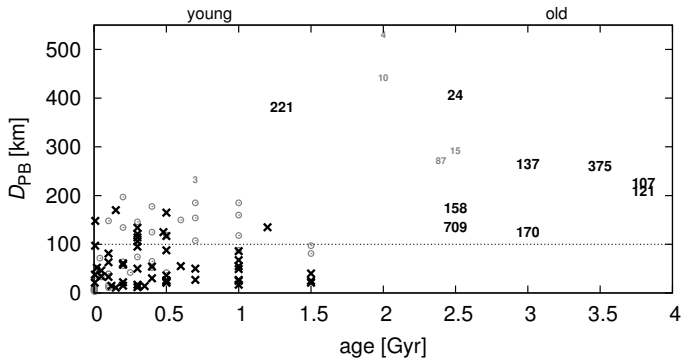


**Figure 9**: The relation between dynamical ages of families and the sizes of their parent bodies. Black crosses (or large labels) correspond to catastrophic disruptions, while cratering events are labelled by gray circles (small labels). Some of the families are denoted by the designation of the largest member. Adapted from Brož et al. (2013) and updated according to Nesvorný et al. (submitted).

the size of the largest fragment (Durda et al. 2007):

$$M_{\rm LF} \quad = \quad 8 \times 10^{-3} \left[ \frac{Q}{Q_D^\star} \exp\left( - \left( \frac{Q}{4Q_D^\star} \right)^2 \right) \right] M_{\rm tot} \,, \tag{20}$$

$$\tag{21}$$

and the slope of the respective size distribution (dtto):

$$q \quad = \quad -10 + 7 \left( \frac{Q}{Q_D^\star} \right)^{0.4} \exp\left( - \frac{Q}{7Q_D^\star} \right) \,, \tag{22}$$

where the index $i$ always corresponds to a target, $j$ to a projectile, $p_{\rm i}$ denotes the (time-dependent) intrinsic collisional probability, $f_{\rm g}$ the gravitational focussing factor (Greenzweig and Lissauer 1990), $D_i$, $d_j$ the diameters, $n_i$, $n_j$ the numbers of bodies (in given bins), $\Delta t$ the time step, $Q \equiv \frac{1}{2} M_j v_{\rm imp}^2(t)/M_{\rm tot}$ the specific energy of a collision, $v_{\rm imp}$ the impact velocity, of course, $Q_D^\star = Q_0 r^a + B\rho r^b$ the scaling law (Benz and Asphaug 1999), and $M_{\rm tot} \equiv M_i + M_j$ is the total mass. So, it is now clear that this is essentially a Monte-Carlo statistical model, which includes parametric relations inferred from SPH simulations of asteroidal collisions and, inevitably, a number of material parameters too.

One of our results is shown in Figure 10. The LHB is indeed capable to create on average more than 100 (synthetic) families with $D_{\rm PB} > 100\,$km, which seems like a *big* problem, since we observe only 20 of them. At the same time, without the LHB we would have problems to explain the number of $D_{\rm PB} > 200\,$km families. However, we tested several processes: i) overlapping of families, ii) dispersion by the Yarkovsky drift, iii) reduction of physical lifetime of comets, iv) perturbation by planetary migration, v) secondary bombardment (comminution), and v) with the help of iii) may decrease the former number while keep the latter.

We also paid a closer attention to the 'pristine zone', i.e. a narrow part of the main belt between the 5:2 and 7:3 mean-motion resonances with Jupiter ($a_{\rm p} = 2.825$ to $2.955\,$AU), in which no big families are located (well, except Koronis at low inclinations) and the number density of asteroids is much lower than in the neighbouring middle and outer belts. Small families are then best visible in the $(e_{\rm p}, \sin I_{\rm p})$ projection. It is possible that some of them are actually remnants of large ($D_{\rm PB} > 100\,$km) families we spoke about above. One of the promising cases is associated with the asteroid (918) Itha (see also Brož et al. 2012).

## 2.6 A six-part collisional model of the main asteroid belt

In our subsequent and somewhat contradicting study Cibulková, Brož and Benavidez (2014), we tried to explain the observed number of families in a classical way, assuming the current values of the impact probability $p_{\rm i}$ velocity $v_{\rm imp}$ (as in Bottke et al. 2005), and a time scale of $4\,$Gyr (i.e. after the LHB). In order to exploit new observational data, especially the albedos measured by WISE (Mainzer et al. 2011), we constructed reliable size-frequency distributions (SFD) for the six individual parts of the main asteroid belt: inner, middle, pristine belt, outer, Cybele zone, and the high-inclination region (Figure 11, black lines).

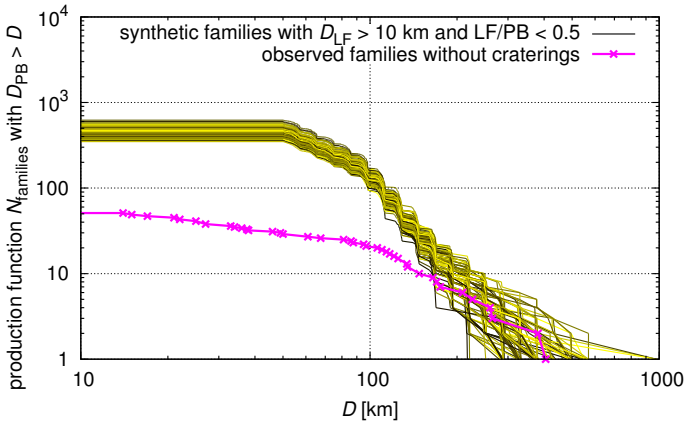


**Figure 10**: The outcomes of the bombardment of the main asteroid belt by trans-neptunian comets, as modeled by Brož et al. (2013). The plot shows the family production functions (i.e. the cumulative number $N(>D)$ of families with parent-body size $D_{\rm PB}$ larger than $D$) and a comparison to the observed one. In order to distinguish 100 individual simulations (differing only by random-seed values) we plot them using lines of different colours, ranging from black to yellow. The assumptions of the model were as follows: a massive ($25\,M_\oplus$) disk of trans-neptunian comets, with a size-frequency distribution having about $10^{12}$ bodies larger than $D > 1\,$km (i.e. corresponding to the observed broken power law for the current Kuiper Belt; Fraser and Kavelaars 2008), intrinsic collisional probabilities reaching up to $6 \times 10^{-21}\,{\rm km}^{-2}\,{\rm yr}^{-1}$, average impact velocities $v_{\rm imp} = 10\,$km/s (according to Vokrouhlický et al. 2008) and a dynamical decay of the main belt population by a factor of $\sim 3$ (Minton and Malhotra 2010).

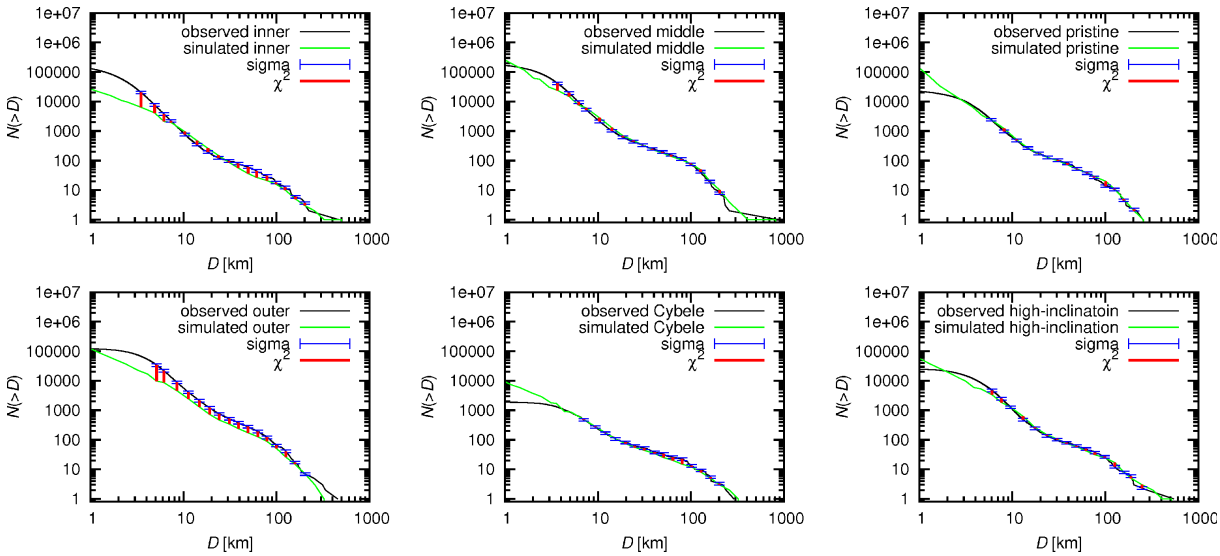


**Figure 11**: The observed (black line) and simulated (green line) size-frequency distributions for the six parts of the main belt: inner, middle, 'pristine' belt ($a \in (2.823, 2.956)\,$AU), outer, Cybele zone, high-inclination region ($\sin I > 0.34$). Sigma error bars denote the (prescribed) uncertainties of the observed SFDs. This result is for the simulation with monoliths, i.e. the scaling law of Benz and Asphaug (1999) and parametric relations from Morbidelli et al. (2009). The largest differences can be seen for the inner and outer belt.

We improved the collisional model presented in the previous section by implementing a $\chi^2$ calculation and a simplex algorithm which allowed us to survey a significant part of the parameter space. One set of simulations for monolithic bodies consisted of more than $10^5$ runs. The evolution is in fact very stochastic, because the outcome depends on individual disruptions of large asteroids and we thus cannot find a global and statistically significant minimum of $\chi^2$. Nonetheless, this allowed us to conclude that it is neither possible nor easy to find a better fit than the one presented in Figure 11. The problems seen in the inner and outer belt (in between $D = 1$ and 10 km) may be possibly solved by incorporating a dynamical decay due to the Yarkovsky effect.

What is even more interesting, we derived parametric relations for rubble-pile bodies with macroporosity, based on SPH modelling of Benavidez et al. (2012). If we assume that the scaling law is simply a scaled-down version of Benz and Asphaug (1999), the corresponding set of simulations led to a $\chi^2$ which is about twice as large as for monoliths. The interpretation of this 'failure' means that majority of asteroids cannot be rubble piles, which is an unexpected result, contradicting previous expectations based on rotational rate distribution (Pravec and Harris 2000).

Well, we have have to admit there are alternative explanations too. Apart from 11 enumerated in our paper, the rubble piles may be actually *microporous*, which have a substantially larger strength (Jutzi et al. 2014). Alternatively, we should use additional observational constraints — apart from the main-belt SFDs and numbers of families — primarily the observed (debiased) SFD of the near-Earth objects (Bottke et al. 2002, Granvik et al. 2014) which would help to constrain the small-size end. Or, what a nice coincidence, we may turn back to Section 2.5.

## 2.7 A study of asteroid pole-latitude distribution based on an extended set of shape models derived by the lightcurve inversion method

Most of the work in Hanuš et al. (2011) was devoted to *lightcurve inversion*, an important technique used to interpret disk-integrated photometric measurements (Kaasalainen and Torppa 2001, Kaasalainen et al. 2001) and to constrain some of the physical properties, most importantly shape, pole direction ($\lambda$, $\beta$), scattering law, size, albedo, even though some of them are often rather assumed than derived. Since the problem for non-convex shapes is degenerate (different shapes may produce the same flux), one usually computes only a *convex hull* as a proxy for the real shape. It was also absolutely necessary to estimate the *bias* of the method itself; the ratio between recovered models in $|\sin\beta| > 0.8$ and $|\sin\beta| < 0.2$ bins is approximately 60 %.

We analysed about 200 convex-hull shape models (80 of them new). While it is not always possible to find a single solution (two mirror solutions in longitude $\lambda$ are very common), the derived latitudes $\beta$ are more reliable, with an uncertainty $\pm 10°$, or in some cases $\pm 20°$ for limited datasets. The observed and debiased distribution of $\sin\beta$ is clearly not uniform (isotropic), but the situation is different for different sizes: $D > 60$ km asteroids exhibit a preference for prograde rotation (cf. Magnusson 1986) and $D < 30$ km a depletion near the ecliptic plane (Drummond et al. 1988). It was worth to verify, if this kind of distribution may be induced by the YORP effect.

To this point, we constructed a dynamical model of the pole-latitude distribution which consisted, in principle, of Equations (12) to (16). Furthermore, we had to account for gravitational torques and spin-orbital resonances (Vokrouhlický et al. 2006). In a crudest approximation, these may be treated as large-amplitude oscillations of $\beta$. Our results shown in Figure 12 confirm the prograde rotation of large asteroids is primordial (Johansen and Lacerda 2010) and indicate that the thermal torques (of Čapek and Vokrouhlický 2004) are capable to deplete small asteroids near the ecliptic. The asymmetry between $\sin\beta > 0.8$ and $\sin\beta < -0.8$ bins is on the other hand caused by the spin-orbital resonances which are only affecting prograde asteroids.

## 2.8 Asteroids' physical models from combined dense and sparse photometry and scaling of the YORP effect by the observed obliquity distribution

Hanuš et al. (2013) is a direct continuation of the previous work (and I actually thought about merging these two Sections into one). Nonetheless, the number of models is substantially higher (330; 119 new) and it allowed us to better constrain the semiempirical scaling by the $c_{\rm YORP}$ parameter, introduced in Eq. (14). We ran 10 sets of simulations, with 100 runs in each of them, and in every time step we computed the $\chi^2$ from simulated and observed $\sin\beta$ distributions. The most probable values of $c_{\rm YORP}$ then range from 0.05 to 0.6.

The scaling above might seem artificial, but it has a very natural explanation. We are missing an important information, namely the small-scale topography. Even small boulders or craters, which cannot

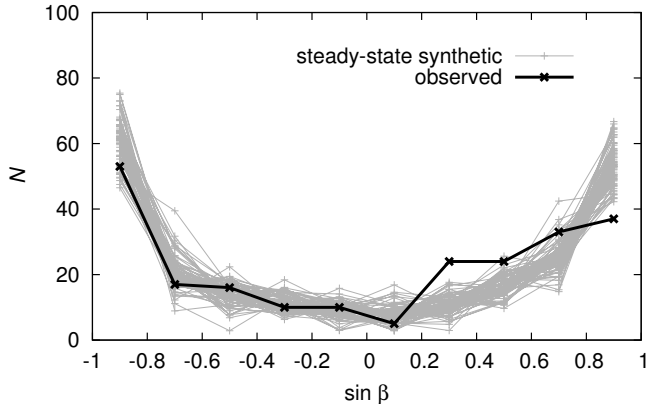


**Figure 12**: Pole latitude sin $\beta$ distribution of the observed main belt asteroids (black), as derived by the lightcurve inversion method (Hanuš et al. 2011), and 100 simulated distributions (gray), which differ only by the random seed. Initially, the distribution of sin $\beta$ was uniform. The dynamical evolution of pole latitudes $\beta$ and spin rates $\omega$ over 4 Gyr was driven by the YORP effect, non-catastrophic collisions, spin-orbital resonances and mass shedding. There is a mismatch for (large) prograde asteroids, which is likely primordial (Johansen and Lacerda 2010).

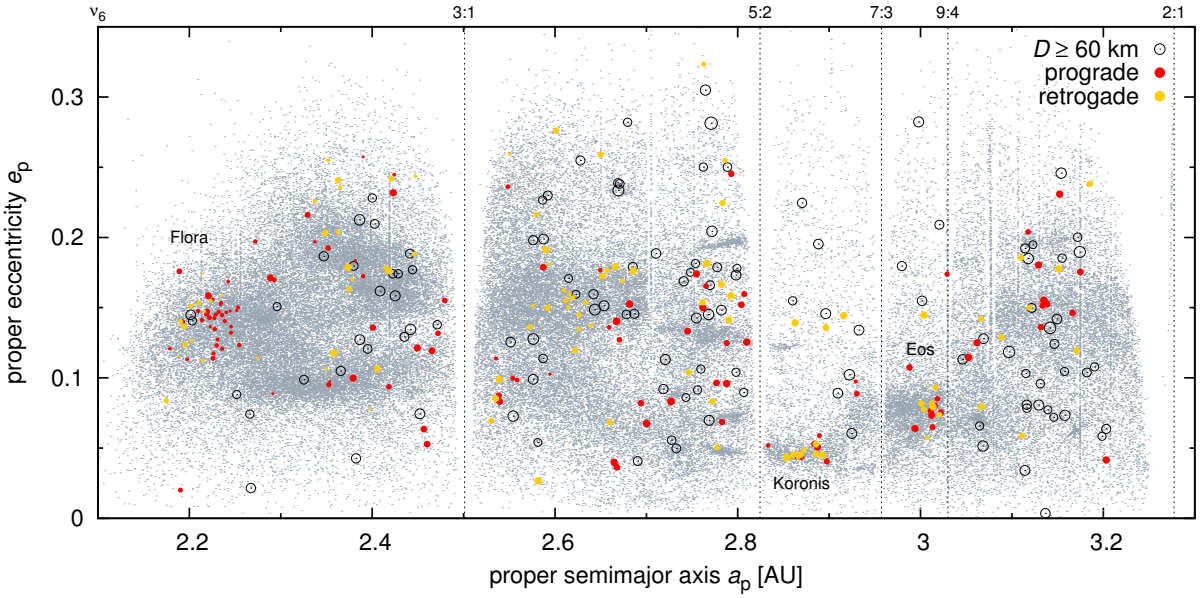


**Figure 13**: The positions of asteroids with convex-hull shape models within the main asteroid belt; the proper semimajor axis $a_{\rm p}$ vs the proper eccentricity $e_{\rm p}$. Large asteroids with diameters $D \leq 60$ km are denoted by open circles, smaller ones by red or yellow circles, depending on their prograde/retrograde sense of rotation. There are three asteroid families (Flora, Koronis, Eos) which seem to already have a significant number of members with derived shape and pole, so that a preference for retrograde asteroids ($\beta < 0°$) at smaller semimajor axes $a_{\rm p}$ (and vice versa) is clearly visible. Adapted from Hanuš et al. (2013) and updated according to the DAMIT database, version Dec 2$^{\rm nd}$ 2014.

be captured by global shape models, may contribute to the total YORP torque (Statler 2009, Golubov and Krugly 2012, Rozitis and Green 2012). Given the values of $c_{\mathrm{YORP}}$ above, the contribution seems to be significant. Another possibility is that there is some systematic difference between the shapes used for the computation of the YORP torques and our convex-hull shapes (and the real shapes, in order not to forget them).

## 2.9 An anisotropic distribution of spin vectors in asteroid families

The number of available shape models and poles will likely increase by an order of magnitude in a few years, because sparse photometric data from ongoing surveys will be processed and infrared photometry will be used to resolve ambiguities (Müller et al. 2011, Ďurech et al. 2012). Already the current situation (shown in Figure 13) is sufficient to preliminarily analyse the distribution of pole latitudes in several asteroid families, a topic of Hanuš, Brož, Ďurech et al. (2013).

We choose the Flora, Koronis, Eos, Eunomia, Phocaea, Themis, Maria, and Alauda families for a detailed inspection. A preliminary membership was taken from Nesvorný (2012), but we had to carefully check for possible or even likely interlopers, e.g. by inspecting reflectance spectra from the SMASS II database (Bus and Binzel 2002) or the distribution in the proper semimajor axis $a_{\mathrm{p}}$ vs the absolute magnitude $H$ diagrams.

All families exhibit a correlation (a positive one) between the proper semimajor axis $a_{\mathrm{p}}$ and the pole latitude $\beta$, although not all bodies strictly follow the rule. To fully understand the distribution including outliers we used by now standard model of Brož et al. (2011) to simulate the long-term evolution of synthetic Flora (Figure 22), Koronis and Eos families. The Flora is a profound example demonstrating the necessity of a *combined* model, accounting for the orbital, spin and collisional evolution: the Yarkovsky drift $\mathrm{d}a/\mathrm{d}t$ pushes the objects in $a_{\mathrm{p}}$, the YORP effect tilts obliquities $\gamma$ (and $\beta$), affecting $\mathrm{d}a/\mathrm{d}t(\gamma)$ too, the $\nu_6$ secular resonance removes objects at small $a_{\mathrm{p}}$, non-disruptive collisions randomly reorient $\beta$, mass shedding occasionally changes the YORP evolution to a random walk. Still, we are missing a detailed treatment of spin-orbital resonances in our model, but it does not seem to be a major flaw with respect to observations. The match is acceptable within uncertainties which are dominated by a limited number of observed family members.

Finally, let us address one of our assumptions. We usually imagine that a parent-body disruption produces an isotropic distribution of poles and a maxwellian distribution of spin rates (cf. experiments of Giblin et al. 1998). Well, everybody knows that this not a ground truth. We may definitely hope that future photometric observations will reach also small (sub-km) members of young families, or next-generation collisional models will be capable to handle shapes, rotation and tidal interaction of fragments. Regarding the models, we shall keep in mind a few 'small' problems: i) total damage of the parent body in the fragmentation phase (Michel et al. 2003), which may correspond to a production of dust particles and leading to interactions of dust clouds (Nesvorný, personal communication); ii) bouncing and friction in the reaccumulation phase (Richardson et al. 2009), with unknown coefficients of restitution, leading to different outcomes and extremely short time steps; iii) phase transitions are often modelled by an approximate equation of state (Tillotson 1962, Melosh 2000), but if chemical reactions in gaseous phase play a role then everything is complicated.

# 3 Physics of stars and interstellar medium

## 3.1 A unified solution for the orbit and light-time effect in the V505 Sgr system

V505 Sagittarii = HR 7571 = HD 187949 is a multiple star, *at least* a triple, with a very interesting data set we used in Brož et al. (2010). The stars denoted hereinafter 1 and 2 form a close eclipsing binary (Algol type, A2V and G5IV), while a star 3 is seen on a more distant orbit. There are speckle-interferometry measurements of the star 3 (namely, $N_{\rm sky} = 20$ of them), minima timings of the stars 1+2 ($N_{\rm lite} = 54$), and also radial velocities of the star 3 ($N_{\rm rv} = 39$). What is actually intriguing, two positional measurements are offset by 50 mas with respect to an elliptical orbit, while the precision of these measurements is 5 mas and we have an indirect evidence that the plate scale was not wrong — these measurements were taken by two different telescopes on two different nights (McAllister et al. 1987a, 1987b). Moreover, the $O-C$ diagram shows a clear light-time effect with a sudden change of the period at around 2000.0 epoch (see Figure 14).

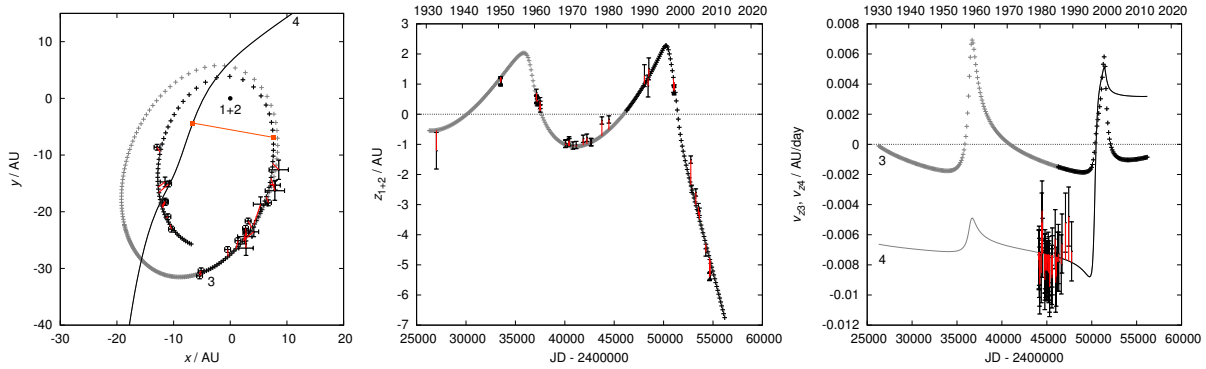


**Figure 14**: A model for the V505 Sagittarii multiple stellar system. The best-fit solution for the trajectory of the 4th body, which explains the observed trajectory of the 3rd body, light-time effect and radial velocities: $m_4 = 0.8\,M_\odot$, $x_{h4} = 45.0\,\mathrm{AU}$, $y_{h4} = 39.5\,\mathrm{AU}$, $z_{h4} = 28.0\,\mathrm{AU}$, $v_{xh4} = -0.0105\,\mathrm{AU/day}$, $v_{yh4} = -0.008\,\mathrm{AU/day}$, $v_{zh4} = -0.0075\,\mathrm{AU/day}$. The resulting $\chi^2 = 331$, with the total number of data points $N = 102$. The motion of the 4th body captured in the left panel spans from 1994 to 2003. The squares connected by a straight line indicate the closest encounter between the 3$^{\rm rd}$ and 4$^{\rm th}$ body.

In order to study this system, we used a general $N$-body integrator and the Bulirsch–Stöer method (Levison and Duncan 1994) which allowed us to simulate all types of orbits. We constructed a $\chi^2$ metric to compare our model with the observations in a usual way:

$$\chi^2 = \chi^2_{\rm sky} + \chi^2_{\rm lite} + \chi^2_{\rm rv}\,, \tag{23}$$

$$\chi^2_{\rm sky} = \sum_{i=1}^{N_{\rm sky}} \frac{(x'_{h3} - x_{h3}[i])^2 + (y'_{h3} - y_{h3}[i])^2}{\sigma^2_{\rm sky}[i]}\,, \tag{24}$$

$$\chi^2_{\rm lite} = \sum_{i=1}^{N_{\rm lite}} \frac{\left(z'_{b1+2} - z_{b1+2}[i]\right)^2}{\sigma^2_{\rm lite}[i]}\,, \tag{25}$$

$$\chi^2_{\rm rv} = \sum_{i=1}^{N_{\rm rv}} \frac{(v'_{zh3} - v_{zh3}[i])^2}{\sigma^2_{\rm rv}[i]}\,, \tag{26}$$

where $x_{h3}$, $y_{h3}$ are the observed sky-plane positions of the 3$^{\rm rd}$ body (with respect to $1+2$), $z_{b1+2}$ is the barycentric radial position of the eclipsing pair $1+2$, $v_{zh3}$ the radial velocity of the 3$^{\rm rd}$ body (again, with respect to $1+2$), $\sigma$'s always denote the corresponding uncertainties, dashed quantities are model values, always interpolated to the times $t[i]$ of observations. We then used a simplex algorithm (Press et al. 1997) to efficiently find local minima of $\chi^2$ and to map an extensive parameter space.

We were able to test the following seven hypotheses: 1. there are three bodies only in V505 Sgr; 2. the third body directly perturbs the central pair; 3. a steady mass transfer causes minima timing variations; 4. there is modulation of mass transfer by the third body; 5. a sudden mass transfer occurred around 2000; 6. Appelgate's (1992) mechanism is operating; 7. a fourth body is present (either on a bound or hyperbolic orbit). Out of these, only the last one may explain *all* the observational data at once (cf. Figure 14).

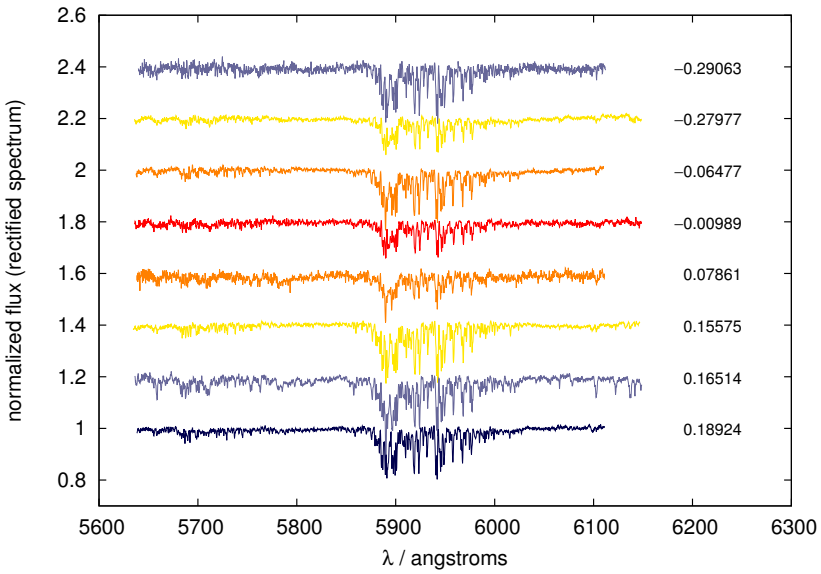


**Figure 15**: Spectra of V505 Sgr obtained from JD = 2454266.5221 to 2456924.3181 at the Ondřejov observatory, with the 2.0-m Perek reflector and the Coudé-focus spectrograph with the CCD camera SITe-005. Their resolution reaches $R = 12\,600$. They were rectified using the Spefo program (Horn et al. 1996, Škoda 1996). The spectra are sorted according to the orbital phase of the eclipsing pair (i.e. stars $1+2$). We are going to interpret these spectra in a subsequent study. We thank all the observers P. Zasche, M. Šlechta, M. Wolf and P. Chadima who acquired these spectra.

The 'only' remaining problem is that either a deep encounter with a passing star, a perturbation caused by a distant passing star, or an intrinsic late instability of the system all have too low probability, given the average number density of stars in the solar neighbourhood $n_\star = 0.073\,\mathrm{pc}^{-3}$ (Fernandéz 2005). On the other hand, there are strong indications that late instabilities are not uncommon among older stars and their exoplanetary systems, indicated for example by an excess IR emission, explained as dust production during collisions (Lisse et al. 2012), or a misalignment of the stellar spin axis and orbit(s) of giant planets, observed thanks to the Rossiter–McLaughlin effect (Rossiter 1924, McLaughlin 1924, Ohta et al. 2005).

Anyway, it seems worthwhile to continue studies of V505 Sgr along following directions: a detailed analysis of new spectra which may potentially confirm the fourth-body hypothesis by a change of the systemic velocity $v_{\mathrm{rad}1+2} = (1.9 \pm 1.4)\,\mathrm{km\,s}^{-1}$, measured previously by Tomkin (1992). Luckily, there are nine spectra from 2010 to 2014 in the archive of Ondřejov observatory (Figure 15). Another opportunity might be an observation by an instrument like the FEROS at the 2.2-m telescope at La Silla, which is capable to cover also the NUV region, with magnetically-sensitive lines CaII H and K, in order to study a correlation between the orbital evolution and magnetic field strength.

## 3.2 V2368 Ophiuchi: an eclipsing and double-lined spectroscopic binary used as a photometric comparison star for U Ophiuchi

V2368 Oph = HR 6412 = HD 156208, selected for our study Harmanec et al. (2011), is a star selected essentially by chance. In the course of the analyses of a really-well-studied eclipsing binary U Oph (cf. Pickering 1896), it turned out that one of the comparison stars is actually variable. While the physical parameters of U Oph are already established, with a clear signature of light-time effect and rapid apsidal motion (Vaz et al. 2007), for V2368 Oph we were able to derive only a preliminary model, using the Phoebe program (Prša and Zwitter 2006). Even though we acquired and collected quite extensive sets of photometric and spectroscopic observations, the $\chi^2$ of the best fit is not yet statistically significant and we were forced to use a more complicated approach: we computed stellar evolution models (Paxton et al. 2011) of both components to reject at least some of the statistically equivalent fits. For example, we can constrain the mass ratio $q \equiv M_1/M_2$ to be close to $1.00 \pm 0.01$, because the luminosities of both components would be otherwise too different. Of course, we have to warn that the parameters derived this way *cannot* be used as independent checks of the stellar evolution models in question.

While the multiplicity of A-type stars is not unusual as it reaches $(69 \pm 7)\,\%$ (De Rosa et al. 2014),

this particular binary is composed of two A stars which have both evolved away from the main sequence. It is also worth to mention that A stars might be sometimes either chemically peculiar (denoted Am; Michaud 1970), magnetic (Ap; Przybylski 1966, Borra and Landstreet 1980), or even rapidly oscillating (roAp; Kurtz 1982, Schöller et al. 2012). However, we were not able to recognise any of these features in the case of V2368 Oph.

### 3.3 Large distance of $\varepsilon$ Aurigae inferred from interstellar absorption and reddening

The eclipsing binary $\varepsilon$ Aurigae is probably the most famous one, known for its record-breaking orbital period of 27.1 years and an exceedingly long eclipse (2 yr) which has to be then caused by an opaque disk rather than by a normal star. This was indeed spectacularly confirmed by interferometric imaging during its last eclipse by Kloppenborg et al. (2010).

In spite of being studied for a *long* time (Vogel 1903), there is still an annoying uncertainty whether the F0Iab primary is a more distant supergiant star (i.e. a high-mass model) or a closer post-AGB star (a low-mass model). Unfortunately, the uncertainty of the parallax (van Leeuwen 2007) does not allow to distinguish between them, so we tried to use an indirect approach, as described in Guinan et al. (2012).

We first constructed a *local* distance calibration based on diffuse interstellar bands (DIBs) observed in spectra of several surrounding stars, located within 1° of $\varepsilon$ Aur, namely HD 31617, HD 31894, HD 32328, HD 277197, and BD+43°1168. Of course, we had to assume that the interstellar medium is smooth enough in the lateral direction and we verified this in COBE/DIRBE reddening maps (Schlegel et al. 1998). Using either parallaxes of nearby stars or spectroscopic distances, we were able to find a well-defined relation between the distance $d$ (in kpc) and the equivalent width $EW$ of the 6613 Å DIB:

$$d(EW) = (1.474 \pm 0.028) \times 10^4 EW\,. \tag{27}$$

The resulting distance of $\varepsilon$ Aur was $d = (1.5 \pm 0.5)$ kpc, strongly supporting the high-mass model, for which the evolution is shown in Figure 16. The uncertainty of $d$ is dominated by the scatter of $EW$ for $\varepsilon$ Aur. We are going to use a similar approach also for other distant supergiant stars which have a long observational record and, at the same time, they will *not* be observed by the GAIA spacecraft due to magnitude limitations (Liu et al. 2012). See an example of a reddening map for V1765 Cygni in Figure 17.

Our calibration is used and discussed in the work of Strassmeier et al. (2013). They were able to measure additional neighbouring star BD+43°1166C (only 28″ from $\varepsilon$ Aur) and claim it is a close (7 pc) white dwarf, since they were unable to find any similar spectrum in the ESO UVES database. Moreover, they can fit its spectrum by a synthetic white-dwarf spectrum. Finally, they speculate the observed DIB at 6613 Å is actually a result of a (hypothetical) debree disk.

However, we find these conclusions questionable. First, a comparison with an extensive database of synthetic spectra shows that it is equally possible to find a reasonable fit using an ordinary A star with a main-sequence $\log g \simeq 4.0$ (P. Harmanec, personal communication). Secondly, it is not likely that the debree disk (which is likely hotter, denser, differentially rotating, having non-zero radial velocity etc.) would cause a spectral line similar to that of *diffuse* interstellar medium.

Muthumariappan et al. (2014), on the other hand, favour a low-mass model. Their arguments are mostly based on observations EWs, RVs and a simplified geometrical model of the optically-thin disk which is eclipsing the F0Ia primary. Moreover, there is a slight overabundance of s-process elements (Y, Zr, Ba) in the photosphere of the F0Ia primary (Sadakane et al. 2010) which would indicate a 3$^{\rm rd}$ dredge-up and a highly evolved post-AGB star.

Again, there seem to be several points worth of a discussion. The authors do no perform any disentangling of (possibly-blended) spectral lines; they only use equivalent width (EW) and radial velocity (RV) measurements, no profile details. Secondly, their model EWs clearly do not agree with observations (cf. their Fig. 11; even though there are no uncertainties declared). We thus consider their argument based on the corresponding RVs to be weak. Third, the above-mentioned overabundances do not seem significant. Indeed, the main conclusion of Sadakane et al. (2010) is just the *opposite*, i.e. the photosperic abundances of $\varepsilon$ Aur are actually very similar to supergiants HD 81471 or $\alpha$ Car. Consequently, this favours (our preffered) high-mass model.

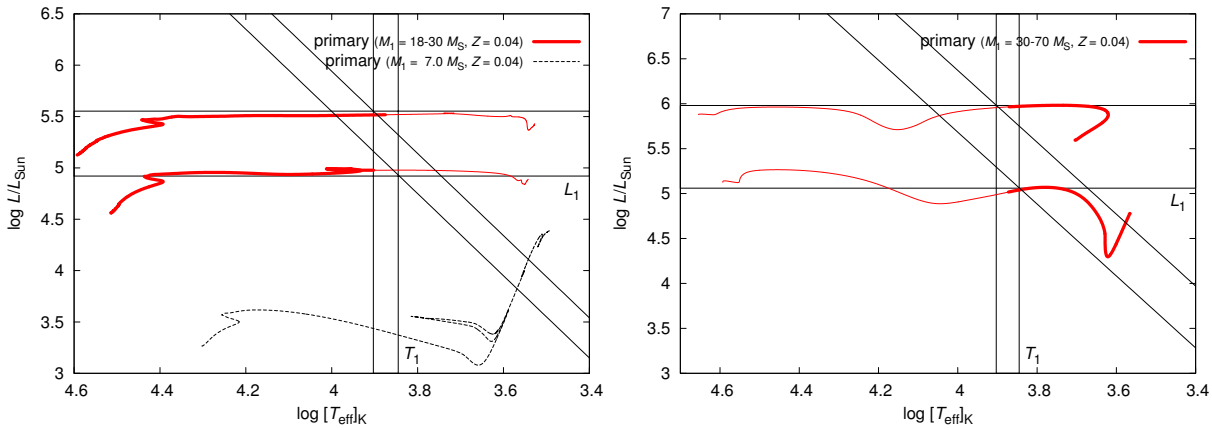


**Figure 16**: Evolutionary tracks computed for $\varepsilon$ Aur in the HR diagram, computed with the MesaStar module (Paxton et al. 2011). Left: the evolution from the zero-age main sequence. The thin black lines correspond to the observed effective temperatures, radii and luminosities of $\varepsilon$ Aur. The range of masses is 18 to 30 $M_\odot$, i.e. corresponding to a high-mass supergiant. We also plot the evolutionary track for a lower-mass star ($m_{\rm ini} = 7\,M_\odot$) for comparison as a dotted line. It never reaches the observed luminosity, even in the post-AGB phase. The post-AGB evolution track (not shown in the plot) is nearly horizontal (at nearly a constant $\log L/L_\odot \simeq 4.4$) as the star moves to the left in the diagram. Right: the pre-main-sequence evolution of $\varepsilon$ Aur. To match the observed luminosity and temperature, the mass would have to be in the range 30 to 70 $M_\odot$. Moreover, the evolution would be too fast in this particular case, which is not supported by observations.

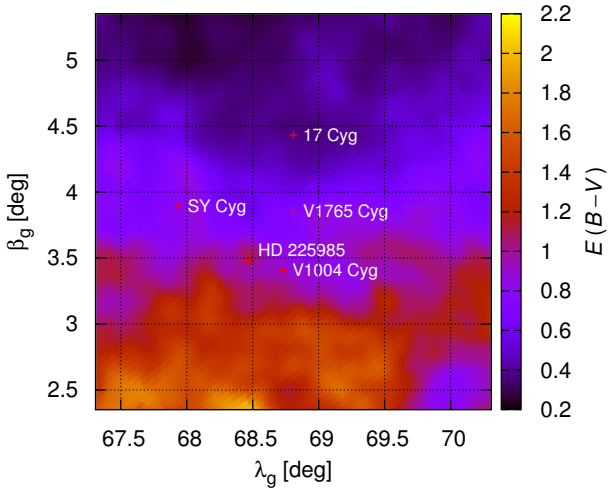


**Figure 17**: Reddening $E(B-V)$ as a function of galactic coordinates in the vicinity of V1765 Cygni, which is another suitable target for an indirect distance determination. The values were computed from IR emission measured by COBE/DIRBE for extragalactic sources (Schlegel et al. 1998). As calibration stars, one can choose for example 17 Cyg, SY Cyg, HD 225985, and V1004 Cyg. The values of $E(B-V)$ range from 0.37 to 1.06 for the positions of the calibration stars (note that these are not $E(B-V)$ for the stars themselves).

# 4 Textbooks

## 4.1 Physics of the Solar System

The book Brož & Šolc (2013) is our attempt to introduce the fundamentals of general astronomy (in Chapter 1), basic properties of the Sun and planets (Chapter 2), and then physics of small Solar System bodies (Chapter 3). While the first two parts are written more or less on a undergraduate level, the third one is a bit more elaborate as it is directly related to our 'beloved' research topics (cf. Sections 2.1 to 2.9). Given the fact that this is a living and active field of research, the relatively new and surprising results we present are not always well-known in a broader community.

Instead of further explaining the actual content, we beg to reprint a complete table of contents here (translated to English, as the textbook was written in Czech).


**Figure 18**: The cover page of the textbook 'Fyzika sluneční soustavy' (Physics of the Solar System).

1.2 Coordinate systems

1.2.1 Space coordinates
1.2.2 Representations of coordinates
1.2.3 Origins
1.2.4 Basic directions

1.3 Coordinate transformations

1.3.1 Transformations with spherical triangles
1.3.2 Transformations with rotation matrices

1.4 Equations of motion, numerical solution

1.4.1 Initial conditions
1.4.2 Euler method
1.4.3 Leap-frog method
1.4.4 Runge-Kutta method of the 4th order
1.4.5 Symplectic integrators
1.4.6 Precision versus accuracy
1.4.7 Propagation of uncertainties
1.4.8 Relativistic equation of motion

1.5 Two-body problem, analytical solution

1.5.1 Newton and Kepler laws
1.5.2 Equations of motion for two gravitating bodies
1.5.3 Motion of the centre of mass (first 6 integrals)
1.5.4 Equation of the relative motion (3 integrals of angular momentum)
1.5.5 Elimination of time and derivation of the trajectory shape
1.5.6 Solution - equation of conic section
1.5.7 Third Kepler law
1.5.8 Speed along the trajectory (1 integral of energy)
1.5.9 Kepler equation
1.5.10 Selected application of Kepler laws
1.5.11 Ephemeris computation for an asteroid

1.6 Three-body problem

1.6.1 Rotating frame. Coriolis and centrifugal acceleration
1.6.2 Jacobi integral
1.6.3 Lagrange libration points
1.6.4 Tisserand parameter
1.6.5 Jupiter-family comets

1.7 Gravitation and resonances

1.7.1 N-body problem and deterministic chaos
1.7.2 Stable and unstable configuration in a resonance
1.7.3 Lagrange equations
1.7.4 Perturbation function
1.7.5 Perturbation function for Sun-Jupiter-asteroid system
1.7.6 Sun-Jupiter-asteroid in a mean-motion resonance
1.7.7 Sun-Jupiter-Saturn
1.7.8 Sun-Jupiter-Saturn-asteroid and secular resonances
1.7.9 Gaps and borders in the main asteroid belt

1.8 Precession and nutation

1.8.1 Precession of a heavy gyroscope
1.8.2 Lunisolar precession of the Earth
1.8.3 Homogeneous ellipsoid
1.8.4 Nutation
1.8.5 Polar wobble

1.9 Theory of relativity

1.9.1 Galilei and Lorentz transformations
1.9.2 Time dilatation and Doppler effect
1.9.3 Length contraction and relativity of simultaneous events
1.9.4 Relativistic dynamics
1.9.5 Minkowski spacetime
1.9.6 Inertial and gravitational mass
1.9.7 Einstein field equations
1.9.8 Schwarzschild solution
1.9.9 World lines
1.9.10 Bending of light, precession of perihelion and redshift
1.9.11 Kerr solution and Lens-Thirring effect

1.10 Non-gravitational accelerations

1.10.1 Rocket effect on comets
1.10.2 Poynting-Robertson effect on dust particles
1.10.3 LAGEOS satellite

1.11 Yarkovsky/YORP effect

1.11.1 First estimate of temperature on the asteroid surface
1.11.2 1-dimensional linear theory of Yarkovsky/YORP effect
1.11.3 Yarkovsky effect on 3-dimensional objects
1.11.4 YORP effect on objects with irregular shape

1.12 Photometry, signal and noise

1.12.1 Photoelectric effect and CCD technology
1.12.2 Offset, dark and flat
1.12.3 Signal and noise
1.12.4 Photometry or "from star to ADU"
1.12.5 Field of view and size of pixels
1.12.6 Apparent and absolute magnitude
1.12.7 Standard photometric system

1.13 Scattering of radiation

1.13.1 Definitions of radiometric quantities
1.13.2 Two-directional distribution function of reflection
1.13.3 Radiant intensity of a sphere
1.13.4 Albedo
1.13.5 Phase function, integrals and albedos for different reflection functions
1.13.6 Apparent and absolute magnitude of an asteroid
1.13.7 HG system
1.13.8 Polarimetry

2 The Sun and planets

2.1 Standard solar model

2.1.1 Atmosphere
2.1.2 Helioseismology and differential rotation
2.1.3 Magnetic activity and solar dynamo
2.1.4 Internal structure
2.1.5 Stellar evolution
2.1.6 Solar analogs

2.2 Basic phenomena on planets

2.2.1 Atmospheres
2.2.2 Magnetospheres

2.2.3 Internal structure

2.3 Extrasolar planets

2.3.1 Basic characteristics
2.3.2 New types of planets
2.3.3 Multiple systems

3 Small bodies in the Solar System

3.1 Protoplanetary disk

3.1.1 Observations of Giant Molecular Clouds and proplyds
3.1.2 Gravitational collapse and Jeans criterion
3.1.3 Isotopic composition and radiometric age of the disk
3.1.4 Structure of the protoplanetary disk

3.2 Dust accretion

3.2.1 Condensation of gas
3.2.2 Collisional growth of particles
3.2.3 Settlement towards the mid-plane of the disk
3.2.4 Spiralling due to gas drag
3.2.5 Turbulence

3.3 Planetesimals and embryos

3.3.1 Collisional growth of planetesimals up to planetary embryos
3.3.2 Gaseous and ice giant - gravitational collapse
3.3.3 Disappearance of the gas
3.3.4 Terrestrial planets - collisions of embryos
3.3.5 Differentiation

3.4 Migration of planets

3.4.1 Types of migration
3.4.2 Migration in the gas disk
3.4.3 Migration in the planetesimal disk and close encounters
3.4.4 Effects on primordial populations of small bodies

3.5 Moons and tides

3.5.1 Gravitational tidal force
3.5.2 Earth-Moon
3.5.3 Moon-Earth
3.5.4 Earth-Sun
3.5.5 Neptune-Triton
3.5.6 Mars-Phobos
3.5.7 Pluto-Charon, binary asteroids
3.5.8 Mercury-Sun, Venus-Sun
3.5.9 Jupiter, Io and Europa

3.6 Rings

3.6.1 Roche limit
3.6.2 Collisions in the ring
3.6.3 Gossamer rings of Jupiter
3.6.4 Main rings of Saturn
3.6.5 Uranus and Neptune rings

3.7 Asteroids

3.7.1 Nomenclature
3.7.2 Orbits

3.7.3 Light curves
3.7.4 Spectra and colours
3.7.5 Internal structure
3.7.6 Near-Earth objects
3.7.7 Binary asteroids

3.8 Asteroid families

3.8.1 Collision probability
3.8.2 Hierarchical clustering method
3.8.3 Size-frequency distribution
3.8.4 Velocity field after disruption
3.8.5 Gauss equations and changes of elements
3.8.6 Kepler differential rotation
3.8.7 Differential precession of nodes and pericentres
3.8.8 Yarkovsky effect and chaotic diffusion
3.8.9 The role of the YORP effect
3.8.10 Families in resonances

3.9 Trans-Neptunian bodies

3.9.1 Orbital structures
3.9.2 Physical characteristics

3.10 Comets

3.10.1 Nomenclature
3.10.2 Activity
3.10.3 Gas
3.10.4 Dust
3.10.5 Nucleus
3.10.6 Physical evolution of comets
3.10.7 Magnetosphere
3.10.8 Orbital classification of comets
3.10.9 Oort cloud and long-period comets

3.11 Dust

3.11.1 Zodiacal light and other observations of the dust
3.11.2 Asteroidal dust bands
3.11.3 Cometary dust trails

3.12 Fireballs and meteors

3.12.1 Atmospheric trajectory of the fireball
3.12.2 Deceleration and ablation
3.12.3 Meteor showers
3.12.4 Radar observations
3.12.5 Meteor spectra

3.13 Meteorites

3.13.1 Known falls and fields
3.13.2 Classification of meteorites
3.13.3 Isotopic ratios
3.13.4 Radiometric methods
3.13.5 Meteorites-asteroids associations
3.13.6 Transport of meteorites to the Earth

3.14 Impacts and craters

3.14.1 Morphology of Ries and Steinheim craters
3.14.2 Processes during an impact
3.14.3 Moldavites and other tectites

3.14.4 Rankine-Hugoniot equations
3.14.5 Age determination of surfaces using cratering
3.14.6 A relation to mass extinctions

3.15 Volcanism

3.15.1 Io
3.15.2 Triton
3.15.3 Europa
3.15.4 Enceladus
3.15.5 Differentiated asteroids
3.15.6 A comparison to planets
3.15.7 Classifications of eruptions

## 4.2 Structure and evolution of stars

In the earlier textbook Harmanec & Brož (2011), we focus on stellar interiors, i.e. the most important part of astrophysics, probably. Ideally, students shall first clearly understand equations of stellar structure and their direct implications (in Chapters 3 to 10), and finally realize the limits and go beyond them (in Chapters 11 to 16). We hope that every reader can appreciate astrophysics as a science in which theory tries to be 'on par' with current observations, acquired by wonderful instruments, by the way.

Similarly as above, we reprint its contents translated to English.

1 Introduction

1.1 Energetic estimates
1.1 Simplifications used for the construction of spherical models
1.2 Model of our Sun

2 Radiation and spectrum

2.1 Electromagnetic radiation

2.1.1 Intensity
2.1.2 Flux
2.1.3 Density of radiation energy
2.1.4 Radiation pressure
2.1.5 Opacity coefficient and optical depth
2.1.6 Mechanical force on a gas layer
2.1.7 Emission coefficient
2.1.8 Radiation transfer equation
2.1.9 Thermodynamic equilibrium
2.1.10 Continuous radiation of a black body
2.1.11 Saha ionisation equation

2.2 Spectra of stars

2.2.1 Transitions in atoms, continuous and discrete spectra
2.2.2 Broadening of spectral lines
2.2.3 Spectral classification

3 State equation

3.1 Mean molecular weight
3.2 Ideal gas
3.3 Radiation pressure
3.4 Electron degeneracy
3.5 Partial ionisation in subsurface layers

4 Basic equations of stellar structure


**Figure 19**: The cover page of the textbook 'Stavba a vývoj hvězd' (Structure and evolution of stars).

4.1 Equation of mass conservation
4.2 Equation of motion and equation of hydrostatic equilibrium
4.3 Equation of thermal equilibrium

4.3.1 Proton-proton chain
4.3.2 CNO cycle
4.3.3 Transformation of helium to carbon and other reactions
4.3.4 Thermal equilibrium and changes of entropy

4.4 Equation of energy transfer

4.4.1 Equation for radiation energy transfer
4.4.2 Equation for convective energy transfer

5 Mathematic structure of equation of stellar interior

5.1 Stationary models
5.2 Evolutionary model
5.3 Dynamic model

6 Initial and boundary conditions

# 5 Conclusions and future work

**Conclusions.** Everybody knows the cliché: the more we know, the more questions we have. It is absolutely true. Usually, a research results in an uncomfortable feeling that we actually know *less* than before, regardless of ever-growing complexity of our models. Indeed, we went from purely gravitational interactions → an addition of non-gravitational forces → non-gravitational torques → analytical planetary migration → $N$-body interactions with planetesimals → Monte-Carlo collisional models → a distinction of monolith and rubble-pile structure → bombardment during ongoing migration, etc. Of course, this means additional initial conditions, additional boundary conditions, more observational data to fit, more uncertainties to account for; and one may only 'pray' for their normal distribution which is often not the case (cf. Figure 20).

Nevertheless, let us conclude that we were able to address (and answer) the following general questions in the framework if this thesis:

- Is the Yarkovsky effect important in first-order resonances? (Yes)
- Can we explain the observed structure of the Hilda family? (Yes)
- Are there many families in the Trojan region? (No)
- Do family halos originate from the planetary migration? (No)
- Was the main asteroid belt affected by the late heavy bombardment? (Yes)
- Have the majority of asteroids a structure of a rubble-pile with macroporosity? (No)
- Is the overall distribution of polar latitudes caused by the YORP effect? (Yes)
- Do asteroid families exhibit the same distribution? (Yes)
- Is it possible to explain all observational data for V505 Sagittarii? (Yes)
- Can we constrain the masses of V2368 Ophiuchi using stellar evolution models? (Yes)
- Is $\varepsilon$ Aurigae a post-asymptotic-giant-branch star? (No)

The list of unanswered questions is *not* appended here, as it would surely be exceedingly long...

**Future work.** Anyway, we shall stop speaking about our old work and focus on the current research. Together with my students, we are about to finish three papers on the following 'hot' topics: (i) a solution of the 3-dimensional heat diffusion equation using a finite element method, with an application to boulders on (25143) Itokawa (Ševeček et al., submitted); (ii) the origin of the stable population in the 2:1 resonance with Jupiter, which may be captured during planetary migration or even be primordial (with Ondřej Chrenko); and (iii) smooth-particle hydrodynamic models of particular asteroidal collisions and gravitational reaccumulation (with Jakub Rozehnal; Figure 21).

There are actually two more papers, as I am a co-author of chapters in the *Asteroids IV* monograph, namely on asteroid families (Nesvorný et al., submitted) and collisional models (Bottke et al., submitted).

From 2013 till 2014, we also cooperate with the ProjectSoft company on a development of a robotic observatory (i.e. a project supported by the Technology Agency of the Czech Republic, grant no. TA 03011171). We were mostly responsible for a high-level control software, called Aitel (Astronomical Institute TELescope control program), Aiview and Aiplan to facilitate fully-autonomous operations. The observatory is ready for testing (see Figure 22) and as a test application, we will perform photometric observations of asteroids suitable for lightcurve inversion and determination of their poles and shapes.

By the way, given the high angular speed and acceleration, which the hardware is capable of, this telescope may be used to observe even fireballs during their flight through the Earth atmosphere! This is one of promising future applications we think about.

Finally, given the vast unexplored areas of knowledge, we plan to prepare a $2^{\text{nd}}$ part of the Physics of the Solar System on advanced modelling which would include e.g.: general hydrodynamics of protoplanetary disks, 3-dimensional heat diffusion using FDM, FEM or FVM methods, Monte-Carlo models of collisional evolution, smooth-particle hydrodynamic models of asteroid breakups, and as an add-on even more 'industrial' applications like a computation of a flexure of a telescope mount, or fully asynchronous object-oriented programming in Python to control (real) hardware.

A definitive conclusion? Life's is too short...

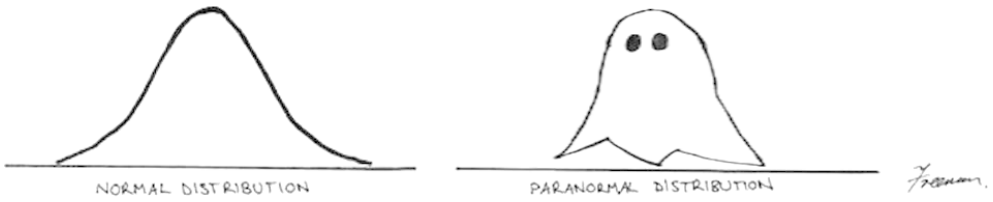


**Figure 20**: A normal distribution compared to a 'paranormal' one. A sketch we sometimes use to demonstrate the importance of thinking about uncertainties of the observational data.

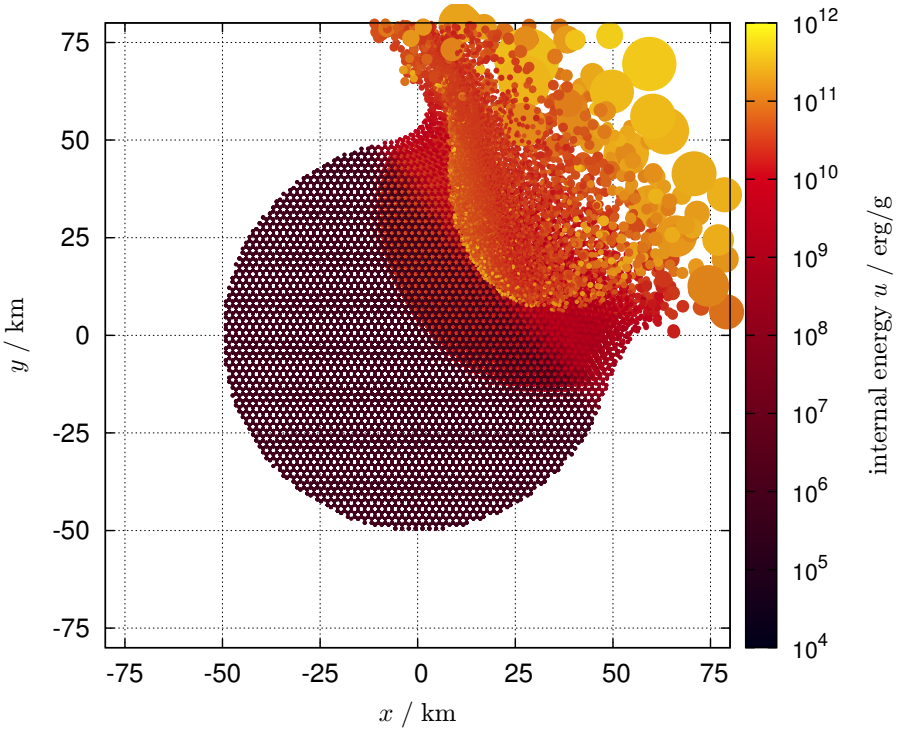


**Figure 21**: A smooth-particle hydrodynamic simulation of a collision between a $D = 100\,\mathrm{km}$ target and a $D = 30\,\mathrm{km}$ projectile, with the impact velocity $v_{\mathrm{imp}} = 15\,\mathrm{km/s}$ and the angle $\varphi_{\mathrm{imp}} = 30°$. The plot shows $(x, y)$ positions of about $1.56 \cdot 10^5$ SPH particles; the colour corresponds to a logarithm of the specific internal energy $u$ (in $\mathrm{erg\,g^{-1}}$ units). The integration was controlled by the Courant number $C = 1.0$, the typical time step thus was $\Delta t \simeq 10^{-5}\,\mathrm{s}$ and time span $t_{\mathrm{stop}} = 2.05\,\mathrm{s}$. We assumed Tillotson equation of state (Tillotson 1962) and basalt material properties (Benz and Asphaug 1999): zero-pressure density $\rho_0 = 2.7\,\mathrm{g\,cm^{-3}}$, bulk modulus $A = 2.67 \cdot 10^{11}\,\mathrm{erg\,cm^{-3}}$, non-linear compressive term $B = 2.67 \cdot 10^{11}\,\mathrm{erg\,cm^{-3}}$, Tillotson parameters $E_0 = 4.87 \cdot 10^{12}\,\mathrm{erg\,g^{-1}}$, $a = 0.5$, $b = 1.5$, $\alpha = 5.0$, and $\beta = 5.0$, incipient vaporization $E_{\mathrm{iv}} = 4.72 \cdot 10^{10}\,\mathrm{erg\,g^{-1}}$, complete vaporization $E_{\mathrm{cv}} = 1.82 \cdot 10^{11}\,\mathrm{erg\,g^{-1}}$, shear modulus $\mu = 2.27 \cdot 10^{11}\,\mathrm{erg\,cm^{-3}}$, yielding $Y = 3.5 \cdot 10^{10}\,\mathrm{erg\,g^{-1}}$, melt energy $E_{\mathrm{melt}} = 3.4 \cdot 10^{10}\,\mathrm{erg\,g^{-1}}$, tensile failure using Weibull flaws, with fracture parameters $k = 4.0 \cdot 10^{29}\,\mathrm{cm^{-3}}$, and $m = 9.0$. Computed with the SPH5 code (Benz and Asphaug 1994).

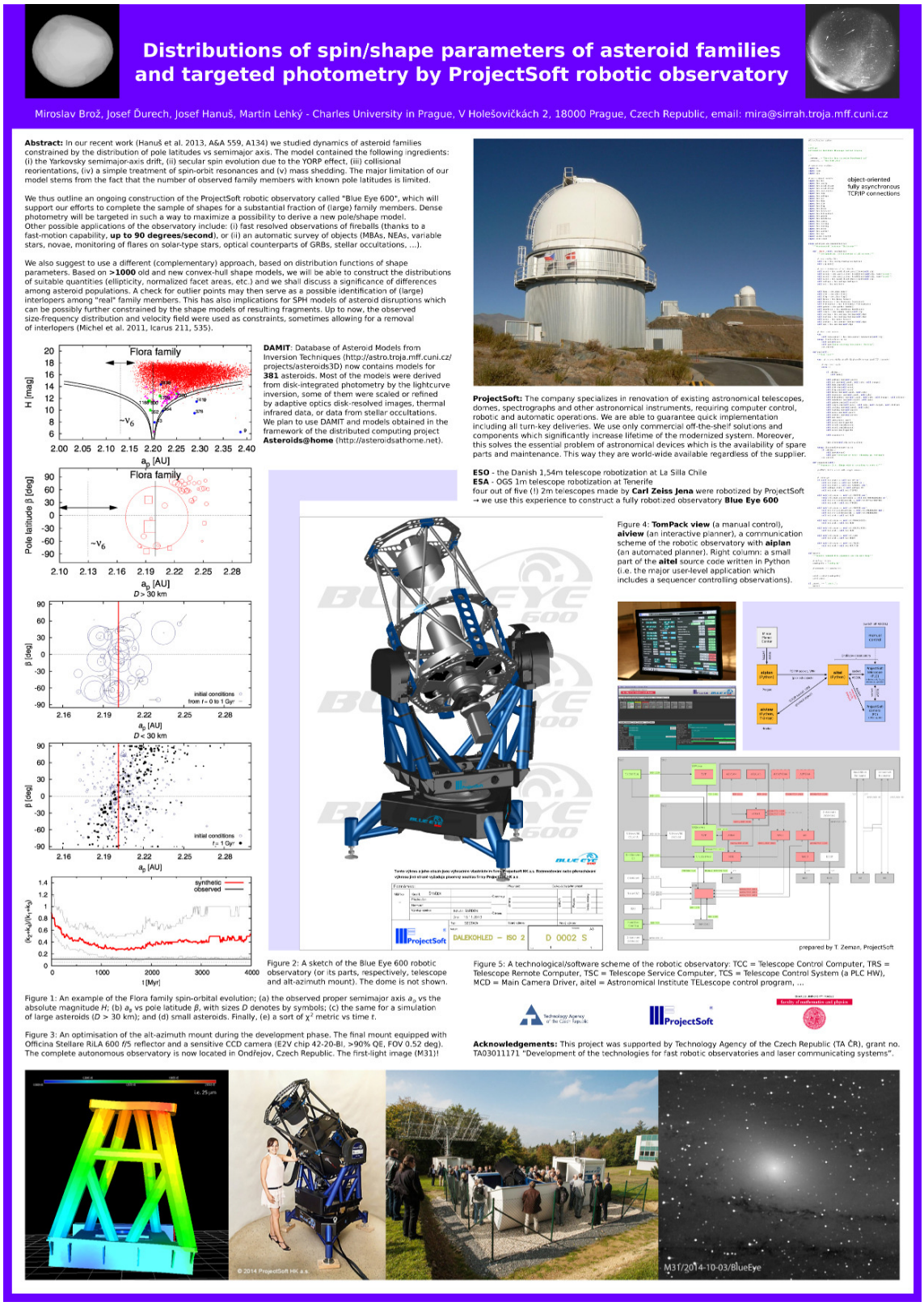


**Figure 22**: A poster about the ProjectSoft robotic observatory, presented at the AAS DPS 2014 conference.

# References


Bottke W.F., D. Vokrouhlický, D.P. Rubincam and M. Brož, Dynamical evolution of asteroids and meteoroids using the Yarkovsky effect, in: *Asteroids III*, Eds. W.F. Bottke, A. Cellino. P. Paolicchi and R. Binzel, (Arizona Univ. Press, Tucson 2003), p. 395.

Nesvorný D., M. Brož and V. Carruba, submitted, Identification and dynamical properties of asteroid families, in: *Asteroids IV*, Eds. P. Michel, F.E. DeMeo and W.F. Bottke, (Arizona Univ. Press, Tucson).

Bottke W.F., M. Brož, D. O'Brien, A.C. Bagatin, A. Morbidelli and S. Marchi, submitted, Collisional evolution of the main asteroid belt, in: *Asteroids IV*, Eds. P. Michel, F.E. DeMeo and W.F. Bottke, (Arizona Univ. Press, Tucson).

Vokrouhlický D. and M. Brož, 1999, An improved model of the seasonal Yarkovsky force for the regolith–covered asteroid fragments, *Astron. Astrophys.* **350**, 1079.

Vokrouhlický D., M. Brož, P. Farinella and Z. Knežević, 2001, Yarkovsky–driven leakage of Koronis family members: I. The case of 2953 Vysheslavia, *Icarus* **150**, 78.

Bottke W.F., D. Vokrouhlický, M. Brož, D. Nesvorný and A. Morbidelli, 2001, Dynamical spreading of asteroid families by the Yarkovsky effect, *Science* **294**, 1693.

Nesvorný D., A. Morbidelli, D. Vokrouhlický, W.F. Bottke and M. Brož, 2002, The Flora family: a case of the dynamically dispersed collisional swarm?, *Icarus* **157**, 155.

Brož M., D. Vokrouhlický, F. Roig, D. Nesvorný, W.F. Bottke and A. Morbidelli, 2005, Yarkovsky origin of the unstable asteroids in the 2/1 mean motion resonance with Jupiter, *Mon. Not. R. Astr. Soc.* **359**, 1437.

Vokrouhlický D., M. Brož, T. Michałowski, S.M. Slivan, F. Colas, L. Šarounová and F.P. Velichko, 2006, Spin axis of (2953) Vysheslavia and its implications, *Icarus* **180**, 217.

Vokrouhlický D., M. Brož, A. Morbidelli, W.F. Bottke, D. Nesvorný, D. Lazzaro and A.S. Rivkin, 2006, Yarkovsky footprints in the Eos family, *Icarus* **182**, 92.

Vokrouhlický D., M. Brož, W.F. Bottke, D. Nesvorný and A. Morbidelli, 2006, The peculiar case of the Agnia asteroid family, *Icarus* **183**, 349.

Vokrouhlický D., M. Brož, W.F. Bottke, D. Nesvorný and A. Morbidelli, 2006, Yarkovsky/YORP chronology of asteroid families, *Icarus* **182**, 118.

Brož M. and D. Vokrouhlický, 2008, Asteroid families in the first-order resonances with Jupiter, *Mon. Not. R. Astr. Soc.* **390**, 715.

Brož M., P. Mayer, T. Pribulla, P. Zasche, D. Vokrouhlický and R. Uhlář, 2010, A unified solution for the orbit and light-time effect in the V505 Sgr system, *Astron. J.* **139**, 6, 2258.

Brož M. and J. Rozehnal, 2011, Eurybates — the only asteroid family among Trojans? *Mon. Not. R. Astr. Soc.* **414**, 565.

Brož M., D. Vokrouhlický, A. Morbidelli, D. Nesvorný and W.F. Bottke, 2011, Hilda collisional family formed during the LHB? *Mon. Not. R. Astr. Soc.* **414**, 2716.

Hanuš J., J. Ďurech, M. Brož *et al.*, 2011, A study of asteroid pole-latitude distribution based on an extended set of shape models derived by the lightcurve inversion method, *Astron. Astrophys.* **530**, 134.

Harmanec P., H. Božić, P. Mayer, P. Eenens, M. Brož, M. Wolf, S. Yang, M. Šlechta, D. Ruždjak, D. Sudar and H. Ak, 2011, V2368 Ophiuchi: an eclipsing and double-lined spectroscopic binary used as a photometric comparison star for U Ophiuchi, *Astron. Astrophys.* **531**, 49.

Guinan E.F., P. Mayer, P. Harmanec, H. Božić, M. Brož, J. Nemravová, S. Engle, M. Šlechta, P. Zasche, M. Wolf, D. Korčaková and C. Johnston, 2012, Large distance of $\epsilon$ Aurigae from interstellar absorption and reddening, *Astron. Astrophys.* **546**, A123.

Hanuš J., J. Ďurech, M. Brož *et al.*, 2013, Asteroids' physical models from combined dense and sparse photometry and scaling of the YORP effect by the observed obliquity distribution, *Astron. Astrophys.* **551**, A67.

Brož M., A. Morbidelli, W.F. Bottke, J. Rozehnal, D. Vokrouhlický and D. Nesvorný, 2013, Constraining the cometary flux through the asteroid belt during the late heavy bombardment, *Astron. Astrophys.* **551**, A117.

Brož M. and A. Morbidelli, 2013, The Eos family halo, *Icarus* **223**, 844.

Hanuš J., M. Brož, J. Ďurech *et al.*, 2013, A spin vector distribution in asteroid families, *Astron. Astrophys.* **559**, A134.

Cibulková H., M. Brož and P. Benavidez, 2014, A six-part collisional model of the main asteroid belt. *Icarus* **241**, 358.

Ševeček P., M. Brož, J. Ďurech, D. Čapek, submitted, The thermal emission from boulders on (25143) Itokawa and general implications for the YORP effect. *Mon. Not. R. Astron. Soc.*.

Harmanec P. and M. Brož, 2011, Stavba a vývoj hvězd, Matfyzpress, Praha (312pp), ISBN 9788073781651.

Brož M. and M. Šolc, 2013, Fyzika sluneční soustavy, Matfyzpress, Praha (422pp), ISBN 9788073782368.


??? finish and sort the list

# Index

# A Reprints of papers

We selected the following papers for this habilitation thesis:

1. Brož et al. (2013) on the late heavy bombardment and the Nice model;
2. Brož and Morbidelli (2013) on the dynamics of the Eos family halo;
3. Brož et al. (2011) on the Hilda family and planetary migration;
4. Brož and Rozehnal (2011) on non-existence of Trojan families;
5. Brož and Vokrouhlický (2008) on the Yarkovsky drift in eccentricity in 1st-order resonances;
6. Cibulková, Brož and Benavidez (2014) on the collisional model of the main asteroid belt;
7. Hanuš et al. (2013) on the pole-latitude distribution in asteroid families;
8. Hanuš et al. (2011) and
9. Hanuš et al. (2013) on the pole-latitude distribution of main-belt asteroids, namely the part on the YORP effect model;
10. Brož et al. (2010) on the V505 Sgr multiple stellar system;
11. Harmanec et al. (2011) on V2368 Oph spectroscopic binary;
12. Guinan et al. (2012) on the distance determination to $\epsilon$ Aur.

We do *not* reprint older papers which were already included in the Ph. D. thesis (Brož et al. 2006):

13. Brož et al. (2005) on the unstable population in the 2:1 resonance with Jupiter,
14. Vokrouhlický et al. (2006) on the Eos family,
15. Vokrouhlický et al. (2006) on the Agnia family,
16. Vokrouhlický et al. (2006) on peculiar orbit and spin axis of (2953) Vysheslavia.

We have to also mention co-authored papers with a relatively minor contribution (less than or equal to 25 %). Again, we do not reprint them here:

17. Vokrouhlický and Brož (1999) on the two-layer model of the seasonal Yarkovsky effect;
18. Bottke et al. (2001) on asteroid families affected by the Yarkovsky effect;
19. Vokrouhlický et al. (2001) on the Yarkovsky drift of (2953) Vysheslavia;
20. Nesvorný et al. (2002) on the dynamical evolution of the Flora family;
21. Bottke et al. (2003), a review of the Yarkovsky effect and the dynamics of meteoroids and asteroids;
22. Vokrouhlický et al. (2006) on the YORP effect and chronology of asteroid families.

Finally, there are three more papers, which are under review at this time:

23. Ševeček et al. (submitted) on a solution of the 3-dimensional heat diffusion equation using the finite elements method;
24. Nesvorný et al. (submitted), a review on asteroid families for the *Asteroids IV* monography;
25. Bottke et al. (submitted), a similar review on collisional models.

A&A 551, A117 (2013)
DOI: 10.1051/0004-6361/201219296


Astronomy & Astrophysics

# Constraining the cometary flux through the asteroid belt during the late heavy bombardment⋆

M. Brož[1], A. Morbidelli[2], W. F. Bottke[3], J. Rozehnal[1], D. Vokrouhlický[1], and D. Nesvorný[3]

[1] Institute of Astronomy, Charles University, Prague, V Holešovičkách 2, 18000 Prague 8, Czech Republic
e-mail: mira@sirrah.troja.mff.cuni.cz, rozehnal@observatory.cz, davok@cesnet.cz
[2] Observatoire de la Côte d'Azur, BP 4229, 06304 Nice Cedex 4, France
e-mail: morby@oca.eu
[3] Department of Space Studies, Southwest Research Institute, 1050 Walnut St., Suite 300, Boulder, CO 80302, USA
e-mail: [bottke;davidn]@boulder.swri.edu

Received 28 March 2012 / Accepted 28 November 2012

**ABSTRACT**

In the Nice model, the late heavy bombardment (LHB) is related to an orbital instability of giant planets which causes a fast dynamical dispersion of a trans-Neptunian cometary disk. We study effects produced by these hypothetical cometary projectiles on main belt asteroids. In particular, we want to check whether the observed collisional families provide a lower or an upper limit for the cometary flux during the LHB. We present an updated list of observed asteroid families as identified in the space of synthetic proper elements by the hierarchical clustering method, colour data, albedo data and dynamical considerations and we estimate their physical parameters. We selected 12 families which may be related to the LHB according to their dynamical ages. We then used collisional models and $N$-body orbital simulations to gain insight into the long-term dynamical evolution of synthetic LHB families over 4 Gyr. We account for the mutual collisions between comets, main belt asteroids, and family members, the physical disruptions of comets, the Yarkovsky/YORP drift in semimajor axis, chaotic diffusion in eccentricity/inclination, or possible perturbations by the giant-planet migration. Assuming a "standard" size-frequency distribution of primordial comets, we predict the number of families with parent-body sizes $D_{\rm PB} \geq 200$ km – created during the LHB and subsequent $\simeq$4 Gyr of collisional evolution – which seems consistent with observations. However, more than 100 asteroid families with $D_{\rm PB} \geq 100$ km should be created at the same time which are not observed. This discrepancy can be nevertheless explained by the following processes: i) asteroid families are efficiently destroyed by comminution (via collisional cascade), ii) disruptions of comets below some critical perihelion distance ($q \lesssim 1.5$ AU) are common. Given the freedom in the cometary-disruption law, we cannot provide stringent limits on the cometary flux, but we can conclude that the observed distribution of asteroid families does not contradict with a cometary LHB.

**Key words.** celestial mechanics – minor planets, asteroids: general – comets: general – methods: numerical

## 1. Introduction

The late heavy bombardment (LHB) is an important period in the history of the solar system. It is often defined as the process that made the huge but relatively young impact basins (a 300 km or larger diameter crater) on the Moon like Imbrium and Orientale. The sources and extent of the LHB, however, has been undergoing recent revisions. In the past, there were two end-member schools of thought describing the LHB. The first school argued that nearly all lunar basins, including the young ones, were made by impacting planetesimals left over from terrestrial planet formation (Neukum et al. 2001; Hartmann et al. 2000, 2007; see Chapman et al. 2007, for a review). The second school argued that most lunar basins were made during a spike of impacts that took place near 3.9 Ga (e.g., Tera et al. 1974; Ryder et al. 2000).

Recent studies, however, suggest that a compromise scenario may be the best solution: the oldest basins were mainly made by leftover planetesimals, while the last 12–15 or so lunar basins were created by asteroids driven out of the primordial main belt by the effects of late giant-planet migration (Tsiganis et al. 2005; Gomes et al. 2005; Minton & Malhotra 2009; Morbidelli et al. 2010; Marchi et al. 2012; Bottke et al. 2012). This would mean the LHB is limited in extent and does not encompass all lunar basins. If this view is correct, we can use studies of lunar and asteroid samples heated by impact events, together with dynamical modelling work, to suggest that the basin-forming portion of the LHB lasted from approximately 4.1–4.2 to 3.7–3.8 billion years ago on the Moon (Bogard 1995, 2011; Swindle et al. 2009; Bottke et al. 2012; Norman & Nemchin 2012).

The so-called "Nice model" provides a coherent explanation of the origin of the LHB as an impact spike or rather a "saw-tooth" (Morbidelli et al. 2012). According to this model, the bombardment was triggered by a late dynamical orbital instability of the giant planets, in turn driven by the gravitational interactions between said planets and a massive trans-Neptunian disk of planetesimals (see Morbidelli 2010, for a review). In this scenario, three projectile populations contributed to the LHB: the comets from the original trans-Neptunian disk (Gomes et al. 2005), the asteroids from the main belt (Morbidelli et al. 2010) and those from a putative extension of the main belt towards Mars, inwards of its current inner edge (Bottke et al. 2012). The last could have been enough of a source for the LHB, as recorded in the lunar crater record (Bottke et al. 2012), while the asteroids from the current main belt boundaries would have only been a minor contributor (Morbidelli et al. 2010).

The Nice model, however, predicts a very intense cometary bombardment of which there seems to be no obvious traces on

⋆ Table 1 is available in electronic form at http://www.aanda.org

the Moon. In fact, given the expected total mass in the original trans-Neptunian disk (Gomes et al. 2005) and the size distribution of objects in this disk (Morbidelli et al. 2009), the Nice model predicts that about $5 \times 10^4$ km-size comets should have hit the Moon during the LHB. This would have formed 20 km craters with a surface density of $1.7 \times 10^{-3}$ craters per km$^2$. But the highest crater densities of 20 km craters on the lunar highlands is less than $2 \times 10^{-4}$ (Strom et al. 2005). This discrepancy might be explained by a gross overestimate of the number of small bodies in the original trans-Neptunian disk in Morbidelli et al. (2009). However, all impact clast analyses of samples associated to major LHB basins (Kring & Cohen 2002; Tagle 2005) show that also the major projectiles were not carbonaceous chondrites or similar primitive, comet-like objects.

The lack of evidence of a cometary bombardment of the Moon can be considered as a fatal flaw in the Nice model. Curiously, however, in the outer solar system we see evidence of the cometary flux predicted by the Nice model. Such a flux is consistent with the number of impact basins on Iapetus (Charnoz et al. 2009), with the number and the size distribution of the irregular satellites of the giant planets (Nesvorný et al. 2007; Bottke et al. 2010) and of the Trojans of Jupiter (Morbidelli et al. 2005), as well as with the capture of D-type asteroids in the outer asteroid belt (Levison et al. 2009). Moreover, the Nice model cometary flux is required to explain the origin of the collisional break-up of the asteroid (153) Hilda in the 3/2 resonance with Jupiter (located at ≃4 AU, i.e. beyond the nominal outer border of the asteroid belt at ≃3.2 AU; Brož et al. 2011).

Missing signs of an intense cometary bombardment on the Moon and the evidence for a large cometary flux in the outer solar system suggest that the Nice model may be correct in its basic features, but most comets disintegrated as they penetrated deep into the inner solar system.

To support or reject this possibility, this paper focusses on the main asteroid belt, looking for constraints on the flux of comets through this region at the time of the LHB. In particular we focus on old asteroid families, produced by the collisional break-up of large asteroids, which may date back at the LHB time. We provide a census of these families in Sect. 2.

In Sect. 3, we construct a collisional model of the main belt population. We show that, on average, this population alone could not have produced the observed number of families with $D_{\rm PB}$ = 200–400 km. Instead, the required number of families with large parent bodies is systematically produced if the asteroid belt was crossed by a large number of comets during the LHB, as expected in the Nice model (see Sect. 4). However, for any reasonable size distribution of the cometary population, the same cometary flux that would produce the correct number of families with $D_{\rm PB}$ = 200–400 km would produce too many families with $D_{\rm PB} \simeq 100$ km relative to what is observed. Therefore, in the subsequent sections we look for mechanisms that might prevent detection of most of these families.

More specifically, in Sect. 5 we discuss the possibility that families with $D_{\rm PB} \simeq 100$ km are so numerous that they cannot be identified because they overlap with each other. In Sect. 6 we investigate their possible dispersal below detectability due to the Yarkovsky effect and chaotic diffusion. In Sect. 7 we discuss the role of the physical lifetime of comets. In Sect. 8 we analyse the dispersal of families due to the changes in the orbits of the giant planets expected in the Nice model. In Sect. 9 we consider the subsequent collisional comminution of the families. Of all investigated processes, the last one seems to be the most promising for reducing the number of visible families with $D_{\rm PB} \simeq 100$ km while not affecting the detectability of old families with $D_{\rm PB}$ = 200–400 km.

Finally, in Sect. 10 we analyse a curious portion of the main belt, located in a narrow semi-major axis zone bounded by the 5:2 and 7:3 resonances with Jupiter. This zone is severely deficient in small asteroids compared to the other zones of the main belt. For the reasons explained in the section, we think that this zone best preserves the initial asteroid belt population, and therefore we call it the "pristine zone". We checked the number of families in the pristine zone, their sizes, and ages and we found that they are consistent with the number expected in our model invoking a cometary bombardment at the LHB time and a subsequent collisional comminution and dispersion of the family members. The conclusions follow in Sect. 11.

## 2. A list of known families

Although several lists of families exist in the literature (Zappalá et al. 1995; Nesvorný et al. 2005; Parker et al. 2008; Nesvorný 2010), we are going to identify the families once again. The reason is that we seek an upper limit for the number of old families that may be significantly dispersed and depleted, while the previous works often focussed on well-defined families. Moreover, we need to calculate several physical parameters of the families (such as the parent-body size, slopes of the size-frequency distribution (SFD), a dynamical age estimate if not available in the literature) which are crucial for further modelling. Last but not least, we use more precise synthetic proper elements from the AstDyS database (Knežević & Milani 2003, version Aug. 2010) instead of semi-analytic ones.

We employed a hierarchical clustering method (HCM, Zappalá et al. 1995) for the initial identification of families in the proper element space ($a_{\rm p}$, $e_{\rm p}$, $\sin I_{\rm p}$), but then we had to perform a lot of manual operations, because i) we had to select a reasonable cut-off velocity $v_{\rm cutoff}$, usually such that the number of members $N(v_{\rm cutoff})$ increases relatively slowly with increasing $v_{\rm cutoff}$. ii) The resulting family should also have a "reasonable" shape in the space of proper elements, which should somehow correspond to the local dynamical features[1]. iii) We checked taxonomic types (colour indices from the Sloan DSS MOC catalogue version 4, Parker et al. 2008), which should be consistent among family members. We can recognise interlopers or overlapping families this way. iv) Finally, the SFD should exhibit one or two well-defined slopes, otherwise the cluster is considered uncertain.

Our results are summarised in online Table 1 and the positions of families within the main belt are plotted in Fig. 1. Our list is "optimistic", so that even not very prominent families are included here[2].

There are, however, several potential problems we are aware of:

1. There may be inconsistencies among different lists of families. For example, sometimes a clump may be regarded as a single family or as two separate families. This may be the case of: Padua and Lydia, Rafita and Cameron.
2. To identify families we used synthetic proper elements, which are more precise than the semi-analytic ones.

[1] For example, the Eos family has a complicated but still reasonable shape, since it is determined by several intersecting high-order mean-motion or secular resonances, see Vokrouhlický et al. (2006).

[2] On the other hand, we do not include all of the small and less-certain clumps in a high-inclination region as listed by Novaković et al. (2011). We do not focus on small or high-$I$ families in this paper.

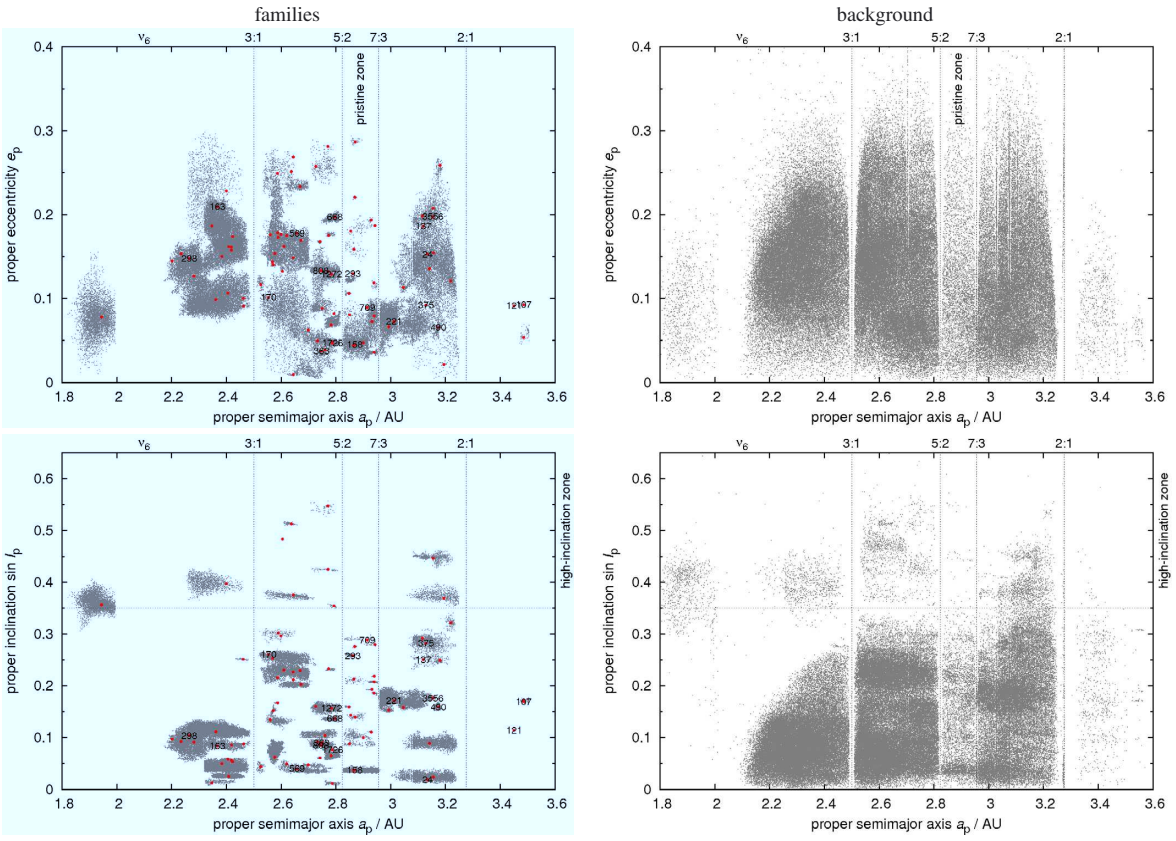


**Fig. 1.** Asteroids from the synthetic AstDyS catalogue plotted in the proper semimajor axis $a_p$ vs. proper eccentricity $e_p$ (*top panels*) and $a_p$ vs. proper inclination sin $I_p$ planes (*bottom panels*). We show the identified asteroid families (*left panels*) with the positions of the largest members indicated by red symbols, and also remaining background objects (*right panels*). The labels correspond to designations of the asteroid families that we focus on in this paper. There are still some structures consisting of small objects in the background population, visible only in the inclinations (*bottom right panel*). These "halos" may arise for two reasons: i) a family has no sharp boundary and its transition to the background is smooth, or ii) there are bodies escaping from the families due to long-term dynamical evolution. Nevertheless, we checked that these halo objects do not significantly affect our estimates of parent-body sizes.

Sometimes the families look more regular (e.g., Teutonia) or more tightly clustered (Beagle) when we use the synthetic elements. This very choice may, however, affect results substantially! A clear example is the Teutonia family, which also contains the big asteroid (5) Astraea if the synthetic proper elements are used, but not if the semi-analytic proper elements are used. This is due to the large differences between the semi-analytic and synthetic proper elements of (5) Astraea. Consequently, the physical properties of the two families differ considerably. We believe that the family defined from the synthetic elements is more reliable.

3. Durda et al. (2007) often claim a larger size for the parent body (e.g., Themis, Meliboea, Maria, Eos, Gefion), because they try to match the SFD of larger bodies and the results of SPH experiments. This way they also account for small bodies that existed at the time of the disruption, but which do not exist today since they were lost due to collisional grinding and the Yarkovsky effect. We prefer to use $D_{\rm Durda}$ instead of the value $D_{\rm PB}$ estimated from the currently observed SFD. The geometric method of Tanga et al. (1999), which uses the sum of the diameters of the first and third largest family members as a first guess of the parent-body size, is essentially similar to our approach[3].

### 2.1. A definition of the production function

To compare observed families to simulations, we define a "production function" as the cumulative number $N(>D)$ of families with parent-body size $D_{\rm PB}$ larger than a given $D$. The observed production function is shown in Fig. 2, and it is worth noting that it is very shallow. The number of families with $D_{\rm PB} \simeq 100$ km is comparable to the number of families in the $D_{\rm PB} = 200$–$400$ km range.

It is important to note that the observed production function is likely to be affected by biases (the family sample may not be complete, especially below $D_{\rm PB} \lesssim 100$ km) and also by long-term collisional/dynamical evolution which may

[3] A complete list of all families' members is available at our web site http://sirrah.troja.mff.cuni.cz/~mira/mp/fams/, including supporting figures.

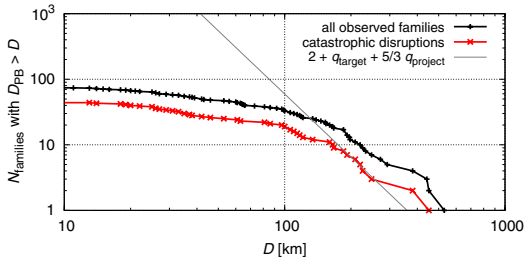


**Fig. 2.** A production function (i.e. the cumulative number $N(>D)$ of families with parent-body size $D_{\rm PB}$ larger than $D$) for all observed families (black) and families corresponding to catastrophic disruptions (red), i.e. with largest remnant/parent body mass ratio lower than 0.5. We also plot a theoretical slope according to Eq. (1), assuming $q_{\rm target} = -3.2$ and $q_{\rm project} = -1.2$, which correspond to the slopes of the main belt population in the range $D = 100$–$200$ km and $D = 15$–$60$ km, respectively.

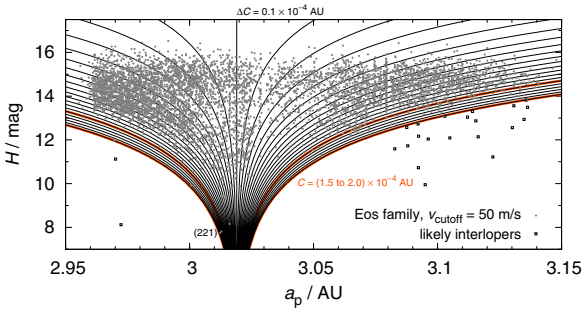


**Fig. 3.** An example of the Eos asteroid family, shown on the proper semimajor axis $a_{\rm p}$ vs. absolute magnitude $H$ plot. We also plot curves defined by Eq. (2) and parameters $a_{\rm c} = 3.019$ AU, $C = 1.5$ to $2.0 \times 10^{-4}$ AU, which is related to the upper limit of the dynamical age of the family.

prevent a detection of old comminutioned/dispersed families today (Marzari et al. 1999).

From the theoretical point of view, the slope $q$ of the production function $N(>D) \propto D^q$ should correspond to the cumulative slopes of the SFDs of the target and projectile populations. It is easy to show[4] that the relation is

$$q = 2 + q_{\rm target} + \frac{5}{3} q_{\rm project}. \quad (1)$$

Of course, real populations may have complicated SFDs, with different slopes in different ranges. Nevertheless, any populations that have a steep SFD (e.g. $q_{\rm target} = q_{\rm project} = -2.5$) would inevitably produce a steep production function ($q \doteq -4.7$).

In the following analysis, we drop cratering events and discuss catastrophic disruptions only, i.e. families which have largest remnant/parent body mass ratio less than 0.5. The reason is that the same criterion LR/PB $< 0.5$ is used in collisional models. Moreover, cratering events were not yet systematically explored by SPH simulations due to insufficient resolution (Durda et al. 2007).

### 2.2. Methods for family age determination

If there is no previous estimate of the age of a family, we used one of the following three dynamical methods to determine it: i) a simple $(a_{\rm p}, H)$ analysis as in Nesvorný et al. (2005); ii) a $C$-parameter distribution fitting as introduced by Vokrouhlický et al. (2006); iii) a full $N$-body simulation described e.g. in Brož et al. (2011).

In the first approach, we assume zero initial velocities, and the current extent of the family is explained by the size-dependent Yarkovsky semimajor axis drift. This way we can obtain only an upper limit for the dynamical age, of course. We show an example for the Eos family in Fig. 3. The extent of the family in the proper semimajor axis vs the absolute magnitude $(a_{\rm p}, H)$ plane can be described by the parametric relation

$$0.2H = \log_{10} \frac{|a_{\rm p} - a_{\rm c}|}{C}, \quad (2)$$

where $a_{\rm c}$ denotes the centre of the family, and $C$ is the parameter. Such relation can be naturally expected when the semimajor-axis drift rate is inversely proportional to the size, $\mathrm{d}a/\mathrm{d}t \propto 1/D$, and the size is related to the absolute magnitude via the Pogson equation $H = -2.5 \log_{10}(p_V D^2 / D_0^2)$, where $D_0$ denotes the reference diameter and $p_V$ the geometric albedo (see Vokrouhlický et al. 2006 for a detailed discussion). The limiting value, for which all Eos family members (except interlopers) are above the corresponding curve, is $C = 1.5$ to $2.0 \times 10^{-4}$ AU. Assuming reasonable thermal parameters (summarised in Table 2), we calculate the expected Yarkovsky drift rates $\mathrm{d}a/\mathrm{d}t$ (using the theory from Brož 2006) and consequently can determine the age to be $t < 1.5$ to $2.0$ Gyr.

**Table 2.** Nominal thermal parameters for S and C/X taxonomic types of asteroids.

| Type | $\rho_{\rm bulk}$ (kg/m$^3$) | $\rho_{\rm surf}$ (kg/m$^3$) | $K$ (W/m/K) | $C_{\rm th}$ (J/kg/K) | $A_{\rm Bond}$ | $\epsilon$ |
|---|---|---|---|---|---|---|
| S | 2500 | 1500 | 0.001 | 680 | 0.1 | 0.9 |
| C/X | 1300 | 1300 | 0.01 | 680 | 0.02 | 0.9 |

**Notes.** $\rho_{\rm bulk}$ denotes the bulk density, $\rho_{\rm surf}$ the surface density, $K$ the thermal conductivity, $C_{\rm th}$ the specific thermal capacity, $A_{\rm Bond}$ the Bond albedo and $\epsilon$ the infrared emissivity.

The second method uses a histogram $N(C, C + \Delta C)$ of the number of asteroids with respect to the $C$ parameter defined above, which is fitted by a dynamical model of the initial velocity field and the Yarkovsky/YORP evolution. This enables us to determine the lower limit for the age too (so the resulting age estimate is $t = 1.3^{+0.15}_{-0.2}$ Gyr for the Eos family).

In the third case, we start an $N$-body simulation using a modified SWIFT integrator (Levison & Duncan 1994), with the Yarkovsky/YORP acceleration included, and evolve a synthetic family up to 4 Gyr. We try to match the shape of the observed family in all three proper orbital elements $(a_{\rm p}, e_{\rm p}, \sin I_{\rm p})$. In principle, this method may provide a somewhat independent estimate of the age. For example, there is a "halo" of asteroids in the surroundings of the nominal Eos family, which are of the same taxonomic type K, and we may fit the ratio $N_{\rm halo}/N_{\rm core}$ of the number of objects in the "halo" and in the family "core" (Brož et al., in prep.).

The major source of uncertainty in all methods are unknown bulk densities of asteroids (although we use the most likely values for the S or C/X taxonomic classes, Carry 2012). The age scales approximately as $t \propto \rho_{\rm bulk}$. Nevertheless, we are still able to distinguish families that are young from those that

[4] Assuming that the strength is approximately $Q_D^\star \propto D^2$ in the gravity regime, the necessary projectile size $d \propto (Q_D^\star)^{1/3} D$ (Bottke et al. 2005), and the number of disruptions $n \propto D^2 D^{q_{\rm target}} d^{q_{\rm project}}$.

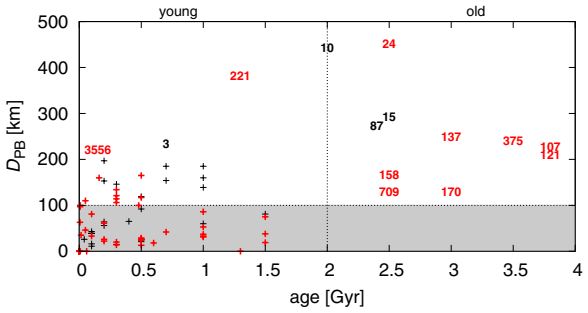


**Fig. 4.** The relation between dynamical ages of families and the sizes of their parent bodies. Red labels correspond to catastrophic disruptions, while cratering events are labelled in black. Some of the families are denoted by the designation of the largest member. The uncertainties of both parameters are listed in Table 1 (we do not include overlapping error bars here for clarity).

are old, because the allowed ranges of densities for S-types (2 to 3 g/cm$^3$) and C/X-types (1 to 2 g/cm$^3$) are limited (Carry 2012) and so are the allowed ages of families.

### 2.3. Which families can be of LHB origin?

The ages of the observed families and their parent-body sizes are shown in Fig. 4. Because the ages are generally very uncertain, we consider that any family whose nominal age is older than 2 Gyr is potentially a family formed ~4 Gyr ago, i.e. at the LHB time. If we compare the number of "young" (<2 Gyr) and old families (>2 Gyr) with $D_{PB}$ = 200–400 km, we cannot see a significant over-abundance of old family formation events. On the other hand, we almost do not find any small old families.

Only 12 families from the whole list may be possibly dated back to the LHB, because their dynamical ages approach ~3.8 Gyr (including the relatively large uncertainties; see Table 3, which is an excerpt from Table 1).

If we drop cratering events and the families of Camilla and Hermione, which do not exist any more today (their existence was inferred from the satellite systems, Vokrouhlický et al. 2010), we end up with only five families created by catastrophic disruptions that may potentially date from the LHB time (i.e. their nominal age is more than 2 Gy). As we shall see in Sect. 4, this is an unexpectedly low number.

Moreover, it is really intriguing that most "possibly-LHB" families are larger than $D_{PB} \simeq 200$ km. It seems that old families with $D_{PB} \simeq 100$ km are missing in the observed sample. This is an important aspect that we have to explain, because it contradicts our expectation of a steep production function.

## 3. Collisions in the main belt alone

Before we proceed to scenarios involving the LHB, we try to explain the observed families with ages spanning 0–4 Gyr as a result of collisions only among main belt bodies. To this purpose, we used the collisional code called Boulder (Morbidelli et al. 2009) with the following setup: the intrinsic probabilities $P_i = 3.1 \times 10^{-18}$ km$^{-2}$ yr$^{-1}$, and the mutual velocities $V_{imp} = 5.28$ km s$^{-1}$ for the MB vs. MB collisions (both were taken from the work of Dahlgren 1998). The assumption of a single $V_{imp}$ value is a simplification, but about 90% collisions have mutual velocities between 2 and 8 km s$^{-1}$ (Dahlgren 1998), which assures a similar collisional regime.

**Table 3.** Old families with ages possibly approaching the LHB.

| Designation | | $D_{PB}$ (km) | $D_{Durda}$ (km) | Note |
|---|---|---|---|---|
| 24 | Themis | 209c | 380–430! | |
| 10 | Hygiea | 410 | 442 | cratering |
| 15 | Eunomia | 259 | 292 | cratering |
| 702 | Alauda | 218c | 290–330! | high-$I$ |
| 87 | Sylvia | 261 | 272 | cratering |
| 137 | Meliboea | 174c | 240–290! | |
| 375 | Ursula | 198 | 240–280 | cratering |
| 107 | Camilla | >226 | – | non-existent |
| 121 | Hermione | >209 | – | non-existent |
| 158 | Koronis | 122c | 170–180 | |
| 709 | Fringilla | 99c | 130–140 | cratering |
| 170 | Maria | 100c | 120–130 | |

**Notes.** They are sorted according to the parent body size, where $D_{Durda}$ determined by the Durda et al. (2007) method is preferred to the estimate $D_{PB}$ inferred from the observed SFD. An additional "c" letter indicates that we extrapolated the SFD down to $D = 0$ km to account for small (unobserved) asteroids, an exclamation mark denotes a significant mismatch between $D_{PB}$ and $D_{Durda}$.

The scaling law is described by the polynomial relation ($r$ denotes radius in cm)

$$Q_D^\star(r) = \frac{1}{q_{fact}} \left( Q_0 r^a + B\rho r^b \right) \quad (3)$$

with the parameters corresponding to basaltic material at 5 km s$^{-1}$ (Benz & Asphaug 1999, Table 4):

**Table 4.** Parameters of the scaling law (Eq. (3)) corresponding to basaltic material at 5 km s$^{-1}$, according to Benz & Asphaug (1999).

| $\rho$ (g/cm$^3$) | $Q_0$ (erg/g) | $a$ | $B$ (erg/g) | $b$ | $q_{fact}$ |
|---|---|---|---|---|---|
| 3.0 | $7 \times 10^7$ | −0.45 | 2.1 | 1.19 | 1.0 |

Even though not all asteroids are basaltic, we use the scaling law above as a mean one for the main belt population. Below, we discuss also the case of significantly lower strengths (i.e. higher $q_{fact}$ values).

We selected the time span of the simulation 4 Gyr (not 4.5 Gyr) since we are interested in this last evolutionary phase of the main belt, when its population and collisional activity is nearly same as today (Bottke et al. 2005). The outcome of a single simulation also depends on the "seed" value of the random-number generator that is used in the Boulder code to decide whether a collision with a fractional probability actually occurs or not in a given time step. We thus have to run multiple simulations (usually 100) to obtain information on this stochasticity of the collisional evolution process.

The initial SFD of the main belt population conditions was approximated by a three-segment power law (see also thin grey line in Fig. 5, 1st row) with differential slopes $q_a = -4.3$ (for $D > D_1$), $q_b = -2.2$, $q_c = -3.5$ (for $D < D_2$) where the size ranges were delimited by $D_1 = 80$ km and $D_2 = 16$ km. We also added a few big bodies to reflect the observed shape of the SFD at large sizes ($D > 400$ km). The normalisation was $N_{norm}(D > D_1) = 350$ bodies in this case.

We used the observed SFD of the main belt as the first constraint for our collisional model. We verified that the outcome

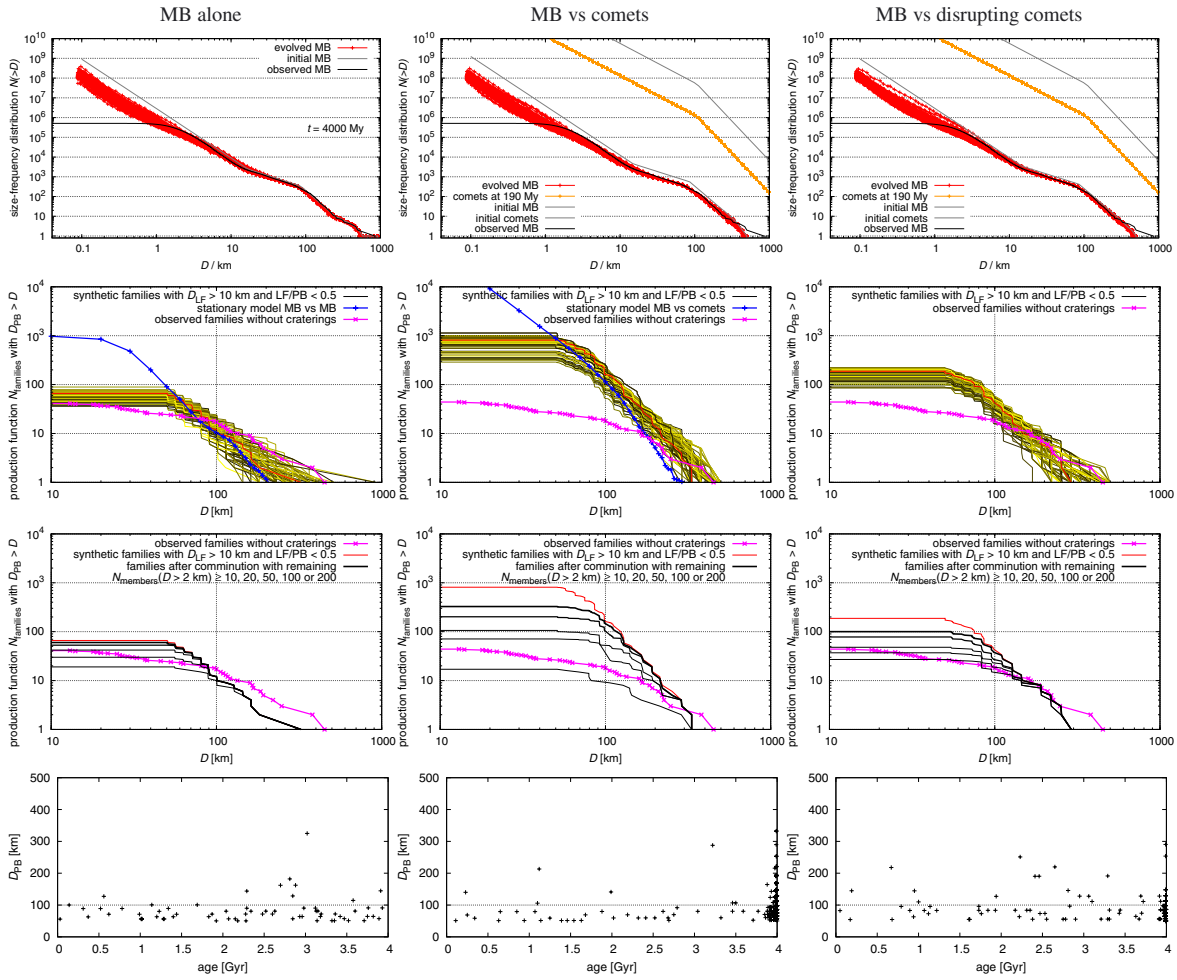


**Fig. 5.** Results of three different collisional models: main belt alone which is discussed in Sect. 3 (*left column*), main belt and comets from Sect. 4 (*middle column*), main belt and disrupting comets from Sect. 7 (*right column*). *1st row*: the initial and evolved SFDs of the main belt populations for 100 Boulder simulations; *2nd row*: the resulting family production functions (in order to distinguish 100 lines we plot them using different colours ranging from black to yellow) and their comparison to the observations; *3rd row*: the production function affected by comminution for a selected simulation; and *4th row*: the distribution of synthetic families with $D_{\rm PB} \geq 50$ km in the (age, $D_{\rm PB}$) plot for a selected simulation, without comminution. The positions of synthetic families in the *4th-row* figures may differ significantly for a different Boulder simulation due to stochasticity and low-number statistics. Moreover, in the middle and right columns, many families were created during the LHB, so there are many overlapping crosses close to 4 Gyr.

our model after 4 Gyr is not sensitive to the value of $q_c$. Namely, a change of $q_c$ by as much as $\pm 1$ does not affect the final SFD in any significant way. On the other hand, the values of the remaining parameters ($q_a$, $q_b$, $D_1$, $D_2$, $N_{\rm norm}$) are enforced by the observed SFD. To obtain a reasonable fit, they cannot differ much (by more than 5–10%) from the values presented above.

We do not use only a single number to describe the number of observed families (e.g. $N = 20$ for $D_{\rm PB} \geq 100$ km), but we discuss a complete production function instead. The results in terms of the production function are shown in Fig. 5 (left column, 2nd row). On average, the synthetic production function is steeper and below the observed one, even though there is approximately a 5% chance that a single realization of the computer model will resemble the observations quite well. This also holds for the distribution of $D_{\rm PB} = 200$–$400$ km families in the course of time (age).

In this case, the synthetic production function of $D_{\rm PB} \gtrsim 100$ km families is not significantly affected by comminution. According to Bottke et al. (2005), most of $D > 10$ km fragments survive intact and a $D_{\rm PB} \gtrsim 100$ km family should be recognisable today. This is also confirmed by calculations with Boulder (see Fig. 5, left column, 3rd row).

To improve the match between the synthetic and the observed production function, we can do the following: i) modify the scaling law, or ii) account for a dynamical decay of the MB population. Using a substantially lower strength ($q_{\rm fact} = 5$ in Eq. (3), which is not likely, though) one can obtain a synthetic production function which is on average consistent with the observations in the $D_{\rm PB} = 200$–$400$ km range.

Regarding the dynamical decay, Minton & Malhotra (2010) suggest that initially the MB was three times more populous than today while the decay timescale was very short: after 100 Myr

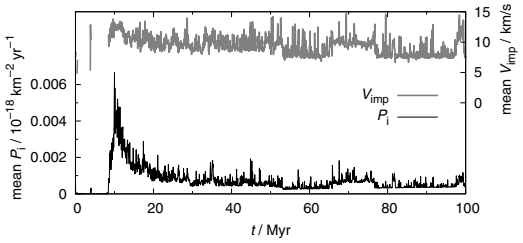


**Fig. 6.** Temporal evolution of the intrinsic collisional probability $P_i$ (*bottom*) and mean collisional velocity $V_{imp}$ (*top*) computed for collisions between cometary-disk bodies and the main belt asteroids. The time $t = 0$ is arbitrary here; the sudden increase in $P_i$ values corresponds to the beginning of the LHB.

of evolution the number of bodies is almost at the current level. In this brief period of time, about 50% more families will be created, but all of them will be old, of course. For the remaining ∼3.9 Gyr, the above model (without any dynamical decay) is valid.

To conclude, it is possible – though not very likely – that the observed families were produced by the collisional activity in the main belt alone. A dynamical decay of the MB population would create more families that are old, but technically speaking, this cannot be distinguished from the LHB scenario, which is discussed next.

## 4. Collisions between a "classical" cometary disk and the main belt

In this section, we construct a collisional model and estimate an expected number of families created during the LHB due to collisions between cometary-disk bodies and main belt asteroids. We start with a simple stationary model and we confirm the results using a more sophisticated Boulder code (Morbidelli et al. 2009).

Using the data from Vokrouhlický et al. (2008) for a "classical" cometary disk, we can estimate the intrinsic collisional probability and the collisional velocity between comets and asteroids. A typical time-dependent evolution of $P_i$ and $V_{imp}$ is shown in Fig. 6. The probabilities increase at first, as the trans-Neptunian cometary disk starts to decay, reaching up to $6 \times 10^{-21}$ km$^{-2}$ yr$^{-1}$, and after 100 Myr they decrease to zero. These results do not differ significantly from run to run.

### 4.1. Simple stationary model

In a stationary collisional model, we choose an SFD for the cometary disk, we assume a current population of the main belt; estimate the projectile size needed to disrupt a given target according to (Bottke et al. 2005)

$$d_{\rm disrupt} = \left(2Q_D^\star / V_{\rm imp}^2\right)^{1/3} D_{\rm target}, \tag{4}$$

where $Q_D^\star$ denotes the specific energy for disruption and dispersion of the target (Benz & Asphaug 1999); and finally calculate the number of events during the LHB as

$$n_{\rm events} = \frac{D_{\rm target}^2}{4}\, n_{\rm target} \int P_{\rm i}(t)\, n_{\rm project}(t)\, {\rm d}t, \tag{5}$$

where $n_{\rm target}$ and $n_{\rm project}$ are the number of targets (i.e. main belt asteroids) and the number of projectiles (comets), respectively.

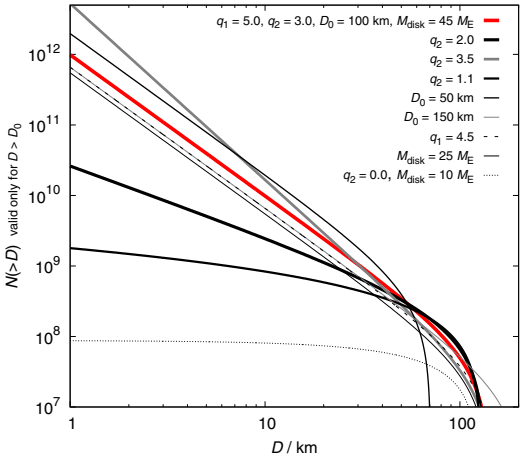


**Fig. 7.** Cumulative SFDs of the cometary disk tested in this work. All the parameters of our nominal choice are given in the top label; the other labels just report the parameters that changed relative to our nominal choice.

The actual number of bodies (27 000) in the dynamical simulation of Vokrouhlický et al. (2008) changes in the course of time, and it was scaled such that it was initially equal to the number of projectiles $N(>d_{\rm disrupt})$ inferred from the SFD of the disk. This is clearly a lower limit for the number of families created, since the main belt was definitely more populous in the past.

The average impact velocity is $V_{\rm imp} \simeq 10$ km s$^{-1}$, so we need the projectile sizes to disrupt given target sizes listed in Table 5.

**Table 5.** Projectile sizes $d_{\rm disrupt}$ needed to disrupt targets with sizes $D_{\rm target}$, as computed from Eq. (4).

| $D_{\rm target}$ (km) | $N_{\rm targets}$ in the MB | $Q_D^\star$ (J/kg) | $d_{\rm disrupt}$ for $\frac{\rho_{\rm target}}{\rho_{\rm project}} = 3$ to 6 (km) |
|---|---|---|---|
| 100 | ∼192 | $1 \times 10^5$ | 12.6 to 23 |
| 200 | ∼23 | $4 \times 10^5$ | 40.0 to 73 |

**Notes.** $N_{\rm targets}$ denotes the number of targets in the main belt, $Q_D^\star$ the specific energy needed for disruption, and $\rho_{\rm target}/\rho_{\rm project}$ the ratio of the respective bulk densities.

We tried to use various SFDs for the cometary disk (i.e., with various differential slopes $q_1$ for $D > D_0$ and $q_2$ for $D < D_0$, the elbow diameter $D_0$ and total mass $M_{\rm disk}$), including rather extreme cases (see Fig. 7). The resulting numbers of LHB families are summarised in Table 6. Usually, we obtain several families with $D_{\rm PB} \simeq 200$ km and about 100 families with $D_{\rm PB} \simeq 100$ km. This result is robust with respect to the slope $q_2$, because even very shallow SFDs should produce a lot of these families[5]. The only way to decrease the number of families significantly is to assume the elbow at a larger diameter $D_0 \simeq 150$ km.

[5] The extreme case with $q_2 = 0$ is not likely at all, e.g. because of the continuous SFD of basins on Iapetus and Rhea, which only exhibits a mild depletion of $D \simeq 100$ km size craters; see Kirchoff & Schenk (2010). On the other hand, Sheppard & Trujillo (2010) report an extremely shallow cumulative SFD of Neptune Trojans that is akin to low $q_2$.

**Table 6.** Results of a stationary collisional model between the cometary disk and the main belt.

| $q_1$ | $q_2$ | $D_0$ (km) | $M_{\rm disk}$ ($M_\oplus$) | $n_{\rm events}$ for $D_{\rm PB} \geq 100$ km | $D_{\rm PB} \geq 200$ km | Vesta craterings | Notes |
|---|---|---|---|---|---|---|---|
| 5.0 | 3.0 | 100 | 45 | 115–55 | 4.9–2.1 | 2.0 | nominal case |
| 5.0 | 2.0 | 100 | 45 | 35–23 | 4.0–2.2 | 1.1 | shallow SFD |
| 5.0 | 3.5 | 100 | 45 | 174–70 | 4.3–1.6 | 1.8 | steep SFD |
| 5.0 | 1.1 | 100 | 45 | 14–12 | 3.1–2.1 | 1.1 | extremely shallow SFD |
| 4.5 | 3.0 | 100 | 45 | 77–37 | 3.3–1.5 | 1.3 | lower $q_1$ |
| 5.0 | 3.0 | 50 | 45 | 225–104 | 7.2–1.7 | 3.2 | smaller turn-off |
| 5.0 | 3.0 | 100 | 25 | 64–40 | 2.7–1.5 | 1.1 | lower $M_{\rm disk}$ |
| 5.0 | 3.0 | 100 | 17 | 34 | 1.2 | 1.9 | $\rho_{\rm comets} = 500\,{\rm kg/m^3}$ |
| 5.0 | 3.0 | 150 | 45 | 77–23 | 3.4–0.95 | 0.74 | larger turn-off |
| 5.0 | 0.0 | 100 | 10 | 1.5–1.4 | 0.5–0.4 | 0.16 | worst case (zero $q_2$ and low $M_{\rm disk}$) |

**Notes.** The parameters characterise the SFD of the disk: $q_1$, $q_2$ are differential slopes for the diameters larger/smaller than the elbow diameter $D_0$, $M_{\rm disk}$ denotes the total mass of the disk, and $n_{\rm events}$ is the resulting number of families created during the LHB for a given parent body size $D_{\rm PB}$. The ranges of $n_{\rm events}$ are due to variable density ratios $\rho_{\rm target}/\rho_{\rm project} = 1$ to 3/1.

**Table 7.** Parameters of the scaling law (Eq. (3)) corresponding to basaltic material at 5 km s$^{-1}$ (first row), and to water ice (second row), according to Benz & Asphaug (1999).

| | $\rho$ (g/cm$^3$) | $Q_0$ (erg/g) | $a$ | $B$ (erg/g) | $b$ | $q_{\rm fact}$ |
|---|---|---|---|---|---|---|
| Asteroids | 3.0 | $7 \times 10^7$ | −0.45 | 2.1 | 1.19 | 1.0 |
| Comets | 1.0 | $1.6 \times 10^7$ | −0.39 | 1.2 | 1.26 | 3.0 |

It is thus no problem to explain the existence of approximately five large families with $D_{\rm PB} = 200$–$400$ km, which are indeed observed, since they can be readily produced during the LHB. On the other hand, the high number of $D_{\rm PB} \simeq 100$ km families clearly contradicts the observations, since we observe almost no LHB families of this size.

### 4.2. Constraints from (4) Vesta

The asteroid (4) Vesta presents a significant constraint for collisional models, being a differentiated body with a preserved basaltic crust (Keil 2002) and a 500 km large basin on its surface (a feature indicated by the photometric analysis of Cellino et al. 1987), which is significantly younger than 4 Gyr (Marchi et al. 2012). It is highly unlikely that Vesta experienced a catastrophic disruption in the past, and even large cratering events were limited. We thus have to check the number of collisions between one $D = 530$ km target and $D \simeq 35$ km projectiles, which are capable of producing the basin and the Vesta family (Thomas et al. 1997). According to Table 6, the predicted number of such events does not exceed ∼2, so given the stochasticity of the results there is a significant chance that Vesta indeed experienced zero such impacts during the LHB.

### 4.3. Simulations with the Boulder code

To confirm results of the simple stationary model, we also performed simulations with the Boulder code. We modified the code to include a time-dependent collisional probability $P_{\rm i}(t)$ and impact velocity $V_{\rm imp}(t)$ of the cometary-disk population.

We started a simulation with a setup for the cometary disk resembling the nominal case from Table 6. The scaling law is described by Eq. (3) with the parameters given in Table 7, suitable for asteroids (basalt) and comets (water ice).

The intrinsic probabilities $P_{\rm i} = 3.1 \times 10^{-18}\,{\rm km^{-2}\,yr^{-1}}$ and velocities $V_{\rm imp} = 5.28\,{\rm km\,s^{-1}}$ for the MB vs MB collisions were again taken from the work of Dahlgren (1998). We do not account for comet-comet collisions since their evolution is dominated by the dynamical decay. The initial SFD of the main belt was similar to the one in Sect. 3, $q_a = -4.2$, $q_b = -2.2$, $q_c = -3.5$, $D_1 = 80$ km, $D_2 = 14$ km, and only the normalisation was increased up to $N_{\rm norm}(D > D_1) = 560$ in this case.

The resulting SFDs of 100 independent simulations with different random seeds are shown in Fig. 5 (middle column). The number of LHB families (approximately 10 with $D_{\rm PB} \simeq 200$ km and 200 with $D_{\rm PB} \simeq 100$ km) is even larger compared to the stationary model, as expected, because we had to start with a larger main belt to get a good fit of the currently observed MB after 4 Gyr of collisional evolution.

To conclude, the stationary model and the Boulder code give results that are compatible with each other, but that clearly contradict the observed production function of families. In particular, they predict far too many families with $D = 100$ km parent bodies. At first sight, this may be interpreted as proof that there was no cometary LHB on the asteroids. Before jumping to this conclusion, however, one has to investigate whether there are biases against identifying of $D_{\rm PB} = 100$ km families. In Sects. 5–9 we discuss several mechanisms that all contribute, at some level, to reducing the number of observable $D_{\rm PB} = 100$ km families over time. They are addressed in order of relevance, from the least to the most effective.

## 5. Families overlap

Because the number of expected $D_{\rm PB} \geq 100$ km LHB families is very high (of the order of 100) we now want to verify if these families can overlap in such a way that they cannot be distinguished from each other and from the background. We thus took 192 main belt bodies with $D \geq 100$ km and selected randomly 100 of them that will break apart. For each one we created an artificial family with $10^2$ members, assume a size-dependent ejection velocity $V \propto 1/D$ (with $V = 50$ m/s for $D = 5$ km) and the size distribution resembling that of the Koronis family. The choice of the true anomaly and the argument of perihelion at the instant of the break-up event was random. We then calculated proper elements $(a_{\rm p}, e_{\rm p}, \sin I_{\rm p})$ for all bodies. This type of analysis is in some respects similar to the work of Bendjoya et al. (1993).

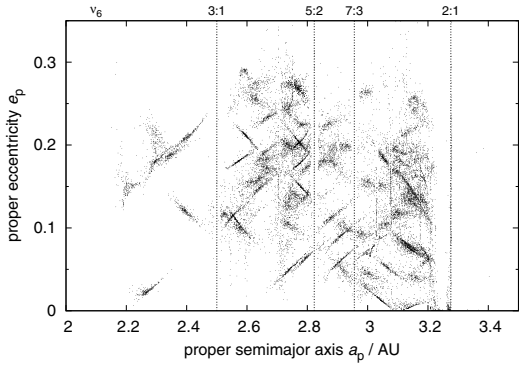


**Fig. 8.** Proper semimajor axis $a_p$ vs. proper eccentricity $e_p$ for 100 synthetic families created in the main belt. It is the initial state, shortly after disruption events. We assume the SFD of bodies in each synthetic family similar to that of the Koronis family (down to $D \simeq 2$ km). Break-ups with the true anomaly $f \simeq 0$ to 30° and 150° to 180° are more easily visible on this plot, even though the choice of both $f$ and the argument of perihelion $\varpi$ was random for all families.

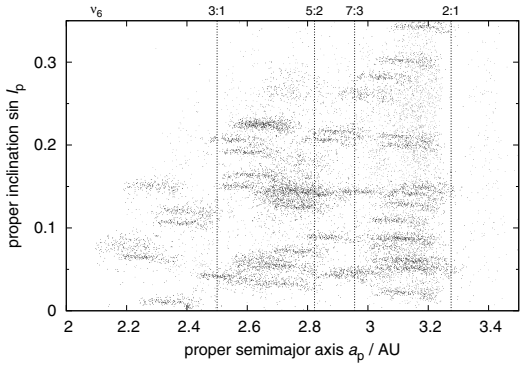


**Fig. 9.** Proper semimajor axis $a_p$ vs. proper inclination $\sin I_p$ for 100 synthetic asteroid families (black dots), evolved over 4 Gyr using a Monte-Carlo model. The assumed SFDs correspond to the Koronis family, but we show only $D > 10$ km bodies here. We also include $D > 10$ km background asteroids (grey dots) for comparison.

According to the resulting Fig. 8 the answer to the question is simple: the families do not overlap sufficiently, and they cannot be hidden that way. Moreover, if we take only bigger bodies ($D > 10$ km), these would be clustered even more tightly. The same is true for proper inclinations, which are usually more clustered than eccentricities, so families could be more easily recognised.

## 6. Dispersion of families by the Yarkovsky drift

In this section, we model long-term evolution of synthetic families driven by the Yarkovsky effect and chaotic diffusion. For one synthetic family located in the outer belt, we have performed a full $N$-body integration with the SWIFT package (Levison & Duncan 1994), which includes also an implementation of the Yarkovsky/YORP effect (Brož 2006) and second-order integrator by Laskar & Robutel (2001). We included 4 giant planets in this simulation. To speed-up the integration, we used ten times smaller sizes of the test particles and thus a ten times shorter time span (400 Myr instead of 4 Gyr). The selected time step is $\Delta t = 91$ d. We computed proper elements, namely their differences $\Delta a_p, \Delta e_p, \Delta \sin I_p$ between the initial and final positions.

Then we used a simple Monte-Carlo approach for the whole set of 100 synthetic families – we assigned a suitable drift $\Delta a_p(D)$ in semimajor axis, and also drifts in eccentricity $\Delta e_p$ and inclination $\Delta \sin I_p$ to each member of 100 families, respecting asteroid sizes, of course. This way we account for the Yarkovsky semimajor axis drift and also for interactions with mean-motion and secular resonances. This Monte-Carlo method tends to smear all structures, so we can regard our results as the upper limits for dispersion of families.

While the eccentricities of small asteroids (down to $D \simeq 2$ km) seem to be dispersed enough to hide the families, there are still some persistent structures in inclinations, which would be observable today. Moreover, large asteroids ($D \geq 10$ km) seem to be clustered even after 4 Gyr, so that more than 50% of families can be easily recognised against the background (see Fig. 9). We thus can conclude that it is not possible to disperse the families by the Yarkovsky effect alone.

## 7. Reduced physical lifetime of comets in the MB crossing zone

To illustrate the effects that the physical disruption of comets (due to volatile pressure build-up, amorphous/crystalline phase transitions, spin-up by jets, etc.) can have on the collisional evolution of the asteroid belt, we adopted here a simplistic assumption. We considered that no comet disrupt beyond 1.5 AU, whereas all comets disrupt the first time that they penetrate inside 1.5 AU. Both conditions are clearly not true in reality: some comets are observed to blow up beyond 1.5 AU, and others are seen to survive on an Earth-crossing orbit. Thus we adopted our disruption law just as an example of a drastic reduction of the number of comets with small perihelion distance, as required to explain the absence of evidence for a cometary bombardment on the Moon.

We then removed all those objects from output of comet evolution during the LHB that had a passage within 1.5 AU from the Sun, from the time of their first passage below this threshold. We then recomputed the mean intrinsic collision probability of a comet with the asteroid belt. The result is a factor ∼3 smaller than when no physical disruption of comets is taken into account as in Fig. 6. The mean impact velocity with asteroids also decreases, from 12 km s$^{-1}$ to 8 km s$^{-1}$.

The resulting number of asteroid disruption events is thus decreased by a factor ∼4.5, which can be also seen in the production function shown in Fig. 5 (right column). The production of families with $D_{PB} = 200$–400 km is consistent with observations, while the number of $D_{PB} \simeq 100$ km families is reduced to 30–70, but is still too high, by a factor 2–3. More importantly, the slope of the production function remains steeper than that of the observed function. Thus, our conclusion is that physical disruptions of comets alone cannot explain the observation, but may be an important factor to keep in mind for reconciling the model with the data.

## 8. Perturbation of families by migrating planets (a jumping-Jupiter scenario)

In principle, families created during the LHB may be perturbed by still-migrating planets. It is an open question what the exact orbital evolution of planets was at that time. Nevertheless, a

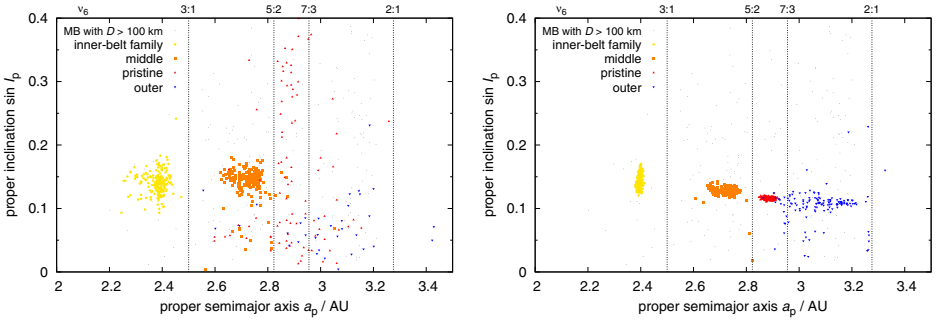


**Fig. 10.** Proper semimajor axis vs. proper inclination for four synthetic families (distinguished by symbols) as perturbed by giant-planet migration. *Left panel*: the case when families were evolved over the "jump" due to the encounter between Jupiter and Neptune. *Right panel*: the families created just after the jump and perturbed only by later phases of migration.

plausible scenario called a "jumping Jupiter" was presented by Morbidelli et al. (2010). It explains major features of the main belt (namely the paucity of high-inclination asteroids above the $\nu_6$ secular resonance), and is consistent with amplitudes of the secular frequencies of both giant and terrestrial planets and also with other features of the solar system. In this work, we thus investigated this particular migration scenario.

We used the data from Morbidelli et al. (2010) for the orbital evolution of giant planets. We then employed a modified SWIFT integrator, which read orbital elements for planets from an input file and calculated only the evolution of test particles. Four synthetic families located in the inner/middle/outer belt were integrated. We started the evolution of planets at various times, ranging from $t_0$ to $(t_0 + 4\,\mathrm{Myr})$ and stopped the integration at $(t_0 + 4\,\mathrm{My})$, in order to test the perturbation on families created in different phases of migration. Finally, we calculated proper elements of asteroids when the planets do not migrate anymore. (We also had to move planets smoothly to their exact current orbital positions.)

The results are shown in Fig. 10. While the proper eccentricities seem to be sufficiently perturbed and families are dispersed even when created at late phases of migration, the proper inclinations are not very dispersed, except for families in the outer asteroid belt that formed at the very beginning of the giant planet instability (which may be unlikely, as there must be a delay between the onset of planet instability and the beginning of the cometary flux through the asteroid belt). In most cases, the LHB families could still be identified as clumps in semi-major axis vs inclination space. We do not see any of such $(a_\mathrm{p}, \sin I_\mathrm{p})$-clumps, dispersed in eccentricity, in the asteroid belt[6].

The conclusion is clear: it is not possible to destroy low-$e$ and low-$I$ families by perturbations arising from giant-planet migration, at least in the case of the "jumping-Jupiter" scenario[7].

## 9. Collisional comminution of asteroid families

We have already mentioned that the comminution is not sufficient to destroy a $D_\mathrm{PB} = 100\,\mathrm{km}$ family in the current environment of the main belt (Bottke et al. 2005).

[6] High-inclination families would be dispersed much more owing to the Kozai mechanism, because eccentricities that are sufficiently perturbed exhibit oscillations coupled with inclinations.

[7] The currently non-existent families around (107) Camilla and (121) Hermione – inferred from the existence of their satellites – cannot be destroyed in the jumping-Jupiter scenario, unless the families were actually pre-LHB and had experienced the jump.

However, the situation in case of the LHB scenario is different. Both the large population of comets and the several-times larger main belt, which has to withstand the cometary bombardment, contribute to the enhanced comminution of the LHB families. To estimate the amount of comminution, we performed the following calculations: i) for a selected collisional simulation, whose production function is close to the average one, we recorded the SFDs of all synthetic families created in the course of time; ii) for each synthetic family, we restarted the simulation from the time $t_0$ when the family was crated until 4 Gyr and saved the final SFD, i.e. after the comminution. The results are shown in Fig. 11.

It is now important to discuss criteria, which enable us to decide if the comminutioned synthetic family would indeed be observable or not. We use the following set of conditions: $D_\mathrm{PB} \geq 50\,\mathrm{km}$, $D_\mathrm{LF} \geq 10\,\mathrm{km}$ (largest fragment is the first or the second largest body, where the SFD becomes steep), LR/PB $< 0.5$ (i.e. a catastrophic disruption). Furthermore, we define $N_\mathrm{members}$ as the number of the remaining family members larger than observational limit $D_\mathrm{limit} \simeq 2\,\mathrm{km}$ and use a condition $N_\mathrm{members} \geq 10$. The latter number depends on the position of the family within the main belt, though. In the favourable "almost-empty" zone (between $a_\mathrm{p} = 2.825$ and 2.955 AU), $N_\mathrm{members} \geq 10$ may be valid, but in a populated part of the MB one would need $N_\mathrm{members} \gtrsim 100$ to detect the family. The size distributions of synthetic families selected this way resemble the observed SFDs of the main belt families.

According to Fig. 5 (3rd row), where we can see the production functions after comminution for increasing values of $N_\mathrm{members}$, families with $D_\mathrm{PB} = 200$–$400\,\mathrm{km}$ remain more prominent than $D_\mathrm{PB} \simeq 100\,\mathrm{km}$ families simply because they contain much more members with $D > 10\,\mathrm{km}$ that survive intact. Our conclusion is thus that comminution may explain the paucity of the observed $D_\mathrm{PB} \simeq 100\,\mathrm{km}$ families.

## 10. "Pristine zone" between the 5:2 and 7:3 resonances

We now focus on the zone between the 5:2 and 7:3 mean-motion resonances, with $a_\mathrm{p} = 2.825$ to 2.955 AU, which is not as populated as the surrounding regions of the main belt (see Fig. 1). This is a unique situation, because both bounding resonances are strong enough to prevent any asteroids from outside to enter this zone owing the Yarkovsky semimajor axis drift. Any family formation event in the surroundings has only a minor influence on this narrow region. It thus can be called "pristine zone" because it may resemble the belt prior to creation of big asteroid families.

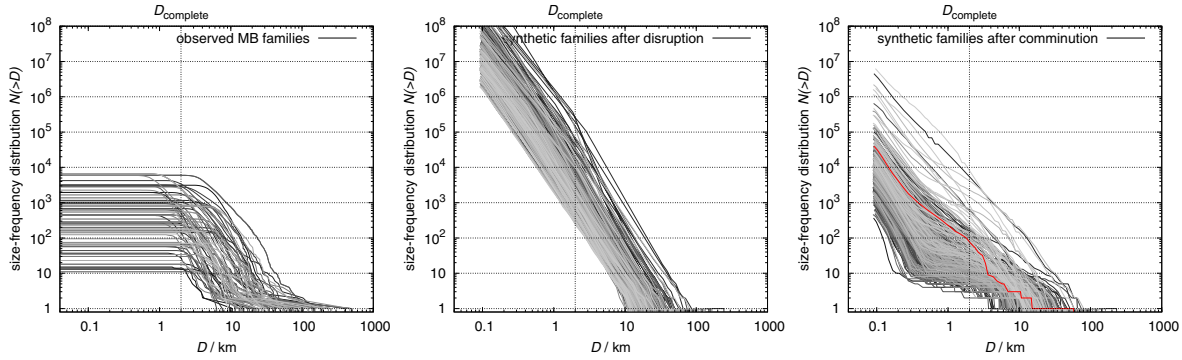


**Fig. 11.** *Left panel*: SFDs of the observed asteroid families. *Middle panel*: SFDs of 378 distinct synthetic families created during one of the collisional simulations of the MB and comets. Initially, all synthetic SFDs are very steep, in agreement with SPH simulations (Durda et al. 2007). We plot only the SFDs that fulfil the following criteria: $D_{\rm PB} \geq 50$ km, $D_{\rm LF} \geq 10$ km, LR/PB $< 0.5$ (i.e. catastrophic disruptions). *Right panel*: the evolved SFDs after comminution. Only a minority of families are observable now, since the number of remaining members larger than the observational limit $D_{\rm limit} \simeq 2$ km is often much smaller than 100. The SFD that we use for the simulation in Sect. 10 is denoted by red.

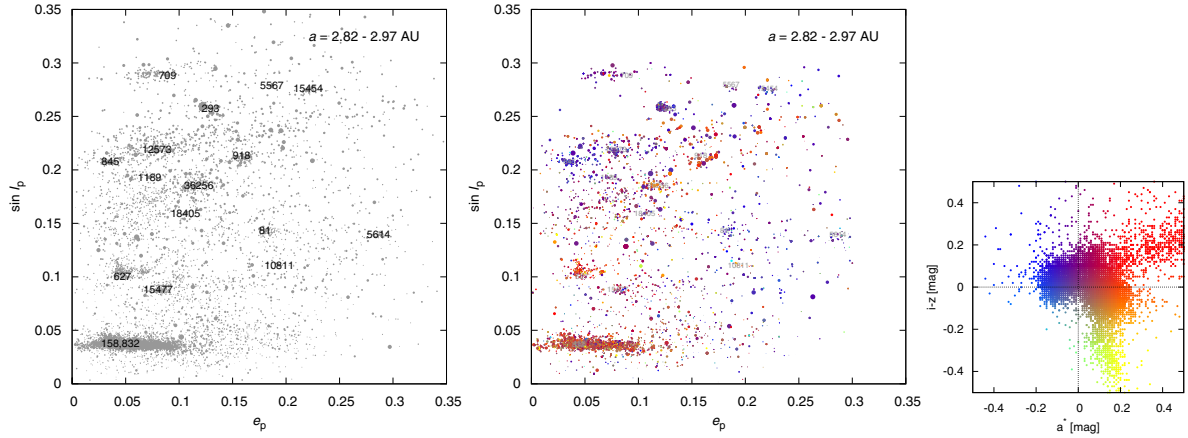


**Fig. 12.** "Pristine zone" of the main belt ($a_{\rm p} = 2.825$ to 2.955 AU) displayed on the proper eccentricity $e_{\rm p}$ vs. proper inclination $\sin I_{\rm p}$ plot. *Left panel*: the sizes of symbols correspond to the sizes of asteroids, the families are denoted by designations. *Right panel*: a subset of bodies for which SDSS data are available; the colours of symbols correspond to the SDSS colour indices $a^*$ and $i - z$ (Parker et al. 2008).

We identified nine previously unknown small families that are visible on the $(e_{\rm p}, \sin I_{\rm p})$ plot (see Fig. 12). They are confirmed by the SDSS colours and WISE albedos, too. Nevertheless, there is only one big and old family in this zone ($D_{\rm PB} \geq 100$ km), i.e. Koronis.

That at most one LHB family (Koronis) is observed in the "pristine zone" can give us a simple probabilistic estimate for the maximum number of disruptions during the LHB. We take the 192 existing main belt bodies which have $D \geq 100$ km and select randomly 100 of them that will break apart. We repeat this selection 1000 times and always count the number of families in the pristine zone. The resulting histogram is shown in Fig. 13. As we can see, there is very low (<0.001) probability that the number of families in the pristine zone is zero or one. On average we get eight families there, i.e. about half of the 16 asteroids with $D \geq 100$ km present in this zone. It seems that either the number of disruptions should be substantially lower than 100 or we expect to find at least some "remnants" of the LHB families here.

It is interesting that the SFD of an old comminutioned family is very flat in the range $D = 1$ to 10 km (see Fig. 11) – similar to those of some of the "less certain" observed families! We may speculate that the families like (918) Itha, (5567) Durisen,

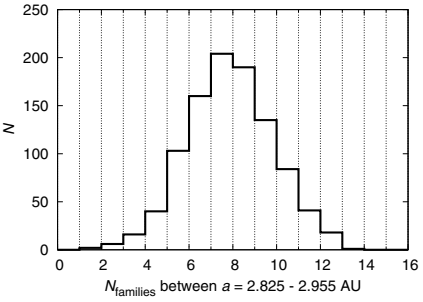


**Fig. 13.** Histogram for the expected number of LHB families located in the "pristine zone" of the main belt.

(12573) 1999 $NJ_{53}$, or (15454) 1998 $YB_3$ (all from the pristine zone) are actually remnants of larger and older families, even though they are denoted as young. It may be that the age estimate based on the $(a_{\rm p}, H)$ analysis is incorrect since small bodies were destroyed by comminution and spread by the Yarkovsky effect too far away from the largest remnant, so they can no longer be identified with the family.

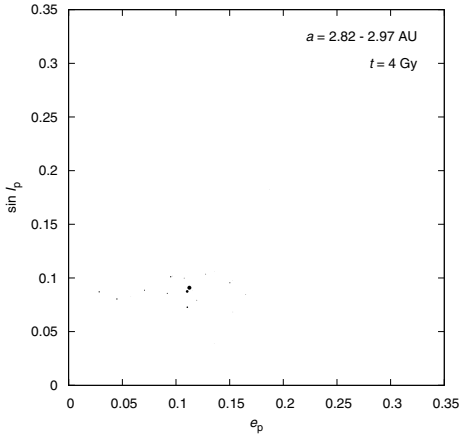


**Fig. 14.** Proper eccentricity vs. proper inclination of one synthetic old/comminutioned family evolved dynamically over 4 Gyr. Only a few family members ($N \simeq 10^1$) remained from the original number of $N(D \geq 2\,\mathrm{km}) \simeq 10^2$. The scales are the same as in Fig. 12, so we can compare it easily to the "pristine zone".

Finally, we have to ask an important question: what does an old/comminutioned family with $D_{\mathrm{PB}} \simeq 100$ km look like in proper-element space? To this aim, we created a synthetic family in the "pristine zone", and assumed the family has $N_{\mathrm{members}} \simeq 100$ larger than $D_{\mathrm{limit}} \simeq 2$ km and that the SFD is already flat in the $D = 1$ to 10 km range. We evolved the asteroids up to 4 Gyr due to the Yarkovsky effect and gravitational perturbations, using the $N$-body integrator as in Sect. 6. Most of the $D \simeq 2$ km bodies were lost in the course of the dynamical evolution, of course. The resulting family is shown in Fig. 14. We can also imagine that this family is placed in the pristine zone among other observed families, to get a feeling of whether it is easily observed or not (refer to Fig. 12).

It is clear that such family is hardly observable even in the almost empty zone of the main belt! Our conclusion is that the comminution (as given by the Boulder code) can explain the paucity of $D_{\mathrm{PB}} \simeq 100$ km LHB families, since we can hardly distinguish old families from the background.

## 11. Conclusions

In this paper we investigated the cometary bombardment of the asteroid belt at the time of the LHB, in the framework of the Nice model. There is much evidence of a high cometary flux through the giant planet region, but no strong evidence of a cometary bombardment on the Moon. This suggests that many comets broke up on their way to the inner solar system. By investigating the collisional evolution of the asteroid belt and comparing the results to the collection of actual collisional families, our aim was to constrain whether the asteroid belt experienced an intense cometary bombardment at the time of the LHB and, if possible, constrain the intensity of this bombardment.

Observations suggest that the number of collisional families is a very shallow function of parent-body size (that we call in this paper the "production function"). We show that the collisional activity of the asteroid belt as a closed system, i.e. without any external cometary bombardment, in general does not produce such a shallow production function. Moreover, the number of families with parent bodies larger than 200 km in diameter is in general too small compared to the observations. However, there is a lot of stochasticity in the collisional evolution of the asteroid belt, and about 5% of our simulations actually fit the observational constraints (shallowness of the production function and number of large families) quite well. Thus, in principle, there is no need for a bombardment due to external agents (i.e. the comets) to explain the asteroid family collection, provided that the real collisional evolution of the main belt was a "lucky" one and not the "average" one.

If one accounts for the bombardment provided by the comets crossing the main belt at the LHB time, predicted by the Nice model, one can easily justify the number of observed families with parent bodies larger than 200 km. However, the resulting production function is steep, and the number of families produced by parent bodies of 100 km is almost an order of magnitude too large.

We have investigated several processes that may decimate the number of families identifiable today with 100 km parent bodies, without considerably affecting the survival of families formed from larger parent bodies. Of all these processes, the collisional comminution of the families and their dispersal by the Yarkovsky effect are the most effective ones. Provided that the physical disruption of comets due to activity reduced the effective cometary flux through the belt by a factor of ≈5, the resulting distribution of families (and consequently the Nice model) is consistent with observations.

To better quantify the effects of various cometary-disruption laws, we computed the numbers of asteroid families for different critical perihelion distances $q_{\mathrm{crit}}$ and for different disruption probabilities $p_{\mathrm{crit}}$ of comets during a given time step ($\Delta t = 500$ yr in our case). The results are summarised in Fig. 15. Provided that comets are disrupted frequently enough, namely the critical perihelion distance has to be at least $q_{\mathrm{crit}} \gtrsim 1$ AU, while the probability of disruption is $p_{\mathrm{crit}} = 1$, the number of $D_{\mathrm{PB}} \geq 100$ km families drops by the aforementioned factor of ≈5. Alternatively, $q_{\mathrm{crit}}$ may be larger, but then comets have to survive multiple perihelion passages (i.e. $p_{\mathrm{crit}}$ have to be lower than 1). It would be very useful to test these conditions by independent models of the evolution and physical disruptions of comets. Such additional constraints on cometary-disruption laws would then enable study of the original SFD of the cometary disk in more detail.

We can also think of two "alternative" explanations: i) physical lifetime of comets was strongly size-dependent so that smaller bodies break up easily compared to bigger ones; ii) high-velocity collisions between hard targets (asteroids) and very weak projectiles (comets) may result in different outcomes than in low-velocity regimes explored so far. Our work thus may also serve as a motivation for further SPH simulations.

We finally emphasize that any collisional/dynamical models of the main asteroid belt would benefit from the following advances:

i) determination of reliable masses of asteroids of various classes. This may be at least partly achieved by the *Gaia* mission in the near future. Using up-to-date sizes and shape models (volumes) of asteroids one can then derive their densities, which are directly related to ages of asteroid families.
ii) Development of methods for identifying asteroid families and possibly targeted observations of larger asteroids addressing their membership, which is sometimes critical for constructing SFDs and for estimating parent-body sizes.
iii) An extension of the SHP simulations for both smaller and larger targets, to assure that the scaling we use now is valid. Studies and laboratory measurements of equations of states for different materials (e.g. cometary-like, porous) are closely related to this issue.

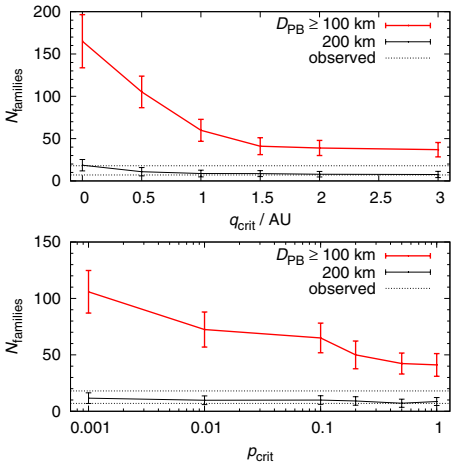


**Fig. 15.** Numbers of collisional families for different critical perihelion distances $q_{crit}$ at which comets break up and disruption probabilities $p_{crit}$ during one time step ($\Delta t$ = 500 yr). In the *top panel*, we vary $q_{crit}$ while keeping $p_{crit}$ = 1 constant. In the *bottom panel*, $q_{crit}$ = 1.5 AU is constant and we vary $p_{crit}$. We always show the number of catastrophic disruptions with parent-body sizes $D_{PB} \geq 100$ km (red line) and 200 km (black line). The error bars indicate typical (1-$\sigma$) spreads of Boulder simulations with different random seeds. The observed numbers of corresponding families are indicated by thin dotted lines.

The topics outlined above seem to be the most urgent developments to be pursued in the future.

*Acknowledgements.* The work of M.B. and D.V. has been supported by the Grant Agency of the Czech Republic (grants no. 205/08/0064, and 13-01308S) and the Research Programme MSM0021620860 of the Czech Ministry of Education. The work of W.B. and D.N. was supported by NASA's Lunar Science Institute (Center for Lunar Origin and Evolution, grant number NNA09DB32A). We also acknowledge the usage of computers of the Observatory and Planetarium in Hradec Králové. We thank Alberto Cellino for a careful review which helped to improve final version of the paper.

## References

Bendjoya, P., Cellino, A., Froeschlé, C., & Zappalà, V. 1993, A&A, 272, 651
Benz, W., & Asphaug, E. 1999, Icarus, 142, 5
Bogard, D. D. 1995, Meteoritics, 30, 244
Bogard, D. D. 2011, Chemie der Erde – Geochemistry, 71, 207
Bottke, W. F., Vokrouhlický, D., Brož, M., Nesvorný, D., & Morbidelli, A. 2001, Science, 294, 1693
Bottke, W. F., Durda, D. D., Nesvorný, D., et al. 2005, Icarus, 175, 111
Bottke, W. F., Nesvorný, D., Vokrouhlický, D., & Morbidelli, A. 2010, AJ, 139, 994
Bottke, W. F., Vokrouhlický, D., Minton, D., et al. 2012, Nature, 485, 78
Brož, M. 2006, Ph.D. Thesis, Charles University
Brož, M., Vokrouhlický, D., Morbidelli, A., Nesvorný, D., & Bottke, W. F. 2011, MNRAS, 414, 2716
Carruba, V. 2009, MNRAS, 398, 1512
Carruba, V. 2010, MNRAS, 408, 580
Carry, B. 2012, Planet. Space Sci., 73, 98
Cellino, A., Zappalà, V., di Martino, M., Farinella, P., & Paolicchi, P. 1987, Icarus, 70, 546
Chapman, C. R., Cohen, B. A., & Grinspoon, D. H. 2007, Icarus, 189, 233
Charnoz, S., Morbidelli, A., Dones, L., & Salmon, J. 2009, Icarus, 199, 413
Cohen, B. A., Swindle, T. D., & Kring, D. A. 2000, Science, 290, 1754
Dahlgren, M. 1998, A&A, 336, 1056
Durda, D. D., Bottke, W. F., Nesvorný, D., et al. 2007, Icarus, 186, 498
Foglia, S., & Masi, G., 2004, Minor Planet Bull., 31, 100
Gil-Hutton, R. 2006, Icarus, 183, 83
Gomes, R., Levison, H. F., Tsiganis, K., & Morbidelli, A. 2005, Nature, 435, 466
Hartmann, W. K., Ryder, G., Dones, L., & Grinspoon, D. 2000, in Origin of the Earth and Moon, eds. R. M. Canup, & K. Righter (Tucson: University of Arizona Press), 493
Hartmann, W. K., Quantin, C., & Mangold, N. 2007, Icarus, 186, 11
Keil, K. 2002, in Asteroids III, eds. W. F. Bottke Jr., A. Cellino, P. Paolicchi, & R. P. Binzel (Tucson: University of Arizona Press), 573
Kirchoff, M. R., & Schenk, P. 2010, Icarus, 206, 485
Knežević, Z., & Milani, A. 2003, A&A, 403, 1165
Koeberl, C. 2004, Geochim. Cosmochim. Acta, 68, 931
Kring, D. A., & Cohen, B. A. 2002, J. Geophys. Res., 107, 41
Laskar, J., & Robutel, P. 2001, Celest. Mech. Dyn. Astron., 80, 39
Levison, H. F., & Duncan, M. 1994, Icarus, 108, 18
Levison, H. F., Bottke, W. F., Gounelle, M., et al. 2009, Nature, 460, 364
Margot, J.-L., & Rojo, P. 2007, BAAS, 39, 1608
Marzari, F., Farinella, P., & Davis, D. R. 1999, Icarus, 142, 63
Masiero, J. P., Mainzer A. K., Grav, T., et al. 2011, ApJ, 741, 68
Michel, P., Tanga, P., Benz, W., & Richardson, D. C. 2002, Icarus, 160, 10
Michel, P., Jutzi, M., Richardson, D. C., & Benz, W. 2011, Icarus, 211, 535
Minton, D. A., & Malhotra, R. 2009, Nature, 457, 1109
Minton, D. A., & Malhotra, R. 2010, Icarus, 207, 744
Morbidelli, A. 2010, Comptes Rendus Phys., 11, 651
Morbidelli, A., Tsiganis, K., Crida, A., Levison, H. F., & Gomes, R. 2007, AJ, 134, 1790
Morbidelli, A., Levison, H. F., Bottke, W. F., Dones, L., & Nesvorný, D. 2009, Icarus, 202, 310
Morbidelli, A., Brasser, R., Gomes, R., Levison, H. F., & Tsiganis, K. 2010, AJ, 140, 1391
Morbidelli, A., Marchi, S., & Bottke, W. F. 2012, LPI Cont. 1649, 53
Molnar, L. A., & Haegert, M. J. 2009, BAAS, 41, 2705
Nesvorný, D. 2010, EAR-A-VARGBDET-5-NESVORNYFAM-V1.0, NASA Planetary Data System
Nesvorný, D., & Vokrouhlický, D. 2006, AJ, 132, 1950
Nesvorný, D., Morbidelli, A., Vokrouhlický, D., Bottke, W. F., & Brož, M. 2002, Icarus, 157, 155
Nesvorný, D., Jedicke, R., Whiteley, R. J., & Ivezić, Ž. 2005, Icarus, 173, 132
Nesvorný, D., Vokrouhlický, D., & Morbidelli, A. 2007, AJ, 133, 1962
Nesvorný, D., Vokrouhlický, D., Morbidelli, A., & Bottke, W. F. 2009, Icarus, 200, 698
Neukum, G., Ivanov, B. A., & Hartmann, W. K. 2001, Space Sci. Rev., 96, 55
Norman, M. D., & Nemchin, A. A. 2012, LPI Cont., 1659, 1368
Novaković, B. 2010, MNRAS, 407, 1477
Novaković, B., Tsiganis, K., & Knežević, Z. 2010, Celest. Mech. Dyn. Astron., 107, 35
Novaković, B., Cellino, A., & Knežević, Z. 2011, Icarus, 216, 69
Parker, A., Ivezić, Ž., Jurić, M., et al. 2008, Icarus, 198, 138
Ryder, G., Koeberl, C., & Mojzsis, S. J. 2000, in Origin of the Earth and Moon, eds. R. M. Canup, & K. Righter (Tucson: University of Arizona Press), 475
Sheppard, S. S., & Trujillo, C. A. 2010, ApJ, 723, L233
Strom, R. G., Malhotra, R., Ito, T., Yoshida, F., & Kring, D. A. 2005, Science, 309, 1847
Swindle, T. D., Isachsen, C. E., Weirich, J. R., & Kring, D. A. 2009, Meteor. Planet. Sci., 44, 747
Tagle, R. 2005, LPI Cont., 36, 2008
Tanga, P., Cellino, A., Michel, P., et al. 1999, Icarus, 141, 65
Tedesco, E. F., Noah, P. V., Noah, M., & Price, S. D. 2002, AJ, 123, 1056
Tera, F., Papanastassiou, D. A., & Wasserburg, G. J. 1974, Earth Planet. Sci. Lett., 22, 1
Tsiganis, K., Gomes, R., Morbidelli, A., & Levison, H. F. 2005, Nature, 435, 459
Thomas, P. C., Binzel, R. P., Gaffey, M. J., et al. 1997, Science, 277, 1492
Vokrouhlický, D., & Nesvorný, D. 2011, AJ, 142, 26
Vokrouhlický, D., Brož, M., Bottke, W. F., Nesvorný, D., & Morbidelli, A. 2006, Icarus, 182, 118
Vokrouhlický, D., Nesvorný, D., & Levison, H. F. 2008, AJ, 136, 1463
Vokrouhlický, D., Nesvorný, D., Bottke, W. F., & Morbidelli, A. 2010, AJ, 139, 2148
Warner, B. D., Harris, A. W., Vokrouhlický, D., Nesvorný, D., & Bottke, W. F. 2009, Icarus, 204, 172
Weidenschilling, S. J. 2000, Space Sci. Rev., 92, 295
Zappalà, V., Bendjoya, Ph., Cellino, A., Farinella, P., & Froeschlé, C. 1995, Icarus, 116, 291

Pages 14 to 16 are available in the electronic edition of the journal at http://www.aanda.org

**Table 1.** A list of asteroid families and their physical parameters.

| Designation | | $v_{cutoff}$ m/s | $N$ | $p_V$ | Tax. | $D_{PB}$ km | $D_{Durda}$ km | LR/PB | $v_{esc}$ m/s | $q_1$ | $q_2$ | Age Gyr | Notes, references |
|---|---|---|---|---|---|---|---|---|---|---|---|---|---|
| 3 | Juno | 50 | 449 | 0.250 | S | 233 | ? | 0.999 | 139 | −4.9 | −3.2 | <0.7 | cratering, Nesvorný et al. (2005) |
| 4 | Vesta | 60 | 11 169 | 0.351w | V | 530 | 425! | 0.995 | 314 | −4.5 | −2.9 | 1.0 ± 0.25 | cratering, Marchi et al. (2012) |
| 8 | Flora | 60 | 5284 | 0.304w | S | 150c | 160 | 0.81–0.68 | 88 | −3.4 | −2.9 | 1.0 ± 0.5 | cut by $\nu_6$ resonance, LL chondrites |
| 10 | Hygiea | 70 | 3122 | 0.055 | C,B | 410 | 442 | 0.976–0.78 | 243 | −4.2 | −3.2 | 2.0 ± 1.0 | LHB? cratering |
| 15 | Eunomia | 50 | 2867 | 0.187 | S | 259 | 292 | 0.958–0.66 | 153 | −5.6 | −2.3 | 2.5 ± 0.5 | LHB? Michel et al. (2002) |
| 20 | Massalia | 40 | 2980 | 0.215 | S | 146 | 144 | 0.995 | 86 | −5.0 | −3.0 | 0.3 ± 0.1 | |
| 24 | Themis | 70 | 3581 | 0.066 | C | 268c | 380–430! | 0.43–0.09 | 158 | −2.7 | −2.4 | 2.5 ± 1.0 | LHB? |
| 44 | Nysa (Polana) | 60 | 9957 | 0.278w | S | 81c | ? | 0.65 | 48 | −6.9 | −2.6(0.5) | <1.5 | overlaps with the Polana family |
| 46 | Hestia | 65 | 95 | 0.053 | S | 124 | 153 | 0.992–0.53 | 74 | −3.3 | −2.0 | <0.2 | cratering, close to J3/1 resonance |
| 87 | Sylvia | 110 | 71 | 0.045 | C/X | 261 | 272 | 0.994–0.88 | 154 | −5.2 | −2.4 | 1.0–3.8 | LHB? cratering, Vokrouhlický et al. (2010) |
| 128 | Nemesis | 60 | 654 | 0.052 | C | 189 | 197 | 0.987–0.87 | 112 | −3.4 | −3.3 | 0.2 ± 0.1 | |
| 137 | Meliboea | 95 | 199 | 0.054 | C | 174c | 240–290! | 0.59–0.20 | 102 | −1.9 | −1.8 | <3.0 | old? |
| 142 | Polana (Nysa) | 60 | 3443 | 0.055w | C | 75 | ? | 0.42 | 45 | −7.0 | −3.6 | <1.5 | overlaps with Nysa |
| 145 | Adeona | 50 | 1161 | 0.065 | C | 171c | 185 | 0.69–0.54 | 101 | −5.2 | −2.8 | 0.7 ± 0.5 | cut by J5/2 resonance |
| 158 | Koronis | 50 | 4225 | 0.147 | S | 122c | 170-180 | 0.024–0.009 | 68 | −3.6(0.3) | −2.3 | 2.5 ± 1.0 | LHB? |
| 163 | Erigone | 60 | 1059 | 0.056 | C/X | 79 | 114 | 0.79–0.26 | 46 | ? | −3.6 | 0.3 ± 0.2 | |
| 170 | Maria | 80 | 3094 | 0.249w | S | 107c | 120-130 | 0.070–0.048 | 63 | −2.5(0.3) | −2.8 | 3.0 ± 1.0 | LHB? |
| 221 | Eos | 50 | 5976 | 0.130 | K | 208c | 381! | 0.13–0.020 | 123 | −3.5 | −2.1 | 1.3 ± 0.2 | |
| 283 | Emma | 75 | 345 | 0.050 | – | 152 | 185 | 0.92–0.51 | 90 | ? | −3.2 | <1.0 | satellite |
| 293 | Brasilia | 60 | 282 | 0.175w | C/X | 34 | ? | 0.020 | 20 | −1.4(0.5) | −3.7 | 0.05 ± 0.04 | (293) is interloper |
| 363 | Padua (Lydia) | 50 | 596 | 0.097 | C/X | 76 | 106 | 0.045–0.017 | 45 | −1.8 | −3.0 | 0.3 ± 0.2 | |
| 396 | Aeolia | 20 | 124 | 0.171 | C/X | 35 | 39 | 0.966–0.70 | 20 | ? | −4.3 | <0.1 | cratering |
| 410 | Chloris | 90 | 259 | 0.057 | C | 126c | 154 | 0.952–0.52 | 74 | ? | −2.1 | 0.7 ± 0.4 | |
| 490 | Veritas | – | – | – | C,P,D | – | 100–177 | – | – | – | – | 0.0083 ± 0.0005 | (490) is likely interloper (Michel et al. 2011) |
| 569 | Misa | 70 | 543 | 0.031 | C | 88c | 117 | 0.58–0.25 | 52 | −3.9 | −2.3 | 0.5 ± 0.2 | |
| 606 | Brangane | 30 | 81 | 0.102 | S | 37 | 46 | 0.92–0.48 | 22 | ? | −3.8 | 0.05 ± 0.04 | |
| 668 | Dora | 50 | 837 | 0.054 | C | 85 | 165! | 0.031–0.004 | 50 | −4.2 | −1.9 | 0.5 ± 0.2 | |
| 808 | Merxia | 50 | 549 | 0.227 | S | 37 | 121! | 0.66–0.018 | 22 | −2.7 | −3.4 | 0.3 ± 0.2 | |
| 832 | Karin | – | – | – | S | – | 40 | – | – | – | – | 0.0058 ± 0.0002 | |
| 845 | Naema | 30 | 173 | 0.081 | C | 77c | 81 | 0.35–0.30 | 46 | −5.2 | −2.9 | 0.1 ± 0.05 | |
| 847 | Agnia | 40 | 1077 | 0.177 | S | 39 | 61 | 0.38–0.10 | 23 | −2.8 | −3.1 | 0.2 ± 0.1 | |
| 1128 | Astrid | 50 | 265 | 0.079 | C | 43c | ? | 0.52 | 25 | −1.7 | −2.6 | 0.1 ± 0.05 | |
| 1272 | Gefion | 60 | 19 477 | 0.20 | S | 74c | 100–150! | 0.001–0.004 | 60 | −4.3 | −2.5 | 0.48 ± 0.05 | Nesvorný et al. (2009), L chondrites |
| 1400 | Tirela | 80 | 1001 | 0.070 | S | 86 | – | 0.12 | 86 | −4.2 | −3.4 | <1.0 | |
| 1658 | Innes | 70 | 621 | 0.246w | S | 27 | ? | 0.14 | 16 | −4.9 | −3.5 | <0.7 | (1644) Rafita is interloper |
| 1726 | Hoffmeister | 40 | 822 | 0.035 | C | 93c | 134 | 0.022–0.007 | 55 | −4.5 | −2.7 | 0.3 ± 0.2 | |
| 3556 | Lixiaohua | 60 | 439 | 0.044w | C/X | 62 | 220! | 0.029–0.001 | 35 | −6.1 | −3.3 | 0.15 ± 0.05 | Novaković et al. (2010) |
| 3815 | Konig | 60 | 177 | 0.044 | C | 33 | ? | 0.32 | 20 | ? | −3.0 | <0.1 | (1639) Bower is interloper |
| 4652 | Iannini | – | – | – | S | – | – | – | – | – | – | 0.005 ± 0.005 | |

**Notes.** There are the following columns: $v_{cutoff}$ is the selected cut–off velocity for the hierarchical clustering, $N$ the corresponding number of family members, $p_V$ the adopted value of the geometric albedo for family members which do not have measured diameters (from Tedesco et al. 2002 or Masiero et al. 2011, a letter "w" indicates it was necessary to use the WISE data to obtain median/mean albedo), taxonomic classification (according to the Sloan DSS MOC 4 colours, Parker et al. 2008), $D_{PB}$ parent body size, an additional "c" letter indicates that we prolonged the SFD slope down to zero $D$ (a typical uncertainty is 10%), $D_{Durda}$ PB size inferred from SPH simulations (Durda et al. 2007), an exclamation mark denotes a significant mismatch with $D_{PB}$, LR/PB the ratio of the volumes of the largest remnant to the parent body (an uncertainty corresponds to the last figure, a range is given if both $D_{PB}$ and $D_{Durda}$ are known), $v_{esc}$ the escape velocity, $q_1$ the slope of the SFD for larger $D$, $q_2$ the slope for smaller $D$ (a typical uncertainty of the slopes is 0.2, if not indicated otherwise), dynamical age including its uncertainty.

**Table 1.** continued.

| Designation | | $v_{cutoff}$ m/s | $N$ | $p_V$ | Tax. | $D_{PB}$ km | $D_{Durda}$ km | LR/PB | $v_{esc}$ m/s | $q_1$ | $q_2$ | Age Gyr | Notes, references |
|---|---|---|---|---|---|---|---|---|---|---|---|---|---|
| 9506 | Telramund | 40 | 146 | 0.217w | S | 22 | – | 0.05 | 13 | −3.9 | −3.7 | <0.5 | |
| 18 405 | 1993 $FY_{12}$ | 50 | 44 | 0.171w | C/X | 15 | – | 0.23 | 15 | −2.4 | −2.4 | <0.2 | cut by J5/2 resonance |
| 158 | $Koronis_{(2)}$ | – | – | – | S | 35 | – | – | – | – | – | 0.015 ± 0.005 | cratering, Molnar & Haegert (2009) |
| 298 | Baptistina | 50 | 1249 | 0.160w | C/X | 35c | – | 0.17 | 21 | −3.6 | −2.4 | <0.3 | overlaps with the Flora family |
| 434 | Hungaria | 200 | 4598 | 0.35 | E | 25 | – | 0.15 | 15 | −5.9 | −3.1 | 0.5 ± 0.2 | Warner et al. (2010) |
| 627 | Charis | 80 | 235 | 0.081 | S | >60 | – | 0.53 | 35 | ? | −3.4 | <1.0 | |
| 778 | Theobalda | 85 | 154 | 0.060 | C | 97c | – | 0.29 | 57 | ? | −2.9 | 0.007 ± 0.002 | cratering, Novaković (2010) |
| 302 | Clarissa | 30 | 75 | 0.054 | C | 39 | – | 0.96 | 23 | ? | −3.1 | <0.1 | cratering, Nesvorný (2010) |
| 656 | Beagle | 24 | 63 | 0.089 | C | 64 | – | 0.56 | 38 | −1.3 | −1.4 | <0.2 | |
| 752 | Sulamitis | 60 | 191 | 0.042 | C | 65 | – | 0.83 | 39 | −6.5 | −2.3 | <0.4 | |
| 1189 | Terentia | 50 | 18 | 0.070 | C | 56 | – | 0.990 | 33 | ? | −2.6? | <0.2 | cratering |
| 1892 | Lucienne | 100 | 57 | 0.223w | S | 14 | – | 0.71 | 8 | ? | −4.4 | <0.3 | |
| 7353 | Kazvia | 50 | 23 | 0.206w | S | 16 | – | 0.57 | 8 | ? | −1.8 | <0.1 | |
| 10 811 | Lau | 100 | 15 | 0.273w | S | 11 | – | 0.77 | 5 | ? | −2.8 | <0.1 | |
| 18 466 | 1995 $SU_{37}$ | 40 | 71 | 0.241w | S | 14 | – | 0.045 | 7 | ? | −5.0 | <0.3 | |
| 1270 | Datura | – | – | – | S | – | – | – | – | – | – | 0.00045–0.00060 | identified in osculating-element space, |
| 14 627 | Emilkowalski | – | – | – | C/X | – | – | – | – | – | – | 0.00019–0.00025 | Nesvorný & Vokrouhlický (2006) |
| 16 598 | 1992 $YC_2$ | – | – | – | S | – | – | – | – | – | – | 0.00005–0.00025 | |
| 21 509 | Lucascavin | – | – | – | S | – | – | – | – | – | – | 0.0003–0.0008 | |
| 2384 | Schulhof | – | – | – | S | – | – | – | – | – | – | 0.0007–0.0009 | Vokrouhlický & Nesvorný (2011) |
| 27 | Euterpe | 70 | 268 | 0.260w | S | 118c | – | 0.998 | 70 | −2.9 | −2.2 | <1.0 | cratering, Parker et al. (2008) |
| 375 | Ursula | 80 | 777 | 0.057w | C | 203c | 240–280 | 0.71–0.43 | 120 | −4.1 | −2.3 | <3.5 | old? |
| 1044 | Teutonia | 50 | 1950 | 0.343 | S | 27–120 | – | 0.17–0.98 | 16–71 | −3.5 | −3.9 | <0.5 | depends on (5) Astraea membership |
| 1296 | Andree | 60 | 401 | 0.290w | S | 17–74 | – | 0.010–0.95 | 10–43 | ? | −2.9(0.5) | <1.0 | depends on (79) Eurynome membership |
| 2007 | McCuskey | 34 | 236 | 0.06 | C | 29 | – | 0.41 | 17 | ? | −5.6 | <0.5 | overlaps with Nysa/Polana |
| 2085 | Henan | 54 | 946 | 0.200w | S | 27 | – | 0.13 | 16 | −4.2 | −3.2 | <1.0 | |
| 2262 | Mitidika | 83 | 410 | 0.064w | C | 49-79c | – | 0.037–0.81 | 26–46 | −4.5 | −2.2 | <1.0 | depends on (785) Zwetana membership, (2262) is interloper, overlaps with Juno |
| 2 | Pallas | 200 | 64 | 0.163 | B | 498c | – | 0.9996 | 295 | ? | −2.2 | <0.5 | high-$I$, Carruba (2010) |
| 25 | Phocaea | 160 | 1370 | 0.22 | S | 92 | – | 0.54 | 55 | −3.1 | −2.4 | <2.2 | old? high-$I/e$, cut by $\nu_6$ resonance, Carruba (2009) |
| 148 | Gallia | 150 | 57 | 0.169 | S | 98 | – | 0.058 | 58 | ? | −3.6 | <0.45 | high-$I$ |
| 480 | Hansa | 150 | 651 | 0.256 | S | 60 | – | 0.83 | 35 | −4.9 | −3.2 | <1.6 | high-$I$ |
| 686 | Gersuind | 130 | 178 | 0.146 | S | 52c | – | 0.48 | 40 | ? | −2.7 | <0.8 | high-$I$, Gil-Hutton (2006) |
| 945 | Barcelona | 110 | 129 | 0.248 | S | 28 | – | 0.77 | 16 | ? | −3.5 | <0.35 | high-$I$, Foglia & Masi (2004) |
| 1222 | Tina | 110 | 37 | 0.338 | S | 21 | – | 0.94 | 12 | ? | −4.1 | <0.15 | high-$I$ |
| 4203 | Brucato | – | – | – | – | – | – | – | – | – | – | <1.3 | in frequency space |
| 31 | Euphrosyne | 100 | 851 | 0.056 | C | 259 | – | 0.97 | 153 | −4.9 | −3.9 | <1.5 | cratering, high-$I$, Foglia & Massi (2004) |
| 702 | Alauda | 120 | 791 | 0.070 | B | 218c | 290-330! | 0.025 | 129 | −3.9 | −2.4 | <3.5 | old? high-$I$, cut by J2/1 resonance, satellite (Margot & Rojo 2007) |
| 107 | Camilla | ? | ? | 0.054 | – | >226 | ? | ? | ? | ? | ? | 3.8? | LHB? Cybele region, non-existent today, |
| 121 | Hermione | ? | ? | 0.058 | – | >209 | ? | ? | ? | ? | ? | 3.8? | LHB? Vokrouhlický et al. (2010) |

**Table 1.** continued.

| Designation | | $v_{cutoff}$ m/s | $N$ | $p_V$ | Tax. | $D_{PB}$ km | $D_{Durda}$ km | LR/PB | $v_{esc}$ m/s | $q_1$ | $q_2$ | Age Gyr | Notes, references |
|---|---|---|---|---|---|---|---|---|---|---|---|---|---|
| 1303 | Luthera | 100 | 142 | 0.043 | X | 92 | – | 0.81 | 54 | −3.9 | −2.7 | <0.5 | above (375) Ursula |
| 1547 | Nele | 20 | 57 | 0.311w | X | 19 | – | 0.85 | 11 | ? | −2.8(0.3) | <0.04 | close to (3) Juno |
| 2732 | Witt | 60 | 985 | 0.260w | S | 25 | – | 0.082 | 15 | −4.0(0.3) | −3.8 | <1.0 | only part with $\sin I > 0.099$, above (363) Padua |
| 81 | Terpsichore | 120 | 70 | 0.052 | C | 119 | – | 0.993 | 71 | ? | −4.4 | <0.5 | cratering, less-certain families in the "pristine zone" |
| 709 | Fringilla | 140 | 60 | 0.047 | X | 99c | 130-140 | 0.93–0.41 | 59 | −6.2 | −1.7 | <2.5 | old? |
| 918 | Itha | 140 | 63 | 0.23 | S | 38 | – | 0.16 | 22 | −2.7 | −1.5 | <1.5 | shallow SFD |
| 5567 | Durisen | 100 | 18 | 0.044w | X | 42 | – | 0.89 | 25 | ? | −1.7 | <0.5 | shallow SFD |
| 5614 | Yakovlev | 100 | 34 | 0.05 | C | 22 | – | 0.28 | 13 | ? | −3.2 | <0.2 | |
| 12 573 | 1999 $NJ_{53}$ | 40 | 13 | 0.190w | C | 15 | – | 0.13 | 9 | ? | −2.0(0.5) | <0.6 | incomplete SFD |
| 15 454 | 1998 $YB_3$ | 50 | 14 | 0.054w | C | 21 | – | 0.41 | 13 | ? | −1.6(0.3) | <0.5 | shallow SFD |
| 15 477 | 1999 $CG_1$ | 110 | 144 | 0.098w | S | 25 | – | 0.065 | 14 | ? | −4.6(0.5) | <1.5 | |
| 36 256 | 1999 $XT_{17}$ | 60 | 30 | 0.210w | S | 17 | – | 0.037 | 10 | ? | −1.4(0.5) | <0.3 | shallow SFD |

Icarus 223 (2013) 844–849

Contents lists available at SciVerse ScienceDirect

Icarus

journal homepage: www.elsevier.com/locate/icarus

# The Eos family halo

M. Brož [a,*], A. Morbidelli [b]

[a] Institute of Astronomy, Charles University, Prague, V Holešovičkách 2, 18000 Prague 8, Czech Republic
[b] Observatoire de la Côte d'Azur, BP 4229, 06304 Nice Cedex 4, France

ARTICLE INFO

*Article history:*
Received 5 November 2012
Revised 6 February 2013
Accepted 6 February 2013
Available online 14 February 2013

*Keywords:*
Asteroids, Dynamics
Resonances, Orbital
Planets, Migration

ABSTRACT

We study K-type asteroids in the broad surroundings of the Eos family because they seem to be intimately related, according to their colours measured by the Sloan Digital Sky Survey. Such 'halos' of asteroid families have been rarely used as constraints for dynamical studies to date. We explain its origin as bodies escaping from the family 'core' due to the Yarkovsky semimajor-axis drift and interactions with gravitational resonances, mostly with the 9/4 mean-motion resonance with Jupiter at 3.03 AU. Our *N*-body dynamical model allows us to independently estimate the age of the family 1.5–1.9 Gyr. This is approximately in agreement with the previous age estimate by Vokrouhlický et al. (2006) based on a simplified model (which accounts only for changes of semimajor axis). We can also constrain the geometry of the disruption event which had to occur at the true anomaly $f \simeq 120$–$180°$.



## 1. Introduction

The Eos family is one of the best-studied families in the main asteroid belt. Although we do not attempt to repeat a thorough review presented in our previous paper Vokrouhlický et al. (2006), we recall that the basic structure of the family is the following: (i) there is a sharp inner boundary coinciding with the 7/3 mean-motion resonance with Jupiter at approximately 2.96 AU; (ii) the 9/4 mean-motion resonance with Jupiter divides the family at 3.03 AU and asteroids with larger sizes are less numerous at larger semimajor axes; (iii) there is an extension of the family along the $z_1$ - $\equiv g - g_6 + s - s_6$ secular resonance towards lower values of proper semimajor axis $a_p$, eccentricity $e_p$ and inclination $\sin I_p$. All these fact seem to be determined by the interaction between the orbits drifting due to the Yarkovsky effect in semimajor axis and the gravitational resonances which may affect eccentricities and inclinations.

In this work, we focus on a 'halo' of asteroids around the nominal Eos family which is clearly visible in the Sloan Digital Sky Survey, Moving Object Catalogue version 4 (SDSS, Parker et al., 2008). As we shall see below, both the 'halo' and the family have the same SDSS colours and are thus most likely related to each other. Luckily, the Eos family seems to be spectrally distinct in this part of the main belt (several Eos family members were classified as K-types by DeMeo et al. (2009)) and it falls in between S-complex and C/X-complex asteroids in terms of the SDSS colour indices. Detailed spectroscopic observations were also performed by Zappalà et al. (2000) which confirmed that asteroids are escaping from the Eos family due to the interaction with the J9/4 resonance.

Our main motivation is to understand the origin of the whole halo and to explain its unusually large spread in eccentricity and inclination which is hard to reconcile with any reasonable initial velocity field. Essentially, this is a substantial extension of work of Vokrouhlický et al. (2006), but here we are interested in bodies which *escaped* from the nominal family.

We were also curious if such halos may be somehow related to the giant-planet migration which would have caused significant gravitational perturbations of all small-body populations (Morbidelli et al., 2005). Of course, in such a case the process is *size-independent* and moreover the age of the corresponding family would have to approach 3.9 Gyr in order to match the Nice model of giant-planet migration.

In Section 2, we define the Eos halo and core populations. Section 3 is devoted to a description of our dynamical model and to a comparison with the SDSS observations. We discuss consequences of our results in Section 4.

## 2. A discernment of the family core and halo

In this section, we proceed as follows: (i) we use a hierarchical clustering method to extract the nominal Eos family; (ii) we look at the members of the family with SDSS colours and we define a colour range; (iii) we select all asteroids with Eos-like colours from the SDSS catalogue; finally, (iv) we define a halo and core using simple 'boxes' in the proper-element space.

### 2.1. Colours of Eos-like asteroids

We want to select asteroids similar to the Eos family, but first we have to choose a criterion to do so. We thus identify the nominal Eos family using a hierarchical clustering method (HCM,

* Corresponding author.
*E-mail addresses:* mira@sirrah.troja.mff.cuni.cz (M. Brož), morby@oca.eu (A. Morbidelli).

0019-1035/$ - see front matter © 2013 Elsevier Inc. All rights reserved.
http://dx.doi.org/10.1016/j.icarus.2013.02.002

Zappalà et al., 1995) with a suitably low cut-off velocity $v_{\rm cutoff}$ = 50 m/s (which leads to a similar extent of the family as in Vokrouhlický et al. (2006)), and extract colour data from the SDSS catalogue (see Fig. 1). The majority of Eos-family asteroids have colour indices in the following intervals:

$$a^* \in (0.0, 0.1)\ \text{mag}, \quad (1)$$
$$i - z \in (-0.03, 0.08)\ \text{mag}, \quad (2)$$

which then serves as a criterion for the selection of Eos-like asteroids in the broad surroundings of the nominal family.

We also used an independent method for the selection of Eos-like asteroids employing a 1-dimensional colour index (which was used in Parker et al. (2008) to construct their colour palette) and we verified that our results are not sensitive to this procedure.

### 2.2. Boundaries in the proper element space

Next, we have to distinguish the family 'core' and 'halo' populations on the basis of proper orbital elements $(a_{\rm p}, e_{\rm p}, \sin I_{\rm p})$ which will be consistently used for both the SDSS observations and our dynamical models. We also need to define 'background' population which enables to estimate how many asteroids might have Eos-like colours by chance. We decided to use a simple box criterion (see Figs. 2, 3 and Table 1), while the range of proper semimajor axis is always the same, $a_{\rm p} \in (2.95, 3.16)$ AU.

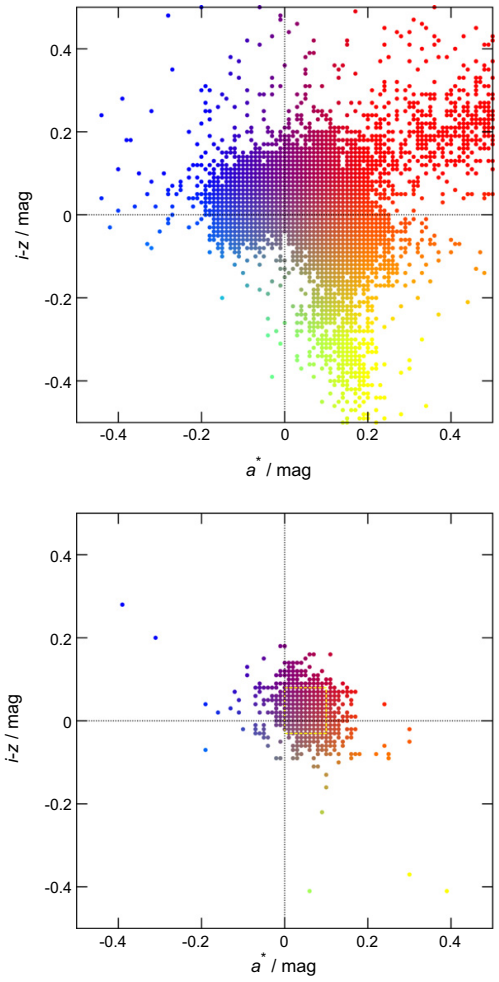


**Fig. 1.** Colour indices $i - z$ and $a^*$ (defined in Parker et al. (2008)) of all asteroids from the Sloan Digital Sky Survey, Moving Object Catalogue version 4 and the corresponding colour palette (top panel) which is used in the following figures to distinguish colours of asteroids. We also plot the Eos family members observed by the SDSS (bottom panel) with small photometric uncertainties (less than 0.03 mag). The inferred range of colour indices (denoted by the dashed yellow rectangle) is then used as a criterion for the selection of the Eos-like asteroids in the broad surroundings of the nominal family. The rectangle does not encompass the outliers. (For interpretation of the references to colour in this figure legend, the reader is referred to the web version of this article.)

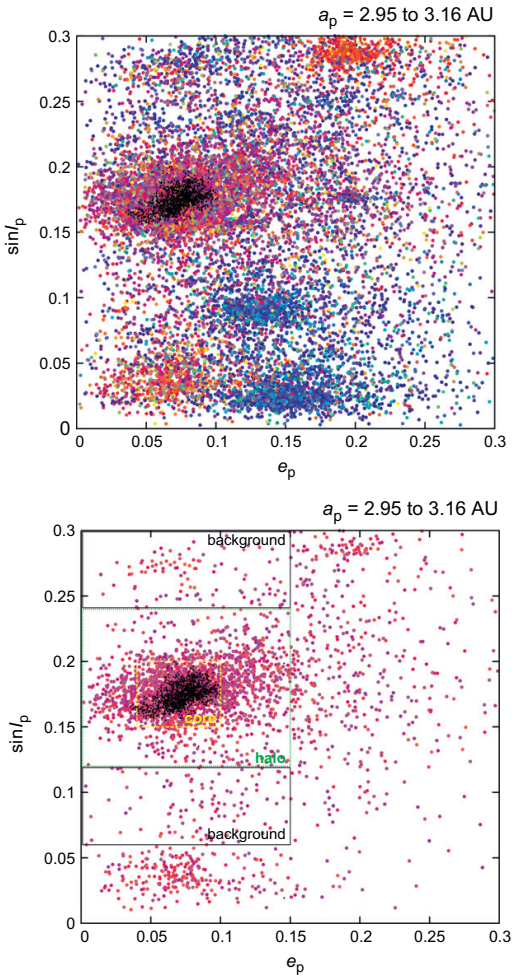


**Fig. 2.** The proper eccentricity $e_{\rm p}$ vs proper inclination $\sin I_{\rm p}$ plot for asteroids included in the SDSS MOC 4 catalogue. The proper semimajor axis is confined to the interval 2.95–3.16 AU, i.e. the Eos family zone. Colour coding corresponds to the SDSS colour indices according to Fig. 1. The top panel includes *all* asteroids (regardless of their colours). The bottom panel shows only a subset of 'Eos-like' asteroids with colours similar to those of the Eos members (see Fig. 1, bottom). Moreover, we denote a box used for the definition of the family 'core' (dashed yellow line) a larger box for the 'halo' (dotted green line) and two boxes considered as 'background' (thin black line). For comparison, we also plot positions of the nominal Eos family members (black dots), identified for the velocity $v_{\rm cutoff}$ = 50 m/s. (For interpretation of the references to colour in this figure legend, the reader is referred to the web version of this article.)

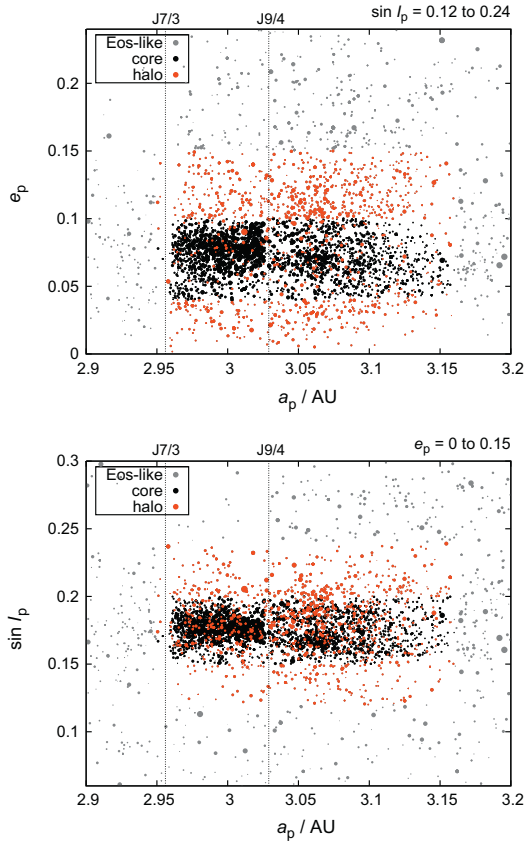


**Fig. 3.** The proper semimajor axis $a_p$ vs proper eccentricity $e_p$ (top panel) and $a_p$ vs proper inclination $\sin I_p$ (bottom panel) for the observed Eos core (black dots), halo (red dots) and remaining Eos-like asteroids (grey dots) in the surroundings. The sizes of symbols are (inversely) proportional to the absolute magnitudes $H$ of asteroids. The positions of important mean-motion resonances with Jupiter are also indicated (dotted vertical lines). (For interpretation of the references to colour in this figure legend, the reader is referred to the web version of this article.)

**Table 1**
The definitions of the core, halo and background populations in terms of intervals of proper eccentricity $e_p$ and proper inclination $\sin I_p$. The range of proper semimajor axis $a_p \in (2.95, 3.16)$ AU is the same in all cases.

| Population | $e_p$ | $\sin I_p$ | Note |
|---|---|---|---|
| Core | 0.04–0.10 | 0.15–0.20 | |
| Halo | 0.00–0.15 | 0.12–0.24 | and *not* in the core |
| Background | 0.00–0.15 | 0.06–0.12 | together with… |
| | 0.00–0.15 | 0.24–0.30 | |

Our results do not depend strongly on the selection criterion. For example, we tested a stringent definition: core was identified by the HCM at $v_{\rm cutoff} = 50$ m/s and all remaining bodies in the surroundings belong to the halo. This approach makes the core as small as possible and the halo correspondingly larger but our results below (based on halo/core ratios) would be essentially the same. According to our tests, not even a different definition of the background/halo boundary changes our results.

We are now ready to construct size–frequency distributions of individual populations. In order to convert absolute magnitudes $H$ to diameters $D$ we computed the median geometric albedo $p_V = 0.16$ from the WISE data (Masiero et al., 2011) for the nominal

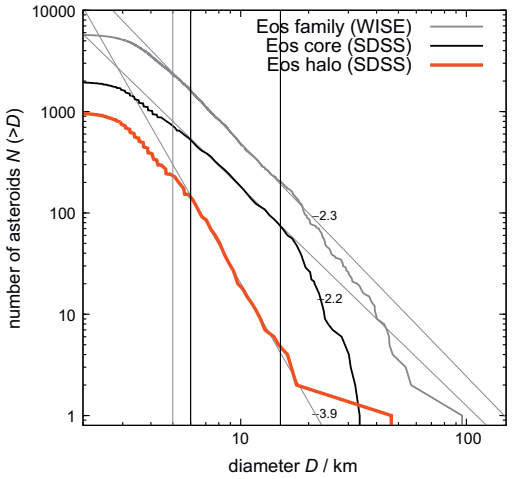


**Fig. 4.** The cumulative size–frequency distributions $N(>D)$ of the Eos core and halo. We show power-law fits and corresponding slopes $\gamma$ which clearly indicate that the halo population is significantly *steeper* than the core population. For comparison, we also plot the SFD of the nominal Eos family (as inferred from the WISE data, Masiero et al., 2011). The SFD's of the core and halo are biased because they include *only* asteroids observed by the SDSS. Consequently, the core seems to be much less populated than the nominal Eos family, even though these SFD's should be very similar. Nevertheless, the slopes and the halo/core ratios which we use in our analysis is not much affected by this bias.

Eos family members. The size–frequency distribution (Fig. 4) of the halo has a cumulative slope $N(>D) \propto D^{\gamma}$ equal to $\gamma = -3.9 \pm 0.2$ in the size range $D = 6$–$15$ km and is significantly *steeper* than that of the core ($\gamma = -2.2 \pm 0.1$). Even this difference of slopes ($1.7 \pm 0.2$) indicates that if there a process transporting asteroids from the core to the halo it must be indeed size-dependent.

A frequency analysis similar as in Carruba and Michtchenko (2007) or Carruba (2009) shows that there is approximately 5% of likely $z_1$ resonators (with the frequency $g - g_6 + s - s_6 < 0.3''$/yr) in the halo region. However, the concentration of objects inside and outside the resonance is roughly the same, so that this secular resonance does not seem to be the most important transport mechanism.

## 3. Yarkovsky-driven origin of the halo

Motivated by the differences of the observed SFD's, we now want to test a hypothesis that the Eos family halo (or at least a part of it) was created by the Yarkovsky semimajor-axis drift, which pushes objects from the core into neighbouring mean-motion resonances and consequently to the halo region.

### 3.1. Initial conditions

We prepared an $N$-body simulation of the long-term evolution of the Eos core and halo with the following initial conditions: we included the Sun and the four giant planets on current orbits. We applied a standard barycentric correction to both massive objects and test particles to prevent a substantial shift of secular frequencies (Milani and Knezevic, 1992). The total number of test particles was 6545, with sizes ranging from $D = 104$ to 1.5 km and the distribution resembling the observed SFD of the Eos family.

Material properties were as follows: the bulk density $\rho = 2500$ kg/m$^3$, the surface density $\rho_s = 1500$ kg/m$^3$, the thermal conductivity $K = 0.001$ W/m/K, the specific thermal capacity

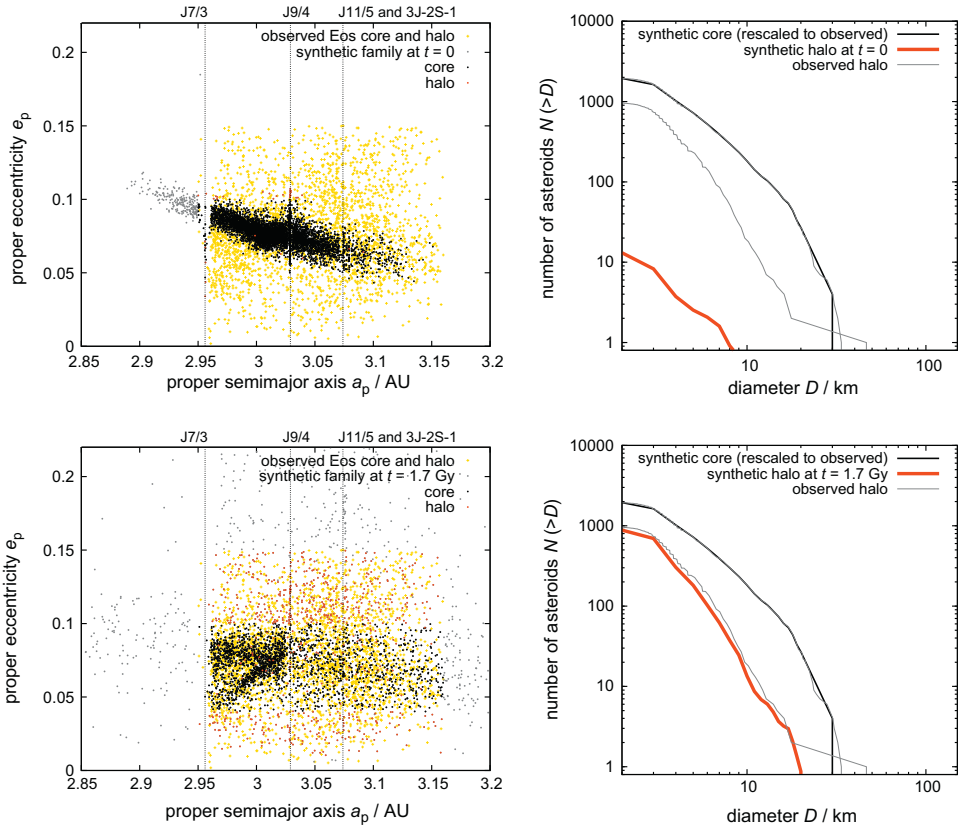


**Fig. 5.** Left panels: the proper semimajor axis $a_p$ vs proper eccentricity $e_p$ plots showing a dynamical evolution of our synthetic family. We can distinguish the core (black dots), the halo (red dots) and objects beyond the halo box (grey dots). There is a comparison to the observed Eos core and halo too (yellow crosses), as inferred from the SDSS data (the same as in Fig. 2, bottom). The positions of important resonances are indicated by vertical dotted lines. We plot the initial situation at $t = 0$ (top panel) and the evolved family at $t = 1.7$ Gyr (bottom panel). The core of the synthetic family exhibits a slightly different structure than the observed core which may indicate that: (i) the initial true anomaly was closer to $f = 180°$, or (ii) the initial velocity field deviated from the assumed $v \propto 1/D$ dependence. Right panels: the corresponding size–frequency distributions of the synthetic core (black line), which was always scaled to the observed SFD of the Eos core, and the synthetic halo (red line) which can be then directly compared to the observed halo (grey line). It is clear that the halo's SFD becomes steeper in the course of time and at $t \simeq 1.7$ Gyr it matches the observed SFD. (For interpretation of the references to colour in this figure legend, the reader is referred to the web version of this article.)

$C = 680$ J/kg/K, the Bond albedo $A = 0.1$, the infrared emissivity $\epsilon = 0.9$, i.e. all typical values for regolith covered basaltic asteroids.

Initial rotation periods were distributed uniformly on the interval 2–10 h and we used random (isotropic) orientations of the spin axes. The YORP model of the spin evolution was described in detail in Brož et al. (2011), while the efficiency parameter was $c_{\mathrm{YORP}} = 0.33$ (i.e. a likely value according to Hanuš et al. (2011)). YORP angular momenta affecting the spin rate and the obliquity were taken from Čapek and Vokrouhlický (2004). We also included spin axis reorientations caused by collisions[1] with a time scale estimated by Farinella et al. (1998): $\tau_{\mathrm{reor}} = B(\omega/\omega_0)^{\beta_1}(D/D_0)^{\beta_2}$, where $B = 84.5$ kyr, $\beta_1 = 5/6$, $\beta_2 = 4/3$, $D_0 = 2$ m and $\omega_0$ corresponds to period $P = 5$ h.

The initial velocity field was size-dependent, $v \propto v_0 D_0/D$, with $v_0 = 93$ m/s and $D_0 = 5$ km (i.e. the best-fit values from Vokrouhlický et al. (2006)). In principle, this type of size–velocity relation was initially suggested by Cellino et al. (1999), but here, we attempt to interpret the structure of the family as a complex interplay between the velocity field and the Yarkovsky drift which is also inversely proportional to size. We assumed isotropic orientations of the velocity vectors. The geometry of collisional disruption was determined by the true anomaly $f = 150°$, and the argument of perihelion $\omega = 30°$. We discuss different geometries in Section 4.

We use a modified version of the SWIFT package (Levison and Duncan, 1994) for numerical integrations, with a second-order symplectic scheme (Laskar and Robutel, 2001), digital filters employing frequency-modified Fourier transform (Šidlichovský and Nesvorný, 1996) and an implementation of the Yarkovsky effect (Brož, 2006). The integration time step was $\Delta t = 91$ days, the output time step after all filtering procedures 10 Myr and the total integration time span reached 4 Gyr.

### 3.2. Results of the N-body simulation

Initially, almost all asteroids are located in the core (see Fig. 5). Only a few outliers may have velocities large enough to belong to the halo. Within a few million years the halo/core ratio quickly increases due to objects located inside the 9/4 resonance and injected to the halo by these size-independent gravitational perturbations. Further increase is caused by the Yarkovsky/YORP semimajor axis drift which pushes additional orbits into the J9/4 and also other resonances.

[1] We do *not* take into account collisional disruptions because we model only that subset of asteroids which survived subsequent collisional grinding (and compare it to the currently observed asteroids). Of course, if we would like to discuss e.g. the size of the parent body, it would be necessary to model disruptive collisions too.

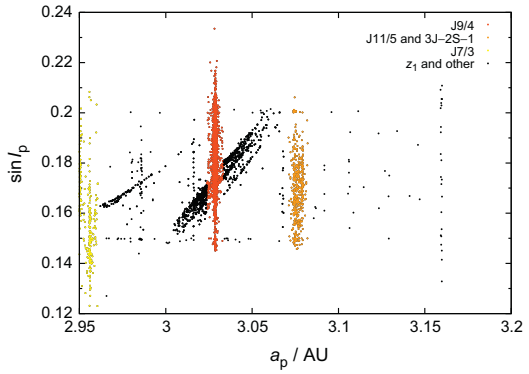


**Fig. 6.** The proper semimajor axis $a_p$ vs proper inclination $\sin I_p$ of the synthetic family members at the moment when they have entered the halo region. It is easy to distinguish objects injected by mean-motion resonances and by secular resonances in this projection, because the former have a particular value of the semimajor axis. The objects injected by the J9/4 resonance are denoted by red colour, the J11/5 and 3J–2S–1 by orange, the J7/3 by yellow, the $z_1$ secular resonance and other resonances by black. (For interpretation of the references to colour in this figure legend, the reader is referred to the web version of this article.)

We checked the orbital elements of bodies at the moment when they enter the halo region (Fig. 6) and we computed the statistics of dynamical routes that had injected bodies in the halo: J9/4 57%, J11/5 (together with a three-body resonance 3J–2S–1 with Jupiter and Saturn) 10%, J7/3 6%, and $z_1$ secular resonance 23%. The remaining few percent of bodies may enter the halo by different dynamical routes.[2] However, if we account for the fact that bodies captured by the $z_1$ resonance usually encounter also the J9/4 resonance that scatters them further away into the halo, we obtain a modified statistics: J9/4 70%, J11/5 12%, J7/3 5%, and $z_1$ 10% that better reflects the importance of different mechanisms.

A saturation of the halo occurs after approximately 1 Gyr, because the halo population is affected by the Yarkovsky/YORP drift too, so that the injection rate roughly matches the removal rate. Nevertheless, the halo/core ratio steadily increases, which is caused by the ongoing decay of the core population.

In order to compare our model and the SDSS observations we compute the ratio $\mathcal{R} = \mathrm{d}N_{\mathrm{halo}}/\mathrm{d}N_{\mathrm{core}}$ between the number of objects in the halo and in the core for a given *differential* size bin. This can be computed straightforwardly from our simulation data. In case of the SDSS observations, however, we think that there is a real *background* of asteroids with Eos-like colours (may be due to observational uncertainties or a natural spread of colours; see Fig. 2). Obviously, such background overlaps with the core and the halo, so we need to subtract this contamination

$$\mathcal{R}_{\mathrm{obs}} \equiv \frac{\mathrm{d}N_{\mathrm{halo}} - 0.833\,\mathrm{d}N_{\mathrm{background}}}{\mathrm{d}N_{\mathrm{core}} - 0.167\,\mathrm{d}N_{\mathrm{background}}}. \tag{3}$$

The numerical coefficients then reflect different 'volumes' of the halo, core and background in the space of proper elements ($a_p$, $e_p$, $\sin I_p$), as defined in Table 1.

As we can see in Fig. 7, a reasonable match to the observed halo/core ratios can be obtained for ages 1.5 Gyr (for smaller bodies) to 2.2 Gyr (for larger bodies). To better quantify the difference between the model and the observations we construct a suitable metric

[2] Other secular resonances intersecting this region, $s - s_6 - 2g_5 + 2g_6$ or $g + 2g_5 - 3g_6$, do not seem to be important with respect to the transport from the core to the halo.

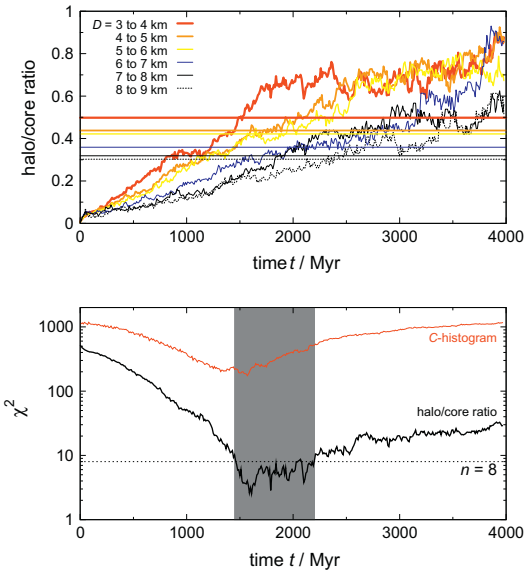


**Fig. 7.** Top panel: the evolution of the halo/core ratio in our simulation for several size bins (colour curves) and its comparison to the observed SDSS ratios in the same bins (horizontal lines). The intersections give age estimates from 1.5 Gyr (for smaller bodies) to 2.2 Gyr (larger bodies). Bottom panel: the corresponding evolution of the $\chi^2$ vs time $t$. The dotted line indicates the number $n = 8$ of size bins (from $D = 2$ km to 10 km) in which the $\chi^2$ was computed. The best fits (with $\chi^2 \simeq n$ or smaller) correspond to ages from 1.5 to 2.2 Gyr. For comparison, we also plot a $\chi^2(t)$ dependence (red line), computed from the histogram of $C \equiv (a - 3.019\ \mathrm{AU})/10^H$ values, which corresponds to the analysis of Vokrouhlický et al. (2006). We use the population of Eos-like asteroids observed by the SDSS in both core and halo for this purpose. (For interpretation of the references to colour in this figure legend, the reader is referred to the web version of this article.)

$$\chi^2(t) \equiv \sum_{i=2}^{9} \frac{(\mathcal{R}_i(t) - \mathcal{R}_{\mathrm{obs}i})^2}{\sigma_i^2(t) + \sigma_{\mathrm{obs}i}^2}, \tag{4}$$

where the summation is over the respective size bins $(D_i, D_i + \mathrm{d}D)$, $D_i \equiv i \cdot 1$ km and $\mathrm{d}D = 1$ km. The uncertainties of the numbers of objects are of the order $\sigma_{\mathrm{halo}} \simeq \sqrt{\mathrm{d}N_{\mathrm{halo}}}$, $\sigma_{\mathrm{core}} \simeq \sqrt{\mathrm{d}N_{\mathrm{core}}}$, and $\sigma_i$ reflects their propagation during the calculation of the ratio in Eq. (3) in a standard way

$$\sigma_i = \sqrt{(\sigma_{\mathrm{halo}}/\mathrm{d}N_{\mathrm{halo}})^2 + (\sigma_{\mathrm{core}}/\mathrm{d}N_{\mathrm{core}})^2}\,\mathrm{d}N_{\mathrm{halo}}/\mathrm{d}N_{\mathrm{core}}$$

and similarly for $\sigma_{\mathrm{obs}i}$. The $\chi^2(t)$ dependence is shown in Fig. 7 and the best-fit is obtained again for the ages $t \simeq 1.5$–2.2 Gyr.

The ratios $\mathcal{R}$ are directly related to the size–frequency distributions and consequently we are indeed able to match the observed SFD's of halo and core, including their slopes and absolute numbers (Fig. 5, right column).

These results are *not* very sensitive to the initial velocity field, because most asteroids fall within the family core; velocities would be unreasonably large to have a substantial halo population initially.

## 4. Conclusions

Yarkovsky-driven origin seems to be a natural explanation of the halo population. A lucky coincidence that the disruption of the Eos-family parent body occurred close to the moderately strong 9/4 mean motion resonance with Jupiter established a mechanism, in which orbits drifting in semimajor axis due to the Yarkovsky effect are mostly perturbed by this resonance and scat-

tered around in eccentricity and inclination. The total spread of the simulated halo (up to 0.2 in eccentricity, Fig. 5), which matches the SDSS observations (Fig. 2), also supports our conclusion.

As an important by-product, the process enabled us to independently constrain the age of the family. Moreover, if we analyse the evolution in the proper semimajor axis vs the absolute magnitude $(a_p, H)$ plane and create a histogram of the quantity $C \equiv (a - 3.019\,\mathrm{AU})/10^H$ (i.e. a similar approach as in Vokrouhlický et al. (2006), but now using a full $N$-body model and the SDSS observations for both the core and halo), we can compute an independent $\chi^2(t)$ evolution (refer to Fig. 7, red line). Since both methods – the halo/core ratios $\mathcal{R}$ and the $C$-histogram – seem to be reasonable, we can infer the most probable age as an overlap of intervals of low $\chi^2(t)$ and this way further decrease its uncertainty, so that $t \simeq 1.5$–$1.9$ Gyr.

It is also interesting that the true anomaly at the time of disruption has to be $f \simeq 120$–$180°$. We performed tests with lower values of $f$ and in these cases the synthetic family has initially a different orientation in the $(a_p, e_p)$ plane: the objects are spread from small $a_p$ and $e_p$ to large $a_p$ and $e_p$ (cf. Fig. 5). Way too many objects thus initially fall into the $z_1$ secular resonance and because such captured orbits cannot drift to small $a_p$ and large $e_p$ it is then impossible to explain the observed structure of the family and consequently $f \lesssim 120°$ is excluded.

Finally, let us emphasise that given the differences between the size–frequency distribution of the halo that of the core, we can exclude a possibility that the Eos halo was created by a *purely* gravitational process (like the perturbations arising from giant-planet migration).

## Acknowledgments

The work of MB has been supported by the Grant Agency of the Czech Republic (Grant No. 13-01308S) and the Research Program MSM0021620860 of the Czech Ministry of Education. We also thank both referees A. Cellino and V. Carruba for careful reviews of this paper.

## References

Brož, M., 2006. Yarkovsky Effect and the Dynamics of the Solar System. PhD Thesis, Charles Univ.
Brož, M., Vokrouhlický, D., Morbidelli, A., Nesvorný, D., Bottke, W.F., 2011. Did the Hilda collisional family form during the late heavy bombardment? Mon. Not. R. Astron. Soc. 414 (July), 2716–2727.
Carruba, V., 2009. The (not so) peculiar case of the Padua family. Mon. Not. R. Astron. Soc. 395 (May), 358–377.
Carruba, V., Michtchenko, T.A., 2007. A frequency approach to identifying asteroid families. Astron. Astrophys. 475 (December), 1145–1158.
Cellino, A., Michel, P., Tanga, P., Zappalà, V., Paolicchi, P., dell'Oro, A., 1999. The velocity–size relationship for members of asteroid families and implications for the physics of catastrophic collisions. Icarus 141 (September), 79–95.
DeMeo, F.E., Binzel, R.P., Slivan, S.M., Bus, S.J., 2009. An extension of the Bus asteroid taxonomy into the near-infrared. Icarus 202 (July), 160–180.
Farinella, P., Vokrouhlický, D., Hartmann, W.K., 1998. Meteorite delivery via Yarkovsky orbital drift. Icarus 132 (April), 378–387.
Hanuš, J. et al., 2011. A study of asteroid pole-latitude distribution based on an extended set of shape models derived by the lightcurve inversion method. Astron. Astrophys. 530 (June), 1–20. A134.
Laskar, J., Robutel, P., 2001. High order symplectic integrators for perturbed Hamiltonian systems. Celest. Mech. Dynam. Astron. 80 (July), 39–62.
Levison, H.F., Duncan, M.J., 1994. The long-term dynamical behavior of short-period comets. Icarus 108 (March), 18–36.
Masiero, J.R. et al., 2011. Main belt asteroids with WISE/NEOWISE. I. Preliminary albedos and diameters. Astrophys. J. 741 (November), 68–88.
Milani, A., Knezevic, Z., 1992. Asteroid proper elements and secular resonances. Icarus 98 (August), 211–232.
Morbidelli, A., Levison, H.F., Tsiganis, K., Gomes, R., 2005. Chaotic capture of Jupiter's trojan asteroids in the early Solar System. Nature 435 (May), 462–465.
Parker, A., Ivezić, Ž., Jurić, M., Lupton, R., Sekora, M.D., Kowalski, A., 2008. The size distributions of asteroid families in the SDSS Moving Object Catalog 4. Icarus 198 (November), 138–155.
Čapek, D., Vokrouhlický, D., 2004. The YORP effect with finite thermal conductivity. Icarus 172 (December), 526–536.
Šidlichovský, M., Nesvorný, D., 1996. Frequency modified Fourier transform and its applications to asteroids. Celest. Mech. Dynam. Astron. 65 (March), 137–148.
Vokrouhlický, D., Brož, M., Morbidelli, A., Bottke, W.F., Nesvorný, D., Lazzaro, D., Rivkin, A.S., 2006. Yarkovsky footprints in the Eos family. Icarus 182 (May), 92–117.
Zappalà, V., Bendjoya, P., Cellino, A., Di Martino, M., Doressoundiram, A., Manara, A., Migliorini, F., 2000. Fugitives from the Eos family: First spectroscopic confirmation. Icarus 145 (May), 4–11.
Zappalà, V., Bendjoya, P., Cellino, A., Farinella, P., Froeschlè, C., 1995. Asteroid families: Search of a 12,487-asteroid sample using two different clustering techniques. Icarus 116 (August), 291–314.

Monthly Notices
of the
ROYAL ASTRONOMICAL SOCIETY

Mon. Not. R. Astron. Soc. **414,** 565–574 (2011) doi:10.1111/j.1365-2966.2011.18420.x

# Eurybates – the only asteroid family among Trojans?

M. Brož[1⋆] and J. Rozehnal[1,2]

[1]*Institute of Astronomy, Charles University, Prague, V Holešovičkách 2, 18000 Prague 8, Czech Republic*
[2]*Štefánik Observatory, Petřín 205, 11800 Prague, Czech Republic*

Accepted 2011 January 24. Received 2011 January 24; in original form 2010 November 11

**ABSTRACT**

We study the orbital and physical properties of Trojan asteroids of Jupiter. We try to discern all the families previously discussed in the literature, but we conclude that there is only one significant family among the Trojans, namely the cluster around the asteroid (3548) Eurybates. This is the only cluster that has all of the following characteristics: (i) it is clearly concentrated in the proper-element space; (ii) the size–frequency distribution is different from that of background asteroids; (iii) we have a reasonable collisional/dynamical model of the family. Henceforth, we can consider it as a real collisional family.

We also report the discovery of a possible family around the asteroid (4709) Ennomos, composed mostly of small asteroids. The asteroid (4709) Ennomos is known to have a very high albedo $p_V \simeq 0.15$, which may be related to the hypothetical cratering event that exposed ice. The relation between the collisional family and the exposed surface of the parent body offers a unique means to study the physics of cratering events. However, more data are needed to confirm the existence of this family and its relationship with Ennomos.

**Key words:** methods: numerical – celestial mechanics – minor planets, asteroids: general.

## 1 INTRODUCTION

Trojans of Jupiter, which reside in the neighbourhood of $L_4$ and $L_5$ Lagrangian points, serve as an important test of the planetary migration theory (Morbidelli et al. 2005). Their inclination distribution, namely the large spread of $I$, can be explained as a result of chaotic capture during a brief period when Jupiter and Saturn encountered a 1:2 mean-motion resonance. Moreover, the Late Heavy Bombardment provides the timing of this resonant encounter $\simeq 3.8$ Gyr ago (Gomes et al. 2005). It is thus important to understand the population of Trojans accurately.

There are several unresolved problems regarding Trojans, however; for example the number of families, which is a stringent constraint for collisional models. Roig, Ribeiro & Gil-Hutton (2008) studied as many as 10 suggested families, using relatively sparse SLOAN data and spectra. They noted that most families seem to be heterogeneous from the spectroscopic point of view, with one exception – the C-type Eurybates family. As we argue in this paper, the number of families (with parent-body size $D \gtrsim 100$ km) is indeed as low as one.

Another strange fact is the ratio of $L_4$ and $L_5$ Trojans. Szabó et al. (2007) used SLOAN colour data to reach fainter than orbital catalogues and estimated the ratio to $N(L_4)/N(L_5) = 1.6 \pm 0.1$. There is no clear explanation for this, since the chaotic capture as a gravitational interaction should be independent of the size or $L_4/L_5$ membership. Any hypothesis involving collisions would require a relatively recent disruption of a huge parent body, which is highly unlikely (O'Brien & Morbidelli 2008, D. O'Brien, private communication). This is again related to the actual observed number of Trojan families.

Brož & Vokrouhlický (2008) studied another resonant population, the so-called Hilda group in the 3/2 mean-motion resonance with Jupiter, and reported only two families: Hilda and Schubart, with approximately 200- and 100-km parent bodies. This number might be in accord with low collisional probabilities, assuming that the Hilda family is very old and experienced the Late Heavy Bombardment (Brož et al. 2011).

Levison et al. (2009) compared the observed distribution of D-type asteroids and the model of their delivery from transneptunian region. They found a good match assuming that the D-types (presumably of cometary origin) are easy-to-disrupt objects (with the strength more than five times lower than that of solid ice). Note that Trojan asteroids are a mixture of C- and D-type objects and we have to discriminate between them with respect to collisional behaviour.

All of the works mentioned above are a good motivation for us to focus on asteroid families in the Trojan population. The paper is organized as follows. First, we describe our data sources and methods in Section 2. A detailed study of orbital and physical properties of families (and other 'false' groupings) is presented in Section 3. Section 4 is devoted to the modelling of long-term dynamical evolution. Finally, there are concluding remarks in Section 5.

⋆E-mail: mira@sirrah.troja.mff.cuni.cz

## 2 METHODS

### 2.1 Resonant elements

We use the symplectic SWIFT integrator (Levison & Duncan 1994) for orbital calculations. Our modifications include a second-order scheme of Laskar & Robutel (2001) and online digital filters, which enable us to compute suitable resonant proper elements: libration amplitude $d$ of the $a - a'$ oscillations, where $a$ is the osculating semimajor axis of an asteroid and $a'$ is that of Jupiter, eccentricity $e$ and inclination $\sin I$. (In figures, we usually plot a mean value $\bar{a}$ of semimajor axis plus the libration amplitude $d$.) We employ their definition from Milani (1993). The source of initial osculating elements is the AstOrb catalogue, version JD = 245 5500.5 (2010 October 31).

There are actually two independent filters running in parallel: in the first one, we sample osculating elements every 1 yr, compute the mean elements using the filter sequence B, B with decimation factors 3, 3 (refer to Quinn, Tremaine & Duncan 1991) and store this data in a buffer spanning 1 kyr. We then estimate the libration frequency $f$ by a linear fit of $\phi(t) = \lambda - \lambda' - \chi$, where $\lambda$, $\lambda'$ are the mean longitudes of an asteroid and Jupiter and $\chi = \pm 60^\circ$ for $L_4$ or $L_5$, respectively. The revolution of angle $\phi(t)$ must not be confined to the interval $[0, 360^\circ)$, of course. The amplitude of $d$ is computed for the already known $f$ by a discrete Fourier transform. Finally, an offline running-average filter with a window of 1 Myr is used to smooth the data.[1]

In the second filter, we compute proper eccentricity $e$ and proper inclination $\sin I$ by sampling osculating elements (1-yr step), computing the mean elements using a filter sequence A, A, B and the decimation factors 10, 10, 3, and then we apply a frequency modified Fourier transform (Šidlichovský & Nesvorný 1996), which gives us the relevant proper amplitudes.

The values of the resonant elements agree very well with those listed in the AstDyS catalogue by Knežević & Milani (2003; see Fig. 1). There are only few outliers, probably due to a different timespan of integration. We computed the proper elements for 2647 $L_4$ and 1496 $L_5$ Trojan asteroids.[2] This sample is roughly twice larger than the one previously analysed. The ratio of populations valid for $H \lesssim 15$ mag asteroids is thus $N(L_4)/N(L_5) \simeq 1.8$.

The overall distribution of Trojans in the ($d$, $e$, $\sin I$) space is shown in Fig. 2. Note that there is only one cluster visible immediately in the bottom-left panel – around (3548) Eurybates. The reason is its tight confinement in inclinations ($\sin I = 0.125$–$0.135$).

### 2.2 Hierarchical clustering

In order to detect clusters in the resonant element space we use a hierarchical clustering method (Zappalá et al. 1994) with a standard metric $d_1$, with $\delta a$ substituted by $d$. We run the HCM code many times with various starting bodies and different cut-off velocities $v_{\rm cut\text{-}off}$ and determine the number of bodies $N$ in the given cluster. We find the $N(v_{\rm cut\text{-}off})$ dependence to be a very useful diagnostic tool. We can see these dependences for $L_4$ and $L_5$ Trojans in Fig. 3.

[1] Equivalently, we may compute the amplitude $D$ of mean longitudes $\lambda - \lambda'$. Anyway, there is a linear relation between $d$ and $D$.

[2] The data are available in an electronic form on our web site http://sirrah.troja.mff.cuni.cz/~mira/mp/. We use also one-apparition orbits for the purposes of physical studies. Of course, orbital studies require more precise multi-apparition data.

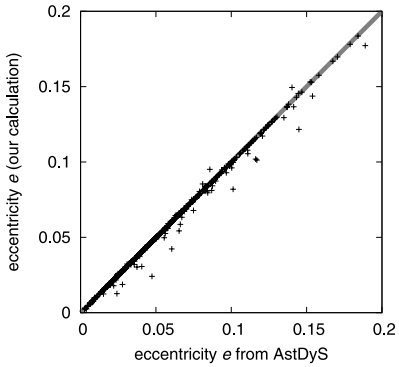


**Figure 1.** Comparison of the resonant eccentricity calculated by our code with that of Knežević & Milani (AstDyS catalogue). There is a line $x = y$ to aid a comparison.

It is easy to recognize if a cluster has a concentration towards the centre – even at a low $v_{\rm cut\text{-}off}$ it must have more than one member ($N \gg 1$). It is also instructive to compare clusters with a random background (thin lines), which we generated artificially by a random-number generator in the same volume of the ($d$, $e$, $I$) space. Insignificant (random) clusters usually exhibit an abrupt increase in $N$ at a high cut-off velocity.

As starting bodies we selected those listed in Roig et al. (2008). Only three clusters, namely the Eurybates, Aneas and 1988 $RG_{10}$, seem to be somewhat concentrated i.e. denser than the background. The Hektor cluster is also concentrated but it contains only a relatively small number of members (20–70) before it merges with the background. In other words, smaller asteroids do not seem to be concentrated around (624) Hektor. The remaining clusters are more or less comparable to the background.

Nevertheless, we report the detection of a previously unknown cluster around (4709) Ennomos in $L_5$. It is relatively compact, since the minimum cut-off velocity is only $70\,{\rm m\,s^{-1}}$. The cluster contains mostly small bodies which were discovered only recently.

Finally, let us point out a very tight cluster around (9799) 1996 RJ, associated already at $v_{\rm cut\text{-}off} = 20\,{\rm m\,s^{-1}}$. It is located at high inclinations and contains nine bodies, three of them having short arcs. The cluster seems to be peculiar in the osculating element space too since it exhibits a non-random distribution of nodes and perihelia (see Table 1). This is similar to very young families such as the Datura (Nesvorný, Vokrouhlický & Bottke 2006), and it makes the 1996 RJ cluster a particularly interesting case with respect to collisional dynamics. Because one has to use slightly different methods for studies of such young families, we postpone its detailed analysis to the next paper.

Let us compare Trojan clusters to the well-known asteroid families in the outer Main Belt (Fig. 4). Most families (e.g. Themis, Koronis, Eos) exhibit a steady increase of $N$ until they merge with another family or the entire outer Main Belt. Eurybates, Aneas and 1988 $RG_{10}$ are the only Trojan clusters which behave in a similar fashion. The Veritas family (dynamically young, Nesvorný et al. 2003) exhibits a different behaviour – for a large interval of $v_{\rm cut\text{-}off}$ the number of members $N$ remains almost the same, which indicates a clear separation from the background population. With respect to the $N(v_{\rm cut\text{-}off})$ dependence, the Ennomos cluster is similar to Veritas.

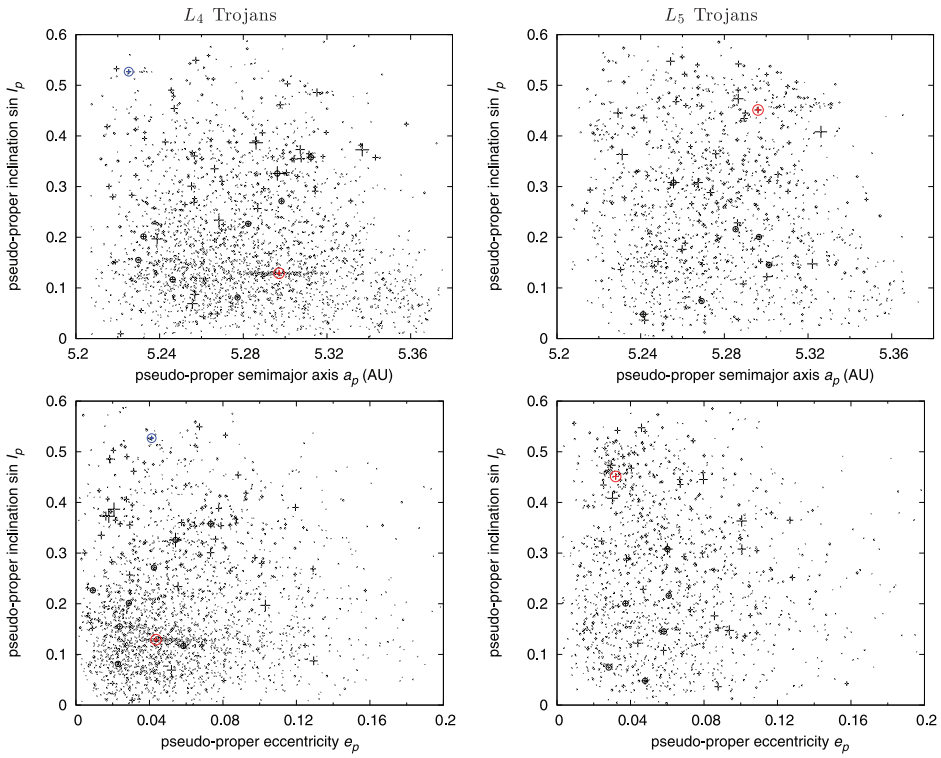


**Figure 2.** The resonant elements ($a \equiv \bar{a} + d$, $\sin I$) and ($e$, $\sin I$) for $L_4$ and $L_5$ Trojans. The crosses indicate relative sizes of bodies, taken either from the AstOrb catalogue or computed from absolute magnitude $H$ and geometric albedo $p_V$. In this plot, we assumed $p_V = 0.058$ for $L_4$ Trojans and 0.045 for those in $L_5$ (it corresponds to medians of known $p_V$s). The asteroids (3548) Eurybates in $L_4$ and (4709) Ennomos in $L_5$, around which significant clusters are visible, are shown in red. Moreover, the asteroid (9799) 1996 RJ in $L_4$, which is surrounded by a small cluster, is denoted by a blue circle. [This cluster is so tight that its members are located inside the circle on the ($e$, $\sin I$) plot.]

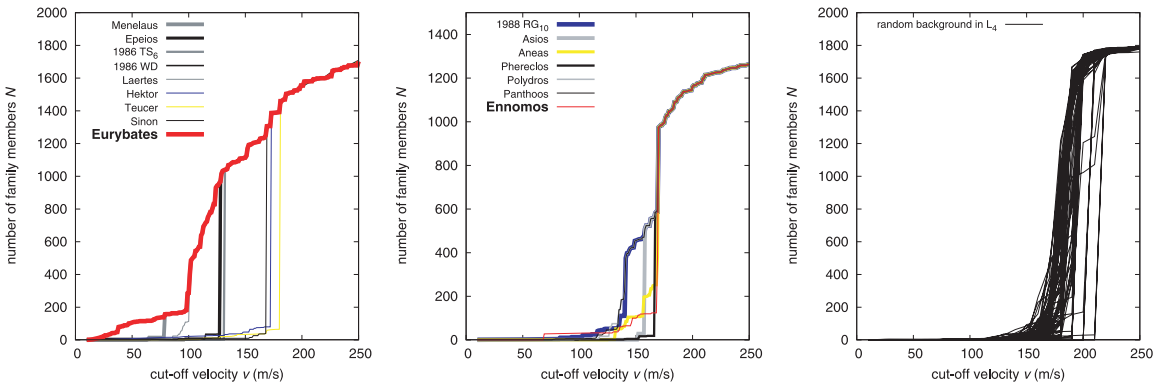


**Figure 3.** Left-hand panel: the dependence of the number of family members $N$ on the cut-off velocity $v_{\rm cut\text{-}off}$ computed by the hierarchical clustering method. Only clusters among $L_4$ Trojans are included in this plot. Middle panel: the same $N(v_{\rm cut\text{-}off})$ dependence for $L_5$ Trojans. Right-hand panel: artificial clusters selected from *random* distribution of asteroids generated in the same volume of the ($d$, $e$, $\sin I$) space.

### 2.3 Size–frequency distribution

At first, let us assume a single value of albedo for all the family members. This is a reasonable assumption provided the family is of collisional origin. We can then calculate sizes from absolute magnitudes and construct size–frequency distributions (SFDs). Fig. 5 shows a comparison of SFDs for the clusters detected by the HCM[3] and for the whole population of $L_4$ and $L_5$ Trojans.

[3] Of course, we have to select a 'suitable' value of the cut-off velocity for all clusters. Usually, we select that value for which $N(v_{\rm cut-off})$ is flat. Size–frequency distribution is not very sensitive to this selection anyway.

**Table 1.** List of nine members of the (9799) 1996 RJ cluster and their proper ($a$, $e$, $\sin I$) and osculating ($\Omega_{\rm osc}$, $\varpi_{\rm osc}$) elements and absolute magnitude $H$. Note that the distribution of nodes and perihelia is not entirely uniform. Asteroids with short-arc orbits (<60 d) are denoted by the * symbol.

| Number | Designation | | $a$ | $e$ | $\sin I$ | $\Omega_{\rm osc}$ | $\varpi_{\rm osc}$ | $H$/mag |
|---|---|---|---|---|---|---|---|---|
| 9799 | 1996 RJ | | 5.2252 | 0.0412 | 0.5269 | 115.4 | 259.6 | 9.9 |
| 89938 | 2002 $FR_4$ | | 5.2324 | 0.0394 | 0.5274 | 70.0 | 23.1 | 12.5 |
| 226027 | 2002 $EK_{127}$ | | 5.2316 | 0.0399 | 0.5263 | 62.8 | 352.9 | 12.6 |
| 243316 | 2008 $RL_{32}$ | | 5.2340 | 0.0398 | 0.5268 | 27.3 | 358.2 | 12.8 |
| | 2005 $MG_{24}$ | | 5.2275 | 0.0404 | 0.5252 | 172.3 | 236.5 | 13.1 |
| | 2008 $OW_{22}$ | * | 5.2276 | 0.0401 | 0.5274 | 53.7 | 340.9 | 13.9 |
| | 2009 $RA_{17}$ | * | 5.2258 | 0.0409 | 0.5272 | 257.7 | 194.5 | 13.7 |
| | 2009 $RK_{63}$ | * | 5.2305 | 0.0407 | 0.5260 | 56.4 | 5.6 | 12.8 |
| | 2009 $SR_{30}$ | | 5.2362 | 0.0409 | 0.5258 | 103.6 | 22.0 | 13.3 |

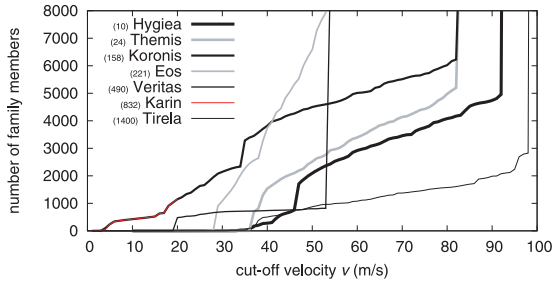


**Figure 4.** The $N(v_{\rm cut\text{-}off})$ dependence for seven outer main-belt families. If we would consider only a subset of asteroids brighter than $H = 15$ mag, which is an approximate observational limit for Trojans, the $N(v_{\rm cut\text{-}off})$ dependencies would be qualitatively the same, only slightly shifted to larger cut-off velocities.

A slope $\gamma$ of the cumulative distribution $N(>D) \propto D^{\gamma}$ is an indicative parameter. For $L_4$ and $L_5$ Trojans, it equals $-2.0 \pm 0.1$ and $-1.9 \pm 0.1$ in the intermediate size range of 15–60 km. (These numbers match the findings of the study of Yoshida & Nakamura 2008.) The slope is steeper at large sizes. The uncertainties are mainly due to a freedom in the selection of the size range, and the difference between $L_4$ and $L_5$ SFDs does not seem significant. The clusters have typically similar slope as background (within 0.1 uncertainty), though sometimes the results are inconclusive due to the small number of members. On the other hand, the slope $-2.5 \pm 0.1$ for the Eurybates family is significantly steeper than the mean slope of the whole Trojan population.[4] There are two more groups that exhibit a relatively steep slope, namely Laertes in $L_4$ ($\gamma = -3.1$) and 1988 $RG_{10}$ in $L_5$ ($\gamma = -2.6$).

We should be aware, however, that even the background exhibits a trend with respect to inclinations (see Fig. 6). Slope $\gamma$ typically decreases with inclination $\sin I$, which is especially prominent in case of the $L_4$ cloud. We have to admit that if we compare the Eurybates family to its surroundings only ($\sin I = 0.1$ to 0.15), the difference in slopes is not so prominent. An interesting feature of the $L_5$ cloud is a dip in the interval $\sin I = 0.05$ to 0.1. This corresponds to the approximate location of the 1988 $RG_{10}$ group.

The $\gamma(\sin I)$ dependence among the Trojans is not unique. For example, low-inclination bodies in the J3/2 resonance also have the SFD steeper than background ($\gamma = -2.5 \pm 0.1$ versus $-1.7 \pm 0.1$), without any clear family and a few big interlopers. Maybe, this feature reflects different *source reservoirs* of low- and high-inclination bodies among Trojans and J3/2?[5] It may also be in concert with the colour–inclination dependence reported by Szabó et al. (2007).

We also test albedo distributions dependent on size, since the measurements by Fernández, Jewitt & Ziffer (2009) suggested that small Trojans are significantly brighter and thus smaller. Large asteroids have $p_V = 0.044 \pm 0.008$ while small $p_V = 0.12 \pm 0.06$. This is a significant change of the SFD, which occurs around the size $D \simeq 30$ km. The SFD thus becomes shallower below this size e.g. for Eurybates we would have $\gamma = -1.6$ and for L4 Trojans $\gamma = -1.5$, so the SFDs become comparable with respect to the slope. Though, as we have stated above, for a real collisional family we expect the albedo distribution to be rather homogeneous and independent of size.

### 2.4 Colour and spectral data

We used the Sloan Digital Sky Survey Moving Object catalogue version 4 (SDSS-MOC4) to check that the families are spectrally homogeneous, similar to what we expect. Due to a larger uncertainty in the $u$ colour in SDSS-MOC4, we used the colour indices $a^*$ and $i - z$, where $a^* = 0.89(g - r) + 0.45(r - i) - 0.57$ (defined by Parker et al. 2008).

The result is shown in Fig. 7. It is clearly visible that the distribution of the Eurybates family in the space of ($a^*$, $i - z$) colours is different from the Trojan background. On the contrary, the 1988 $RG_{10}$ group covers essentially the same area as the background. The Aneas is only slightly shifted towards larger $a^*$ and $i - z$ with respect to the background. There is a lack of data for the Ennomos group – three bodies are not sufficient to compare the colour distributions.

Alternatively, we may use principal component analysis of the SDSS colour indices. We use only data with uncertainties smaller than 0.2 mag, which resulted in 70 887 records. We calculated eigenvalues ($\lambda_{1,2,3,4} = 0.173$, 0.0532, 0.0249, 0.0095), corresponding eigenvectors and constructed the following three principal components (Trojanová 2010):

$$\begin{aligned} \mathrm{PC}_1 = {} & 0.235\,(u - g) + 0.416\,(g - r) + 0.598\,(g - i) \\ & + 0.643\,(g - z), \end{aligned} \quad (1)$$

[4] Though the number of the Eurybates members (105) is so small that it almost does not affect the mean slope of the whole $L_4$ population.

[5] Both the Trojan and J3/2 regions are dynamically unstable during Jupiter–Saturn 1:2 mean-motion resonance, so we expect that the same bodies entering Trojan region may also enter J3/2.

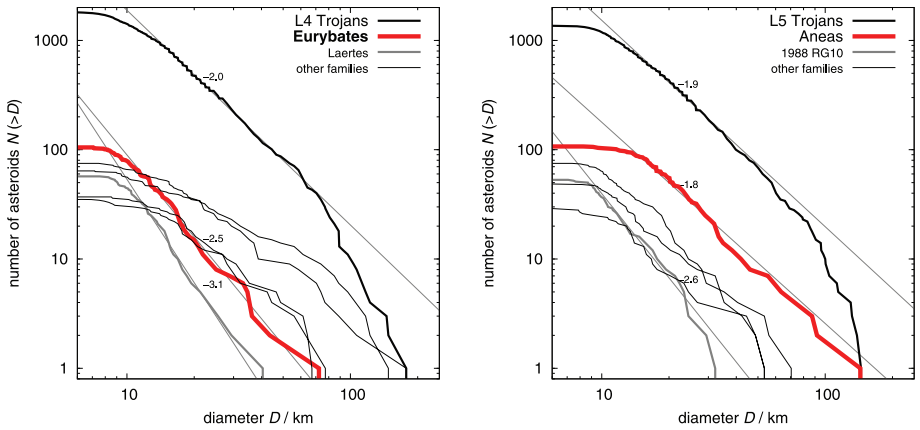


**Figure 5.** Left-hand panel: size–frequency distributions of $L_4$ Trojans and the following clusters (the selected cut-off velocities are given in the parentheses): Eurybates ($v_{\rm cut\text{-}off} = 50\,{\rm m\,s^{-1}}$), Laertes (94), Hektor (160), Teucer (175), Sinon (163), 1986 WD (120). Right-hand panel: SFDs of $L_5$ Trojans and the following clusters: 1988 $RG_{10}$ (at $v_{\rm cut\text{-}off} = 130\,{\rm m\,s^{-1}}$), Aneas (150), Asios (155), Panthoos (130), Polydoros (130).

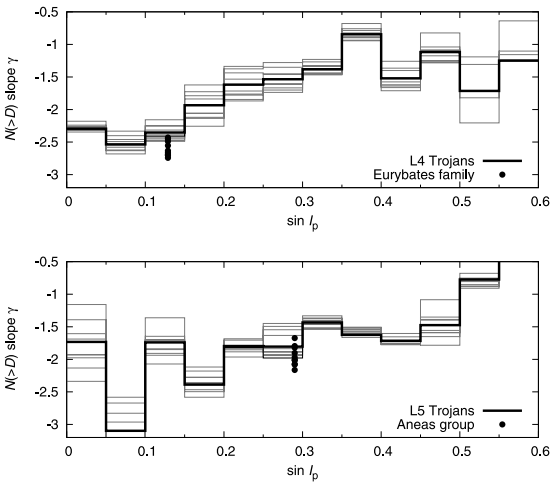


**Figure 6.** Slopes $\gamma$ of the size–frequency distributions $N(>D)$ for $L_4$ and $L_5$ Trojans and their dependence on the inclination $\sin I$. The range of diameters for which the SFDs were fitted is $D_{\rm min} = 12$ km, $D_{\rm max} = 30$ km. Thin lines were calculated for different ranges, which were varied as $D_{\rm min} \in (10, 15)$ km, $D_{\rm max} \in (20, 40)$ km. Their spread indicates the uncertainty of $\gamma$ in a given interval of $\sin I$. The populations are observationally complete down to $D \simeq 10$ km, because the characteristic change of slope due to the incompleteness occurs at smaller sizes (see also Yoshida & Nakamura 2008).

$$\begin{aligned} {\rm PC}_2 = {} & 0.968\,(u-g) - 0.173\,(g-r) - 0.147\,(g-i) \\ & - 0.106\,(g-z), \end{aligned} \tag{2}$$

$$\begin{aligned} {\rm PC}_3 = {} & 0.078\,(u-g) + 0.601\,(g-r) + 0.330\,(g-i) \\ & - 0.724\,(g-z), \end{aligned} \tag{3}$$

which have a clear physical interpretation: $PC_1$ corresponds to an overall slope, $PC_2$ is a variability in the $u$ band and $PC_3$ a depth of the 1-μm absorption band. The Eurybates family is different

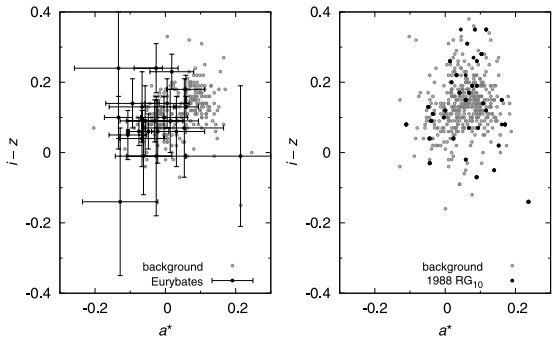


**Figure 7.** Left-hand panel: the $(a^*, i-z)$ colours for the $L_4$ Trojans (grey dots) and the Eurybates family (black dots with error bars). The distributions differ significantly in this case. Right-hand panel: a similar comparison for the $L_5$ Trojans and the 1988 $RG_{10}$ group, which seem to be indistinguishable.

from Trojans in all the three principal components (mean $PC_1$ of the Eurybates members is smaller, $PC_2$ and $PC_3$ larger). The Aneas group has the same distribution of $PC_2$ and $PC_3$ as Trojans and the 1988 $RG_{10}$ group is similar to Trojans even in all three components.

Hence, we confirm that the Eurybates family seems distinct in colour even in the fourth version of the SDSS-MOC. This fact is consistent with the work of Roig et al. (2008), who used the third version of the same catalogue and classified Eurybates family members as C-type asteroids.

Finally, note that De Luise et al. (2010) pointed out an absence of ice spectral features at 1.5 and 2.0 μm on several Eurybates members and Yang & Jewitt (2007) concluded the same for (4709) Ennomos. This puzzling fact may indicate that pure ice covers at most 10 per cent of the Ennomos surface.

### 2.5 Impact disruption model

We use a simple model of an isotropic disruption from Farinella, Froeschlé & Gonczi (1994). The distribution of velocities 'at infinity' follows the function

$$dN(v) = C v (v^2 + v_{\rm esc}^2)^{-(\alpha+1)/2}, \tag{4}$$

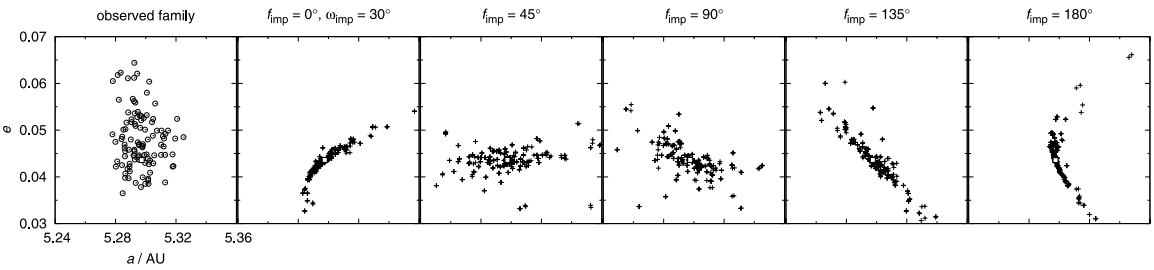


**Figure 8.** A comparison between the observed Eurybates family (open circles) and synthetic families (crosses) just after the impact disruption computed for several values of $f_{\rm imp} = 0^\circ, 45^\circ, 90^\circ, 135^\circ, 180^\circ$ and $\omega_{\rm imp} = 30^\circ$, $R_{\rm PB} = 47$ km, $\rho_{\rm PB} = 1300\,{\rm kg\,m^{-3}}$. Different geometry in $f$, $\omega$ produces a slightly different cluster; nevertheless, it is always tighter than the observed family. The position of the asteroid (3548) Eurybates is denoted by a square.

with the exponent $\alpha$ being a free parameter, $C$ a normalization constant and $v_{\rm esc}$ the escape velocity from the parent body, which is determined by its size $R_{\rm PB}$ and mean density $\rho_{\rm PB}$. The distribution is cut at a selected maximum allowed velocity $v_{\rm max}$ to prevent outliers. We typically use $v_{\rm max} = 300\,{\rm m\,s^{-1}}$. The orientations of velocity vectors in space are assigned randomly. We assume that the velocity of fragments is independent on their size.[6]

There are several more free parameters, which determine the initial shape of the family in the space of proper elements: initial osculating eccentricity $e_{\rm i}$ of the parent body, initial inclination $i_{\rm i}$ as well as true anomaly $f_{\rm imp}$ and argument of perihelion $\omega_{\rm imp}$ at the time of impact disruption.

An example of a synthetic family just after disruption and its comparison to the observed Eurybates family is shown in Fig. 8. Usually, there is a significant disagreement between this simple model of impact disruption and the observations. Synthetic families usually look like thin 'filaments' in the $(d, e, \sin I)$ space, which are curved due to the mapping from osculating elements to resonant ones. On the other hand, the observed groups among Trojans are much more spread. However, this only indicates the importance of the further long-term evolution by chaotic diffusion and possibly by planetary migration.[7]

In case of the Ennomos group members, they are distributed mostly on larger semimajor axes compared to (4709) Ennomos, though isotropic impact disruptions produce fragments distributed evenly on larger and smaller $a$. Is it possibly the indication of an anisotropic velocity field? Or is it a different parent body of this cluster?

### 2.6 Planetary migration

If asteroid families are very old, planetary migration might influence their current shape. In order to study of late stages of planetary migration, which is caused by interactions with a planetesimal disc, we construct the following model. We treat the migration analytically within a modified version of the numerical symplectic SWIFT-RMVS3 integrator (Levison & Duncan 1994), which accounts for gravitational perturbations of the Sun and four giant planets and includes also an energy-dissipation term, as described in Brož et al. (2011). The speed of migration is characterized by the exponential time-scale $\tau_{\rm mig}$ and the required total change of semimajor axis $a_{\rm i} - a_{\rm f}$. We use an eccentricity damping formula too, which simulates the effects of dynamical friction and prevents an unrealistic increase in eccentricities (Morbidelli et al. 2010). The amount of damping is determined by the parameter $e_{\rm damp}$.

We try to adjust initial orbital parameters of planets and the parameters of migration in such a way as to end up at the currently observed orbits. The integration time-step is $\Delta t = 36.525$ d and the time-span is usually equal to $3\tau_{\rm mig}$, when planetary orbits almost stop migrating.

### 2.7 Inefficient Yarkovsky/YORP effect

On long time-scales, the Yarkovsky thermal force might cause significant perturbations of orbits. We use an implementation of the Yarkovsky thermal effect in the SWIFT $N$-body integrator (Vokrouhlický et al. 2006). It includes both the diurnal and the seasonal variants.

The YORP effect (thermal torques affecting spin states; Vokrouhlický et al. 2006) was not taken into account in our simulations. The reason is that the respective time-scale $\tau_{\rm YORP}$ is of the order of 100 Myr to 1 Gyr. So, as a 'zero' approximation, we neglect the YORP effect on these 'short' time-scales and keep the orientations of the spin axes fixed.

For Trojan asteroids captured in a zero-order mean-motion resonance, the Yarkovsky perturbation only affects the position of libration centre (Moldovan et al. 2010). Note that the perturbation acts 'instantly' – there is no systematic secular drift in eccentricity nor in other proper elements which is an important difference from first-order resonances, where an $e$-drift is expected (Brož & Vokrouhlický 2008, appendix A). This is another reason that we do not need a detailed YORP model here.

The thermal parameters we use are reasonable estimates for C/X-type bodies: $\rho_{\rm surf} = \rho_{\rm bulk} = 1300\,{\rm kg\,m^{-3}}$ for the surface and bulk densities, $K = 0.01\,{\rm W\,m^{-1}\,K^{-1}}$ for the surface thermal conductivity, $C = 680\,{\rm J\,kg^{-1}}$ for the heat capacity, $A = 0.02$ for the Bond albedo and $\epsilon_{\rm IR} = 0.95$ for the thermal emissivity.

## 3 ASTEROID FAMILIES AND INSIGNIFICANT GROUPS

In this section, we briefly discuss the properties of selected clusters: Eurybates, Ennomos, Aneas and 1988 $RG_{10}$. We focus on these four clusters, since they seem most prominent according to our previous analysis.

[6] If we use a size-dependent relation for velocities similar to Vokrouhlický et al. (2006), our results do not change much, because the overall shape of the velocity distribution is quite similar to the size-independent case.

[7] Only very young clusters like the Karin family (Nesvorný et al. 2002) exhibit this kind of a 'filament' shape.

### 3.1 Eurybates family

The Eurybates family can be detected by the hierarchical clustering method for cut-off velocities $v_{\text{cut-off}} = 38$ to $78\,\text{m}\,\text{s}^{-1}$, when it merges with Menelaus (see Fig. 3). Yet, we do not rely just on the HCM! Another selection criterion we use is a 'meaningful' shape of the family and its changes with respect to $v_{\text{cut-off}}$. A very important characteristic of the Eurybates family at low values of $v_{\text{cut-off}}$ is a tight confinement of inclinations ($\sin I$ within 0.01). It breaks down at $v_{\text{cut-off}} \simeq 68\,\text{m}\,\text{s}^{-1}$, so we consider this value as an upper limit. The Eurybates family is also confined in the semimajor axis, being approximately twice smaller than other groups.

The diameter of the parent body is $D_{\text{PB}} \doteq 97$ km for albedo $p_V = 0.055$ if we sum the volumes of the known bodies. Of course, in reality it is slightly larger due to observational incompleteness. If we prolong the slope of the SFD $\gamma = -2.5$ down to zero, we obtain $D_{\text{PB}} \doteq 110$ km. The geometric method of Tanga et al. (1999) gives the upper limit $D_{\text{PB}} \simeq 130$ km.

Spectral slopes of family members are rather homogeneous and correspond to C/P-types (Roig et al. 2008).

### 3.2 Ennomos group

The cluster around (4709) Ennomos can be recognized for a wide interval of cut-off velocities $v_{\text{cut-off}} \in (69, 129)\,\text{m}\,\text{s}^{-1}$ when it stays compact and confined in inclinations ($\sin I = 0.451$ to 0.466). Very probably, there are several interlopers, because we can count four to 10 asteroids in the surroundings i.e. in the same volume of the ($d$, $e$, $\sin I$) space (see Fig. 9). Since small bodies dominate the Ennomos group, we suspect that large bodies might actually be interlopers.

A very intriguing feature is a high albedo of (4709) Ennomos $p_V \simeq 0.15$ measured by Fernández et al. (2003). Apart from other explanations, the authors speculated that it may result from a recent impact which covered the surface with pristine ice. If it is true, the relation between the fresh surface and the collisional family might be a unique opportunity to study cratering events.

We cannot exclude the possibility that (4709) Ennomos is actually an interloper and the family is not related to it at all. Nevertheless, our hypothesis is testable: family members should exhibit a similarity in spectra and albedos. The only information we have to date are SDSS colours for three members: 98362, 2005 $\text{YG}_{204}$ are probably C-types and 2005 $\text{AR}_{72}$ is a D-type. In case new data become available, we would be able to remove interlopers from our sample and improve our analysis.

The size distribution of the Ennomos group is barely constrained, since small bodies are at the observational limit. Moreover, removal of interlopers can change the SFD slope completely (from $\gamma = -1.4$ to $-3.2$ or so). The minimum parent body size is about $D_{\text{PB}} \simeq 67$ km if all members have a high albedo $p_V = 0.15$.

### 3.3 Group called Aneas

The Aneas group looks like the middle portion of the $L_5$ cloud with an approximate background density. It spans the whole range of semimajor axes, as background asteroids do.

The minimum size of a hypothetical parent body is $D_{\text{PB}} = 160$ to 170 km (for albedo $p_V = 0.055$–$0.041$). This size is very large and an impact disruption of such body is less probable (see Section 4.4). The size–frequency distribution is shallow, with approximately the same slope as that of the background.

According to Roig et al. (2008) the colours are rather homogeneous and correspond to D-types, with $\simeq$10 per cent of probable interlopers.

### 3.4 Group called 1988 $\text{RG}_{10}$

The group around asteroid (11487) 1988 $\text{RG}_{10}$ again looks like a lower portion of the $L_5$ cloud at low inclinations, with $\sin I \in (0.06, 0.1)$. The SFD is steeper ($\gamma = -2.6 \pm 0.1$) than the surroundings in $L_5$ and the resulting parent body size $D \simeq 60$ km is relatively small. The colours seem heterogeneous (Roig et al. 2008) and we can confirm this statement based on the new SDSS-MOC version 4 data.

The remaining clusters (Hektor, Teucer, Sinon, 1986 WD, Laertes, Asios, Polydoros, Panthoos, etc.) may be characterized as follows: (i) they have a density in ($d$, $e$, $\sin I$) space comparable to that of background (surroundings); (ii) when identified by the HCM their semimajor axes span the whole range of Trojan region; (iii) the slopes of their SFDs are comparable to the background; (iv) they are often inhomogeneous with respect to colours (according to Roig et al. 2008). These reasons lead us to a conclusion that these clusters are not necessarily real collisional families.

## 4 LONG-TERM EVOLUTION OF TROJAN FAMILIES

### 4.1 Evolution due to chaotic diffusion

We try to model long-term evolution of the Eurybates family. At first, we generate a synthetic family (consisting of 42 bodies) by an

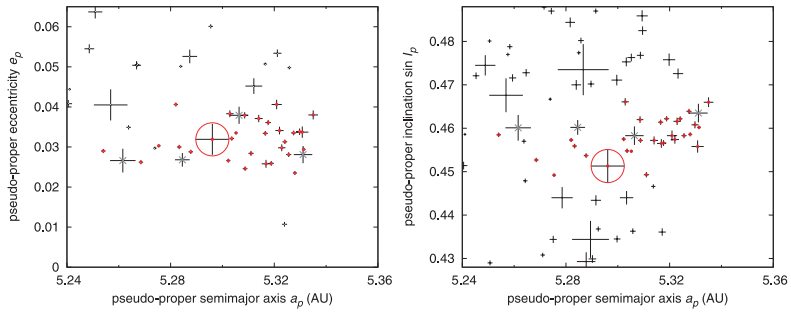


**Figure 9.** Details of the $L_5$ Trojan population where the Ennomos group is visible. Left-hand panel: the resonant semimajor axis $a$ versus eccentricity $e$. Only asteroids occupying the same range of inclinations as the Ennomos group $\sin I \in (0.448, 0.468)$ are plotted to facilitate a comparison with the density of surroundings space (background). The sizes of plus signs are proportional to diameters of the asteroids. The probable family members are denoted by small red circles and the possible interlopers by small grey crosses. Right-hand panel: $a$ versus inclination $\sin I$, with the range of eccentricities $e \in (0.02, 0.045)$.

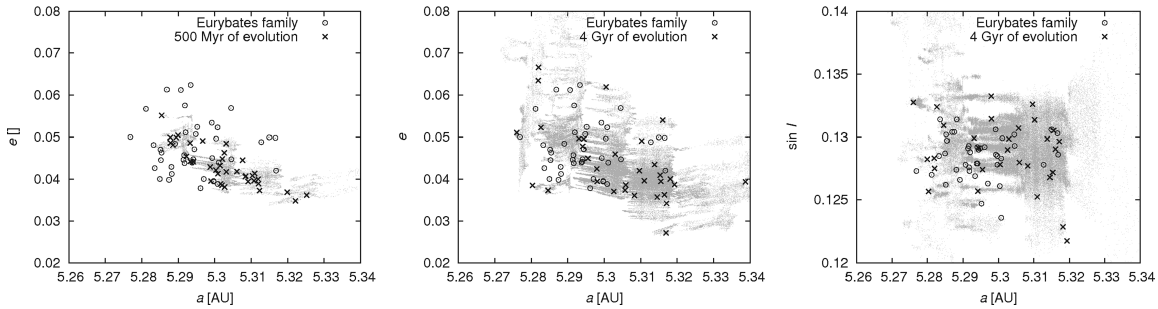


**Figure 10.** Orbital evolution of the synthetic family and its comparison with the observed Eurybates family. Left-hand panel: the situation in the $(a, e)$ plane at 500 Myr. Middle panel: the situation after 4 Gyr. Chaotic diffusion disperses the synthetic family in course of time (see shaded tracks of particles). Right-hand panel: the $(a, \sin I)$ plane at the same time. Inclinations evolve only barely.

impact disruption of the parent body with required size. Then we integrate the synthetic family and compare it at a particular time to the observed Eurybates family. The time-span of the integration is 4 Gyr.

The main driving mechanism is slow *chaotic diffusion* (the Yarkovsky effect is present but inefficient in the Trojan region). Initially, the spread of inclinations of the synthetic family is consistent with the observed one. On the other hand, the shape in $(a, e)$ elements is clearly inconsistent.

Since the inclinations evolve only barely, we focus on the evolution in the $(a, e)$ plane (see Fig. 10). The point is the synthetic family, namely the 'filament' structure, has to disperse sufficiently. After 500 Myr it is still recognizable but after 1 Gyr of evolution it is not. So we may constrain the age of the Eurybates family from 1 to 4 Gyr.[8]

A similar analysis for the Ennomos group indicates that the chaotic diffusion is faster in this region (given the large inclination) and the most probable age thus seems to be from 1 to 2 Gyr. Beyond 2 Gyr the inclinations of the synthetic family become too large compared to the observed Ennomos group, while the eccentricities are still compatible.

We try to model Aneas and 1988 $RG_{10}$ groups too (see Fig. 11). In these two cases, there is a strong disagreement between our model and observations. The observed groups are much larger and the chaotic diffusion in the respective regions is very slow. Even after 4 Gyr of orbital evolution, the synthetic family remains too small.

The only free parameter that may substantially change our results is the initial velocity distribution. Theoretically, the distribution might have been strongly anisotropic. However, we cannot choose initial velocities entirely freely, since their magnitude should be comparable to the escape velocity from the parent body, which is fixed by the size $D_{\rm PB}$ and is only weakly dependent on the a priori unknown density $\rho_{\rm PB}$.

Another solution of this problem is possible if we assume that families are very old and that they experienced perturbations due to planetary migration.

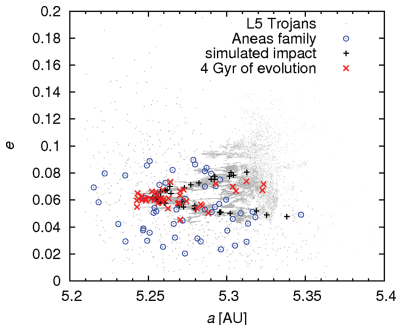


**Figure 11.** Evolution of the synthetic family over 4 Gyr versus the observed Aneas group. Chaotic diffusion is slow and it seems impossible to match the large spread of the observed group even after 4 Gyr.

### 4.2 Stability during planetary migration

The major perturbation acting on Trojans are *secondary resonances* between the libration period $P_{J1/1}$ of the asteroid in the J1/1 mean-motion resonance with Jupiter and the period $P_{1J-2S}$ of the critical argument of Jupiter–Saturn 1:2 resonance (Morbidelli et al. 2005):

$$P_{J1/1} = n P_{1J-2S}, \tag{5}$$

where $n$ is a small integer number. Typical libration periods are $P_{J1/1} \simeq 150$ yr, and $P_{1J-2S}$ changes as planets migrate (it decreases because Jupiter and Saturn recede from their mutual 1:2 resonance).[9]

All synthetic families are strongly unstable when $P_{1J-2S} \simeq 150$ yr and even during the later stages of migration with $P_{1J-2S} \simeq 75$ yr the eccentricities of family members are perturbed too much to match the observed families such as Eurybates or Ennomos (see Fig. 12). There are practically no plausible migration scenarios – regardless of time-scale $\tau_{\rm mig}$ – that would produce a sufficiently compact group, unless Jupiter and Saturn are almost on their current orbits. We tested $\tau_{\rm mig} = 0.3$, 3, 30 Myr and even for $\Delta a_{\rm J} \equiv a_{\rm Jf} - a_{\rm Ji}$ as small as $-0.08$ au and $\Delta a_{\rm S} = +0.25$ au the perturbation was

[8] We verified these estimates by a two-dimensional Kolmogorov–Smirnov test of the $(a, e)$ distributions: initially the KS distance is $D_{\rm KS} = 0.30$ and the probability $p_{\rm KS}(>D) = 0.02$, which means the distribution are incompatible. At $t = 1$ Gyr, the values are $D_{\rm KS} = 0.20$ and $p_{\rm KS}(>D) = 0.32$, which indicate a reasonable match.

[9] Another source of instability might be a secondary resonance with $P_{2J-5S}$ (the so-called Great Inequality period) though it is weaker than $P_{1J-2S}$. We find no asteroids perturbed by secondary resonances connected with $P_{3J-7S}$ or $P_{4J-9S}$ which are present 'en route'. Neither Uranus nor Neptune plays an important role.

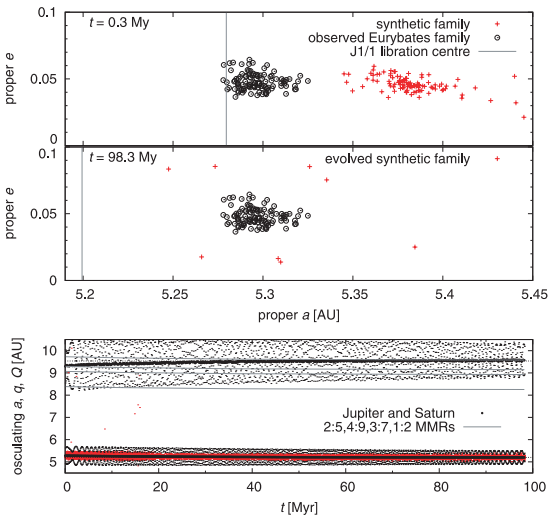


**Figure 12.** Evolution of a synthetic family during the late phases of planetary migration ($\tau_{\rm mig} = 30$ Myr in this case). Top panel: the state at 0 Myr, middle: 100 Myr; bottom panel: the respective orbital evolution of Jupiter and Saturn. The family is almost destroyed and it is definitely incompatible with the observed Eurybates family.

too strong. The reason is that one has to avoid $n = 2$ secondary resonance to preserve the low spread of a synthetic family.

Let us conclude that if any of Trojan families was created during planetary migration and if the migration was smooth (exponential), then the family cannot be visible today. However, we cannot exclude the possibility that the final stages of migration were entirely different e.g. similar to the 'jumping-Jupiter' scenario (Morbidelli et al. 2010).

### 4.3 Families lost by the ejection of fragment outside the resonance

We have studied the possibility that some families cannot be identified because the breakup occurred on the outskirts of the stable libration zone and some fragments were ejected outside the J1/1 resonance. We thus chose 30 largest asteroids near the edge of the $L_4$ libration zone and we simulated the breakups of these asteroids which create families with 30 fragments each. We assumed the diameter of all parent bodies to be $D_{\rm PB} = 100$ km and their density $\rho_{\rm PB} = 1.3\,{\rm g\,cm^{-3}}$. The breakups always occurred at the same geometry $f_{\rm imp} = 0^\circ$, $\omega_{\rm imp} = 30^\circ$. After the breakup, we calculated proper elements of the family members and plotted their distribution (see Fig. 13). We found that all the 30 synthetic families could be easily identified. In most cases, more than 95 per cent of the family members remained within the stable libration zone. We can thus conclude that the ejection of fragments outside the libration zone does not affect the number of observed families among the Trojans.

### 4.4 Collisional rates

We can estimate collisional activity by means of a simple stationary model. Trojan–Trojan collisions play a major role here, because Trojans are detached from the Main Belt. In case of Eurybates, the target (parent body) diameter $D_{\rm target} = 110$ km, the mean impact velocity $V_{\rm imp} = 4.7\,{\rm km\,s^{-1}}$ (Dell'Oro et al. 1998), the strength $Q^\star_D =$

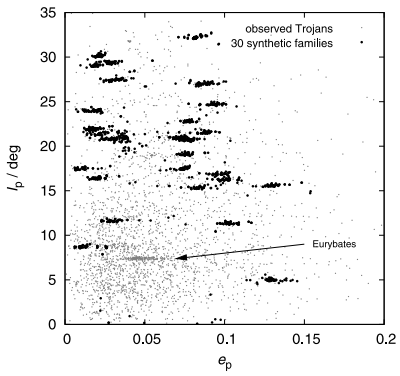


**Figure 13.** Proper eccentricities and inclinations of 30 *synthetic* families (black dots), which originated near the border of stable libration zone, compared to the observed L4 Trojans (grey dots).

$10^5\,{\rm J\,kg^{-1}}$ (Benz & Asphaug 1999) and thus the necessary impactor size (Bottke et al. 2005)

$$d_{\rm disrupt} = \left(2Q^\star_D/V^2_{\rm imp}\right)^{1/3} D_{\rm target} \simeq 23\,{\rm km}. \quad (6)$$

The number of $\geq$23 km projectiles among the $L_4$ Trojans is $n_{\rm project} = 371$ and we have $n_{\rm target} = 8$ available targets. The intrinsic collision probability for Trojan–Trojan collisions $P_{\rm i} = 7.8 \times 10^{-18}\,{\rm km^{-2}\,yr^{-1}}$ (Dell'Oro et al. 1998) and the corresponding frequency of disruptions is

$$f_{\rm disrupt} = P_{\rm i}\frac{D^2_{\rm target}}{4} n_{\rm project} n_{\rm target} \simeq 7 \times\ 10^{-11}\,{\rm yr^{-1}}. \quad (7)$$

Over the age of the Solar system $T_{\rm SS} \simeq 4$ Gyr (after the LHB), we have a very small number of such events $n_{\rm events} = T_{\rm SS} f_{\rm disrupt} \simeq 0.28$. This number seems to be in concert with only one $D \geq 100$ km family currently observed among the Trojans.[10] In a less likely case, the material of the Eurybates parent body was very weak and its strength may be at most 1 order of magnitude lower, $Q^\star_D \simeq 10^4\,{\rm J\,kg^{-1}}$ (see Leinhardt & Stewart 2009, Bottke et al. 2010). We then obtain $d_{\rm disrupt} \simeq 10$ km and $n_{\rm events} \simeq 1.0$, so the conclusion about the low number of expected Trojan families remains essentially the same.

The parent body of Aneas group is 1.5 larger and consequently the resulting number of events is more than 1 order of magnitude lower. On the other hand, clusters with smaller parent bodies ($D_{\rm PB} \ll 100$ km) or those that are significantly weaker ($Q^\star_D \ll 10^5\,{\rm J\,kg^{-1}}$) might be more frequent.

During the Late Heavy Bombardment epoch we may assume a substantial increase of collisional activity (Levison et al. 2009). Hypothetical old families were, however, probably 'erased' due to the late phases of planetary migration (see Section 4.2) unless the migration time-scale for Jupiter and Saturn was significantly shorter than the time-scale of the impactor flux from transneptunian region which is mainly controlled by the migration of Uranus and Neptune.

[10] A similar stationary estimate valid for the Main Asteroid Belt gives the number of events 12 while the number of observed families with $D_{\rm PB} \gtrsim 100$ km is about 20 (Durda et al. 2007). These two numbers are comparable at least to order-of-magnitude.

## 5 CONCLUSIONS

The increasing number of Trojan asteroids with available proper elements enables us to get new insights into this important population. Essentially, the new faint/small asteroids filled the 'gaps' in the proper-element space between previously known clusters, and today it seems most clusters are rather comparable to background. One should be aware of the fact that the number of families among the Trojans may be small and one should not take the number of $\simeq$10 families as a rule.

Only the C-type Eurybates family fulfils all the criteria to be considered a collisional family. This is probably also true for the newly discovered Ennomos group. Moreover, there might be a potentially interesting relation between the high-albedo surface of (4709) Ennomos and the collisional family though we do not have enough data yet to prove it independently (by colours, spectra or albedos).

Note that there may exist clusters among Trojans which are not of collisional origin. They may be caused by (i) differences in chaotic diffusion rates, (ii) $a$-/$e$-/$I$-dependent efficiency of original capture mechanism; or (iii) it may somehow reflect the orbital distribution in the source regions.

We cannot exclude the hypothetical existence of old families which were totally dispersed by dynamical processes e.g. by perturbations due to planetary migration which is especially efficient in the Trojan region.

Finally, note that there seem to be no D-type families anywhere in the Solar system – neither in the Trojan region, nor in the J3/2 (Brož et al. 2011) and Cybele regions (Vokrouhlický et al. 2010). Is it that the D-type parent bodies are too weak and the target is completely pulverized by a collision? This might have important implications for collisional models of icy bodies.

## ACKNOWLEDGMENTS

We thank David Vokrouhlický, David Nesvorný, Alessandro Morbidelli and William F. Bottke for valuable discussions on the subject. We also thank Lenka Trojanová for the principal component analysis of the SDSS-MOC4 data and Gonzalo Carlos de Elía for his review which helped to improve the final version of the paper. The work has been supported by the Grant Agency of the Czech Republic (grant 205/08/P196) and the Research Program MSM0021620860 of the Czech Ministry of Education. We acknowledge the usage of computers of the Observatory and Planetarium in Hradec Králové and Observatory and Planetarium of Prague.

## REFERENCES

Benz W., Asphaug E., 1999, Icarus, 142, 5
Bottke W. F., Durda D. D., Nesvorný D., Jedicke R., Morbidelli A., Vokrouhlický D., Levison H. F., 2005, Icarus, 175, 111
Bottke W. F., Nesvorný D., Vokrouhlický D., Morbidelli A., 2010, AJ, 139, 994
Brož M., Vokrouhlický D., 2008, MNRAS, 390, 715
Brož M., Vokrouhlický D., Morbidelli A., Bottke W. F., Nesvorný D., 2011, MNRAS, in press
De Luise F., Dotto E., Fornasier S., Barucci M. A., Pinilla Alonso N., Perna D., Marzari F., 2010, Icarus, 209, 586
Dell'Oro A., Marzari F., Paolicchi P., Dotto E., Vanzani V., 1998, A&A, 339, 272
Durda D. D., Bottke W. F., Nesvorný D., Enke B. L., Merline W. J., Aspaugh E., Richardson D. C., 2007, Icarus, 186, 498
Farinella P., Froeschlé C., Gonczi R., 1994, in Milani A., Di Martino M., Cellino A., eds, Asteroids, Comets, Meteors 1993. Kluwer, Dordrecht, p. 205
Fernández Y. R., Sheppard S. S., Jewitt D. C., 2003, AJ, 126, 1536
Fernández Y. R., Jewitt D. C., Ziffer J. E., 2009, AJ, 138, 240
Gomes R., Levison H. F., Tsiganis K., Morbidelli A., 2005, Nat, 435, 466
Knežević Z., Milani A., 2003, A&A, 403, 1165
Laskar J., Robutel P., 2001, Celest. Mech. Dynamical Astron., 80, 39
Leinhardt Z. M., Stewart S. T., 2009, Icarus, 199, 542
Levison H. F., Duncan M., 1994, Icarus, 108, 18
Levison H. F., Bottke W. F., Gounelle M., Morbidelli A., Nesvorný D., Tsiganis K., 2009, Nat, 460, 364
Milani A., 1993, Celest. Mech. Dynamical Astron, 57, 59
Moldovan R., Matthews J. M., Gladman B., Bottke W. F., Vokrouhlický D., 2010, ApJ, 716, 315
Morbidelli A., Levison H. F., Tsiganis K., Gomes R., 2005, Nat, 435, 462
Morbidelli A., Brasser R., Gomes R., Levison H. F., Tsiganis K., 2010, AJ, 140, 1391
Nesvorný D., Bottke W. F., Dones L., Levison H. F., 2002, Nat, 417, 720
Nesvorný D., Bottke W. F., Levison H. F., Dones L., 2003, ApJ, 591, 486
Nesvorný D., Vokrouhlický D., Bottke W. F., 2006, Sci, 312, 1490
O'Brien D., Morbidelli A., 2008, LPI Contr., 1405, 8367
Parker A., Ivezić Ž, Jurić M., Lupton R., Sekora M. D., Kowalski A., 2008, Icarus, 198, 138
Quinn T. R., Tremaine S., Duncan M., 1991, AJ, 101, 2287
Roig F., Ribeiro A. O., Gil-Hutton R., 2008, A&A, 483, 911
Šidlichovský M., Nesvorný D., 1997, Celest. Mech. Dynamical Astron., 65, 137
Szabó Gy. M., Ivezić Ž, Jurić M., Lupton R., 2007, MNRAS, 377, 1393
Tanga P., Cellino A., Michel P., Zappalà V., Paolicchi P., Dell'Oro A., 1999, Icarus, 141, 65
Trojanová L., 2010, B.Sc. thesis, Univ. Hradec Králové
Vokrouhlický D., Brož M., Bottke W. F., Nesvorný D., Morbidelli A., 2006, Icarus, 182, 118
Vokrouhlický D., Nesvorný D., Bottke W. F., Morbidelli A., 2010, AJ, 139, 2148
Yang B., Jewitt D., 2007, AJ, 134, 223
Yoshida F., Nakamura T., 2008, PASJ, 60, 297
Zappalá V., Cellino A., Farinella P., Milani A., 1994, AJ, 107, 772

This paper has been typeset from a TEX/LATEX file prepared by the author.

Monthly Notices
of the
ROYAL ASTRONOMICAL SOCIETY

Mon. Not. R. Astron. Soc. **414,** 2716–2727 (2011) doi:10.1111/j.1365-2966.2011.18587.x

# Did the Hilda collisional family form during the late heavy bombardment?

M. Brož,[1⋆] D. Vokrouhlický,[1] A. Morbidelli,[2] D. Nesvorný[3] and W. F. Bottke[3]

[1]*Institute of Astronomy, Charles University, Prague, V Holešovičkách 2, 18000 Prague 8, Czech Republic*
[2]*Observatoire de la Côte d'Azur, BP 4229, 06304 Nice Cedex 4, France*
[3]*Department of Space Studies, Southwest Research Institute, 1050 Walnut St., Suite 300, Boulder, CO 80302, USA*

Accepted 2011 February 22. Received 2011 February 3; in original form 2011 January 5

**ABSTRACT**

We model the long-term evolution of the Hilda collisional family located in the 3/2 mean-motion resonance with Jupiter. Its eccentricity distribution evolves mostly due to the Yarkovsky/YORP effect and assuming that (i) impact disruption was isotropic and (ii) albedo distribution of small asteroids is the same as for large ones, we can estimate the age of the Hilda family to be $4^{+0}_{-1}$ Gyr. We also calculate collisional activity in the J3/2 region. Our results indicate that current collisional rates are very low for a 200-km parent body such that the number of expected events over gigayears is much smaller than 1.

The large age and the low probability of the collisional disruption lead us to the conclusion that the Hilda family might have been created during the late heavy bombardment (LHB) when the collisions were much more frequent. The Hilda family may thus serve as a test of orbital behaviour of planets during the LHB. We have tested the influence of the giant-planet migration on the distribution of the family members. The scenarios that are consistent with the observed Hilda family are those with fast migration time-scales $\simeq$0.3–3 Myr, because longer time-scales produce a family that is depleted and too much spread in eccentricity. Moreover, there is an indication that Jupiter and Saturn were no longer in a compact configuration (with period ratio $P_S/P_J > 2.09$) at the time when the Hilda family was created.

**Key words:** methods: numerical – celestial mechanics – minor planets, asteroids: general.

## 1 INTRODUCTION

There are many independent lines of evidence that the orbits of planets of the Solar system were not the same all the time, but that they have changed substantially over billions of years. The major arguments are based on the observed orbital distribution of Kuiper belt objects (Malhotra 1995; Levison et al. 2008) or small but non-negligible eccentricities and inclinations of the giant planets (Tsiganis et al. 2005). Observations of Jupiter's Trojans (Morbidelli et al. 2005), main-belt asteroids (Minton & Malhotra 2009; Morbidelli et al. 2010), the amplitudes of secular oscillations of the planetary orbits (Brasser et al. 2009; Morbidelli et al. 2009), or the existence of irregular moons (Nesvorný, Vokrouhlický & Morbidelli 2007) provide important constraints for planetary migration scenarios.

Asteroids are a fundamental source of information about the evolution of the planetary system. Some of the resonant groups, i.e. those which are located in the major mean-motion resonances with Jupiter, might also have been influenced by planetary migration, because their current distribution does not match the map of the currently stable regions. For instance, there are two stable islands denoted by A and B in the J2/1 resonance and only the B island is populated (Nesvorný & Ferraz-Mello 1997).

In this work we focus on the Hilda asteroid family in the 3/2 resonance with Jupiter. We exploit our ability to model long-term evolution of asteroid families, which is usually dominated by the Yarkovsky effect on the orbital elements (Bottke et al. 2001), often coupled to the YORP effect on the spin rate and obliquity (Vokrouhlický et al. 2006b). Chaotic diffusion in eccentricity and sometimes interactions with weak mean-motion or secular resonances (Vokrouhlický et al. 2006a) also play important roles. In case of asteroids inside strong mean-motion resonances, one has to account for the 'resonant' *Yarkovsky effect*, which causes a systematic drift in eccentricity (Brož & Vokrouhlický 2008). This is different from usual non-resonant orbits where the Yarkovsky effect causes a drift in semimajor axis.

The Hilda collisional family – a part of the so-called Hilda group in the 3/2 mean motion resonance with Jupiter – was already briefly discussed by Brož & Vokrouhlický (2008). However, the modelling presented in that paper was not very successful, since the resulting age of the family seemed to be too large (exceeding 4 Gyr). This was an important motivation for our current work. We think that we missed an important mechanism in our previous model, namely perturbations arising from the migration of the giant planets and also an appropriate treatment of the YORP effect. Indeed, the age

⋆E-mail: mira@sirrah.troja.mff.cuni.cz

$\gtrsim$4 Gyr suggests that the planetary migration might have played a *direct* role during the early evolution of the Hilda family. In this paper we thoroughly test this hypothesis.

The paper is organized as follows. First we study the observed properties of the J3/2 resonance population in Section 2. Our dynamical model of the Hilda family (without migration first) is described in Section 3. Then we estimate the collisional activity in the J3/2 region in Section 4. The results of our simulations of the giant-planet migration are presented in Section 5. Finally, Section 6 is devoted to conclusions.

## 2 CURRENT ASTEROID POPULATION IN THE J3/2 RESONANCE

Asteroids located in the 3/2 mean motion resonance with Jupiter have osculating semimajor axes around $(3.96 \pm 0.04)$ au, i.e. beyond the main asteroid belt. Contrary to the Kirkwood gaps (associated with J3/1, J7/3 or J2/1 resonances), this resonance is populated by asteroids while its neighbourhood is almost empty. The Hilda collisional family we are going to discuss in detail is a small part of the whole J3/2 resonant population.

Our identification procedure of the J3/2 resonant population was described in the previous paper, Brož & Vokrouhlický (2008). Using the AstOrb catalogue of orbits (version JD = 245 5500.5, 2010 October 31) we identified 1787 numbered and multi-opposition bodies with the librating critical argument

$$\sigma = \frac{p+q}{q}\lambda' - \frac{p}{q}\lambda - \varpi\,, \tag{1}$$

where $p = 2$, $q = 1$, $\lambda'$ is the mean longitude of Jupiter, $\lambda$ the mean longitude of the asteroid and $\varpi$ the longitude of perihelion of the asteroid.

In order to study the detailed distribution of the bodies librating inside the resonance, we have to use pseudo-proper resonant elements defined as approximate surfaces of sections (Roig, Nesvorný & Ferraz-Mello 2002), i.e. the intersection of the trajectory with a plane defined by

$$|\sigma| < 5^\circ\,, \quad \frac{\Delta\sigma}{\Delta t} > 0\,, \quad |\varpi - \varpi'| < 5^\circ\,. \tag{2}$$

These conditions correspond to the maximum of the semimajor axis $a$ over several oscillations and the minimum of the eccentricity $e$ or the inclination $I$. We need to apply a digital filter to $\sigma(t)$ prior to using equation (2), namely filter A from Quinn, Tremaine & Duncan (1991), by sampling 1 yr and with a decimation factor of 10, to suppress fast $\simeq$80 yr oscillations, which would otherwise disturb slower $\simeq$280 yr oscillations associated with resonant librations. Finally, we apply an averaging of the sections $a$, $e$, $I$ over 1-Myr running window and these averages are the pseudo-proper elements $a_\mathrm{p}, e_\mathrm{p}, I_\mathrm{p}$. The accuracy of the pseudo-proper elements is of the order of $10^{-4}$ au for $a_\mathrm{p}$ and $10^{-4}$ for $e_\mathrm{p}$ or $\sin I_\mathrm{p}$, which is much smaller than those of the structures we are interested in.

The overall dynamical structure of the J3/2 resonance is determined by secular resonances $\nu_5$, $\nu_6$ at high eccentricities $e_\mathrm{p} \gtrsim 0.3$ and secondary resonances at lower values of $e_\mathrm{p} \lesssim 0.13$ (according to Morbidelli & Moons 1993; Nesvorný & Ferraz-Mello 1997; Ferraz-Mello et al. 1998; Roig & Ferraz-Mello 1999). They destabilize the orbits at the borders of a stable island. The orbits inside the island exhibit very low chaotic diffusion rates, so bodies can remain there for 4 Gyr (without non-gravitational perturbation).

Next we apply a hierarchical clustering method (Zappalà et al. 1994) to detect significant clusters. We use a standard metric in the pseudo-proper element space $(a_\mathrm{p}, e_\mathrm{p}, \sin I_\mathrm{p})$:

$$\delta v = na\sqrt{\frac{5}{4}\left(\frac{\delta a_\mathrm{p}}{a_\mathrm{p}}\right)^2 + 2\left(\delta e_\mathrm{p}^2\right) + 2(\delta \sin I_\mathrm{p})^2}\,. \tag{3}$$

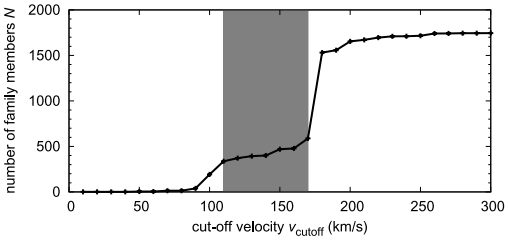


**Figure 1.** The number $N$ of the Hilda family members versus the selected cut-off velocity $v_{\text{cut-off}}$.

In the following, we do not discuss the known Schubart family, which was sufficiently analysed elsewhere (Brož & Vokrouhlický 2008), but we focus on the family associated with (153) Hilda. A suitable cut-off velocity for the Hilda family seems to be $v_{\text{cut-off}} = 140\,\mathrm{m\,s^{-1}}$, because the number of members does not change substantially around this value (see Fig. 1). The number of members at this cut-off is 400.

The resulting plots $(a_\mathrm{p}, H)$, $(e_\mathrm{p}, H)$ and $(I_\mathrm{p}, H)$ of the Hilda family show very interesting features (see Fig. 2). The distribution of semimajor axis and inclination seems rather uniform and almost independent of absolute magnitude $H$, but the eccentricities of small asteroids (i.e. with high $H$) are clearly concentrated at the outskirts of the family and depleted in the centre.

In order to explain the distribution of asteroids in the $(e_\mathrm{p}, H)$ plane we have to recall that asteroids orbiting about the Sun are affected by non-gravitational forces, mostly by the Yarkovsky/YORP effect, i.e. the recoil force/torque due to anisotropic emission of thermal radiation. We consider the concentrations in the $(e_\mathrm{p}, H)$ plane to be a strong indication of the ongoing Yarkovsky/YORP evolution, because they are very similar to those observed among the several main-belt families in the $(a_\mathrm{p}, H)$ plane and successfully modelled by Vokrouhlický et al. (2006b). The difference between these two cases stems from the fact that the main-belt families are non-resonant and the Yarkovsky/YORP effect thus increases or decreases the semimajor axis (depending on the actual obliquity of the spin axis), while in our resonant case, the same perturbation results instead in a systematic increase or decrease of eccentricity. A detailed modelling of the $e$-distribution is postponed to Section 3.5.

The central part of the $(e_\mathrm{p}, H)$ distribution, from $e = 0.17$–$0.23$, seems rather extended. The large asteroids ($H < 12.5$ mag) are spread over this interval of eccentricities even though their Yarkovsky drift rates must have been small. Only 2–4 of them are likely to be interlopers, because there is a very small number of background asteroids in the surroundings of the family (see Fig. 3). We think this shape might actually be the result of the initial-size-independent perturbation that the family distribution received by the migration of the giant planets (which we discuss in Section 5.1).

Regarding the $(a_\mathrm{p}, H)$ distribution, the largest asteroid (153) Hilda is offset with respect to the centre, but this is a natural outcome of the definition of the pseudo-proper elements – fragments that fall to the left of the libration centre are mapped to the right, which creates the offset.

The geometric albedos for Hilda family objects are poorly known. There are only six measured values for the family members: 0.064,

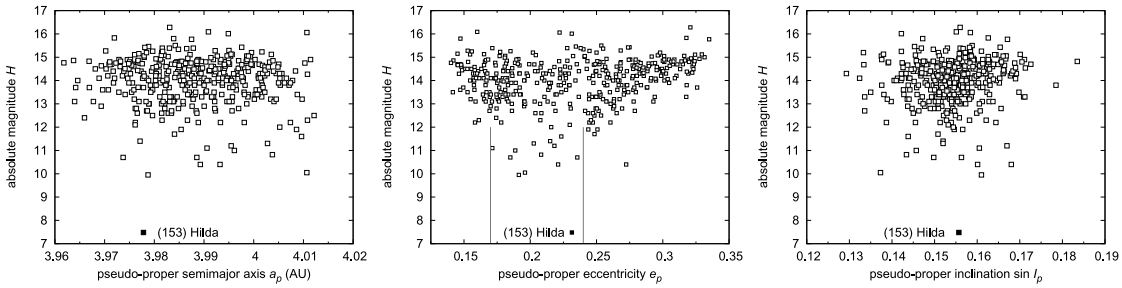


**Figure 2.** The Hilda family displayed in resonant semimajor axis $a_\mathrm{p}$ (left), eccentricity $e_\mathrm{p}$ (middle) and inclination $\sin I_\mathrm{p}$ (right) versus absolute magnitude $H$. The libration centre is located at $a \simeq 3.96$ au and all the bodies are displayed to the right of it. The 'ears' in ($e_\mathrm{p}$, $H$), i.e. both the concentration of small asteroids on the outskirts of the family and their depletion at the centre are very prominent here. The thin vertical lines denote the central part of the ($e_\mathrm{p}$, $H$) distribution discussed in the text. The family has 400 members at $v_\mathrm{cut\text{-}off} = 140\,\mathrm{m\,s^{-1}}$.

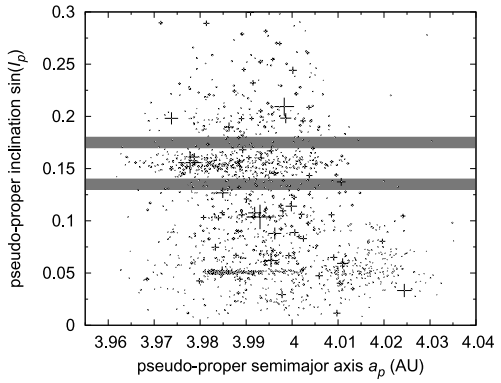


**Figure 3.** The J3/2 region displayed in ($a_\mathrm{p}$, $I_\mathrm{p}$) plot. A very prominent Schubart cluster (studied by Brož & Vokrouhlický 2008) is visible around $\sin I_\mathrm{p} \doteq 0.05$. The close surroundings of the Hilda family, where only a low number of bodies is present, are highlighted by grey rectangles.

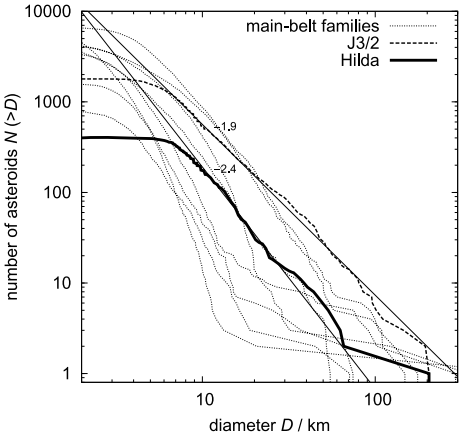


**Figure 4.** Cumulative size distributions of the J3/2 population and the Hilda family. The polynomial fits of the form $N(>D) = CD^\gamma$ are plotted as thin lines, together with the respective values of the $\gamma$ exponent. Several main-belt families are plotted for comparison: Eos (with slope $\gamma = -2.8$), Eunomia ($-5.0$), Hygiea ($-3.8$), Koronis ($-2.8$), Themis ($-2.9$), Tirela ($-3.3$), Veritas ($-3.4$) and Vesta ($-5.4$).

0.046, 0.038, 0.089, 0.044, 0.051 (Davis & Neese 2002). Given the small number of values and the possibility of selection effects, we prefer to assume that the family members have a mean value $p_V = 0.044$, which corresponds to the whole J3/2 population. The size of the parent body can be then estimated to be $D_\mathrm{PB} = (200 \pm 20)$ km. We employ two independent methods to determine the diameter $D_\mathrm{PB}$: (i) we sum the volumes of the observed bodies larger than an assumed completeness limit $D_\mathrm{complete} = 10$ km and then we prolong the slope of the size–frequency distribution down to $D = 0$ to account for unobservable bodies (see Brož & Vokrouhlický 2008), which results in $D_\mathrm{PB} \simeq 185$ km; (ii) we also use a geometric method developed by Tanga et al. (1998) which gives $D_\mathrm{PB} \simeq 210$ km. A test with different albedo values will be described in Section 3.6.

The size–frequency distribution $N(>D)$ versus $D$ of the Hilda family is steeper than that of background J3/2 population, but shallower than for usual main-belt families (Fig. 4). Interestingly, the slope $\gamma = -2.4 \pm 0.1$ of the distribution $N(>D) = CD^\gamma$ is close to a collisional equilibrium calculated by Dohnanyi (1969).

Colour data extracted from the Sloan Digital Sky Survey Moving Object Catalogue version 4 (Parker et al. 2008) confirm that the Hilda family belongs to the taxonomic type C, because most of the spectral slopes are small. Recall that the whole J3/2 population exhibits a bimodal distribution of slopes, i.e. it contains a mixture of C- and D-type asteroids.

## 3 THE HILDA FAMILY MODEL WITH RADIATION FORCES

To understand the long-term evolution of the Hilda family, we construct a detailed numerical model, extending efforts in Brož & Vokrouhlický (2008), which includes the following processes: (i) impact disruption, (ii) the Yarkovsky effect, (iii) the YORP effect, (iv) collisions and spin-axis reorientations. We describe the individual parts of the model in the following subsections.

### 3.1 Impact disruption

To obtain initial conditions for the family just after the breakup event, we need a model for the ejection velocities of the fragments. We use a very simple model of an isotropic ejection from the work of Farinella, Froeschlé & Gonczi (1994). The distribution of velocities 'at infinity' follows the function

$$\mathrm{d}N(v)\mathrm{d}v = Cv(v^2 + v_\mathrm{esc}^2)^{-(\alpha+1)/2}\mathrm{d}v\,, \tag{4}$$

with the exponent $\alpha$ being a free parameter, $C$ a normalization constant and $v_\mathrm{esc}$ the escape velocity from the parent body, which

is determined by its size $D_{\rm PB}$ and mean density $\rho_{\rm PB}$ as $v_{\rm esc} = \sqrt{(2/3)\pi G \rho_{\rm PB}}\, D_{\rm PB}$ . The distribution is usually cut at a selected maximum allowed velocity $v_{\rm max}$ to prevent outliers. The actual values of all these parameters are given in Section 3.5. Typically, the overall distribution of velocities has a peak close to the escape velocity, which is approximately $100\,{\rm m\,s^{-1}}$ for a 200-km parent body. The initial velocities $|v|$ of individual bodies are generated by a straightforward Monte Carlo code and the orientations of the velocity vectors $\boldsymbol{v}$ in space are assigned randomly.

Here, we assume the velocity of fragments is independent of their size, which seems reasonable with respect to the observed uniform distribution of the Hilda family in the ($a_{\rm p}$, $H$) and ($I_{\rm p}$, $H$) planes (Fig. 2). We also perform tests with non-isotropic distributions in Section 3.7.

We must also select initial osculating eccentricity $e_{\rm i}$ of the parent body, initial inclination $i_{\rm i}$, as well as true anomaly $f_{\rm imp}$ and argument of perihelion $\omega_{\rm imp}$ at the time of impact disruption. All of these parameters determine the initial shape of the synthetic 'Hilda' family just after the disruption of the parent body. Initial semimajor axis $a_{\rm i}$ is not totally free, instead it is calculated from the initial semimajor axis of Jupiter $a_{\rm Ji}$ and the Kepler's law, since the parent body has to be confined to the J3/2 resonance.

### 3.2 Yarkovsky effect in a resonance

The long-term evolution of asteroid orbits is mainly driven by the Yarkovsky thermal effect. The implementation of the Yarkovsky effect in the *SWIFT* integrator was described in detail in Brož (2006). Only minor modifications of the code were necessary to incorporate spin rate evolution, which is driven by the YORP effect (see Section 3.3).

The thermal parameter we use are reasonable estimates for C/X-type bodies: $\rho_{\rm surf} = \rho_{\rm bulk} = 1300\,{\rm kg\,m^{-3}}$ for the surface and bulk densities, $K = 0.01\,{\rm W\,m^{-1}\,K^{-1}}$ for the surface thermal conductivity, $C = 680\,{\rm J\,kg^{-1}}$ for the heat capacity, $A = 0.02$ for the Bond albedo and $\epsilon_{\rm IR} = 0.95$ for the thermal emissivity parameter.

We can use a standard algorithm for the calculation of the Yarkovsky acceleration which results in a semimajor-axis drift in case of non-resonant bodies. The drift in eccentricity in case of resonant bodies arises 'automatically' due to the gravitational part of the integrator. In Fig. 5 we can see a comparison between the expected drift $\Delta a$ in semimajor axis and the resulting drift $\Delta e$ in eccentricity, computed for the Hilda family (see the explanation in appendix A of Brož & Vokrouhlický 2008). The data can be approximated by a linear relationship, where the departures from linearity are caused mainly by interactions of drifting orbits with embedded weak secular or secondary resonances.

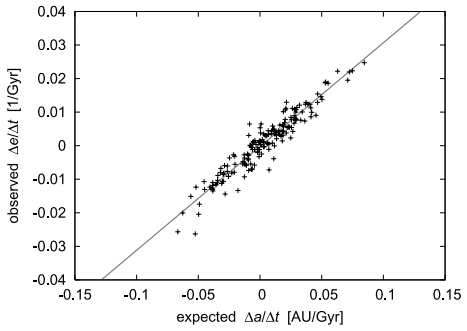


**Figure 5.** An almost linear relation between the expected drift $\Delta a$ in semimajor axis and the simulated drift $\Delta e$ in eccentricity, computed for 360 members of the Hilda family located inside the J3/2 resonance.

Note that according to a standard solar model the young Sun was faint (Güdel 2007), i.e. its luminosity 4 Gyr ago was 75 per cent of the current $L_\odot$. We can then expect a lower insolation and consequently weaker thermal effects acting on asteroids. Since we assume a constant value of $L_\odot$ in our code, the age estimated for the Hilda family (in Section 3.5) can be 12.5 per cent larger.

### 3.3 YORP effect

The magnitude of the Yarkovsky drift sensitively depends on the orientation of the spin axis with respect to the orbital plane and, to a lesser extent, on the angular velocity too. We thus have to account for the long-term evolution of spins of asteroids which is controlled by torques arising from the emission of thermal radiation, i.e. the YORP effect. The implementation of the YORP effect follows Vokrouhlický et al. (2006b). We assume the following relations for the rate of angular velocity and obliquity:

$$\frac{{\rm d}\omega}{{\rm d}t} = f_i(\epsilon)\,, \qquad i = 1, \ldots, 200\,, \tag{5}$$

$$\frac{{\rm d}\epsilon}{{\rm d}t} = \frac{g_i(\epsilon)}{\omega}\,, \tag{6}$$

where $f$- and $g$-functions are given by Čapek & Vokrouhlický (2004) for a set of 200 shapes with mean radius $R_0 = 1$ km, bulk density $\rho_0 = 2500\,{\rm kg\,m^{-3}}$, located on a circular orbit with semimajor axis $a_0 = 2.5$ au. The shapes of the Hilda family members are not known, so we assign one of the artificial shapes (denoted by the index $i$) randomly to each individual asteroid. We only have to scale the $f$- and $g$-functions by the factor

$$c = c_{\rm YORP} \left(\frac{a}{a_0}\right)^{-2} \left(\frac{R}{R_0}\right)^{-2} \left(\frac{\rho_{\rm bulk}}{\rho_0}\right)^{-1}\,, \tag{7}$$

where $a$, $R$, $\rho_{\rm bulk}$ are semimajor axis, radius and density of the simulated body, and $c_{\rm YORP}$ is a free scaling parameter, which can account for an additional uncertainty of the YORP model. Because the values of $f$ and $g$ were computed for only a limited set of obliquities (with a step $\Delta\epsilon = 30^\circ$) we use interpolation by Hermite polynomials (Hill 1982) of the data in Čapek & Vokrouhlický (2004) to obtain a smooth analytical function each for $f_i(\epsilon)$ and $g_i(\epsilon)$.

If the angular velocity approaches a critical value,

$$\omega_{\rm crit} = \sqrt{\frac{8}{3}\pi G \rho_{\rm bulk}}\,, \tag{8}$$

we assume a mass-shedding event, so we keep the orientation of the spin axis and the sense of rotation, but we reset the orbital period $P = 2\pi/\omega$ to a random value from the interval (2.5, 9) h. We also change the assigned shape to a different one, since any change of shape may result in a different YORP effect.

The differential equations (5) and (6) are integrated numerically by a simple Euler integrator. The usual time-step is $\Delta t = 1000$ yr. An example of the results computed by the spin integrator for the Hilda family is displayed in Fig. 6. The typical time-scale of the spin-axis evolution is $\tau_{\rm YORP} \simeq 500$ Myr. After $\simeq 3$ times $\tau_{\rm YORP}$ most bodies have spin axes perpendicular to their orbits, what maximizes the Yarkovsky drift rate of eccentricity.

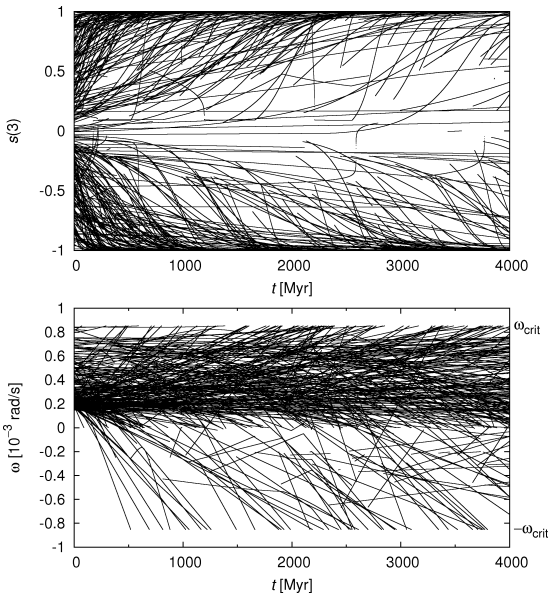


**Figure 6.** An example of the YORP-driven evolution of obliquities (namely a $z$-component of the spin-axis unit vector, top panel) and angular velocities $\omega$ (bottom panel) for the members of the synthetic 'Hilda' family. At the beginning, all values of $\omega$ were selected positive and spin axes were distributed isotropically. The evolution may force $\omega$ to become negative, which simply corresponds to an opposite orientation of the spin axis. The scaling parameter selected for this run was $c_{\rm YORP} = 0.33$.

### 3.4 Collisions and spin-axis reorientations

In principle, collisions may directly affect the size distribution of the synthetic Hilda family, but we neglect this effect because most of the asteroids are large enough to remain intact.

However, we include spin-axis reorientations caused by collisions. We use an estimate of the time-scale by Farinella, Vokrouhlický & Hartmann (1998):

$$\tau_{\rm reor} = B \left(\frac{\omega}{\omega_0}\right)^{\beta_1} \left(\frac{D}{D_0}\right)^{\beta_2}, \qquad (9)$$

where $B = 84.5\,{\rm kyr}$, $\beta_1 = 5/6$, $\beta_2 = 4/3$, $D_0 = 2\,{\rm m}$ and $\omega_0$ corresponds to period $P = 5$ h. These values are characteristic of the main belt and we use them as an upper limit of $\tau_{\rm reor}$ for the J3/2 region. Even so, the time-scale is $\tau_{\rm reor} \simeq 3\,{\rm Gyr}$ for the smallest observable ($D \simeq 5\,{\rm km}$) bodies, and reorientations are thus only of minor importance. Note that the probability of the reorientation is enhanced when the YORP effect drives the angular velocity $\omega$ close to zero.

### 3.5 Results for the Yarkovsky/YORP evolution

We start a simulation with an impact disruption of the parent body and create 360 fragments. Subsequent evolution of the synthetic Hilda family due to the Yarkovsky/YORP effect is computed up to 6 Gyr in order to estimate the time-span needed to match the observed family even though the family cannot be older than $\simeq$4 Gyr, of course. Planets are started on their current orbits. A typical outcome of the simulation is displayed in Fig. 7.

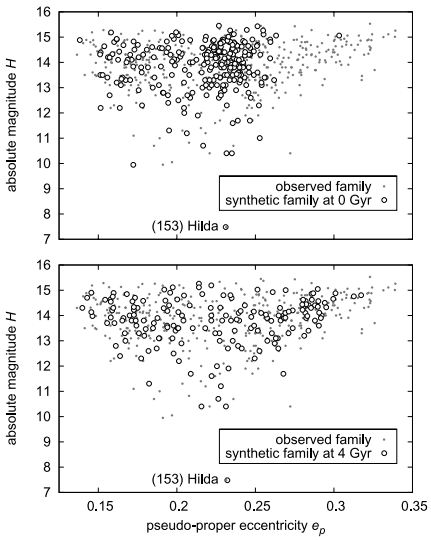


**Figure 7.** Eccentricity versus absolute magnitude plot for the synthetic 'Hilda' family just after the impact disruption (time $t = 0$, top panel) and after 4 Gyr of evolution due to the Yarkovsky/YORP effect (bottom panel). There is a comparison with the observed Hilda family (grey dots).

Due to the long integration time-span and large number of bodies, we were able to compute only four simulations with the following values of true anomaly and YORP efficiency:

(i) $f_{\rm imp} = 0^\circ$, $c_{\rm YORP} = 0$;
(ii) $f_{\rm imp} = 180^\circ$, $c_{\rm YORP} = 0$;
(iii) $f_{\rm imp} = 0^\circ$, $c_{\rm YORP} = 1$;
(iv) $f_{\rm imp} = 0^\circ$, $c_{\rm YORP} = 0.33$.

The remaining parameters were fixed: $e_{\rm i} = 0.14$, $i_{\rm i} = 7\overset{\circ}{.}8$, $\omega_{\rm imp} = 30^\circ$, $\alpha = 3.25$, $v_{\rm max} = 300\,{\rm m\,s^{-1}}$, $R_{\rm PB} = 93.5\,{\rm km}$, $\rho_{\rm PB} = 1300\,{\rm kg\,m^{-3}}$, $p_V = 0.044$.

We are mainly concerned with the distribution of eccentricities $e_{\rm p}$, because the observed family has a large spread of $e_{\rm p}$ values, while the initial synthetic family is very compact. For this purpose we constructed a Kolmogorov–Smirnov test (Press et al. 1999) of the normalized cumulative distributions $N(<e)$:

$$D_{\rm KS} = \max_{0<e<1} |N(<e)_{\rm syn} - N(<e)_{\rm obs}|\,, \qquad (10)$$

which provides a measure of the difference between the synthetic Hilda family, at a given time, and the observed Hilda family (see Fig. 8 for an example). The results of the KS tests are summarized in Fig. 9 (the first four panels).

There is an easy possibility to asses the sensitivity of results with respect to the $v_{\rm max}$ parameter too, without the need to compute the simulation again. We simply select bodies fulfilling the condition $v < v'_{\rm max}$, with $v'_{\rm max} = 200$, 100 or $50\,{\rm m\,s^{-1}}$, and recompute only the KS statistics for this subset. The results are plotted in Fig. 9 as thin lines. We can state that values lower than $v_{\rm max} \simeq 100\,{\rm m\,s^{-1}}$ are surely excluded.

As a preliminary conclusion we may say that all simulations point to a large age of the Hilda family. The $e_{\rm p}$-distributions are most compatible with the observed family for ages $t = (4.0 \pm 1.0)$ Gyr. This suggests that the Hilda family might have experienced the giant-planet migration period which is dated by the late heavy bombardment to $t_{\rm LHB} \simeq 3.85\,{\rm Gyr}$ (Gomes et al. 2005). The large

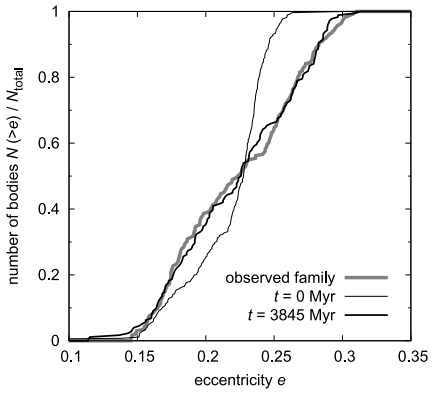


**Figure 8.** Normalized cumulative distributions $N(<e)$ of eccentricities for (i) the observed Hilda family, (ii) the synthetic 'Hilda' family at time $t = 0$ (just after the impact disruption), (iii) evolved due to the Yarkovsky/YORP effect (at time $t = 3845$ Myr). In this figure we show the best fit for the simulation with parameters $f_{\rm imp} = 0^\circ$, $c_{\rm YORP} = 0.33$. Note that the 'bent' shape of the observed distribution corresponds to the 'ears' on the ($e_{\rm p}$, $H$) plot (Fig. 2). There is no perturbation by planetary migration in this particular case.

uncertainty of the age stems from the fact that the runs including the YORP effect ($c_{\rm YORP} \geq 0.33$) tend to produce ages at a lower limit of the interval while the YORP-less runs (with $c_{\rm YORP} = 0$) tend to the upper limit.

### 3.6 Alternative hypothesis: high albedos of small asteroids

We now discuss two scenarios that further reduce the minimal age of the family: (i) high albedos of small asteroids (i.e. larger Yarkovsky/YORP drift); (ii) strongly asymmetric velocity field after impact (like that of the Veritas family).

Albedo is the most important unknown parameter, which can affect results on the Yarkovsky/YORP evolution. Fernández, Jewitt & Ziffer (2009) measured albedos of small Trojan asteroids and found systematically larger values than those for large Trojans. If we assume that the J3/2 asteroids behave similarly to Trojans, we may try a simulation with a rather high value of geometric albedo $p_V = 0.089$ (compared to previous $p_V = 0.044$). Moreover, we decrease density $\rho_{\rm bulk} = 1200\,{\rm kg\,m^{-3}}$, increase maximum velocity of fragments $v_{\rm max} = 500\,{\rm m\,s^{-1}}$ (though the velocity distribution is still determined by equation 4) and select true anomaly $f_{\rm imp} = 90^\circ$ to maximize the spread of $e_{\rm p}$ values.

The KS test is included in Fig. 9, panel (e). The most probable age is $(2.3 \pm 0.5)$ Gyr in this case. However, we do not think that the size-dependent albedo is very plausible because both large and small family members should originate from the same parent body and their albedos, at least just after the disruption, should be similar. Nevertheless, the albedos may change to a certain degree due to space weathering processes (Nesvorný et al. 2005). Unfortunately, we do not have enough data for small asteroids to assess a possible albedo difference between large and small family members.

### 3.7 Alternative hypothesis: strongly asymmetric velocity field

Another possibility to reduce the estimate of the family age is that the original velocity was highly anisotropic. A well-known example from the main belt is the Veritas family. Let us assume that the anisotropy is of the order of Veritas, i.e. approximately four times larger in one direction. Note that Veritas is a young family and can be modelled precisely enough to compensate for chaotic diffusion in resonances (Nesvorný et al. 2003; Tsiganis, Knežević & Varvoglis 2007). This family is characterized by a large spread of inclinations, which corresponds to large out-of-plane components of velocities. In case of the Hilda family we multiply by 4 the radial components of initial velocities to maximize the dispersion of eccentricities, assuming the most favourable geometry of disruption ($f_{\rm imp} \doteq 90^\circ$).

The fit in Fig. 9, panel (f), is seemingly better at the beginning of the simulation, but bodies on unstable orbits are quickly eliminated and the fit gets much worse at $t \simeq 500$ Myr. We can see that the synthetic Hilda family is similar to the observed Hilda family quite early (at $t \simeq 2.5$ Gyr); however, the best fit is at later times ($t \simeq 3.5$ Gyr), so there is no significant benefit compared to isotropic velocity-distribution cases.

## 4 DISRUPTION RATES IN THE J3/2 POPULATION

### 4.1 Present collisional activity

The results presented above show that the Hilda family is old. However, the uncertainty of the age is too large to conclude whether or not the family formed during the late heavy bombardment (LHB) period. An alternative constraint is the collisional lifetime of the parent body. If the probability that the parent body broke in the last 4 Gyr in the current collisional environment is negligible, it would argue that the family broke during the LHB when the collisional bombardment was much more severe. Thus, here we estimate the collisional lifetime of the parent body.

In our case, the target (parent body) has a diameter $D_{\rm target} = 200$ km, a mean impact velocity $V_{\rm i} = 4.8\,{\rm km\,s^{-1}}$ (Dahlgren 1998), and a probable strength $Q^\star_{\rm D} = 4 \times 10^5\,{\rm J\,kg^{-1}}$ (Benz & Asphaug 1999), and thus the necessary impactor size (Bottke et al. 2005) is

$$d_{\rm disrupt} = \left(2Q^\star_{\rm D}/V_{\rm i}^2\right)^{1/3} D_{\rm target} \simeq 65\,{\rm km}\,. \quad (11)$$

The population of $\geq$65 km projectiles is dominated by main-belt bodies: $n_{\rm project} \simeq 160$, according to Bottke et al. (2006), and we have only one 200-km target in the J3/2 region, so $n_{\rm target} = 1$. The intrinsic collisional probability for Hilda versus main belt collisions is $P_{\rm i} = 6.2 \times 10^{-19}\,{\rm km^{-2}\,yr^{-1}}$ (Dahlgren 1998) and the corresponding frequency of disruptions is

$$f_{\rm disrupt} = P_{\rm i} \frac{D^2_{\rm target}}{4} n_{\rm project} n_{\rm target} \simeq 10^{-12}\,{\rm yr^{-1}}\,. \quad (12)$$

Thus, over the age of the Solar system $T_{\rm SS} \simeq 4$ Gyr (after LHB), we expect a very small number of such events $n_{\rm events} = T_{\rm SS} f_{\rm disrupt} \simeq 0.004$.

The value of strength $Q^\star_{\rm D}$ used above corresponds to strong targets. Though there is a theoretical possibility that the Hilda parent body was weaker, it does not seem to us likely, because the Hilda family is of the C taxonomic type. Thus, it is rather similar to (presumably stronger) main belt asteroids, than to (likely weaker) D-type objects. Anyway, even if we use an order of magnitude lower strength inferred for weak ice, $Q^\star_{\rm D} \simeq 4 \times 10^4\,{\rm J\,kg^{-1}}$ (see Leinhardt & Stewart 2009; Bottke et al. 2010), we obtain $d_{\rm disrupt} \simeq 30$ km, $n_{\rm project} \simeq 360$ and $n_{\rm events} \simeq 0.009$, so the conclusion about the low number of expected families remains essentially the same.

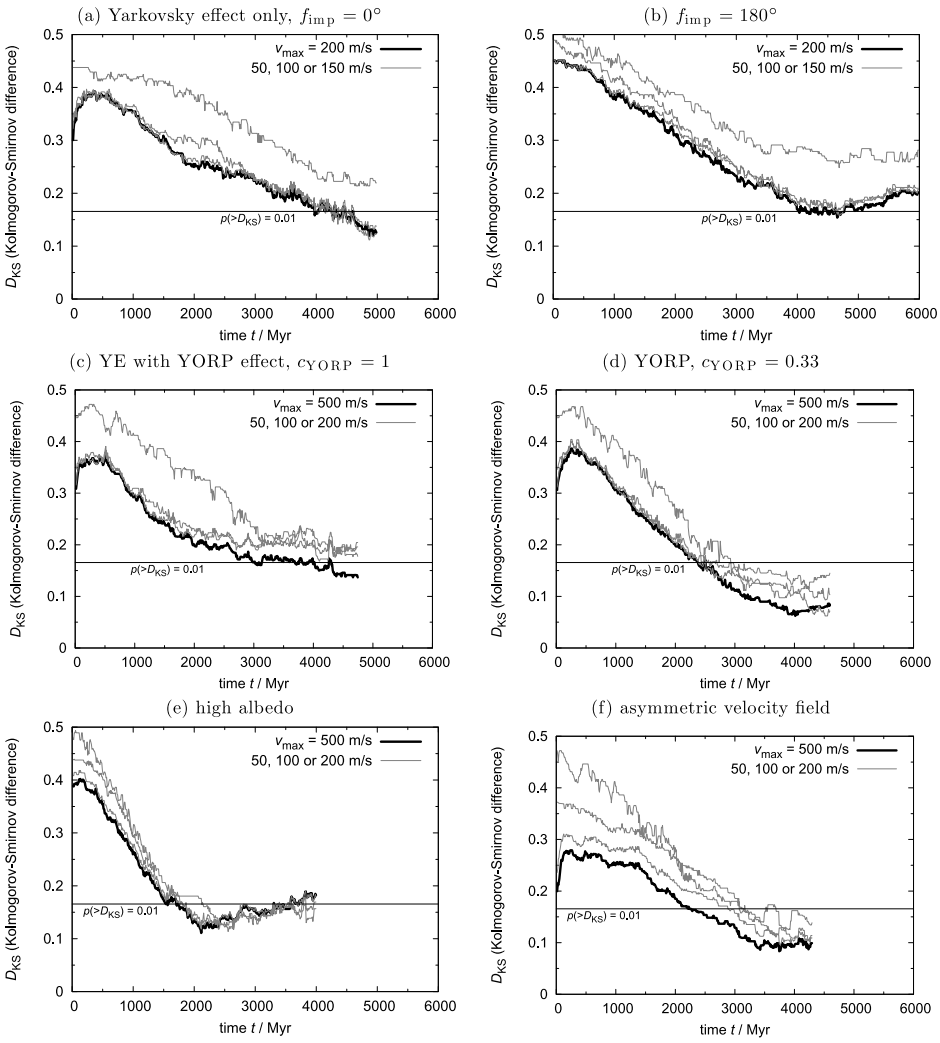


**Figure 9.** Kolmogorov–Smirnov tests of the synthetic 'Hilda' family: (a) no migration, only initial disruption (at anomaly $f_{\rm imp} = 0°$, $\varpi_{\rm i} = 30°$) and subsequent Yarkovsky evolution; (b) the case with $f_{\rm imp} = 180°$; (c) including the YORP effect; (d) YORP with efficiency factor $c_{\rm YORP} = 0.33$; (e) high albedo values (i.e. small bodies); (f) strongly asymmetric velocity field. The horizontal line denotes the distance $D_{\rm KS} = 0.165$ for which the probability $p(>D_{\rm KS})$ that the two eccentricity distributions differ by this amount equals 0.01.

### 4.2 The late heavy bombardment

We now compute the probability that the parent body broke during the LHB. We can think of two projectile populations: (i) transient decaying cometary disc; (ii) D-type asteroids captured in the J3/2. Models like that of Levison et al. (2009) suggest that the decay time-scale of the cometary bombardment is of the order of 10–100 Myr and the flux of impactors integrated over this time-span might have been 100 times larger than it is today. Higher mean collisional velocities, due to projectiles on high-$e$ and high-$i$ orbits, are also favourable.

In order to estimate collisional activity we use a self-consistent model of the cometary disc from Vokrouhlický, Nesvorný & Levison (2008). Their $N$-body simulations included four giant planets and 27 000 massive particles with a total mass of $M_{\rm disc} = 35\,{\rm M}_\oplus$. The orbital evolution was propagated by the SyMBA integrator for 100 Myr. Using the output of these simulations, we calculate the mean intrinsic collisional probabilities $P_{\rm i}(t)$ between the cometary-disc population (at given time $t$) and the current J3/2 population. We use an algorithm described in Bottke et al. (1994) for this purpose. Typically, the $P_{\rm i}$ reaches 2to3 $\times$ $10^{-21}\,{\rm km^{-2}\,yr^{-1}}$ and the corresponding mean impact velocities are $V_{\rm imp} = 7$–$10\,{\rm km\,s^{-1}}$ (see Fig. 10).

The necessary impactor size is slightly smaller than before, $d_{\rm disrupt} = 40$–$50\,{\rm km}$ due to larger $V_{\rm imp}$. To estimate the number of such projectiles we assume that the cometary disc had a size distribution described by a broken power law with differential slopes $q_1 = 5.0$ for $D > D_0$, $q_2 = 2.5 \pm 0.5$ for $D < D_0$, where the diameter corresponding to the change of slopes is $D_0 = 50$–$70\,{\rm km}$. We then use the following expressions to calculate the number of bodies

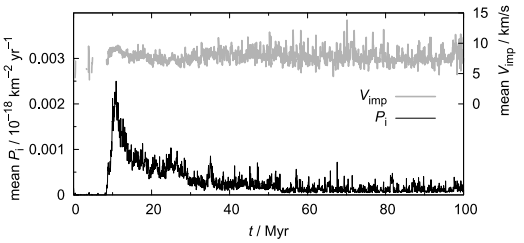


**Figure 10.** Mean intrinsic collisional probability $P_i$ and mean impact velocity $V_{imp}$ versus time for one of the disc simulations from Vokrouhlický et al. (2008).

larger than the given threshold (Vokrouhlický et al. 2008):

$$D_1 = D_0 \left[ \frac{(q_1-4)(4-q_2)}{(q_1-1)(q_1-q_2)} \frac{M_{\rm disc}}{M_0} \right]^{\frac{1}{q_1-1}}, \tag{13}$$

$$N(>D) = \frac{q_1-1}{q_2-1} \left(\frac{D_1}{D_0}\right)^{q_1-1} \left(\frac{D_0}{D}\right)^{q_2-1} - \frac{q_1-q_2}{q_2-1} \left(\frac{D_1}{D_0}\right)^{q_1-1}, \tag{14}$$

where $M_0 = \frac{\pi}{6}\rho D_0^3$ and $\rho = 1300\,\mathrm{kg\,m^{-3}}$. The result of this calculation is $N(>d_{\rm disrupt}) \doteq 0.3$ to $1.7 \times 10^9$. The actual number of bodies in the simulation (27 000) changes in course of time and it was scaled such that initially it was equal to $N(>d_{\rm disrupt})$. The resulting number of events is

$$n_{\rm events} = \frac{D_{\rm target}^2}{4} n_{\rm target} \int P_i(t)\, n_{\rm project}(t)\, {\rm d}t \simeq 0.05 \text{ to } 0.2\,, \tag{15}$$

which is 10–50 times larger than the number found in Section 4.1.

Regarding the captured D-type asteroids, they were probably not so numerous and their impact velocities were lower but their collisional probabilities were larger and the population might have had a substantially longer time-scale of decay (Levison et al. 2009). Using the reasonable values $V_i = 4.0\,\mathrm{km\,s^{-1}}$, $d_{\rm disrupt} = 70\,\mathrm{km}$, $n_{\rm project} = 5000$, $P_i = 2.3 \times 10^{-18}\,\mathrm{km^{-2}\,yr^{-1}}$, $T_{\rm LHB} \simeq 1\,\mathrm{Gyr}$, we obtain the number of events $\simeq$0.1 which is again 25 times larger than the number presented in Section 4.1.

We conclude that the Hilda family was likely created during the LHB when the collisions were much more frequent than in the current collisional environment. We must now test whether the structure of the family is consistent with the giant-planet migration, since it is connected with the LHB.

## 5 PLANETARY MIGRATION

At the LHB-time the planetary migration was most probably caused by the presence of a massive cometary disc. Instead of a full $N$-body model we use a simpler *analytic migration*, with an artificial dissipation applied to the planets. This is the only realistic possibility in our case, because we need to test not only a large number of various migration scenarios but also various initial configurations of the synthetic Hilda family.

For this purpose we use a modified version of the symplectic *SWIFT*–RMVS3 integrator (Levison & Duncan 1994). We account for four giant planets and include the following dissipation term

**Table 1.** Free parameters of our Hilda family model.

| No. | Parameter | Description |
|---|---|---|
| 1 | $a_{\rm Ji}$ | Initial semimajor axis of Jupiter |
| 2 | $a_{\rm Si}$ | Saturn |
| 3 | $e_{\rm Ji}$ | Initial eccentricity of Jupiter |
| 4 | $e_{\rm Si}$ | Saturn |
| 5 | $\tau_{\rm mig}$ | Migration time-scale |
| 6 | $e_{\rm dampJ}$ | Eccentricity damping for Jupiter |
| 7 | $e_{\rm dampS}$ | Saturn |
| 8 | $e_{\rm i}$ | Initial eccentricity of the parent body |
| 9 | $i_{\rm i}$ | Initial inclination |
| 10 | $f_{\rm imp}$ | True anomaly at the impact disruption |
| 11 | $\omega_{\rm imp}$ | Argument of perihelion |
| 12 | $\alpha$ | Slope of the velocity distribution |
| 13 | $v_{\rm max}$ | Maximum velocity of fragments |
| 14 | $R_{\rm PB}$ | Radius of parent body |
| 15 | $\rho_{\rm PB}$ | Bulk density |
| 16 | $p_V$ | Geometric albedo of fragments |
| 17 | $c_{\rm YORP}$ | Efficiency of the YORP effect |

**Table 2.** Fixed (assumed) parameters of the Hilda family model. There are also a number of less important parameters, such as the thermal ones ($\rho_{\rm surf}$, $K$, $C$, $A$, $\epsilon_{\rm IR}$) or the collisional ones ($B$, $\beta_1$, $\beta_2$).

| No. | Parameter | Description |
|---|---|---|
| 18 | $a_{\rm Jf}$ | Final semimajor axis of Jupiter |
| 19 | $a_{\rm Sf}$ | Saturn |
| 20 | $N(<H)$ | (observed) absolute magnitude distribution |

applied to the planets in every time-step:

$$\boldsymbol{v} = \boldsymbol{v} \left[ 1 + \frac{\Delta v}{v} \frac{\Delta t}{\tau_{\rm mig}} \exp\left( -\frac{t-t_0}{\tau_{\rm mig}} \right) \right], \tag{16}$$

where $\boldsymbol{v}$ denotes a velocity vector of a given planet, $v$ is the absolute value of velocity, $\Delta t$ is the time-step, $\tau_{\rm mig}$ is the selected migration time-scale, $\Delta v = \sqrt{GM/a_{\rm i}} - \sqrt{GM/a_{\rm f}}$ the required total change of velocity (i.e. the difference of mean velocities between the initial and the final orbit), $t$ is the time and $t_0$ is some reference time. If there are no perturbations other than (16), the semimajor axis of the planet changes smoothly (exponentially) from the initial value $a_{\rm i}$ to the final $a_{\rm f}$. We use time-step $\Delta t = 36.525$ d and the total time-span of the integration is usually equal to $3\tau_{\rm mig}$ when planetary orbits practically stop to migrate.

We would like to resemble evolution of planetary orbits similar to the Nice model so it is necessary to use an eccentricity-damping formula, which simulates the effects of dynamical friction (Morbidelli et al. 2010). This enables us to model a decrease of eccentricities of the giant planets to relatively low final values. The amount of eccentricity damping is characterized by a parameter $e_{\rm damp}$.

Because inclinations of the planets are not very important for what concerns the perturbation of minor bodies (the structure of resonances is mainly determined by planetary eccentricities), we usually start with the current values of inclination of the planets.

We admit that the analytic migration is only a crude approximation of the real evolution, but we can use it as a first check to see which kinds of migration scenarios are allowed and which are not with respect to the existence and structure of the Hilda family.

As a summary we present a list of free and fixed (assumed) parameters of our model in Tables 1 and 2. According to our numerical tests the initial configuration of Uranus and Neptune is not very important, as these planets do not produce significant direct

perturbations on asteroids located in the J3/2 resonance. We thus do not list the initial semimajor axes and eccentricities of Uranus and Neptune among our free parameters though we include these planets in our simulations.

The problem is that we cannot tune all the 17 parameters together, since the 17-dimensional space is enormous. We thus first select a reasonable set of impact parameters for the family (No. 8–17 in Table 1), keep them fixed, and experiment with various values of migration parameters (No. 1–7). We test roughly $10^3$ migration scenarios. Then, in the second step, we vary impact parameters for a single (successful) migration scenario and check the sensitivity of results.

### 5.1 Results for planetary migration

In the first test we compute an evolution of the synthetic Hilda family during planetary migration phase for the following parameter space (these are not intervals but lists of values): $a_{\rm Ji} = (5.2806$ and $5.2027)$ au, $a_{\rm Si} = (8.6250, 8.8250, 9.3000)$ au, $e_{\rm Ji} = (0.065, 0.045)$, $e_{\rm Si} = (0.08, 0.05)$, $\tau_{\rm mig} = (0.3, 3, 30, 300)$ Myr, $e_{\rm dampJ} = 10^{-11}$, $e_{\rm dampS} = 10^{-11}$.[1] The values of $a_{\rm Ji}$ and $a_{\rm Si}$ correspond to period ratios $P_{\rm S}/P_{\rm J}$ from 2.09 to 2.39 (the current value is 2.49), i.e. the giant planets are placed already *beyond* the 2:1 resonance, since the 2:1 resonance crossing would destroy the Hilda family (Brož & Vokrouhlický 2008). Impact parameters were fixed except $f_{\rm imp}$: $e_{\rm i} = 0.14$, $i_{\rm i} = 7\overset{\circ}{.}8$, $f_{\rm imp} = (0^\circ, 180^\circ)$, $\omega_{\rm imp} = 30^\circ$, $\alpha = 3.25$, $v_{\rm max} = 300\,{\rm m\,s^{-1}}$, $R_{\rm PB} = 93.5$ km, $\rho_{\rm PB} = 1300\,{\rm kg\,m^{-3}}$.

The synthetic Hilda family has 360 bodies in case of short simulations ($\tau_{\rm mig} = 0.3$or3 Myr). In case of longer simulations we create 60 bodies only. Their absolute magnitudes (sizes) were thus selected randomly from 360 observed values. This is a minimum number of bodies necessary to compare the distributions of eccentricities. We performed tests with larger numbers of bodies and the differences do not seem significant.

A comparison of the final orbits of the planets with the current planetary orbits shows we have to exclude some migration simulations (mostly those with Uranus and Neptune on compact orbits). One of the reasons for the unsuccessful scenarios is that a compact configuration of planets is inherently unstable. If the migration time-scale is too large or the eccentricity damping too low, it may result in a violent instability, close encounters between planets and eventually an unrealistic final configuration.

The change in the structure of the synthetic Hilda family due to migration can be seen in Fig. 11. The family is shifted in semimajor axis, because it moves together with the resonance with migrating Jupiter. Moreover, the eccentricities are dispersed while the inclinations are barely affected.

We have found that the eccentricity distribution is modified when secondary resonances occur between the libration frequency $f_{J3/2}$ of an asteroid in the J3/2 resonance and the frequency $f_{\rm 1J-2S}$ of the critical argument of Jupiter–Saturn 1:2 resonance (see Kortenkamp, Malhotra & Michtchenko 2004; Morbidelli et al. 2005 for the case of Trojans):

$$n f_{J3/2} = f_{\rm 1J-2S}\,, \tag{17}$$

[1] In order to increase the statistics we ran simulations multiple times with different initial conditions for Uranus and Neptune: $a_{\rm Ui} = (18.4479,$ $12.3170)$ au, $a_{\rm Ni} = (28.0691, 17.9882)$ au, $e_{\rm Ui} = (0.06, 0.04)$, $e_{\rm Ni} = (0.02,$ $0.01)$.

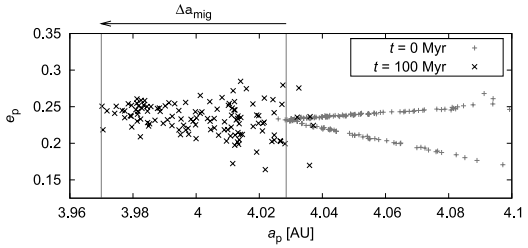


**Figure 11.** A usual evolution of the synthetic 'Hilda' family in the pseudo-proper semimajor axis versus eccentricity plot. The initial ($t = 0$ Myr) and final stages ($t = 100$ Myr) are plotted. The migration time-scale was $\tau_{\rm mig} =$ 30 Myr in this particular example. We selected this longer time-scale because secular frequencies can then be computed more precisely (see Fig. 12). The arrow indicates a total change of the position of the J3/2 resonance due to migration of Jupiter.

where $n$ is a small integer number, $n = 2$, 3 or 4 in our case.[2] We can see the evolution of resonant semimajor axes and the corresponding dominant frequencies, computed by means of periodogram, in Fig. 12.

Because the resonances are localized – they act only at particular values of semimajor axes of planets – it is *not* necessary to have a dense grid in $a_{\rm Ji}$, $a_{\rm Si}$ parameters to study the dependence of the synthetic Hilda family shape on $a_{\rm Ji}$, $a_{\rm Si}$. Essentially, there are only three situations when the Hilda family is strongly perturbed, otherwise the spread in $e$ does not change much in course of time.

A very simple test, which allows us to quickly select allowed migration scenarios, is the number of remaining Hilda family members. We may assume that the depletion by dynamical effects was probably low (say 50 per cent at most), otherwise we would obtain a much larger parent body than $D \simeq 200$ km, which has a much lower probability of collisional disruption. The fractions of the remaining bodies $N_{\rm left}/N_{\rm initial}$ versus initial conditions for planets are displayed in Fig. 13.

The small number of remaining bodies $N_{\rm left}$ indicates that perturbations acting on the synthetic family were too strong. It means either the family had to be formed later (when fewer and weaker secondary resonances are encountered) to match the observed family or this migration scenario is not allowed. The same applies to the dispersion of $e$-distribution (see below): if it is too large compared to the observed Hilda family, the synthetic Hilda had to be formed later or the scenario is not allowed. Our results indicate that

(i) a faster migration time-scale $\tau_{\rm mig} \simeq 0.3$–30 Myr is preferred over slower time-scales;

(ii) Jupiter and Saturn were not in the most compact configuration ($a_{\rm Ji} = 5.2806$ au, $a_{\rm Si} = 8.6250$ au) at the time when the Hilda family was created.

### 5.2 A sensitivity to the impact-related parameters

Another important test was devoted to the impact parameters, which were varied in relatively larger steps: $e_{\rm i} = (0.12, 0.15)$, $i_{\rm i} = (6\overset{\circ}{.}8,$ $8\overset{\circ}{.}8)$, $f_{\rm imp} = (45^\circ, 90^\circ, 135^\circ)$, $\omega_{\rm imp} = (60^\circ, 90^\circ)$, $\alpha = (2.25, 4.25)$, $v_{\rm max} = (200, 400)\,{\rm m\,s^{-1}}$, $R_{\rm PB} = (83.5, 103.5)$ km, $\rho_{\rm PB} = (1000,$ $2000)\,{\rm kg\,m^{-3}}$. Note that the selected impact parameters are rather extreme, reason that we do not expect them to ever be out of these

[2] We also looked for secondary resonances connected with the 4:9, 3:7 and 2:5 Jupiter–Saturn resonances, but we found no significant effects.

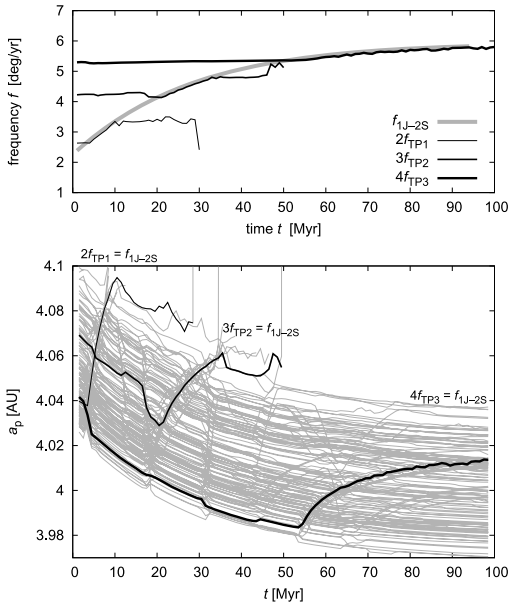


**Figure 12.** Top panel: the frequency $f_{1J-2S}$ of the Jupiter–Saturn 1:2 mean motion critical argument (thick grey curve) versus time $t$. The frequency changes due to the migration of planets with the time-scale $\tau_{mig} = 30$ Myr. We also computed dominant frequencies $f_{J3/2}$ of librations in the J3/2 resonance for three selected members of the synthetic Hilda family (black curves). We do not plot the frequency itself but a selected multiple of it $nf_{J3/2}$. Captures in the secondary resonances of type $nf_{J3/2} = f_{1J-2S}$ are then clearly visible when the frequencies are equal. For the test particle number 1 it occurs between 4 and 10 Myr, particle 2 was captured from 21 to 32 Myr and particle 3 from 54 Myr till the end of the simulation. Bottom panel: the corresponding changes of the pseudo-proper semimajor axes $a_p$ versus time $t$ due to the secondary resonances. The three test particles from the top panel are shown (black curves) together with the remaining members of synthetic 'Hilda' family (grey curves). Note that some particles may be pushed to the border of the stable libration zone and then escape from the J3/2 resonance.

bounds. The total number of simulations is 384. The migration parameters were fixed (they correspond to one successful migration scenario): $a_{Ji} = 5.2806$ au, $a_{Si} = 8.8250$ au, $e_{Ji} = 0.065$, $e_{Si} = 0.08$, $\tau_{mig} = 3$ Myr, $e_{dampJ} = 10^{-11}$, $e_{dampS} = 10^{-11}$.

This time, we decided to use a simple quantity to discuss the results, namely the eccentricity dispersion $\sigma_e$ of the synthetic family at the end of the giant-planet migration. The most frequent values of the dispersion are $\sigma_e = 0.015$–$0.04$ (see the histograms in Fig. 14). Further evolution by the Yarkovsky/YORP effect would increase the dispersions up to $\sigma_e = 0.045$–$0.06$, while the observed dispersion of the Hilda family is $\sigma_e = 0.046$.

It is notable that the histograms look similar for *all* the impact parameters, there is even no apparent correlation between them. The explanation for this 'lack of dependence' is that the eccentricity distribution is mainly determined by the perturbations of the giant planets. A given planetary evolution therefore gives a characteristic value of $\sigma_e$ whatever the impact parameters are. The dispersion in $\sigma_e$ values is due to the fact that the planetary evolutions that we have computed change widely from one simulation to another. Though planet migration was prescribed analytically, there are mutual interactions between planets and random captures in resonances (or jumps across resonances) which may affect the eccentricity distribution of the synthetic Hilda family. An extreme case is shown in Fig. 15. In this particular simulation, Jupiter and Saturn were captured in the mutual 3:7 resonance for 0.5 Myr which resulted in a large eccentricity dispersion $\sigma_e = 0.044$ of the synthetic family. Our conclusion is that the impact parameters are less important than the parameters related to migration.

### 5.3 Matching results together

Even though we do not perform a joint integration which includes both the planetary migration and Yarkovsky/YORP effect, we try to match the previous results from Sections 5.1 and 3.5. We do it by using a straightforward Monte Carlo approach: (i) we take the pseudo-proper eccentricities $e_{mig}$ of bodies at the end of planetary migration from Section 5.1; (ii) we compute the total Yarkovsky/YORP drifts $\Delta e_{YE}$ in eccentricity from Section 3.5; (iii) we assign every body a drift randomly ($e_{final} = e_{mig} + \Delta e_{YE}$) and this way we construct an

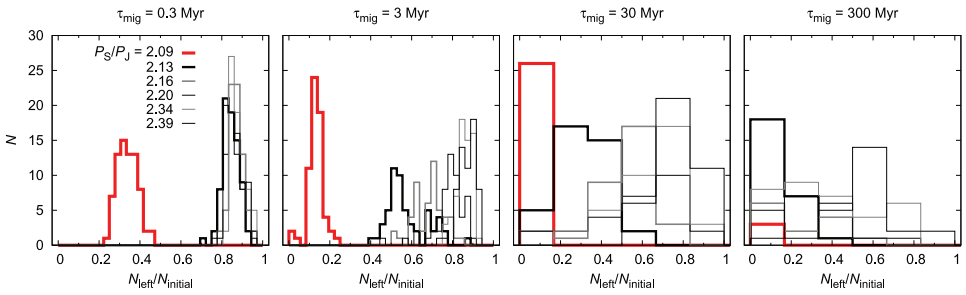


**Figure 13.** The number of simulations $N$ versus the fraction of remaining bodies $N_{left}/N_{initial}$ from the synthetic 'Hilda' family. The histograms are plotted for four different time-scales of migration $\tau_{mig}$ and six different initial configurations of Jupiter and Saturn ($a_{Ji}$, $a_{Si}$; we indicate period ratios $P_{Si}/P_{Ji}$ instead of semimajor axes here). The ranges of the remaining free parameters are mentioned in the text. We only plot the successful migration scenarios with $\Delta v_{planets} \leq 2000\,\mathrm{m\,s^{-1}}$, where $\Delta v_{planets} = \sum_1^4 \delta v_i$ is a sum of the velocity differences $\delta v$ (defined similarly as in the HCM metric, equation 3) between the final simulated orbit of the $i$th planet and the currently observed one. This way we join differences in orbital elements $a$, $e$, $I$ into a single quantity which has the dimension of velocity.

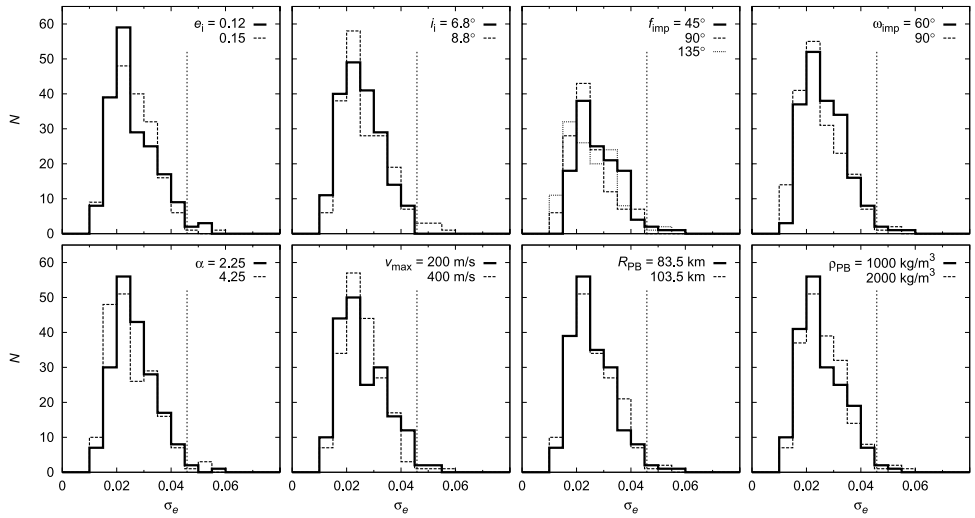


**Figure 14.** Eccentricity dispersions of the synthetic 'Hilda' families at the end of the giant-planet migration for the various initial conditions of the impact disruption: initial eccentricity $e_i$, inclination $i_i$, true anomaly $f_{imp}$, argument of perihelion $\omega_{imp}$, exponent $\alpha$, maximum velocity $v_{max}$, radius of the parent body $R_{PB}$ and its bulk density $\rho_{PB}$. The values of the remaining parameters related to migration are mentioned in the text. Note that there is no evolution by the Yarkovsky/YORP effect in this simulation. The dotted vertical line denotes the value $\sigma_e = 0.046$ of the observed Hilda family.

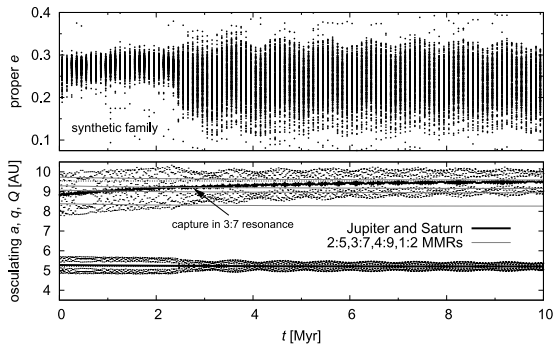


**Figure 15.** An example of the orbital evolution of Jupiter and Saturn with a rare temporary capture in the mutual 3:7 resonance (bottom panel). This sort of evolution leads to a large spread of pseudo-proper eccentricities of the synthetic 'Hilda' family by the end of the migration (top panel).

evolved synthetic family.[3] Finally, we compare the synthetic family to the observed Hilda family by computing a Kolmogorov–Smirnov test for $N(<e_{final})$ and $N(<e_{obs})$ distributions.

To avoid problems with the small number of bodies (60 in case of planetary migration), we perform the above procedure 100 times, always with a different random seed for the assignment of the $\Delta e_{YE}$. We then take a median of the 100 KS statistics as a result for one particular run. The resulting histograms of the median $D_{KS}$ for various initial conditions are shown in Fig. 16.

We confirm the conclusions from Section 5.1 – those migration scenarios that preserve the largest number of family members (i.e. high $N_{left}$) are the same, for which we can find a good fit of eccentricity distribution (low $D_{KS}$). Moreover, it seems we can exclude also the time-scale of migration $\tau_{mig} = 30$ Myr since the total number of successful simulations is significantly smaller in this case.

[3] Note that gravitational perturbations, caused by planetary migration, are independent of size (mass), so a large body may be easily found at the outskirts of the family. This is another reason for the random assignment of Yarkovsky/YORP drifts.

## 6 CONCLUSIONS

Results of this paper can be summarized as follows.

(i) The Hilda family evolves mainly due to the Yarkovsky/YORP effect and the observed large spread of eccentricities indicates the age $4^{+0}_{-1}$ Gyr.

(ii) The collisional disruption of a $D \simeq 200$ km parent body is unlikely in the current environment. Instead, it rather occurred during the LHB when collisions with comets dominated and were up to 50 times more frequent. Another possible source of projectiles is the population of D-type asteroids captured in the J3/2 resonance (Levison et al. 2009).

(iii) In case the Hilda family was created during giant-planet migration, which seems to us likely, the major perturbations of the family were due to secondary resonances between libration frequency and the frequency of Jupiter–Saturn 1:2 critical argument.

(iv) On the basis of our simulations, we argue that the migration was relatively fast (with time-scale $\tau_{mig} \simeq 0.3$–$3$ Myr) and Jupiter and Saturn were relatively closer to the current configuration (with period ratio $P_S/P_J \geq 2.13$ or more) at the moment when the Hilda family was created, otherwise the family would be 'destroyed' by migration. Slower migration time scales are only allowed for larger values of $P_S/P_J$ ratios.

The Hilda family thus proved to be one of the oldest families in the main asteroid belt.

There are emerging indications that orbital evolution of planets was rather violent and close encounters between planets were present (Nesvorný et al. 2007; Brasser et al. 2009). This might be still consistent with our model of the Hilda family, but of course we have to assume that the family formed after severe perturbations

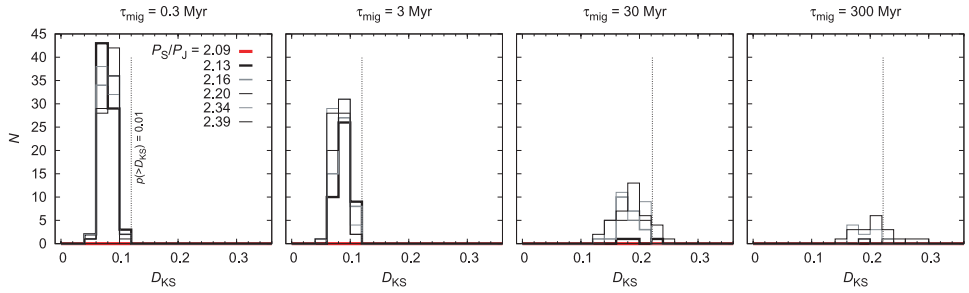


**Figure 16.** The number of simulations $N$ versus the Kolmogorov–Smirnov distance $D_{\rm KS}$ between the synthetic and the observed Hilda family. The simulations differ by the time-scale of migration $\tau_{\rm mig}$ and the initial conditions for Jupiter and Saturn ($a_{\rm Ji}$, $a_{\rm Si}$). We only plot the successful migration scenarios with $\Delta v_{\rm planets} \leq 2000\,{\rm m\,s^{-1}}$ and the number of bodies left $N_{\rm left} > N_{\rm initial}/2$. The dotted vertical line denotes the distance $D_{\rm KS}$ for which the probability $p(>D_{\rm KS})$ that the two eccentricity distributions differ by this amount equals 0.01.

in the J3/2 region ended. A more complicated migration scenario like that of 'jumping Jupiter' (Morbidelli et al. 2010) even seems favourable in our case because Jupiter and Saturn very quickly reach a high period ratio ($P_{\rm S}/P_{\rm J} \gtrsim 2.3$, i.e. the planets are quite close to their current orbits). Then, the perturbations acting on the J3/2 region are already small and the flux of impactors becomes high just *after* the jump. The Hilda family thus might have formed exactly during this brief period of time.

Regarding future improvements of our model, knowledge of geometric albedos for a large number of small asteroids may significantly help and decrease uncertainties. The *WISE* infrared mission seems to be capable of obtaining these data in near future.

## ACKNOWLEDGMENTS

We thank Hal Levison for his code on eccentricity damping, David Čapek for sending us the YORP effect data in an electronic form and an anonymous referee for constructive comments.

The work of MB and DV has been supported by the Grant Agency of the Czech Republic (grants 205/08/P196 and 205/08/0064) and the Research Program MSM0021620860 of the Czech Ministry of Education. We also acknowledge the provision of computers to us at the Observatory and Planetarium in Hradec Králové.

## REFERENCES

Benz W., Asphaug E., 1999, Icarus, 142, 5
Bottke W. F., Nolan M. C., Greenberg R., Kolvoord R. A., 1994, Icarus, 107, 255
Bottke W. F., Vokrouhlický D., Brož M., Nesvorný D., Morbidelli A., 2001, Sci, 294, 1693
Bottke W. F., Durda D. D., Nesvorný D., Jedicke R., Morbidelli A., Vokrouhlický D., Levison H. F., 2005, Icarus, 175, 111
Bottke W. F., Nesvorný D., Grimm R. E., Morbidelli A., O'Brien D. P., 2006, Nat, 439, 821
Bottke W. F., Nesvorný D., Vokrouhlický D., Morbidelli A., 2010, AJ, 139, 994
Brasser R., Morbidelli A., Gomes R., Tsiganis K., Levison H. F., 2009, A&A, 507, 1053
Brož M., 2006, PhD thesis, Charles Univ.
Brož M., Vokrouhlický D., 2008, MNRAS, 390, 715
Čapek D., Vokrouhlický D., 2004, Icarus, 172, 526
Dahlgren M., 1998, A&A, 336, 1056
Davis D. R., Neese C., eds, 2002, Asteroid Albedos. EAR-A-5-DDR-ALBEDOS-V1.1. NASA Planetary Data System
Dohnanyi J. W., 1969, J. Geophys. Res., 74, 2531



Farinella P., Froeschlé C., Gonczi R., 1994, in Milani A., Di Martino M., Cellino A., eds, Asteroids, Comets, Meteors 1993. Kluwer, Dordrecht, p. 205
Farinella P., Vokrouhlický D., Hartmann W. K., 1998, Icarus, 132, 378
Fernández Y. R., Jewitt D., Ziffer J. E., 2009, AJ, 138, 240
Ferraz-Mello S., Michtchenko T. A., Nesvorný D., Roig F., Simula A., 1998, P&SS, 46, 1425
Gomes R., Levison H. F., Tsiganis K., Morbidelli A., 2005, Nat, 435, 466
Güdel M., 2007, Living Rev. Solar Phys., 4, 3
Hill G., 1982, Publ. Dom. Astrophys. Obser. Victoria BC, 16, 67
Kortenkamp S. J., Malhotra R., Michtchenko T., 2004, Icarus, 167, 347
Leinhardt Z. M., Stewart S. T., 2009, Icarus, 199, 542
Levison H. F., Duncan M., 1994, Icarus, 108, 18
Levison H. F., Morbidelli A., Vanlaerhoven Ch., Gomes R., Tsiganis K., 2008, Icarus, 196, 258
Levison H. F., Bottke W. F., Gounelle M., Morbidelli A., Nesvorný D., Tsiganis K., 2009, Nat, 460, 364
Malhotra R., 1995, AJ, 110, 420
Minton D. A., Malhotra R., 2009, Nat, 457, 1109
Morbidelli A., Moons M., 1993, Icarus, 102, 316
Morbidelli A., Levinson H. F., Tsiganis K., Gomes R., 2005, Nat, 435, 459
Morbidelli A., Brasser R., Tsiganis K., Gomes R., Levison H. F., 2009, A&A, 507, 1041
Morbidelli A., Brasser R., Gomes R., Levison H. F., Tsiganis K., 2010, AJ, 140, 1391
Nesvorný D., Ferraz-Mello S., 1997, Icarus, 130, 247
Nesvorný D., Bottke W. F., Levison H. F., Dones L., 2003, ApJ, 591, 486
Nesvorný D., Jedicke R., Whiteley R. J., Ivezić Ž., 2005, Icarus, 173, 132
Nesvorný D., Vokrouhlický D., Morbidelli A., 2007, AJ, 133, 1962
Parker A., Ivezić Ž., Jurić M., Lupton R., Sekora M. D., Kowalski A., 2008, Icarus, 198, 138
Press W. H., Teukolsky S. A., Vetterlink W. T., Flannery B. P., 1999, Numerical Recipes in Fortran 77. Cambridge Univ. Press, Cambridge
Quinn T. R., Tremaine S., Duncan M., 1991, AJ, 101, 2287
Roig F., Ferraz-Mello S., 1999, Planet. Space Sci., 47, 653
Roig F., Nesvorný D., Ferraz-Mello S., 2002, MNRAS, 335, 417
Tanga P., Cellino A., Michel P., Zappatà V., Paolicchi P., Dell'Oro A., 1998, Icarus, 141, 65
Tsiganis K., Gomes R., Morbidelli A., Levison H. F., 2005, Nat, 435, 459
Tsiganis K., Knežević Z., Varvoglis H., 2007, Icarus, 186, 484
Vokrouhlický D., Brož M., Bottke W. F., Nesvorný D., Morbidelli A., 2006a, Icarus, 182, 92
Vokrouhlický D., Brož M., Bottke W. F., Nesvorný D., Morbidelli A., 2006b, Icarus, 182, 118
Vokrouhlický D., Nesvorný D., Levison H. F., 2008, AJ, 136, 1463
Zappalà V., Cellino A., Farinella P., Milani A., 1994, AJ, 107, 772

This paper has been typeset from a TEX/LATEX file prepared by the author.

Mon. Not. R. Astron. Soc. **390,** 715–732 (2008) doi:10.1111/j.1365-2966.2008.13764.x

# Asteroid families in the first-order resonances with Jupiter

M. Brož★ and D. Vokrouhlický★

*Institute of Astronomy, Charles University, Prague, V Holešovičkách 2, 18000 Prague 8, Czech Republic*

Accepted 2008 July 26. Received 2008 July 20; in original form 2008 June 23

**ABSTRACT**

Asteroids residing in the first-order mean motion resonances with Jupiter hold important information about the processes that set the final architecture of giant planets. Here, we revise current populations of objects in the J2/1 (Hecuba-gap group), J3/2 (Hilda group) and J4/3 (Thule group) resonances. The number of multi-opposition asteroids found is 274 for J2/1, 1197 for J3/2 and three for J4/3. By discovering a second and third object in the J4/3 resonance (186024) 2001 $QG_{207}$ and (185290) 2006 $UB_{219}$, this population becomes a real group rather than a single object. Using both hierarchical clustering technique and colour identification, we characterize a collisionally born asteroid family around the largest object (1911) Schubart in the J3/2 resonance. There is also a looser cluster around the largest asteroid (153) Hilda. Using *N*-body numerical simulations we prove that the Yarkovsky effect (infrared thermal emission from the surface of asteroids) causes a systematic drift in eccentricity for resonant asteroids, while their semimajor axis is almost fixed due to the strong coupling with Jupiter. This is a different mechanism from main belt families, where the Yarkovsky drift affects basically the semimajor axis. We use the eccentricity evolution to determine the following ages: $(1.7 \pm 0.7)$ Gyr for the Schubart family and $\gtrsim 4$ Gyr for the Hilda family. We also find that collisionally born clusters in the J2/1 resonance would efficiently dynamically disperse. The steep size distribution of the stable population inside this resonance could thus make sense if most of these bodies are fragments from an event older than $\simeq 1$ Gyr. Finally, we test stability of resonant populations during Jupiter's and Saturn's crossing of their mutual mean motion resonances. In particular, we find primordial objects in the J3/2 resonance were efficiently removed from their orbits when Jupiter and Saturn crossed their 1:2 mean motion resonance.

**Key words:** methods: *N*-body simulations – celestial mechanics – minor planets, asteroids.

## 1 INTRODUCTION

Populations of asteroids in the Jovian first-order mean motion resonances – J2/1, J3/2 and J4/3 – are closely linked to the orbital evolution of the giant planets. This is because of their orbital proximity to Jupiter.[1] Stability or instability of these asteroid populations directly derives from the orbital configuration of the giant planets. As such, it is also sensitive on the nature and amount of Jupiter's migration and other finer details of its dynamics. As a result, the currently observed asteroids in the Jovian first-order resonances contain valuable information about the early evolution of planets and, if correctly understood and properly modelled, they may help to constrain it.

Apart from the Trojan clouds (not studied in this paper), the largest known population in the Jovian mean motion resonances occupies the J3/2 resonance, and is frequently called the Hilda group. It was carefully studied in a parallel series of papers by Schubart and Dahlgren and collaborators during the past few decades. Schubart (1982a,b, 1991) analysed short-term dynamics of Hilda-type orbits and introduced quasi-constant orbital parameters that allowed their first classification. While pioneering, Schubart's work had the disadvantage of having much smaller sample of known asteroids and computer power than today. Dahlgren & Lagerkvist (1995) and Dahlgren et al. (1997); Dahlgren (1998); Dahlgren, Lahulla & Lagerkvist (1999) conducted the first systematic spectroscopic and rotation-rate investigation of Hildas. They found about equal abundance of D- and P-type asteroids[2] and suggested spectral-size correlation such that P-types dominate large Hildas and D-types dominate smaller Hildas. They also suggested that small Hildas have large light-curve amplitudes, as an indication of elongated or

★E-mail: mira@sirrah.troja.mff.cuni.cz (MB); vokrouhl@cesnet.cz (DV)

[1] Interestingly, at their discovery (158) Hilda and (279) Thule, residing in the J3/2 and J4/3 resonances, immediately attracted attention of astronomers by vastly extending asteroid zone towards giant planets and by their ability to apparently approach Jupiter near aphelia of their orbits (e.g. Kühnert 1876; Krueger 1889).

[2] Note the former P-type objects were reclassified to X-type in a newer taxonomy by Bus and Binzel (e.g. Bus, Vilas & Barucci 2002).

irregular shape, and that the distribution of their rotation rates is non-Maxwellian. Further analysis using the Sloan Digital Sky Survey (SDSS) data, however, does not support significant dominance of either of the two spectral types for small sizes and indicates about equal mix of them (Gil-Hutton & Brunini 2008; see also below). Smaller populations of asteroids in the J2/1 and J4/3 received comparatively less observational effort.

Since the late 1990s, powerful enough computers allowed a more systematic analysis of fine details of the longer term dynamics in the Jovian first-order resonances. Ferraz-Mello & Michtchenko (1996) and Ferraz-Mello et al. (1998a); Ferraz-Mello, Michtchenko & Roig (1998b) determined that asteroids in the J2/1 resonance can be very long-lived, possibly primordial, yet their motion is comparatively more chaotic than those in the J3/2 resonance. The latter paper showed that commensurability between the libration period and the period of Jupiter's and Saturn's Great Inequality (GI) might have played an important role in depletion of the J2/1 resonance. This would have occurred when both giant planets were farther from their mutual 2:5 mean motion configuration in the past. A still more complete analysis was obtained by Nesvorný & Ferraz-Mello (1997) who also pointed out that the J4/3 resonance stable zone is surprisingly void of asteroids, containing only (279) Thule. Roig et al. (2002) and Brož et al. (2005) recently revised the population of asteroids in the J2/1 resonance and classified them into several groups according to their long-term orbital stability. While the origin of the unstable resonant population was successfully interpreted using a model of a steady-state flow of main belt objects driven by the Yarkovsky semimajor axis drift, the origin of the long-lived asteroids in the J2/1 remains elusive. Population of Hildas and Thule was assumed primordial or captured by an adiabatic migration of Jupiter (e.g. Franklin et al. 2004).

It has been known for some time that the current configuration of giant planets does not correspond to that at their birth. However, a new momentum to that hypothesis was given by the so-called Nice model (Gomes et al. 2005; Morbidelli et al. 2005; Tsiganis et al. 2005). The Nice model postulates the initial configuration of the giant planets was such that Jupiter and Saturn were interior of their mutual 1:2 mean motion resonance (see also Morbidelli et al. 2007). The event of crossing this resonance had a major influence on the final architecture of giant planets and strongly influenced structure of small-body populations in the Solar system. Morbidelli et al. (2005) showed that the population of Jupiters Trojan asteroids was destabilized and repopulated during this phase. In what follows we show that, within the Nice model, the same most probably occurs for populations of asteroids in the J3/2 and J4/3 resonances.

The paper is organized as follows. In Section 2 we revise information about the current populations of asteroids in the Jovian first-order resonances. We use an up-to-date AstOrb data base of asteroid orbits from the Lowell Observatory (ftp.lowell.edu) as of 2007 September and eliminate only single-opposition cases to assure accurate orbital information.

In Section 3 we apply clustering techniques and extract two families of asteroids on similar orbits in the J3/2 resonance. We strengthen their case with an additional colour analysis using the SDSS broad-band data. We model the long-term orbital evolution of these families and estimate their ages on the basis of Yarkovsky-driven dispersion in eccentricity.

In Section 4 we determine an orbital stability of the putative primordial populations of planetesimals in the Jovian first-order resonances. We show that those in the J3/2 and J4/3 are very efficiently eliminated when Jupiter and Saturn cross their mutual 1:2 mean motion resonance. We also determine the removal rate of very small resonant asteroids due to the Yarkovsky/YORP effects.

## 2 CURRENT ASTEROID POPULATIONS IN THE JOVIAN FIRST-ORDER RESONANCES

Dynamics of asteroid motion in the Jovian first-order resonances has been extensively studied by both analytical and numerical methods in the past few decades (e.g. Murray 1986; Ferraz-Mello 1988; Sessin & Bressane 1988; Lemaitre & Henrard 1990; Morbidelli & Moons 1993; Nesvorný & Ferraz-Mello 1997; Moons, Morbidelli & Migliorini 1998; Roig, Nesvorný & Ferraz-Mello 2002; Schubart 2007). In what follows we review a minimum information needed to understand our paper, referring an interested reader to the literature mentioned above for more insights.

In the simplest framework of a circular restricted planar three-body problem (Sun–Jupiter–asteroid) the fundamental effects of the resonant dynamics is reduced to a one degree of freedom problem defined by a pair of variables $(\Sigma, \sigma)$. For $J(p+1)/p$ resonance ($p = 1, 2$ and 3 in our cases) we have

$$\Sigma = \sqrt{a}\left(1 - \sqrt{1-e^2}\right), \tag{1}$$

$$\sigma = (p+1)\,\lambda' - p\,\lambda - \varpi, \tag{2}$$

where $a$ is the semimajor axis, $e$ is the eccentricity, $\varpi$ is the longitude of pericentre and $\lambda$ is the mean longitude in orbit of the asteroid, and $\lambda'$ is the mean longitude in orbit of Jupiter.

If the asteroid motion is not confined into the orbital plane of the planet, we have an additional pair of resonant variables $(\Sigma_z, \sigma_z)$ such that

$$\Sigma_z = 2\sqrt{a\left(1-e^2\right)}\,\sin^2\frac{i}{2}, \tag{3}$$

$$\sigma_z = (p+1)\,\lambda' - p\,\lambda - \Omega, \tag{4}$$

where $i$ denotes the inclination of asteroids orbit and $\Omega$ the longitude of its node. Remaining still with the simple averaged model, orbital effects with shorter periods are neglected, the motion obeys an integral of motion $N$ given by

$$N = \sqrt{a}\left(\frac{p+1}{p} - \sqrt{1-e^2}\cos i\right). \tag{5}$$

Because of this integral of motion, variations of $\Sigma$ imply oscillations of both $a$ and $e$.

The two degree of freedom character of the resonant motion prevents integrability. However, as an approximation we may introduce a hierarchy by noting that perturbation described by the $(\Sigma, \sigma)$ variables is larger than that described by the $(\Sigma_z, \sigma_z)$ terms (e.g. Moons et al. 1998). This is usually true for real resonant asteroids of interest. Only the angle $\sigma$ librates and $\sigma_z$ circulates with a very long period. The $(\Sigma_z, \sigma_z)$ dynamics thus produces a long-period perturbation of the $(\Sigma, \sigma)$ motion.

Within this model the minimum value of $\Sigma$ in one resonant cycle (typically several hundreds of years) implies $a$ is minimum and $e$ is maximum. These values do not conserve exactly from one cycle to another because the $(\Sigma_z, \sigma_z)$ motion produces small oscillations. Since $\Sigma + \Sigma_z - N = -\sqrt{a}/p$ one needs to wait until $\Sigma_z$ reaches maximum over its cycle to attain 'real' minimum of $a$ values and 'real' maximum of $e$ values over a longer time interval. From (3) we note the maximum of $\Sigma_z$ occurs for the maximum of $i$ variations. This situations occurs typically once in a few thousands of years.

In an ideal situation, these extremal values of ($a$, $e$, $i$) would be constant and may serve as a set of proper orbital elements.

The motion of real asteroids in the Solar system is further complicated by Jupiter having non-zero and oscillating value of eccentricity. This brings further perturbations (e.g. Ferraz-Mello 1988; Sessin & Bressane 1988 for a simple analytic description) and sources of instability inside the resonance. Despite the non-integrability, we follow Roig et al. (2001) and introduce *pseudo-proper orbital elements* ($a_\mathrm{p}$, $e_\mathrm{p}$, $\sin i_\mathrm{p}$) as the osculating elements ($a$, $e$, $\sin i$) at the moment, when the orbit satisfies the condition

$$\sigma = 0 \wedge \frac{\mathrm{d}\sigma}{\mathrm{d}t} < 0 \wedge \varpi - \varpi' = 0 \wedge \Omega - \Omega' = 0, \quad (6)$$

where $\varpi'$ and $\Omega'$ denote the longitude of pericentre and the longitude of node of Jupiter. As above, when (6) holds the osculating orbital elements are such that $a$ attains minimum, $e$ attains maximum and $i$ attains maximum. Numerical experiments show that with a complete perturbation model and a finite time-step it is difficult to satisfy all conditions of (6) simultaneously. Following Roig et al. (2001) we thus relax (6) to a more practical condition

$$|\sigma| < 5^\circ \wedge \frac{\Delta\sigma}{\Delta t} < 0 \wedge |\varpi - \varpi'| < 5^\circ. \quad (7)$$

Because this condition is only approximate, we numerically integrate orbits of resonant asteroids for 1 Myr, over which the pseudo-proper orbital elements are recorded. We then compute their mean value and standard deviation, which is an expression of the orbital stability over that interval of time.

In the case of the J3/2 and J4/3 resonances, we use condition (7) with a different sign $\Delta\sigma/\Delta t > 0$ and, moreover, we apply a digital filter (denoted as A in Quinn, Tremaine & Duncan (1991), using 1-yr sampling and a decimation factor of 10) to $\sigma(t)$. This intermediate stage serves to suppress oscillations faster than the libration period. The different sign of $\Delta\sigma/\Delta t$ just means that our pseudo-proper orbital elements correspond to maximum value of $a$ and minimum values of $e$ and $i$, in order to allow more direct comparison with previous analyses.

Aside to this short-term integration we perform long-term runs to determine the stability of a particular resonant orbit. With this aim we conduct integrations spanning 4 Gyr for all resonant asteroids. Because of the inherent uncertainty in the initial conditions (orbital elements at the current epoch), we perform such integration for the nominal orbit and 10 clones that randomly span the uncertainty ellipsoid. We then define *dynamical lifetime* of the orbit as the median of time intervals, for which the individual clones stayed in the resonance.

All integrations are performed using the SWIFT package (Levison & Duncan 1994), slightly modified to include necessary online digital filters and a second-order symplectic integrator (Laskar & Robutel 2001). Most of numerical simulations take into account gravitational interactions only, but in specific cases – and when explicitly mentioned – we include also Yarkovsky (thermal) accelerations. In this case we use an implementation described in detail by Brož (2006). Our simulations include four outer planets. We modify the initial conditions of the planets and asteroids by a barycentric correction to partially account for the influence of the terrestrial planets. The absence of the terrestrial planets as perturbers is a reasonable approximation in the outer part of the main belt and for orbits with $e < 0.8$ in general. We nevertheless checked the short-term computations (determination of pseudo-proper resonant elements) using a complete planetary model and noticed no significant difference in results. The second-order symplectic scheme allows us to use a time-step of 91 d.

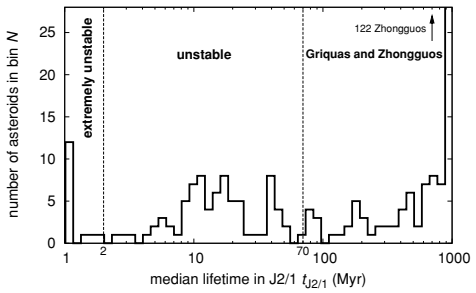


**Figure 1.** A distribution of the median dynamical lifetimes for objects in the J2/1 resonance. A division to several groups is denoted: extremely unstable objects ($t_{J2/1} \leq 2$ Myr), short-lived objects ($t_{J2/1} \leq 70$ Myr) and long-lived objects (Griquas and Zhongguos, $t_{J2/1} > 70$ Myr).

### 2.1 Hecuba-gap group

In order to determine, which objects are located in the J2/1 mean motion resonance, we first extracted orbits from the AstOrb data base with osculating orbital elements in a broad box around this resonance (see e.g. Roig et al. 2001 for a similar procedure). We obtained 7139 orbits, which we numerically integrated for 10 kyr. We recorded and analysed behaviour of the resonance angle $\sigma = 2\lambda' - \lambda - \varpi$ from equation (2). Pericentric librators, for which $\sigma$ oscillates about $0^\circ$ were searched. We found 274 such cases; this extends the previous catalogue of Brož et al. (2005) almost twice. The newly identified resonant objects are mainly asteroids discovered or recovered after 2005 with accurate enough orbits. We disregard from our analysis asteroids at the border of the resonance, for which $\sigma(t)$ exhibits alternating periods of libration and circulation, and also those asteroids for which $\sigma$ oscillates but are not resonant anyway ($N \leq 0.8$ in equation 5; see e.g. Morbidelli & Moons 1993). The latter reside on low-eccentricity orbits in the main asteroid belt adjacent to the J2/1 resonance.

We conducted short- and long-term integrations of the resonant asteroids as described above. They allowed us to divide the population into 182 long-lived asteroids (with the median dynamical lifetime longer than 70 Myr, as defined in Brož et al. 2005) and 92 short-lived asteroids (the lifetime shorter than 70 Myr), see Fig. 1.[3] Among the short-lived objects we found 14 have dynamical lifetimes even less than 2 Myr and we call them extremely unstable. Brož et al. (2005) suggested the unstable orbits in the J2/1 resonance are resupplied from the adjacent main belt due to a permanent flux driven by the Yarkovsky force, the extremely unstable objects are most probably temporarily captured Jupiter-family comets. The origin of the long-lived population in this resonance is still not known.

Fig. 2 shows the pseudo-proper orbital elements of the J2/1 asteroids projected on to the ($a_\mathrm{p}$, $e_\mathrm{p}$) and ($a_\mathrm{p}$, $\sin i_\mathrm{p}$) planes. Our data confirm that the unstable population of J2/1 asteroids populates the resonance outskirts near its separatrix, where several secular resonances overlap and trigger chaotic motion (e.g. Morbidelli & Moons 1993; Nesvorný & Ferraz-Mello 1997; Moons et al. 1998).

[3] Our results for both J2/1 and J3/2 resonances are summarized in tables available through a web site http://sirrah.troja.mff.cuni.cz/yarko-site/ (those for J4/3 bodies are given in Table 1). These contain listing of all resonant asteroids, their pseudo-proper orbital elements with standard deviations, their dynamical residence time and some additional information.

**Table 1.** Data on presently known population of asteroids residing in the J4/3 Jovian mean motion resonance (Thule group). Pseudo-proper orbital elements ($a_\mathrm{p}$, $e_\mathrm{p}$, $\sin i_\mathrm{p}$) are given together with their standard deviations ($\delta a_\mathrm{p}$, $\delta e_\mathrm{p}$, $\delta \sin i_\mathrm{p}$) determined from a 1-Myr numerical integration. $\sigma_{p,\max}$ is the maximum libration amplitude in the Sessin's ($K$, $H$) variables (see Fig. 8), $H$ is the absolute magnitude from the AstOrb catalogue and $D$ is the estimated size using $p_V = 0.04$ geometric albedo (Tedesco et al. 2002).

| No. | Name | $a_\mathrm{p}$ (au) | $e_\mathrm{p}$ | $\sin i_\mathrm{p}$ | $\delta a_\mathrm{p}$ (au) | $\delta e_\mathrm{p}$ | $\delta \sin i_\mathrm{p}$ | $\sigma_{p,\max}$ (°) | $H$ (mag) | $D$ (km) |
|---|---|---|---|---|---|---|---|---|---|---|
| 279 | Thule | 4.2855 | 0.119 | 0.024 | 0.0005 | 0.012 | 0.003 | ∼50 | 8.57 | 126.6 |
| 186024 | 2001 $QG_{207}$ | 4.2965 | 0.244 | 0.042 | 0.0003 | 0.014 | 0.003 | 25 | 14.36 | 8.9 |
| 185290 | 2006 $UB_{219}$ | 4.2979 | 0.234 | 0.102 | 0.0003 | 0.014 | 0.004 | 25 | 13.75 | 11.8 |

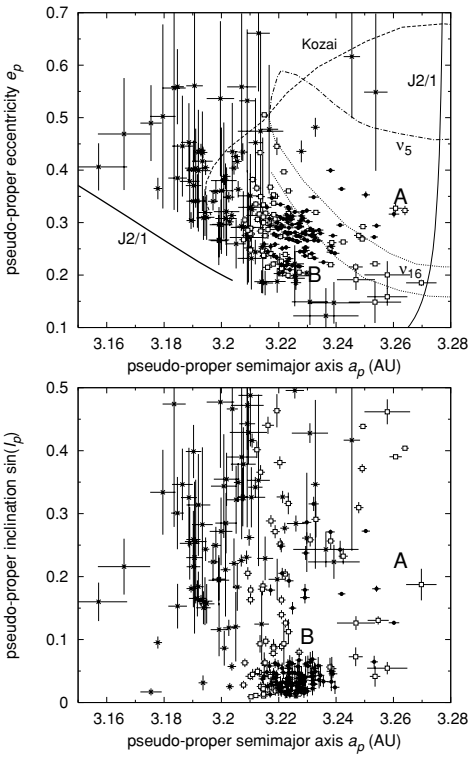


**Figure 2.** Pseudo-proper orbital elements for the 247 objects in the J2/1 resonance projected on to the planes of semimajor axis $a_\mathrm{p}$ versus eccentricity $e_\mathrm{p}$ (top) and semimajor axis $a_\mathrm{p}$ versus sine of inclination $\sin i_\mathrm{p}$ (bottom). Bars are standard deviations of the elements derived from 1-Myr numerical integration. Position of several secular resonances embedded in J2/1 is shown in the upper panel. The unstable population of asteroids (crosses) occupies the region of their overlap; the stable population (full circles) occupies two distinct zones – A and B – of low-eccentricity and low-inclination orbits (e.g. Nesvorný & Ferraz-Mello 1997). The population of marginally stable asteroids (open squares) resides in region adjacent to the unstable borders of the resonance or near the bridge over the stable regions associated with the $\nu_{16}$ secular resonance.

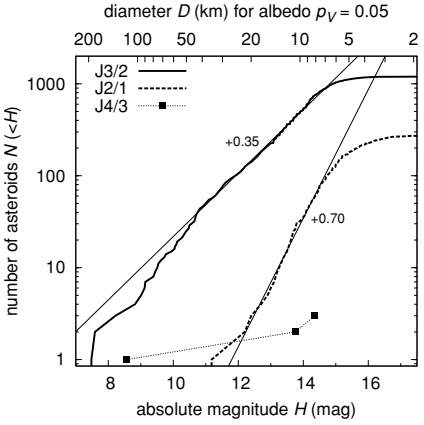


**Figure 3.** Cumulative distributions $N(< H)$ of the absolute magnitude $H$ values for population of asteroids in the Jovian first-order mean motion resonances: (i) J2/1 (dashed curve), (ii) J3/2 (solid curve) and (iii) J4/3 (dotted curve). The straight lines show best-fitting approximations $N(< H) \propto 10^{\gamma H}$ with the values of $\gamma$ indicated by the corresponding label. The fit matches $N(< H)$ for $H$ in the interval (12, 15) mag for J2/1 and (10.5, 14.5) mag for J3/2; no such approximation is available for J4/3 where only three objects are currently known. The $H$ values where the straight line approximations level off from the data roughly correspond to the completeness limit of the population (R. Jedicke, personal communication). For sake of a rough comparison, the upper abscissa gives an estimate of sizes for the albedo value $p_V = 0.05$, average of the outer belt population.

At low-eccentricities the chaos is also caused by an overlap on numerous secondary resonances (e.g. Lemaitre & Henrard 1990). Two 'islands' of stability – A and B – harbour the long-lived population of bodies. The high-inclination island A, separated from the low-inclination island B by the $\nu_{16}$ secular resonance, is much less populated. Our current search identifies nine asteroids in the island A. The origin of the asymmetry in A/B islands is not known, but since the work of Michtchenko & Ferraz-Mello (1997) and Ferraz-Mello et al. (1998a,b) it is suspected to be caused by instability due to the libration period commensurability with the forcing terms produced by the GI.

The size–frequency distribution of objects of a population is an important property, complementing that of the orbital distribution. Fig. 3 shows cumulative distribution $N(< H)$ of the absolute magnitudes $H$ for bodies in the J2/1 (and other Jovian first-order resonances as well). In between $H = 12$ mag and 14.5 mag (an approximate completeness limit; R. Jedicke, personal communication) it can be matched by a simple power-law $N(< H) \propto 10^{\gamma H}$, with $\gamma = (+0.70 \pm 0.02)$.[4] We thus confirm that the J2/1 population is steeper than it would correspond to a standard collisionally evolved system (e.g. Dohnanyi 1969; O'Brien & Greenberg 2003) with

[4] This is equivalent to a cumulative size distribution law $N(> D) \propto D^{\alpha}$ with $\alpha = -5\gamma = (-3.5 \pm 0.1)$, assuming all bodies have the same albedo.

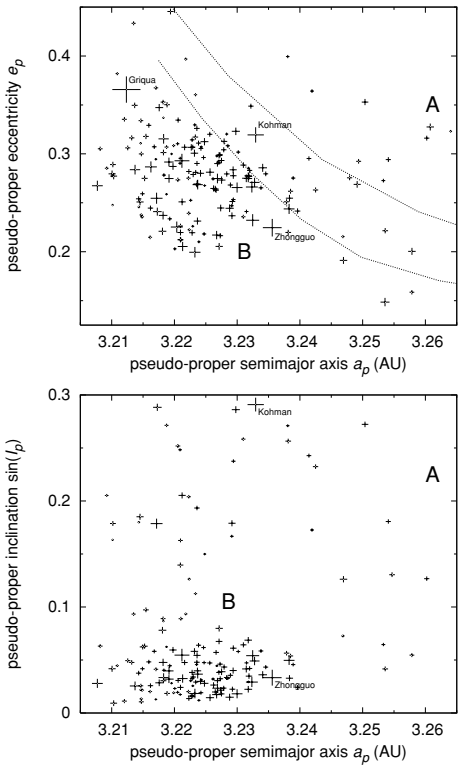


**Figure 4.** A zoom on the ($a_p$, $e_p$) and ($a_p$, $\sin i_p$) plots from Fig. 2 with relative size of the resonant asteroids indicated by size of the crosses. Note the large bodies, some of which are labelled, reside far from each other.

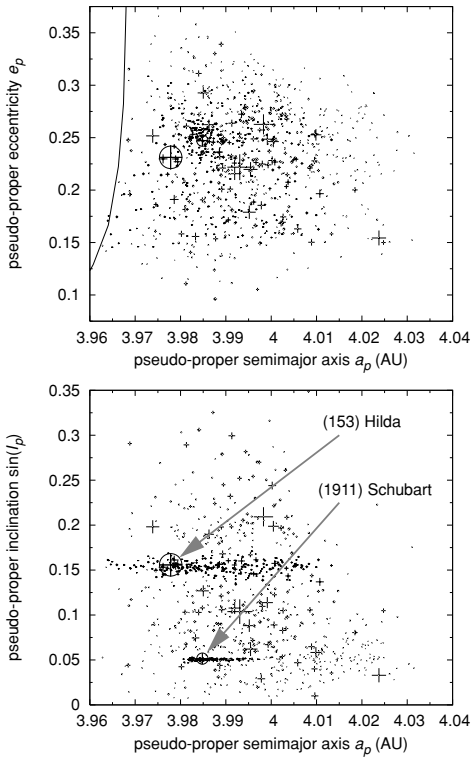


**Figure 5.** Pseudo-proper orbital elements for 1197 Hildas projected on to the planes of semimajor axis $a_p$ versus eccentricity $e_p$ (top) and semimajor axis $a_p$ versus sine of inclination $\sin i_p$ (bottom). Larger size of the symbol indicates larger physical size of the asteroid. Because of Hildas orbital stability, the uncertainty in the pseudo-proper element values is typically smaller than the symbol size. Note a tight cluster around the proper inclination value $\sin i_p \simeq 0.0505$, led by the largest asteroid (1911) Schubart, and a somewhat looser cluster around the proper inclination value $\sin i_p \simeq 0.151$, led by the largest asteroid (153) Hilda. Both are discussed in more detail in Section 3. Solid line denotes the libration centre of the J3/2 resonance.

$\gamma = +0.5$. The same result holds for both the short- and long-lived subpopulations in this resonance separately.

Albedos of J2/1 bodies are not known, except for (1362) Griqua for which Tedesco et al. (2002) give $p_V = 0.067$. The surrounding main belt population has an average $p_V = 0.05$. For sake of simplicity we convert absolute magnitudes to sizes using this averaged value when needed. For instance in Fig. 4 we show a zoom on the long-lived population of objects in the J2/1 resonance with symbol size weighted by the estimated size of the body. We note large objects are located far from each other and they are quite isolated – no small asteroids are in close surroundings. Both these observations suggest that the long-lived J2/1 population does not contain recently born collisional clusters.

### 2.2 Hilda group

Because asteroids in the J3/2 constitute a rather isolated group, it is easy to select their candidates: we simply extracted from the AstOrb data base those asteroids with semimajor axis in between 3.8 and 4.1 au. With that we obtained 1267 multi-opposition objects. We numerically integrated these orbits for 10 kyr and analysed the behaviour of the resonance angle $\sigma = 3\lambda' - 2\lambda - \varpi$. We obtained 1197 cases for which $\sigma$ librates about 0° and which have $N \geq 0.44$, a threshold of the resonance zone (e.g. Morbidelli & Moons 1993); see Fig. 5.

The long-term evolution of Hildas indicates that not all of them are stable over 4 Gyr, but 20 per cent escape earlier. A brief inspection of Fig. 6 shows that the escapees are essentially asteroids located closer to the outer separatrix and exhibiting large amplitudes of librations. If the Hilda group has been constituted during the planetary formation some 4 Gyr ago, some non-conservative process must have placed these objects on to their currently unstable orbits. We suspect mutual collisions or gravitational scattering on the largest Hilda members might be the corresponding diffusive mechanisms. Small enough members might be also susceptible to the resonant Yarkovsky effect (see Section 4.2 and Appendix A).

Data in Fig. 3 confirm earlier findings that the Hilda group is characterized by an anomalously shallow size distribution. In between absolute magnitudes $H = 10.5$ and 14.5 mag the cumulative distribution can be well matched by $N(< H) \propto 10^{\gamma H}$ with $\gamma = (+0.35 \pm 0.02)$ only. The distribution of albedo values is shown in Fig. 7.

Subpopulations among Hilda asteroids, namely two collisional families, are studied in Section 3.

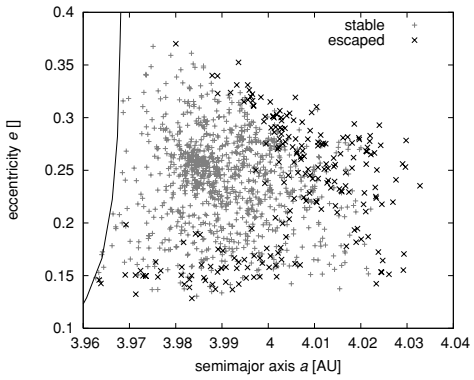


**Figure 6.** Pseudo-proper semimajor axis versus eccentricity plot for asteroids in the J3/2 resonance. Bold crosses denote orbits, which escaped during the 4 Gyr of evolution. Solid line is the position of the libration centre (the outer separatrix is located further to the right-hand side).

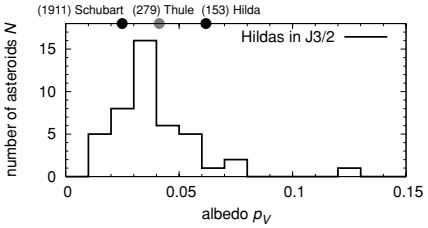


**Figure 7.** The histogram shows distribution of values of the geometric albedo $p_V$ determined by Tedesco et al. (2002) for asteroids located inside the J3/2 resonance. Three individual values – (153) Hilda, (1911) Schubart and (279) Thule (a J4/3 asteroid) – are indicated on top.

### 2.3 Thule group

In spite of a frequent terminology 'Thule group', asteroids in the J4/3 resonance consisted of a single object (279) Thule up to now. Nesvorný & Ferraz-Mello (1997) considered this situation anomalous because the extent of the stable zone of this resonance is not much smaller than that of the J3/2 resonance (see also Franklin et al. 2004). In the same way, our knowledge about the low-$e$ and low-$i$ Thule-type stable orbits (e.g. $a = 4.27$ au, $e = 0.1$ and $i = 5^\circ$) should be observationally complete at about magnitudes $H = 12.5$–13 mag (R. Jedicke, personal communication). A rough estimate also shows that even one magnitude in $H$ beyond this completeness limit the Thule population should be known at $\sim$10 per cent completeness, leaving only about 90 per cent undiscovered population. We thus conclude that the objects in the magnitude range $H = 9$–13 mag are very likely missing in this resonance. Where does the existing population of small Thule-type asteroids begin?

Our initial search in the broad box around the J4/3 resonance detected only 13 objects. Six of them, including the well-known extinct comet (3552) Don Quixote (e.g. Weissman, Bottke & Levison 2002), are on typical orbits of Jupiter-family comets that happen to reside near this resonance with very high eccentricity and moderately high inclination. Two more are single-opposition objects and one has only poorly constrained orbit, leaving us with (279) Thule and three additional candidate objects: (52007) 2002 EQ47, (186024) 2001 $QG_{207}$ and (185290) 2006 $UB_{219}$.

Fig. 8 (top panels) shows short-term tracks of (279) Thule, (186024) 2001 $QG_{207}$ and (185290) 2006 $UB_{219}$ in resonant variables $\sqrt{2\Sigma}\,(\cos\sigma, \sin\sigma) \simeq (e\cos\sigma, e\sin\sigma)$ of the J4/3 resonance ($\sigma = 4\lambda' - 3\lambda - \varpi$ in this case). In all cases their orbits librate about the pericentric branch ($\sigma = 0^\circ$) of this resonance, although this is complicated – mainly in the low-eccentricity case of (279) Thule – by the forced terms due to Jupiter's eccentricity (see e.g. Ferraz-Mello 1988; Sessin & Bressane 1988; Tsuchida 1990). The leftmost panel recovers the 40°–50° libration of (279) Thule, determined previously by Tsuchida (1990, fig. 3). The other two smaller asteroids show librations with comparable amplitudes. The last object, (52007) 2002 EQ47, appears to reside on an unstable orbit outside the J4/3 resonance. Our search thus lead to the detection of two new asteroids in this resonance, increasing its population by a factor of 3.[5]

Results of a long-term numerical integration of the nominal orbits plus 10 close clones, placed within an orbital uncertainty, reveal that the orbit of (279) Thule is stable over 4 Gyr, but the orbits of (186024) 2001 $QG_{207}$ and (185290) 2006 $UB_{219}$ are partially unstable. They are not 'short-lived' but 45 and 60 per cent of clones, respectively, escaped before 4 Gyr. Fig. 9 shows pseudo-proper semimajor axis versus time for nominal orbits and their clones of all J4/3 objects; the escaping orbits leave the figure before the simulation was ended at 4 Gyr. We suspect similar non-conservative effects as mentioned above for the 20 per cent fraction of long-term-unstable Hildas to bring these two Thule members on to their marginally stable orbits.

We would like to point out that it took more than a century from the discovery of (279) Thule (Palisa 1888; Krueger 1889) until further objects in this resonance were finally discovered. This is because there is an anomalously large gap in size of these bodies: (279) Thule is 127 km in size with $p_V = 0.04$ au (e.g. Tedesco et al. 2002), while the estimated sizes of (186024) 2001 $QG_{207}$ and (185290) 2006 $UB_{219}$ for the same value of albedo are 8.9 and 11.8 km only. It will be interesting to learn as much as possible about the Thule population in the $H = 13$–15 mag absolute magnitude range using future-generation survey projects such as Pan-STARRS (e.g. Jedicke et al. 2007). Such a completed population may present an interesting constraint on the planetesimal size distribution 4 Gyr ago.

## 3 COLLISIONAL FAMILIES AMONG HILDA ASTEROIDS

Collisions and subsequent fragmentations are ubiquitous processes since planets formed in the Solar system. Because the characteristic dispersal velocities of the ejecta (as a rule of thumb equal to the escape velocity of the parent body) are usually smaller than the orbital velocity, the resulting fragments initially reside on nearby orbits. If the orbital chaoticity is not prohibitively large in the formation zone, we can recognize the outcome of such past fragmentations as distinct clusters in the space of sufficiently stable orbital elements. More than 30 collisional families are known and studied in the main asteroid belt (e.g. Zappalà et al. 2002) with important additions in the recent years (e.g. Nesvorný et al. 2002; Nesvorný, Vokrouhlický & Bottke 2006). Similarly, collisional families have been found among the Trojan clouds of Jupiter (e.g. Milani 1993;

[5] While our initial search used AstOrb catalogue from 2007 September, we repeated it using the catalogue as of 2008 June. No additional J4/3 objects were found.

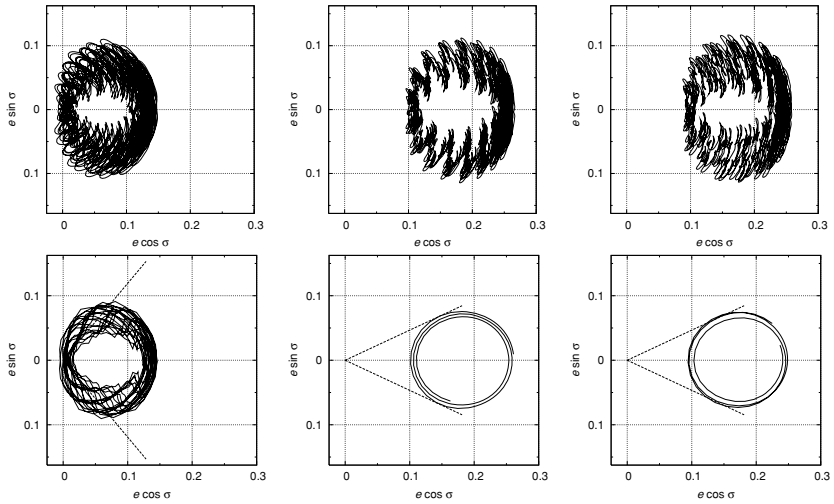


**Figure 8.** Top panels: orbits of (279) Thule (left-hand side), (186024) 2001 $QG_{207}$ (middle) and (185290) 2006 $UB_{219}$ (right-hand side) in resonant variables ($e\cos\sigma$, $e\sin\sigma$) of the J4/3 resonance. Here $e$ is the eccentricity and $\sigma = 4\lambda' - 3\lambda - \varpi$, with $\lambda$ and $\lambda'$ the mean longitude in orbit of the asteroid and Jupiter and $\varpi$ is the longitude of asteroid's pericentre (in all cases the osculating orbital elements are used). Each panel shows results of a short-term, 10-kyr numerical integration. In all three cases the orbits librate about the pericentric branch ($\sigma = 0^\circ$) of the resonance. Perturbations due to Jupiter's eccentricity and its variations make the regular libration move in an epicyclic manner (e.g. Ferraz-Mello 1988; Sessin & Bressane 1988). Bottom panels: filtered resonant variables ($e\cos\sigma$, $e\sin\sigma$), with short-period oscillations forced by Jupiter removed by digital filtering. They are similar to Sessin's ($K$, $H$) coordinates in Sessin & Bressane (1988) or Tsuchida (1990). In each of the cases the pericentric libration is clearly revealed. The maximum libration amplitude in these coordinates is denoted by $\sigma_{p,\,max}$ in Table 1.

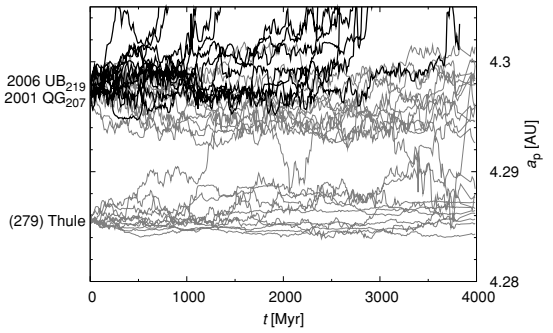


**Figure 9.** Pseudo-proper semimajor axis $a_p$ versus time $t$ plot for the three orbits of asteroids located inside the J4/3 resonance and 10 close clones orbits (placed randomly within the uncertainty ellipsoids) for each of them. Thin lines denote the stable orbits and thick lines unstable, which escaped from the J4/3 before the completion of the simulation at 4 Gyr.

Beaugé & Roig 2001; Roig, Ribeiro & Gil-Hutton 2008), irregular satellites of Jupiter (e.g. Nesvorný et al. 2003, 2004) and even trans-Neptunian objects (e.g. Brown et al. 2007). Mean motion resonances, other than the Trojan librators of Jupiter, are typically too chaotic to hold stable asteroid populations, or the populations were too small to enable search for families. The only remaining candidate populations are those in the Jovian first-order resonances, with Hilda asteroids the most promising group. However, low expectations for an existence of collisional families likely demotivated systematic search. Note that the estimated intrinsic collisional probability of Hilda asteroids is about a factor of 3 smaller than in the main asteroid belt (e.g. Dahlgren 1998; Dell'Oro et al. 2001) and the population is more than two orders of magnitude smaller.

In spite of the situation outlined above, Schubart (1982a, 1991) repeatedly noticed groups of Hilda-type asteroids with very similar proper elements. For instance, in his 1991 paper he lists five members of what we call Schubart family below and pointed out their nearly identical values of the proper inclination. Already in his 1982 paper Schubart mentions a similarity of such clusters to Hirayama families, but later never got back to the topic to investigate this problem with sufficient amount of data provided by the growing knowledge about the J3/2 population.[6] Even a zero-order inspection of Fig. 5, in particular the bottom panel, implies the existence of two large clusters among the J3/2 population. In what follows we pay a closer analysis to both of them.

We adopt an approach similar to the hierarchical clustering method (HCM) frequently used for identification of the asteroid families in the main belt (e.g. Zappalà et al. 1990, 1994, 2002). In the first step of our analysis, we compute the number of bodies $N_{\rm min}$ which is assumed to constitute a statistically significant cluster for a given value of the cut-off velocity $v_{\rm cut-off}$. We use a similar approach to that of Beaugé & Roig (2001): for all asteroids in the J3/2 resonance we determine the number $N_i(v_{\rm cut-off})$ of asteroids which are closer than $v_{\rm cut-off}$. Then we compute the average value $N_0 = \bar{N}_i$. According to Zappalà et al. (1994), a cluster may be considered significant if $N > N_{\rm min} = N_0 + 2\sqrt{N_0}$. The plots $N_0(v_{\rm cut-off})$ and the corresponding $N_{\rm min}(v_{\rm cut-off})$ for Hilda population are shown in Fig. 10. We use a standard metric ($d_1$ defined by Zappalà et al.

[6] Schubart lists 11 additional asteroids in the group on his web site http://www.rzuser.uni-heidelberg.de/~s24/hilda.htm, but again he does not go into details of their putative collisional origin.

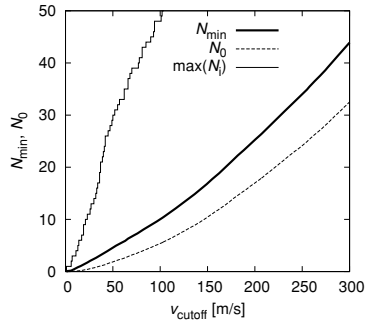


**Figure 10.** The dependence of the minimum number of asteroids $N_{\rm min}$, to be considered a statistically significant cluster, on the cut-off velocity $v_{\rm cut-off}$ (thick curve). The average number $N_0$ and the maximum number max ($N_i$) of asteroids, which are closer than $v_{\rm cut-off}$, is shown by dashed and thin curves. All quantities are valid for the J3/2 population. The fact that max ($N_i$) is much larger than $N_0$ and $N_{\rm min}$ indicates a presence of a significant cluster (or clusters) among the Hilda group.

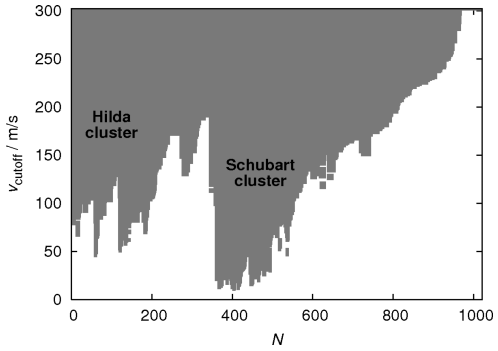


**Figure 11.** A stalactite diagram computed for the J3/2 population (Hildas). Two prominent groupings, the Schubart family and the Hilda family, are indicated. Every group plotted here has at least five or $N_{\rm min}$ members, whichever is larger (see Fig. 10).

1994), namely

$$\delta v = n a_{\rm p} \sqrt{\frac{5}{4}\left(\frac{\delta a_{\rm p}}{a_{\rm p}}\right)^2 + 2\,(\delta e_{\rm p})^2 + 2\,(\delta \sin i_{\rm p})^2}, \qquad (8)$$

where ($a_{\rm p}$, $e_{\rm p}$, $\sin i_{\rm p}$) are 10 Myr averaged values of the resonant pseudo-proper elements (we checked that our results practically do not depend on the width of this averaging interval).

Next, we construct a stalactite diagram for Hildas in a traditional way (e.g. Zappalà et al. 1990): we start with (153) Hilda as the first central body and we find all bodies associated with it at $v_{\rm cut-off} = 300\,{\rm m\,s^{-1}}$, using an HCM (Zappalà et al. 1990, 1994). Then we select the asteroid with the lowest number (catalogue designation) from remaining (not associated) asteroids and repeat the HCM association again and again, until no asteroids are left. Then we repeat the whole procedure recursively for all clusters detected at $v_{\rm cut-off} = 300\,{\rm m\,s^{-1}}$, but now for a lower value, e.g. $v_{\rm cut-off} = 299\,{\rm m\,s^{-1}}$. We may continue until $v_{\rm cut-off} = 0\,{\rm m\,s^{-1}}$, but of course, for too low values of the cut-off velocity, no clusters can be detected and all asteroids are single. The resulting stalactite diagram at Fig. 11 is simply the asteroid number (designation) versus $v_{\rm cut-off}$ plot: a dot

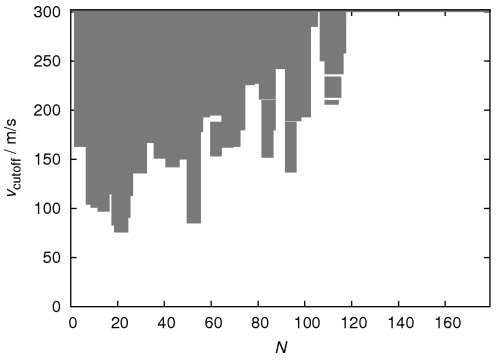


**Figure 12.** A stalactite diagram computed for the long-lived J2/1 population. There are no prominent groupings; 60 asteroids are not associated with any others, even at $v_{\rm cut-off} = 300\,{\rm m\,s^{-1}}$. Every group plotted here has at least five members.

at a given place is plotted only if the asteroids belongs to a cluster of at least max (5, $N_{\rm min}(v_{\rm cut-off})$) bodies. We are not interested in clusters with less than five members; they are most probably random flukes.

We can see two prominent clusters among Hildas: the first one around the asteroid (153) Hilda itself, and the second one around (1911) Schubart. In the remaining part of this Section we discuss each of them separately.

The stalactite diagram constructed in the same way for Zhongguos and Griquas is shown in Fig. 12. No grouping seems to be significant enough to be considered an impact-generated cluster. This is consistent with the discussion of the ($a_{\rm p}$, $e_{\rm p}$, $\sin i_{\rm p}$) plots in Section 2.1.

### 3.1 Schubart family

The Schubart family can be distinguished from the remaining population of Hildas on a large range of cut-off velocities: from $50\,{\rm m\,s^{-1}}$ to more than $100\,{\rm m\,s^{-1}}$ (Fig. 11). It merges with the Hilda family at $200\,{\rm m\,s^{-1}}$. For the purpose of our analysis we selected $v_{\rm cut-off} = 60\,{\rm m\,s^{-1}}$ as the nominal value. While the total number of Schubart family members is not too sensitive to this cut-off value, we refrain from using too high $v_{\rm cut-off}$, for which we would expect and increasing number of interlopers to be associated with the family, and the family would attain a rather peculiar shape in the ($a_{\rm p}$, $e_{\rm p}$, $\sin i_{\rm p}$) space.

Fig. 13 shows the cumulative distribution of the absolute magnitudes for the Schubart family members, compared to the rest of the J3/2 population. Importantly, the slope $\gamma = (+0.48 \pm 0.02)$ of the $N(<H) \propto 10^{\gamma H}$ fit is quite *steeper* for the Schubart family, which supports the hypothesis of its collisional origin.

We also analysed the available SDSS catalogue of moving objects (ADR3; Ivezić et al. 2002). We searched for the J3/2 asteroids among the entries of this catalogue and computed the principal component $\rm PC_1$ of the spectrum in the visible band. Note the $\rm PC_1$ value is an indicator of the spectral slope and allows thus to broadly distinguish principal spectral classes of asteroids (e.g. Bus et al. 2002). Fig. 14 shows our results. The top panel confirms the bimodal character of the J3/2 population (see also Dahlgren et al. 1997; Dahlgren 1998; Dahlgren et al. 1999 and Gil-Hutton & Brunini 2008). More importantly, though, the bottom panel indicates a spectral homogeneity of the Schubart family, placing all members

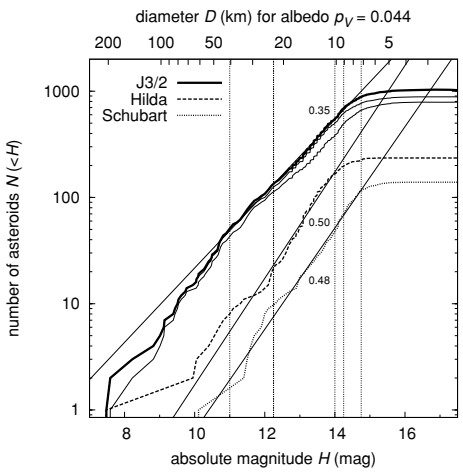


**Figure 13.** Cumulative distributions $N(<H)$ of absolute magnitudes $H$ for the whole J3/2 population (solid) and for the members of the families around (153) Hilda (dashed) and (1911) Schubart (dotted). Thin dotted curves denote $N(<H)$ of the J3/2 population with one and both families subtracted. Labels are the best-fitting values of $\gamma$ using $N(<H) \propto 10^{\gamma H}$ (straight lines) in the interval (12.25, 14.25) for Hilda and (12.25, 14.75) for Schubart clusters. For sake of a rough comparison, the upper abscissa gives an estimate of the sizes for an albedo value $p_V = 0.044$, average of the J3/2 population.

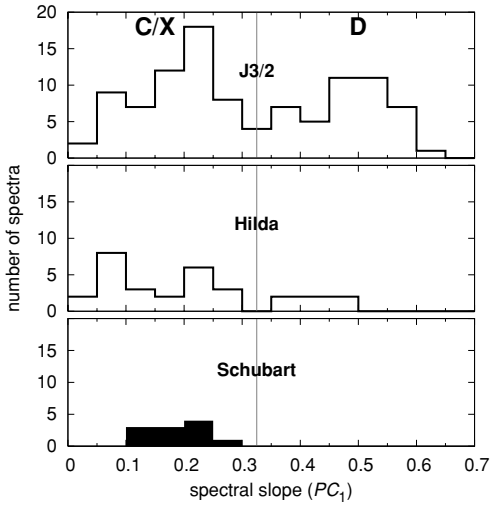


**Figure 14.** Distribution of spectral slopes ($PC_1$ components of the five broad-band colours) of 153 asteroids in the J3/2 resonance (top), 21 Hilda family members (middle) and four Schubart family members (bottom). Data computed from the third release of the SDSS catalogue of moving objects (ADR3; Ivezić et al. 2002). Note some objects have been observed multiple times by SDSS and the histograms show distribution of all observations (rather than averages for a given body). The slope values of Hildas range from neutral to steep, with roughly two groups separated by the value $PC_1 = 0.3$: (i) C/X types with $PC_1 < 0.3$ and (ii) D types with $PC_1 > 0.3$. Importantly, the Schubart family members are spectrally similar; the median value $PC_1 = 0.20$ corresponds to a C- or X-type parent body.

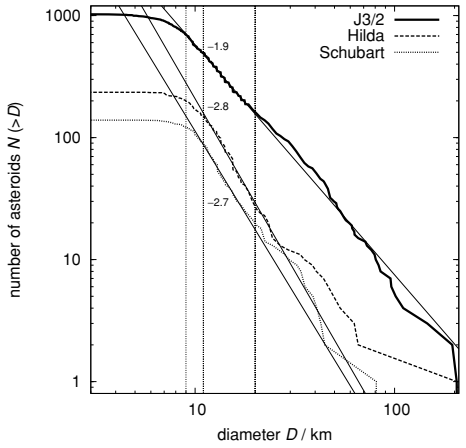


**Figure 15.** Cumulative size distribution $N(> D)$ for the whole J3/2 population (solid) and for members of the two suggested collisional clusters: Hilda (dashed) and Schubart (dotted). We assumed the geometric albedo $p_V = 0.044$ (and 0.025 in the Schubart-family case; see the text) for the conversion of absolute magnitudes $H$ to diameters $D$. Labels are the best-fitting values of $\alpha$ using $N(> D) \propto D^{\alpha}$ (straight lines) in the interval (11, 20) km for the two families and (9, 20) km for the J3/2 population.

within the C/X taxonomy class branch. This finding strongly supports collisional origin of the Schubart family.

Tedesco et al. (2002) derive $D = 80$ km size for (1911) Schubart, corresponding to a very low albedo $p_V = 0.025$. The same authors determine $D = 38$ km size of (4230) van den Bergh and exactly the same albedo; this asteroid is among the five largest in the family. Assuming the same albedo for all other family members, we can construct a size–frequency distribution (Fig. 15). The slope $\alpha \simeq (-2.7 \pm 0.1)$ fitted to the small end of the distribution, where we still assume observational completeness, is rather shallow, but marginally within the limits of population slopes produced in the numerical simulations of disruptions (e.g. Durda et al. 2007).[7]

If we sum the volumes of the observed members, we end up with a lower limit for the parent body size $D_{\rm PB} = 110$ km, provided there are no interlopers. We can also estimate the contribution of small (unobserved) bodies using the following simple method: (i) we sum only the volumes of the observed bodies larger than an assumed completeness limit $D_{\rm complete} = 10$ km [$V_{\rm complete} = \sum_i (\pi/6) D_i^3$]; (ii) we fit the cumulative size distribution by a power law $\{\log N(> D) = \alpha \log [D]_{\rm km} + \beta$; $\alpha = -2.68, \beta = 4.73$ for the Schubart$\}$; (iii) we prolong this slope from $D_{\rm complete}$ down to $D_{\rm min} = 0$ and calculate the total volume of the parent body (provided $\alpha > -3$):

$$V_{\rm PB} = V_{\rm complete} + \frac{\pi}{6} 10^{\beta} \frac{\alpha}{\alpha + 3} \left[ D_{\rm min}^{\alpha+3} - D_{\rm complete}^{\alpha+3} \right] . \quad (9)$$

The result is $D_{\rm PB} = \sqrt[3]{(6/\pi) V_{\rm PB}} \doteq 130$ km, some sort of an upper limit. The volumetric ratio between the largest fragment and the parent body is then $V_{\rm LF}/V_{\rm PB} \doteq 0.2$, a fairly typical value for asteroid families in the main asteroid belt. Obviously, the assumption of a single power-law extrapolation of the $N(> D)$ at small sizes is only approximate and can lead to a result with a 10 per cent

[7] We also mention that so far asteroid disruption simulations did not explore cases of weak-strength materials appropriate for the suggested C/X spectral taxonomy of the Schubart family parent body.

uncertainty. However, if we use an entirely different geometric method, developed by Tanga et al. (1999), we obtain $D_{\rm PB} \simeq 120$–130 km, i.e. comparable to our previous estimate.

What is an approximate size $d_{\rm disrupt}$ of a projectile necessary to disrupt the parent body of the Schubart family? Using equation (1) from Bottke et al. (2005):

$$d_{\rm disrupt} = \left(2Q_D^*/V_{\rm imp}^2\right)^{1/3} D_{\rm target}. \quad (10)$$

and substituting $Q_D^* = 10^5\,{\rm J\,kg^{-1}}$ for the strength (somewhat lower than that of basaltic objects to accommodate the assumed C/X spectral type; e.g. Kenyon et al. 2008 and references therein), $V_{\rm imp} = 4.78\,{\rm km\,s^{-1}}$ for the typical impact velocity (see Dahlgren 1998) and $D_{\rm target} \simeq 130$ km, we obtain $d_{\rm disrupt} \simeq 25$ km. At this size the projectile population is dominated by main belt bodies. Considering also different intrinsic collisional probabilities between Hilda–Hilda asteroids ($2.3 \times 10^{-18}\,{\rm km^{-2}\,yr^{-1}}$; Dahlgren 1998) and Hilda–main belt asteroids ($0.6 \times 10^{-18}\,{\rm km^{-2}\,yr^{-1}}$), we find it more likely the Schubart family parent body was hit by a projectile originating from the main belt.

### 3.2 Hilda family

We repeated the same analysis as in Section 3.1 for the Hilda family. The family remains statistically distinct from the whole J3/2 population in the range of cut-off velocities (130, 170) m s$^{-1}$; we choose $v_{\rm cut-off} = 150\,{\rm m\,s^{-1}}$ as the nominal value.

The slope $\gamma$ of the cumulative absolute magnitude distribution $N(<H)$ is $(+0.50 \pm 0.02)$ (Fig. 13), again steeper than for the total J3/2 population and comparable to that of the Schubart family. The spectral slopes ($PC_1$) are somewhat spread from flat (C/X-compatible values; $PC_1 < 0.3$) to redder (D-compatible values; $PC_1 > 0.3$) – see Fig. 14. Overall, though, the C/X members prevail such that the D-type objects might be actually interlopers, at least according to a simple estimate based on the volume of the Hilda family in the ($a_{\rm p}$, $e_{\rm p}$, $\sin i_{\rm p}$) space, compared to the total volume of the J3/2 population.

Tedesco et al. (2002) determine albedos for six family members. They range from 0.037 to 0.087, but three values are close to the median albedo 0.044 of all J3/2 asteroids. We thus consider this value to be representative of the Hilda family. The corresponding cumulative size distribution is plotted in Fig. 15. Using the same method as in Section 3.1 we estimate the size of the parent body $D_{\rm PB} = 180$–190 km, with $V_{\rm LF}/V_{\rm PB} \simeq 0.8$. With the model of Tanga et al. (1999) we would obtain $D_{\rm PB} \simeq 210$ km and thus $V_{\rm LF}/V_{\rm PB} \simeq 0.5$. This family forming event seems to be thus characterized in between the catastrophic disruption and a huge cratering. The necessary projectile size is $d_{\rm disrupt} = 50$–55 km.

While not so prominent as the Schubart family, we consider the group of asteroids around Hilda a fairly robust case of a collisionally born family too.

### 3.3 Simulated disruption events

In order to asses some limits for the age of the Schubart and Hilda families, we perform a number of numerical tests. In particular, we simulate a disruption of a parent body inside the resonance and numerically determine the long-term orbital evolution of fragments. The evolved synthetic family at different time-steps is then compared with the observed family. Ideally, this approach should allow to constrain the time elapsed since the family formed.

As a first step, we need to create a synthetic family inside the resonance. We use current orbital elements of the largest family member, (1911) Schubart in this case, as representative to the parent body and only allow changes in the true anomaly $f$ and in the argument of pericentre $\omega$ at the break-up event. By changing these two geometric parameters we can produce different initial positions of the fragments in the orbital element space. For sake of our test, fragments are assumed to be dispersed isotropically with respect to the parent body, with a velocity distribution given by the model of Farinella et al. (1993); Farinella, Froeschlé & Gonczi (1994). The number of fragments $\mathrm{d}N(v)$ launched with relative velocities in the interval $(v, v + \mathrm{d}v)$ is given by

$$\mathrm{d}N(v) = Cv(v^2 + v_{\rm esc}^2)^{-(\kappa+1)/2}\,\mathrm{d}v, \quad (11)$$

with $C$ a normalization constant, $v_{\rm esc}$ the escape velocity from the parent body and $\kappa = 3.25$. To prevent excessive escape velocities we introduce a maximum allowed value $v_{\rm max}$. Nominally, we set $v_{\rm max} = 200\,{\rm m\,s^{-1}}$, but in Section 3.4 we also use restricted values of this parameter to test sensitivity of our results to initial conditions.

To simulate an impact that might have created the Schubart family, we generated velocities randomly for 139 fragments with $v_{\rm esc} = 65\,{\rm m\,s^{-1}}$ (note the number of fragments in the synthetic family is equal to the number of the Schubart family members). The resulting swarm of fragments is shown in Fig. 16, for the impact geometry $f = 0^\circ$ and $\omega + f = 180^\circ$. We show both the initial osculating orbital elements and the pseudo-proper elements.

The synthetic family extends over significantly larger range of the semimajor axis than the observed Schubart family, but all fragments still fall within the J3/2 resonance. The eccentricity distribution is, on the other hand, substantially more compact. Only the distribution of inclinations of the synthetic family roughly matches that of the observed family. We verified this holds also for other isotropic-impact geometries (such as $f = 135^\circ$ and $\omega + f = 180^\circ$ shown in Fig. 17). The peculiar shape of the synthetic family in the pseudo-proper element space ($a_{\rm p}$, $e_{\rm p}$) is an outcome of the isotropic disruption, simply because some fragments fall to the left-hand side from the libration centre of the J3/2 resonance (at 3.97 au) and they are 'mapped' to the right-hand side. This is because the pseudo-proper

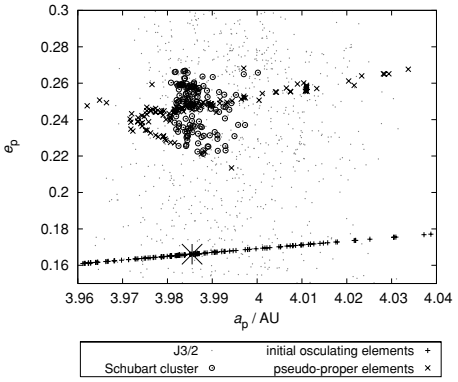


**Figure 16.** The initial osculating elements of an impact-generated swarm of 139 fragments at the location of (1911) Schubart (bottom crosses), the corresponding pseudo-proper elements computed from the first Myr of evolution (upper crosses) and the pseudo-proper elements of the observed Schubart family (circles). We show here projection on to the plane defined by semimajor axis and eccentricity. Dots are the pseudo-proper elements of the background J3/2-population asteroids. The initial synthetic swarm of asteroids poorly matches the observed family: it is both too extent in semimajor axis and too compact in eccentricity.

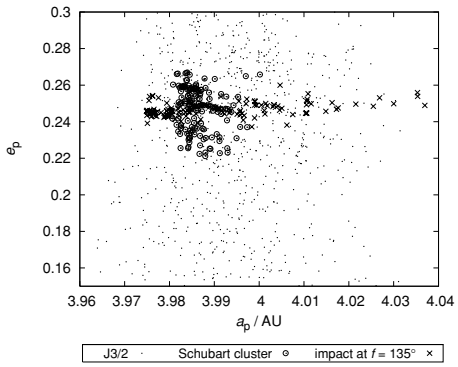


**Figure 17.** The same as Fig. 16, but for a different impact geometry ($f = 135°, \omega + f = 180°$). This choice of $f$ maximizes the initial spread of the synthetic family in proper eccentricity. In this case we do not show the initial osculating orbital elements.

elements are the maxima and minima of $a$ and $e$, respectively, over their resonant oscillations.

The initial configuration of the synthetic family was propagated for 4 Gyr, using the integrator described in Section 2. At this stage, we use only the gravitational perturbations from the four exterior giant planets. We performed such simulation for several impact geometries, as determined by $f$ and $\omega$, with similar results.

Fig. 18 shows the long-term evolution of the synthetic family. Because the family resides mostly in the stable zone of the J3/2 resonance, only little evolution can be seen for most of the bodies. This is in accord with findings of Nesvorný & Ferraz-Mello (1997) who concluded that the stable region in this resonance shows little or no diffusion over time-scales comparable to the age of the Solar system. Only about 10 per cent of orbits that initially started at the outskirts of the stable zone (with large libration amplitudes) escaped from the resonance during the 4-Gyr simulation.

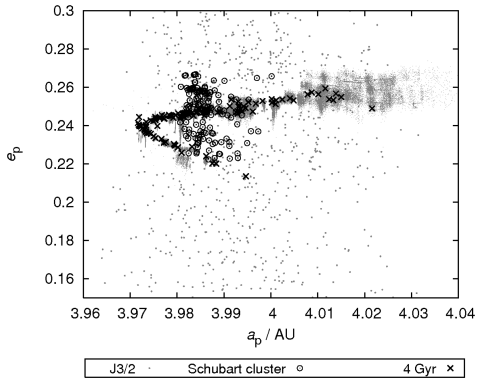


**Figure 18.** The synthetic family from Fig. 16 evolved over 4 Gyr: the grey dots show evolutionary tracks of the fragments in the pseudo-proper orbital element space. Overall, stability of the J3/2 resonance makes many fragments to stay very close to their initial values. Only ∼10 per cent of fragments with the initial extremal values of $a_p$ (and thus the libration amplitude) escape from the resonance during the simulation. This helps in part to reduce the mismatch with the observed family (circles) in semimajor axis, but is not sufficient to attain the Schubart-family full eccentricity dispersion.

The removal of orbits with large semimajor axis $a_p$ helps in part to reconcile the mismatch with the distribution of the observed Schubart family. However, the dispersion in eccentricity $e_p$ does not evolve much and it still shows large mismatch if compared to the observed family. Even in the case $f = 135°$ ($\omega + f = 180°$; Fig. 17), which maximizes the initial eccentricity dispersion of the synthetic fragments, the final value at 4 Gyr is about three times smaller than that of the Schubart family. Clearly, our model is missing a key element to reproduce the current orbital configuration of this family.

One possibility to resolve the problem could be to release the assumption of an isotropic impact and explore anisotropies in the initial velocity field. This is an obvious suspect in all attempts to reconstruct orbital configurations of the asteroid families, but we doubt it might help much in this case. Exceedingly large relative velocities, compared to the escape velocity of the estimated parent body, would be required. Recall, the fragments located in the stable region of the J3/2 resonance would hardly evolve over the age of the Solar system.

A more radical solution is to complement the force model, used for the long-term propagation, by additional effects. The only viable mechanism for the size range we are dealing with is the Yarkovsky effect. This tiny force, due to anisotropic thermal emission, has been proved to have determining role in understanding fine structures of the asteroid families in the main belt (e.g. Bottke et al. 2001; Vokrouhlický et al. 2006a,b). In these applications the Yarkovsky effect produces a steady drift of the semimajor axis, leaving other orbital elements basically constant.

However, the situation is different for resonant orbits. The semimajor axis evolution is locked by the strong gravitational influence of Jupiter. For that reason we first ran simplified simulations with the Yarkovsky forces – results of these tests are briefly described in Appendix A. We next applied the model containing both gravitational and Yarkovsky perturbations to the evolution of the synthetic family. Results of these experiments are described in Section 3.4.

### 3.4 Yarkovsky drift in eccentricity

We ran our previous simulation of the long-term evolution of the synthetic family with the Yarkovsky forces included. Our best guess of thermal parameters for bodies of the C/X type is: $\rho_s = \rho_b = 1300\,\mathrm{kg\,m^{-3}}$ for the surface and bulk densities, $K = 0.01\,\mathrm{W\,m^{-1}\,K^{-1}}$ for the surface thermal conductivity, $C = 680\,\mathrm{J\,kg^{-1}}$ for the heat capacity, $A = 0.02$ for the Bond albedo and $\epsilon = 0.95$ for the thermal emissivity parameter. Rotation periods are bound in the 2–12 h range. Spin axes orientations are assumed isotropic in space. Finally, we assign sizes to our test particles equal to the estimate of sizes for Schubart family members, based on their reported absolute magnitudes and albedo $p_V = 0.025$. The dependence of the Yarkovsky force on these parameters is described, e.g. in Bottke et al. (2002, 2006). We note the uncertainties of the thermal parameters, assigned to individual bodies, do not affect our results significantly, mainly because we simulate a collective evolution of more than 100 bodies; we are not interested in evolution of individual orbits.

We let the synthetic family evolve for 4 Gyr and recorded its snapshots every 50 kyr. As discussed in Appendix A, the *resonant Yarkovsky effect* produces mainly secular changes of eccentricity (Fig. 19). We recall this systematic drift in $e$ must not be confused with the chaotic diffusion in $e$. We also note that inclination of the orbits remains stable, in accord with a good match of the Schubart family by the initial inclination distribution.

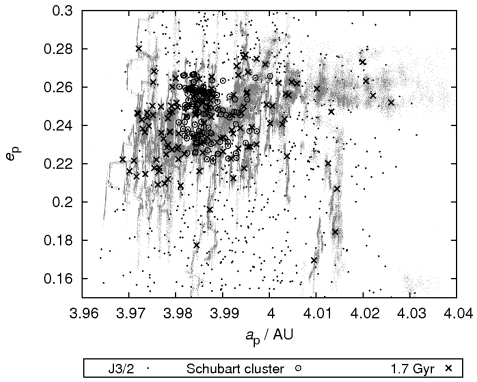


**Figure 19.** The impact-generated swarm from Fig. 16 evolved by planetary perturbations and the Yarkovsky forces, in the projection on the pseudo-proper semimajor axis $a_p$ versus eccentricity $e_p$ plane. The grey dots indicate the evolutionary tracks over the whole 4-Gyr time-span and crosses denote the configuration at 1.7 Gyr, when the eccentricity dispersion of the synthetic family particles roughly matches that of the observed Schubart family (circles).

Because the initial eccentricity dispersion of the synthetic family is much smaller than that of the observed one, its steady increase due to the combined effects of the Yarkovsky forces and the resonant lock gives us a possibility to date the origin of the family (see Vokrouhlický et al. 2006a for a similar method applied to families in the main belt). To proceed in a quantitative way, we use a one-dimensional Kolmogorov–Smirnov (KS) test to compare cumulative distribution of pseudo-proper eccentricity values $e_p$ of the observed and synthetic families (e.g. Press et al. 2007).

Fig. 20 shows the KS distance $D_{KS}$ of the two eccentricity distributions as a function of time. For sake of a test, we also use smaller $v_{max}$ values of the initial velocity field (essentially, this is like to start with a more compact synthetic family). Regardless of the $v_{max}$ value, our model rejects Schubart family ages smaller than 1 Gyr

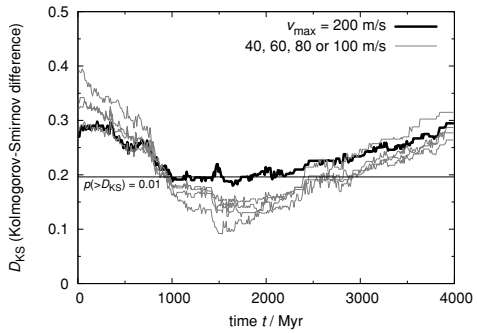


**Figure 20.** The difference between the cumulative distribution of eccentricities for the observed Schubart family and our synthetic families expressed as the Kolmogorov–Smirnov (KS) distance $D_{KS}$ versus time $t$. All models assume $f = 0^\circ$ and $\omega + f = 180^\circ$ but they have different maximum values $v_{max}$ of the ejected particles: $v_{max} = 40$, 60, 80, 100 and 200 m s$^{-1}$ (labels). For $t < 1$ Gyr and $t > 2.4$ Gyr the KS distance is large such that the KS probability is $p(> D_{KS}) < 0.01$. Thus with a 99 per cent probability level we can exclude such age for the Schubart family. The best matches are achieved for $v_{max} = 40$ and 60 m s$^{-1}$, for which the most extreme particles have been eliminated from the synthetic family.

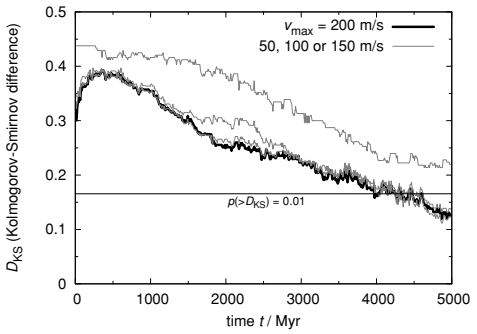


**Figure 21.** The same as Fig. 20 but for the Hilda family. The KS distance $D_{KS}$ of the observed and modelled pseudo-proper eccentricity $e_p$ distribution for several synthetic clusters with different maximum velocities $v_{max}$ are plotted versus time $t$. In this case, $t \leq 3.5$ Gyr seems to be ruled out at a 99 per cent probability level.

and larger than 2.4 Gyr with a 99 per cent confidence level. For ages in between 1.5 and 1.7 Gyr the KS-tested likelihood of a similarity of the synthetic-family and the observed-family $e_p$ distributions can reach up to 50 per cent. We thus conclude the most likely age of the Schubart cluster is $(1.7 \pm 0.7)$ Gyr.

We repeated the same analysis for Hilda family by creating a synthetic family of 233 particles about (153) Hilda. In this case we used $v_{esc} = 110$ m s$^{-1}$. The situation is actually very similar to the Schubart – there is again a problem with the small dispersion of eccentricities in case of a purely gravitational model. Using the model with the Yarkovsky effect, we can eventually fit the spread of eccentricities and according to the KS test (Fig. 21) the age of the family might be $\gtrsim$4 Gyr. The match is still not perfect, but this problem might be partly due to numerous interlopers in the family. We also note that a 10 per cent relative uncertainty of the mean albedo of the Hilda family members would lead to a 5 per cent uncertainty of their sizes and, consequently, to a 5 per cent uncertainty of the family age.

The Hilda family seems to be dated back to the Late Heavy Bombardment era (Morbidelli et al. 2005; see also Section 4.1). We would find such solution satisfactory, because the population of putative projectiles was substantially more numerous than today (note that a disruption of the Hilda family parent body is a very unlikely event during the last 3.5 Gyr).

We finally simulated a putative collision in the J2/1 resonance, around the asteroid (3789) Zhongguo (the largest asteroid in the stable island B). There are two major differences as compared to the J3/2 resonance.

(i) The underlying chaotic diffusion due to the gravitational perturbations is larger in the J2/1 resonance (e.g. Nesvorný & Ferraz-Mello 1997), such that an initially compact cluster would fill the whole stable region in 1–1.5 Gyr and consequently becomes unobservable.

(ii) Sizes of the observed asteroids are generally smaller, which together with a slightly smaller heliocentric distance, accelerates the Yarkovsky drift in $e_p$. The latter effect would likely shorten the time-scale to 0.5–1 Gyr.

Thus the non-existence of any significant orbital clusters in the J2/1 resonance (Section 3 and Fig. 12) does not exclude a collisional origin of the long-lived population by an event older than

1 Gyr. This would also solve the apparent problem of the very steep size distribution of the stable J2/1 population (Brož et al. 2005 and fig. 3). Note the expected collisional lifetime of the smallest observed J2/1 asteroids is several Gyr (e.g. Bottke et al. 2005).

## 4 RESONANT POPULATION STABILITY WITH RESPECT TO PLANETARY MIGRATION AND THE YARKOVSKY EFFECT

We finally pay a brief attention to the overall stability of asteroid populations in the first-order resonances with respect to different configurations of giant planets. We are focusing on the situations when the orbits of Jupiter and Saturn become resonant. This is motivated by currently adopted views about final stages of building planetary orbits architecture, namely planet migration in a diluted planetesimal disc (e.g. Malhotra 1995; Hahn & Malhotra 1999; Gomes et al. 2005; Morbidelli et al. 2005; Tsiganis et al. 2005 – these last three references are usually described as the Nice model). Morbidelli et al. (2005) proved that the primordial Trojan asteroids were destabilized when Jupiter and Saturn crossed their mutual 1:2 mean motion resonance and, at the same time, the Trojan region was repopulated by particles of the planetesimal disc. Since the mutual 1:2 resonance of Jupiter and Saturn plays a central role in the Nice model, and since these two planets had to cross other (weaker) mutual resonances such as 4:9 and 3:7 before they acquired today's orbits, one can naturally pose a question about the stability of primordial populations in the first-order mean motion resonances with Jupiter. Ferraz-Mello et al. (1998a,b) demonstrated that even subtler effects can influence the J2/1 population, namely the resonances between the asteroid libration period in the J2/1 resonance and the period of the GI terms in planetary perturbations (i.e. those associated with Jupiter and Saturn proximity to their mutual 2:5 mean motion resonance; Fig. 22). A first glimpse to the stability of the first-order resonance populations with respect to these effects is given in Section 4.1.

In Section 4.2 we also briefly estimate the change of dynamical lifetimes for small J2/1 and J3/2 bodies caused by the Yarkovsky effect.

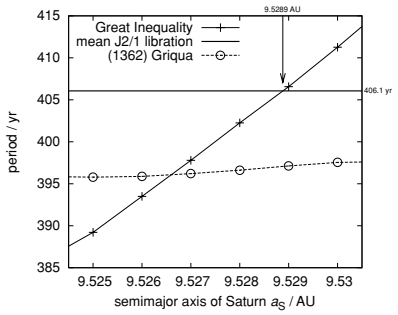


**Figure 22.** Dependence of the period associated with circulation of the GI angle $5\lambda_S - 2\lambda_J$($\lambda_S$ and $\lambda_J$ are mean longitude in orbit for Saturn and Jupiter) on the osculating semimajor axis $a_S$ of Saturn (crosses); Jupiter's orbit is fixed. Moving Saturn farther away from the location of 2:5 resonance with Jupiter (at $a_S = 9.584$ au) makes the GI period shorter (with today's $a_S = 9.5289$ au the GI period is about 880 yr). In the interval of $a_S$ values shown in this figure the GI period becomes comparable to the average period $\bar{P}_{J2/1}$ of librations in the J2/1 resonance (solid line). Libration period for a particular case of asteroid (1362) Griqua is shown by circles.

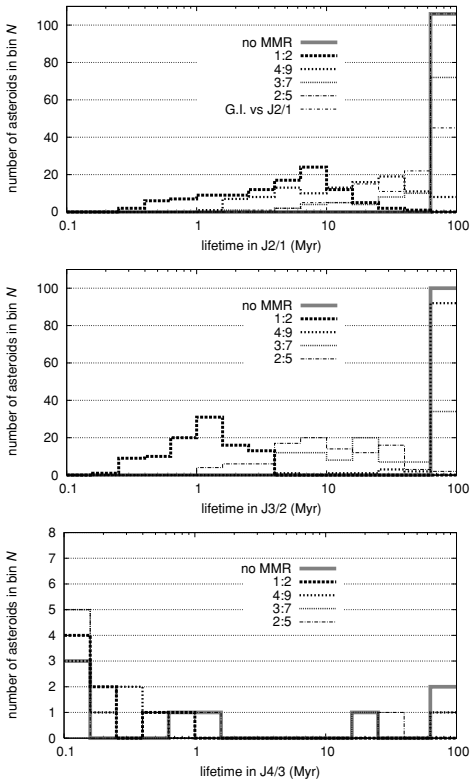


**Figure 23.** Histograms of dynamical lifetimes for asteroids in the J2/1 (top), J3/2 (middle) and J4/3 (bottom) resonances, in case Jupiter and Saturn are at their current orbits, or in a mutual 1:2, 4:9, 3:7, 2:5 resonance, or in a GI resonance (in case of the J2/1 only). The histograms were computed for 106 long-lived asteroids in the J2/1, first 100 Hildas in the J3/2 and 8 in the J4/3 (including short-lived).

### 4.1 Planetary migration effects

In what follows we use a simple approach by only moving Saturn's orbit into different resonance configurations with Jupiter's orbit. We do not let orbits of these planets migrate, but consider them static. With such a crude approach we can only get a first hint about a relative role of depletion of the asteroid populations in the first-order resonances (note in reality the planets undergo steady, but likely not smooth, migration and exhibit jumps over different mutual resonant states; e.g. supplementary materials of Tsiganis et al. 2005).

The results are summarized in Fig. 23.

(i) The Hilda group in the J3/2 resonance is very unstable (on the time-scale ∼1 Myr) with respect to the 1:2 Jupiter–Saturn resonance[8]; on the contrary J2/1 asteroids may survive several 10 Myr in this configuration of Jupiter and Saturn, so this population is not much affected by this phase by planetary evolution (note, moreover, that Jupiter and Saturn would likely cross the zone of other

[8] Jupiter Trojans, which are already known to be strongly unstable (Morbidelli et al. 2005), would have the dynamical lifetime of the order of 0.1 Myr in this kind of simulation.

mutual 1:2 resonance in ∼1 Myr only; e.g. Tsiganis et al. 2005 and Morbidelli et al. 2005).

(ii) The 4:9 resonance has a larger influence on the J2/1 population than on Hildas.

(iii) In the case of 3:7 resonance it is the opposite: the J3/2 is more unstable than the J2/1.

(iv) The GI resonance does indeed destabilize the J2/1 on a timescale 50 Myr. Provided the last phases of the migration proceed very slowly, it may cause a significant depletion of the primordial J2/1 population. In the exact 2:5 resonance, the J2/1 population would not be affected at all.

According to our preliminary tests with a more complete *N*-body model for planetary migration which includes a disc of $10^3$ planetesimals beyond Neptune, the strong instability of the J3/2 asteroids indeed occurs during the Jupiter–Saturn 1:2 resonance crossing (see Fig. 24). A vast reservoir of planetesimals residing beyond the giant planets, and to some extent also nearby regions of the outer asteroid belt, are probably capable to repopulate the J3/2 resonance zone at the same time and form the currently observed populations. This is similar to the Trojan clouds of Jupiter (Morbidelli et al. 2005).

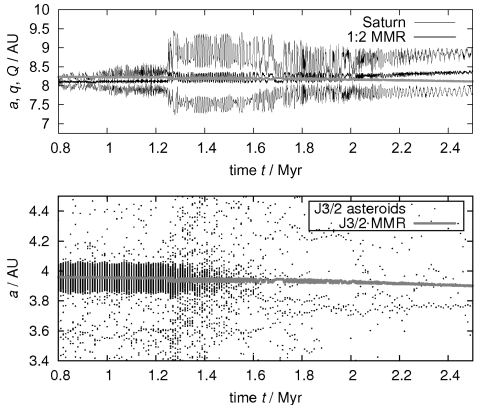


**Figure 24.** An *N*-body simulation of planetary migration driven by dynamically cold planetesimal disc beyond Neptune, with $10^3$ particles and total mass $50\,M_\oplus$, and including also $10^3$ massless particles in the J3/2 resonance with Jupiter. Top: The semimajor axis $a_S$ of Saturn versus time and the position of the 1:2 mean motion resonance with Jupiter [estimated from the Kepler law $(1/2)^{-2/3}\,a_J$]. Bottom: The same for asteroids initially located inside the J3/2 resonance with Jupiter. The J3/2 asteroids are strongly destabilized at the very time of the 1:2 Jupiter–Saturn resonance crossing ($t = 1.25$ Myr) and none of the 1000 test particles survived in the J3/2 region after a mere 0.5 Myr. This means more than 99.9 per cent depletion of the primordial population. None of the planetesimal disc particles got trapped in the J3/2 during or after Jupiter's and Saturn's passage through the 1:2 resonance, indicating that more particles are needed to study this process. We used the Mercury hybrid-scheme integrator (Chambers 1999) for the purpose of this test. The gravitational interactions between planets and massive planetesimals are accounted for, but planetesimals do not interact with each other, nor with massless test particles. The time-step was 36 d and the accuracy parameter $10^{-10}$. Initial conditions of planets were: $a_J = 5.2$ au, $a_S = 8.05$ au, $a_U = 12.3$ au, $a_N = 17.5$ au, with all eccentricities and inclination of the order of $10^{-3}$. We took the current orbits of Hildas as the initial conditions for our test particles. Note the destabilization of the Hilda region is neither sensitive to precise initial conditions nor to the mass of the planetesimal disc; the only relevant condition is that Jupiter and Saturn cross their mutual 1:2 resonance.

### 4.2 The Yarkovsky effect

In Section 3.4 we already discussed the influence of the Yarkovsky effect on the families located inside the J3/2 resonance. In course of time it modified eccentricities of their members, but did not cause a large-scale instability; the families remained inside the resonance all the time. Here we seek the size threshold for which the Yarkovsky would case overall instability by quickly removing the bodies from the resonance.

We perform the following numerical test: we multiply sizes of the long-lived J2/1 objects by fudge factors of 0.2, 0.02 and 0.002, for which the Yarkovsky effect is stronger, and compare respective dynamical lifetimes with the original long-lived objects. Results are summarized in Fig. 25. We can conclude that a significant destabilization of the J2/1 resonant population occurs for sizes ∼0.1 km and smaller (provided the nominal population has sizes mostly 4–12 km).

We do not include the YORP effect (i.e. the torque induced by the infrared thermal emission) at this stage. The YORP is nevertheless theoretically capable to significantly decelerate (or accelerate) the rotation rate, especially of the smallest asteroids, which can lead to random reorientations of the spin axes due to collisions, because the angular momentum is low in this spin-down state. These reorientations can be simulated by a Monte Carlo model with a typical time-scale (Čapek & Vokrouhlický 2004; $R$ is radius in kilometres and $a$ orbital semimajor axis in au):

$$\tau_{\rm YORP} \simeq 25\,{\rm Myr}\,(R/1\,{\rm km})^2\,(2.5\,{\rm au}/a)^2. \qquad (12)$$

Since the Yarkovsky effect depends on the obliquity value, the systematic drift would be changed to a random walk for bodies whose spin axis undergo frequent re-orientations by the YORP effect. We can thus expect that the YORP effect might significantly prolong dynamical lifetimes of resonant objects with sizes ∼0.1 km or smaller, because $\tau_{\rm YORP} < 0.25$ Myr for them.

We can also check which orientation of the spin axis makes the escape from the J2/1 resonance more likely to happen. We consider 0.08–0.24 km bodies, clone them five times and assign them different values of the obliquity $\gamma = 0^\circ, 45^\circ, 90^\circ, 135^\circ$ and $180^\circ$. Fig. 26 shows clearly that the retrograde rotation increases the probability of the escape. This is consistent with the structure of the J2/1 resonance, for which low-$a$ separatrix does not continue

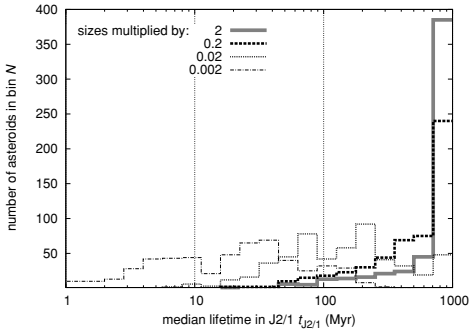


**Figure 25.** Logarithmic histograms of dynamical lifetimes for the originally long-lived asteroids in the J2/1 resonance, in case the Yarkovsky effect perturbs the orbits. The sizes of the objects (4–12 km) were multiplied by 2, 0.2, 0.02 and 0.002 for comparison. Note a stronger instability starts to occur for the factor of 0.02 (i.e. for the sizes 0.08–0.24 km). The YORP reorientations are not included in this model.

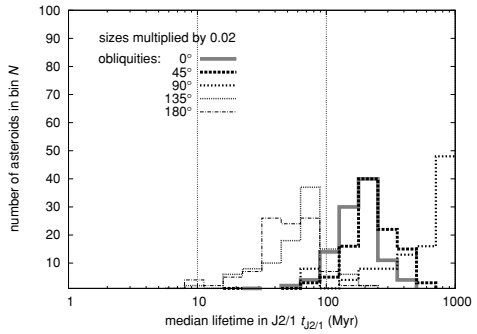


**Figure 26.** The same as Fig. 25, but now the Yarkovsky effect is calculated only for small bodies (0.08–0.24 km) and varies due to different values of the obliquity $\gamma = 0, 45^\circ, 90^\circ, 135^\circ$ and $180^\circ$. Note the retrograde bodies (i.e. with a negative drift $\mathrm{d}a/\mathrm{d}t < 0$) are significantly more unstable.

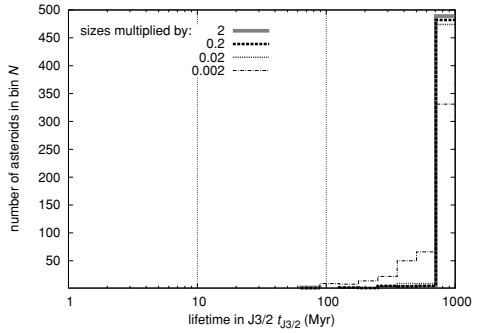


**Figure 27.** The same as Fig. 25, but for the J3/2 resonance. Instability occurs for the sizes multiplied by 0.002 (i.e. 0.02–0.12 km). The YORP effect and corresponding reorientations of the spin axes are included in this case.

to $e = 0$. We conclude the remaining very small (yet unobservable) asteroids inside the J2/1 may exhibit a preferential prograde rotation.

We perform a similar simulation for the J3/2 population (first 100 bodies with sizes 10–60 km), but now with YORP reorientations (equation 12) included. The results (Fig. 27) show the J3/2 population is much less affected than the J2/1 by the Yarkovsky/YORP perturbation.

We conclude the Yarkovsky/YORP effect may destabilize the J2/1 and J3/2 bodies only partially on the 100-Myr time-scale and only for sizes smaller than $\sim 0.1$ km. It is obviously a remote goal to verify this conclusion by observations (note the smallest bodies in these resonances have several kilometres size). Nevertheless, the dynamical lifetimes of small asteroids determined in this section, might be useful for collisional models of asteroid populations, which include also dynamical removal.

## 5 CONCLUSIONS AND FUTURE WORK

The main results of this paper can be summarized as follows.

(i) We provided an update of the observed J2/1, J3/2 and J4/3 resonant populations.

(ii) We discovered two new objects in the J4/3 resonance.

(iii) We described two asteroid families located inside the J3/2 resonance (Schubart and Hilda) and provided an evidence that they are of a collisional origin.

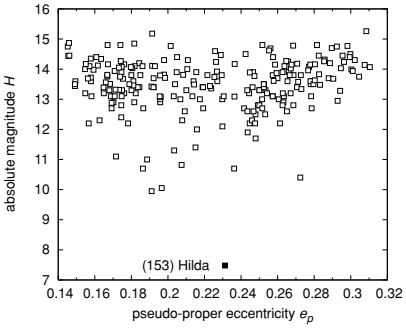


**Figure 28.** Pseudo-proper eccentricity $e_\mathrm{p}$ versus absolute magnitude $H$ plot for the members of the Hilda family. The triangular shape and the depletion of asteroids in the centre of the family (around $e_\mathrm{p} \simeq 0.22$) is discussed in the text.

(iv) We reported a new mechanism how the Yarkovsky effect systematically changes *eccentricities* of resonant asteroids; we used this phenomenon to estimate the ages of the Schubart and Hilda families [$(1.7 \pm 0.7)$ Gyr and $\gtrsim$4 Gyr respectively].

(v) Collisionally born asteroid clusters in the stable region of J2/1 would disperse in about 1 Gyr.

(vi) 20 per cent of Hildas may escape from the J3/2 resonance within 4 Gyr in the current configuration of planets.

(vii) Hildas are strongly unstable when Jupiter and Saturn cross their mutual 1:2 mean motion resonance.

The J3/2 resonance is a unique 'laboratory' – the chaotic diffusion is so weak, that families almost do not disperse in eccentricity and inclination due to this effect over the age of the Solar system. What is even more important, they almost do not disperse in semimajor axis, even thought the Yarkovsky effect operates. The drift in $a$ is transformed to a drift in $e$, due to a strong gravitational coupling with Jupiter. We emphasize, this is not a chaotic diffusion in $e$, but a *systematic drift in e*.

Another piece of information about the families in J3/2 resonance is hidden in the eccentricity $e_\mathrm{p}$ versus absolute magnitude $H$ plots (see Fig. 28 for the Hilda family). The triangular shape (larger eccentricity dispersion of the family members for larger $H$) is a well-known combination of two effects: (i) larger ejection speed and (ii) faster dispersal by the Yarkovky forces for smaller fragments. Interestingly, there is also a noticeable depletion of small bodies in the centre of the family and their concentration at the outskirts – a phenomenon known from ($a$, $H$) plots of main belt families, which was interpreted as an interplay between the Yarkovsky and YORP effects (Vokrouhlický et al. 2006b).[9] Indeed the estimated $\sim$4 Gyr age for this family matches the time-scale of a YORP cycle for $D \simeq 10$ km asteroids in the Hilda region (e.g. Vokrouhlický & Brož 2002; Čapek & Vokrouhlický 2004). Vokrouhlický et al. (2006a) pointed out that this circumstance makes the uneven distribution of family members most pronounced.

We postpone the following topics for the future work.

[9] The YORP effect tilts the spin axes of asteroids preferentially towards obliquity $\gamma = 0^\circ$ or $180^\circ$ and this enhances the diurnal Yarkovsky drift due to its $\cos\gamma$ dependence.

(i) A more precise age determination for the resonant asteroid families, based on the Yarkovsky/YORP evolution in the ($e$, $H$) space.

(ii) A more detailed modelling of analytic or $N$-body migration of planets and its influence on the stability of resonant populations.

## ACKNOWLEDGMENTS

We thank David Nesvorný, Alessandro Morbidelli and William F. Bottke for valuable discussions on the subject and also Rodney Gomes for a constructive review. The work has been supported by the Grant Agency of the Czech Republic (grants 205/08/0064 and 205/08/P196) and the Research Programme MSM0021620860 of the Czech Ministry of Education. We also acknowledge the usage of the Metacentrum computing facilities (http://meta.cesnet.cz/) and computers of the Observatory and Planetarium in Hradec Králové (http://www.astrohk.cz/).

## REFERENCES

Beaugé C., Roig F., 2001, Icarus, 153, 391
Bottke W. F., Vokrouhlický D., Brož M., Nesvorný D., Morbidelli A., 2001, Sci, 294, 1693
Bottke W. F., Vokrouhlický D., Rubincam D. P., Brož M., 2002, in Bottke W. F., Cellino A., Paolicchi P., Binzel R. P., eds, Asteroids III. University of Arizona Press, Tucson, p. 395
Bottke W. F., Durda D. D., Nesvorný D., Jedicke R., Morbidelli A., Vokrouhlický D., Levison H. F., 2005, Icarus, 179, 63
Bottke W. F., Vokrouhlický D., Rubincam D. P., Nesvorný D., 2006, Annu. Rev. Earth Planet. Sci., 34, 157
Brown M. E., Barkume K. M., Ragozzine D., Schaller E. L., 2007, Nat, 446, 294
Brož M., 2006, PhD thesis, Charles University (see at http://sirrah.troja.mff.cuni.cz/~mira/mp/)
Brož M., Vokrouhlický D., Roig F., Nesvorný D., Bottke W. F., Morbidelli A., 2005, MNRAS, 359, 1437
Bus S. J., Vilas F., Barucci M. A., 2002, in Bottke W. F., Cellino A., Paolicchi P., Binzel R. P., eds, Asteroids III. University of Arizona Press, Tucson, p. 169
Čapek D., Vokrouhlický D., 2004, Icarus, 172, 526
Chambers J. E., 1999, MNRAS, 304, 793
Dahlgren M., 1998, A&A, 336, 1056
Dahlgren M., Lagerkvist C.-I., 1995, A&A, 302, 907
Dahlgren M., Lagerkvist C.-I., Fitzsimmons A., Williams I. P., Gordon M., 1997, A&A, 323, 606
Dahlgren M., Lahulla J. F., Lagerkvist C.-I., Lagerros J., Mottola S., Erikson A., Gonano-Beurer M., di Martino M., 1998, Icarus, 133, 247
Dahlgren M., Lahulla J. F., Lagerkvist C.-I., 1999, Icarus, 138, 259
Davis D. R., Durda D. D., Marzari F., Campo Bagatin A., Gil-Hutton R., 2002, in Bottke W. F., Cellino A., Paolicchi P., Binzel R. P., eds, Asteroids III. University of Arizona Press, Tucson, p. 545
Dell'Oro A., Marzari F., Paolicchi P., Vanzani A., 2001, A&A, 366, 1053
Dohnanyi J. W., 1969, J. Geophys. Res., 74, 2531
Durda D., Bottke W. F., Nesvorny D., Encke B., Merline W. J., Asphaug E., Richardson D. C., 2007, Icarus, 186, 498
Farinella P., Gonczi R., Froeschlé Ch., Froeschlé C., 1993, Icarus, 101, 174
Farinella P., Froeschlé C., Gonczi R., 1994, in Milani A., Di Martino M., Cellino A., eds, Asteroids, Comets, Meteors 1993. Kluwer, Dordrecht, p. 205
Ferraz-Mello S., 1988, AJ, 96, 400
Ferraz-Mello S., Michtchenko T. A., 1996, A&A, 310, 1021
Ferraz-Mello S., Michtchenko T. A., Nesvorný D., Roig F., Simula A., 1998a, Planet. Space Sci., 46, 1425
Ferraz-Mello S., Michtchenko T. A., Roig F., 1998b, AJ, 116, 1491
Franklin A., Lewis N. K., Soper P. R., Holman M. J., 2004, ApJ, 128, 1391
Gil-Hutton R., Brunini A., 2008, Icarus, 193, 567
Gomes R., Levison H. L., Tsiganis K., Morbidelli A., 2005, Nat, 435, 466
Hahn J. M., Malhotra R., 1999, AJ, 117, 3041
Henrard J., 1982, Celest. Mech., 27, 3
Ivezić Z., Jurić M., Lupton R. H., Tabachnik S., Quinn T., 2002, in Tyson J. A., Wolff S., eds, Proc. SPIE, Vol. 4836, Survey and Other Telescope Technologies and Discoveries. SPIE, Bellingham, 98
Jedicke R., Magnier E. A., Kaiser N., Chambers K. C., 2007, in Milani A., Valsecchi G. B., Vokrouhlický D., eds, Near Earth Asteroids, Our Celestial Neighbors. Cambridge Univ. Press, Cambridge, p. 341
Kenyon S. J., Bromley B. C., O'Brien D. P., Davis D. R., 2008, in Barucci M. A., Boehnhardt H., Cruikshank D. P., Morbidelli A., eds, The Solar System Beyond Neptune. University of Arizona Press, Tucson, p. 293
Krueger A., 1889, Astron. Nachr., 120, 221
Kühnert F., 1876, Astron. Nachr., 87, 173
Landau L. D., Lifschitz E. M., 1976, Mechanics. Pergamon Press, Oxford
Laskar J., Robutel P., 2001, Celest. Mech. Dyn. Astron., 80, 39
Lemaitre A., Henrard J., 1990, Icarus, 83, 391
Levison H., Duncan M., 1994, Icarus, 108, 18
Malhotra R., 1995, AJ, 110, 420
Michtchenko T. A., Ferraz-Mello S., 1997, Planet. Space Sci., 45, 1587
Milani A., 1993, Celest. Mech. Dyn. Astron., 57, 59
Milani A., Farinella P., 1995, Icarus, 115, 209
Morbidelli A., Moons M., 1993, Icarus, 102, 316
Morbidelli A., Levison H. L., Tsiganis K., Gomes R., 2005, Nat, 435, 462
Morbidelli A., Tsiganis K., Crida A., Levison H. F., Gomes R., 2007, AJ, 134, 1790
Moons M., Morbidelli A., Migliorini F., 1998, Icarus, 135, 458
Murray C. D., 1986, Icarus, 65, 70
Murray C. D., Dermott S. F., 1999, Solar System Dynamics. Cambridge Univ. Press, Cambridge
Nesvorný D., Ferraz-Mello S., 1997, Icarus, 130, 247
Nesvorný D., Bottke W. F., Dones L., Levison H. F., 2002, Nat, 417, 720
Nesvorný D., Alvarellos J. L. A., Dones L., Levison H. F., 2003, AJ, 126, 398
Nesvorný D., Beaugé C., Dones L., 2004, AJ, 127, 1768
Nesvorný D., Jedicke R., Whiteley R. J., Ivezić Z., 2005, Icarus, 173, 132
Nesvorný D., Vokrouhlický D., Bottke W. F., 2006, Sci, 312, 1490
O'Brien D. P., Greenberg R., 2003, Icarus, 164, 334
Palisa J., 1888, Astron. Nachr., 120, 111
Press W. R., Teukolsky S. A., Vetterling W., Flannery B. P., 2007, Numerical Recipes: The Art of Scientific Computing. Cambridge Univ. Press, Cambridge
Quinn T. R., Tremaine S., Duncan M., 1991, AJ, 101, 2287
Roig F., Gil-Hutton R., 2006, Icarus, 183, 411
Roig F., Nesvorný D., Ferraz-Mello S., 2002, MNRAS, 335, 417
Roig F., Ribeiro A. O., Gil-Hutton R., 2008, A&A, 483, 911
Schubart J., 1982a, A&A, 114, 200
Schubart J., 1982b, Celest. Mech. Dyn. Astron., 28, 189
Schubart J., 1991, A&A, 241, 297
Schubart J., 2007, Icarus, 188, 189
Sessin W., Bressane B. R., 1988, Icarus, 75, 97
Tanga P., Cellino A., Michel P., Zappalà V., Paolicchi P., Dell'Oro A., 1999, Icarus, 141, 65
Tedesco E. F., Noah P. V., Noah M., Price S. D., 2002, AJ, 123, 1056
Tsiganis K., Gomes R., Morbidelli A., Levison H. L., 2005, Nat, 435, 459
Tsuchida M., 1990, Rev. Mex. Astron. Astrofis., 21, 585
Vokrouhlický D., Brož M., 2002, in Celletti A., Ferraz-Mello S., Henrard J., eds, Modern Celestial Mechanics: From Theory to Applications. Kluwer, Dordrecht, p. 467
Vokrouhlický D., Brož M., Bottke W. F., Nesvorný D., Morbidelli A., 2006a, Icarus, 182, 118
Vokrouhlický D., Brož M., Morbidelli A., Bottke W. F., Nesvorný D., Lazzaro D., Rivkin A. S., 2006b, Icarus, 182, 92
Weissman P. R., Bottke W. F., Levison H. L., 2002, in Bottke W. F., Cellino A., Paolicchi P., Binzel R. P., eds, Asteroids III. University of Arizona Press, Tucson, p. 669
Zappalà V., Cellino A., Farinella P., Knežević Z., 1990, AJ, 100, 2030

Zappalà V., Cellino A., Farinella P., Milani A., 1994, AJ, 107, 772
Zappalà V., Cellino A., Dell'Oro A., Paolicchi P., 2002, in Bottke W. F., Cellino A., Paolicchi P., Binzel R. P., eds, Asteroids III. University of Arizona Press, Tucson, p. 619

## APPENDIX A: RESONANT YARKOVSKY EFFECT

The effects of weak dissipative forces, such as the tidal force, gas-drag force and the Poynting–Robertson force, on both non-resonant and resonant orbits were extensively studied in the past (e.g. Murray & Dermott 1999 and references therein). Interaction of the Yarkovsky drifting orbits with high-order, weak resonances was also numerically studied to some extent (e.g. Vokrouhlický & Brož 2002) but no systematic effort was paid to study Yarkovsky evolving orbits in strong low-order resonances. Here we do not intend to develop a detailed theory, rather give a numerical example that can both help to explain results presented in the main text and motivate a more thorough analytical theory.

*The Yarkovsky effect outside the resonance.* We constructed the following simple numerical experiment: we took the current orbit of (1911) Schubart as a starting condition and integrated the motion of two 0.1-km-sized objects with extreme obliquity values 0° and 180°. Their thermal parameters were the same as in Section 3.4. Because the diurnal variant of the Yarkovsky effect dominates the evolution, the extreme obliquities would mean the two test bodies would normally (outside any resonances) drift in semimajor axis in two opposite directions (e.g. Bottke et al. 2002, 2006). The two orbits would secularly acquire $\Delta a \simeq +0.25$ or $-0.25$ au in 100 Myr, about the extent shown by the arrow on top of the left-hand panel of Fig. A1. Since the strength of the Yarkovsky forces is inversely proportional to the size, we can readily scale the results for larger bodies.

*The resonance without the Yarkovsky effect.* If we include gravitational perturbations by Jupiter only, within a restricted circular three body problem ($e_J = 0$), and remove short-period oscillations by a digital filter, the parameter $N$ from equation (5) would stay constant. The orbit would be characterized by a stable libration in ($\Sigma$, $\sigma$) variables with about 30° amplitude in $\sigma$ (see the curve labelled 0 Myr in the middle panel of Fig. A1).

While evolving, some parameters known as the adiabatic invariants are approximately conserved (see e.g. Landau & Lifschitz 1976; Henrard 1982; Murray & Dermott 1999). One of the adiabatic invariants is $N$ itself. Another, slightly more involved quantity, is the area $J$ enclosed by the resonant path in the $\sqrt{2\Sigma}\,(\cos\sigma, \sin\sigma)$ space:

$$J = \oint \sqrt{2\Sigma}\,\mathrm{d}\sigma. \tag{A1}$$

We would thus expect these parameters be constant, except for strong enough perturbation or long enough time-scales (recall the adiabatic invariants are constant to the second order of the perturbing parameter only).

*Resonant Yarkovsky effect.* Introducing the Yarkovsky forces makes the system to evolve slowly. The lock in the resonance prevents the orbits to steadily drift away in the semimajor axis and the perturbation by the Yarkovsky forces acts adiabatically. This is because (i) the time-scale of the resonance oscillations is much shorter than the characteristic time-scale of the orbital evolution driven by the Yarkovsky forces and (ii) the strength of the resonant terms in the equations of motion are superior to the strength of the Yarkovsky accelerations.

We let the two J3/2 orbits evolve over 100 Myr (Fig. A1). At the end of our simulation the orbits moved from $N_0 \simeq 0.45$ to $N_+ \simeq 0.46$ (for the outward migrating orbit) or to $N_- \simeq 0.44$ (for the inward migrating orbit), respectively. During this evolution, both orbits remained permanently locked in the J2/1 resonance, librating about the periodic orbit (dashed line in the left-hand panel of Fig. A1). Because the position of this centre has a steep progression in the eccentricity and only small progression in the semimajor axis, the evolution across different $N$ planes makes the orbital eccentricity evolve significantly more than the semimajor axis. This is also seen in the middle panel of Fig. A1, where the librating orbits significantly split farther/closer with respect to origin of coordinates (note the polar distance from the origin is basically a measure of the eccentricity). The shape of the librating orbit is modified such that the area $J$ stays approximately constant. We have verified that

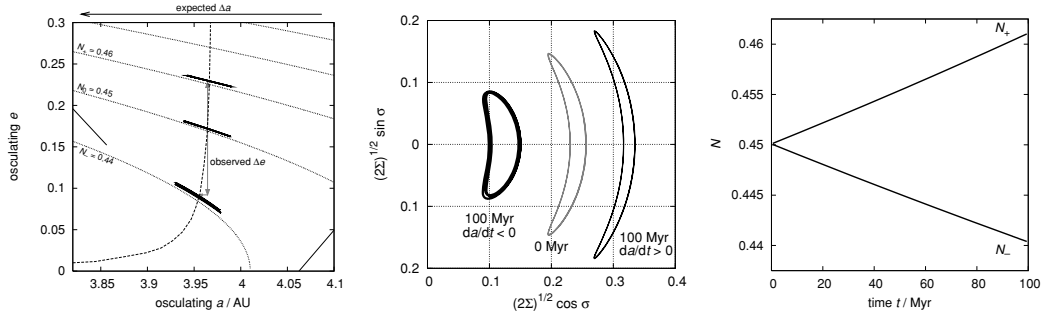


**Figure A1.** Orbital evolution of two $D = 0.1$ km asteroids in the J3/2 resonance within a circular restricted three-body problem (Jupiter on a circular orbit). Obliquities 0° and 180° were assigned to the two bodies, such that outside the resonance they would migrate by the Yarkovsky forces in opposite direction. The expected change $\Delta a$ of the semimajor axis in 100 Myr is depicted by the arrow on top of the left-hand panel. The left-hand and middle panels show 1-kyr orbital segments at the beginning and at the end of the simulation: (i) in the semimajor axis $a$ versus eccentricity $e$ projection (left-hand panel) and (ii) in the projection of Cartesian resonant variables $\sqrt{2\Sigma}\,(\cos\sigma, \sin\sigma)$ (see equations 1 and 2; short-period variations have been removed for better visibility) (middle). The orbits slowly evolve from the initial $N_0 \simeq 0.45$ level-curve of the integral given by equation (5) to their final values of $\simeq$0.44 ($N_+$ with $\mathrm{d}a/\mathrm{d}t > 0$) and $\simeq$0.46 ($N_-$ with $\mathrm{d}a/\mathrm{d}t < 0$), respectively (see also the right-hand panel). During this evolution the libration centre follows the position of the exact periodic orbit in the J3/2 (dashed curve in the left-hand panel). Because the latter has a steep progression in $e$ as $a$ changes, orbital evolution is characterized by a significant change of the eccentricity $\Delta e$ (also $e_\mathrm{p}$) but only a small change in $a$ (also $a_\mathrm{p}$).

the relative change in both adiabatic invariants, acquired during the 100 Myr of evolution, is about the same: $\delta N/N \sim \delta J/J \sim 5 \times 10^{-2}$. It is a direct expression of the strength of the perturbation by the Yarkovsky forces.

We can conclude the Yarkovsky effect results in a significantly different type of secular evolution for orbits initially inside strong first-order mean motion resonances with Jupiter. Instead of secularly pushing the orbital semimajor axis inward or outward from the Sun, it drives the orbital eccentricity to smaller or larger values, while leaving the semimajor axis to follow the resonance centre.

If we were to leave the orbital evolution continue in our simple model, the inward-migrating orbit would leave the resonance towards the zone of low-eccentricity apocentric librators. Such bodies are observed just below the J2/1 resonance. On the other hand, the outward-migrating orbit would finally increase the eccentricity to the value when the orbit starts to cross the Jupiters orbit. Obviously, in a more complete model, with all planets included, the orbits would first encounter the unstable region surrounding the stable resonant zone. Such marginally stable populations exist in both the J3/2 and J2/1 resonances.

This paper has been typeset from a TEX/LATEX file prepared by the author.

Icarus 241 (2014) 358–372

Contents lists available at ScienceDirect

Icarus

journal homepage: www.elsevier.com/locate/icarus

# A six-part collisional model of the main asteroid belt

H. Cibulková [a,*], M. Brož [a], P.G. Benavidez [b]

[a] Institute of Astronomy, Charles University in Prague, V Holešovičkách 2, 18000 Prague 8, Czech Republic
[b] Departamento de Física, Ingeniería de Sistemas y Teoría de la Señal, Universidad de Alicante, P.O. Box 99, 03080 Alicante, Spain

ARTICLE INFO

*Article history:*
Received 24 December 2013
Revised 25 June 2014
Accepted 11 July 2014
Available online 22 July 2014

*Keywords:*
Asteroids
Collisional physics
Origin, Solar System

ABSTRACT

In this work, we construct a new model for the collisional evolution of the main asteroid belt. Our goals are to test the scaling law of Benz and Asphaug (Benz, W., Asphaug, E. [1999]. Icarus, 142, 5–20) and ascertain if it can be used for the whole belt. We want to find initial size–frequency distributions (SFDs) for the considered six parts of the belt (inner, middle, "pristine", outer, Cybele zone, high-inclination region) and to verify if the number of synthetic asteroid families created during the simulation matches the number of observed families as well. We used new observational data from the WISE satellite (Masiero et al., 2011) to construct the observed SFDs. We simulate mutual collisions of asteroids with a modified version of the Boulder code (Morbidelli, A., et al. [2009]. Icarus, 204, 558–573), where the results of hydrodynamic (SPH) simulations of Durda et al. (Durda, D.D., et al. [2007]. Icarus, 498–516) and Benavidez et al. (Benavidez, P.G., et al. [2012]. 219, 57–76) are included. Because material characteristics can significantly affect breakups, we created two models — for monolithic asteroids and for rubble-piles. To explain the observed SFDs in the size range $D = 1$ to 10 km we have to also account for dynamical depletion due to the Yarkovsky effect. The assumption of (purely) rubble-pile asteroids leads to a significantly worse fit to the observed data, so that we can conclude that majority of main-belt asteroids are rather monolithic. Our work may also serve as a motivation for further SPH simulations of disruptions of smaller targets (with a parent body size of the order of 1 km).



## 1. Introduction

The collisional evolution of the main asteroid belt has been studied for more than 60 years (Dohnanyi, 1969; Davis et al., 1979 etc.). The first collisional model was created by Dohnanyi (1969) and his important result was that a size–frequency distribution for a population of mutually colliding asteroids will reach an equilibrium. If the cumulative distribution is described by a power law, the corresponding slope (exponent) will be close to −2.5. An overview of previous modeling of the main belt and subsequent advances can be found in a relatively recent paper by Bottke et al. (2005), so that we shall not repeat it here. Nevertheless, it is worth to mention another development, which is an attempt to merge a classical particle-in-a-box collisional model with (parametrized) results of smooth-particle hydrodynamic (SPH) codes as done in Morbidelli et al. (2009). We are going to use this kind of method in this work.

Every collisional model should comply with two important constraints: (1) the size–frequency distribution (SFD) of main belt at the end of a simulation must fit the observed SFD; (2) the number of asteroid families created during this simulation must fit the observed number of families. It is important to note, that the models were improved in the course of time not only due to the progress of technology or new methods but also thanks to an increasing amount of observational data. In this work, we could exploit new data obtained by the WISE satellite (Wide-field Infrared Survey Explorer; Masiero et al., 2011), specifically, diameters and geometric albedos for 129,750 asteroids.

Moreover, several tens of asteroid families are observed in the main belt as shown by many authors (Zappalà et al., 1995; Nesvorný et al., 2005, 2010; Brož et al., 2013; Masiero et al., 2013; Milani et al., 2013). The lists of collisional families are also steadily improved, they become more complete and (luckily) compatible with each other.

In order to fully exploit all new data, we created a new collisional model in which we divided the whole main belt into six parts (see Section 2 for a detailed discussion and Section 3 for the description of observational data). Our aims are: (1) to check the number of families in individual parts of the belt — we use the list of families from Brož et al. (2013) (which includes also their physical properties) with a few modifications; (2) to verify whether a single scaling law (e.g. Benz and Asphaug, 1999) can

* Corresponding author.
*E-mail addresses:* cibulkova@sirrah.troja.mff.cuni.cz (H. Cibulková), mira@sirrah.troja.mff.cuni.cz (M. Brož), paula.benavidez@ua.es (P.G. Benavidez).

http://dx.doi.org/10.1016/j.icarus.2014.07.016
0019-1035/

be used to fit the *whole* asteroid belt, or it is necessary to use two different scaling laws, e.g. one for the inner belt and second for the outer belt; (3) and we also test a hypothesis, if the main belt is mostly composed of monolithic or rubble-pile objects.

In this paper, we assume that *all* families observed today were created in the last ∼4 Gyr (without any influence of the late heavy bombardment dated approximately 4.2 to 3.85 Gyr ago).[1] We thus focus on an almost steady-state evolution of the main belt, without any significant changes of collisional probabilities or dynamical characteristics. This is different from the work of Bottke et al. (2005). We must admit here that the assumption of the steady-state evolution could be disputable, since Dell'Oro et al. (2001) showed that the formation of big asteroid families may influence the impact probability.

We model collisions with the statistical code called Boulder (Morbidelli et al., 2009) that we slightly extended to account for six populations of asteroids (Sections 5 and 6). As mentioned above, the Boulder code incorporates the results of the SPH simulations by Durda et al. (2007) for *monolithic* $D_{PB} = 100$ km parent bodies, namely for the masses of the largest remnant and fragment and an overall slope of fragment's SFD. For asteroids larger or smaller than $D_{PB} = 100$ km a scaling is used for sake of simplicity.

Material characteristics definitely have significant influence on mutual collisions (e.g. Michel et al., 2011; Benavidez et al., 2012). Therefore, we also run simulations with *rubble-pile* objects, which are less firm (refer to Section 7). A set of simulations analogous to Durda et al. (2007) for rubble-pile targets with $D_{PB} = 100$ km was computed by Benavidez et al. (2012).

First, we try to explore the parameter space using a simplex algorithm while we keep the scaling law fixed. Considering a large number of free parameters and the stochasticity of the system, we look only for some local minima of $\chi^2$ and we do not expect to find a statistically significant global minimum. Further possible improvements and extensions of our model are discussed in Sections 8 and 9.

## 2. A definition of the six parts of the main belt

We divided the main belt into six parts (sub-populations) according the synthetic orbital elements (the semimajor axis $a$ and the inclination $I$, Fig. 1). Five parts separated by major mean-motion resonances with Jupiter are well-defined — if an asteroid enters a resonance due to the Yarkovsky effect (Bottke et al., 2006), its eccentricity increases and the asteroid becomes a near-Earth object. Consequently, vast majority of large asteroids do not cross the resonances[2] and we do not account for resonance crossing in our model. The sixth part is formed by asteroids with high inclinations, $\sin I_p > 0.34$. This value corresponds approximately to the position of the $\nu_6$ secular resonance.

Namely, the individual parts are defined as follows:

1. inner belt – from $a = 2.1$ to 2.5 AU (i.e. the resonance 3:1);
2. middle belt – from 2.5 to 2.823 AU (5:2);

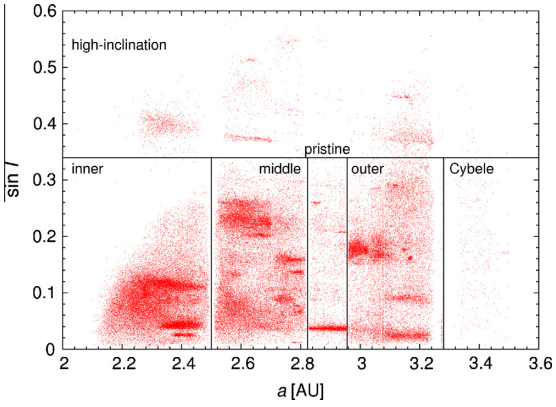


**Fig. 1.** A definition of the six parts of the main asteroids belt according to the semimajor axis a and the inclination I: inner, middle, "pristine", outer, Cybele zone and high-inclination region. The numbers of objects in these parts are the following: 177,756; 186,307; 23,132; 121,186; 1894 and 25,501, respectively.

3. "pristine" belt – from 2.823 to 2.956 AU (7:3; as explained in Brož et al. (2013));
4. outer belt – from 2.956 to 3.28 AU (2:1);
5. Cybele zone – from 3.3 to 3.51 AU;
6. high-inclination region – $\sin I > 0.34$.

For $a$ and $\sin I$ we preferentially used the proper values from the AstDyS catalog (Asteroids Dynamic Site; Knežević and Milani, 2003).[3] For remaining asteroids, not included in AstDyS, we used osculating orbital elements from the AstOrb catalog (The Asteroid Orbital Elements Database).[4]

More precisely, we used proper values from AstDyS for 403,674 asteroids and osculating values from AstOrb for 132,102 not-yet-numbered (rather small) asteroids, which is a minority. We thus think that mixing of proper and osculating orbital elements cannot affect the respective size–frequency distributions in a significant way. Moreover, if we assign (erroneously) e.g. a high-inclination asteroid to the outer main belt, then it is statistically likely that another asteroid from the outer main belt may be assigned (erroneously) to the high-inclination region, so that overall the SFDs remain almost the same.

## 3. Observed size–frequency distributions

To construct SFDs we used the observational data from the WISE satellite (Masiero et al., 2011)[5] — for 123,306 asteroids. Typical diameter and albedo relative uncertainties are ∼10% and ∼20%, respectively (Mainzer et al., 2011), but since we used a statistical approach ($10^4$ to $10^5$ bodies), this should not present a problem. For asteroids not included there we could exploit the AstOrb catalog (i.e. data from IRAS; Tedesco et al., 2002) — for 451 bodies. For remaining asteroids (412,019), we calculated their diameters according the relation (Bowell et al., 1989)

$$D = 10^{0.5(6.259 - \log p_V) - 0.4H}, \quad (1)$$

where $H$ denotes the absolute magnitude from the AstOrb catalog and $p_V$ the (assumed) geometric albedo. We assigned albedos to asteroids without a known diameter randomly, by a Monte-Carlo method, from the distributions of albedos constructed according

[1] This is an approach different from Brož et al. (2013), where (at most) 5 large ($D_{PB} > 200$ km) catastrophic disruptions were attributed to the LHB. Nevertheless, there was a possibility (at a few-percent level) that all the families were created without the LHB. So our assumptions here do not contradict Brož et al. (2013) and we will indeed discuss a possibility that the number of post-LHB families is lower than our 'nominal' value.

[2] For very small asteroids ($D \lesssim 10$ m) we must be more careful. Nevertheless, if an asteroid is able to cross the resonance between e.g. the pristine and the middle belt (i.e. increasing the population of the middle belt) then another asteroid is able to cross the resonance between the middle and the inner belt (decreasing the population of the middle belt). The crossing of the resonances essentially corresponds to a longer time scale of the dynamical decay, which we shall discuss in Section 8.

[3] http://hamilton.dm.unipi.it/astdys/.

[4] ftp://ftp.lowell.edu/pub/elgb/astorb.html.

[5] http://wise2.ipac.caltech.edu/staff/bauer/NEOWISE_pass1/.

to the WISE data. Differences in albedo distributions can influence the resulting SFDs, therefore for each part of the main belt, we constructed a distribution of albedos separately.

We checked that the WISE distributions of albedos are (within a few percent) in agreement with the distributions found by Tedesco et al. (2005). The (minor) differences can be attributed for example to a substantially larger sample (119,876 asteroids compared to 5983), which includes also a lot of asteroids with smaller sizes ($D \lesssim 10$ km). The resulting observed SFDs are shown in Fig. 2. We can see clearly that the individual SFDs differ significantly in terms of slopes and total numbers of asteroids.

To verify a validity of this method, we perform the following test (for the whole main belt). We assume a known set of diameters. We then assign albedos randomly to the individual diameters according to the distribution of WISE albedos. We calculate the values of the absolute magnitudes $H$ by the inversion of Eq. (1). Now, we try to reconstruct the SFD from $H$ and $p_V$. The new "unknown" values of diameters are computed according to Eq. (1) and for the values of $p_V$ we test three following options: (1) a fixed albedo $p_V = 0.15$; (2) the mean value $p_V = 0.13$ (derived from the distribution of WISE albedos); (3) for $H < 15$ mag we used the known albedos, for other bodies we assigned albedos by the Monte-Carlo method as above. The known SFD and the three reconstructed SFDs are shown in Fig. 3.

The largest uncertainties of the reconstruction are given by the method of assignment of geometric albedos, but we verified that the third method is the best one and that these uncertainties (Fig. 3) are much smaller than the differences between individual SFDs (Fig. 2).

Another possible difficulty, especially for asteroids with diameters $D < 10$ km, is the observational bias. In Fig. 2, we can see that for sizes smaller than some $D_{\mathrm{limit}}$ the total number of asteroids remains constant. We also probably miss same asteroids with $D_{\mathrm{limit}} < D < 10$ km. These objects are less bright than the reach of current surveys: LINEAR (Stuart, 2001), Catalina,[6] Spacewatch (Bottke et al., 2002), or Pan-STARRS (Hodapp et al., 2004). Nevertheless, for $D > 10$ km we do not need to perform debiasing and neither for smaller asteroids we do not account for the bias, because the range of diameters $D$ where we fit out model is limited (see Table 4).

## 4. Collisional probabilities and impact velocities

To model the collisional evolution of the main belt by the Boulder code we need to know the intrinsic probabilities $p_i$ of collisions between individual parts and the mutual impact velocities $v_{\mathrm{imp}}$. The values of $p_i$ and $v_{\mathrm{imp}}$ were computed by the code written by W.F. Bottke (Bottke and Greenberg, 1993; Greenberg, 1982). For this calculation, we used only the osculating elements from the AstOrb catalog.

We calculated $p_i$'s and $v_{\mathrm{imp}}$'s between each pair of asteroids of different populations. We used first 1000 asteroids from each population (first according to the catalog nomenclature). We checked that this selection does not significantly influence the result. We constructed the distributions of eccentricities and inclinations of first 1000 objects from each region and we verified that they approximately correspond with the distributions for the whole population. We also tried a different selection criterion (last 1000 orbits), but this changes neither $p_i$ nor $v_{\mathrm{imp}}$ values substantially.

From these sets of $p_i$'s and $v_{\mathrm{imp}}$'s, we computed the mean values $\overline{p_i}$ and $\overline{v}_{\mathrm{imp}}$ (for $v_{\mathrm{imp}}$ only if corresponding $p_i \neq 0$). We checked that the distributions are relatively close to the Gauss distribution and the computations of the mean values are reasonable.

We found out that the individual $p_i$ and $v_{\mathrm{imp}}$ differ significantly (values from $0.35 \times 10^{-18}$ to $11.98 \times 10^{-18}$ km$^{-2}$ yr$^{-1}$ and from 2.22 to 10.09 km s$^{-1}$) — see Table 1. The collision probability decreases with an increasing difference between semimajor axis of two asteroids (the lowest value is for the interaction between the inner belt and the Cybele zone, while the highest for the interactions inside the inner belt). The highest impact velocities are for interactions between the high-inclination region and any other population.

The uncertainties of $\overline{p_i}$ are of the order $0.1 \times 10^{-18}$ km$^{-2}$ yr$^{-1}$ and for $\overline{v}_{\mathrm{imp}}$ about 0.1 km s$^{-1}$. Values computed by Dahlgren (1998), $p_i = 3.1 \times 10^{-18}$ km$^{-2}$ yr$^{-1}$ and $v_{\mathrm{imp}} = 5.28$ km s$^{-1}$ (mean values for the whole main belt), are in accordance with our results as well as values computed by Dell'Oro and Paolicchi (1998) — from 3.3 to $3.5 \times 10^{-18}$ km$^{-2}$ yr$^{-1}$ (depending on assumptions for orbital angles distributions). However, it seems to be clear that considering only a single value of $p_i$ and $v_{\mathrm{imp}}$ for the *whole* main belt would result in a systematic error of the model.

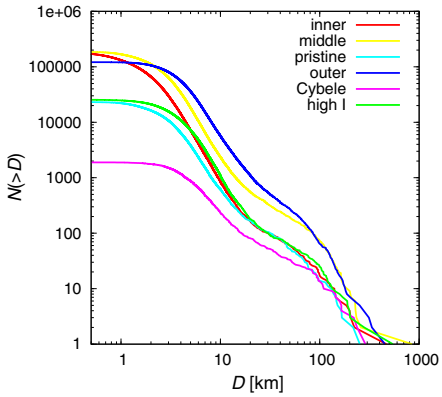


**Fig. 2.** The observed cumulative size–frequency distributions $N(>D)$ of the six parts of the main belt. We used the observational data from the WISE satellite (Masiero et al., 2011) and the AstOrb catalog for their construction. For asteroids which have no albedos in the WISE database, we assigned albedos by a Monte Carlo method from the distribution of WISE albedos.

## 5. A construction of the model

In this section, we are going to describe free and fixed input parameters of our model, the principle how we explore the parameter space and we also briefly describe the Boulder code.

The initial SFDs of the six parts of the main belt are described by 36 free parameters — six for every part: $q_a$, $q_b$, $q_c$, $d_1$, $d_2$ and $n_{\mathrm{norm}}$. Parameter $q_a$ denotes the slope of the SFD for asteroids with diameters $D > d_1$, $q_b$ the slope between $d_1$ and $d_2$, $q_c$ the slope for $D < d_2$ (in other words, $d_1$ and $d_2$ are the diameters separating different power laws) and $n_{\mathrm{norm}}$ is the normalization of the SFD at $d_1$, i.e. the number of asteroids with $D > d_1$ (see also Table 4).

We must also "manually" add biggest asteroids, which likely stay untouched from their formation, to the input SFDs: (4) Vesta with a diameter 468.3 km (according to AstOrb) in the inner belt, (1) Ceres with a diameter 848.4 km (AstOrb) in the middle belt, and (2) Pallas with a diameter 544 km (Masiero et al., 2011) in the high-inclination region. These asteroids are too big and "solitary" in the respective part of the SFD and consequently cannot be described by the slope $q_a$.

The list of fixed input parameters is as follows: collision probabilities and impact velocities from Section 4; the scaling law parameters according to Benz and Asphaug (1999); initial (−4 Gyr) and final (0) time and the time step (10 Myr).

[6] http://www.lpl.arizona.edu/css/.

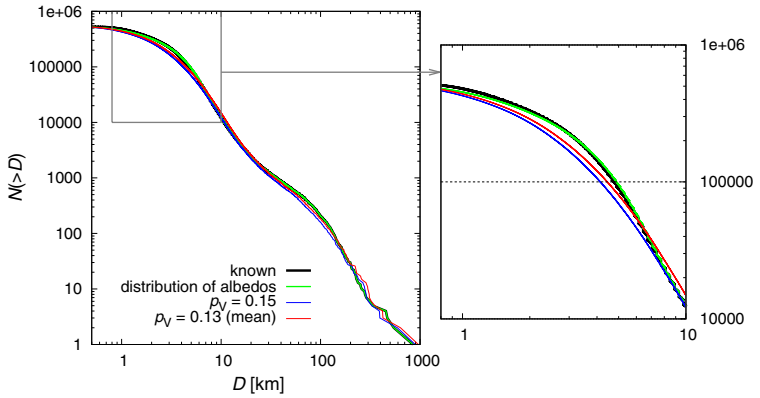


**Fig. 3.** A test of three reconstructions of a "known" size–frequency distribution. Diameters were calculated according to Eq. (1) and for values of $p_V$ we try to use: (1) $p_V = 0.15$ (blue line), (2) $p_V = 0.13$, i.e. the mean value from the distribution of WISE albedos (red line), and (3) we used albedos from WISE for $H < 15$ mag; for other bodies we assigned albedos by a Monte-Carlo method according to the distribution of WISE albedos (green line). We can see that the third method is the best one. (For interpretation of the references to colour in this figure legend, the reader is referred to the web version of this article.)

### 5.1. The scaling law

One of the input parameters is the scaling law described by a parametric relation

$$Q_D^\star = \frac{1}{q_{\text{fact}}}(Q_0 r^a + B\rho r^b), \tag{2}$$

where $r$ denotes the radius in cm, $\rho$ the density in g/cm$^3$, parameters $q_{\text{fact}}$, $Q_0$ and $B$ are the normalization parameters, $a$ and $b$ characterize the slope of the corresponding power law. $Q_D^\star$ is the specific impact energy required to disperse half of the total mass of a target. A scaling law which is often used is that of Benz and Asphaug (1999) (Fig. 4), which was derived on the basis of SPH simulations. Parameters in Eq. (2), corresponding to Benz and Asphaug (1999), are listed in Table 2.

In our simulations, we used three different scaling laws, one for monolithic bodies and two for rubble-pile bodies (to be studied in Section 7). Densities we assumed are within the ranges reported by Carry (2012) for major taxonomical classes (C-complex 1.3 to 2.9 g/cm$^3$; S-complex 2 to 4 g/cm$^3$; for X-types the interval is wide; see Fig. 7 or Table 3 therein).

### 5.2. A definition of the $\chi^2$ metric

To measure a match between our simulations and the observations we calculate $\chi^2$ prescribed by the relation

$$\chi^2 = \sum_{i=1}^{n} \frac{(\text{syn}_i - \text{obs}_i)^2}{\sigma_i^2}, \tag{3}$$

where $\text{syn}_i$ denotes the synthetic data (i.e. results from Boulder simulations) and $\text{obs}_i$ denotes the observed data, $\sigma_i$ is the uncertainty of the corresponding $\text{obs}_i$. The quantities $\text{syn}_i$ and $\text{obs}_i$ are namely the cumulative SFDs $N(>D)$ or the numbers of families $N_{\text{families}}$. More exactly, we calculate $\chi^2_{\text{sfd}}$ for the 96 points in the cumulative SFDs of the six populations (we verified that this particular choice does not influence our results) and we add $\chi^2_{\text{fam}}$ for the numbers of families in these populations.[7]

To minimize $\chi^2$ we use a simplex numerical method (Press et al., 1992). Another approach we could use is a genetic algorithm which is not-so-prone to "fall" into a local minimum as simplex.

[7] We should mention that more sophisticated techniques of assessing the goodness-of-fit (based on bi-truncated Pareto distributions and maximum likelihood techniques) exist, as pointed out by Cellino et al. (1991).

**Table 1**
The computed intrinsic collisional probabilities $\overline{p_i}$ and the mutual impact velocities $\overline{v}_{\text{imp}}$ (for $v_{\text{imp}}$ only if $p_i \neq 0$) between objects belonging to the different parts of the main belt. The uncertainties are of the order $0.1 \times 10^{-18}$ km$^{-2}$ yr$^{-1}$ for $\overline{p_i}$ and 0.1 km s$^{-1}$ for $\overline{v}_{\text{imp}}$.

| Interacting populations | $\overline{p_i}$ ($10^{-18}$ km$^{-2}$ yr$^{-1}$) | $\overline{v}_{\text{imp}}$ (km s$^{-1}$) |
|---|---|---|
| Inner–inner | 11.98 | 4.34 |
| Inner–middle | 5.35 | 4.97 |
| Inner–pristine | 2.70 | 3.81 |
| Inner–outer | 1.38 | 4.66 |
| Inner–Cybele | 0.35 | 6.77 |
| Inner–high Inc. | 2.93 | 9.55 |
| Middle–middle | 4.91 | 5.18 |
| Middle–pristine | 4.67 | 3.96 |
| Middle–outer | 2.88 | 4.73 |
| Middle–Cybele | 1.04 | 5.33 |
| Middle–high Inc. | 2.68 | 8.84 |
| Pristine–pristine | 8.97 | 2.22 |
| Pristine–outer | 4.80 | 3.59 |
| Pristine–Cybele | 1.37 | 4.57 |
| Pristine–high Inc. | 2.45 | 7.93 |
| Outer–outer | 3.57 | 4.34 |
| Outer–Cybele | 2.27 | 4.45 |
| Outer–high Inc. | 1.81 | 8.04 |
| Cybele–Cybele | 2.58 | 4.39 |
| Cybele–high Inc. | 0.98 | 7.87 |
| High Inc.–high Inc. | 2.92 | 10.09 |

Nevertheless, we decided to rather explore the parameter space in a more systematic/controlled way and we start the simplex many times with (729) different initial conditions. We thus do not rely on a single local minimum.

The $\chi^2$ prescribed by Eq. (3) is clearly not a "classical" $\chi^2$, but a "pseudo"-$\chi^2$, because we do not have a well-determined $\sigma_i$.[8] Using $\chi^2$ we can only decide, if our model corresponds to the observations within the prescribed uncertainties $\sigma_i$. Specifically, we used $\sigma_i = 10\%$, $\text{obs}_i$ for the SFDs[9] (similarly as Bottke et al. (2005)) and $\sigma_i = \sqrt{\text{obs}_i}$ for the families.

[8] We *cannot* use a usual condition $\chi^2 \approx n$ or the probability function $q(\chi^2|n)$ to asses a statistical significance of the match between the synthetic and observed data.

[9] We prefer to use cumulative values $N(>D)$ instead of differential, even though the bins are not independent of each other. The reason is more-or-less technical: the Boulder code can create new bins (or merge existing bins) in the course of simulation and this would create a numerical artefact in the $\chi^2$ computation.

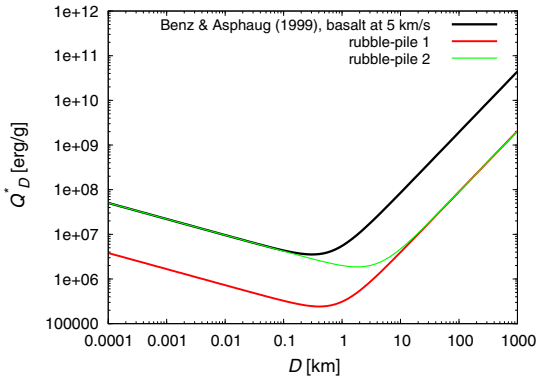


**Fig. 4.** The scaling law for basaltic material at 5 km/s (black line) according to Benz and Asphaug (1999). The red a green lines represent two scaling laws assumed for rubble-pile bodies (1. with less strength than monoliths at all sizes; 2. with less strength than monoliths at large sizes). Their derivations are described in Section 7. (For interpretation of the references to colour in this figure legend, the reader is referred to the web version of this article.)

We are aware that the observed $N_{\mathrm{fam}}$ values do not follow a Poissonian distribution, and that was actually a motivation for us to use a higher value of weighting for families $w_{\mathrm{fam}} = 10$ (we multiply $\chi^2_{\mathrm{fam}}$ by $w_{\mathrm{fam}}$), i.e. we effectively decreased the uncertainty of $N_{\mathrm{fam}}$ in the $\chi^2$ sum. The weighting also emphasizes families, because six values of $\chi^2_{\mathrm{fam}}$ would have only small influence on the total $\chi^2$. Unfortunately, there are still not enough and easily comparable family identifications. Even though there are a number of papers (Parker et al., 2008; Nesvorný, 2012; Masiero et al., 2013; Carruba et al., 2013; Milani et al., 2013), they usually do not discuss parent-body sizes of families.

If a collision between asteroids is not energetic enough (i.e. a cratering event), then only a little of the mass of the target (parent body) is dispersed to the space. In this case, the largest remaining body is called the *largest remnant*. The second largest body, which has a much lower mass, is called the *largest fragment*. If a collision is catastrophic, the first two fragments have comparable masses and in such a case, the largest body is called the largest fragment.

In our simulations, we focused on asteroid families with the diameter of the parent body $D_{\mathrm{PB}} \geq 100$ km and the ratio of the largest remnant/fragment to the parent body $M_{\mathrm{LF}}/M_{\mathrm{PB}} < 0.5$ only (i.e. catastrophic disruptions), though the Boulder code treats also cratering events, of course. For that sample we can be quite sure that the observed sample is complete and not biased. This approach is also consistent with the work of Bottke et al. (2005). The numbers of observed families $N_{\mathrm{fam}}$ in individual parts are taken from Brož et al. (2013), except for the inner belt, where two additional families were found by Walsh et al. (2013) (i.e. three families in total, see Table 3). Our synthetic families then simply correspond to individual collisions between targets and projectiles — which are energetic enough to catastrophically disrupt the target of given minimum size ($D \geqslant 100$ km) — as computed by the Boulder code.

In order to avoid complicated computations of the observational bias we simply limit a range of the diameters $D_{\max}$ to $D_{\min}$ where $\chi^2$ is computed (see Table 4) and we admit a possibility that $\chi^2$ is slightly increased for $D$ approaching $D_{\min}$. We estimated $D_{\max}$ and $D_{\min}$ for each population separately from the observed SFDs shown in Fig. 2.

### 5.3. The Boulder code

A collisional evolution of the size–frequency distributions is modeled with the statistical code called Boulder (Morbidelli et al., 2009), originally developed for studies of the formation of planetary embryos. Our simulations were always running from 0 to 4 Gyr. The Boulder code operates with particles separated to populations, which can differ in values of the intrinsic impact probability $p_i$, mutual velocity $v_{\mathrm{imp}}$, in material characteristics, etc. The populations are then characterized by their distribution of mass. The total mass range is divided to logarithmic bins, whose width and center evolve dynamically. The processes which are realized in every time step are:

1. the total numbers of collisions among all populations and all mass bins are calculated according to the mutual $p_i$'s;
2. the mass of the largest remnant $M_{\mathrm{LR}}$ and the largest fragment $M_{\mathrm{LF}}$ and the slope $q$ of the SFD of fragments are determined for each collision;
3. the largest remnant and all fragments are distributed to the mass bins of the respective population;
4. it is also possible to prescribe a statistical decay of the populations by dynamical processes;
5. finally, the mass bins are redefined in order to have an optimal resolution and an appropriate next time step $\Delta t$ is chosen.

The relations for $M_{\mathrm{LR}}$, $M_{\mathrm{LF}}$ and $q$, derived from the works of Benz and Asphaug (1999) and Durda et al. (2007), are

$$M_{\mathrm{LR}} = \left[-\frac{1}{2}\left(\frac{Q}{Q^\star_D} - 1\right) + \frac{1}{2}\right] M_{\mathrm{tot}} \quad \text{for } Q < Q^\star_D, \tag{4}$$

$$M_{\mathrm{LR}} = \left[-0.35\left(\frac{Q}{Q^\star_D} - 1\right) + \frac{1}{2}\right] M_{\mathrm{tot}} \quad \text{for } Q > Q^\star_D, \tag{5}$$

$$M_{\mathrm{LF}} = 8 \times 10^{-3}\left[\frac{Q}{Q^\star_D}\exp\left(-\left(\frac{Q}{4Q^\star_D}\right)^2\right)\right] M_{\mathrm{tot}}, \tag{6}$$

$$q = -10 + 7\left(\frac{Q}{Q^\star_D}\right)^{0.4}\exp\left(-\frac{Q}{7Q^\star_D}\right), \tag{7}$$

where $M_{\mathrm{tot}}$ denotes the sum of the masses of target and of projectile, $Q^\star_D$ the strength of the asteroid and $Q$ the specific kinetic energy of the projectile

**Table 2**
Parameters of the scaling law according to Benz and Asphaug (1999) (see Eq. (2)). Parameters $q_{\mathrm{fact}}$, $Q_0$ and $B$ are the normalization parameters, $a$ and $b$ characterize the slope of the corresponding power law. The procedure how we obtained the parameters for rubble-pile bodies is described in Section 7.

| | $\rho$ (g/cm$^3$) | $Q_0$ (erg/g) | $a$ | $B$ (erg/g) | $b$ | $q_{\mathrm{fact}}$ |
|---|---|---|---|---|---|---|
| Basalt | 3.0 | $9 \times 10^7$ | −0.36 | 0.5 | 1.36 | 1.0 |
| Rubble-pile 1 | 1.84 | $9 \times 10^7$ | −0.36 | 0.5 | 1.36 | 13.2 |
| Rubble-pile 2 | 1.84 | $118.8 \times 10^7$ | −0.36 | 0.5 | 1.36 | 13.2 |

**Table 3**
The list of asteroid families in individual parts of the main belt according to Brož et al. (2013) and Walsh et al. (2013). Only families with the diameter of the parent body $D_{\mathrm{PB}} > 100$ km and the ratio of the largest remnant/fragment to the parent body $M_{\mathrm{LF}}/M_{\mathrm{PB}} < 0.5$ are listed.

| Belt | $N_{\mathrm{fam}}$ | Families | | |
|---|---|---|---|---|
| Inner | 3 | Erigone | Eulalia | Polana |
| Middle | 8 | Maria | Padua | Misa |
| | | Dora | Merxia | Teutonia |
| | | Gefion | Hoffmeister | |
| Pristine | 2 | Koronis | Fringilla | |
| Outer | 6 | Themis | Meliboea | Eos |
| | | Ursula | Veritas | Lixiaohua |
| Cybele | 0 | | | |
| High Inc. | 1 | Alauda | | |

$$Q = \frac{\frac{1}{2} M_{\text{projectile}} v_{\text{imp}}^2}{M_{\text{tot}}}. \quad (8)$$

The disruptions of large bodies have only a small probability during one time step $\Delta t$. In such situations the Boulder uses a pseudo-random-number generator. The processes thus become stochastic and for the same set of initial conditions we may obtain different results, depending on the value of the random seed (Press et al., 1992).

The Boulder code also includes additional "invisible" bins of the SFD (containing the smallest bodies) which should somewhat prevent artificial "waves" on the SFDs, which could be otherwise created by choosing a fixed minimum size.

## 6. Simulations for monolithic objects

We can expect a different evolution of individual populations as a consequence of their different SFDs, collision probabilities and impact velocities. Therefore, in this section we are going to run simulations with a new collisional model with six populations.

### 6.1. An analysis of an extended parameter space

First, we explored the parameter space on larger scales and started the simplex[10] with many different initial conditions (see Fig. 5). The calculation had 36 free parameters, as explained above. To reduce the total computational time, we change the same parameter in each part of the main belt with every initialisation of the simplex. For example, we increase all parameters $q_{a1}$, $q_{a2}$, $q_{a3}$, $q_{a4}$, $q_{a5}$, $q_{a6}$ together and then we search for a neighboring local minimum with the simplex which has all 36 parameters free — we call this one cycle. In total, we run $3^6 = 729$ cycles (i.e. initialisations of the simplex), for each parameter we examined 3 values (within the ranges from Table 4). The maximum permitted number of iterations of the simplex was 300 in one cycle (and we verified that this is sufficient to find a $\chi^2$ value which is already close to a local minimum). In total, we run 218,700 simulations of the collisional evolution of the main belt.

The argument which would (partly) justify simultaneous changes of all parameters in the 6 parts of the main belt is that we use the same scaling law for each of them, therefore we can expect a similar behavior in individual belts and it then seems logical to choose initial conditions (SFDs) simultaneously.

The input parameters are summarized in Table 4. The mid-in-the-range values were derived "manually" after several preliminary simulations of collisional evolution (without simplex or $\chi^2$ calculations). The changes of parameters between cycles and the steps of simplex within one cycle are listed in Table 5.

The minimum value of $\chi^2$, which we obtained, is $\chi^2 = 562$, but we found many other values, that are statistically equivalent (see Fig. 6 as an example). Therefore, we did not find a statistically significant global minimum. The parameters $q_{b1-b6}$ seem to be well-determined within the parameter space, parameters $q_{a1-a6}$, $d_{11-6}$, $d_{21-6}$ and $n_{\text{norm}\,1-6}$ are slightly less constrained. For the remaining parameters $q_{c1-c6}$ we essentially cannot determine the best values. This is caused by the fact that the 'tail' of the SFD is created easily during disruptions of larger asteroids, so that the initial conditions essentially do not matter. The influence of the initial conditions at the smallest sizes ($D < d_2$) on the final SFDs was carefully checked. As one can see e.g. from the dependence $\chi^2(q_{c1})$, i.e. the resulting $\chi^2$ values as a function of the initial slope of the tail, the outcome is essentially not dependent on the tail slope, but rather on other free parameters of our model.

[10] The simplex as well as $\chi^2$ calculation is not a direct part of the Boulder code.

The differences between simulated and observed SFDs and numbers of families for individual populations corresponding to $\chi^2 = 562$ are shown in Figs. 7 and 8. We can see that the largest differences are for the inner and outer belt. Note that it is *not* easy to improve these results, e.g. by increasing the normalization $n_{\text{norm}4}$ of the outer belt, because this would affect all of the remaining populations too.

From Fig. 7, we can also assess the influence of the choice of $D_{\min}$ and $D_{\max}$ values on the resulting $\chi^2$ — for example, an increase of $D_{\min}$ would mean that the $\chi^2$ will be lower (because we would drop several points of comparison this way). However, as this happens in all main belt parts (simultaneously), it cannot change our results significantly. We ran one complete set of simulations with $D_{\min} = 15$ km (i.e. with $q_c$ unconstrained) to confirm it and we found out that the resulting SFDs, at both larger and smaller sizes than $D_{\min}$, are not significantly different from the previous ones.

The parameters of the initial SFDs for the minimal $\chi^2$ are summarized in Table 6. Comparing with Table 4, the best initial slopes $q_{a1-6}$ and $q_{c1-6}$ are both significantly steeper than the mid-in-the-range values (from Table 4) and they exceed the value −3.5 derived by Dohnanyi. We can also see that the SFD of the Cybele zone is significantly flatter than the SFDs of the other populations and is more affected by observational biases (incompleteness) which actually corresponds to our choice of (relatively large) $D_{\min} = 6$ km.

Another approach to the initial conditions we tested is the following: we generated a completely *random* set of 729 initial conditions — generated within the ranges simulated previously — and without simultaneous (i.e. with uncorrelated) changes in the 6 parts of the main belt. We then started the simplex algorithms again, i.e. we computed 729 initial conditions for the simplex ×300 iterations = 218,700 collisional models in total. Results are very similar to the previous ones, with the best $\chi^2 = 544$, which is statistically equivalent to 562, reported above. In Fig. 6, we compare the dependence of the $\chi^2$ on the parameter $q_{b2}$ for simultaneous (correlated) changes of parameters and for the randomized (uncorrelated) sets of initial parameters. Both results are equivalent in terms of residuals and we can conclude that there is no significantly better local minimum on the interval of parameters we studied.

To test the influence of the choice of $w_{\text{fam}}$, we ran simulation with $w_{\text{fam}} = 0$. The resulting SFDs for monoliths were similar (i.e. exhibiting the same problems) and $\chi^2_{\text{sfd}} = 612$ (among ≈100,000 simulations) remained high. We thus think that the choice of $w_{\text{fam}}$ is not critical. While this seems like the families do not determine the result at all, we treat this as an indication that the numbers of families and SFDs are consistent.

### 6.2. A detailed analysis of the parameters space

We also tried to explore the parameter space in detail — with smaller changes of input parameters between cycles and also smaller steps of the simplex. The best $\chi^2$ which we found is however statistically equivalent to the previous value and we did not obtain a significant improvement of the SFDs. Parameters are not well-constrained in this limited parameter space, because the simulations were performed in a surroundings of a local minimum and the simplex was mostly contracting. An even more-detailed exploration of the parameter space thus would not lead to any improvement and we decided to proceed with a model for rubble-pile asteroids.

## 7. Simulations for rubble-pile objects

The material characteristics of asteroids can significantly influence their mutual collisions. We can modify the Boulder code for

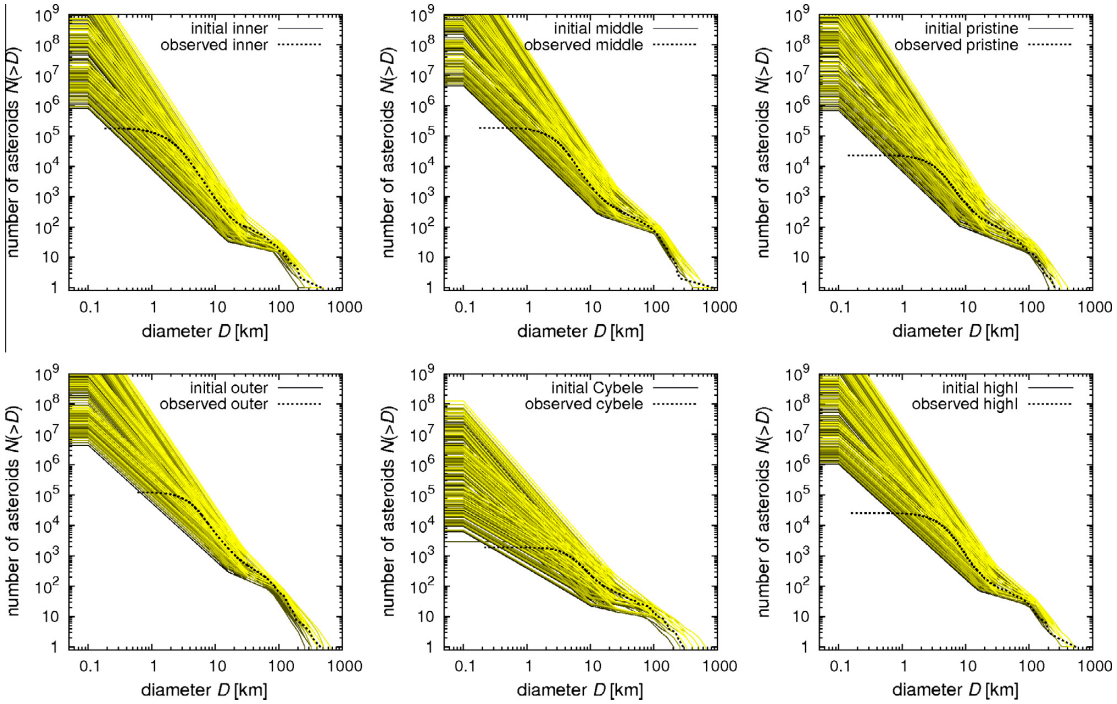


**Fig. 5.** A set of 729 synthetic size–frequency distributions (for six parts of the main belt), which served as starting points for the simplex algorithm and subsequent simulations of collisional evolution. Thin lines (with various colors) denote the synthetic SFDs, while the thick lines corresponds to the observed SFDs. Note that we tested quite a large range of possible initial conditions. The number of simplex steps was limited to 300 because the convergence to a local minimum is difficult due to the stochasticity of the collisional evolution. The total number of collisional simulations we ran was thus $729 \times 300 = 218,700$. (For interpretation of the references to colour in this figure legend, the reader is referred to the web version of this article.)

**Table 4**
The ranges of input parameters describing the size–frequency distributions (SFDs) of the six parts of the main belt: $q_a$ denotes the slope of the SFD for asteroids with diameters $D > d_1$, $q_b$ the slope between $d_1$ and $d_2$, $q_c$ the slope for $D < d_2$ and $n_{norm}$ is the normalization of the SFD at $d_1$. $N_{fam}$ denotes the number of observed families and $D_{max}$ and $D_{min}$ the range of diameters in the SFD, where the $\chi^2$ is calculated.

| Population | $d_1$ (km) | $d_2$ (km) | $q_a$ | $q_b$ | $q_c$ | $n_{norm}$ | $N_{fam}$ | $D_{max}$ (km) | $D_{min}$ (km) |
|---|---|---|---|---|---|---|---|---|---|
| Inner | 75 to 105 | 14 to 26 | −3.6 to −4.2 | −1.5 to −2.7 | −3.0 to −4.2 | 14 to 26 | 3 | 250 | 3 |
| Middle | 90 to 120 | 12 to 24 | −4.0 to −4.6 | −1.7 to −2.9 | −3.0 to −4.2 | 60 to 90 | 8 | 250 | 3 |
| Pristine | 85 to 115 | 7 to 19 | −3.3 to −3.9 | −1.8 to −3.0 | −3.0 to −4.2 | 15 to 27 | 2 | 250 | 5 |
| Outer | 65 to 95 | 14 to 26 | −3.4 to −4.0 | −1.9 to −3.1 | −2.9 to −4.1 | 75 to 105 | 6 | 250 | 5 |
| Cybele | 65 to 95 | 9 to 21 | −2.2 to −2.8 | −1.4 to −2.6 | −2.2 to −3.4 | 11 to 23 | 0 | 250 | 6 |
| High-inclination | 85 to 115 | 14 to 26 | −3.6 to −4.2 | −1.6 to −2.8 | −2.9 to −4.1 | 24 to 36 | 1 | 250 | 5 |

rubble-pile bodies on the basis of Benavidez et al. (2012) work, who ran a set of SPH simulation for rubble-pile $D_{PB} = 100$ km parent bodies. We used data from their Fig. 8, namely diameters of fragments inferred for simulations with various projectile diameters and impact velocities.

### 7.1. Modifications of the Boulder code for rubble-pile bodies

We need to modify the parameters of the scaling law first. We were partly inspired by the shape of scaling laws presented in Levison et al. (2009) for icy bodies (Fig. 3 therein). The modified versions used by these authors are all scaled-down by a factor (i.e. $q_{fact}$ in our notation). Thus, the only two parameters we changed are $q_{fact}$ and density. For the density of asteroids, we used $\rho = 1.84\ \mathrm{g\,cm^{-3}}$ as Benavidez et al. (2012). We determined the specific impact energy $Q^*_D$ required to disperse half of the total mass of a $D = 100$ km rubble-pile target from the dependence of the mass of the largest remnant $M_{LR}$ as a function of the kinetic energy of projectile $Q$ (see Fig. 9). $Q^*_D$ is then equal to $Q$ corresponding to $M_{LR}/M_{target} = 0.5$. So the result is $Q^*_D = (9 \pm 1) \times 10^7\ \mathrm{erg\,g^{-1}}$ and the corresponding parameter $q_{fact}$ in the scaling law is then $13.2 \pm 1.5$ (calculated according to Eq. (2) with $\rho = 1.84\ \mathrm{g\,cm^{-3}}$, $r = 5 \times 10^6$ cm, parameters $Q_0$, $a$, $B$ and $b$ remain same as for the monolithic bodies). The scaling law for rubble-pile bodies was already shown graphically in Fig. 4 (red line).

We must also derive new dependencies of the slope $q(Q)$ of the fragments' SFD and for the mass of the largest fragment $M_{LF}(Q)$ on

**Table 5**
The changes of input parameters between cycles, and steps of the simplex within one cycle. $d_1$, $d_2$, $q_a$, $q_b$, $q_c$ and $n_{norm}$ denote the same parameters as in Table 4. For the middle and outer belt, which are more populous, we used $\Delta n_{norm} = 15$ and $\delta n_{norm} = 5$.

| | $d_1$ (km) | $d_2$ (km) | $q_a$ | $q_b$ | $q_c$ | $n_{norm}$ |
|---|---|---|---|---|---|---|
| Cycles | ±15 | ±6 | ±0.3 | ±0.6 | ±0.6 | ±6; 15 |
| Steps | 5 | 2 | 0.1 | 0.2 | 0.2 | 2; 5 |

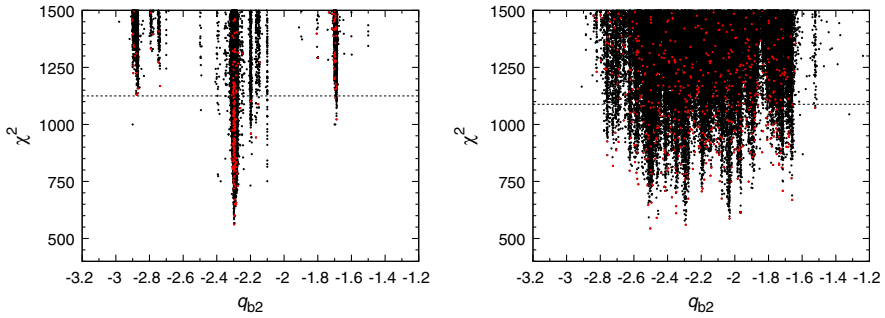


**Fig. 6.** The values of $\chi^2$ for all simulations of collisional evolution as a function of the parameter $q_{b2}$ (i.e. the slope of the SFD of the middle belt for asteroids with diameters $D < d_1$ and $D > d_2$). Black points display all initial conditions of the collisional models (within the ranges of the figure), red points display the initial conditions for which simplex converged to a local minimum (i.e. 729 points in total, but less within the ranges of the figure). The dotted line is a value twice larger than the best $\chi^2$. Values below this line we consider statistically equivalent. Left: simultaneous (correlated) changes of parameters in individual parts of the main belt. Right: randomized (uncorrelated) set of initial parameters (as described in the text). (For interpretation of the references to colour in this figure legend, the reader is referred to the web version of this article.)

the specific energy $Q$ of the impact. The cumulative SFDs of the fragments cannot be always described with only one single slope. We thus divided the fragments according to their diameters to small ($D < 10$ km) and large ($D > 10$ km) and we determined two slopes. Then we calculated the mean value and we used the differences between the two values as error bars (see Fig. 10).

For some of the SPH simulations outcomes it can be difficult to determine the largest fragment, in other words, to distinguish a catastrophic disruption from a cratering event, as explained in Section 5.2. The error bars in Fig. 11 correspond to the points, which we would get if we choose the other of the two above-mentioned possibilities.

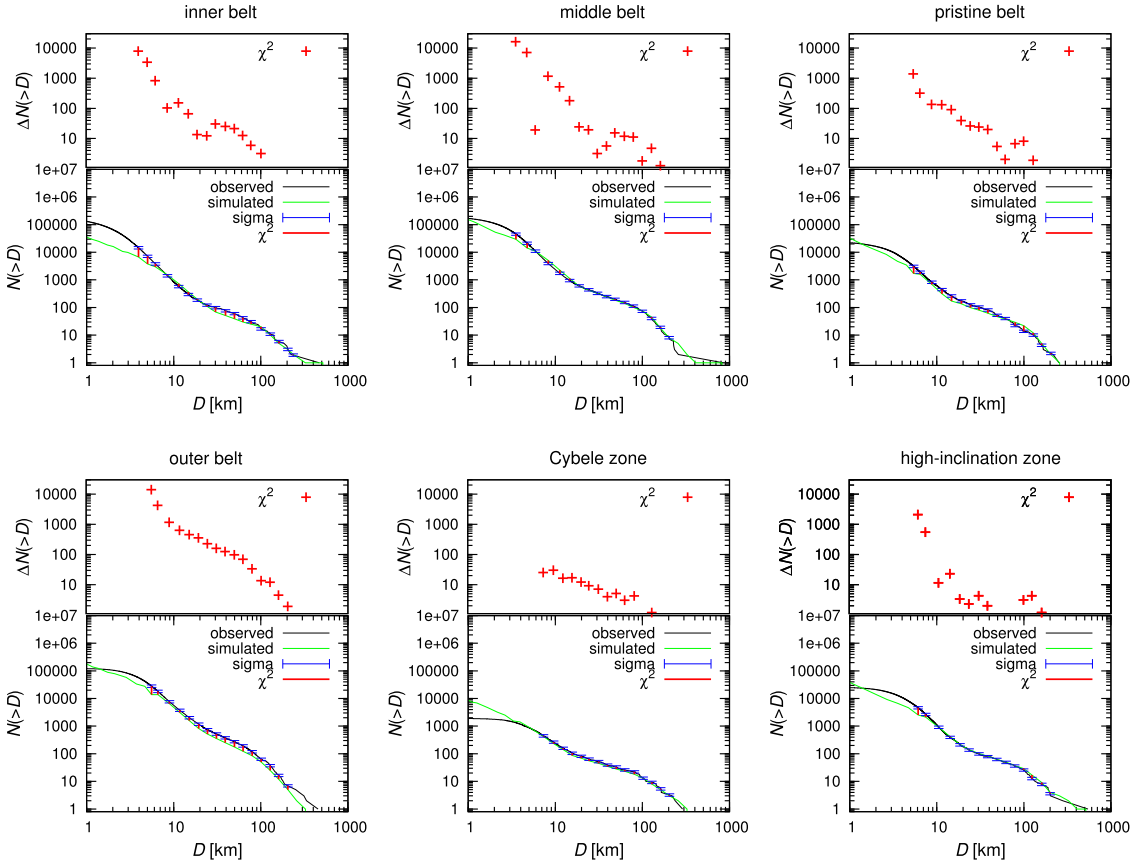


**Fig. 7.** The observed (black line) and simulated (green line) SFDs and the differences between them for the simulation with $\chi^2 = 562$. Sigma error bars denote the (prescribed) uncertainties of the observed SFDs. This result is for the simulation with monoliths. The largest differences can be seen for the inner and outer belt. (For interpretation of the references to colour in this figure legend, the reader is referred to the web version of this article.)

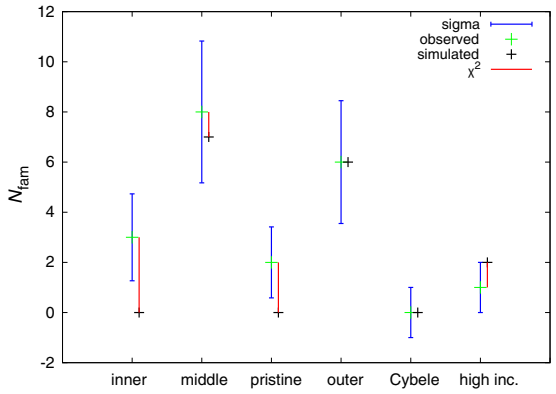


**Fig. 8.** The differences between simulated and observed numbers of families $N_{\text{fam}}$ in individual populations, corresponding to the total $\chi^2 = 562$. Sigma error bars denote the uncertainties of the observed numbers of families. This results is for simulations with monoliths. The simulated and observed numbers of families seem to be consistent within the uncertainties.

The parametric relations we determined for rubble-pile bodies are the following

$$q = -6.3 + 3.16\left(\frac{Q}{Q_D^\star}\right)^{0.01} \exp\left(-0.008\frac{Q}{Q_D^\star}\right), \quad (9)$$

$$M_{\text{LF}} = \frac{0.6}{13\left(\frac{Q}{Q_D^\star}\right)^{-1.2} + 1.5\frac{Q}{Q_D^\star}} M_{\text{tot}}. \quad (10)$$

When we approximate scattered data with functions, we must carefully check their limits. In the case of low-energetic collisions there is one largest remnant and other fragments are much smaller, therefore for decreasing $Q$ we need $M_{\text{LF}}$ to approach zero. The slope $q$ we need to stay negative and not increasing above 0 (that would signify an unphysical power law and zero number of fragments). These conditions are the reasons why our functions do not go through all of the data points (not even within the range of uncertainties). This problem is most pronounced for the dependence of $M_{\text{LF}}(Q)$ for small $Q$ (Fig. 11). Nevertheless, we think that it is more important that the functions fit reasonably the data for high $Q$'s, because highly-energetic collisions produce a lot of fragments and they influence the SFD much more significantly.

### 7.2. A comparison of results for monoliths and rubble-piles with less strength at all sizes

We explored the parameter space in a similar way as for monoliths: with 729 different initial SFDs (i.e. 729 cycles), the maximum permitted number of iterations 300 and 218,700 simulations in total. The changes of parameters between cycles and the steps of the simplex within one cycle are the same as for simulations with monolithic bodies (see Table 5).

**Table 6**
The parameters describing the initial SFDs (for time $t = -4$ Gyr) of the six parts of the main belt for which we obtained the best fit ($\chi^2 = 562$) of the observed SFDs and the number of families. $d_1$, $d_2$, $q_a$, $q_b$, $q_c$ and $n_{\text{norm}}$ denote the same parameters as in Table 4 and are rounded to two decimal places.

| Population | $d_1$ (km) | $d_2$ (km) | $q_a$ | $q_b$ | $q_c$ | $n_{\text{norm}}$ |
|---|---|---|---|---|---|---|
| Inner | 90.07 | 20.03 | −4.20 | −2.10 | −4.20 | 20.03 |
| Middle | 105.07 | 18.03 | −4.60 | −2.30 | −4.20 | 75.07 |
| Pristine | 100.07 | 13.03 | −3.90 | −2.30 | −4.20 | 21.03 |
| Outer | 80.07 | 20.03 | −4.00 | −2.50 | −4.10 | 90.07 |
| Cybele | 80.07 | 15.03 | −2.80 | −2.00 | −3.40 | 17.03 |
| High-inclination | 100.07 | 20.03 | −4.20 | −2.20 | −4.10 | 30.03 |

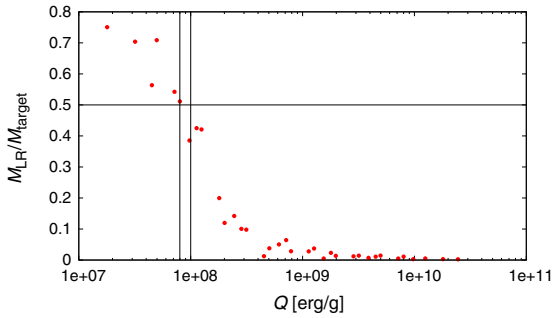


**Fig. 9.** The dependence of the mass of the largest remnant $M_{\text{LR}}$ on the kinetic energy $Q$ of the projectile for rubble-pile bodies. We mark the value $M_{\text{LR}}/M_{\text{target}} = 0.5$ with a horizontal line, according to this value we determine $Q_D^*$. The uncertainties of the determination of $Q_D^*$ are denoted by vertical lines. The result is $Q_D^* = (9 \pm 1) \times 10^7$ erg g$^{-1}$.

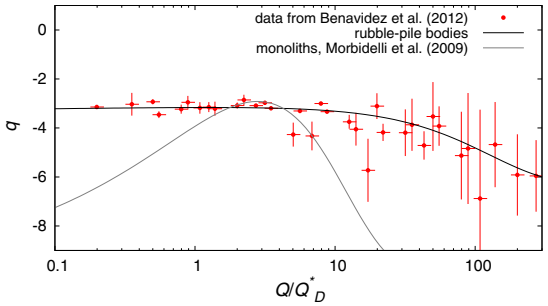


**Fig. 10.** The slope $q$ of the SFD of fragments as a function of the impact energy $Q/Q_D^*$ for the rubble-pile parent bodies with $D_{\text{PB}} = 100$ km. The horizontal axis is in a logarithmic scale. The SFD of fragments is characterized by two slopes (for fragments $D < 10$ km and $D > 10$ km) and we calculated the mean value. The displayed uncertainties of $q$ are the differences between real and mean values. The horizontal error bars are given by the uncertainties of $Q_D^*$. The gray line corresponds to the dependence for monoliths (Morbidelli et al., 2009), which we used in Section 6.

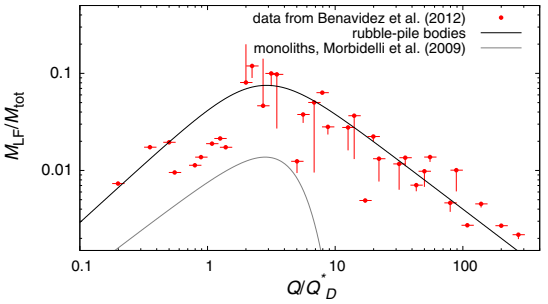


**Fig. 11.** The ratio $M_{\text{LF}}/M_{\text{tot}}$ (the mass of the largest fragment divided by the sum of the mass of target and the mass of projectile) as a function of the impact energy $Q/Q_D^*$ for the rubble-pile parent bodies with the diameter $D_{\text{PB}} = 100$ km. The horizontal axis is in a logarithmic scale. The uncertainties of $M_{\text{LF}}/M_{\text{tot}}$ are caused by a problematic determination of the largest fragment and the largest remnant. The horizontal error bars are given by the uncertainties of $Q_D^*$. The gray line corresponds to the dependence for monoliths (Morbidelli et al., 2009) which we used in Section 6.

The minimum $\chi^2$ which we obtained was 1321. The differences between the simulated and observed SFDs and the numbers of families for individual populations corresponding to $\chi^2 = 1321$ are shown in Figs. 12 and 13. These values are significantly higher than what we obtained for monoliths ($\chi^2 = 562$ at best). Given that the set of initial conditions was quite extensive (refer to Fig. 5), we think that this difference is fundamental and constitutes a major result of our investigation.

It seems that, at least within our collisional model, we can preliminarily conclude that the main belt does not contain *only* rubble-pile bodies, because otherwise the corresponding fit would not be that worse than for monoliths (see Figs. 7 and 8 for a comparison).

It would be interesting to run a simulation with two different population of the main belt — monolithic and rubble-pile bodies. Also because Benavidez et al. (2012) concluded that some asteroid families were more likely created by a disruption of a rubble-pile parent body: namely the Meliboea, Erigone, Misa, Agnia, Gefion and Rafita. Such simulation remains to be done.

### 7.3. Simulations for rubble-piles with less strength at large sizes

Large rubble-piles objects can be also assumed to be composed of monolithic blocks with sizes of the order of 100 m. Then, at and below this size, the scaling law $Q_D^\star$ should be a duplicate of the Benz and Asphaug (1999) — see Fig. 4 (green line). We computed a new set of $729 \times 300 = 218{,}700$ collisional simulations with the scaling law modified in this way. The resulting smallest $\chi^2$ is 1393, which should be compared to the previous result $\chi^2 = 1321$ — i.e. no statistically significant improvement.

We thus can conclude that this kind of $Q_D^\star$ modification does not lead to an improvement of the model. We think that the collisional evolution and overall shape of the SFDs are more affected by disruptions of large asteroids.

## 8. Improvements and extensions of the model

We think that the match between our collisional model and the observational data as presented in Sections 6 and 7 is not entirely convincing. In this section we thus try to improve the model by the following procedures: (i) we use a longer 'tail' of the SFD (down to $D = 0.01$ km), which is a straightforward modification. Nevertheless, the longer tail means a significant increase of the required CPU time (which is proportional to $N_{\mathrm{bins}}^2$). (ii) We account for the Yarkovsky effect whose time scales for small bodies ($D \lesssim 0.1$ km) are already comparable to the collisional time scales (see Section 8.1). (iii) We do not converge all 36 free parameters at once but we free only 6 of them ($d_1$, $d_2$, $q_{\mathrm{a}}$, $q_{\mathrm{b}}$, $q_{\mathrm{c}}$ and $n_{\mathrm{norm}}$ for one popu-

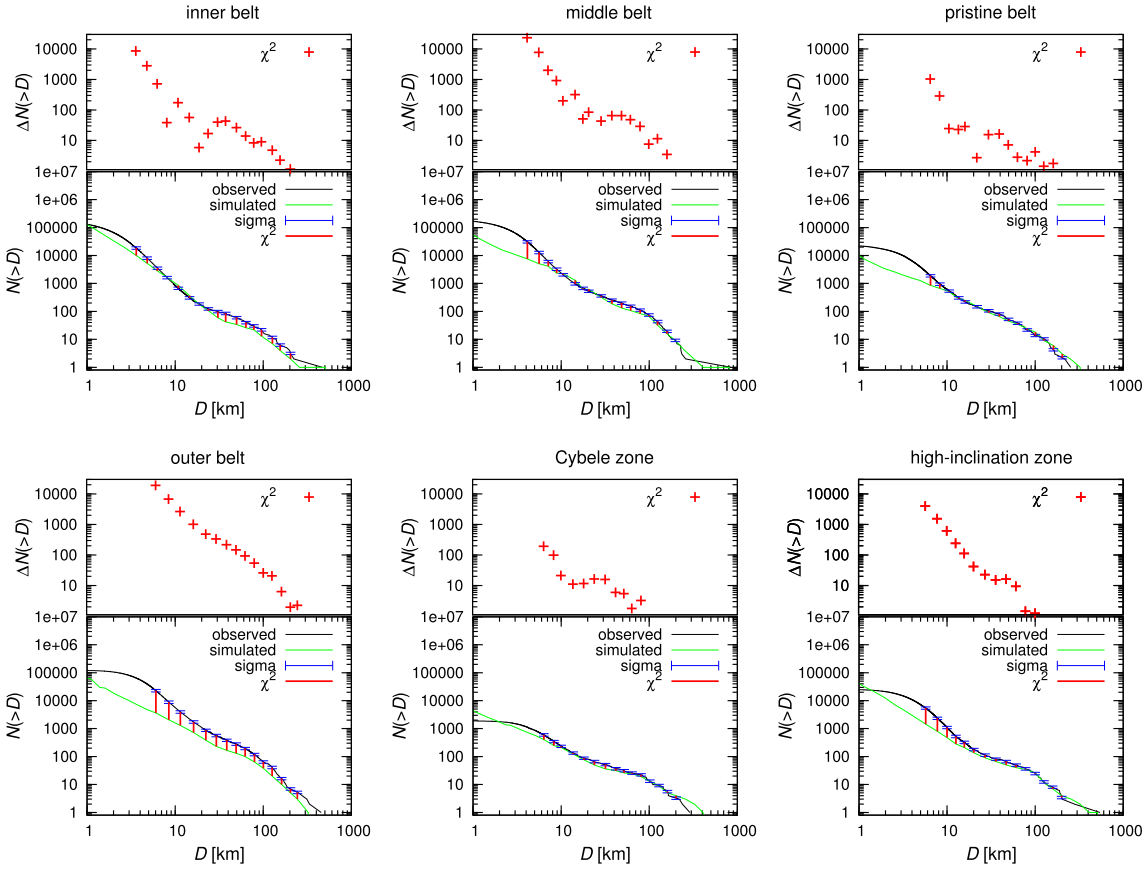


**Fig. 12.** The observed (black line) and simulated (green line) SFDs and the differences between them for the simulation with rubble-piles with total $\chi^2 = 1321$. Sigma error bars denote the adopted uncertainties of the observed SFDs. (For interpretation of the references to colour in this figure legend, the reader is referred to the web version of this article.)

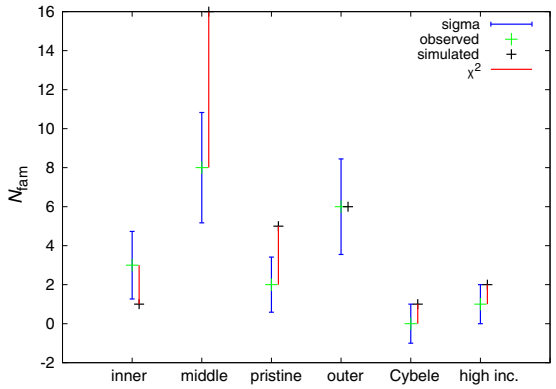


**Fig. 13.** The simulated and the observed numbers of families $N_{\rm fam}$ in individual populations for the simulation with rubble-piles, corresponding to the total $\chi^2 = 1321$. Sigma error bars denote the uncertainties of the observed numbers of families.

lation only) and proceed sequentially with six parts of the main belt (see Section 8.2). (iv) Finally, we try to use a scaling law different from Benz and Asphaug (1999) (see Section 8.3).

### 8.1. Dynamical decay caused by the Yarkovsky effect

In order to improve the Boulder code and use a more complete dynamical model, we try to account for the Yarkovsky effect as follows. We assume that the Yarkovsky effect causes a dynamical decay of the population which can be described by the following relation

$$N(t+\Delta t) = N(t)\exp\left(\frac{\Delta t}{\tau_{\rm YE}}\right), \tag{11}$$

where $N(t)$ denotes the number of bodies at time $t$, $\Delta t$ the time step of the integrator and $\tau_{\rm YE}$ is the characteristic timescale.

We can compute the semimajor-axis drift rate $\mathrm{d}a/\mathrm{d}t$, for both the diurnal and seasonal variants of the Yarkovsky effect, using the theory of Vokrouhlický (1998), Vokrouhlický and Farinella (1999) and the (size-dependent) time scale is then

$$\tau_{\rm YE}(D) = \frac{\Delta a}{\mathrm{d}}\, a/\mathrm{d}t(D), \tag{12}$$

where $\Delta a$ is the range of semimajor axis given by the positions of major mean-motion resonances which are capable to remove objects from the respective populations. It differs for different zones of the main belt, of course (see Table 7).

In the thermal model, we assume the following parameters: the thermal conductivity $K = 0.01\ \mathrm{W\,m^{-1}\,K^{-1}}$ for $D > D_{\rm YE}$, i.e. a transition diameter, and $1.0\ \mathrm{W\,m^{-1}\,K^{-1}}$ for $D \leqslant D_{\rm YE}$. The break in $K(D)$ reflects the rotational properties of small bodies, as seen in Fig. 14 (and Warner et al., 2009): they rotate too fast, above the critical limit of about 11 revolutions/day, to retain low-conductivity regolith on their surfaces. This is also in accord with infrared observations of Delbo' et al. (2007), even though the authors propose a linear relationship between the thermal intertia $\Gamma = \sqrt{K\rho C}$ and size $D$ (their Fig. 6), a step-like function may be also compatible with the data. The thermal capacity was $C = 680\ \mathrm{J\,kg^{-1}\,K^{-1}}$, the infrared emissivity $\epsilon = 0.95$ and the Bond albedo $A_{\rm B} = 0.02$. The latter value of $A_{\rm B}$ corresponds to the geometric albedo $p_V = 0.05$, which is typical for C-complex asteroids (e.g. Masiero et al., 2013), with $A_{\rm B} = p_V q$, where $q$ denotes the phase integral (with a typical value of 0.39; Bowell et al., 1989). If we assume higher $p_V = 0.15$ (typical of S-complex) and $A_{\rm B} = 0.06$, the Yarkovsky dynamical time scale would remain almost the same, because it is driven by the factor $(1 - A_{\rm B})$. Remaining thermal parameters, namely the densities, are summarized in Table 7.

**Table 7**
The parameters of the Yarkovsky-driven decay which are dependent on the zone of the main asteroid belt: $\Delta a$ is half of the zone size (or a typical distance from neighboring strong mean-motion resonances), $\rho$ denotes the (bulk and surface) density assumed for respective bodies.

| Zone | $\Delta a$ AU | $\rho$ kg m$^{-3}$ |
|---|---|---|
| Inner | 0.2 | 2500 |
| Middle | 0.1615 | 2500 |
| Pristine | 0.0665 | 1300 |
| Outer | 0.162 | 1300 |
| Cybele | 0.105 | 1300 |
| High-$I$ | 0.135 | 1300 |

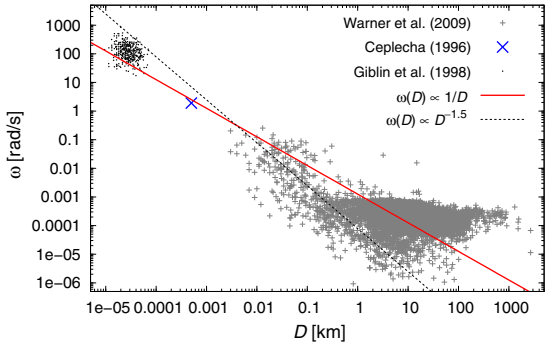


**Fig. 14.** The spin rate $\omega$ vs size $D$ dependence for asteroids (observational data from Warner et al., 2009), the Lost City fireball (Ceplecha, 1996) and fragments in laboratory experiments (Giblin et al., 1998). Two approximations are given: $\omega(D) \propto 1/D$, and $\omega(D) \propto D^{-1.5}$, which better fits the observational data in the size range $D \in (0.01, 1)$ km where the Yarkovsky drift is the most important with respect to the collisional model. Nevertheless, we cannot yet exclude a possibility that the observed $\omega(D)$ distribution is still strongly biased for small $D \lesssim 1$ km.

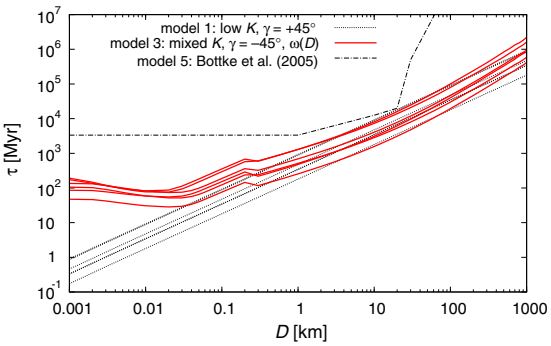


**Fig. 15.** The time scale $\tau_{\rm YE}$ of the Yarkovsky-driven decay (as defined by Eq. (12)) vs size $D$ for three different models (denoted 1, 3 and 5), or in other words, assumptions of the thermal conductivity $K(D)$ and the spin rate $\omega(D)$, which were described in the text. The obliquities $\gamma$ of the spin axes were assumed moderate, $|\gamma| = 45°$. Model 2 is quite similar to 1 and model 4 is similar to 3, so we decided not to plot them in order to prevent many overlapping lines. For each model, we plot six lines corresponding to the six zones of the main belt: inner, middle, 'pristine', outer, Cybele and high inclination. Bottke et al. (2005) time scales were used for the whole main belt (regarded as a single population).

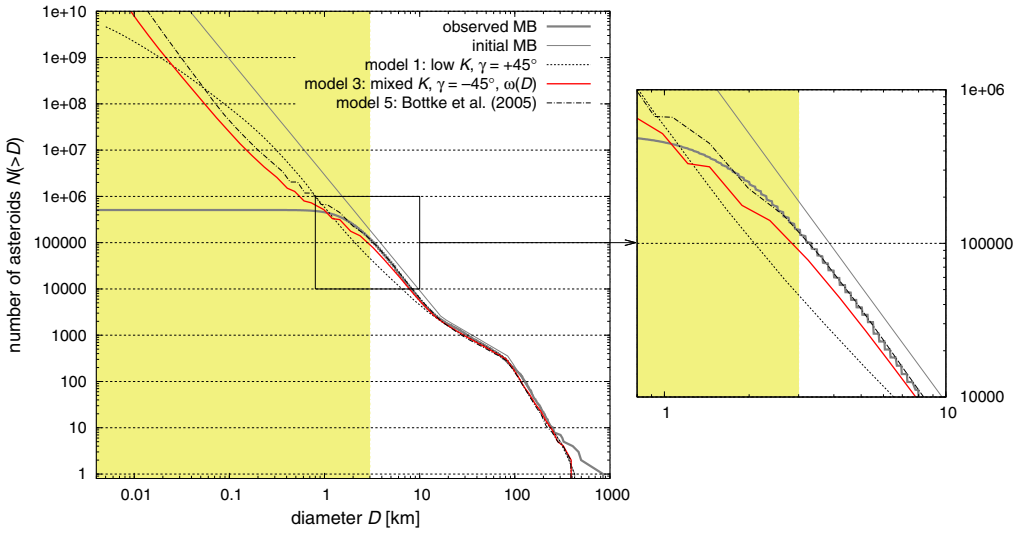


**Fig. 16.** Resulting synthetic size–frequency distributions of the main belt (regarded as a single population) after 4 Gyr of collisional evolution, as computed by the Boulder code. We show results for three different models of the Yarkovsky-driven decay (denoted 1, 3 and 5 in the text). Model 1 (dotted line) is clearly inconsistent with the observed SFD (thick gray line). The shaded region corresponds to the sizes well below the observational completeness.

We tested five different models (assumptions):

1. low thermal conductivity $K = 0.01\ \mathrm{W\,m^{-1}\,K^{-1}}$ only, i.e. $D_{\mathrm{YE}} = 0$ km, fixed rotation period $P = 5$ h;
2. both low/high $K$ with $D_{\mathrm{YE}} = 200$ m, again $P = 5$ h;
3. the same $K(D)$ dependence, but size-dependent spin rate $\omega(D) = \frac{2\pi}{P_0}\frac{D_0}{D}$, $P_0 = 5$ h, $D_0 = 5$ km;
4. $\omega(D) = \frac{2\pi}{P_0}\left(\frac{D}{D_0}\right)^{-1.5}$, $P_0 = 2$ h, $D_0 = 0.2$ km (see Fig. 14);
5. we used Bottke et al. (2005) time scales.

It is important to explain that these spin rate dependencies are not meant to describe bigger asteroids but rather smaller ones ($D \lesssim 1$ km) that comprise the majority of impactors but mostly fall below the detection threshold.

We then computed the Yarkovsky time scales $\tau_{\mathrm{YE}}(D)$ (Fig. 15) and constructed a 'testing' collisional model in order to check the influence of the dynamical decay on the evolution of the main belt SFD. Note that for small sizes $D \lesssim 1$ km, $\tau_{\mathrm{YE}}(D)$ can be even smaller than corresponding collisional time scales $\tau_{\mathrm{col}}(D)$.

Regarding the asteroid families, we use the most straightforward approach: we simply count only families large enough (original $D_{\mathrm{PB}} > 100$ km, $m_{\mathrm{LR}}/m_{\mathrm{PB}} < 0.5$) which *cannot* be completely destroyed by a collisional cascade (Bottke et al., 2005) or by the Yarkovsky drift (Bottke et al., 2001). We verified this statement (implicitly) also in our recent work (Brož et al., 2013) in which the evolution of SFDs for individual synthetic families was studied. At the same time, we use *original* parent-body sizes $D_{\mathrm{PB}}$ of the observed families — inferred by using methods of Durda et al. (2007) or Tanga et al. (1999); as summarized in Brož et al. (2013) — so that we can directly compare them to synthetic families, as output from the Boulder code.

The results of models 1 and 2 above are clearly not consistent with the observed SFD (see Fig. 16). The results of 3, 4 and 5 seem to be equivalent and consistent with observations, however, we cannot distinguish between them. We can thus exclude 'extreme' Yarkovsky drift rates and conclude that only lower or 'reasonable' drift rates provide a reasonable fit to the observed SFD of the main belt.

### 8.2. Subsequent fits for individuals parts of the main belt

In order to improve our 'best' fit from Section 6 (and 7), we ran simplex sequentially six times, with only 6 parameters free in each case, namely $d_1$, $d_2$, $q_{\mathrm{a}}$, $q_{\mathrm{b}}$, $q_{\mathrm{c}}$, $n_{\mathrm{norm}}$ for a given part of the main belt. We included a longer tail ($D_{\mathrm{min}} = 0.01$ km) and the Yarkovsky model discussed above.[11] The number of simplex iterations was always limited to 100.

We shall not be surprised if we obtain a $\chi^2$ value which is (slightly) larger than before because we changed the collisional model and this way we moved *away* from the previously-found local minimum. At the same time, we do not perform that many iterations as before (600 vs. 218,700), so we cannot 'pick-up' the deepest local minima.

For monoliths, we tried to improve the 'best' fit with $\chi^2 = 562$. However, the initial value at the very start of the simplex was $\chi^{2\prime} \simeq 803$ (due to the changes in the collisional model) and the final value after the six subsequent fits $\chi^{2\prime\prime} = 520$. This is only slightly smaller than the previous $\chi^2$ and statistically equivalent ($\chi^{2\prime\prime} \simeq \chi^2$). For rubble-piles, a similar procedure for the $\chi^2 = 1321$ fit lead to the initial $\chi^{2\prime} \simeq 1773$ and the final $\chi^{2\prime\prime} = 1470$. Again, a statistically-equivalent result.

We interpret this as follows: our simplex algorithm naturally selects deep local minima. It seems that the lowest $\chi^2$ (for a given set of initial conditions) can be achieved by a 'lucky' sequence of disruptions of relatively large bodies ($D_{\mathrm{PB}} \gtrsim 100$ km) which results in synthetic SFDs and the numbers of families best matching the observed properties. Of course, this sequence depends on the 'seed' value of the random-number generator.

To conclude, our improvements of the collisional model do not seem significant and the $\chi^2$ values are of the same order. This can be considered as an indication that we should probably use an even more complicated model. (Nevertheless, there is still a significant

[11] This more complicated model runs about 10 times slower, because we have both larger number of bins to account for smaller bodies and a shorter time step to account for their fast dynamical removal. It is thus not easy to run a whole set of simulations from Sections 6 and 7 again.

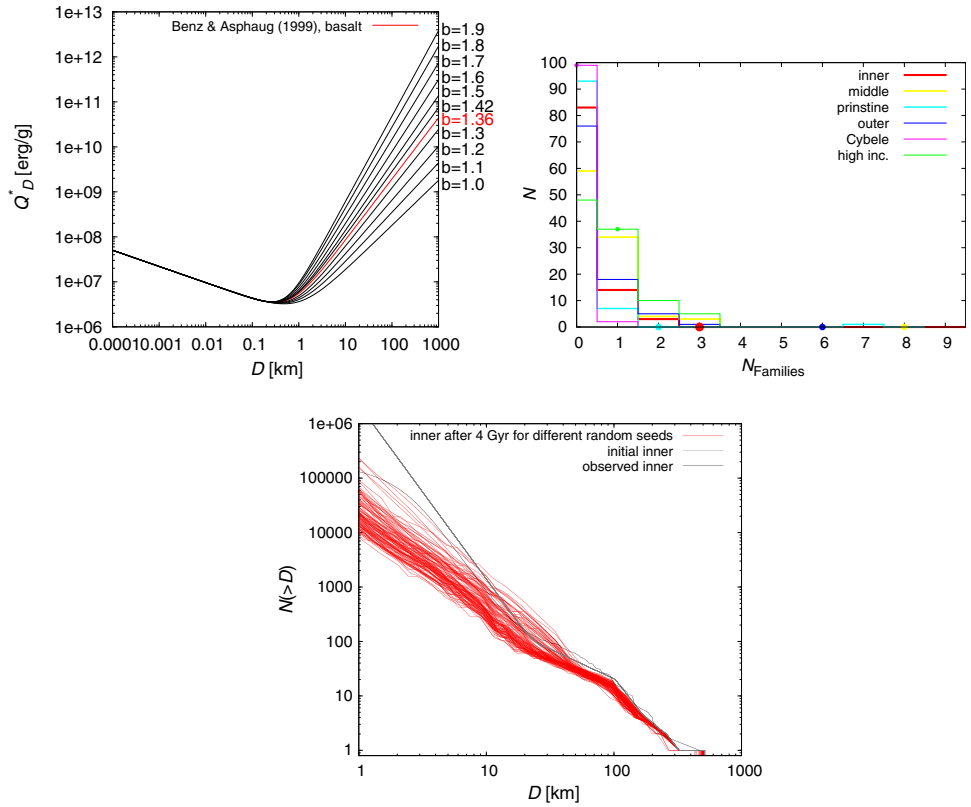


**Fig. 17.** Left: A number of scaling laws with modified strength of large bodies (a similar set as in Bottke et al. (2005)). The red line represents the nominal scaling law of Benz and Asphaug (1999). Middle: histograms representing the number $N$ of simulations (out of 100) a given number of families $N_{\text{families}}$ was created; we assumed the scaling law with an increased strength of large bodies ($b = 1.9$). The observed numbers of families are displayed as filled circles for comparison. Right: the final size–frequency distributions of the inner belt for 100 simulations with different random seeds and for the scaling law with a decreased strength of large bodies ($b = 1.0$). Neither of these two mentioned simulations is consistent with the observations (their $\chi^2$ would be clearly much larger than the best fit from Section 6). (For interpretation of the references to colour in this figure legend, the reader is referred to the web version of this article.)

difference between monoliths and rubble-piles and the assumption of monolithic structure matches the observations better.)

### 8.3. Simulations with various scaling laws

So far we used the scaling law of Benz and Asphaug (1999) for all simulations. In this section, we are going to test different scaling laws. Similarly as Bottke et al. (2005), we changed the specific impact energy $Q^*_D$ of asteroids with $D > 200$ m (see Fig. 17, left). For each scaling law we ran 100 simulations of the collisional evolution with different random seeds. The initial parameters of SFDs are fixed and correspond to the best-fit initial parameters found in Section 6.

In order to decide which scaling laws are suitable, we can simply compare the resulting synthetic SFDs and the numbers of families to the observed ones. It is clear that if we increase the strength of $D \simeq 100$ km bodies by a factor of 10 or more, the number of synthetic families (namely catastrophic disruptions with $D_{\text{PB}} \geqslant 100$ km) is much smaller than the observed number (usually 4 vs 20, see in Fig. 17, middle). On the other hand, if we decrease the strength by a factor of 10, the synthetic SFDs exhibit a significant deficit of small bodies with $D < 10$ km due to a collisional cascade (especially in the inner belt, see Fig. 17, right). Moreover, the number of synthetic families is then significantly larger, of course. The fact that the number of synthetic families is dependent on the scaling law confirm our statement that families are important observational constraints.

These results lead us to the conclusion, that the 'extreme' scaling laws (i.e. much different from Benz and Asphaug, 1999) cannot be used for the main asteroid belt. This result is also in accord with Bottke et al. (2005).

## 9. Conclusions

In this work, we created a new collisional model of the evolution of the main asteroid belt. We divided the main belt into six parts and constructed the size–frequency distribution for each part. The observed SFDs differ significantly in terms of slopes and total numbers of asteroids. We then ran two sets of simulations — for monolithic bodies and for rubble-piles.

In the case of monoliths, there seem to be (relatively minor) discrepancies between the simulated and observed SFDs in individual parts of the main belt, nevertheless, the numbers of families (catastrophic disruptions) correspond within uncertainties. On the other hand, the $\chi^2$ value for rubble-pile bodies is more than twice as large because there are systematic differences between the SFDs and the number of families is substantially larger (usually 30 or more) than the observed one (20 in total). We can thus conclude

that within our collisional model, monolithic asteroids provide a better match to the observed data than rubble-piles, even though we cannot exclude a possibility that a certain part of the population is indeed of rubble-pile structure, of course.

We tried to improve our model by: (i) introducing a longer 'tail' of the SFD[12] (down to $D = 0.01$ km); (ii) incorporating the Yarkovsky effect, i.e. a size-dependent dynamical decay; (iii) running many simulations with different random seeds, in order to find even low-probability scenarios. Neither of these improvements provided a substantially better match in *all* parts of the main belt at once.

However, we can think of several other possible reasons, why the match between our collisional model and the observed SFDs is not perfect:

1. There are indeed different scaling laws for different parts of the main belt. This statement could be supported by the observed distribution of albedo, which is not uniform in the main belt, and by the diverse compositions of asteroids (DeMeo and Carry, 2014). This topic is a natural continuation of our work (and a detailed analysis is postponed to a forthcoming paper).
2. The scaling of the SPH simulations from $D_{\rm PB} = 100$ km by one or even two orders of magnitude is likely problematic. Our work is thus a motivation to study disruptions of both smaller ($D_{\rm PB} \simeq 1$ km) and larger (400 km) targets. Similar sets of SPH simulations as in Durda et al. (2007) and Benavidez et al. (2012) would be very useful for further work.
3. To explain the SFD of the inner belt, namely its 'tail', we would need to assume a recent disruption (during the last ~100 Myr) of a large parent body ($D_{\rm PB} \gtrsim 200$ km). In that case the SFD is temporarily steep — and may be closer to the observed SFD in the particular part of the main belt — but only for a limited period of time which is typically about 200 Myr. After that time, the collisional cascade eliminates enough bodies and consequently the SFD becomes flatter. On the other hand, there must not have occurred a recent large disruption in the middle or the outer belt, otherwise the synthetic SFD is more populous than the observed one. It is not likely, that all such conditions are fulfilled together in our model, in which collisions occur randomly.
4. When we split the main belt into 6 parts, the evolution seems too stochastic (the number of large events in individual part is of the order of 1). It may be even useful to prepare a 'deterministic model', in which large disruptions are *prescribed*, according to the observed families and their ages. Of course, the completeness of the family list and negligible bias are then crucial.
5. Our model does not yet include an YORP-induced fission (Marzari et al., 2011), even though there are indications that these 'additional' disruptions might affect the tail of the SFD if they are frequent enough as stated by Jacobson et al. (2014).
6. We can improve the modeling of the Yarkovsky/YORP effect, e.g. by assuming a more realistic distribution of spin rates (not only the $\omega(D)$ dependence, Fig. 14) and performing an *N*-body simulation of the orbital evolution to get a more accurate estimate of the (exponential) time scale $\tau_{\rm YE}(D)$. It may be difficult to estimate biases in the $\omega(D)$ plot, because the respective dataset is heterogeneous. Luckily, the Gaia spacecraft is expected to provide a large homogeneous database of asteroid spin properties (Mignard et al., 2007).
7. May be, the intrinsic collisional probabilities $p_{\rm i}$ were substantially different (lower) in the past, e.g. before major asteroid families were created (as suggested by Dell'Oro et al. (2001)).
8. Some of the mutual impact velocities $v_{\rm imp}$, especially with high-inclination objects, are substantially larger than the nominal 5 km s$^{-1}$, so the outcomes of these collisions are most-likely different. On the other hand, these collisions are usually of lower probability and the high-inclination region is not that populous, so that this effect has likely a minor contribution only. One should properly account for observational biases acting against discoveries of high-inclination objects, thought (Novaković et al., 2011).
9. Collisions occur not only at the mean impact velocity $v_{\rm imp}$, but there is rather a distribution of velocities. It would be then useful and logical to use a *velocity-dependent* scaling law (Leinhardt and Stewart, 2012; Stewart and Leinhardt, 2009).
10. There might be several large undiscovered families, or in other words, the lists of $D_{\rm PB} \leqslant 100$ km families (Brož et al., 2013, or Masiero et al., 2013) might be strongly biased, because comminution is capable to destroy most of the fragments.[13]
11. Possibly, parent-body sizes $D_{\rm PB}$ of the observed families are systematically underestimated or their mass ratios $M_{\rm LR}/M_{\rm PB}$ of the largest remnant to parent body are offset, even though they were determined by best available methods (Durda et al., 2007; Tanga et al., 1999).

The topics outlined above seem to be good starting points for (a lot of) further work.

## Acknowledgments

The work of M.B. has been supported by the Grant Agency of the Czech Republic (Grant No. 13-01308S) and the Research Programme MSM0021620860 of the Czech Ministry of Education. We thank Alessandro Morbidelli for valuable discussions on the subject and William F. Bottke for a computer code suitable for computations of collisional probabilities. We are also grateful to Alberto Cellino and an anonymous referee for constructive and detailed reviews which helped us to improve the paper.

## References

Benavidez, P.G., Durda, D.D., Enke, B.L., Bottke, W.F., Nesvorný, D., Richardson, D.C., Asphaug, E., Merline, W.J., 2012. A comparison between rubble-pile and monolithic targets in impact simulations: Application to asteroid satellites and family size distributions. Icarus 219, 57–76. http://dx.doi.org/10.1016/j.icarus.2012.01.015.

Benz, W., Asphaug, E., 1999. Catastrophic disruptions revisited. Icarus 142, 5–20. http://dx.doi.org/10.1006/icar.1999.6204.

Bottke, W.F. et al., 2005. The fossilized size distribution of the main asteroid belt. Icarus 175, 111–140. http://dx.doi.org/10.1016/j.icarus.2004.10.026.

Bottke, W.F., Greenberg, R., 1993. Asteroidal collision probabilities. Geophys. Res. Lett. 20, 879–881. http://dx.doi.org/10.1029/92GL02713.

Bottke, W.F., Vokrouhlický, D., Broz, M., Nesvorný, D., Morbidelli, A., 2001. Dynamical spreading of asteroid families by the Yarkovsky effect. Science 294, 1693–1696. http://dx.doi.org/10.1126/science.1066760.

Bottke, W.F., Morbidelli, A., Jedicke, R., Petit, J.-M., Levison, H.F., Michel, P., Metcalfe, T.S., 2002. Debiased orbital and absolute magnitude distribution of the near-Earth objects. Icarus 156, 399–433. http://dx.doi.org/10.1006/icar.2001.6788.

Bottke Jr, W.F., Vokrouhlický, D., Rubincam, D.P., Nesvorný, D., 2006. The Yarkovsky and Yorp effects: Implications for asteroid dynamics. Annu. Rev. Earth Planet. Sci. 34, 157–191. http://dx.doi.org/10.1146/annurev.earth.34.031405.125154.

Bowell, E., Hapke, B., Domingue, D., Lumme, K., Peltoniemi, J., Harris, A.W., 1989. Application of photometric models to asteroids. In: Binzel, R.P., Gehrels, T.,

[12] Plus the 'invisible' tail implemented in the Boulder code to prevent artificial waves on the SFD.

[13] It seems that the late heavy bombardment is indeed capable to destroy $D_{\rm PB} \leqslant 100$ km families, as concluded by Brož et al. (2013), but in this paper we focus on the last ~ 4 Gyr only and we do not simulate the LHB.

Matthews, M.S. (Eds.), Asteroids II, University of Arizona Press, Tucson, AZ, pp. 524–556.
Brož, M., Morbidelli, A., Bottke, W.F., Rozehnal, J., Vokrouhlický, D., Nesvorný, D., 2013. Constraining the cometary flux through the asteroid belt during the late heavy bombardment. Astron. Astrophys. 551, 16. http://dx.doi.org/10.1051/0004-6361/201219296. Article Id: A117.
Carruba, V., Domingos, R.C., Nesvorný, D., Roig, F., Huaman, M.E., Souami, D., 2013. A multidomain approach to asteroid families' identification. Mon. Not. R. Astron. Soc. 433, 2075–2096. http://dx.doi.org/10.1093/mnras/stt884.
Carry, B., 2012. Density of asteroids. Planet. Space Sci. 73, 98–118. http://dx.doi.org/10.1016/j.pss.2012.03.009.
Cellino, A., Zappala, V., Farinella, P., 1991. The size distribution of main-belt asteroids from IRAS data. Mon. Not. R. Astron. Soc. 253, 561–574.
Ceplecha, Z., 1996. Luminous efficiency based on photographic observations of the Lost City fireball and implications for the influx of interplanetary bodies onto Earth. Astron. Astrophys. 311, 329–332.
Dahlgren, M., 1998. A study of Hilda asteroids. III. Collision velocities and collision frequencies of Hilda asteroids. Astron. Astrophys. 336, 1056–1064.
Davis, D.R., Chapman, C.R., Greenberg, R., Weidenschilling, S.J., Harris, A.W., 1979. Collisional Evolution of Asteroids – Populations, Rotations, and Velocities, In: Asteroids. (A80-24551 08-91), University of Arizona Press, NASA-supported research, Tucson, Ariz., pp. 528–557.
Delbo', M., dell'Oro, A., Harris, A.W., Mottola, S., Mueller, M., 2007. Thermal inertia of near-Earth asteroids and implications for the magnitude of the Yarkovsky effect. Icarus 190, 236–249. http://dx.doi.org/10.1016/j.icarus.2007.03.007.
Dell'Oro, A., Paolicchi, P., 1998. Statistical properties of encounters among asteroids: A new, general, purpose, formalism. Icarus 136, 328–339. http://dx.doi.org/10.1006/icar.1998.6025.
Dell'Oro, A., Paolicchi, P., Cellino, A., Zappalà, V., Tanga, P., Michel, P., 2001. The role of families in determining collision probability in the asteroid main belt. Icarus 153, 52–60. http://dx.doi.org/10.1006/icar.2001.6621.
DeMeo, F.E., Carry, B., 2014. Solar System evolution from compositional mapping of the asteroid belt. Nature 505, 629–634. http://dx.doi.org/10.1038/nature12908.
Dohnanyi, J.S., 1969. Collisional model of asteroids and their debris. J. Geophys. Res. 74, 2531. http://dx.doi.org/10.1029/JB074i010p02531.
Durda, D.D., Bottke, W.F., Nesvorný, D., Enke, B.L., Merline, W.J., Asphaug, E., Richardson, D.C., 2007. Size–frequency distributions of fragments from SPH/N-body simulations of asteroid impacts: Comparison with observed asteroid families. Icarus 186, 498–516. http://dx.doi.org/10.1016/j.icarus.2006.09.013.
Giblin, I., Martelli, G., Farinella, P., Paolicchi, P., di Martino, M., Smith, P.N., 1998. The properties of fragments from catastrophic disruption events. Icarus 134, 77–112. http://dx.doi.org/10.1006/icar.1998.5937.
Greenberg, R., 1982. Orbital interactions – A new geometrical formalism. Astron. J. 87, 184–195. http://dx.doi.org/10.1086/113095.
Hodapp, K.W. et al., 2004. Design of the Pan-STARRS telescopes. Astron. Nachrichten 325, 636–642. http://dx.doi.org/10.1002/asna.200410300.
Jacobson, S.A., Marzari, F., Rossi, A., Scheeres, D.J., Davis, D.R., 2014. Effect of rotational disruption on the size-frequency distribution of the main belt asteroid population. Mon. Not. R. Astron. Soc. 439, L95–L99. http://dx.doi.org/10.1093/mnrasl/slu006.
Knežević, Z., Milani, A., 2003. Proper element catalogs and asteroid families. Astron. Astrophys. 403, 1165–1173. http://dx.doi.org/10.1051/0004-6361:20030475.
Leinhardt, Z.M., Stewart, S.T., 2012. Collisions between gravity-dominated bodies. I. Outcome Regimes and scaling laws. Astrophys. J. 745 (1), 27. http://dx.doi.org/10.1088/0004-637X/745/1/79. Article Id: 79.
Levison, H.F., Bottke, W.F., Gounelle, M., Morbidelli, A., Nesvorný, D., Tsiganis, K., 2009. Contamination of the asteroid belt by primordial trans-Neptunian objects. Nature 460, 364–366. http://dx.doi.org/10.1038/nature08094.
Mainzer, A. et al., 2011. Thermal model calibration for minor planets observed with wide-field infrared survey explorer/NEOWISE. Astrophys. J. 736 (2), 9. http://dx.doi.org/10.1088/0004-637X/736/2/100. Article Id: 100.
Marzari, F., Rossi, A., Scheeres, D.J., 2011. Combined effect of YORP and collisions on the rotation rate of small main belt asteroids. Icarus 214, 622–631. http://dx.doi.org/10.1016/j.icarus.2011.05.033.
Masiero, J.R., Mainzer, A.K., Grav, T., Bauer, J.M., Cutri, R.M., Dailey, J., Eisenhardt, P.R.M., McMillan, R.S., Spahr, T.B., Skrutskie, M.F., Tholen, D., Walker, R.G., Wright, E.L., DeBaun, E., Elsbury, D., Gautier IV, T., Gomillion, S., Wilkins, A., 2011. Main belt asteroids with WISE/NEOWISE.I. Preliminary albedos and diameters. Astrophys. J. 741 (2), 20. http://dx.doi.org/10.1088/0004-637X/741/2/68. Article Id: 68.
Masiero, J.R., Mainzer, A.K., Bauer, J.M., Grav, T., Nugent, C.R., Stevenson, R., 2013. Asteroid family identification using the hierarchical clustering method and WISE/NEOWISE physical properties. Astrophys. J. 770 (1), 22. http://dx.doi.org/10.1088/0004-637X/770/1/7. Article Id: 7.
Michel, P., Jutzi, M., Richardson, D.C., Benz, W., 2011. The asteroid veritas: An intruder in a family named after it? Icarus 211, 535–545. http://dx.doi.org/10.1016/j.icarus.2010.10.01.
Mignard, F. et al., 2007. The Gaia mission: Expected applications to asteroid science. Earth Moon Planets 101, 97–125. http://dx.doi.org/10.1007/s11038-007-9221-z.
Milani, A., Cellino, A., Knezevic, Z., Novakovic, B., Spoto, F., Paolicchi, P., 2013. Asteroid families classification: Exploiting very large data sets. ArXiv e-prints.
Morbidelli, A., Bottke, W.F., Nesvorný, D., Levison, H.F., 2009. Asteroids were born big. Icarus 204, 558–573. http://dx.doi.org/10.1016/j.icarus.2009.07.011.
Nesvorný, D., Jedicke, R., Whiteley, R.J., Ivezić, Ž., 2005. Evidence for asteroid space weathering from the Sloan Digital Sky Survey. Icarus 173, 132–152. http://dx.doi.org/10.1016/j.icarus.2004.07.026.
Nesvorný, D., 2010. Nesvorný HCM Asteroid Families V1.0, NASA Planetary Data System 133.
Nesvorný, D., 2012. Nesvorný HCM Asteroid Families V2.0, NASA Planetary Data System 189.
Novaković, B., Cellino, A., Knežević, Z., 2011. Families among high-inclination asteroids. Icarus 216, 69–81. http://dx.doi.org/10.1016/j.icarus.2011.08.016.
Parker, A., Ivezić, Ž., Jurić, M., Lupton, R., Sekora, M.D., Kowalski, A., 2008. The size distributions of asteroid families in the SDSS moving object catalog 4. Icarus 198, 138–155. http://dx.doi.org/10.1016/j.icarus.2008.07.002.
Press, W.H., Teukolsky, S.A., Vetterling, W.T., Flannery, B.P., 1992. Numerical Recipes in FORTRAN. The Art of Scientific Computing.
Stewart, S.T., Leinhardt, Z.M., 2009. Velocity-dependent catastrophic disruption criteria for planetesimals. Astrophys. J. 691, L133–L137. http://dx.doi.org/10.1088/0004-637X/691/2/L133.
Stuart, J.S., 2001. A near-Earth asteroid population estimate from the LINEAR survey. Science 294, 1691–1693. http://dx.doi.org/10.1126/science.1065318.
Tanga, P., Cellino, A., Michel, P., Zappalà, V., Paolicchi, P., dell'Oro, A., 1999. On the size distribution of asteroid families: The role of geometry. Icarus 141, 65–78. http://dx.doi.org/10.1006/icar.1999.6148.
Tedesco, E.F., Noah, P.V., Noah, M., Price, S.D., 2002. The supplemental IRAS minor planet survey. Astron. J. 123, 1056–1085. http://dx.doi.org/10.1086/338320.
Tedesco, E.F., et al., 2005. Albedo distributions of near-Earth and intermediate source region asteroids. In: AAS/Division for Planetary Sciences Meeting Abstracts #37. Bulletin of the American Astronomical Society, vol. 37, pp. 643.
Vokrouhlický, D., 1998. Diurnal Yarkovsky effect as a source of mobility of meter-sized asteroidal fragments. I. Linear theory. Astron. Astrophys. 335, 1093–1100.
Vokrouhlický, D., Farinella, P., 1999. The Yarkovsky seasonal effect on asteroidal fragments: A nonlinearized theory for spherical bodies. Astron. J. 118, 3049–3060. http://dx.doi.org/10.1086/301138.
Walsh, K.J., Delbó, M., Bottke, W.F., Vokrouhlický, D., Lauretta, D.S., 2013. Introducing the Eulalia and new Polana asteroid families: Re-assessing primitive asteroid families in the inner main belt. Icarus 225, 283–297. http://dx.doi.org/10.1016/j.icarus.2013.03.005.
Warner, B.D., Harris, A.W., Pravec, P., 2009. The asteroid lightcurve database. Icarus 202, 134–146. http://dx.doi.org/10.1016/j.icarus.2009.02.003.
Zappalà, V., Bendjoya, P., Cellino, A., Farinella, P., Froeschlé, C., 1995. Asteroid families: Search of a 12,487-asteroid sample using two different clustering techniques. Icarus 116, 291–314. http://dx.doi.org/10.1006/icar.1995.1127.

A&A 530, A134 (2011)
DOI: 10.1051/0004-6361/201116738


Astronomy & Astrophysics

# A study of asteroid pole-latitude distribution based on an extended set of shape models derived by the lightcurve inversion method⋆

J. Hanuš[1], J. Ďurech[1], M. Brož[1], B. D. Warner[2], F. Pilcher[3], R. Stephens[4], J. Oey[5], L. Bernasconi[6], S. Casulli[7], R. Behrend[8], D. Polishook[9], T. Henych[10], M. Lehký[11], F. Yoshida[12], and T. Ito[12]

[1] Astronomical Institute, Faculty of Mathematics and Physics, Charles University in Prague, V Holešovičkách 2, 18000 Prague, Czech Republic
e-mail: hanus.home@gmail.com
[2] Palmer Divide Observatory, 17995 Bakers Farm Rd., Colorado Springs, CO 80908, USA
[3] 4438 Organ Mesa Loop, Las Cruces, NM 88011, USA
[4] Goat Mountain Astronomical Research Station, 11355 Mount Johnson Court, Rancho Cucamonga, CA 91737, USA
[5] Kingsgrove, NSW, Australia
[6] Observatoire des Engarouines, 84570 Mallemort-du-Comtat, France
[7] Via M. Rosa 1, 00012 Colleverde di Guidonia, Rome, Italy
[8] Geneva Observatory, 1290 Sauverny, Switzerland
[9] Benoziyo Center for Astrophysics, The Weizmann Institute of Science, Rehovot 76100, Israel
[10] Astronomical Institute, Academy of Sciences of the Czech Republic, Fričova 1, 25165 Ondřejov, Czech Republic
[11] Severni 765, 50003 Hradec Kralove, Czech republic
[12] National Astronomical Observatory, Osawa 2-21-1, Mitaka, 181-8588 Tokyo, Japan

Received 17 February 2011 / Accepted 13 April 2011

**ABSTRACT**

*Context.* In the past decade, more than one hundred asteroid models were derived using the lightcurve inversion method. Measured by the number of derived models, lightcurve inversion has become the leading method for asteroid shape determination.
*Aims.* Tens of thousands of sparse-in-time lightcurves from astrometric projects are publicly available. We investigate these data and use them in the lightcurve inversion method to derive new asteroid models. By having a greater number of models with known physical properties, we can gain a better insight into the nature of individual objects and into the whole asteroid population.
*Methods.* We use sparse photometry from selected observatories from the AstDyS database (Asteroids – Dynamic Site), either alone or in combination with dense lightcurves, to determine new asteroid models by the lightcurve inversion method. We investigate various correlations between several asteroid parameters and characteristics such as the rotational state and diameter or family membership. We focus on the distribution of ecliptic latitudes of pole directions. We create a synthetic uniform distribution of latitudes, compute the method bias, and compare the results with the distribution of known models. We also construct a model for the long-term evolution of spins.
*Results.* We present 80 new asteroid models derived from combined data sets where sparse photometry is taken from the AstDyS database and dense lightcurves are from the Uppsala Asteroid Photometric Catalogue (UAPC) and from several individual observers. For 18 asteroids, we present updated shape solutions based on new photometric data. For another 30 asteroids we present their partial models, i.e., an accurate period value and an estimate of the ecliptic latitude of the pole. The addition of new models increases the total number of models derived by the lightcurve inversion method to ~200. We also present a simple statistical analysis of physical properties of asteroids where we look for possible correlations between various physical parameters with an emphasis on the spin vector. We present the observed and de-biased distributions of ecliptic latitudes with respect to different size ranges of asteroids as well as a simple theoretical model of the latitude distribution and then compare its predictions with the observed distributions. From this analysis we find that the latitude distribution of small asteroids ($D < 30$ km) is clustered towards ecliptic poles and can be explained by the YORP thermal effect while the latitude distribution of larger asteroids ($D > 60$ km) exhibits an evident excess of prograde rotators, probably of primordial origin.

**Key words.** minor planets, asteroids: general – thechniques: photometric – methods: numerical – methods: statistical

## 1. Introduction

The lightcurve inversion method (LI) is a powerful tool that allows us to derive basic physical properties of asteroids (the rotational state and the shape) from their disk-integrated photometry (see Kaasalainen & Torppa 2001; Kaasalainen et al. 2001, 2002). This photometry can be *dense-in-time*, which typically consists of tens to a few hundreds of individual data points observed during one revolution. This is in contrast to *sparse-in-time*, where the typical separation of individual measurements is large compared to the rotation period. For sparse data, we usually have a few measurements per night, such as in the case of astrometric sky surveys. In the following text, we use the terms "dense lightcurves" and "sparse lightcurves".

To obtain a unique spin and shape solution, we need a set of at least a few tens of dense lightcurves observed during at least three apparitions. Based on simulated photometric data and the survey cadence of the Panoramic Survey Telescope And Rapid

⋆ Tables 3–6 are available in electronic form at http://www.aanda.org

Response System (Pan-STARRS), Kaasalainen (2004) showed that we can also use only sparse data for the inversion technique. In this case, a unique model can be derived from more than about one hundred calibrated measurements observed during 3−5 years if the photometric accuracy is better than ∼5% (Ďurech et al. 2005, 2007). Sparse data available so far are not that accurate. Nevertheless, for many asteroids with high lightcurve amplitudes, it is possible to derive their models from current sparse data (see Sect. 2 for more details). We can also combine sparse and dense data to derive models. First results from this approach were presented by Ďurech et al. (2009), where sparse data from the US Naval Observatory in Flagstaff (USNO) were used.

Currently (January 2011), there are 113 models of asteroids derived by the lightcurve inversion method; most of them are stored in the Database of Asteroid Models from Inversion Techniques (DAMIT[1], Ďurech et al. 2010). Most of these models were derived from dense lightcurves. Only 24 of them were computed from combined dense and sparse data (Ďurech et al. 2009). The AstDyS database (Asteroids – Dynamic Site[2]), which contains data from astrometric projects, is another possible source of sparse data. However, most of the data are not accurate enough to be used for inversion alone. On the other hand, even noisy sparse data in combination with a few dense lightcurves can give us, in many cases, a unique solution (Ďurech et al. 2007). The aim of our work was to gather these data, keep only those that were useful, and then combine them with dense lightcurves in the lightcurve inversion method.

Dense data are best used to define the rotational period and constrain the period interval that must be searched during the model computation (see Sect. 3.1 for more details). On the other hand, sparse data usually cover a long time interval, typically over several apparitions, and carry information about brightness variations for different geometries, which constrains the pole directions.

A priori information about rotational periods of asteroids plays an important role in the process of model determination. When an approximate period is known, we search for the solution near this value (details in Sect. 3.1) and thus save considerable computational time. We use the latest update of the Minor Planet Lightcurve Database[3] published by Warner et al. (2009) to check for previously derived periods. For many asteroids, there are only a few sparse lightcurves from different astrometric observatories available but no dense lightcurves. In these cases, we must scan the whole interval of expected period values (2–30 h). This approach is time-consuming and there is no guarantee that the correct period will lie in the scanned interval.

The knowledge of rotational states of asteroids is fundamental for understanding the history of the Solar System, specifically the accretion of planets or the collisional processes. For example, it was presumed that due to collisional evolution, the spin-vector distribution of main belt asteroids (MBAs) should be nearly isotropic, possibly with a small excess of prograde spins (Davis et al. 1989). Johansen & Lacerda (2010) performed a hydrodynamical simulation of the accretion of pebbles and rocks onto protoplanets and speculated that the trend of prograde rotators among the largest asteroids is primordial.

First statistical analyses of the spin-vector distribution were presented by Magnusson (1986, 1990) and Drummond et al. (1988, 1991), later by Pravec et al. (2002) and Skoglöv & Erikson (2002). They all observed a lack of poles close to the ecliptic plane. Kryszczyńska et al. (2007) used more objects in the analysis, finding that the distribution was strongly anisotropic with a moderate excess of prograde spins in the limited size range from 100 to 150 km. Interpretation of this depopulation of poles close to the ecliptic plane is still unclear. Probable candidates are selection effects, the role of inclination, the YORP effect[4] (Rubincam 2000; Vokrouhlický et al. 2003), or a combination of these. The YORP effect acts only on small bodies with $D \lesssim 40$ km. Asteroids with these sizes have non-Maxwellian spin rate distribution (Pravec & Harris 2000) and is particularly evident for asteroids with $D < 14$ km (Warner et al. 2009). It is believed that the YORP effect is responsible for this trend since it can either spin up or spin down an irregularly-shaped asteroid on the timescale shorter than the typical time between collisions and also affects the obliquity of spin axes (Rubincam 2000; Bottke et al. 2006).

In the near Earth asteroids (NEAs) population, the latitude distribution of poles is different from that of MBAs (La Spina et al. 2004; Kryszczyńska et al. 2007), i.e., there is a significant excess of retrograde spins probably caused by the transport mechanism of MBAs to Earth-crossing space by gravitational resonances and the Yarkovsky effect[5] (Morbidelli & Vokrouhlický 2003). There is no statistically significant clustering in the longitude of poles of either MBAs or NEAs (Kryszczyńska et al. 2007).

As the number of asteroid models with known physical properties grows, we can have a better insight into the nature of individual objects and into the asteroid population as a whole. In Sect. 2, we describe available dense and sparse photometric data and the selection of astrometric observatories with quality sparse data. In Sect. 3, we present new asteroid models derived from combined photometric data sets or from sparse data alone, mentioning a few individual objects and define several procedures on how to test the reliability of new models. In Sect. 4, we present a statistical analysis of asteroid physical parameters that we derived using the lightcurve inversion method or adopted from different sources (proper elements from the AstDyS database, diameters from IRAS, ...). We also present results of a numerical simulation that allowed us to estimate the bias in pole directions of the lightcurve inversion method. Using these results, we then corrected the observed pole distributions for this effect. Finally, in order to explain the observed latitude distributions, we present a simple theoretical model of the latitude distribution in Sect. 5.

## 2. Photometric data

The main source of dense photometric lightcurves is the Uppsala Asteroid Photometric Catalogue (UAPC, Lagerkvist et al. 1987; Piironen et al. 2001), where the lightcurves for about 1 000 asteroids are stored. We also used data from several individual observers (Table 6).

Sparse photometry was first used in combination with dense data for lightcurve inversion by Ďurech et al. (2009). These sparse data were from the USNO-Flagstaff station and had a typical photometric uncertainty of ∼8−10%. Other sparse photometric measurements are produced by many astrometric surveys,

[1] http://astro.troja.mff.cuni.cz/projects/asteroids3D
[2] http://hamilton.dm.unipi.it/
[3] http://cfa-www.harvard.edu/iau/lists/LightcurveDat.html

[4] Yarkovsky-O'Keefe-Radzievskii-Paddack effect, a torque caused by the recoil force from anisotropic thermal emission.
[5] A thermal force acting on a rotating asteroid.

**Table 1.** Comparison of estimated characteristics of residuals for 13 selected observatories: mode, "*FWHM*" and median.

| Obs | $N_{LC}$ | Mode | *FWHM* | Median | $\overline{N_P}$ | Weight | Observatory name |
|---|---|---|---|---|---|---|---|
| 608 | 2459 | 0.26 | 0.20 | 0.27 | 37 | 0 | Haleakala-AMOS |
| 644 | 2567 | 0.22 | 0.22 | 0.24 | 36 | 0 | Palomar Mountain/NEAT |
| 683 | 218 | 0.18 | 0.25 | 0.20 | 39 | 0 | Goodricke-Pigott Observatory, Tucson |
| 689 | 1970 | 0.14 | 0.12 | 0.15 | 118 | 0.3 | U.S. Naval Observatory, Flagstaff |
| 691 | 1893 | 0.23 | 0.22 | 0.24 | 39 | 0 | Steward Observatory, Kitt Peak-Spacewatch |
| 699 | 546 | 0.17 | 0.11 | 0.18 | 33 | 0.1 | Lowell Observatory-LONEOS |
| 703 | 8350 | 0.17 | 0.16 | 0.19 | 54 | 0.15 | Catalina Sky Survey |
| 704 | 8333 | 0.42 | 0.17 | 0.42 | 311 | 0 | Lincoln Laboratory ETS, New Mexico |
| 950 | 80 | 0.14 | 0.11 | 0.15 | 180 | 0.15 | La Palma |
| E12 | 1354 | 0.14 | 0.16 | 0.15 | 41 | 0.1 | Siding Spring Survey |
| G96 | 1810 | 0.14 | 0.22 | 0.17 | 43 | 0.1 | Mt. Lemmon Survey |
| H07 | 161 | 0.20 | 0.18 | 0.23 | 47 | 0 | 7300 Observatory, Cloudcroft |
| Hip | 49 | 0.10 | 0.10 | 0.11 | 53 | 0.3 | Hipparcos satellite |

**Notes.** For each observatory, the table gives also the number of sparse lightcurves $N_{LC}$, and the average number of data points for a single lightcurve $\overline{N_P}$.

but mostly as a by-product. In most cases, asteroid magnitudes are given to only one decimal place, i.e., the accuracy is 0.1 mag at best. Whether or not this is sufficient for a unique shape determination for reasonable number of asteroids can be deduced from asteroids lightcurve amplitude distribution. We used lightcurve amplitude data for ~2500 asteroids from the Minor Planet Lightcurve Database (Warner et al. 2009) and found that the mean lightcurve amplitude is ~0.3 mag. For 19% of asteroids, the amplitude is ≥0.5 mag. This means that, in principle, photometry with an accuracy of ~0.1 mag carries sufficient information about rotational states and shapes for a significant number of asteroids.

Our goal was to find out which observatories produce photometry suitable for lightcurve inversion and to use these data for determining new asteroid models. Through to September 2009 (the time of the data download), data for more than 350 000 objects from almost 1500 observatories were archived on the AstDyS server. Some of the observatories contributed with only a few data points, while others contributed tens of thousands of photometric measurements (e.g., large sky surveys such as the Catalina Sky Survey, LONEOS, or Siding Spring Survey).

### 2.1. Data reduction

The quality of the sparse photometry archived on the AstDyS varies significantly. We investigated the photometry carefully by establishing criteria for its quality. Then, using those criteria, we choose only those data that were useful for inversion.

For each observatory, we extracted photometric data for the first 10 000 numbered asteroids if there were at least 30 data points for a single lightcurve. We then transformed this photometry to the standard format used in lightcurve inversion: we computed geometry of observation (astrocentric ecliptic coordinates of the Sun and the Earth), corrected for light-time, normalized the brightness to the distance of 1 AU from the Sun and the Earth, and excluded clear outliers.

For further investigation, we selected 13 observatories that fulfilled the condition of having data for more than ~50 asteroids. This resulted in almost 30 000 sparse lightcurves for ~9000 asteroids. In the next step, we estimated mean uncertainties of individual observatories and, based on these uncertainties, we assigned a relative weight to the data from each observatory. In this process, we assumed that the brightness vs. solar phase angle relation can be fitted with a simple relation for each sparse lightcurve:

$$f(\alpha) = \cos^2\left(\frac{\alpha}{2}\right)\left[a\,\exp\left(-\frac{\alpha}{b}\right) + c\,\alpha + d\right], \quad (1)$$

where $\alpha$ is the solar phase angle[6] and $a, b, c$ and $d$ are free parameters. Then, we constructed a histogram of residuals (rms) for each observatory comparing actual data against the model given by Eq. (1). Four examples are plotted in Fig. 1. The dispersion is caused by observational uncertainties and by the amplitudes of the lightcurves. From these histograms, we estimated the "*FWHM*"[7] values and the most frequent residual (the mode); median values of the residual distributions for each location (Table 1) were computed. Observatories with a high median or "*FWHM*" value (≳0.2 mag for both) are not suitable for the lightcurve inversion (e.g. observatory 691 in Fig. 1). Data from only seven observatories, listed in Table 1 with non-zero weights, had sufficient accuracy and so could be used for modeling. Based on the values of medians and "*FWHM*s", we estimated a weight for the photometric data from each observatory relative to dense data, which has a unity weight (see Table 1). We assumed that the typical accuracy of dense lightcurves is ~0.02 mag.

The USNO in Flagstaff (MPC code 689) and the Hipparcos satellite are clearly the best observatories with respect to photometric accuracy. Other observatories are less accurate but they still hold some information about rotational states and shapes of asteroids. For any given asteroid, we have typically 2−4 sparse lightcurves from different observatories covering the last ~10−15 years. Data from USNO were already used by Ďurech et al. (2009). We updated those data along with adding another 20−30% of new data from the years 2008 and 2009 if there was an apparition for the asteroid.

## 3. Results

### 3.1. Models of asteroids

Our lightcurve inversion (LI) method is based on the optimization of unknown parameters of the shape (modeled as a *convex* hull), the rotational state, and the scattering law (see Kaasalainen & Torppa 2001; Kaasalainen et al. 2001). The parameter space have many local minims. Since LI is a gradient-based method

[6] The Sun-asteroid-Earth angle.
[7] The width of the distribution in the half of its maximum.

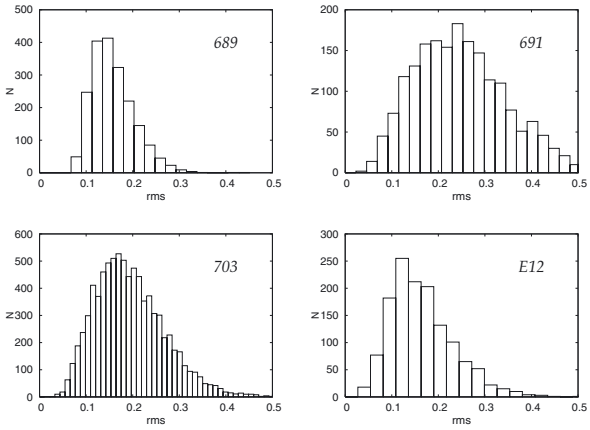


**Fig. 1.** Four histograms of residuals comparing actual data against the model given by Eq. (1) of all sparse lightcurves belonging to the following observatories: 689 USNO, 691 Steward Observatory, 703 Catalina Sky Survey and E12 Siding Spring Survey. Number of bins is $\sim\sqrt{N}$, where $N$ is the total number of sparse lightcurves used for histogram construction.

that converges to a local minimum near the initial choice of parameter values, it is critical to find the global minimum for the data set and then do the modeling. Finding a global minimum involves a systematic search through all relevant parameter values. Each model corresponding to a particular local minimum is characterized by a single value $\chi^2$, which corresponds to the quality of the fit.

A unique solution is defined as follows: (i) the best period has at least 10% lower $\chi^2$ than all other periods in the scanned interval; (ii) for this period, there is only one pole solution with at least 10% lower $\chi^2$ than the others (with a possible ambiguity for $\lambda \pm 180°$); and (iii) this solution fulfills our additional tests (see Sect. 3.3).

The most time-consuming part of the lightcurve inversion method is scanning through all periods within a chosen interval, which we determined by using the periods and reliability codes given in the Minor Planet Lightcurve Database[8]. For each asteroid, we scanned an interval centered at the reported period value $P$ with a range of ±1%, ±5% and ±20% of $P$ for reliability codes 4, 3 and 2, respectively. Half and double periods were tested later on.

We combined relative lightcurves from the UAPC and from individual observers together with sparse data obtained from the AstDyS site to create a data set for each asteroid. This gave us data sets for ~2300 asteroids (in ~900 cases there were only sparse data available) to which we then applied the lightcurve inversion method and then we ran the additional tests described in Sect. 3.3. We derived 80 new unique models, 16 of which are based only on sparse data. Basic characteristics of these models are listed in Table 3. We estimated the uncertainty in the pole direction as ±10–20° based on previous results with limited data sets. As might be expected, the uncertainty seems dependent on the number of dense and sparse photometric data. The longitude uncertainty increases for higher latitudes because meridians on a $(\lambda, \beta)$-sphere are more dense with increasing latitude. These uncertainties are discussed in more detail in Sect. 4.3. The uncertainty of the rotational period depends on the time interval covered by observational data and is of the order of the last decimal place of period values $P$ in Tables 3–5.

In some cases, we were able to determine a unique rotational period, but we had multiple pole solutions with similar ecliptic latitudes $\beta$. These models give us accurate period values and rough estimates of ecliptic latitudes $\beta$, which are also important parameters. In Table 4, we present results for 30 partial models, where $\beta$ is the mean value for all different models if the dispersion is smaller than 50°. We defined a parameter $\Delta = |\beta_{\max} - \beta_{\min}|/2$ as being the estimated uncertainty of $\beta$, where $\beta_{\max}$ and $\beta_{\min}$ are the extremal values within all $\beta$.

All new unique shape models are now included in DAMIT.

### 3.2. Comments to selected models

In DAMIT there are several solutions designated as "preliminary". These models do not have a well-constrained pole solution or are based on combined data sets. For 18 of those asteroids we derived updated model solutions based on additional photometric data (see Table 5). The difference between the old and new model for asteroid (1223) Neckar was significant. The new model has a slightly different period, but the pole directions and shapes are nearly similar to the old model. The current data suggest a period of $P = 7.82401$ h (previous value was $P = 7.82123$ h).

The asteroid (4483) Petofi was recently observed by Brian Warner. We derived a shape solution from three poor dense lightcurves and one sparse lightcurve from Catalina Sky Survey. Warner used these four lightcurves in combination with his new observations and also derived the shape model of Petofi (Warner 2011a). His period of $P = 4.3330$ h and pole direction (90°, 35°) are close to our solution of $P = 4.33299$ h and (107°, 40°).

The asteroid (832) Karin was also studied by Slivan & Molnar (2010); their solution with $P = 18.352$ h and pole (51° or 228°, 41°) confirms our results, see Table 3.

In past decades, occultations of stars by several asteroids were observed. These events give us additional information about the shape and can help resolve which mirror solutions of a model is the correct one. According to the recent work of Ďurech et al. (2011), asteroid occultation measurements prefer pole solutions of (122°, −44°) for (10) Hygiea, (347°, 47°) for (152) Atala, (28°, −72°) for (302) Clarissa, (223°, 67°) for (471) Papagena, and (296°, 41°) for (925) Alphonsina. Spin solutions preferred by asteroid occultations appear in bold font in Tables 3 and 5.

### 3.3. Models and method testing

We constructed five additional tests to be sure that the new models are reliable. We performed the first two tests for all models. For models derived only from sparse data, which are presented for the first time, we performed three additional tests:

Inertia tensor of the shape model. The lightcurve inversion method we use assumes that asteroids are in a relaxed rotational state, which means that derived models should rotate around the axis with a maximum moment of inertia. For each derived shape, we computed principal moments using equations presented by Dobrovolskis (1996) and checked if the rotation axis was close to the principal axis of the maximum momentum of inertia. We rejected those models for which the angle between the spin axis and the axis with a maximum momentum of inertia was larger

[8] http://cfa-www.harvard.edu/iau/lists/LightcurveDat.html, there is also an explanation and more details about the reliability codes too.

than ±30°. However, this criterion is too strict for elongated models with similar sizes along the rotational axis and the axis that is both perpendicular to the rotational axis and is the minimal size of the model. In this case, the principal moments for these two axes are similar. Under these circumstances, the angle between the spin axis and the axis with a maximum momentum of inertia can be large even for realistic shapes and so we allowed these models to pass this test.

Half- and double-period models. In cases where we have only a few dense lightcurves for a given asteroid, it is easy to confuse the correct rotational period with its half or double value. When the a priori period value in the Minor Planet Lightcurve Database is uncertain, which corresponds to a low reliability code (see Sect. 3.1), it is reasonable to check if the half and double period value give a better fit. If the period was in doubt, we searched for a solution also around $2P$ and $P/2$; if the $\chi^2$ was lower than $1.1\chi^2$ of the solution with period $P$, we rejected the model as unreliable.

Reduction of the number of sparse photometric data. In this test, we used only the sparse data sets for modeling. For 63 asteroids, this led to unique shape and spin state solutions (after performing the tests described above). For each solution, we randomly reduced the original amount of observed sparse data points to 90% and used these new limited data sets again in the lightcurve inversion. Our expectation was that we would not get a unique solution when using less data. This was true for five asteroids. These models, when using the full sparse data sets, are not necessarily wrong, but the amount of available data is probably just at the level when a unique solution can be derived. The important point of this test is that, for a given asteroid, we did not find two different but formally correct solutions when using the full versus reduced data sets. In Table 3, we present 16 models successfully derived only from sparse data that passed this test.

Models from sparse data vs. DAMIT. Here, we used previously derived models based only on relative photometry which are stored in DAMIT. As can seen in the previous test, sparse data are sometimes sufficient to produce a unique model of an asteroid. In 16 cases, we were able to derive a model for an asteroid which was already included in DAMIT and thus a model based on entirely different photometric data sets is available. These two independent models can be then compared and should be similar. We obtained similar resulting models for all 16 asteroids.

Models of "mock" objects. For each asteroid shape model derived only from sparse data, we created a set of ten "mock" objects of roughly the same appearance and spin state (see an example of such shape in Fig. 2). For these synthetic objects, we computed their photometric data using same epochs and geometries and with similar random noise level. These synthetic photometric data sets were then used in the lightcurve inversion method. A check that the original model using actual data is reliable is to be able to derive most of the models of the "mock" objects. The dispersions between the periods and pole directions of the "mock" objects represent the typical uncertainties of these parameters. For all studied asteroids, we were able to derive unique models for most of their "mock" objects. In all cases when we did not get a unique solution for the "mock" object, the best fit corresponded to the correct solution although other solutions could not be ruled out. The typical uncertainty in pole direction was ±10° and, for the period, ~0.1 times the difference between the two local minimums as determined by the period value and the time span of the data.

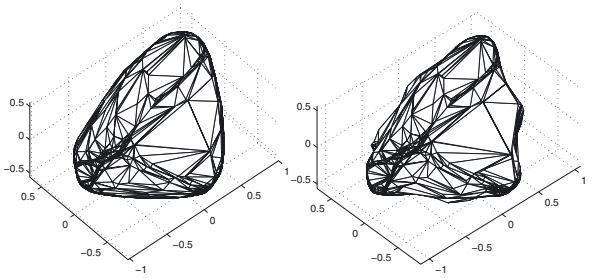

**Fig. 2.** Asteroid (810) Atossa: shape model (*left panel*) and an example of a "mock" shape model (*right panel*).

## 4. An analysis of periods, poles and sizes of asteroid models

Previous studies have been looking on spin state results using different techniques, e.g. amplitude-epoch, lightcurve inversion or radar methods. If there were multiple solutions for a given asteroid, the most probable one or simply the weighted mean was taken. However, this could cause systematic deviations. In our study, we used only results based on the lightcurve inversion method – i.e., unique and partial models presented in this work and models from the DAMIT. Our sample consists of 221 asteroid models: 80 new models, 18 updates for models from DAMIT, 30 new partial models, 84 models from DAMIT and 9 new models presented by Ďurech et al. (2011). Our sample consists of models for 206 MBAs, 10 NEAs, 3 Hungaria, 1 Trojan, and 1 Hilda and so a statistical study is only possible for the MBAs. In many cases there is an ambiguity in the pole direction since there are two, undistinguishable mirror solutions. For our statistical analysis we randomly chose only one.

In Fig. 3, we show (among other things to be discussed later) the relation between the proper semi-major axis and the proper eccentricity for asteroids in our sample and for all main belt asteroids. It is obvious that the positions of studied asteroids strongly correlate with the MBAs population and so derived models are not significantly biased with respect to orbits, e.g. they do not lie in the inner main belt. Several asteroids in Fig. 3 with semi-major axis $a > 3.3$ AU belong to the Cybele group, e.g. (121) Hermione.

### 4.1. Pole distribution analysis

In the following study of spin axis directions, we did not use the Koronis family members because their spin states are correlated, i.e., their spin vectors are clustered towards two values of the obliquity (Slivan 2002). In Fig. 4a, we show the ecliptic latitude distribution of our MBA sample. As in all similar plots, the width of the latitude and longitude bins corresponds to equal surfaces on the ($\lambda$, $\beta$)-sphere (bins are equidistant in $\sin\beta$ for latitudes and in $\lambda$ for longitudes). We confirmed the expectation that there is a lack of asteroids with latitudes close to the ecliptic plane. The latitude distribution is clearly not symmetric: about half of the retrograde rotators have latitudes in the bin (−53°, −90°). On the other hand, less than a third of asteroids with prograde spins are in the corresponding bin (53°, 90°). Moreover, the remaining prograde bins are more populated than the corresponding retrograde ones. From a detailed look at the plot we can see that there are up to 10% more prograde rotators among the MBAs.

In Fig. 5, we show the dependence of the ecliptic latitude $\beta$ of the pole direction on the diameter $D$ (most of the diameters

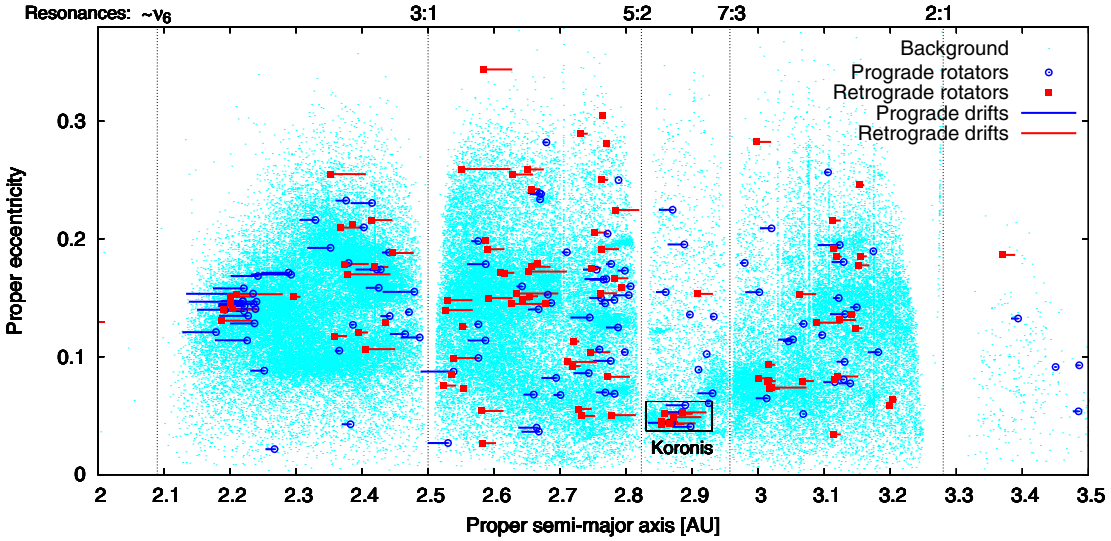


**Fig. 3.** Relation between the proper semi-major axis and the proper eccentricity for asteroids in our sample and for the first 100 000 numbered asteroids for comparison. Main resonances are shown by dotted lines. Prograde rotators are plotted with blue circles and retrograde rotators with red squares. The horizontal lines represent for each asteroid its estimated past drift (i.e. where the asteroid came from) during the collisional lifetime computed with Eq. (7). Proper elements are from the AstDyS database.

used are based on the IRAS data (Tedesco et al. 2002) or occultations profiles and have an uncertainty ±10%). Even for diameters $D \lesssim 50$ km, the clustering of the latitudes towards higher absolute values, and conversely, the depletion close to the ecliptic plane is obvious and markedly so for $D \lesssim 30$ km. Asteroids with larger diameters have a more isotropic distribution of latitudes and only a moderate excess of prograde. In Fig. 6, we plotted the latitude and longitude distributions of asteroids with respect to their diameters. Based on Fig. 5, we resolved three different size groups: 0–30 km, 30–60 km and >60 km.

The latitude distribution for asteroids with $D > 60$ km (Fig. 6a) is close to the uniform distribution for latitudes lower than 11° and for larger latitudes it exhibits an evident excess of prograde rotators. This is in agreement with theoretical arguments presented by Davis et al. (1989) and recently by Johansen & Lacerda (2010). On the other hand, the latitude distribution for asteroids with $D < 30$ km (Fig. 6e) exhibits a strong depopulation of pole vectors close to the ecliptic plane (i.e. small absolute values of latitudes $\beta$). The few asteroids with small latitudes have diameters $D > 25$ km. The latitude distribution for asteroids with intermediate diameters of 30–60 km (Fig. 6c) is also somewhat clustered towards higher latitudes but the bins for small latitudes are more populated. Therefor, it is probably a transition region between the two distinct distributions.

It is evident that the depopulation concerns mainly objects with diameters $D \lesssim 30$ km (the distribution for the intermediate size sample shows that the limit is probably ~50 km). This size roughly corresponds to the value, when the YORP effect starts to act and hence it is a natural candidate for a physical explanation. It is known from previous studies (Pravec & Harris 2000; Rubincam 2000) that the YORP effect is significantly altering the *periods* and also *spin vectors* of these objects on a timescale shorter than the typical collisional lifetime of these objects (timescales are discussed in more details in Sect. 5). In Fig. 7, we show the relation between the spin rate and the latitude for the small ($D < 30$ km) and large ($D > 60$ km) groups of asteroids. In concert with YORP theory, the spin up and spin down and the simultaneous evolution of the latitudes towards higher absolute values are evident in the small asteroid sample.

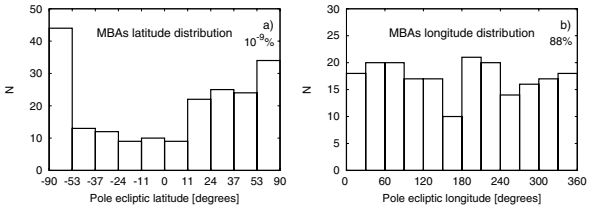


**Fig. 4. a)** Shows the ecliptic latitude distribution of all MBAs in our sample except the Koronis family members. The width of bins in latitude $\beta$ corresponds to similar surfaces on the $(\lambda, \beta)$-sphere, so the bins are equidistant in sin$\beta$. In **b)**, the longitude distribution of all MBAs is plotted, again except the Koronis family members. The longitude bins are equidistant in $\lambda$. In the top right corners, there are the probability values of the $\chi^2$-tests (that the observed distributions are randomly drown from a uniform distribution, see Table 2).

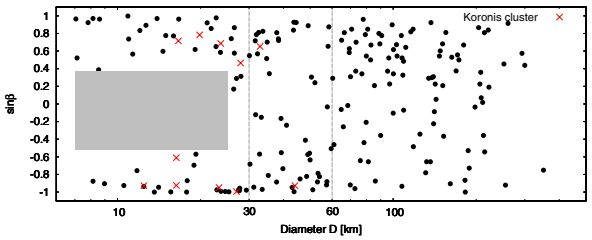


**Fig. 5.** Dependence of the ecliptic latitude $\beta$ (plotted as sin $\beta$) of the pole direction on the models diameter $D$. The gray box shows the gap of small latitudes for asteroids with $D < 30$ km. Members of the Koronis cluster are plotted with crosses.

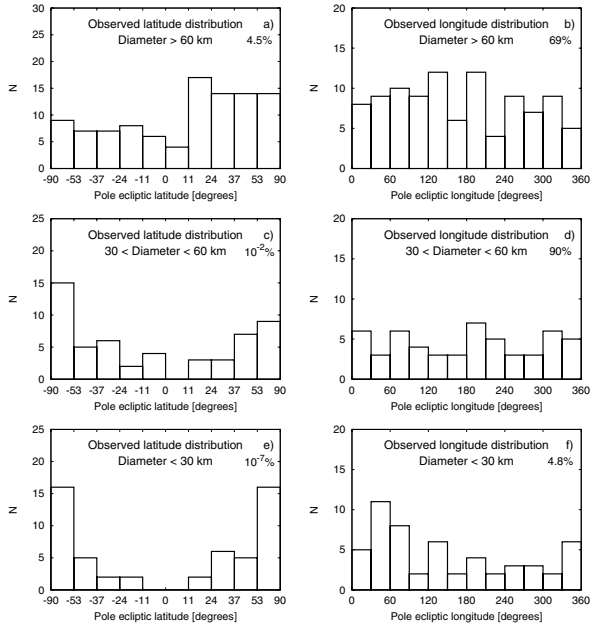


**Fig. 6.** Histograms showing the observed latitude and longitude distributions of MBAs (except Koronis cluster members) for different size ranges. **a)** Shows the latitude distribution for asteroids with diameters larger than 60 km, **c)** for asteroids with diameters in the range of 30−60 km, **e)** for asteroids with diameters smaller than 30 km, and similarly **b)**, **d)** and **f)** for longitudes. The width of bins in the latitude $\beta$ and longitude lambda $\lambda$ corresponds to similar surfaces on the $(\lambda, \beta)$-sphere, so the bins are equidistant in $\sin\beta$ and $\lambda$. In the top right corners, there are the probability values of the $\chi^2$-tests (that the observed distributions are randomly drown from a uniform distribution, see Table 2).

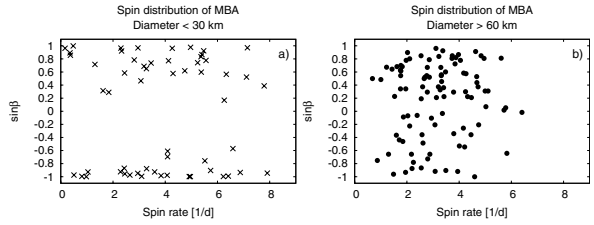


**Fig. 7.** Dependence of the ecliptic latitude $\beta$ (plotted as $\sin\beta$) of the pole direction on the models spin rate, **a)** for asteroids with diameter $D < 30$ km and **b)** for asteroids with diameter $D > 60$ km.

Note that observed latitude and longitude distributions can be biased by the convex inversion method and, therefore, this bias should be taken into consideration. In general, models for asteroids with higher amplitudes are more often successfully derived than those asteroids with lower amplitudes. This is because, while the accuracy of the sparse photometry in both cases is roughly the same, the signal-to-noise ratio is significantly better for higher amplitude lightcurves. If we assume two bodies with the same shapes and orbits and *different* ecliptic latitudes of the poles, the body with higher absolute value of ecliptic latitude usually has a higher amplitude. This effect is numerically investigated in Sect. 4.3.

Skoglöv & Erikson (2002) discussed the role of orbital inclination in the observed distribution of latitudes. No indications of this effect were found in the asteroids sample of

**Table 2.** Test of the hypothesis that the observed pole distributions and de-biased latitude distribution are drown from uniform distributions (a $\chi^2$-test).

| | $\beta$ $N=9$ | | $\lambda$ $N=11$ | | $\beta_{\rm deb}$ $N=9$ | |
|---|---|---|---|---|---|---|
| Diameter | $\chi^2$ | % | $\chi^2$ | % | $\chi^2$ | % |
| all | 63 | $10^{-9}$ | 5.9 | 88 | 39 | $10^{-3}$ |
| >60 km | 17 | 4.5 | 8.2 | 69 | 17 | 4.7 |
| 30−60 km | 30 | $10^{-2}$ | 5.6 | 90 | 18 | 2.9 |
| <30 km | 59 | $10^{-7}$ | 20 | 4.8 | 37 | $10^{-3}$ |

**Notes.** $N$ is the degree of freedom.

Kryszczyńska et al. (2007). We also did not find any indications of such correlation in our sample and so we conclude that orbital inclination does not affect the observed distribution of latitudes.

We are not aware of any other physical effects in the main belt that could explain the non-uniform observed latitude distribution of small asteroids ($D < 30$ km). Collisions are believed to produce uniform spin distributions and close encounters with planets are common only among NEAs.

There are many additional selection effects that influence the properties of derived models, e.g. the role of amplitude, orbit, time, accuracy and geometry of observations, among others. The significance of this bias is unknown and cannot be easily determined. The main problem here is that for almost every asteroid, the photometric data are from different observers with a different number of measurements, quality, and purpose. The significance of this effect can be determined only from a comparison of models derived from real and synthetic data of known properties. This may be possible in a few years when the photometry from the Pan-STARRS is available, but not now. In the meantime, the role of the selection effects seems to be small and does not significantly affect, for example, the latitude distribution.

The longitude distributions of the MBAs are plotted in Figs. 4b and 6b, d, f. They are, contrary to the latitude distributions, without any statistically significant features and have very close to uniform distributions. The only exception are the asteroids with $D < 30$ km, but the excess appears to be just a random coincidence than a result of some physical process.

In all cases, we tested a hypothesis that the observed distribution of latitudes or longitudes is uniform (using a $\chi^2$-test[9]). The computed chi-squares and corresponding probabilities are listed in Table 2. Higher $\chi^2$-values and lower probabilities mean that the supposed hypothesis "the observed distribution is uniform" does not fit the observed data. If we assume a probability of 5% or lower as statistically significant, we can say that the latitude distributions for the whole sample and for asteroids with $D < 30$ km and $30 < D < 60$ km do not agree with a uniform distribution. On the other hand, all longitude distributions are consistent with uniform distributions. Latitude distribution for the MBAs with diameters $D > 60$ km also disagrees with the uniform distribution; this is because of the excess of prograde rotators.

The overall view on the model positions within the main belt of asteroids, together with their estimated total drifts and the information about whether they are prograde or retrograde rotators (Fig. 3), shows behavior consistent with the Yarkovsky/YORP theory: there is an asymmetry of prograde and retrograde rotators near the main resonances and prograde aster-

[9] The results based on the $\chi^2$-test are also in agreement with the Kolmogorov-Smirnov test.

oids drift outwards from the Sun and can reach the resonance only from the left. On the other hand, retrograde rotators drift the opposite direction and depopulate the zone left of the resonance because the resonance prevents the entry of new retrograde asteroids. This creates an excess of prograde rotators. The same mechanism works also in the zone right of the resonance, except, in this case, only an excess of retrograde asteroids is now created. This effect is obvious in the neighborhood of the $\nu_6$ and 3:1 resonances. The total drift from an asteroid's original location during the collisional lifetime computed with Eq. (7) are inversely proportional to the size of the asteroids. Larger asteroids ($D \gtrsim 50$ km) do not drift significantly while smaller asteroids frequently drift ±0.05 AU. Note that small-sized asteroids are found mainly in the inner or middle part of the main belt (due to selection effect; they have high albedos and/or are closer to the Earth). Asteroids drifting through the resonances during their collisional lifetime are interesting from the point of the dynamical evolution. These asteroids were either recently collisionally-affected or their shape models are wrong. There seems to be three such models, two near the 3:1 resonance and one near the resonance 5:2.

### 4.2. The Koronis family members

The analysis of rotational state solutions for ten members of the Koronis asteroid family revealed a clustered distribution of their spin vectors (Slivan 2002; Slivan et al. 2003). This spin distribution was later explained by Vokrouhlický et al. (2003) as the result of the thermal torques and spin-orbital resonances that modify the spin states over time of 2−3 Gyr. The modeling suggested an existence of two groups of asteroids: (a) low-obliquity retrograde objects with rotational periods $P < 5$ h or $P > 13$ h, and (b) prograde rotators with periods $4 < P < 7$ h that became trapped in a spin-orbit resonance with secular frequency $s_6$ and thus have similar spin obliquities (42−51°) and also similar ecliptic longitudes in the range of (24−73°) and (204−259°). All ten members of the Koronis family studied by Slivan (2002) and Slivan et al. (2003) had the expected properties: periods for prograde rotators were shifted only to higher values of 7−10 h. Slivan et al. (2009) published spin state solutions for another four members of Koronis family. Only the solution for (253) Dresda was not in agreement with the theoretical expectation.

Here, we present three new models of asteroids belonging to the Koronis family: (832) Karin, (1482) Sebastiana, and (1635) Bohrmann, along with two partial models for (1350) Rosselina and (1389) Onnie. Only the spin state solutions for Bohrmann and Onnie fit the theoretical expectations. Rotational parameters for Karin ($P = 18.3512$ h, $\lambda = 242°$, $\beta = 46°$) are outside both groups. Asteroids Sebastiana and Rosselina are low-obliquity retrograde rotators, but their periods (10.49 h for Sebastiana and 8.14 h for Rosselina) are in the middle of the "wrong" range of $P = 5$−13 h. Karin is the namesake and largest member of a small and young (~5.8 My, Nesvorný & Bottke 2004) collisional family that is confined within the larger Koronis family. The spin state of Karin was thus likely affected during this catastrophic event and changed to a random state that disagrees with the clustered distribution.

We are not able to give a satisfactory explanation for the peculiar spin state solutions for Sebastiana and Rosselina. Nevertheless, we are aware of two possible scenarios: (i) the initial rotational state and shape did not allow being captured in the resonance or (ii) the objects were randomly reoriented by non-catastrophic collisions. The timescales of such collisions (given by Eq. (7)) are for Sebastiana $\tau_{reor} \sim 7.5$ Gyr and for Rosselina $\tau_{reor} \sim 14.7$ Gyr. This leads to the probability of a collision during the Koronis cluster lifetime (estimated to ~2.5 Gyr, Bottke et al. 2001) ~1/3 for Sebastiana and ~1/6 for Rosselina, respectively, which means that random collisional reorientation of the spin axis is likely for at least a few of 19 asteroids in the Koronis cluster with known spin state solutions (most of them have $\tau_{reor} \lesssim 20$ Gyr).

### 4.3. Biases of the LI method

We developed a numerical algorithm to estimate the selection effect of the lightcurve inversion method and used this approach to de-bias the observed distribution of asteroid's pole directions. The algorithm was as follows:

1. for a model with a known shape, we randomly generated a new pole direction (while the overall distribution of poles was isotropic);
2. for each shape with a new rotational state but with the period unchanged, we computed synthetic lightcurves for the same epochs as observed ones;
3. to each data point $i$, we added the corresponding noise $\delta_i$ given by:

$$\delta_i = \frac{L_i^{\rm obs} - L_i^{\rm mod}}{L_i^{\rm mod}}, \quad (2)$$

   where $L_i^{\rm obs}$ is $i$th brightness observed and $L_i^{\rm mod}$ is $i$th brightness computed, both for the original model. This gave us synthetic lightcurve data equivalent to the original observed data, but for a new pole direction;
4. finally, we performed a lightcurve inversion the same way as with the actual data and tried to derive a model;
5. we repeated steps 1–4 for 50 random poles for each asteroid model.

In this simulation, we used 80 models derived from combined dense and sparse data sets and 89 models from the DAMIT.

For each successfully derived model we have the generated pole direction ($\lambda_{\rm gen}$, $\beta_{\rm gen}$) and period $P_{\rm gen}$, and also the computed pole and period: $\lambda_{\rm comp}$, $\beta_{\rm comp}$, $P_{\rm comp}$. We computed the angular differences between the generated and derived ecliptic latitude and longitude of the pole direction: $\beta_{\rm comp} - \beta_{\rm gen}$ and $(\lambda_{\rm comp} - \lambda_{\rm gen})\cos\beta_{\rm gen}$ (the $\cos\beta_{\rm gen}$ factor is used for the correction of the different distances of meridians near the equator and poles). In Fig. 8, we show the histograms of these differences in a) ecliptic latitudes and b) ecliptic longitudes. We assumed that the histograms can be described by a normal distribution and we computed the mean and the standard deviation ($\mu$; $\sigma$). We found values of (−0.2; 10.2) for latitudes and (−0.2; 5.2) for longitudes. The standard deviation $\sigma$ is directly related to the typical uncertainty that we can expect in pole determination by the lightcurve inversion method, which is ~5°/ $\cos\beta$ in $\lambda$ and ~10° in $\beta$.

In Fig. 9a, we constructed a histogram of the latitude distribution for all successful models. The bins in $\beta$ were again equally spaced in $\sin\beta$. The latitude distribution of all generated models was not exactly uniform, the amount of latitudes in bins slightly differed. To remove this effect, we divided the latitude distribution of successfully derived models by the latitude distribution of all generated models normalized to unity. This correction was also applied to latitude distributions in Figs. 10a, c, e. It is obvious that the LI method is more efficient for asteroids with higher $|\beta|$. The amount of successfully derived models with $|\beta| \sim 0°$ is about 30% lower than with $|\beta| > 53°$.

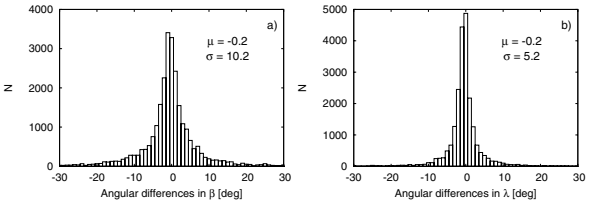


**Fig. 8.** Histograms of the angular differences between the generated and derived ecliptic latitudes and longitudes of the pole directions for all successfully derived synthetic models: **a)** $\beta_{\rm comp} - \beta_{\rm gen}$, where $\beta_{\rm gen}$ and $\beta_{\rm comp}$ are generated and computed ecliptic latitudes and similarly **b)** $(\lambda_{\rm comp} - \lambda_{\rm gen})\cos\beta_{\rm gen}$ for ecliptic longitudes.

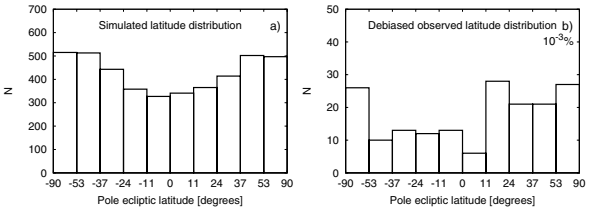


**Fig. 9. a)** Shows the simulated ecliptic latitude distribution of all successfully derived models. In **b)**, the de-biased observed latitude distribution is plotted. The bins are equidistant in $\sin\beta$. In the top right corner, there is the probability value of the $\chi^2$-test (that the observed distribution is drown from a uniform one, see Table 2).

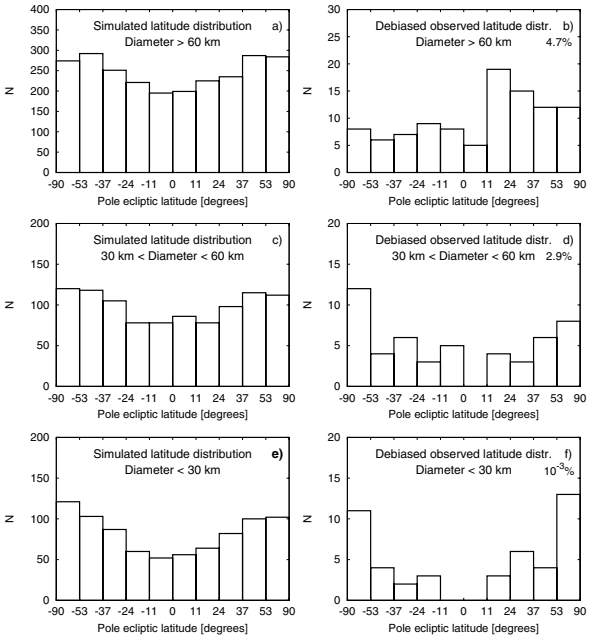


**Fig. 10.** Histograms showing the simulated and corrected (de-biased) observed latitude distributions of MBAs for different size groups, excluding the Koronis cluster members. **a)** Shows the simulated latitude distribution for asteroids with the diameters larger than 60 km, **c)** for asteroids with the size in range of 30–60 km, e) for asteroids with diameters smaller than 30 km. Similarly **b)**, **d)** and **f)** show the observed latitude distributions corrected by the bias of the LI method. The bins are equidistant in $\sin\beta$. In the top right corners, there are the probability values of the $\chi^2$-tests (that the observed distributions are drown from a uniform distribution, see Table 2).

In Figs. 10a, c, e, we constructed the histograms of latitude distributions for successfully derived models and distinguished three size ranges. All three plots look very similar, except that with decreasing size, the ratio between models with $|\beta| \sim 0°$ and $|\beta| > 53°$ goes down. This ratio is ~75% for $D > 60$ km, ~65% for $30 < D < 60$ km and ~60% for $D < 30$ km.

The histograms in Figs. 9a and 10a, c, e define the bias in latitude of the LI method and can be used for de-biasing the observed latitude distributions presented in Figs. 4a and 6a, c, e. The de-biased histograms of latitudes are plotted in Figs. 9b and 10b, d, f. The histograms changed only slightly and the conclusions from Sect. 4.1 are still valid, i.e., the latitude distribution differs significantly from a uniform distribution, and especially so for $D < 30$ km. The distribution of latitudes for asteroids with $D > 60$ has an evident excess of prograde rotators while the distribution for a subsample with 30 km $< D <$ 60 km shows an enrichment of asteroids with large latitudes ($|\beta| > 53°$). Other bins have similar populations. We also performed a $\chi^2$–test in the same way as for the observed distributions (see Table 2, Cols. 6 and 7).

We did not find any significant correlation between the ecliptic longitude and the efficiency of the model determination.

## 5. A theoretical model of the latitude distribution

In order to understand observations of main-belt asteroids, namely the de-biased distribution of their ecliptic latitudes $\beta$ (Fig. 9b), we constructed a simple model for spin evolution that contains the following processes: (i) the YORP effect, i.e., torques arising from the emission of thermal radiation, (ii) random reorientations induced by non-catastrophic collisions, and (iii) mass shedding after a critical rotational frequency is reached.

On the other hand, we did *not* include gravitational torques of the Sun, spin-orbital resonances, damping (dissipation of rotational energy), or tumbling. Even though individual asteroids may be substantially affected by these processes, our model is for a large statistical sample of asteroids and the effect on the *overall* latitude distribution is assumed to be only minor. For example, gravitational torques and spin-orbital resonances usually cause large oscillations of $\beta$ for prograde-rotating asteroids, but they remain bound to a certain interval (Vokrouhlický et al. 2006). Moreover, we tried to account for these (rather random) oscillations in our model as well (see below).

Our sample of 220 asteroids was the same as the observed sample discussed in Sect. 4. This means that the orbits and sizes correspond to real asteroids. The model for spin evolution was similar to that of Brož et al. (2011), where it was used for studies of the long-term evolution of asteroid families. We assumed the following relations for the rate of the angular velocity $\omega$ and the obliquity $\epsilon$ due to the YORP effect

$$\frac{{\rm d}\omega}{{\rm d}t} = f_i(\epsilon)\,, \qquad i = 1 \ldots 200\,, \tag{3}$$

$$\frac{{\rm d}\epsilon}{{\rm d}t} = \frac{g_i(\epsilon)}{\omega}\,, \tag{4}$$

where $f$- and $g$-functions were given by Čapek & Vokrouhlický (2004) for a set of 200 shapes with mean radius $R_0 = 1$ km, bulk density $\rho_0 = 2500\,{\rm kg/m^3}$, located on a circular orbit with semi-major axis $a_0 = 2.5$ AU. We assigned one of the artificial shapes

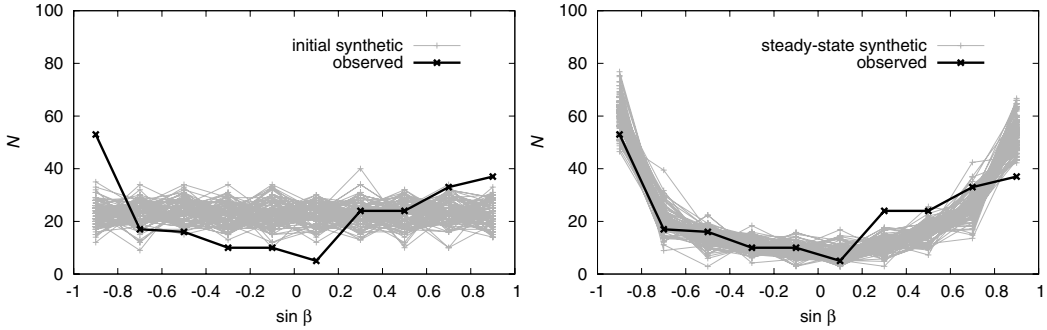


**Fig. 11.** *Left panel*: the distribution of the ecliptic latitudes $\beta$ for the observed asteroids (thick line) and 100 synthetic samples (generated with a different random seed) at time $t = 0$ (thin lines). *Right panel*: steady-state synthetic latitude distributions at time $t = 4$ Gyr (thin lines), evolved by the YORP effect, collisions, mass shedding and spin-orbit resonances. We also applied an observational bias to it. The steady state was reached already within $\simeq$1 Gyr.

(denoted by the index $i$) randomly to each individual asteroid[10]. We had only to scale the $f$- and $g$-functions by a factor

$$c = c_{\rm YORP}\left(\frac{a}{a_0}\right)^{-2}\left(\frac{R}{R_0}\right)^{-2}\left(\frac{\rho_{\rm bulk}}{\rho_0}\right)^{-1}, \quad (5)$$

where $a$, $R$, $\rho_{\rm bulk}$ are semi-major axis, radius, and density of the simulated body, respectively, and $c_{\rm YORP}$ is a free scaling parameter, which can account for an additional uncertainty of the YORP model. Because the values of $f$'s and $g$'s were computed for only a limited set of obliquities (with a step $\Delta\epsilon = 30°$) we used interpolation by Hermite polynomials (Hill 1982) of the data in Čapek & Vokrouhlický (2004) to obtain a smooth analytical functions for $f_i(\epsilon)$ and $g_i(\epsilon)$.

When the angular velocity approached a critical value (i.e., the gravity was equal to the centrifugal force)

$$\omega_{\rm crit} = \sqrt{\frac{4}{3}\pi G\rho_{\rm bulk}}, \quad (6)$$

we assumed a mass shedding event. We kept the orientation of the spin axis and the sense of rotation but reset the orbital period $P = 2\pi/\omega$ to a random value from the interval $(P_1, P_2) = (2.5, 9)$ h. We also altered the assigned shape since any change of shape can produce a different YORP effect. We did not change the mass, however.

The differential Eqs. (3) and (4) were integrated numerically by a simple Euler integrator. The usual time step was $\Delta t = 1000$ yr. The time scale of the spin axis evolution for small bodies ($D \simeq 10$ km) is $\tau_{\rm YORP} \simeq 500$ Myr. After $\simeq 3$ times $\tau_{\rm YORP}$ most of these bodies have spin axes perpendicular to the ecliptic.

We also included a Monte-Carlo model for spin axis reorientations caused by collisions[11]. We used an estimate of the time scale by Farinella et al. (1998)

$$\tau_{\rm reor} = B\left(\frac{\omega}{\omega_0}\right)^{\beta_1}\left(\frac{D}{D_0}\right)^{\beta_2}, \quad (7)$$

where $B = 84.5$ kyr, $\beta_1 = 5/6, \beta_2 = 4/3$, $D_0 = 2$ m and $\omega_0$ corresponds to period $P = 5$ h. These values are characteristic for the main belt. After a collision, we reset the spin axis periods to random values, using the interval $(P_1', P_2') = (2.5, 9)$ h for the period. Since the time scale is $\tau_{\rm reor} \simeq 3$ Gyr for the smallest ($D \simeq 5$ km) bodies, reorientations are only of minor importance. However, note that the probability of the reorientation is enhanced when the YORP effect drives the angular velocity $\omega$ close to zero.

There were several free parameters in our model: the $c_{\rm YORP}$ parameter, thermal conductivity $K$, bulk density $\rho_{\rm bulk}$, initial distribution of $\beta$ and initial distribution of $\omega$.

Our aim was to start with a simple $\beta$- and $\omega$-distribution, wait until a steady state was reached, and then compare the resulting synthetic to observed latitude distributions. We applied an observational bias derived in Sect. 4.3 to the synthetic distribution.

We partly accounted for spin-orbital resonances acting on prograde asteroids by adding a sinusoidal oscillations to $\beta$ with a random phase and an amplitude $\simeq$40°, which are typically induced by resonances. This procedure naturally decreased the right-most bin ($\sin\beta = (0.8, 1)$) of the synthetic distribution and increased the next bin ($\sin\beta = (0.6, 0.8)$).

We started with reasonable parameters of $c_{\rm YORP} = 0.33$, $K = 10^{-2}$ W/K/m, $\rho_{\rm bulk} = 2500$ kg/m$^3$, a Maxwellian distribution of $\omega$, a uniform distribution of $\sin\beta$ (i.e., an isotropic distribution of spin axes). We ran 100 such simulations with different random seeds. A steady state was reached within $\simeq$1 Gyr. The resulting latitude distributions are shown in Figs. 11 and 12.

From these it can be seen that: (i) the observed distribution of $\beta$ for small asteroids seems compatible with our model; the YORP effect is capable of creating such an uneven distribution and (ii) there is a discrepancy for large asteroids (especially in bins $\sin\beta \in (-1, -0.8)$ and $(0.2, 0.4)$), which can be explained as a preference for prograde rotators in the primordial population (see Davis et al. 1989; Johansen & Lacerda 2010). The results regarding the spin rates agree with Pravec et al. (2008), so we do not repeat the discussion here.

We also tested the sensitivity of our results with respect to the free parameters. The thermal conductivity did not seem important (we tested $K = 10^{-3}$ W/K/m). A simulation with $c_{\rm YORP} = 0.66$, $\rho = 1300$ kg/m$^3$, and a uniform distribution of

[10] We did not use the convex-hull shapes derived in this work for two reasons: (i) the two samples of shapes are believed to be statistically equivalent and it is thus not necessary to compute the YORP torques again; (ii) the YORP effect seems sensitive to small-scale surface structure (Scheeres & Mirrahimi 2007) which cannot be caught by our shape model. Nevertheless, the YORP torque remains of the same order, so the random assignment of shapes seems reasonable.

[11] Collisional disruptions are not important, since we are only interested in the steady state. We can imagine that whenever an asteroid from our sample is disrupted, another one with a randomly oriented spin axis is created by a disruption of a larger body.

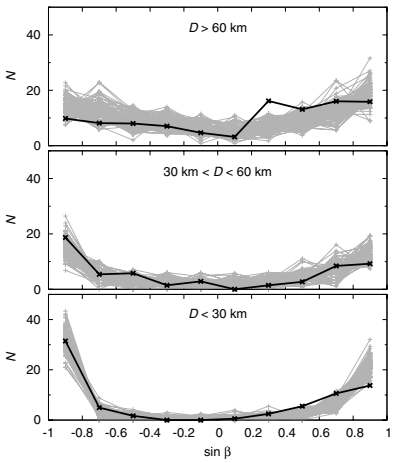


**Fig. 12.** Steady-state synthetic latitude distributions for three different size ranges: $D > 60$ km (*top*), 30 km $< D <$ 60 km (*middle*) and $D <$ 30 km (*bottom*). The synthetic distributions are plotted by thin gray lines while the observed distribution by a thick black line.

orbital periods $P \propto 1/\omega$ produced almost the same resulting latitude distribution. Nevertheless, a value of $c_{\rm YORP} = 1.00$ seems too high because the extreme bins of the $\beta$-distribution were overpopulated[12]. There is only a weak dependence of our results on the period ranges that we used for resetting the orbital period after a mass-shedding event $(P_1, P_2)$ and collision $(P'_1, P'_2)$. As would be expected, the values $P_1, P_2, P'_1, P'_2$ significantly affect the period distribution. The relatively weak dependence on the free parameters likely stems from the fact that we presume the steady-state. Even though the free parameters change, e.g., the strength of the YORP effect and the evolution of spins is slower and/or faster, after reaching a steady state, the basic characteristics of the latitude distribution remain similar. The observed $\beta$-distribution of small asteroids ($D <$ 30 km) cannot be explained by our simulation without accounting the YORP effect.

## 6. Conclusions

The results of this paper can be summarized as follows.

We used combined dense and sparse data to derive new asteroid shape models. We systematically gathered and processed all available sparse photometry from astrometric surveys and employed valuable data from seven observatories (see Table 1) in lightcurve inversion.

We derived 80 new unique models of asteroids, from which 16 are based only on sparse data. We also present 30 partial models with accurate rotational periods and estimated ecliptic latitudes of the pole directions and 18 updated solutions based on new data for asteroids already included in DAMIT.

In the future, quality sparse data sets will be produced by all-sky surveys such as Pan-STARRS, the Large Synoptic Survey Telescope (LSST), and the Gaia satellite. When these data are available, we will be able to apply the same methods in order to derive many more new asteroid models. These surveys will have one advantage over dense data: their selection effects (e.g., with respect to the orbit) will be known. This will allow us to make a more accurate analysis of the asteroid population.

As expected, the observed ecliptic *longitude* distribution of asteroid spin vector is independent of diameter and is compatible with a uniform distribution. Unlike the latitude distribution, the observed ecliptic longitude distribution is not significantly biased by the LI method. However, the effect of the LI bias is only minor and the global features of the observed latitude distribution do not change. The observed (and de-biased) *latitude* distribution for asteroids with diameters $D > 60$ km shows an excess of prograde rotators in the latitude interval (11°, 90°). This excess is probably primordial. On the other hand, the latitude distributions for the entire sample and in particular for asteroids with $D < 30$ km, is strongly anisotropic.

The dynamical evolution of asteroid spins seems to be dominated by the YORP effect and also by collisions and mass shedding for asteroids with diameters $D \lesssim 30$ km. We calculate that YORP (with a small contribution for the LI method's bias) is capable of producing the observed depopulation of spin vectors for small asteroids.

We are not yet able to study small asteroids in individual families (small bodies at the outskirts of a family should have extreme spins); this is an aim of future work.

[12] As an alternative hypothesis, we assumed the spin axis evolution without a YORP effect ($c_{\rm YORP} = 0$). In this case, the initial $\beta$-distributions (Fig. 11, left panel, thin lines) do not change significantly in time.

*Acknowledgements.* The work of J.H. has been supported by the grant GA UK 134710 of the Grant agency of the Charles University, by the project SVV 261301 of the Charles University in Prague and by the grant GACR 205/08/H005 of the Czech grant agency. The work of J.H. and J.Ď. has been supported by the grant GACR 209/10/0537 of the Czech grant agency, the work of J.D. and M.B. by the Research Program MSM0021620860 of the Czech Ministry of Education and the work of M.B. has been also supported by the Grant Agency of the Czech Republic (grant 205/08/P196). The calculations were performed on the computational cluster Tiger at the Astronomical Institute of Charles University in Prague (`http://sirrah.troja.mff.cuni.cz/tiger`).
We thank Brian D. Warner for significantly improving the linguistic quality of this paper and David Čapek for sending us the YORP effect data in an electronic form.

## References

Bottke, W. F., Vokrouhlický, D., Brož, M., Nesvorný, D., & Morbidelli, A. 2001, Science, 294, 1693
Bottke, J. W. F., Vokrouhlický, D., Rubincam, D. P., & Nesvorný, D. 2006, Ann. Rev. Earth Planet. Sci., 34, 157
Brož, M., Vokrouhlický, D., Morbidelli, A., Nesvorný, D., & Bottke, W. F. 2011, MNRAS, in press
Čapek, D., & Vokrouhlický, D. 2004, Icarus, 172, 526
Davis, D. R., Weidenschilling, S. J., Farinella, P., Paolicchi, P., & Binzel, R. P. 1989, in Asteroids II, ed. R. P. Binzel, T. Gehrels, & M. S. Matthews, 805
Dobrovolskis, A. R. 1996, Icarus, 124, 698
Drummond, J. D., Weidenschilling, S. J., Chapman, C. R., & Davis, D. R. 1988, Icarus, 76, 19
Drummond, J. D., Weidenschilling, S. J., Chapman, C. R., & Davis, D. R. 1991, Icarus, 89, 44
Ďurech, J., Grav, T., Jedicke, R., Denneau, L., & Kaasalainen, M. 2005, Earth Moon and Planets, 97, 179
Ďurech, J., Scheirich, P., Kaasalainen, M., et al. 2007, IAU Symp. 236, ed. G. B. Valsecchi, D. Vokrouhlický, & A. Milani, 191
Ďurech, J., Kaasalainen, M., Warner, B. D., et al. 2009, A&A, 493, 291
Ďurech, J., Sidorin, V., & Kaasalainen, M. 2010, A&A, 513, A46
Ďurech, J., Kaasalainen, M., Herald, D., et al. 2011, Icarus, accepted
Farinella, P., Vokrouhlicky, D., & Hartmann, W. K. 1998, Icarus, 132, 378
Hill, G. 1982, Publ. Dom. Astrophys. Obs. Victoria BC, 16, 67
Ito, T., & Yoshida, F. 2007, PASJ, 59, 269
Johansen, A., & Lacerda, P. 2010, MNRAS, 404, 475
Kaasalainen, M. 2004, A&A, 422, L39
Kaasalainen, M., & Torppa, J. 2001, Icarus, 153, 24
Kaasalainen, M., Torppa, J., & Muinonen, K. 2001, Icarus, 153, 37
Kaasalainen, M., Mottola, S., & Fulchignoni, M. 2002, Asteroids III, 139
Kryszczyńska, A., La Spina, A., Paolicchi, P., et al. 2007, Icarus, 192, 223

La Spina, A., Paolicchi, P., Kryszczyńska, A., & Pravec, P. 2004, Nature, 428, 400
Lagerkvist, C., Barucci, M. A., Capria, M. T., et al. 1987, Asteroid photometric catalogue., ed. C.-I. Lagerkvist, M. A. Barucci, M. T. Capria, M. Fulchignoni, L. Guerriero, E. Perozzi, & V. Zappala
Magnusson, P. 1986, Icarus, 68, 1
Magnusson, P. 1990, Icarus, 85, 229
Morbidelli, A., & Vokrouhlický, D. 2003, Icarus, 163, 120
Nesvorný, D., & Bottke, W. F. 2004, Icarus, 170, 324
Piironen, J., Lagerkvist, C., Torppa, J., Kaasalainen, M., & Warner, B. 2001, in BAAS, 33, 1562
Pilcher, F. 2008, Minor Planet Bulletin, 35, 135
Pilcher, F. 2009, Minor Planet Bulletin, 36, 133
Pilcher, F. 2010, Minor Planet Bulletin, 37, 167
Pilcher, F., & Cooney, J. W. R. 2006, Minor Planet Bulletin, 33, 13
Pilcher, F., & Jardine, D. 2009, Minor Planet Bulletin, 36, 52
Pilcher, F., & Oey, J. 2010, Minor Planet Bulletin, 37, 144
Pravec, P., & Harris, A. W. 2000, Icarus, 148, 12
Pravec, P., Harris, A. W., & Michalowski, T. 2002, Asteroids III, 113
Pravec, P., Harris, A. W., Vokrouhlický, D., et al. 2008, Icarus, 197, 497
Rubincam, D. P. 2000, Icarus, 148, 2
Scheeres, D. J., & Mirrahimi, S. 2007, in BAAS, 38, 416
Skoglöv, E., & Erikson, A. 2002, Icarus, 160, 24
Slivan, S. M. 2002, Nature, 419, 49
Slivan, S. M., & Molnar, L. A. 2010, in BAAS, 42, 1036
Slivan, S. M., Binzel, R. P., Crespo da Silva, L. D., et al. 2003, Icarus, 162, 285
Slivan, S. M., Binzel, R. P., Kaasalainen, M., et al. 2009, Icarus, 200, 514
Stephens, R. D. 2003, Minor Planet Bulletin, 30, 46
Stephens, R. D. 2004, Minor Planet Bulletin, 31, 40
Stephens, R. D. 2005a, Minor Planet Bulletin, 32, 82
Stephens, R. D. 2005b, Minor Planet Bulletin, 32, 27
Stephens, R. D. 2005c, Minor Planet Bulletin, 32, 2
Stephens, R. D., & Warner, B. D. 2004, Minor Planet Bulletin, 31, 3
Tedesco, E. F., Noah, P. V., Noah, M., & Price, S. D. 2002, AJ, 123, 1056
Vokrouhlický, D., Nesvorný, D., & Bottke, W. F. 2003, Nature, 425, 147
Vokrouhlický, D., Nesvorný, D., & Bottke, W. F. 2006, Icarus, 184, 1
Warner, B. D. 2002, Minor Planet Bulletin, 29, 74
Warner, B. D. 2003, Minor Planet Bulletin, 30, 21
Warner, B. D. 2005a, Minor Planet Bulletin, 32, 54
Warner, B. D. 2005b, Minor Planet Bulletin, 32, 26
Warner, B. D. 2011a, Minor Planet Bulletin, 38, 25
Warner, B. D. 2011b, Minor Planet Bulletin, 38, 52
Warner, B. D. 2011c, Minor Planet Bulletin, 38, 63
Warner, B. D., Harris, A. W., & Pravec, P. 2009, Icarus, 202, 134
Yoshida, F., Dermawan, B., Ito, T., et al. 2004, PASJ, 56, 1105

Pages 13 to 16 are available in the electronic edition of the journal at http://www.aanda.org

**Table 3.** List of new asteroid models derived from combined data sets or sparse data alone.

| | Asteroid | $\lambda_1$ [deg] | $\beta_1$ [deg] | $\lambda_2$ [deg] | $\beta_2$ [deg] | $P$ [h] | $N_{\rm lc}$ | $N_{\rm app}$ | $N_{689}$ | $N_{699}$ | $N_{703}$ | $N_{\rm E12}$ | $N_{\rm G96}$ | $N_{950}$ | $N_{\rm Hip}$ |
|---|---|---|---|---|---|---|---|---|---|---|---|---|---|---|---|
| 10 | Hygiea | 312 | −42 | **122** | **−44** | 27.6591 | 23 | 9 | 263 | | | | | 405 | 50 |
| 13 | Egeria | 44 | 21 | 238 | 11 | 7.04667 | 13 | 4 | 255 | | 74 | | | 203 | 34 |
| 14 | Irene | 97 | −22 | 268 | −24 | 15.02991 | 20 | 8 | 250 | | | 48 | | 161 | 45 |
| 37 | Fides | 270 | 19 | 89 | 27 | 7.33253 | 23 | 5 | 270 | | 61 | | | 135 | 31 |
| 40 | Harmonia | 22 | 31 | 206 | 39 | 8.90848 | 19 | 6 | 210 | | 48 | | | 255 | 102 |
| 42 | Isis | 106 | 40 | 302 | 28 | 13.58364 | 28 | 7 | 210 | | 36 | | | 128 | 51 |
| 62 | Erato | 87 | 22 | 269 | 23 | 9.21819 | 1 | 1 | 164 | | 48 | | | | |
| 68 | Leto | 103 | 43 | 290 | 23 | 14.84547 | 12 | 2 | 174 | | 85 | 30 | | 152 | |
| 69 | Hesperia | 250 | 17 | 71 | −2 | 5.65534 | 35 | 7 | 222 | | 44 | 40 | | | |
| 97 | Klotho | −1 | 30 | 161 | 40 | 35.2510 | 25 | 6 | 309 | | 31 | | | 202 | |
| 119 | Althaea | 339 | −67 | 181 | −61 | 11.46514 | 4 | 2 | 149 | | 59 | | | 222 | |
| 162 | Laurentia | 139 | 64 | 313 | 51 | 11.86917 | 4 | 2 | 166 | 31 | 40 | | | | |
| 174 | Phaedra | 94 | 36 | 266 | 14 | 5.75025 | 2 | 1 | 173 | | 36 | | | | |
| 188 | Menippe | 32 | 48 | 198 | 25 | 11.9765 | 4 | 1 | 145 | | 40 | | | | |
| 258 | Tyche | 224 | −4 | 40 | −9 | 10.04008 | 10 | 2 | 162 | | 44 | | | | |
| 264 | Libussa | 157 | 18 | 338 | −9 | 9.22794 | 19 | 3 | 129 | | 39 | 49 | | | |
| 291 | Alice | 69 | 51 | 249 | 56 | 4.316011 | 9 | 4 | 75 | | 46 | | | | |
| 302 | Clarissa | **28** | **−72** | 190 | −72 | 14.47670 | 8 | 2 | 102 | | 104 | | | | |
| 310 | Margarita | 225 | −35 | 42 | −33 | 12.0710 | 27 | 1 | 88 | 31 | 51 | | | | |
| 312 | Pierretta | 82 | −39 | 256 | −58 | 10.20764 | 4 | 1 | 176 | | 36 | 52 | | | |
| 336 | Lacadiera | 194 | 39 | 37 | 54 | 13.69552 | 3 | 1 | 121 | | 36 | 32 | | | |
| 340 | Eduarda | 188 | −43 | 18 | −47 | 8.00613 | 2 | 1 | 117 | | 76 | 31 | 36 | | |
| 354 | Eleonora | 144 | 54 | | | 4.277186 | 37 | 9 | 258 | | 40 | | | 139 | 96 |
| 355 | Gabriella | 341 | 78 | 197 | 70 | 4.82899 | 4 | 1 | 128 | | | | | | |
| 367 | Amicitia | 203 | 38 | 21 | 32 | 5.05502 | 2 | 1 | 128 | | 34 | | | | |
| 372 | Palma | 221 | −47 | 44 | 17 | 8.58189 | 28 | 6 | 214 | | 52 | 36 | | | |
| 376 | Geometria | 239 | 45 | 63 | 53 | 7.71097 | 39 | 9 | 158 | | 76 | | | | |
| 399 | Persephone | 36 | 63 | | | 9.14639 | | | 166 | | 36 | | | | |
| 400 | Ducrosa | 328 | 56 | 158 | 62 | 6.86788 | 3 | 1 | 103 | | | | | | |
| 413 | Edburga | 202 | −45 | | | 15.7715 | 2 | 1 | 148 | | 43 | | | | |
| 436 | Patricia | 124 | −30 | 339 | −58 | 16.1320 | 4 | 1 | 97 | | 53 | 91 | | | |
| 440 | Theodora | 80 | −88 | | | 4.83658 | | | 123 | | 103 | | 48 | | |
| 471 | Papagena | **223** | **67** | 22 | 18 | 7.11539 | 13 | 2 | 293 | | 72 | | | 203 | 112 |
| 486 | Cremona | 227 | 59 | 31 | 30 | 65.151 | 1 | 1 | 127 | | 55 | 35 | | | |
| 499 | Venusia | 37 | 50 | 212 | 46 | 13.4871 | 4 | 1 | 122 | | 39 | | 31 | | |
| 544 | Jetta | 275 | −84 | 31 | −67 | 7.74528 | 3 | 1 | 139 | | 60 | | | | |
| 573 | Recha | 74 | −24 | 252 | −48 | 7.16586 | 3 | 1 | 161 | | 85 | | | | |
| 584 | Semiramis | 106 | −56 | 315 | −32 | 5.06893 | 24 | 6 | 150 | | 59 | 49 | | | |
| 590 | Tomyris | 273 | −47 | 120 | −46 | 5.55248 | 3 | 1 | 91 | | 32 | | | | |
| 601 | Nerthus | 173 | 44 | 20 | 32 | 13.5899 | | | 139 | | 94 | | | | |
| 606 | Brangane | 183 | 20 | 354 | 26 | 12.29067 | 2 | 1 | 108 | | 70 | | | | |
| 629 | Bernardina | 40 | 33 | 236 | 48 | 3.76360 | | | 91 | | 48 | | | | |
| 631 | Philippina | 183 | −2 | | | 5.90220 | 6 | 2 | 171 | | 38 | | | | |
| 685 | Hermia | 197 | 87 | 29 | 79 | 50.387 | | | 93 | | 148 | | | | |
| 695 | Bella | 87 | −55 | 314 | −56 | 14.21900 | 8 | 1 | 184 | | 90 | 30 | | | |
| 753 | Tiflis | 5 | 36 | 199 | 57 | 9.8259 | | | 129 | | 64 | | | | |
| 800 | Kressmannia | 345 | 37 | 172 | 34 | 4.460963 | 8 | 2 | 108 | | 51 | | | | |
| 808 | Merxia | 26 | 54 | 192 | 57 | 30.630 | 4 | 1 | 158 | | 87 | | 32 | | |
| 810 | Atossa | 12 | 67 | 188 | 69 | 4.38547 | | | 99 | | 71 | | 60 | | |
| 825 | Tanina | 46 | 48 | 231 | 60 | 6.93981 | 2 | 1 | 114 | | 40 | | | | |
| 832 | Karin | 242 | 46 | 59 | 44 | 18.3512 | 13 | 3 | 84 | | | 39 | | | |
| 847 | Agnia | 341 | 18 | 162 | 13 | 14.8247 | 3 | 1 | 136 | | | | | | |
| 889 | Erynia | 187 | −60 | 335 | −74 | 9.8749 | | | 94 | | 65 | | | | |
| 925 | Alphonsina | **296** | **41** | 147 | 22 | 7.87754 | 4 | 1 | 134 | | 48 | 79 | | | |
| 934 | Thuringia | 120 | −52 | | | 8.16534 | | | 123 | | 59 | | | | |
| 1002 | Olbersia | 220 | 35 | 16 | 54 | 10.2367 | | | 87 | | 48 | 54 | | | |
| 1087 | Arabis | 334 | −7 | 155 | 12 | 5.79501 | 3 | 1 | 156 | | 92 | | | | |
| 1102 | Pepita | 25 | −34 | 231 | −30 | 5.10532 | | | 147 | | 47 | | | | |
| 1140 | Crimea | 12 | −73 | 175 | −22 | 9.7869 | 3 | 1 | 96 | | 116 | | | | |
| 1148 | Rarahu | 148 | −9 | 322 | −9 | 6.54449 | | | 95 | | 64 | | | | |
| 1207 | Ostenia | 310 | −77 | 124 | −51 | 9.07129 | 2 | 2 | 87 | | 71 | | | | |
| 1291 | Phryne | 106 | 35 | 277 | 59 | 5.58414 | 2 | 1 | 129 | | 72 | | | | |
| 1301 | Yvonne | 39 | 41 | | | 7.31968 | | | 78 | | 56 | 33 | | | |
| 1333 | Cevenola | 38 | −86 | 220 | −44 | 4.87932 | 3 | 1 | 104 | | 91 | | | | |
| 1382 | Gerti | 268 | 23 | 87 | 28 | 3.081545 | 2 | 1 | 60 | | 56 | | 52 | | |
| 1419 | Danzig | 22 | 76 | 193 | 62 | 8.11957 | 1 | 1 | 135 | | 87 | | | | |

**Table 3.** continued.

| Asteroid | | $\lambda_1$ [deg] | $\beta_1$ [deg] | $\lambda_2$ [deg] | $\beta_2$ [deg] | $P$ [h] | $N_{\rm lc}$ | $N_{\rm app}$ | $N_{689}$ | $N_{699}$ | $N_{703}$ | $N_{\rm E12}$ | $N_{\rm G96}$ | $N_{950}$ | $N_{\rm Hip}$ |
|---|---|---|---|---|---|---|---|---|---|---|---|---|---|---|---|
| 1482 | Sebastiana | 262 | −68 | 91 | −67 | 10.48965 | 2 | 1 | 131 | | 39 | 30 | | | |
| 1514 | Ricouxa | 251 | 75 | 68 | 69 | 10.42468 | 3 | 1 | 68 | | 56 | | | | |
| 1568 | Aisleen | 109 | −68 | | | 6.67597 | | | 82 | | 37 | | | | |
| 1635 | Bohrmann | 5 | −38 | 185 | −36 | 5.86427 | 8 | 1 | 108 | | 47 | | | | |
| 1659 | Punkaharju | 259 | −71 | 75 | −22 | 5.01327 | 2 | 1 | 118 | | 66 | | | | |
| 1682 | Karel | 232 | 32 | 51 | 41 | 3.37485 | | | 54 | | 84 | | 36 | | |
| 1709 | Ukraina | 165 | −61 | 2 | −40 | 7.30517 | 2 | 1 | 46 | | 79 | | | | |
| 1742 | Schaifers | 198 | 57 | 47 | 55 | 8.53270 | 3 | 1 | 106 | | | | | | |
| 1747 | Wright | 227 | 31 | | | 5.28796 | | | 70 | | 55 | | | | |
| 1889 | Pakhmutova | 22 | −76 | 167 | −40 | 17.5157 | | | 68 | | 46 | 35 | | | |
| 1930 | Lucifer | 32 | 17 | 211 | −19 | 13.0536 | 6 | 1 | 106 | | 43 | 66 | | | |
| 2156 | Kate | 49 | 74 | | | 5.62215 | 4 | 1 | | | 44 | | | | |
| 3678 | Mongmanwai | 125 | −65 | | | 4.18297 | 2 | 1 | | | 103 | | 31 | | |
| 4483 | Petofi | 107 | 40 | | | 4.33299 | 3 | 1 | | | 36 | | | | |

**Notes.** For each asteroid, the table gives also the number of dense lightcurves $N_{\rm lc}$ observed during $N_{\rm app}$ apparitions and the number of sparse data points for the corresponding observatory: $N_{689}$, $N_{699}$, $N_{703}$, $N_{\rm E12}$, $N_{\rm G96}$, $N_{950}$ and $N_{\rm Hip}$. Pole solutions preferred by asteroid occultation measurements (Ďurech et al. 2011) are emphasized by a bold font.

**Table 4.** List of partial models derived from combined data sets.

| Asteroid | $\beta$ [deg] | $\Delta$ [deg] | $P$ [h] | $N_{lc}$ | $N_{app}$ | $N_{689}$ | $N_{699}$ | $N_{703}$ | $N_{E12}$ | $N_{G96}$ | $N_{950}$ | $N_{Hip}$ |
|---|---|---|---|---|---|---|---|---|---|---|---|---|
| 163 Erigone | −60 | 14 | 16.1403 | 3 | 1 | 168 | | 72 | | | | |
| 187 Lamberta | −58 | 9 | 10.66703 | 9 | 2 | 159 | | 52 | 53 | | | |
| 233 Asterope | 49 | 8 | 19.6981 | 13 | 3 | 184 | | 80 | | | 165 | |
| 272 Antonia | −70 | 6 | 3.85480 | 5 | 1 | 109 | | 60 | | 36 | | |
| 281 Lucretia | −54 | 11 | 4.349710 | 6 | 3 | 123 | 30 | 62 | | | | |
| 313 Chaldaea | 33 | 18 | 8.38992 | 9 | 3 | 176 | | 80 | | | | |
| 390 Alma | −60 | 22 | 3.74116 | 2 | 1 | 109 | | | 34 | | | |
| 510 Mabella | −59 | 12 | 19.4304 | 6 | 2 | 145 | | 60 | | | | |
| 550 Senta | −63 | 13 | 20.5726 | 9 | 1 | 151 | | | 61 | | | |
| 622 Esther | −61 | 9 | 47.5042 | 5 | 1 | 120 | | 60 | | | | |
| 692 Hippodamia | −52 | 25 | 8.99690 | 3 | 1 | 114 | | 78 | 32 | | | |
| 733 Mocia | 36 | 16 | 11.37611 | 2 | 1 | 175 | | 44 | | | | |
| 746 Marlu | −54 | 18 | 7.78887 | 3 | 1 | 133 | | 47 | 34 | | | |
| 784 Pickeringia | 58 | 15 | 13.1699 | 1 | 1 | 188 | | 67 | 32 | | | |
| 823 Sisigambis | 57 | 9 | 146.58 | 8 | 1 | 123 | | 90 | | | | |
| 877 Walkure | 53 | 12 | 17.4217 | 3 | 1 | 141 | 45 | 104 | | 32 | | |
| 899 Jokaste | −58 | 19 | 6.24812 | 3 | 1 | 140 | | | 43 | | | |
| 1010 Marlene | 46 | 7 | 31.066 | 8 | 1 | 104 | | 52 | | | | |
| 1103 Sequoia | −48 | 19 | 3.037977 | 2 | 1 | 111 | | 36 | 30 | | | |
| 1185 Nikko | 46 | 12 | 3.78615 | 3 | 1 | 91 | | 46 | 32 | | | |
| 1188 Gothlandia | −63 | 19 | 3.491820 | 2 | 1 | 129 | 33 | 67 | 41 | | | |
| 1214 Richilde | −59 | 15 | 9.86687 | 4 | 1 | 101 | | 78 | | | | |
| 1282 Utopia | −39 | 21 | 13.6228 | 4 | 1 | 116 | | 72 | | | | |
| 1350 Rosselia | −58 | 13 | 8.14011 | 1 | 1 | 114 | | 48 | | | | |
| 1368 Numidia | −50 | 14 | 3.640740 | 3 | 1 | 129 | | 47 | | | | |
| 1379 Lomonosowa | −62 | 17 | 24.4845 | 2 | 1 | 96 | | 100 | | | | |
| 1389 Onnie | −56 | 10 | 23.0447 | 2 | 1 | 85 | 33 | 47 | 32 | 40 | | |
| 1665 Gaby | 49 | 17 | 67.905 | 1 | 1 | 81 | | 80 | | | | |
| 1719 Jens | −56 | 19 | 5.87016 | 2 | 1 | 78 | | 48 | 40 | | | |
| 2001 Einstein | −51 | 22 | 5.4850 | 2 | 1 | | | 84 | | | | |

**Notes.** For each asteroid, there is the mean ecliptic latitude $\beta$ of the pole direction and its dispersion $\Delta$, the other parameters have the same meaning as in Table 3.

**Table 5.** List of improved asteroid models that were originally designated in DAMIT as "preliminary".

| Asteroid | $\lambda_1$ [deg] | $\beta_1$ [deg] | $\lambda_2$ [deg] | $\beta_2$ [deg] | $P$ [h] | $N_{lc}$ | $N_{app}$ | $N_{689}$ | $N_{699}$ | $N_{703}$ | $N_{E12}$ | $N_{G96}$ | $N_{950}$ | $N_{Hip}$ |
|---|---|---|---|---|---|---|---|---|---|---|---|---|---|---|
| 73 Klytia | 266 | 68 | 44 | 83 | 8.28307 | 21 | 7 | 131 | 36 | 98 | 47 | | | |
| 82 Alkmene | 164 | −28 | 349 | −33 | 13.00079 | 11 | 1 | 158 | | 72 | 36 | 38 | 192 | |
| 132 Aethra | 326 | 67 | | | 5.16827 | 4 | 2 | 204 | | 55 | | | | |
| 152 Atala | **347** | **46** | 199 | 61 | 6.24472 | 2 | 1 | 101 | | 32 | | | | |
| 277 Elvira | 121 | −84 | | | 29.6922 | 22 | 5 | 142 | | 36 | 51 | | | |
| 278 Paulina | 307 | 31 | 118 | 38 | 6.49387 | 3 | 1 | 195 | | 51 | | | | |
| 311 Claudia | 214 | 43 | 30 | 40 | 7.53138 | 23 | 6 | 114 | 33 | 108 | | 40 | | |
| 484 Pittsburghia | 70 | 46 | | | 10.64977 | 2 | 1 | 100 | | 52 | | | | |
| 516 Amherstia | 254 | 22 | 81 | 54 | 7.48431 | 5 | 3 | 162 | | 32 | | | | |
| 534 Nassovia | 66 | 41 | 252 | 42 | 9.46889 | 16 | 6 | 151 | | 64 | 32 | | | |
| 614 Pia | 348 | 48 | 162 | 27 | 4.57872 | 2 | 1 | 121 | | 78 | | | | |
| 714 Ulula | 224 | −10 | 41 | −5 | 6.99837 | 9 | 2 | 177 | | 67 | | | | |
| 770 Bali | 70 | 50 | 262 | 45 | 5.81894 | 2 | 1 | 131 | | 52 | | | | |
| 915 Cosette | 350 | 56 | 189 | 61 | 4.469742 | 1 | 1 | 106 | | 32 | 35 | | | |
| 1012 Sarema | 45 | 67 | 253 | 63 | 10.30708 | 2 | 1 | 74 | | 42 | | | | |
| 1022 Olympiada | 46 | 10 | 242 | 52 | 3.83359 | 5 | 2 | 107 | | 91 | | | | |
| 1088 Mitaka | 280 | −71 | | | 3.035378 | 1 | 1 | 104 | | 39 | 41 | | | |
| 1223 Neckar | 252 | 28 | 69 | 30 | 7.82401 | 16 | 7 | 132 | 33 | 60 | | 36 | | |

**Notes.** Pole solutions preferred by asteroid occultation measurements (Ďurech et al. 2011) are emphasized by a bold font.

**Table 6.** Observations used for successful model determination that are not included in the UAPC.

| Asteroid | Date | Observer | Asteroid | Date | Observer |
|---|---|---|---|---|---|
| 13 Egeria | 2007.9−2009.3 | Pilcher (2009) | 808 Merxia | 2003 1 26.8 | Casulli[a] |
| 14 Irene | 2007.11−2009.5 | Pilcher (2009) | | 2003 1 28.8 | Casulli[a] |
| | 2008 2 3.7 | Polishook | | 2003 2 7.0 | Bernasconi[a] |
| 40 Harmonia | 2008.12-2009.1 | Pilcher (2009) | | 2003 2 8.0 | Bernasconi[a] |
| | 2010.5−2010.6 | Pilcher (2010) | 832 Karin | 2003.8−2003.9 | Yoshida et al. (2004) |
| 68 Leto | 2008 1 26.0 | Pilcher[b] | | 2004.9−2004.9 | Ito & Yoshida (2007) |
| | 2008 1 30.0 | Pilcher[b] | 899 Jokaste | 2003.11−2003.12 | Stephens (2004) |
| | 2008 2 6.1 | Pilcher[b] | 1010 Marlene | 2005.1−2005.3 | Warner (2005a) |
| 264 Libussa | 2005.2−2005.3 | Pilcher & Cooney (2006) | 1022 Olympiada | 1999.6−1999.6 | Warner (2005b) |
| | 2008.10−2008.12 | Pilcher & Jardine (2009) | 1087 Arabis | 2003 2 23.0 | Lehký |
| 272 Antonia | 2007.12−2008.1 | Pilcher (2008) | 1140 Crimea | 2005.4−2005.4 | Stephens (2005a) |
| 310 Margarita | 2010.3−2010.5 | Pilcher & Oey (2010) | 1185 Nikko | 2004.11−2004.11 | Stephens (2005b) |
| 390 Alma | 2004.8−2004.8 | Stephens (2005c) | 1282 Utopia | 2000.11−2000.11 | Warner (2011b) |
| 400 Ducrosa | 2005.1−2005.1 | Warner (2005a) | 1333 Cevenola | 2002.2−2002.2 | Warner (2002) |
| 436 Patricia | 2002.12−2003.1 | Warner (2003) | 1635 Bohrmann | 2003.9−2003.10 | Stephens & Warner (2004) |
| 544 Jetta | 2004.8−2004.8 | Stephens (2005c) | 1659 Punkaharju | 2000.11−2000.11 | Warner (2011c) |
| 573 Recha | 2001.1−2001.1 | Warner (2011b) | 1719 Jens | 2000.9−2000.9 | Warner (2011c) |
| 714 Ulula | 2005 9 23.8 | Henych | 1930 Lucifer | 2003.10−2003.10 | Warner (2005a) |
| | 2005 9 25.8 | Henych | 2001 Einstein | 2004.12−2004.12 | Warner (2005a) |
| | 2005 9 30.8 | Henych | 3678 Mongmanwai | 2003.3−2003.3 | Stephens (2003) |
| | 2005 10 1.8 | Henych | | | |
| | 2005 10 10.8 | Henych | | | |

**Notes.** [(a)] Online at `http://obswww.unige.ch/~behrend/page_cou.html`. [(b)] Online at `http://aslc-nm.org/Pilcher.html`

A&A 551, A67 (2013)
DOI: 10.1051/0004-6361/201220701


Astronomy & Astrophysics

# Asteroids' physical models from combined dense and sparse photometry and scaling of the YORP effect by the observed obliquity distribution⋆

J. Hanuš[1], J. Ďurech[1], M. Brož[1], A. Marciniak[2], B. D. Warner[3], F. Pilcher[4], R. Stephens[5], R. Behrend[6], B. Carry[7], D. Čapek[8], P. Antonini[9], M. Audejean[10], K. Augustesen[11], E. Barbotin[12], P. Baudouin[13], A. Bayol[11], L. Bernasconi[14], W. Borczyk[2], J.-G. Bosch[15], E. Brochard[16], L. Brunetto[17], S. Casulli[18], A. Cazenave[12], S. Charbonnel[12], B. Christophe[19], F. Colas[20], J. Coloma[21], M. Conjat[22], W. Cooney[23], H. Correira[24], V. Cotrez[25], A. Coupier[11], R. Crippa[26], M. Cristofanelli[17], Ch. Dalmas[11], C. Danavaro[11], C. Demeautis[27], T. Droege[28], R. Durkee[29], N. Esseiva[30], M. Esteban[11], M. Fagas[2], G. Farroni[31], M. Fauvaud[12,32], S. Fauvaud[12,32], F. Del Freo[11], L. Garcia[11], S. Geier[33,34], C. Godon[11], K. Grangeon[11], H. Hamanowa[35], H. Hamanowa[35], N. Heck[20], S. Hellmich[36], D. Higgins[37], R. Hirsch[2], M. Husarik[38], T. Itkonen[39], O. Jade[11], K. Kamiński[2], P. Kankiewicz[40], A. Klotz[41,42], R. A. Koff[43], A. Kryszczyńska[2], T. Kwiatkowski[2], A. Laffont[11], A. Leroy[12], J. Lecacheux[44], Y. Leonie[11], C. Leyrat[44], F. Manzini[45], A. Martin[11], G. Masi[11], D. Matter[11], J. Michałowski[46], M. J. Michałowski[47], T. Michałowski[2], J. Michelet[48], R. Michelsen[11], E. Morelle[49], S. Mottola[36], R. Naves[50], J. Nomen[51], J. Oey[52], W. Ogłoza[53], A. Oksanen[49], D. Oszkiewicz[34,54], P. Pääkkönen[39], M. Paiella[11], H. Pallares[11], J. Paulo[11], M. Pavic[11], B. Payet[11], M. Polińska[2], D. Polishook[55], R. Poncy[56], Y. Revaz[57], C. Rinner[31], M. Rocca[11], A. Roche[11], D. Romeuf[11], R. Roy[58], H. Saguin[11], P. A. Salom[11], S. Sanchez[51], G. Santacana[12,30], T. Santana-Ros[2], J.-P. Sareyan[59,60], K. Sobkowiak[2], S. Sposetti[61], D. Starkey[62], R. Stoss[51], J. Strajnic[11], J.-P. Teng[63], B. Trégon[64,12], A. Vagnozzi[65], F. P. Velichko[66], N. Waelchli[67], K. Wagrez[11], and H. Wücher[30]

*(Affiliations can be found after the references)*

Received 5 November 2012 / Accepted 15 January 2013

**ABSTRACT**

*Context.* The larger number of models of asteroid shapes and their rotational states derived by the lightcurve inversion give us better insight into both the nature of individual objects and the whole asteroid population. With a larger statistical sample we can study the physical properties of asteroid populations, such as main-belt asteroids or individual asteroid families, in more detail. Shape models can also be used in combination with other types of observational data (IR, adaptive optics images, stellar occultations), e.g., to determine sizes and thermal properties.

*Aims.* We use all available photometric data of asteroids to derive their physical models by the lightcurve inversion method and compare the observed pole latitude distributions of all asteroids with known convex shape models with the simulated pole latitude distributions.

*Methods.* We used classical dense photometric lightcurves from several sources (Uppsala Asteroid Photometric Catalogue, Palomar Transient Factory survey, and from individual observers) and sparse-in-time photometry from the U.S. Naval Observatory in Flagstaff, Catalina Sky Survey, and La Palma surveys (IAU codes 689, 703, 950) in the lightcurve inversion method to determine asteroid convex models and their rotational states. We also extended a simple dynamical model for the spin evolution of asteroids used in our previous paper.

*Results.* We present 119 new asteroid models derived from combined dense and sparse-in-time photometry. We discuss the reliability of asteroid shape models derived only from Catalina Sky Survey data (IAU code 703) and present 20 such models. By using different values for a scaling parameter $c_{\rm YORP}$ (corresponds to the magnitude of the YORP momentum) in the dynamical model for the spin evolution and by comparing synthetic and observed pole-latitude distributions, we were able to constrain the typical values of the $c_{\rm YORP}$ parameter as between 0.05 and 0.6.

**Key words.** minor planets, asteroids: general

## 1. Introduction

The lightcurve inversion method (LI) was developed by Kaasalainen & Torppa (2001) and Kaasalainen et al. (2001). This powerful tool allows us to derive physical models of asteroids (their rotational states and the shapes) from series of disk-integrated photometry.

*Convex* asteroid shape models can be derived from two different types of disk-integrated photometry: dense or sparse-in-time. Originally, only dense photometry was used. About 20 such dense lightcurves from at least four or five apparitions are necessary for a unique shape determination. By this approach, ~100 asteroid models have been derived (e.g., Kaasalainen et al. 2002; Michałowski et al. 2004; Ďurech et al. 2007; Marciniak et al. 2007, 2008). To significantly enlarge the number of asteroid models, sparse photometric data were studied and used in the LI. Ďurech et al. (2009) determined 24 asteroid models from a combination of dense data with sparse photometry from the U.S. Naval Observatory in Flagstaff (USNO-Flagstaff station, IAU code 689). Sparse data from seven astrometric surveys (including USNO-Flagstaff station) were used in the LI by

⋆ Table 3 is available in electronic form at http://www.aanda.org

Hanuš et al. (2011), who presented 80 asteroid models. Sixteen models were based only on sparse data, the rest on combined dense and sparse data.

Models of asteroids derived by the lightcurve inversion method are stored in the Database of Asteroid Models from Inversion Techniques (DAMIT[1], Ďurech et al. 2010). In October 2012, models of 213 asteroids were included there.

A larger number of asteroids with derived models of their convex shapes and rotational states is important for further studies. Large statistical samples of physical parameters can tell us more about processes that take place in the asteroids' populations (near-Earth asteroids, main-belt asteroids, or asteroids in individual families). For example, an anisotropy of spin-axis directions is present in the population of main-belt asteroids with diameters $\lesssim$30 km (Hanuš et al. 2011), where the YORP effect[2], together with collisions and mass shedding, is believed to be responsible. There are similar effects on the rotational states of main-belt binaries (Pravec et al. 2012). Convex shape models were also used in combination with stellar occultations by asteroids where global nonconvexities can be detected, and the diameter can be estimated with a typical uncertainty of 10% (see Ďurech et al. 2011).

In Sect. 2, we describe the dense and sparse photometric data used in the lightcurve inversion method and present new asteroid models derived from combined photometric data sets or from the sparse-in-time data from the Catalina Sky Survey Observatory (IAU code 703) alone. The reliability tests for derived models are also described. In Sect. 3, we use a theoretical model of the latitude distribution of pole directions published in Hanuš et al. (2011) in a numerical simulation to constrain the free scaling parameter $c_{\rm YORP}$ describing our uncertainty in the shape and the magnitude of the YORP momentum.

## 2. Asteroid models

We used four main sources of dense photometric lightcurves: (i) the Uppsala Asteroid Photometric Catalogue (UAPC[3], Lagerkvist et al. 1987; Piironen et al. 2001), where lightcurves for about 1000 asteroids are stored; (ii) data from a group of individual observers provided via the Minor Planet Center in the Asteroid Lightcurve Data Exchange Format (ALCDEF[4], Warner et al. 2009); (iii) data from another group of individual observers available online via Courbes de rotation d'astéroïdes et de comètes (CdR[5]); and (iv) data from the Palomar Transient Factory survey (PTF[6], Rau et al. 2009). Polishook et al. (2012) recently analyzed a small fraction of PTF data and presented dense lightcurves for 624 asteroids. So far, only a fraction of photometric data from the PTF has been processed (four overlapping fields on four consecutive nights), which means that this source will become very important in the near future.

We downloaded sparse data from the AstDyS site (Asteroids – Dynamic Site[7]) and gathered sparse lightcurves from the USNO-Flagstaff station (IAU code 689) for ~1000 asteroids, from Roque de los Muchachos Observatory, La Palma (IAU code 950) for ~500 asteroids and $\gtrsim$100 sparse data points from the Catalina Sky Survey Observatory (CSS for short, IAU code 703, Larson et al. 2003) for ~4000 asteroids. We present 119 asteroid models derived from combined dense and sparse data (Sect. 2.2) and 20 models based only on CSS data (Sect. 2.3).

During the model computation, a priori information about the rotational period of the asteroid was used, which significantly reduced the volume of the multidimensional parameter space that had to be searched, and saved computational time. Period values were taken from the regularly updated Minor Planet Lightcurve Database[8] (Warner et al. 2009). If the period was unknown or insecure, we searched the model over all possible period values of 2–100 h (usually, when only sparse data are available).

### 2.1. Reliability tests

We carefully tested the reliability of derived models. If we had several dense lightcurves and sparse data from USNO-Flagstaff station for an asteroid, we considered a model as unique if: (i) the modeled sidereal rotational period was close to the synodic rotational period determined from a single apparition dense data set (synodic period values have usually been previously published and were available in the Minor Planet Lightcurve Database); (ii) the shape model rotated close to its axis with a maximum momentum of inertia (it was in a relaxed rotational state); and (iii) models with half and double period values gave significantly worse fits.

It was necessary to apply additional tests to models derived from sparse-in-time data alone. We used the tests presented in Hanuš et al. (2011, for more details, see Sect. 3.3 there), and they were sufficient if photometry from USNO-Flagstaff station was present. In Hanuš & Ďurech (2012), we have shown that reliable asteroid models can also be derived from the Catalina Sky Survey data alone, and we described a convenient procedure for how to proceed during the computation when the rotational period is unknown: the solution should be searched for all periods in an interval of 2–100 h, and the stability of the solution should be tested for at least two different shape parametrizations[9]. The correct solution had to be stable for both low ($n = 3$) and high ($n = 6$) shape resolutions. We followed these recommendations: we searched for the model in the multidimensional parameter space for shape resolutions $n = 3$ and $n = 6$ and checked that we derived solutions with similar rotational states. In Hanuš & Ďurech (2012), we tested values $n = 2, 3, 4, 5, 6$ for the shape resolution. Correct solutions (i.e., models from the CSS data were similar to the models based on different data sets) were reproduced for most values of $n$. On the other hand, incorrect solutions were derived only for values $n = 6$ and sometimes also for $n = 4$ or $n = 5$, but never for $n = 2$ or $n = 3$.

### 2.2. Models from combined dense and sparse data

The shape model determination scheme was very similar to the one used in Hanuš et al. (2011). 119 new asteroid models were

[1] http://astro.troja.mff.cuni.cz/projects/asteroids3D

[2] Yarkovsky–O'Keefe–Radzievskii–Paddack effect, a torque caused by the recoil force from anisotropic thermal emission, which can alter the rotational periods and orientation of spin axes, see e.g., Rubincam (2000), Vokrouhlický et al. (2003).

[3] http://asteroid.astro.helsinki.fi/

[4] http://www.minorplanet.info/alcdef.html

[5] http://obswww.unige.ch/~behrend/page2cou.html

[6] http://www.astro.caltech.edu/ptf/

[7] http://hamilton.dm.unipi.it/

[8] http://cfa-www.harvard.edu/iau/lists/LightcurveDat.html

[9] Shape is represented by coefficients of its expansion into spherical harmonic functions to the order $n$. We call $n$ the shape resolution, the number of shape parameters is then $(n + 1)^2$, and our typical value for the shape resolution is $n = 6$.

derived because we gathered ∼1000 new dense lightcurves from ALCDEF, another ∼1000 lightcurves from PTF, ∼300 from individual observers, and also additional sparse data observed by the CSS during the second half of the year 2010 and the first half of the year 2011. Derived rotational states with basic information about the photometry used for 119 asteroids are listed in Table 1. Out of them, 18 models are based only on *combined* sparse data from various sources, but in all cases, sparse data from USNO-Flagstaff station were present[10]. In Table 3, we list the references to the dense lightcurves we used for the new model determination.

Although the amount of photometric data from PTF was similar to that from ALCDEF, only two new shape models (for asteroids with numbers 52 820 and 57 394, see Table 1) were derived with their contribution. The first reason was a significantly worse quality of PTF data: only for 84 asteroids out of 624 were the data sufficient for determining a synodic period, while other lightcurves were noisy or burdened with systematic errors. In many cases they allowed only for an estimate of a lower limit for the lightcurve amplitude (presented in Polishook et al. 2012). The second reason was that PTF data alone were not sufficient for a unique model determination (they covered only one apparition), no other dense lightcurves were usually available, and sparse data were available for only fewer than a half of these asteroids. Many asteroids detected by the PTF survey were previously unknown.

There are previously published models available for 15 of the asteroids modeled here: (11) Parthenope, (79) Eurynome, (272) Antonia, (281) Lucretia, (351) Yrsa, (352) Gisela, (390) Alma, (787) Moskva, (852) Wladilena, (1089) Tama, (1188) Gothlandia, (1389) Onnie, (1572) Posnania, (1719) Jens, and (4954) Eric (see databases by Kryszczyńska et al. 2007; and Warner et al. 2009). As these models were usually based on limited datasets, our solutions differ from some of them substantially, while agreeing for some in the spin axis latitude or the sidereal period value. We fully confirmed previous models for six objects of that sample: the spin models of (79) Eurynome by Michałowski (1996), (787) Moskva by Svoren et al. (2009), and (1572) Posnania by Michałowski et al. (2001), as well as our preliminary solutions for (390) Alma, (1389) Onnie, and (1719) Jens obtained in Hanuš et al. (2011).

The shape models and their spin solutions can be found in the DAMIT database (Ďurech et al. 2010). We noticed that for the models based only on sparse data, their shapes tend to be very angular, with sharp edges and large planar areas, thus can be treated only as crude approximations of the real asteroid shapes. However, a substantial addition ($\gtrsim$10 lightcurves from $\gtrsim$2 apparitions) of dense lightcurves smooths the shape models out, making them look more realistic, as confirmed by their better fit to occultation chords.

From observations of star occultations by asteroids, we can reconstruct asteroid projected silhouettes. These silhouettes can then be compared with the predicted contours of the convex shape models and used for the asteroid size determination by scaling the shape models to fit the occultation chords. A reasonable number of observations were available for three asteroids from our sample. By using the same methods as in Ďurech et al. (2011), we rejected mirror solutions for the asteroids (345) Tercidina and (578) Happelia, and also determined equivalent diameters (corresponding to spheres with the same volume as the scaled convex shape models): 96 ± 10 km for (345) Tercidina, 101 ± 5 km for (404) Arsinoe, and 70 ± 5 km for (578) Happelia. Two different stellar occultations are available for all three asteroids, and are plotted in Figs. 1–3.

[10] Models based only on data from the Catalina Sky Survey are described later in Sect. 2.3.

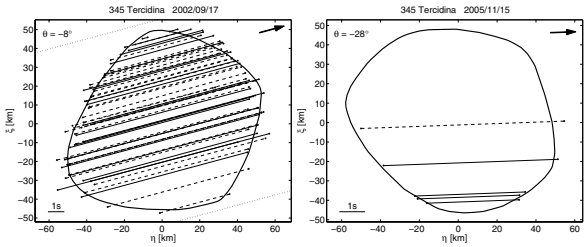


**Fig. 1.** Two observations of star occultations by asteroid (345) Tercidina. The solid contour corresponds to a scaled projected silhouette of the shape model with the pole (346°, −55°), each chord represents one occultation observation (solid lines are CCD, video, or photoelectric observations; dashed lines are visual observations, and dotted lines negative observations). Each plot also contains the time scale (lower left corner), the latitude of the sub-Earth point $\theta$ for the time of occultation (upper left corner), and the direction of the relative velocity (the arrow in the upper right corner). East points to the left and north up.

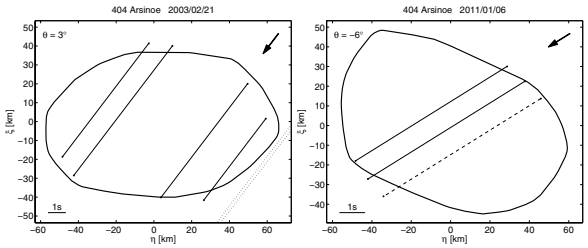


**Fig. 2.** Two observations of star occultations by asteroid (404) Arsinoe. The solid contour corresponds to a scaled projected silhouette of the shape model with the pole (25°, 57°). See Fig. 1 for line types and symbols explanation.

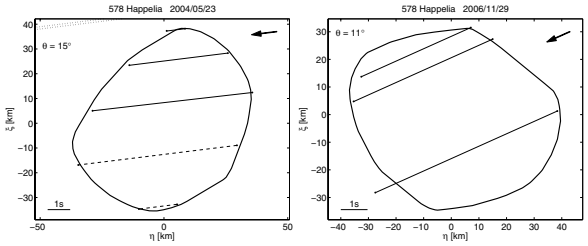


**Fig. 3.** Two observations of star occultations by asteroid (578) Happelia. The solid contour corresponds to a scaled projected silhouette of the shape model with the pole (339°, 62°). See Fig. 1 for line types and symbols explanation.

During the apparition in 2004, the lightcurves of asteroid (1089) Tama have shown features typical of close binary systems (Behrend et al. 2004) and indeed, the system was later interpreted as a synchronous close binary (Behrend et al. 2006). Our *brick-like* convex shape model is strongly elongated with sharp edges and is similar to a convex shape model of a close binary system (90) Antiope. Such a shape appearance for close binaries was predicted from synthetic data (Ďurech & Kaasalainen 2003).

**Table 1.** List of new asteroid models derived from combined dense and sparse data or from sparse data alone.

| Asteroid | $\lambda_1$ [deg] | $\beta_1$ [deg] | $\lambda_2$ [deg] | $\beta_2$ [deg] | $P$ [h] | $N_{\rm lc}$ | $N_{\rm app}$ | $N_{689}$ | $N_{703}$ | $N_{950}$ |
|---|---|---|---|---|---|---|---|---|---|---|
| 11 Parthenope | 311 | 14 | 128 | 14 | 13.72205 | 107 | 13 | 297 | 24 | 147 |
| 25 Phocaea | 347 | 10 | | | 9.93540 | 22 | 5 | 272 | 100 | |
| 72 Feronia | 287 | −39 | 102 | −55 | 8.09068 | 20 | 5 | 196 | 124 | 127 |
| 79 Eurynome | 228 | 30 | 54 | 24 | 5.97772 | 36 | 4 | 240 | 168 | |
| 147 Protogeneia | 269 | 15 | 90 | 14 | 7.85232 | 11 | 3 | 152 | 80 | |
| 149 Medusa | 333 | −73 | 156 | −76 | 26.0454 | 13 | 4 | 134 | 60 | |
| 157 Dejanira | 319 | −64 | 146 | −33 | 15.8287 | 14 | 2 | 94 | 123 | |
| 166 Rhodope | 345 | −22 | 173 | −3 | 4.714793 | 7 | 2 | 141 | 111 | |
| 178 Belisana | 260 | 20 | 79 | 9 | 12.32139 | 35 | 3 | 147 | 127 | |
| 183 Istria | 85 | 20 | | | 11.76897 | 8 | 2 | 142 | 174 | |
| 193 Ambrosia | 141 | −11 | 328 | −17 | 6.58166 | 18 | 4 | 169 | 87 | |
| 199 Byblis | 344 | −24 | 165 | 9 | 5.22063 | 22 | 5 | 184 | 108 | |
| 220 Stephania | 26 | −50 | 223 | −62 | 18.2087 | 9 | 2 | 117 | 99 | |
| 222 Lucia | 106 | 50 | 293 | 49 | 7.83671 | 9 | 4 | 160 | 100 | |
| 242 Kriemhild | 100 | −40 | 285 | −15 | 4.545174 | 25 | 7 | 179 | 144 | |
| 257 Silesia | 5 | −53 | 176 | −46 | 15.7097 | 18 | 2 | 167 | 88 | |
| 260 Huberta | 23 | −28 | 206 | −19 | 8.29055 | 6 | 2 | 162 | 90 | |
| 265 Anna | 109 | −53 | | | 11.6903 | | | 114 | 79 | |
| 272 Antonia | 293 | −90 | | | 3.85480 | 7 | 2 | 109 | 92 | |
| 281 Lucretia | 128 | −49 | 309 | −61 | 4.349711 | 8 | 4 | 129 | 83 | |
| 290 Bruna | 286 | −80 | 37 | −74 | 13.8055 | 9 | 1 | 97 | 66 | |
| 297 Caecilia | 223 | −53 | 47 | −33 | 4.151388 | 15 | 5 | 149 | 130 | |
| 345 Tercidina | 346 | −55 | | | 12.37082 | 42 | 8 | 161 | 155 | |
| 351 Yrsa | 20 | −70 | 193 | −41 | 13.3120 | 2 | 1 | 183 | 52 | |
| 352 Gisela | 24 | −21 | 206 | −28 | 7.48008 | 6 | 4 | 134 | 140 | |
| 371 Bohemia | 93 | 49 | 256 | 43 | 10.73965 | 30 | 4 | 181 | 79 | |
| 390 Alma | 53 | −50 | 275 | −76 | 3.74117 | 5 | 2 | 142 | 58 | |
| 403 Cyane | 65 | 35 | 230 | 33 | 12.2700 | 7 | 3 | 186 | 104 | |
| 404 Arsinoe | 25 | 57 | | | 8.88766 | 49 | 9 | 199 | 104 | |
| 406 Erna | 357 | −49 | 161 | −60 | 8.79079 | 8 | 1 | 134 | 93 | |
| 441 Bathilde | 285 | 55 | 122 | 43 | 10.44313 | 32 | 7 | 158 | 112 | |
| 507 Laodica | 102 | −55 | 312 | −49 | 4.70657 | | | 162 | 103 | |
| 509 Iolanda | 245 | 65 | 98 | 38 | 12.2907 | 4 | 2 | 178 | 85 | |
| 512 Taurinensis | 324 | 45 | | | 5.58203 | 11 | 2 | 124 | 111 | |
| 519 Sylvania | 106 | 9 | 286 | −13 | 17.9647 | 5 | 2 | 147 | 76 | |
| 528 Rezia | 176 | −59 | 46 | −66 | 7.33797 | 6 | 2 | 151 | 77 | |
| 531 Zerlina | 78 | −84 | | | 16.7073 | 28 | 3 | 48 | 52 | |
| 543 Charlotte | 333 | 59 | 172 | 49 | 10.7184 | 4 | 1 | 138 | 98 | |
| 572 Rebekka | 1 | 54 | 158 | 39 | 5.65009 | 5 | 2 | 155 | 63 | |
| 578 Happelia | 339 | 62 | | | 10.06450 | 20 | 4 | 183 | 80 | |
| 600 Musa | 0 | −74 | 208 | −46 | 5.88638 | 23 | 7 | 96 | 132 | |
| 669 Kypria | 31 | 40 | 189 | 49 | 14.2789 | 5 | 1 | 142 | 126 | |
| 708 Raphaela | 37 | 27 | 217 | 22 | 20.8894 | 5 | 1 | 140 | 95 | |
| 725 Amanda | 145 | −63 | 320 | −70 | 3.74311 | 18 | 7 | 70 | 77 | |
| 731 Sorga | 83 | 40 | 275 | 21 | 8.18633 | 7 | 2 | 131 | 136 | |
| 732 Tjilaki | 160 | 23 | 353 | 24 | 12.3411 | 3 | 1 | 140 | 153 | |
| 787 Moskva | 331 | 59 | 126 | 27 | 6.05581 | 15 | 4 | 160 | 92 | |
| 792 Metcalfia | 88 | −14 | 274 | −13 | 9.17821 | 9 | 3 | 164 | 56 | |
| 803 Picka | 218 | 34 | 53 | 41 | 5.07478 | | | 154 | 50 | |
| 807 Ceraskia | 325 | 23 | 132 | 26 | 7.37390 | 2 | 1 | 132 | 111 | |
| 812 Adele | 301 | 44 | 154 | 69 | 5.85746 | | | 65 | 119 | |
| 816 Juliana | 124 | −8 | 304 | 10 | 10.5627 | 11 | 2 | 158 | 107 | |
| 819 Barnardiana | 169 | 46 | 334 | 47 | 66.698 | | | 121 | 86 | |
| 852 Wladilena | 181 | −48 | 46 | −53 | 4.613301 | 30 | 8 | 138 | 101 | |
| 857 Glasenappia | 227 | 48 | 38 | 34 | 8.20757 | 4 | 2 | 140 | 116 | |
| 867 Kovacia | 200 | −44 | 38 | −50 | 8.67807 | | | 78 | 76 | |
| 874 Rotraut | 201 | −41 | 2 | −36 | 14.3007 | 3 | 1 | 129 | 68 | |
| 875 Nymphe | 42 | 31 | 196 | 42 | 12.6213 | 6 | 1 | 94 | 100 | |
| 900 Rosalinde | 276 | 70 | 90 | 39 | 16.6868 | 3 | 2 | 125 | 170 | |
| 920 Rogeria | 238 | −15 | 47 | −35 | 12.5749 | | | 137 | 79 | |

**Notes.** For each asteroid, the table gives the ecliptic coordinates $\lambda_1$ and $\beta_1$ of the pole solution with the lowest chi-square, the corresponding mirror solution $\lambda_2$ and $\beta_2$, the sidereal rotational period $P$, the number of dense lightcurves $N_{\rm lc}$ observed during $N_{\rm app}$ apparitions, and the number of sparse data points for the corresponding observatory: $N_{689}$, $N_{703}$ and $N_{950}$. The uncertainty of the sidereal rotational period corresponds to the last decimal place of $P$ and of the pole direction to 10–20°.

**Table 1.** continued.

| Asteroid | $\lambda_1$ [deg] | $\beta_1$ [deg] | $\lambda_2$ [deg] | $\beta_2$ [deg] | $P$ [h] | $N_{\rm lc}$ | $N_{\rm app}$ | $N_{689}$ | $N_{703}$ | $N_{950}$ |
|---|---|---|---|---|---|---|---|---|---|---|
| 958 Asplinda | 41 | 48 | 226 | 35 | 25.3050 | 2 | 1 | 98 | 68 | |
| 994 Otthild | 183 | −50 | 41 | −39 | 5.94819 | 26 | 5 | 140 | 125 | |
| 1040 Klumpkea | 172 | 48 | | | 56.588 | | | 114 | 88 | |
| 1056 Azalea | 252 | 51 | 64 | 41 | 15.0276 | 3 | 1 | 122 | 112 | |
| 1089 Tama | 193 | 32 | 9 | 28 | 16.4461 | 90 | 7 | 108 | 79 | |
| 1111 Reinmuthia | 356 | 68 | 153 | 78 | 4.007347 | 13 | 3 | 137 | 65 | |
| 1126 Otero | 44 | 75 | 240 | 56 | 3.64800 | 2 | 1 | 101 | 110 | |
| 1130 Skuld | 24 | 36 | 200 | 35 | 4.80764 | 14 | 1 | 92 | 106 | |
| 1188 Gothlandia | 334 | −84 | | | 3.491820 | 36 | 5 | 134 | 91 | |
| 1241 Dysona | 125 | −68 | | | 8.60738 | 7 | 1 | 156 | 64 | |
| 1249 Rutherfordia | 32 | 74 | 197 | 65 | 18.2183 | 6 | 2 | 187 | 75 | |
| 1317 Silvretta | 45 | −57 | 161 | −46 | 7.06797 | 13 | 3 | 120 | 69 | |
| 1386 Storeria | 227 | −67 | 297 | −67 | 8.67795 | 10 | 1 | 33 | 78 | |
| 1389 Onnie | 183 | −75 | 0 | −79 | 23.0447 | 2 | 1 | 90 | 97 | |
| 1393 Sofala | 319 | 28 | 134 | 41 | 16.5931 | | | 69 | 91 | |
| 1401 Lavonne | 204 | 23 | 27 | 44 | 3.93261 | 3 | 1 | 109 | 88 | |
| 1432 Ethiopia | 41 | 44 | 225 | 54 | 9.84425 | 11 | 1 | 88 | 101 | |
| 1436 Salonta | 223 | 18 | 57 | 35 | 8.86985 | 10 | 2 | 132 | 90 | |
| 1450 Raimonda | 231 | −56 | 71 | −60 | 12.6344 | | | 74 | 116 | |
| 1472 Muonio | 249 | 61 | 42 | 62 | 8.70543 | 6 | 1 | 99 | 93 | |
| 1490 Limpopo | 319 | 22 | 142 | 2 | 6.65164 | 5 | 1 | 103 | 107 | |
| 1495 Helsinki | 355 | −39 | | | 5.33131 | 13 | 2 | 62 | 109 | |
| 1518 Rovaniemi | 62 | 60 | 265 | 45 | 5.25047 | 2 | 1 | 100 | 73 | |
| 1528 Conrada | 250 | −51 | 93 | −66 | 6.32154 | 2 | 1 | 93 | 126 | |
| 1554 Yugoslavia | 281 | −34 | 78 | −64 | 3.88766 | 3 | 1 | 75 | 75 | |
| 1559 Kustaanheimo | 275 | 29 | 94 | 33 | 4.30435 | | | 53 | 82 | |
| 1572 Posnania | 205 | −82 | 85 | −63 | 8.04945 | 46 | 7 | 141 | 83 | |
| 1607 Mavis | 0 | 59 | 222 | 70 | 6.14775 | 4 | 1 | 141 | 179 | |
| 1630 Milet | 304 | 34 | 121 | 40 | 32.485 | 3 | 1 | 72 | 92 | |
| 1634 Ndola | 261 | 45 | 66 | 34 | 64.255 | 7 | 1 | 71 | 110 | |
| 1704 Wachmann | 267 | 41 | 90 | 40 | 3.31391 | | | 54 | 135 | |
| 1715 Salli | 95 | −24 | 254 | −48 | 11.08867 | 2 | 1 | 84 | 97 | |
| 1719 Jens | 286 | −88 | 55 | −42 | 5.87016 | 4 | 2 | 78 | 53 | |
| 1785 Wurm | 11 | 57 | 192 | 47 | 3.26934 | 2 | 1 | 43 | 115 | |
| 1837 Osita | 167 | −64 | 352 | −54 | 3.81879 | | | 82 | 62 | |
| 1905 Ambartsumian | 52 | −64 | 241 | −68 | 92.153 | | | 50 | 101 | |
| 1927 Suvanto | 74 | 73 | 278 | 23 | 8.16154 | 4 | 1 | 64 | 119 | |
| 1933 Tinchen | 113 | 26 | 309 | 36 | 3.67062 | | | 72 | 103 | |
| 1950 Wempe | 90 | −41 | 258 | −45 | 16.7953 | 1 | 1 | 96 | 46 | |
| 1963 Bezovec | 219 | 7 | | | 18.1655 | 12 | 2 | 103 | 40 | |
| 1996 Adams | 107 | 55 | | | 3.31114 | | | 82 | 120 | |
| 2002 Euler | 30 | 44 | 188 | 47 | 5.99264 | 7 | 2 | | 85 | |
| 2094 Magnitka | 107 | 57 | 272 | 48 | 6.11219 | | | 25 | 84 | |
| 2510 Shandong | 256 | 27 | 71 | 27 | 5.94639 | 4 | 1 | | 132 | |
| 2606 Odessa | 25 | −81 | 283 | −88 | 8.2444 | 3 | 1 | 25 | 129 | |
| 2709 Sagan | 302 | −14 | 124 | −35 | 5.25636 | 6 | 2 | | 160 | |
| 2839 Annette | 341 | −49 | 154 | −36 | 10.4609 | 8 | 1 | | 99 | |
| 2957 Tatsuo | 81 | 45 | 248 | 32 | 6.82043 | 13 | 1 | 33 | 102 | |
| 2991 Bilbo | 277 | 54 | 90 | 51 | 4.06175 | 3 | 1 | | 97 | |
| 3722 Urata | 260 | −22 | 77 | −9 | 5.5671 | 10 | 3 | | 70 | |
| 4954 Eric | 86 | −54 | | | 12.05207 | 7 | 2 | | 68 | |
| 5281 Lindstrom | 238 | −72 | 84 | −81 | 9.2511 | 2 | 1 | | 76 | |
| 7517 1989 AD | 314 | −60 | 123 | −51 | 9.7094 | 4 | 1 | | 81 | |
| 8132 Vitginzburg | 33 | −66 | 193 | −48 | 7.27529 | 3 | 1 | | 100 | |
| 8359 1989 WD | 121 | −68 | 274 | −68 | 2.89103 | 6 | 1 | | 105 | |
| 10772 1990 YM | 16 | 46 | | | 68.82 | 5 | 1 | | 73 | |
| 31383 1998 $XJ_{94}$ | 110 | −74 | 279 | −63 | 4.16818 | 4 | 1 | | 71 | |
| 52820 1998 $RS_2$ | 228 | −57 | 58 | −48 | 2.13412 | 1 | 1 | | 45 | |
| 57394 2001 $RD_{84}$ | 65 | 68 | 241 | 59 | 6.7199 | 4 | 1 | | 47 | |

**Table 2.** List of new asteroid models derived from the Catalina Sky Survey data alone.

| Asteroid | $\lambda_1$ [deg] | $\beta_1$ [deg] | $\lambda_2$ [deg] | $\beta_2$ [deg] | $P$ [h] | $N_{703}$ | $P_{\rm publ}$ [h] | Period reference |
|---|---|---|---|---|---|---|---|---|
| 2112 Ulyanov | 156 | 48 | 334 | 65 | 3.04071 | 118 | 3.000 | Maleszewski & Clark (2004) |
| 2384 Schulhof | 196 | −60 | 45 | −42 | 3.29367 | 121 | 3.294 | Ditteon et al. (2002) |
| 2617 Jiangxi | 224 | 76 | 1 | 54 | 11.7730 | 124 | 11.79 | Carbo et al. (2009) |
| 3170 Dzhanibekov | 217 | 60 | 21 | 64 | 6.07168 | 105 | 6.0724 | Molnar et al. (2008) |
| 4507 1990 FV | 143 | 55 | 323 | 49 | 6.57933 | 84 | 6.58 | Yoshida et al. (2005) |
| 5647 1990 TZ | 253 | 77 | 119 | −19 | 6.13867 | 87 | 6.144 | Bembrick & Bolt (2003) |
| 10826 1993 $SK_{16}$ | 260 | −56 | 60 | −34 | 13.8327 | 90 | 13.835 | Galad (2008) |
| 19848 Yeungchuchiu | 190 | −68 | | | 3.45104 | 104 | 3.450 | Yeung (2006) |
| 3097 Tacitus | 229 | 71 | 72 | 62 | 8.7759 | 99 | | |
| 4611 Vulkaneifel | 5 | −86 | 197 | −50 | 3.75635 | 148 | | |
| 5461 Autumn | 249 | −26 | 79 | −43 | 20.0929 | 106 | | |
| 5625 1991 $AO_2$ | 265 | −52 | 97 | −78 | 6.67411 | 110 | | |
| 5960 Wakkanai | 226 | −69 | 69 | −61 | 4.96286 | 102 | | |
| 7201 Kuritariku | 22 | 67 | 249 | 64 | 48.849 | 103 | | |
| 7632 Stanislav | 234 | −50 | 46 | −45 | 5.29073 | 99 | | |
| 7905 Juzoitami | 105 | −76 | 226 | −55 | 2.72744 | 118 | | |
| 13002 1982 $BJ_{13}$ | 58 | −50 | 245 | −57 | 3.13844 | 110 | | |
| 16009 1999 $CM_8$ | 283 | 44 | | | 8.3476 | 124 | | |
| 16847 Sanpoloamosciano | 91 | −24 | | | 8.1845 | 114 | | |
| 26792 1975 LY | 226 | 68 | | | 79.15 | 140 | | |

**Notes.** For each asteroid, the table gives the ecliptic coordinates $\lambda_1$ and $\beta_1$ of the pole solution, the corresponding mirror solution $\lambda_2$ and $\beta_2$, the sidereal rotational period $P$, the number of sparse data points from the CSS $N_{703}$, and the previously published period value $P_{\rm publ}$ with the reference. The uncertainty of the sidereal rotational period corresponds to the last decimal place of $P$ and of the pole direction to 20–40°.

### 2.3. Models based on data from the Catalina Sky Survey astrometric project

There are two different groups of asteroid models based on CSS data: (i) models with previously reported synodic periods determined from dense data (we did not have these dense data, so period values were taken from the literature, usually from the Minor Planet Lightcurve Database); and (ii) models with previously unknown rotational periods. In the first case, we could compare the published period value with the period value derived by the LI (see Table 2, Cols. 7 and 9). If both periods agreed within their uncertainties, we considered the solution reliable. This test could not be performed for the second group of models, so we had to use additional reliability tests (see Sect. 2.1).

In Table 2, we present 20 asteroid models based only on the CSS data. The previous period estimates were not available for 12 of them. All of these 20 models have higher uncertainties of the pole orientations and lower shape resolution than models based on combined data, and all are possible candidates for follow-up lightcurve observations for period confirmation and more detailed shape determination.

## 3. Semi-empirical scaling of the YORP effect

Our enlarged sample of physical parameters for ~330 asteroids[11] validates our previous results based on a smaller asteroid sample (220 asteroids) presented in Hanuš et al. (2011). In Fig. 4, we show the observed *debiased* (i.e., we removed the systematic effect of the lightcurve inversion method caused by the method having a higher probability of deriving a unique solution for asteroids with larger pole latitudes. The debiasing procedure was based on a numerical simulation presented in Hanuš et al. 2011, see Sect. 4.3 there) latitude distributions of pole directions for main-belt asteroids with diameters $D < 30$ km and $D > 60$ km. The population of larger asteroids ($D > 60$ km) exhibits an excess of prograde rotators, probably of primordial origin (predicted also from numerical simulations by Johansen & Lacerda 2010). On the other hand, smaller asteroids ($D < 30$ km) have a clearly bimodal latitude distribution – most of the asteroids have ecliptic pole latitudes > 53°.

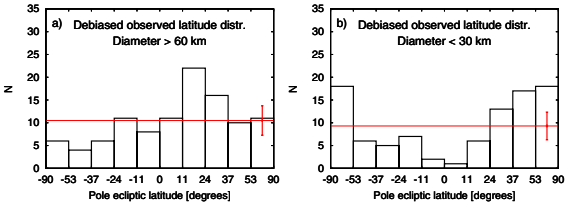


**Fig. 4.** Debiased observed latitude distribution of main-belt asteroids with diameters $D > 60$ km (*left panel*) and $D < 30$ km (*right panel*). The latitude bins are equidistant in $\sin\beta$. The thin horizontal line corresponds to the average value $\bar{N}$ and the errorbar to $\sqrt{\bar{N}}$.

The debiased observed latitude distribution of the pole directions of MBAs represents fingerprints from the past evolution of this population. Direct comparison between the observed asteroid properties and predictions of theoretical models can validate/exclude some of the asteroid dynamical evolution theories or constrain specific free parameters.

In Hanuš et al. (2011), we introduced a simple dynamical model for the spin evolution of asteroids, where we included (i) the YORP thermal effect; (ii) random reorientations induced by noncatastrophic collisions; (iii) oscillations caused by gravitational torques and spin-orbital resonances; and also (iv) mass shedding when a critical rotational frequency is reached. Because we studied a large statistical sample of

[11] According to the asteroid size distribution function of Davis et al. (2002), we have in our sample ~30% of all asteroids with $D > 100$ km, ~15% asteroids with 60 km < $D$ < 100 km, and ~14% asteroids with 30 km < $D$ < 60 km.

asteroids, the effect on the overall latitude distribution of pole directions caused by other processes (gravitational torques by the Sun, damping, or tumbling) was assumed to be only minor.

The model was based on the relations for the rate of the angular velocity $\omega$ ($\omega = 2\pi/P$) and the obliquity $\epsilon$ (Euler equations)

$$\frac{\mathrm{d}\omega}{\mathrm{d}t} = c f_i(\epsilon), \qquad i = 1 \ldots 200, \tag{1}$$

$$\frac{\mathrm{d}\epsilon}{\mathrm{d}t} = \frac{c g_i(\epsilon)}{\omega}, \tag{2}$$

where $f$- and $g$-functions describing the YORP effect for a set of 200 shapes with the effective radius $R_0 = 1$ km, the bulk density $\rho_0 = 2500\,\mathrm{kg/m^3}$, located on a circular orbit with the semi-major axis $a_0 = 2.5$ AU, were calculated numerically by Čapek & Vokrouhlický (2004). We assigned one of the artificial shapes (denoted by the index $i$) for each individual asteroid from our sample[12]. The $f$- and $g$-functions were scaled by a factor

$$c = c_{\mathrm{YORP}} \left(\frac{a}{a_0}\right)^{-2} \left(\frac{R}{R_0}\right)^{-2} \left(\frac{\rho_{\mathrm{bulk}}}{\rho_0}\right)^{-1}, \tag{3}$$

where $a$, $R$, $\rho_{\mathrm{bulk}}$ denote the semi-major axis, the radius, and the density of the simulated body, respectively, and $c_{\mathrm{YORP}}$ is a *free* scaling parameter reflecting our uncertainty in the shape models and the magnitude of the YORP torque, which dependents on small-sized surface features (even boulders, Statler 2009) and other simplifications in the modeling of the YORP torque.

We enhanced the simulation of the spin evolution of asteroids presented in Hanuš et al. (2011), by testing different values of the free parameter $c_{\mathrm{YORP}}$ and comparing the resulting synthetic latitude distributions with the observed debiased latitude distributions. Thanks to the new asteroid models, we had an updated observed spin vector distribution. We added 50% more observed asteroids, so we used 307 instead of 220 models for this comparison.

We used the following values of the parameter $c_{\mathrm{YORP}}$: 0.01, 0.05, 0.1, 0.2, 0.3, 0.4, 0.5, 0.6, 0.8. Values of $c_{\mathrm{YORP}} \gtrsim 1$ were already recognized as unrealistic.

For each value of $c_{\mathrm{YORP}}$, we ran 100 simulations with different random seeds to generate different initial $\omega$ and spin vector distributions. We integrated Eqs. (1) and (2) numerically. The time span was 4 Gyr with the time step of the explicit Euler scheme $\Delta t = 10$ Myr. As initial conditions, we assumed a Maxwellian distribution of angular velocities $\omega$ and isotropically distributed spin vectors. We also used $K = 10^{-2}\,\mathrm{W/K/m}$, $\rho_{\mathrm{bulk}} = 2500\,\mathrm{kg/m^3}$.

Every time a critical angular velocity ($\omega_{\mathrm{crit}} = \sqrt{4/3\pi G\rho_{\mathrm{bulk}}}$) was reached for an asteroid, we assumed a mass shedding event, so that we reset the rotational period to a random value from an interval of 2.5, 9 h. We altered the assigned shape, but we kept the sense of the rotation and the orientation of the spin axis. We also included a simple Monte-Carlo model for the spin axis reorientations caused by collisions (with $\tau_{\mathrm{reor}} = B\left(\frac{\omega}{\omega_0}\right)^{\beta_1}\left(\frac{D}{D_0}\right)^{\beta_2}$, where $B = 84.5\,\mathrm{kyr}$, $\beta_1 = 5/6$, $\beta_2 = 4/3$, $D_0 = 2\,\mathrm{m}$, and $\omega_0$ corresponds to period $P = 5$ h, Farinella et al. 1998). After the collision, we reset the spin axis and period to random values (new period was from an interval of 2.5, 9 h). Collisional disruptions are not important in our case so they were not considered.

[12] We did not use the convex-hull shape models derived in this work because the two samples of shapes are believed to be statistically equivalent, and moreover, the YORP effect seems sensitive to small-scale surface structure (Scheeres & Mirrahimi 2007), which cannot be caught by our shape models.

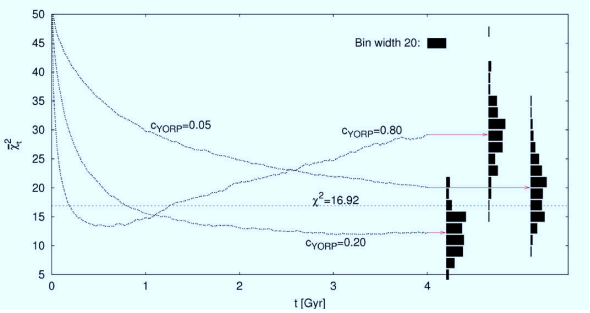


**Fig. 5.** Temporal evolution of the $\chi^2$ that corresponds to the difference between the simulated latitude distributions, averaged over all 100 runs, and the debiased observed latitude distribution (i.e., $\bar{\chi}^2_t$) for three different values of parameter $c_{\mathrm{YORP}} = 0.05$, 0.20, and 0.80 (we performed a chi-square test). Vertical histograms on the righthand side represent the distributions of $\chi^2_{tj}$ at time $t = 4$ Gy for all 100 runs. Dotted line: the statistically significant probability value of 5%, i.e. $\chi^2 = 16.92$.

We also accounted for spin-orbital resonances by adding a sinusoidal oscillation to $\beta$ (to prograde rotators, only, Vokrouhlický et al. 2006b) with a random phase and an amplitude $\simeq 40°$.

The spin states of our synthetic asteroids evolve during the simulation. At each time $t$ of the simulation, we can construct a latitude distribution of the pole directions with the latitude values split into ten bins with a variable width corresponding to constant surface on the celestial sphere. Because we used ecliptic coordinates with the longitude $\lambda$ and the latitude $\beta$, the bins were equidistant in $\sin\beta$. To describe the temporal evolution of the simulated latitude distributions, we computed a $\chi^2$ metric between the simulated and the debiased observed latitude distributions of asteroids with diameters $D < 60$ km. The assumption of isotropically distributed initial spin vectors is not fulfilled for larger asteroids ($D > 60$ km), because this population has an excess of prograde rotators (see Fig. 4), which is believed to have a primordial origin (Johansen & Lacerda 2010). The second reason we rejected asteroids with $D > 60$ km from latitude comparison is that their evolution is rather slow compared to the simulation time span.

For each time $t$ within the simulation run $j$ ($j = 1...100$), the corresponding chi-square value $\chi^2_{tj}$ is defined by

$$\chi^2_{tj} \equiv \sum_i \frac{(S_{tji} - O_i)^2}{\sigma^2_{tji}}, \tag{4}$$

where $S_{tji}$ denotes the number of synthetic bodies with latitudes in bin $i$, $O_i$ the number of observed latitudes in bin $i$, and $\sigma_{tji} \equiv \sqrt{S_{tji} + O_i}$ corresponds to the uncertainty estimate.

In Fig. 5, we show the temporal evolution of the *average* chi-square $\bar{\chi}^2_t = \sum_j \chi^2_{tj}/100$ in the course of our numerical simulations for different $c_{\mathrm{YORP}}$ values. As we see in Fig. 5, the average synthetic latitude distribution evolves in course of the time (while the debiased observed latitude distribution is fixed). We can distinguish three basic cases of the temporal evolution:

– When the YORP effect is weak ($c_{\mathrm{YORP}} \lesssim 0.1$), the synthetic latitude distribution only evolves slowly and is never similar to the observed latitude distribution, even at the end of the simulation, because $\bar{\chi}^2_t$ is still large (for $N = 9$, a statistically significant probability value of 5% corresponds to $\chi^2 = 16.92$).

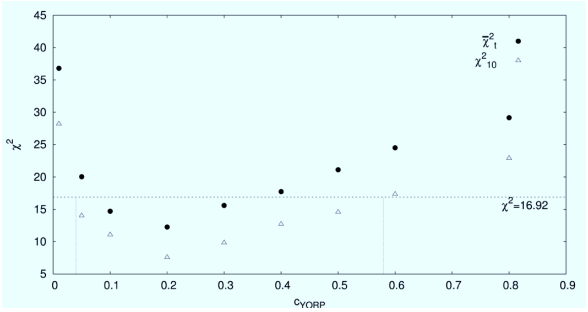


**Fig. 6.** Dependence of $\bar{\chi}^2_t$ and $\chi^2_{10}$ values calculated for the time $t$ = 4 Gyr (i.e. the final state of the simulation) on different values of the $c_{YORP}$ parameter. We also plotted the statistically significant probability value of 5% which corresponds to $\chi^2$ = 16.92 and the interval of plausible $c_{YORP}$ values from 0.05 to 0.6.

- A steady state (i.e., the state when the synthetic latitude distribution does not significantly evolve in time, and thus the $\bar{\chi}^2_t$ is approximately constant) is only reached for $c_{YORP}$ values close to 0.2.
- For values $c_{YORP} \gtrsim 0.3$, the synthetic latitude distribution evolves faster and, at a certain time, is most similar to the observed latitude distribution (i.e., the minimum of $\bar{\chi}^2_t$). After that, the $\bar{\chi}^2_t$ grows, because the YORP significantly develops also larger asteroids, and thus the bins with low latitudes are depopulated more than is observed.

Vertical histograms on the righthand side of Fig. 5 represent the distributions of $\chi^2_{tj}$ at the time $t$ = 4 Gy for all 100 runs. The average chi-square $\bar{\chi}^2_t$ of the model with $c_{YORP}$ = 0.05 is substantially higher than 16.92, so this model can be considered wrong. However, from the distributions of $\chi^2_{tj}$ we can see that about 25% of individual runs have $\chi^2_{tj}$ lower than 16.92. To avoid rejecting those $c_{YORP}$ values that are partially compatible with the observations, we should instead use a more representative value of $\chi^2$ than the average $\bar{\chi}^2_t$, namely a value $\chi^2_{10}$, for which 10% runs have lower $\chi^2_{tj}$ (see Fig. 6). Based on the $\chi^2_{10}$, the most probable values of the $c_{YORP}$ parameter are between 0.05 and 0.6.

## 4. Discusion and conclusions

Our preferred interpretation of the optimal $c_{YORP}$ value being much lower than one is that small-scale features (boulders) tend to decrease the YORP torque. This hypothesis is supported by the independent modeling of Rozitis & Green (2012), who estimate, by including rough surface thermal-infrared beaming effects in their long-term spin evolution model, that the surface roughness is on average responsible for damping the magnitude of the YORP effect typically by half of the smooth surface predictions. This would correspond to $c_{YORP}$ = 0.5 in our notation. The YORP effect is sensitive to the sizes of the boulders and can vary tens of percent, so the results of Rozitis & Green (2012) agree with our model.

As an important application, we mention that the constraint for the value of $c_{YORP}$ can be used in simulations of the long-term dynamical evolution of asteroid families. So far, $c_{YORP}$ has been used as a free parameter (e.g., in the method presented by Vokrouhlický et al. 2006a). Constraining $c_{YORP}$ therefore *removes* one free parameter from the simulations and should thus lead to a better determination of the ages of asteroid families.

Finally, the results of this paper can be briefly summarized as follows.

- For 119 asteroids, we derived the convex shape models and rotational states from their combined disk-integrated dense and sparse photometric data. This effort was achieved with the help of ~100 individual observers who were willing to share their lightcurves. The typical uncertainty of the sidereal rotational period is $\sim 10^{-5}$ h and of the pole direction 10–20°. All new models are now included in the DAMIT database.
- We also derived 20 asteroid models based purely on sparse-in-time photometry from the Catalina Sky Survey Observatory. The reliability of these models is supported by the fact that for eight of them, we obtained similar rotational period values that were previously reported in the literature and derived from an independent data set (dense photometry). We do not have any previous information about the rotational periods for the 12 other asteroids. Due to relatively larger uncertainties of the CSS sparse data, the typical uncertainty of the sidereal rotational period is $\sim 10^{-4}$–$10^{-5}$ h and of the pole direction 20–40°.
- By combining observations of stellar occultations by asteroids with derived convex shape models, we determined equivalent diameters for the asteroids (345) Tercidina, (404) Arcinoe, and (578) Happelia to $96 \pm 10$ km, $101 \pm 5$ km, and $70 \pm 5$ km, respectively.
- We updated a simple dynamical model for the spin evolution of asteroids and compared the synthetic pole latitude distributions to the debiased observed latitude distributions of 307 asteroids. By using several values of the scaling parameter $c_{YORP}$ defined by Eq. (3) (from 0.01 to 0.8), we constrained its value to $c_{YORP} \in [0.05, 0.6]$. We interpreted the low value of $c_{YORP}$ as a result of the surface roughness.

*Acknowledgements.* The work of JH has been supported by grant GA UK 134710 of the Grant agency of the Charles University and by the project SVV 265301 of the Charles University in Prague. The work of J.H. and J.Ď. has been supported by grants GACR 209/10/0537 and P209/12/0229 of the Czech Science Foundation, the work of J.D. and M.B. by the Research Program MSM0021620860 of the Czech Ministry of Education, and the work of MB also by the grant GACR 13-01308S of the Grant Agency of the Czech Republic. The work of TSR was carried out through the Gaia Research for European Astronomy Training (GREAT-ITN) network. He has received funding from the European Union Seventh Framework Program (FP7/2007-2013) under grant agreement no. 264895. This work is partially based on observations made at the South African Astronomical Observatory (SAAO). It was based on observations made with the Nordic Optical Telescope, operated on the island of La Palma jointly by Denmark, Finland, Iceland, Norway, and Sweden, in the Spanish Observatorio del Roque de los Muchachos of the Instituto de Astrofisica de Canarias. This work is partially based on observations carried out with the Pic du Midi Observatory 0.6 m telescope, a facility operated by the Observatoire Midi-Pyrénées and Association T60, an amateur association. The calculations were performed on the computational cluster Tiger at the Astronomical Institute of Charles University in Prague (http://sirrah.troja.mff.cuni.cz/tiger).

## References

Baker, R. E., Pilcher, F., & Klinglesmith III, D. A. 2012, Minor Planet Bulletin, 39, 60
Behrend, R., Roy, R., Rinner, C., et al. 2004, IAU Circ., 8265, 2
Behrend, R., Bernasconi, L., Roy, R., et al. 2006, A&A, 446, 1177
Bembrick, C., & Bolt, G. 2003, Minor Planet Bulletin, 30, 42
Bembrick, C., Crawford, G., Oey, J., & Allen, B. 2007, Minor Planet Bulletin, 34, 67
Brinsfield, J. W. 2008a, Minor Planet Bulletin, 35, 179
Brinsfield, J. W. 2008b, Minor Planet Bulletin, 35, 86
Brinsfield, J. W. 2009, Minor Planet Bulletin, 36, 169
Buchheim, R. K. 2005, Minor Planet Bulletin, 32, 35
Buchheim, R. K. 2007, Minor Planet Bulletin, 34, 68

Buchheim, R. K. 2010, Minor Planet Bulletin, 37, 41
Buchheim, R. K., Conjat, M., Roy, R., Baudoin, P., & Behrend, R. 2004, Minor Planet Bulletin, 31, 90
Čapek, D., & Vokrouhlický, D. 2004, Icarus, 172, 526
Carbo, L., Kragh, K., Krotz, J., et al. 2009, Minor Planet Bulletin, 36, 91
Davis, D. R., Durda, D. D., Marzari, F., Campo Bagatin, A., & Gil-Hutton, R. 2002, Asteroids III, 545
Ditteon, R., Bixby, A. R., Sarros, A. M., & Waters, C. T. 2002, Minor Planet Bulletin, 29, 69
Ďurech, J., & Kaasalainen, M. 2003, A&A, 404, 709
Ďurech, J., Scheirich, P., Kaasalainen, M., et al. 2007, in IAU Symp., 236, eds. G. B. Valsecchi, D. Vokrouhlický, & A. Milani, 191
Ďurech, J., Kaasalainen, M., Warner, B. D., et al. 2009, A&A, 493, 291
Ďurech, J., Sidorin, V., & Kaasalainen, M. 2010, A&A, 513, A46
Ďurech, J., Kaasalainen, M., Herald, D., et al. 2011, Icarus, 214, 652
Farinella, P., Vokrouhlicky, D., & Hartmann, W. K. 1998, Icarus, 132, 378
Galad, A. 2008, Minor Planet Bulletin, 35, 128
Hanuš, J., & Ďurech, J. 2012, Planet. Space Sci., 73, 75
Hanuš, J., Ďurech, J., Brož, M., et al. 2011, A&A, 530, A134
Higgins, D. 2008, Minor Planet Bulletin, 35, 30
Higgins, D., & Goncalves, R. M. D. 2007, Minor Planet Bulletin, 34, 16
Higgins, D., & Warner, B. D. 2009, Minor Planet Bulletin, 36, 159
Higgins, D., Pravec, P., Kusnirak, P., et al. 2006, Minor Planet Bulletin, 33, 89
Higgins, D., Pravec, P., Kusnirak, P., et al. 2008, Minor Planet Bulletin, 35, 123
Johansen, A., & Lacerda, P. 2010, MNRAS, 404, 475
Kaasalainen, M., & Torppa, J. 2001, Icarus, 153, 24
Kaasalainen, M., Torppa, J., & Muinonen, K. 2001, Icarus, 153, 37
Kaasalainen, M., Torppa, J., & Piironen, J. 2002, Icarus, 159, 369
Koff, R. A., & Brincat, S. M. 2000, Minor Planet Bulletin, 27, 49
Kryszczyńska, A., La Spina, A., Paolicchi, P., et al. 2007, Icarus, 192, 223
Lagerkvist, C., Barucci, M. A., Capria, M. T., et al. 1987, Asteroid photometric catalogue, eds. C.-I. Lagerkvist, M. A. Barucci, M. T. Capria, et al.
Larson, S., Beshore, E., Hill, R., et al. 2003, in BAAS, 35, AAS/Division for Planetary Sciences Meeting Abstracts #35, 982
López-González, M. J., & Rodríguez, E. 2000, A&AS, 145, 255
Maleszewski, C., & Clark, M. 2004, Minor Planet Bulletin, 31, 93
Marciniak, A., Michałowski, T., Kaasalainen, M., et al. 2007, A&A, 473, 633
Marciniak, A., Michałowski, T., Kaasalainen, M., et al. 2008, A&A, 478, 559
Michałowski, T. 1996, Icarus, 123, 456
Michałowski, T., Pych, W., Kwiatkowski, T., et al. 2001, A&A, 371, 748
Michałowski, T., Kwiatkowski, T., Kaasalainen, M., et al. 2004, A&A, 416, 353
Molnar, L. A., Haegert, J. M., Beaumont, C. N., et al. 2008, Minor Planet Bulletin, 35, 9
Oey, J. 2008, Minor Planet Bulletin, 35, 132
Oey, J. 2009, Minor Planet Bulletin, 36, 4
Oey, J., & Krajewski, R. 2008, Minor Planet Bulletin, 35, 47
Oey, J., Behrend, R., Pravec, P., et al. 2007, Minor Planet Bulletin, 34, 2
Piironen, J., Lagerkvist, C., Torppa, J., Kaasalainen, M., & Warner, B. 2001, in BAAS, 33, 1562
Pilcher, F. 2008, Minor Planet Bulletin, 35, 135
Pilcher, F. 2009a, Minor Planet Bulletin, 36, 133
Pilcher, F. 2009b, Minor Planet Bulletin, 36, 25
Pilcher, F. 2009c, Minor Planet Bulletin, 36, 100
Pilcher, F. 2010, Minor Planet Bulletin, 37, 119
Pilcher, F. 2011a, Minor Planet Bulletin, 38, 183
Pilcher, F. 2011b, Minor Planet Bulletin, 38, 76
Pilcher, F., & Brinsfield, J. W. 2011, Minor Planet Bulletin, 38, 206
Pilcher, F., Benishek, V., & Oey, J. 2009, Minor Planet Bulletin, 36, 68
Polishook, D. 2012, Minor Planet Bulletin, 39, 242
Polishook, D., & Brosch, N. 2008, Icarus, 194, 111
Polishook, D., & Brosch, N. 2009, Icarus, 199, 319
Polishook, D., Ofek, E. O., Waszczak, A., et al. 2012, MNRAS, 421, 2094
Pravec, P., Scheirich, P., Vokrouhlický, D., et al. 2012, Icarus, 218, 125
Rau, A., Kulkarni, S. R., Law, N. M., et al. 2009, PASP, 121, 1334
Rozitis, B., & Green, S. F. 2012, MNRAS, 423, 367
Rubincam, D. P. 2000, Icarus, 148, 2
Ruthroff, J. C. 2010, Minor Planet Bulletin, 37, 102
Scheeres, D. J., & Mirrahimi, S. 2007, in BAAS, 38, 416
Statler, T. S. 2009, Icarus, 202, 502
Stephens, R. D. 2005a, Minor Planet Bulletin, 32, 82
Stephens, R. D. 2005b, Minor Planet Bulletin, 32, 2
Stephens, R. D. 2008, Minor Planet Bulletin, 35, 126
Stephens, R. D. 2009a, Minor Planet Bulletin, 36, 59
Stephens, R. D. 2009b, Minor Planet Bulletin, 36, 18
Svoren, J., Husarik, M., Ambroz, J., Drbohlav, J., & Medek, J. 2009, Earth Moon and Planets, 105, 361
Vokrouhlický, D., Brož, M., Morbidelli, A., et al. 2006a, Icarus, 182, 92
Vokrouhlický, D., Nesvorný, D., & Bottke, W. F. 2003, Nature, 425, 147
Vokrouhlický, D., Nesvorný, D., & Bottke, W. F. 2006b, Icarus, 184, 1
Warner, B. D. 2004, Minor Planet Bulletin, 31, 85
Warner, B. D. 2005a, Minor Planet Bulletin, 32, 90
Warner, B. D. 2005b, Minor Planet Bulletin, 32, 4
Warner, B. D. 2006a, Minor Planet Bulletin, 33, 58
Warner, B. D. 2006b, Minor Planet Bulletin, 33, 35
Warner, B. D. 2007, Minor Planet Bulletin, 34, 72
Warner, B. D. 2008a, Minor Planet Bulletin, 35, 56
Warner, B. D. 2008b, Minor Planet Bulletin, 35, 163
Warner, B. D. 2009a, Minor Planet Bulletin, 36, 109
Warner, B. D. 2009b, Minor Planet Bulletin, 36, 172
Warner, B. D. 2011a, Minor Planet Bulletin, 38, 52
Warner, B. D. 2011b, Minor Planet Bulletin, 38, 63
Warner, B. D. 2011c, Minor Planet Bulletin, 38, 96
Warner, B. D., Harris, A. W., & Pravec, P. 2009, Icarus, 202, 134
Yeung, K. W. 2006, Minor Planet Bulletin, 33, 49
Yoshida, F., Dermawan, B., Nakamura, T., et al. 2005, Abstr. IAU Symp., 229, 82

[1] Astronomical Institute, Faculty of Mathematics and Physics, Charles University in Prague, V Holešovičkách 2, 18000 Prague, Czech Republic
e-mail: hanus.home@gmail.com
[2] Astronomical Observatory Institute, Faculty of Physics, A. Mickiewicz University, Słoneczna 36, 60-286 Poznań, Poland
[3] Palmer Divide Observatory, 17995 Bakers Farm Rd., Colorado Springs, CO 80908, USA
[4] 4438 Organ Mesa Loop, Las Cruces, NM 88011, USA
[5] Goat Mountain Astronomical Research Station, 11355 Mount Johnson Court, Rancho Cucamonga, CA 91737, USA
[6] Geneva Observatory, 1290 Sauverny, Switzerland
[7] European Space Astronomy Centre, Spain, PO Box 78, 28691 Villanueva de la Cañada, Madrid, Spain
[8] Astronomical Institute of the Academy of Sciences, Fričova 298, 25165 Ondřejov, Czech Republic
[9] Observatoire de Bédoin, 47 rue Guillaume Puy, 84000 Avignon, France
[10] Observatoire de Chinon, Mairie de Chinon, 37500 Chinon, France
[11] Courbes de rotation d'astéroïdes et de comètes, CdR
[12] Association T60, 14 avenue Édouard Belin, 31400 Toulouse, France
[13] Harfleur, France
[14] Observatoire des Engarouines, 84570 Mallemort-du-Comtat, France
[15] Collonges Observatory, 90 allée des résidences, 74160 Collonges, France
[16] Paris and Saint-Savinien, France
[17] 139 Antibes, France
[18] Via M. Rosa, 1, 00012 Colleverde di Guidonia, Rome, Italy
[19] 947 Saint-Sulpice, France
[20] IMCCE – Paris Observatory – UMR 8028 CNRS, 77 Av. Denfert-Rochereau, 75014 Paris, France
[21] A90 San Gervasi, Spain
[22] l'Observatoire de Cabris, 408 chemin Saint Jean Pape, 06530 Cabris, France
[23] 929 Blackberry Observatory, USA
[24] Plateau du Moulin à Vent, St-Michel l'Observatoire, France
[25] J80 Saint-Hélène, France
[26] B13 Tradate, Italy
[27] 138 Village-Neuf, France
[28] TASS = The Amateur Sky Survey
[29] Shed of Science Observatory, 5213 Washburn Ave. S, Minneapolis, MN 55410, USA
[30] Association AstroQueyras, 05350 Saint-Véran, France
[31] Association des Utilisateurs de Détecteurs Électroniques (AUDE), France
[32] Observatoire du Bois de Bardon, 16110 Taponnat, France
[33] Dark Cosmology Centre, Niels Bohr Institute, University of Copenhagen, Juliane Maries Vej 30, 2100 Copenhagen, Denmark
[34] Nordic Optical Telescope, Apartado 474, 38700 Santa Cruz de La Palma, Santa Cruz de Tenerife, Spain
[35] Hamanowa Astronomical Observatory, Hikarigaoka 4–34, Motomiya, Fukushima, Japan

[36] Institute of Planetary Research, German Aerospace Center, Rutherfordstrasse 2, 12489, Berlin, Germany
[37] Hunters Hill Observatory, 7 Mawalan Street, Ngunnawal ACT 2913, Australia
[38] 056 Skalnaté Pleso, Slovakia
[39] A83 Jakokoski, Finland
[40] Astrophysics Division, Institute of Physics, Jan Kochanowski University, Świętokrzyska 15, 25–406 Kielce, Poland
[41] Université de Toulouse, UPS-OMP, IRAP, 31400 Toulouse, France
[42] CNRS, IRAP, 14 avenue Édouard Belin, 31400 Toulouse, France
[43] 980 Antelope Drive West, Bennett, CO 80102, USA
[44] LESIA-Observatoire de Paris, CNRS, UPMC Univ. Paris 06, Univ. Paris-Diderot, 5 place Jules Janssen, 92195 Meudon, France
[45] Stazione Astronomica di Sozzago, 28060 Sozzago, Italy
[46] Forte Software, Os. Jagiełły 28/28 60-694 Poznań, Poland
[47] SUPA (Scottish Universities Physics Alliance), Institute for Astronomy, University of Edinburgh, Royal Observatory, Edinburgh, EH9 3HJ, UK
[48] Club d'Astronomie Lyon Ampère, 37 rue Paul Cazeneuve, 69008 Lyon, France
[49] 174 Nyrölä, Finland
[50] Observatorio Montcabre, C/Jaume Balmes 24, 08348 Cabrils, Barcelona, Spain
[51] Observatori Astronómico de Mallorca, Camí de l'Observatori, s/n 07144 Costitx, Mallorca, Spain
[52] Kingsgrove, NSW, Australia
[53] Mt. Suhora Observatory, Pedagogical University, Podchorążych 2, 30-084, Cracow, Poland
[54] University of Helsinki, Department of Physics, PO Box 64, 00014 Helsinki
[55] Department of Earth, Atmospheric, and Planetary Sciences, Massachusetts Institute of Technology, Cambridge, MA 02139, USA
[56] 2 rue des Écoles, 34920 Le Crès, France
[57] F.-X. Bagnoud Observatory, 3961 St.-Luc, Switzerland
[58] Blauvac Observatory, 84570 St.-Estéve, France
[59] Observatoire de la Côte d'Azur, BP 4229, 06304 Nice Cedex 4, France
[60] Observatoire de Paris-Meudon, LESIA, 92190 Meudon, France
[61] 143 Gnosca, Switzerland
[62] DeKalb Observatory, 2507 CR 60, Auburn, IN 46706, USA
[63] 181 Les Makes, la Réunion, France
[64] CNRS-LKB-École Normale Supérieure – UMR 8552 – 24 rue Lhomond, 75005 Paris, France
[65] ANS Collaboration, c/o Osservatorio Astronomico di Padova, Sede di Asiago, 36032 Asiago (VI), Italy
[66] Institute of Astronomy, Karazin Kharkiv National University, Sums'ka 35, 61022 Kharkiv, Ukraine
[67] Observatoire Francois-Xavier Bagnoud, 3961 St.-Luc, Switzerland

Pages 11 to 16 are available in the electronic edition of the journal at http://www.aanda.org

**Table 3.** Observations used for the successful model determinations that are not included in the UAPC.

| Asteroid | Date | Observer | Observatory (MPC code) |
|---|---|---|---|
| 11 Parthenope | 2008 5–2008 9 | Warner | Palmer Divide Observatory (716) |
| | 2008 7–2008 7 | Pilcher[b] | Organ Mesa Observatory (G50) |
| | 2009 11–2010 1 | Pilcher (2010) | |
| | 2011 2–2011 5 | Pilcher (2011a) | |
| | 2011 3–2011 3 | Audejean | Observatoire de Chinon, France (B92) |
| | 2011 4–2011 4 | Naves | Observatorio Montcabre (213) |
| 25 Phocaea | 2006 10–2006 10 | Buchheim | Altimira Observatory, USA (G76) |
| | 2006 10 21.9 | Strajnic, Grangeon, Coupier, Godon, Roche Danavaro, Dalmas, Bayol, Behrend | Haute-Provence Observatory, France (511) |
| | 2008 1–2009 4 | Pilcher (2009a) | |
| | 2010 9–2010 12 | Pilcher (2011b) | |
| 72 Feronia | 2004 3–2004 4 | Bernasconi | Les Engarouines Observatory, France (A14) |
| | 2005 7–2005 8 | Bernasconi | Les Engarouines Observatory, France (A14) |
| | 2007 1 20.9 | Coliac | Observatoire Farigourette, France |
| | 2011 3–2011 4 | Marciniak | Borowiec, Poland (187) |
| | 2011 5 9.9 | Hirsch | Borowiec, Poland (187) |
| 147 Protogeneia | 2004 11–2004 12 | Buchheim (2005) | |
| | 2005 1 4.9 | Roy | Blauvac Observatory, France (627) |
| | 2005 1–2005 1 | Bernasconi | Les Engarouines Observatory, France (A14) |
| | 2008 5 29.7 | Higgins[a] | Hunters Hill Observatory, Ngunnawal (E14) |
| 149 Medusa | 2010 10–2010 11 | Pilcher (2011b) | |
| | 2010 11–2010 12 | Martin | Tzec Maun Observatory, Mayhill (H10) |
| 157 Dejanira | 2005 3–2005 3 | Poncy | Le Crés, France (177) |
| | 2005 4–2005 5 | Warner (2005a) | |
| | 2008 12–2009 2 | Pilcher (2009c) | |
| 166 Rhodope | 2010 12–2011 1 | Conjat | Cabris, France |
| 178 Belisana | 2007 4-2007 7 | Oey & Krajewski (2008) | |
| | 2008 9–2008 10 | Pilcher et al. (2009) | |
| 183 Istria | 2004 2 14.1 | Bernasconi | Les Engarouines Observatory, France (A14) |
| 193 Ambrosia | 2009 4–2009 4 | Warner (2009b) | |
| | 1999 10 15.0 | Hirsch | Borowiec, Poland (187) |
| | 2005 4–2005 4 | Kaminski | Borowiec, Poland (187) |
| | 2005 4 3.9 | Marciniak | Borowiec, Poland (187) |
| | 2005 4–2005 4 | Hirsch | Borowiec, Poland (187) |
| | 2009 3–2009 3 | Audejean | Observatoire de Chinon, France (B92) |
| | 2009 4–2009 5 | Hirsch | Borowiec, Poland (187) |
| | 2009 4 29.9 | Kaminski | Borowiec, Poland (187) |
| | 2010 4 19.1 | Borczyk | SAAO, Sutherland, South Africa |
| 199 Byblis | 2003 3–2003 4 | Casulli | Vallemare di Bordona, Italy (A55) |
| | 2003 5–2003 5 | Bernasconi | Les Engarouines Observatory, France (A14) |
| | 2005 10–2005 10 | Roy | Blauvac Observatory, France (627) |
| | 2005 10–2005 10 | Casulli | Vallemare di Bordona, Italy (A55) |
| | 2005 11–2005 11 | Stoss, Nomen, Sanchez, Behrend | OAM, Mallorca (620) |
| | 2005 11 20.9 | Farroni | |
| | 2006 12–2006 12 | Roy | Blauvac Observatory, France (627) |
| | 2008 2 9.1 | Manzini | Stazione Astronomica di Sozzago, Italy (A12) |
| | 2011 9 24.1 | Sobkowiak | Borowiec, Poland (187) |
| | 2011 11–2011 11 | Marciniak | Borowiec, Poland (187) |
| 220 Stephania | 2004 10–2004 10 | Koff | Antelope Hills Observatory, Bennett (H09) |
| 222 Lucia | 1999 4 18.2 | Warner | Palmer Divide Observatory (716) |
| | 2008 12–2008 12 | Stephens (2009a) | |
| | 2010 4–2010 5 | Audejean | Observatoire de Chinon, France (B92) |
| | 2010 4–2010 4 | Bosch | Collonges Observatory, France (178) |
| 242 Kriemhild | 2004 7–2004 7 | Bosch | Collonges Observatory, France (178) |
| | 2004 8–2004 8 | Warner (2005b) | |
| | 2004 9–2004 9 | Rinner | Ottmarsheim Observatory, France (224) |
| | 2005 11 7.9 | Roy | Blauvac Observatory, France (627) |
| | 2007 1–2007 1 | Bembrick et al. (2007) | |
| | 2009 8–2009 8 | Audejean | Observatoire de Chinon, France (B92) |
| | 2010 8–2011 3 | Marciniak | Borowiec, Poland (187) |
| | 2010 10 10.1 | T. Michałowski | Borowiec, Poland (187) |
| | 2011 11–2012 1 | Marciniak | Borowiec, Poland (187) |
| | 2011 11 13.1 | Sobkowiak | Borowiec, Poland (187) |

**Notes.** [(a)] On line at http://www.david-higgins.com/Astronomy/asteroid/lightcurves.htm; [(b)] On line at http://aslc-nm.org/Pilcher.html; [(c)] Observations, reductions, and calibration methods are described in Polishook & Brosch (2008, 2009).

**Table 3.** continued.

| Asteroid | Date | Observer | Observatory (MPC code) |
|---|---|---|---|
| 257 Silesia | 2004 12–2004 12 | Casulli, Behrend | Vallemare di Bordona, Italy (A55) |
| | 2004 12–2005 1 | Roy | Blauvac Observatory, France (627) |
| | 2005 1 31.1 | Starkey | DeKalb Observatory, USA (H63) |
| | 2005 12 1.1 | Strajnic, Paulo, Wagrez, Jade, Rocca, Del Freo, Behrend | Haute-Provence Observatory, France (511) |
| | 2005 12–2006 1 | Roy | Blauvac Observatory, France (627) |
| | 2005 12–2005 12 | Antonini | Observatoire de Bédoin, France (132) |
| 260 Huberta | 2005 3–2005 3 | Roy | Blauvac Observatory, France (627) |
| | 2007 7–2007 8 | Roy | Blauvac Observatory, France (627) |
| 272 Antonia | 2007 12–2008 1 | Pilcher (2008) | |
| | 2011 10–2011 10 | S. Fauvaud, M. Fauvaud | Observatoire du Bois de Bardon, France |
| 281 Lucretia | 2011 10–2011 10 | S.Fauvaud, M. Fauvaud | Observatoire du Bois de Bardon, France |
| 290 Bruna | 2008 3–2008 4 | Pilcher (2009b) | |
| 297 Caecilia | 2004 11–2004 12 | Roy | Blauvac Observatory, France (627) |
| | 2006 1–2006 1 | Manzini | Stazione Astronomica di Sozzago, Italy (A12) |
| | 2006 1 11.0 | Antonini | Observatoire de Bédoin, France (132) |
| | 2006 1 13.1 | Roy | Blauvac Observatory, France (627) |
| | 2009 12 11.8 | Salom, Esteban | Caimari (B81) |
| | 2011 2–2011 3 | Marciniak | Borowiec, Poland (187) |
| | 2012 1 30.2 | Marciniak | Borowiec, Poland (187) |
| | 2012 1 31.2 | Polinska | Borowiec, Poland (187) |
| | 2012 2–2012 3 | Hirsch | Borowiec, Poland (187) |
| 345 Tercidina | 2002 9–2002 10 | Barbotin | Villefagnan Observatory, France |
| | 2002 9–2002 12 | Bernasconi | Les Engarouines Observatory, France (A14) |
| | 2002 9–2002 10 | Rinner | Ottmarsheim Observatory, France (224) |
| | 2002 9–2002 9 | Starkey, Bernasconi | Les Engarouines Observatory, France (A14) |
| | 2002 9–2002 9 | Waelchli, Revaz | F.-X. Bagnoud Observatory, Switzerland (175) |
| | 2002 10 1.1 | Michelet | |
| | 2002 10 5.2 | Barbotin | Villefagnan Observatory, France |
| | 2002 11 22.9 | Bosch | Collonges Observatory, France (178) |
| | 2002 11-2002 12 | Starkey | DeKalb Observatory, USA (H63) |
| | 2004 4–2004 5 | Bernasconi | Les Engarouines Observatory, France (A14) |
| | 2004 4–2004 5 | Roy | Blauvac Observatory, France (627) |
| | 2005 8–2005 8 | Bernasconi | Les Engarouines Observatory, France (A14) |
| | 2005 8 27.0 | Stoss, Nomen, Sanchez, Behrend | OAM, Mallorca (620) |
| | 2005 9 8.0 | Farroni | |
| | 2008 7 5.0 | Trégon, Leroy | Pic du Midi Observatory (586) |
| | 2009 8–2009 10 | Naves | Observatorio Montcabre (213) |
| | 2011 4 22.9 | Sobkowiak | Borowiec, Poland (187) |
| 352 Gisela | 2002 10 8.7 | Droege | |
| | 2004 2 13.1 | Bernasconi, Klotz, Behrend | Haute-Provence Observatory, France (511) |
| | 2005 7–2005 8 | Bernasconi | Les Engarouines Observatory, France (A14) |
| 371 Bohemia | 2001 6–2004 3 | Buchheim et al. (2004) | |
| | 2006 9 2.0 | Bernasconi | Les Engarouines Observatory, France (A14) |
| | 2011 8–2011 11 | Marciniak | Borowiec, Poland (187) |
| | 2011 11 2.9 | W. Ogłoza | Mnt. Suhora, Poland |
| | 2011 11 30.9 | Santana-Ros | Borowiec, Poland (187) |
| 390 Alma | 2004 8–2004 8 | Stephens (2005b) | |
| | 2008 8–2008 10 | Roy | Blauvac Observatory, France (627) |
| 403 Cyane | 2001 12 9.1 | Brunetto | Le Florian, France (139) |
| | 2001 12–2001 12 | Bernasconi | Les Engarouines Observatory, France (A14) |
| | 2001 12 22.2 | Cooney | |
| | 2005 10 1.0 | Bernasconi | Les Engarouines Observatory, France (A14) |
| | 2007 2–2007 2 | Roy | Blauvac Observatory, France (627) |
| 404 Arsinoe | 1999 3–1999 4 | Kryszczynska | Borowiec, Poland (187) |
| | 1999 3 19.0 | Hirsch | Borowiec, Poland (187) |
| | 1999 3 20.0 | T. Michałowski | Borowiec, Poland (187) |
| | 2001 10–2001 10 | S. Fauvaud, Heck, Santacana, Wucher | Pic de Château-Renard Observatory |
| | 2001 11–2001 12 | Bernasconi | Les Engarouines Observatory, France (A14) |
| | 2003 4–2003 4 | Roy | Blauvac Observatory, France (627) |
| | 2005 8 10.1 | Fagas | Borowiec, Poland (187) |
| | 2005 10–2005 10 | Hirsch | Borowiec, Poland (187) |
| | 2005 10–2005 11 | Roy | Blauvac Observatory, France (627) |
| | 2006 11–2007 1 | Fagas | Borowiec, Poland (187) |
| | 2007 1–2007 4 | Marciniak | Borowiec, Poland (187) |
| | 2007 2 17.0 | Hirsch | Borowiec, Poland (187) |

**Table 3.** continued.

| Asteroid | Date | Observer | Observatory (MPC code) |
|---|---|---|---|
| | 2007 4–2007 4 | Kaminski | Borowiec, Poland (187) |
| | 2007 4 22.0 | Kankiewicz | Kielce, Poland (B02) |
| | 2008 6–2008 6 | Marciniak | SAAO, Sutherland, South Africa |
| | 2009 8–2009 10 | Marciniak | SAAO, Sutherland, South Africa |
| | 2009 9 27.0 | Hirsch | Borowiec, Poland (187) |
| | 2009 10 30.0 | Polinska | Borowiec, Poland (187) |
| | 2009 12 3.0 | Kaminski | Borowiec, Poland (187) |
| | 2010 12 5.0 | Sobkowiak | Borowiec, Poland (187) |
| | 2011 1–2011 5 | Marciniak | Borowiec, Poland (187) |
| | 2011 3–2011 3 | Hirsch | Borowiec, Poland (187) |
| 406 Erna | 2005 9–2005 10 | Casulli | Vallemare di Bordona, Italy (A55) |
| | 2005 11–2005 11 | Crippa, Manzini | Stazione Astronomica di Sozzago, Italy (A12) |
| | 2005 11–2005 11 | Poncy | Le Crés, France (177) |
| 441 Bathilde | 2003 1–2003 1 | Roy | Blauvac Observatory, France (627) |
| | 2003 2–2003 2 | Bernasconi | Les Engarouines Observatory, France (A14) |
| | 2003 2–2003 3 | Vagnozzi, Cristofanelli, Paiella | Santa Lucia Stroncone (589) |
| | 2005 7–2005 8 | Bernasconi | Les Engarouines Observatory, France (A14) |
| | 2006 12 11.9 | Poncy | Le Crés, France (177) |
| | 2010 9–2010 10 | Marciniak | Borowiec, Poland (187) |
| | 2010 10 4.8 | Kaminski | Borowiec, Poland (187) |
| | 2010 10 9.9 | T. Michałowski | Borowiec, Poland (187) |
| | 2011 10 14.0 | Sobkowiak | Borowiec, Poland (187) |
| | 2011 10–2011 11 | Marciniak | Borowiec, Poland (187) |
| 507 Laodica | 2001 8–2001 8 | Charbonnel | Durtal (949) |
| | 2001 8–2001 9 | Leyrat | |
| 509 Iolanda | 1996 10–1996 10 | López-González & Rodríguez (2000) | |
| | 2000 6 8.3 | Koff & Brincat (2000) | |
| 512 Taurinensis | 2004 12–2005 1 | Poncy | Le Crés, France (177) |
| | 2005 1 5.0 | Correia | Haute-Provence Observatory, France (511) |
| 528 Rezia | 2011 3–2011 3 | Mottola | |
| 531 Zerlina | 2002 6 2.9 | Christophe | |
| | 2007 9–2007 10 | Brinsfield (2008b) | |
| | 2011 3–2011 6 | Pilcher & Brinsfield (2011) | |
| 543 Charlotte | 2006 11–2006 12 | Poncy | Le Crés, France (177) |
| 572 Rebekka | 2007 2–2007 2 | Warner (2007) | |
| | 2009 8–2009 8 | Audejean | Observatoire de Chinon, France (B92) |
| 578 Happelia | 2006 12–2006 12 | Leroy | Uranoscope, France (A07) |
| | 2008 4–2008 4 | Warner (2008b) | |
| | 2010 11–2010 12 | Antonini | Observatoire de Bédoin, France (132) |
| | 2012 2–2012 4 | Mottola, Hellmich | |
| 600 Musa | 2001 4 6.0 | Hirsch | Borowiec, Poland (187) |
| | 2001 4 29.0 | Colas | Pic du Midi Observatory (586) |
| | 2005 2–2005 3 | Bernasconi | Les Engarouines Observatory, France (A14) |
| | 2005 3–2005 4 | Hirsch | Borowiec, Poland (187) |
| | 2005 4 1.0 | Marciniak | Borowiec, Poland (187) |
| | 2007 10–2007 10 | S. Fauvaud, Santacana, M. Fauvaud | Pic du Midi Observatory (586) |
| | 2009 3 25.8 | Kaminski | Borowiec, Poland (187) |
| | 2009 3 30.9 | Marciniak | Borowiec, Poland (187) |
| | 2010 4–2010 6 | Marciniak | Borowiec, Poland (187) |
| | 2011 11–2011 11 | Marciniak | Borowiec, Poland (187) |
| | 2011 11 29.8 | Hirsch | Borowiec, Poland (187) |
| 669 Kypria | 2006 3–2006 4 | Bernasconi | Les Engarouines Observatory, France (A14) |
| 708 Raphaela | 2007 2–2007 2 | Warner (2007) | |
| 725 Amanda | 2002 12 12.8 | Marciniak | Borowiec, Poland (187) |
| | 2002 12 31.8 | T. Michałowski | Borowiec, Poland (187) |
| | 2006 10–2006 10 | S. Fauvaud, Santacana, Sareyan, Wucher | Pic de Château-Renard Observatory |
| | 2006 10 30.1 | Hirsch | Borowiec, Poland (187) |
| | 2009 8–2009 8 | Marciniak | SAAO, Sutherland, South Africa |
| | 2010 10–2010 10 | Audejean | Observatoire de Chinon, France (B92) |
| | 2010 10 31.0 | Marciniak | Borowiec, Poland (187) |
| | 2012 3 3.1 | Marciniak | Borowiec, Poland (187) |
| | 2012 3–2012 3 | Hirsch | Borowiec, Poland (187) |
| | 2012 4 10.1 | Oszkiewicz, Geier | NOT, La Palma, Canary Islands |
| 731 Sorga | 2005 4–2005 4 | Warner (2005a) | |
| | 2009 2–2009 2 | Warner (2009a) | |
| 732 Tjilaki | 2004 3–2004 4 | Bernasconi | Les Engarouines Observatory, France (A14) |
| 787 Moskva | 1999 5–1999 5 | Warner (2011a) | |

**Table 3.** continued.

| Asteroid | Date | Observer | Observatory (MPC code) |
|---|---|---|---|
| | 2003 4–2003 5 | Husarik, Behrend | Skalnate Pleso, Slovakia (056) |
| | 2003 5–2003 5 | Bernasconi | Les Engarouines Observatory, France (A14) |
| | 2004 8–2004 8 | Bernasconi | Les Engarouines Observatory, France (A14) |
| | 2011 5–2011 5 | Audejean | Observatoire de Chinon, France (B92) |
| | 2011 5–2011 5 | Morelle | Observatoire Farigourette, France |
| 792 Metcalfa | 2010 7–2010 8 | Roy | Blauvac Observatory, France (627) |
| 803 Picka | 2006 12 10.8 | Bosch | Collonges Observatory, France (178) |
| | 2007 4–2007 4 | Antonini | Observatoire de Bédoin, France (132) |
| | 2010 11–2010 11 | Antonini | Observatoire de Bédoin, France (132) |
| 812 Adele | 2002 10–2002 10 | Roy | Blauvac Observatory, France (627) |
| 816 Juliana | 2005 4–2005 4 | Stephens (2005a) | |
| | 2005 5–2005 6 | Conjat | Cabris, France |
| | 2010 3–2010 3 | Conjat | Cabris, France |
| 852 Wladilena | 2003 2 23.2 | J. Michałowski | Borowiec, Poland (187) |
| | 2003 2 24.2 | Marciniak | Borowiec, Poland (187) |
| | 2003 2 26.2 | T. Michałowski | Borowiec, Poland (187) |
| | 2007 5–2007 5 | Marciniak | SAAO, Sutherland, South Africa |
| | 2008 8 22.2 | M. J. Michałowski | NOT, La Palma, Canary Islands |
| | 2008 10–2009 1 | Kaminski | Borowiec, Poland (187) |
| | 2008 9–2008 10 | Marciniak | Borowiec, Poland (187) |
| | 2008 12–2009 1 | Sobkowiak | Borowiec, Poland (187) |
| | 2010 2–2010 3 | Antonini | Observatoire de Bédoin, France (132) |
| | 2010 3–2010 5 | Marciniak | Borowiec, Poland (187) |
| | 2010 3–2010 3 | Polishook (2012)[c] | Wise Observatory, Mitzpeh Ramon (097) |
| | 2010 3–2010 4 | Sobkowiak | Borowiec, Poland (187) |
| 857 Glasenapia | 2006 12 23.0 | Poncy | Le Crés, France (177) |
| 867 Kovacia | 2006 11 22.8 | Crippa, Manzini | Stazione Astronomica di Sozzago, Italy (A12) |
| | 2008 1–2008 2 | Roy | Blauvac Observatory, France (627) |
| | 2008 2 8.9 | Casulli | Vallemare di Bordona, Italy (A55) |
| | 2008 2 9.0 | Colas | Pic du Midi Observatory (586) |
| | 2008 2–2008 2 | Manzini | Stazione Astronomica di Sozzago, Italy (A12) |
| | 2008 2–2008 2 | Leroy | Uranoscope, France (A07) |
| | 2008 2–2008 2 | Demeautis | Village-Neuf Observatory, France (138) |
| | 2008 2–2008 3 | Coliac | Observatoire Farigourette, France |
| 874 Rotraut | 2002 7–2002 7 | Charbonnel | Durtal (949) |
| | 2002 8 16.0 | Rinner | Ottmarsheim Observatory, France (224) |
| 875 Nymphe | 2003 7–2003 7 | Warner (2011c) | |
| | 2003 7–2003 7 | Roy | Blauvac Observatory, France (627) |
| 900 Rosalinde | 2007 5 19.0 | Roy | Blauvac Observatory, France (627) |
| 994 Otthild | 2001 9 22.0 | Velichko, T. Michałowski | Kharkov (101) |
| | 2001 10–2001 10 | J. Michałowski | Borowiec, Poland (187) |
| | 2001 10–2001 10 | Conjat | Cabris, France |
| | 2001 11–2001 11 | T. Michałowski | Borowiec, Poland (187) |
| | 2001 11–2001 11 | Kwiatkowski | Borowiec, Poland (187) |
| | 2005 8–2005 11 | Stoss, Nomen, Sanchez, Behrend | OAM, Mallorca (620) |
| | 2005 10 1.9 | Bernasconi | Les Engarouines Observatory, France (A14) |
| | 2005 10–2005 10 | Fagas | Borowiec, Poland (187) |
| | 2005 10 19.9 | T. Michałowski | Borowiec, Poland (187) |
| | 2007 2 26.9 | S. Fauvaud, Esseiva, Michelet, Saguin, Sareyan | Pic de Château-Renard Observatory |
| | 2011 3 19.9 | Polinska | Borowiec, Poland (187) |
| | 2011 3 29.8 | Marciniak | Borowiec, Poland (187) |
| 1056 Azalea | 2004 2–2004 2 | Klotz, Behrend | Haute-Provence Observatory, France (511) |
| 1089 Tama | 2003 12–2004 3 | Roy | Blauvac Observatory, France (627) |
| | 2003 12–2004 2 | Rinner | Ottmarsheim Observatory, France (224) |
| | 2004 1–2004 1 | Antonini | Observatoire de Bédoin, France (132) |
| | 2004 1–2004 1 | Sposetti, Behrend | Gnosca Observatory, Switzerland (143) |
| | 2004 1 4.9 | Klotz | Haute-Provence Observatory, France (511) |
| | 2004 1–2004 1 | Lecacheux, Colas | Pic du Midi Observatory (586) |
| | 2004 1 22.8 | Colas | Pic du Midi Observatory (586) |
| | 2004 1 26.9 | Michelsen, Augustesen, Masi | Brorfelde (054) |
| | 2004 1–2004 1 | Cotrez, Behrend | Saint-Hélène Observatory, France (J80) |
| | 2004 1–2004 2 | Durkee | Shed of Science Observatory, USA (H39) |
| | 2004 2 7.9 | Bernasconi | Les Engarouines Observatory, France (A14) |
| | 2004 2 9.8 | Coloma | Sabadell (619) |
| | 2004 2–2004 2 | Oksanen | Nyrölä Observatory, Finland (174) |
| | 2004 2 11.9 | Itkonen, Pääkkönen | Jakokoski Observatory, Finland (A83) |

**Table 3.** continued.

| Asteroid | Date | Observer | Observatory (MPC code) |
|---|---|---|---|
| | 2004 2 15.0 | Brochard | |
| | 2004 2 20.9 | Demeautis, Matter | Village-Neuf Observatory, France (138) |
| | 2004 2 24.1 | Barbotin, Cotrez, Cazenave, Laffont | Pic du Midi Observatory (586) |
| | 2005 6–2005 7 | Stoss, Nomen, Sanchez, Behrend | OAM, Mallorca (620) |
| | 2005 7–2005 8 | Teng, Behrend | Observatoire Les Makes, France (181) |
| | 2006 9–2006 12 | Sposetti, Pavic | Gnosca Observatory, Switzerland (143) |
| | 2006 9–2006 12 | Polishook (2012)[c] | Wise Observatory, Mitzpeh Ramon (097) |
| | 2006 11 26.9 | Sposetti, Behrend | Gnosca Observatory, Switzerland (143) |
| | 2008 4 5.1 | Klotz, Strajnic | Haute-Provence Observatory, France (511) |
| | 2008 5–2008 5 | Roy | Blauvac Observatory, France (627) |
| | 2008 5–2008 5 | Polishook (2012)[c] | Wise Observatory, Mitzpeh Ramon (097) |
| | 2009 10–2009 11 | Polishook (2012)[c] | Wise Observatory, Mitzpeh Ramon (097) |
| | 2011 2–2011 3 | Crippa, Manzini | Stazione Astronomica di Sozzago, Italy (A12) |
| 1111 Reinmuthia | 2007 10–2007 11 | Hiromi Hamanowa, Hiroko Hamanowa | |
| 1126 Otero | 2008 2–2008 2 | Stephens (2008) | |
| 1130 Skuld | 2004 1 22.0 | Colas | Pic du Midi Observatory (586) |
| | 2009 10–2009 11 | Buchheim (2010) | |
| 1188 Gothlandia | 2006 1 2.9 | Pallares | Sabadell (619) |
| | 2006 1 11.9 | Coloma | Agrupación Astronómica de Sabadell, Spain (A90) |
| | 2006 2 2.9 | Coloma, Garcia | Agrupación Astronómica de Sabadell, Spain (A90) |
| | 2007 5–2007 5 | Antonini | Observatoire de Bédoin, France (132) |
| | 2008 12–2009 1 | H. Hamanowa, H. Hamanowa | |
| | 2011 8–2011 12 | Baker et al. (2012) | |
| | 2011 9–2011 9 | S. Fauvaud, M. Fauvaud | Observatoire du Bois de Bardon, France |
| 1241 Dysona | 2002 9–2002 11 | Bosch | Collonges Observatory, France (178) |
| | 2002 10 2.0 | Brunetto | Le Florian, France (139) |
| | 2006 4–2006 5 | Oey | Leura (E17) |
| 1249 Rutherfordia | 2001 8–2001 8 | Bernasconi | Les Engarouines Observatory, France (A14) |
| | 2008 8 22.0 | Demeautis | Village-Neuf Observatory, France (138) |
| | 2004 7–2004 7 | Roy | Blauvac Observatory, France (627) |
| 1317 Silvretta | 2006 4–2006 4 | Bernasconi | Les Engarouines Observatory, France (A14) |
| | 2009 12–2010 1 | Ruthroff (2010) | |
| 1386 Storeria | 2004 6–2004 6 | Warner (2004) | |
| | 2004 7 15.0 | Behrend, Klotz | Haute-Provence Observatory, France (511) |
| | 2004 7 17.0 | Bernasconi | Les Engarouines Observatory, France (A14) |
| | 2004 7 21.0 | Coloma | Agrupación Astronómica de Sabadell, Spain (A90) |
| | 2004 7 28.0 | Roy | Blauvac Observatory, France (627) |
| 1401 Lavonne | 2008 8 8.3 | Durkee | Shed of Science Observatory, USA (H39) |
| | 2008 9–2008 9 | Antonini | Observatoire de Bédoin, France (132) |
| 1432 Ethiopia | 2007 7–2007 9 | Oey (2008) | |
| 1436 Salonta | 2007 8–2007 9 | Warner (2008a) | |
| | 2007 10–2007 10 | Antonini | Observatoire de Bédoin, France (132) |
| | 2008 11–2008 11 | Antonini | Observatoire de Bédoin, France (132) |
| | 2008 11 27.8 | Roy | Blauvac Observatory, France (627) |
| 1472 Muonio | 2008 9–2008 9 | Stephens (2009b) | |
| | 2008 10–2008 10 | Higgins[a] | Hunters Hill Observatory, Ngunnawal (E14) |
| 1490 Limpopo | 2005 8–2005 8 | Bernasconi | Les Engarouines Observatory, France (A14) |
| 1495 Helsinki | 2006 4–2006 5 | Oey et al. (2007) | |
| | 2006 6 4.0 | Payet, Teng, Leonie, Behrend | Observatoire Les Makes, France (181) |
| | 2006 6–2006 7 | Teng, Behrend | Observatoire Les Makes, France (181) |
| | 2011 9–2011 9 | S. Fauvaud, M. Fauvaud | Observatoire du Bois de Bardon, France |
| 1518 Rovaniemi | 2009 1–2009 1 | Warner (2009a) | |
| | 2009 1–2009 1 | Roy | Blauvac Observatory, France (627) |
| 1528 Conrada | 2008 5–2008 5 | Warner (2008b) | |
| 1554 Yugoslavia | 2007 4–2007 4 | Higgins (2008) | |
| 1559 Kustaanheimo | 2005 3–2005 3 | Bernasconi | Les Engarouines Observatory, France (A14) |
| 1572 Posnania | 1993 9–1999 11 | Michałowski et al. (2001) | |
| | 2004 9–2004 9 | Roy | Borowiec, Poland (187) |
| | 2010 12 5.1 | Sobkowiak | Borowiec, Poland (187) |
| | 2011 2–2011 2 | Kaminski | Borowiec, Poland (187) |
| | 2011 2 8.8 | Marciniak | Borowiec, Poland (187) |
| | 2012 2–2012 3 | Roy | Blauvac Observatory, France (627) |
| 1607 Mavis | 2007 9–2007 9 | Oey (2008) | |
| 1630 Milet | 2005 2–2005 2 | Bernasconi | Les Engarouines Observatory, France (A14) |
| 1634 Ndola | 2006 9–2006 9 | Higgins[a] | Hunters Hill Observatory, Ngunnawal (E14) |
| 1719 Jens | 2000 9–2000 9 | Warner (2011b) | |
| | 2006 1–2006 2 | Bernasconi | Les Engarouines Observatory, France (A14) |

**Table 3.** continued.

| Asteroid | Date | Observer | Observatory (MPC code) |
|---|---|---|---|
| 1785 Wurm | 2008 3–2008 3 | Oey (2009) | |
| 1837 Osita | 2006 1–2006 3 | Roy | Blauvac Observatory, France (627) |
| 1927 Suvanto | 2005 2–2005 2 | Bernasconi | Les Engarouines Observatory, France (A14) |
| 1933 Tinchen | 2005 3 14.0 | Roy | Blauvac Observatory, France (627) |
| 1950 Wempe | 2006 2 1.9 | Bernasconi | Les Engarouines Observatory, France (A14) |
| 1963 Bezovec | 2005 1–2005 1 | Bernasconi | Les Engarouines Observatory, France (A14) |
| | 2009 3–2009 3 | Romeuf | |
| | 2009 4 6.9 | Manzini | Stazione Astronomica di Sozzago, Italy (A12) |
| | 2009 4–2009 4 | Martin | Tzec Maun Observatory, Mayhill (H10) |
| 2002 Euler | 2006 5–2006 5 | Koff | Antelope Hills Observatory, Bennett (H09) |
| | 2007 10–2007 10 | Higgins[a] | Hunters Hill Observatory, Ngunnawal (E14) |
| 2510 Shandong | 2006 8–2006 9 | Higgins & Goncalves (2007) | |
| 2606 Odessa | 2008 2–2008 2 | Higgins et al. (2008) | |
| | 2008 3 3.6 | Oey | Leura (E17) |
| 2709 Sagan | 2008 3–2008 3 | Higgins et al. (2008) | |
| | 2011 1–2011 2 | Oey | Leura (E17) |
| 2839 Annette | 2005 10–2005 11 | Buchheim (2007) | |
| | 2005 12–2005 12 | Warner (2006a) | |
| 2957 Tatsuo | 2005 8–2005 8 | Bernasconi | Les Engarouines Observatory, France (A14) |
| | 2005 8–2005 9 | Poncy | Le Crés, France (177) |
| | 2005 9–2005 9 | Warner (2006b) | |
| 2991 Bilbo | 2007 4–2007 4 | Higgins[a] | Hunters Hill Observatory, Ngunnawal (E14) |
| 3722 Urata | 2004 12–2004 12 | Antonini | Observatoire de Bédoin, France (132) |
| | 2006 9 3.0 | Manzini | Stazione Astronomica di Sozzago, Italy (A12) |
| | 2007 8–2007 8 | Roy | Blauvac Observatory, France (627) |
| | 2007 8–2007 8 | Stephens | Goat Mountain Astronomical Research Station (G79) |
| 5281 Lindstrom | 2008 6–2008 6 | Brinsfield | Via Capote Sky Observatory, Thousand Oaks (G69) |
| 7517 1989 AD | 2007 11–2007 11 | Stephens | Goat Mountain Astronomical Research Station (G79) |
| 8132 Vitginzburg | 2008 6–2008 6 | Brinsfield (2008a) | |
| 8359 1989 WD | 2009 4–2009 4 | Higgins & Warner (2009) | |
| | 2009 5–2009 5 | Brinsfield (2009) | |
| 10772 1990 YM | 2006 3–2006 3 | Koff | Antelope Hills Observatory, Bennett (H09) |
| | 2006 4–2006 4 | Warner | Palmer Divide Observatory (716) |
| 31383 1998 $XJ_{94}$ | 2006 4–2006 4 | Higgins et al. (2006) | |

A&A 559, A134 (2013)
DOI: 10.1051/0004-6361/201321993


Astronomy & Astrophysics

# An anisotropic distribution of spin vectors in asteroid families⋆

J. Hanuš[1], M. Brož[1], J. Ďurech[1], B. D. Warner[2], J. Brinsfield[3], R. Durkee[4], D. Higgins[5], R. A. Koff[6], J. Oey[7], F. Pilcher[8], R. Stephens[9], L. P. Strabla[10], Q. Ulisse[10], and R. Girelli[10]

[1] Astronomical Institute, Faculty of Mathematics and Physics, Charles University in Prague, V Holešovičkách 2, 18000 Prague, Czech Republic
e-mail: hanus.home@gmail.com
[2] Palmer Divide Observatory, 17995 Bakers Farm Rd., Colorado Springs, CO 80908, USA
[3] Via Capote Observatory, Thousand Oaks, CA 91320, USA
[4] Shed of Science Observatory, 5213 Washburn Ave. S, Minneapolis, MN 55410, USA
[5] Hunters Hill Observatory, 7 Mawalan Street, ACT 2913 Ngunnawal, Australia
[6] 980 Antelope Drive West, Bennett, CO 80102, USA
[7] Kingsgrove, NSW, Australia
[8] 4438 Organ Mesa Loop, Las Cruces, NM 88011, USA
[9] Center for Solar System Studies, 9302 Pittsburgh Ave, Suite 105, Rancho Cucamonga, CA 91730, USA
[10] Observatory of Bassano Bresciano, via San Michele 4, Bassano Bresciano (BS), 25020 Brescia, Italy

Received 30 May 2013 / Accepted 16 September 2013

**ABSTRACT**

*Context.* The current number of ~500 asteroid models derived from the disk-integrated photometry by the lightcurve inversion method allows us to study the spin-vector properties of not only the whole population of main-belt asteroids, but also of several individual collisional families.
*Aims.* We create a data set of 152 asteroids that were identified by the hierarchical clustering method (HCM) as members of ten collisional families, among which are 31 newly derived unique models and 24 new models with well-constrained pole-ecliptic latitudes of the spin axes. The remaining models are adopted from the DAMIT database or a few individual publications.
*Methods.* We revised the preliminary family membership identification by the HCM according to several additional criteria: taxonomic type, color, albedo, maximum Yarkovsky semi-major axis drift, and the consistency with the size-frequency distribution of each family, and consequently we remove interlopers. We then present the spin-vector distributions for asteroidal families Flora, Koronis, Eos, Eunomia, Phocaea, Themis, Maria, and Alauda. We use a combined orbital- and spin-evolution model to explain the observed spin-vector properties of objects among collisional families.
*Results.* In general, for studied families we observe similar trends in $(a_p, \beta)$ space (proper semi-major axis vs. ecliptic latitude of the spin axis): (i) larger asteroids are situated in the proximity of the center of the family; (ii) asteroids with $\beta > 0°$ are usually found to the right of the family center; (iii) on the other hand, asteroids with $\beta < 0°$ to the left of the center; (iv) the majority of asteroids have large pole-ecliptic latitudes ($|\beta| \gtrsim 30°$); and finally (v) some families have a statistically significant excess of asteroids with $\beta > 0°$ or $\beta < 0°$. Our numerical simulation of the long-term evolution of a collisional family is capable of reproducing the observed spin-vector properties well. Using this simulation, we also independently constrain the age of families Flora ($1.0 \pm 0.5$ Gyr) and Koronis (2.5–4 Gyr).

**Key words.** methods: observational – minor planets, asteroids: general – techniques: photometric – methods: numerical

## 1. Introduction

An analysis of rotational state solutions for main belt asteroids has been performed by many authors. All these authors observed the deficiency of poles close to the ecliptic plane (e.g., Magnusson 1986; Drummond et al. 1988; Pravec et al. 2002; Skoglöv & Erikson 2002; Kryszczyńska et al. 2007). Hanuš et al. (2011) showed that this depopulation of spin vectors mainly concerns smaller asteroids ($D \lesssim 40$ km), while the larger asteroids ($60 \lesssim D \lesssim 130$–$150$ km, Kryszczyńska et al. 2007; Paolicchi & Kryszczyńska 2012) have a statistically significant excess of prograde rotators, but no evident lack of poles close to the ecliptic plane. The observed anisotropy of pole vectors of smaller asteroids is now believed to be a result of YORP thermal torques[1], and of collisions that systematically evolve the spin axes away from the ecliptic plane. The prograde excess of larger asteroids is probably caused by a primordial preference that agrees with the theoretical work of Johansen & Lacerda (2010). While the number of asteroids with known rotational states grows, we can not only study the spin vector distribution in the whole main-belt asteroids (MBAs) or near-Earth asteroids (NEAs) populations, but we can also focus on individual groups of asteroids within these populations, particularly on collisional families (i.e., clusters of asteroids with similar proper orbital elements and often spectra that were formed by catastrophic breakups of parent bodies or cratering events).

⋆ Tables 3–5 are available in electronic form at http://www.aanda.org

[1] Yarkovsky-O'Keefe-Radzievskii-Paddack effect, a torque caused by the recoil force due to anisotropic thermal emission, which can alter both rotational periods and orientation of spin axes, see e.g., Rubincam (2000).

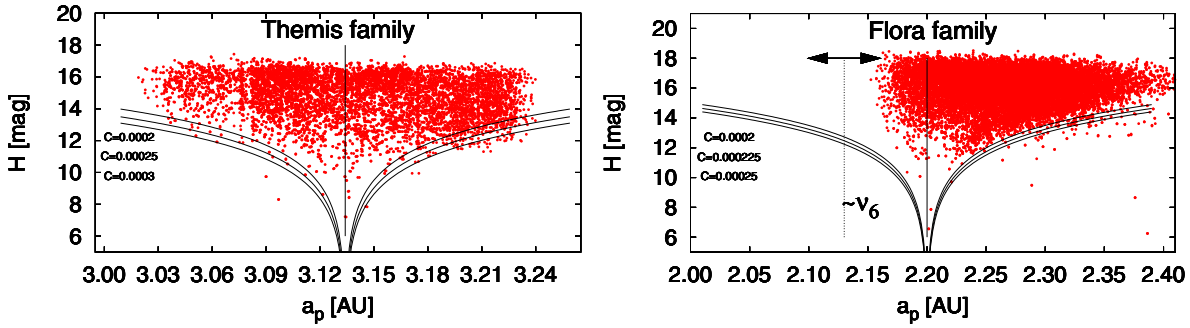


**Fig. 1.** Dependence of the absolute magnitude $H$ on the proper semi-major axis $a_p$ for the Themis family (*left*) and for the Flora family (*right*) with the likely positions of the family centers (vertical lines). We also plot three ($a_p$, $H$) borders of the family for different parameters $C$ (different values correspond to a different initial extent of the family or different age and magnitude of the Yarkovsky semi-major axis drift) by gray lines, the optimal border corresponds to the middle line. The vertical dotted line represents the approximate position of the secular $\nu_6$ resonance for the inclination typical for Flora family members and the horizontal arrow its approximate range.

The theory of dynamical evolution of asteroid families (e.g., Bottke et al. 2006) suggests that the Yarkovsky[2]/YORP effects change orbital parameters of smaller asteroids (≲30–50 km) – the semi-major axis of prograde rotators slowly grows the course of time, unlike retrograde rotators whose semi-major axis decreases. This phenomenon is particularly visible when we plot the dependence of the absolute magnitude $H$ on the proper semi-major axis $a_p$ (see an example of such a plot for Themis family in Fig. 1, left panel). In addition, various resonances (e.g., mean-motion resonances with Jupiter or Mars, or secular resonances) can intersect the family and cause a decrease in the number of asteroids in the family by inducing moderate oscillations to their orbital elements (Bottke et al. 2001) as can be seen in Fig. 1 for the Flora family, where the secular $\nu_6$ resonance with Saturn almost completely eliminated objects to the left of the center of the family. The $\nu_6$ resonance has its center at 2.13 AU for objects with $\sin I \sim 0.09$, which is typical of Flora family members. It develops objects which then approach the proximity of the resonance. Some resonances can, for example, capture some asteroids on particular semi-major axes (Nesvorný & Morbidelli 1998).

Laboratory experiments strongly suggest that a collisionally-born cluster should initially have a rotational frequency distribution close to Maxwellian (Giblin et al. 1998) and an isotropic spin vector distribution. For several families, we already know their age estimates (e.g., 2.5 ± 1.0 Gyr for Koronis family, Bottke et al. 2001), and so we have a constraint on the time at which the family was evolving towards its current state. As shown in Bottke et al. (2001), the family evolution is dominated by Yarkovsky and YORP effects, as well as by collisions and spin-orbital resonances. The knowledge of the age should constrain some free parameters in various evolutionary models.

The spin-vector properties in an asteroid family were first studied by Slivan (2002) and Slivan et al. (2003), who reveal an anisotropy of spin vectors for ten members of the Koronis family. This was an unexpected result because collisionallyborn population should have an isotropic spin-vector distribution. The peculiar spin-vector alignment in the Koronis family was explained by Vokrouhlický et al. (2003) as a result of the YORP torques and spin-orbital resonances that modified the spin states over the timespan of 2–3 Gyr. The secular $s_6$ spin-orbital resonance with Saturn may affect the Koronis family members, according to the numerical simulations, it can (i) capture some objects and create a population of prograde rotators with periods $P \in (4, 7)$ h, similar obliquities (42° to 51°) and also with similar ecliptic longitudes in the ranges of (24° to 73°) and (204° to 259°); or (ii) create a group of low-obliquity retrograde rotators with rotational periods $P < 5$ h or $P > 13$ h. The prograde rotators trapped in the $s_6$ spin-orbital resonance were referred to by Vokrouhlický et al. (2003) as being in *Slivan states*. Most members of the Koronis family with known rotational states (determined by the lightcurve inversion by Slivan et al. 2003, 2009; Hanuš et al. 2011, 2013) had the expected properties except for the periods of observed prograde rotators were shifted to higher values of 7–10 h. Rotational states of asteroids that did not match the properties of the two groups were probably reorientated by recent collisions, which are statistically plausible during the family existence for at least a few Koronis members (e.g., asteroid (832) Karin was affected by a collision when a small and young collisional family within the Koronis family was born, Slivan & Molnar 2012).

Another study of rotational states in an asteroid family was made by Kryszczyńska (2013), who focuses on the Flora family. She distinguishes prograde and retrograde groups of asteroids and reports an excess of prograde rotators. This splitting into two groups is most likely caused by the Yarkovsky effect, while the prograde excess by the secular $\nu_6$ resonance that significantly depopulates the retrograde part of the family. See Fig. 1b, only retrograde rotators can drift via the Yarkovsky/YORP effects towards the resonance.

Future studies of rotational properties of collisional families should reveal the influence of the Yarkovsky and YORP effects, and possibly a capture of asteroids in spin-orbital resonances similar to the case of the Koronis family. The Yarkovsky effect should be responsible for spreading the family in a semi-major axis (retrograde rotators drift from their original positions towards the Sun, on the other hand, prograde rotators drift away from the Sun, i.e. towards larger $a_p$'s), and the YORP effect should eliminate the spin vectors close to the ecliptic plane.

Disk-integrated photometric observations of asteroids contain information about an object's physical parameters, such as the shape, the sidereal rotational period, and the orientation of the spin axis. Photometry acquired at different viewing geometries and apparitions can be used in many cases in a lightcurve inversion method (e.g., Kaasalainen & Torppa 2001; Kaasalainen et al. 2001) and a convex 3D shape model including its rotational

[2] A thermal recoil force affecting rotating asteroids.

state can be derived. This inverse method uses all available photometric data, both the classical dense-in-time lightcurves or the sparse-in-time data from astrometric surveys. Most of the asteroid models derived by this technique are publicly available in the Database of Asteroid Models from Inversion Techniques (DAMIT[3], Ďurech et al. 2010). In February 2013, models of 347 asteroids were included there. About a third of them can be identified as members of various asteroid families. This large number of models of asteroids that belong to asteroid families allows us to investigate the spin-vector properties in at least several families with the largest amount of identified members. Comparison between the observed and synthetic (according to a combined orbital- and spin-evolution model) spin-vector properties could even lead to independent family age estimates.

The paper is organized as follows. In Sect. 2, we investigate the family membership of all asteroids for which we have their models derived by the lightcurve inversion method and present 31 new asteroid models that belong to ten asteroid families. An analysis of spin states within these asteroid families with at least three identified members with known shape models is presented in Sect. 3.1. A combined spin-orbital model for the long-term evolution of a collisional family is described in Sect. 4, where we also compare the synthetic and observed spin-vector properties and constrain the ages of families Flora and Koronis.

## 2. Determination of family members

### 2.1. Methods for family membership determination

For a *preliminary* family membership determination, we adopted an online catalog published by Nesvorný (2012), who used the hierarchical clustering method[4] (HCM, Zappalà et al. 1990, 1994). Nesvorný (2012) used two different types of proper elements for the family membership identification: semi-analytic and synthetic. The more reliable dataset is the one derived from synthetic proper elements, which were computed numerically using a more complete dynamical model. The majority of asteroids are present in both datasets. A few asteroids that are only in one of the datasets are included in the study as well (e.g., asteroids (390) Alma in the Eunomia family or (19848) Yeungchuchiu in the Eos family), because at this stage it is not necessary to remove objects that still could be real family members.

The HCM selects a group of objects that are separated in the proper element space by less than a selected distance. However, not all of these objects are actually real members of the collisionallyborn asteroid family. A fraction of objects have orbital elements similar to typical elements of the asteroid family members only by a coincidence, the so-called interlopers. Interlopers can be identified (and removed), for example, by

- inspection of reflectance spectra. Because they are usually of different taxonomic types those that of the family members, we use the SMASSII (Bus & Binzel 2002) or Tholen taxonomy (Tholen 1984, 1989);
- inspection of colors based on the Sloan Digital Sky Survey Moving Object Catalog 4 (SDSS MOC4, Parker et al. 2008).

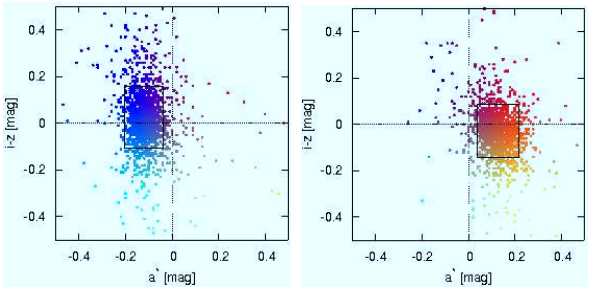


**Fig. 2.** Dependence of the color indexes $a^\star$ and $i - z$ (from the Sloan Digital Sky Survey Moving Object Catalog 4) for a C-type family Themis and S-type family Eunomia. The family corresponds to a compact structure in this parameter space marked by a rectangle. There is a qualitative difference between C- and S-types asteroids.

We used the color indexes $a^\star$ and $i - z$, which usually define the core of the family well (see examples for Themis and Eunomia families in Fig. 2), and for each asteroid with available color indexes, we compared values $a^\star$ and $i - z$ to those that define the family;

- inspection of albedos based on the WISE data (Masiero et al. 2011);
- construction of a diagram of the proper semi-major axis vs. the absolute magnitude (see Fig. 1), estimating the *V-shape* defined by the Yarkovsky semi-major axis drift and excluding outliers, i.e. relatively large asteroids outside the V-shape (see Vokrouhlický et al. 2006b, for the case of the Eos family). We refer here to the ($a_p$, $H$) border of the family as the border of the V-shape; or by
- construction of a size-frequency distribution (SFD) of the cluster. Some asteroids can be too large to be created within the family and thus are believed to be interlopers (see, e.g., numerical simulations by Michel et al. 2011, who excluded the asteroid (490) Veritas from the Veritas family).

These methods for determining family membership have one common characteristic – we have to determine or choose a range for a quantity that defines the family members (range of spectra, sizes, or distance from the family center), which affects the number of objects we include in the family. Our criteria correspond to the fact that usually 99% of the objects are within the ranges.

### 2.2. New asteroid models

From the DAMIT database, we adopt 96 models of asteroids that are, according to the HCM, members of collisional families. Currently, we have about 100 new asteroid models that have not yet been published. Here, we present new physical models of 31 asteroids from this sample that are identified as members of asteroid families by the HCM. We choose only asteroids that belong to ten specific families for which we expect a reasonable amount of members, i.e., at least three. These convex shape models are derived by the lightcurve inversion method from combined dense and sparse photometry. The derivation process is similar to the one used in Hanuš et al. (2013). The dense photometry was from two main sources: (i) the Uppsala Asteroid Photometric Catalogue (UAPC[5], Lagerkvist et al. 1987; Piironen et al. 2001), where lightcurves for about 1000 asteroids are stored; and (ii) the data from a group of individual observers provided by the Minor Planet Center in the

[3] http://astro.troja.mff.cuni.cz/projects/asteroids3D

[4] In this method, mutual distances in proper semi-major axis ($a_d$), proper eccentricity ($e_d$), and proper inclination ($i_d$) space are computed. The members of the family are then separated in the proper element space by less than a selected distance (usually, it has a unit of velocity), a free parameter often denoted as "cutoff velocity".

[5] http://asteroid.astro.helsinki.fi/

**Table 1.** List of new asteroid models derived from combined dense and sparse data or from sparse data alone.

| Asteroid | | $\lambda_1$ [deg] | $\beta_1$ [deg] | $\lambda_2$ [deg] | $\beta_2$ [deg] | $P$ [hours] | $N_{lc}$ | $N_{app}$ | $N_{689}$ | $N_{703}$ | $N_{950}$ |
|---|---|---|---|---|---|---|---|---|---|---|---|
| 243 | Ida | 259 | −66 | 74 | −61 | 4.633632 | 53 | 6 | 134 | 122 | 25 |
| 364 | Isara | 282 | 44 | 86 | 42 | 9.15751 | 4 | 1 | 98 | 104 | |
| 540 | Rosamunde | 301 | 81 | 127 | 62 | 9.34779 | 3 | 1 | 135 | 83 | |
| 550 | Senta | 63 | −40 | 258 | −58 | 20.5726 | 9 | 1 | 151 | 85 | |
| 553 | Kundry | 197 | 73 | 359 | 64 | 12.6025 | 5 | 1 | 61 | 80 | |
| 621 | Werdandi | 247 | −86 | 66 | −77 | 11.77456 | 12 | 2 | 146 | 71 | |
| 936 | Kunigunde | 47 | 57 | 234 | 50 | 8.82653 | | | 154 | 88 | |
| 951 | Gaspra | 20 | 23 | 198 | 15 | 7.042027 | 71 | 4 | 117 | 89 | |
| 1286 | Banachiewicza | 214 | 62 | 64 | 60 | 8.63043 | | | 81 | 51 | |
| 1353 | Maartje | 266 | 73 | 92 | 57 | 22.9926 | | | 154 | 139 | |
| 1378 | Leonce | 210 | −67 | 46 | −77 | 4.32527 | | | 89 | 113 | |
| 1423 | Jose | 78 | −82 | | | 12.3127 | | | 121 | 134 | |
| 1446 | Sillanpaa | 129 | 76 | 288 | 63 | 9.65855 | 2 | 1 | 76 | 73 | |
| 1464 | Armisticia | 194 | −54 | 35 | −69 | 7.46699 | 2 | 1 | 231 | 67 | |
| 1503 | Kuopio | 170 | −86 | 27 | −61 | 9.9586 | | | 116 | 68 | |
| 1527 | Malmquista | 274 | 80 | | | 14.0591 | | | 49 | 107 | |
| 1618 | Dawn | 39 | −60 | 215 | −51 | 43.219 | | | 93 | 91 | |
| 1633 | Chimay | 322 | 77 | 116 | 81 | 6.59064 | 2 | 1 | 127 | 83 | |
| 1691 | Oort | 45 | 68 | 223 | 58 | 10.2684 | | | 86 | 60 | |
| 1703 | Barry | 46 | −76 | 221 | −71 | 107.04 | | | 89 | 138 | |
| 1805 | Dirikis | 364 | 48 | 188 | 61 | 23.4543 | | | 117 | 91 | |
| 1835 | Gajdariya | 34 | 74 | 204 | 69 | 6.33768 | | | 66 | 86 | |
| 1987 | Kaplan | 357 | −58 | | | 9.45950 | 8 | 2 | 81 | 28 | |
| 2430 | Bruce Helin | 177 | −68 | | | 129.75 | 15 | 1 | | 112 | |
| 3279 | Solon | 268 | −70 | | | 8.1043 | 3 | 1 | | 137 | |
| 3492 | Petra-Pepi | 9 | −57 | 202 | −16 | 46.570 | 15 | 1 | 25 | 111 | |
| 4399 | Ashizuri | 266 | −48 | 45 | −61 | 2.830302 | 4 | 1 | 20 | 84 | |
| 4606 | Saheki | 44 | 59 | 222 | 68 | 4.97347 | 6 | 1 | | 123 | |
| 6159 | 1991 YH | 266 | 67 | 62 | 67 | 10.6590 | 3 | 1 | | 102 | |
| 6262 | Javid | 93 | 76 | 275 | 69 | 8.02054 | 3 | 1 | | 106 | |
| 6403 | Steverin | 246 | 77 | 109 | 73 | 3.49119 | 2 | 1 | | 74 | |
| 7043 | Godart | 73 | 62 | 235 | 80 | 8.4518 | 4 | 1 | | 121 | |
| 7169 | Linda | 11 | −60 | 198 | −61 | 27.864 | 5 | 1 | | 95 | |

**Notes.** For each asteroid, the table gives the ecliptic coordinates $\lambda_1$ and $\beta_1$ of the pole solution with the lowest $\chi^2$, the corresponding mirror solution $\lambda_2$ and $\beta_2$, the sidereal rotational period $P$, the number of dense lightcurves $N_{lc}$ observed during $N_{app}$ apparitions, and the number of sparse data points for the corresponding observatory: $N_{689}$, $N_{703}$, and $N_{950}$. The uncertainty of the sidereal rotational period corresponds to the last decimal place of $P$ and of the pole direction to 5–10° if we have multi-apparition dense data or 10–20° if the model is based mainly on sparse data (i.e., only a few dense lightcurves from 1–2 apparitions).

Asteroid Lightcurve Data Exchange Format (ALCDEF[6], Warner et al. 2009). The sparse-in-time photometry is downloaded from the AstDyS site (Asteroids – Dynamic Site[7]). We use data from the three most accurate observatories: USNO–Flagstaff station (IAU code 689), Roque de los Muchachos Observatory, La Palma (IAU code 950), and Catalina Sky Survey Observatory (CSS for short, IAU code 703, Larson et al. 2003).

To increase the number of asteroid models for our study of asteroid families, we performed additional analysis of our previous results of the lightcurve inversion. For many asteroids, we are able to determine a unique rotational period, but get multiple pole solutions (typically 3–5) with similar ecliptic latitudes $\beta$, which is an important parameter. In Hanuš et al. (2011), we presented a reliability test where we checked the physicality of derived solutions by the lightcurve inversion (i.e., if the shape model rotated around its axis with a maximum momentum of inertia). By computing models for all possible pole solutions and by checking their physicality, we removed the pole ambiguity for several asteroids, and thus determined their unique solutions (listed in Table 1). For other asteroids, the pole ambiguity remain and the models give us accurate period values and also rough estimates of ecliptic latitudes $\beta$ (if the biggest difference in latitudes of the models is <50°). We call these models *partial* and present them in Table 2. For the ecliptic latitude $\beta$, we use the mean value of all different models. We define parameter $\Delta \equiv |\beta_{max} - \beta_{min}|/2$ as being the estimated uncertainty of $\beta$, where $\beta_{max}$ and $\beta_{min}$ are the extremal values within all $\beta$. The threshold for partial models is $\Delta < 25°$.

We present 31 new models and 24 partial models. References to the dense lightcurves used for the model determination are listed in Table 3. In Sect. 4, we compare the numbers of asteroids in four quadrants of the ($a_p$, $\beta$) diagram (defined by the center of the family and the value $\beta = 0°$) with the same quantities based on the synthetic family population. The uncertainties in $\beta$ are rarely greater than 20°, and the assignment to a specific quadrant is usually not questionable (only in 4 cases out of 136 does the uncertainty interval lie in both quadrants, and most of the asteroids have latitudes $|\beta| \gtrsim 30°$), and thus give us useful information about the rotational properties in asteroid families. Partial models represent about 20% of our sample of asteroid models.

[6] http://www.minorplanet.info/alcdef.html
[7] http://hamilton.dm.unipi.it/

**Table 2.** List of partial models derived from combined data sets.

| Asteroid | | $\beta$ [deg] | $\Delta$ [deg] | $P$ [hours] | $N_{lc}$ | $N_{app}$ | $N_{689}$ | $N_{703}$ |
|---|---|---|---|---|---|---|---|---|
| 391 | Ingeborg | −60 | 7 | 26.4145 | 24 | 2 | 141 | 96 |
| 502 | Sigune | −44 | 3 | 10.92667 | 9 | 2 | 157 | 52 |
| 616 | Elly | 67 | 23 | 5.29771 | 4 | 1 | 101 | 133 |
| 1003 | Lilofee | 65 | 10 | 8.24991 | | | 107 | 83 |
| 1160 | Illyria | 47 | 23 | 4.10295 | | | 96 | 100 |
| 1192 | Prisma | −65 | 14 | 6.55836 | 5 | 1 | 44 | 43 |
| 1276 | Ucclia | −49 | 22 | 4.90748 | | | 114 | 45 |
| 1307 | Cimmeria | 63 | 9 | 2.820723 | 2 | 1 | 91 | 54 |
| 1339 | Desagneauxa | 65 | 17 | 9.37510 | | | 78 | 120 |
| 1396 | Outeniqua | 62 | 7 | 3.08175 | 2 | 1 | 112 | 68 |
| 1493 | Sigrid | 78 | 7 | 43.179 | | | 78 | 103 |
| 1619 | Ueta | 39 | 6 | 2.717943 | 5 | 1 | 122 | 51 |
| 1623 | Vivian | −75 | 8 | 20.5235 | | | 77 | 58 |
| 1738 | Oosterhoff | −72 | 8 | 4.44896 | | | 109 | 105 |
| 1838 | Ursa | 47 | 17 | 16.1635 | | | 102 | 91 |
| 2086 | Newell | −60 | 12 | 78.09 | 10 | 1 | 24 | 84 |
| 3017 | Petrovic | −73 | 8 | 4.08037 | 3 | 1 | | 114 |
| 3786 | Yamada | 56 | 2 | 4.03294 | 3 | 1 | | 71 |
| 3896 | Pordenone | −32 | 9 | 4.00366 | 3 | 1 | 22 | 71 |
| 4209 | Briggs | −56 | 25 | 12.2530 | 2 | 1 | | 64 |
| 4467 | Kaidanovskij | 54 | 13 | 19.1454 | | | 20 | 107 |
| 6179 | Brett | −42 | 20 | 9.4063 | 6 | 1 | | 93 |
| 7055 | 1989 KB | −61 | 11 | 4.16878 | 7 | 1 | | 117 |
| 7360 | Moberg | −18 | 18 | 4.58533 | 3 | 1 | | 103 |

**Notes.** For each asteroid, there is the mean ecliptic latitude $\beta$ of the pole direction and its dispersion $\Delta$. The other parameters have the same meaning as in Table 1. The uncertainty of the sidereal rotational period corresponds to the last decimal place of $P$.

The typical error for the orientation of the pole is (5–10°)/cos$\beta$ in longitude $\lambda$ and 5–20° in latitude $\beta$. Both uncertainties depend on the amount, timespan, and quality of used photometry. Models based purely on dense photometry are typically derived from a large number (~30–50) of individual dense lightcurves observed during about five to ten apparitions, and thus the uncertainties of parameters of the rotational state correspond to lower values of the aforementioned range. On the other hand, models based on combined sparse-in-time data have larger uncertainties, owing to the poor photometric quality of the sparse data (corresponds to the upper bound of the aforementioned range).

Models of asteroids (281) Lucretia and (1188) Gothlandia published by Hanuš et al. (2013) were recently determined also by Kryszczyńska (2013) from partly different photometric data sets. Parameters of the rotational state for both models agree within their uncertainties.

The spin vector solution of asteroid (951) Gaspra based on Galileo images obtained during the October 1991 flyby was already published by Davies et al. (1994b). Similarly, the solution of a Koronis-family member (243) Ida based on Galileo images and photometric data was previously derived by Davies et al. (1994a) and Binzel et al. (1993). Here we present convex shape models for both these asteroids. Our derived pole orientations agree within only a few degrees with the previously published values (see Table 5), which again demonstrates the reliability of the lightcurve inversion method.

### 2.3. Family members and interlopers

We revise the family membership assignment by the HCM according to the criteria described above for interlopers or borderline cases. Interlopers are asteroids that do not clearly belong to the family; for example, they have different taxonomic types or incompatible albedos or are far from the ($a_p$, $H$) border. On the other hand, borderline cases cannot be directly excluded from the family, since their physical or orbital properties are just not typical in the context of other members (higher/lower albedos, close to the ($a_p$, $H$) border). These asteroids are possible family members, but can just as easily be interlopers. In the penultimate column of Table 5, we show our revised membership classification for each object (M is a member, I an interloper, and B a borderline case), the table also gives the rotational state of the asteroid (the ecliptic coordinates of the pole orientation $\lambda$ and $\beta$ and the period $P$), the semi-major axis $a$, the diameter $D$, and the albedo $p_V$ from WISE (Masiero et al. 2011), the SMASS II (Bus & Binzel 2002), and Tholen (Tholen 1984, 1989) taxonomic types, and the reference to the model).

Although we got several members by the HCM for Vesta and Nysa/Polana families, we excluded these two families from further study of spin states. The Vesta family was created by a cratering event, and thus a majority of the fragments are rather small and beyond the capabilities of the model determination. Most of the models we currently have (recognized by the HCM) are not compatible with the SFD of the Vesta family and thus are interlopers. On the other hand, Nysa/Polana family is a complex of two families (of different age and composition), hence should be treated individually. Additionally, we only have five member candidates for the whole complex, so even if we assign them to the subfamilies, the numbers would be too low to make any valid conclusions.

In Table 4, we list asteroids for which the HCM suggested a membership in families Flora, Koronis, Eos, Eunomia, Phocaea and Alauda, but using the additional methods for the family membership determination described above, we identified them as interlopers or borderline cases. In Fig. 3, we show the ($a_p$, $H$)

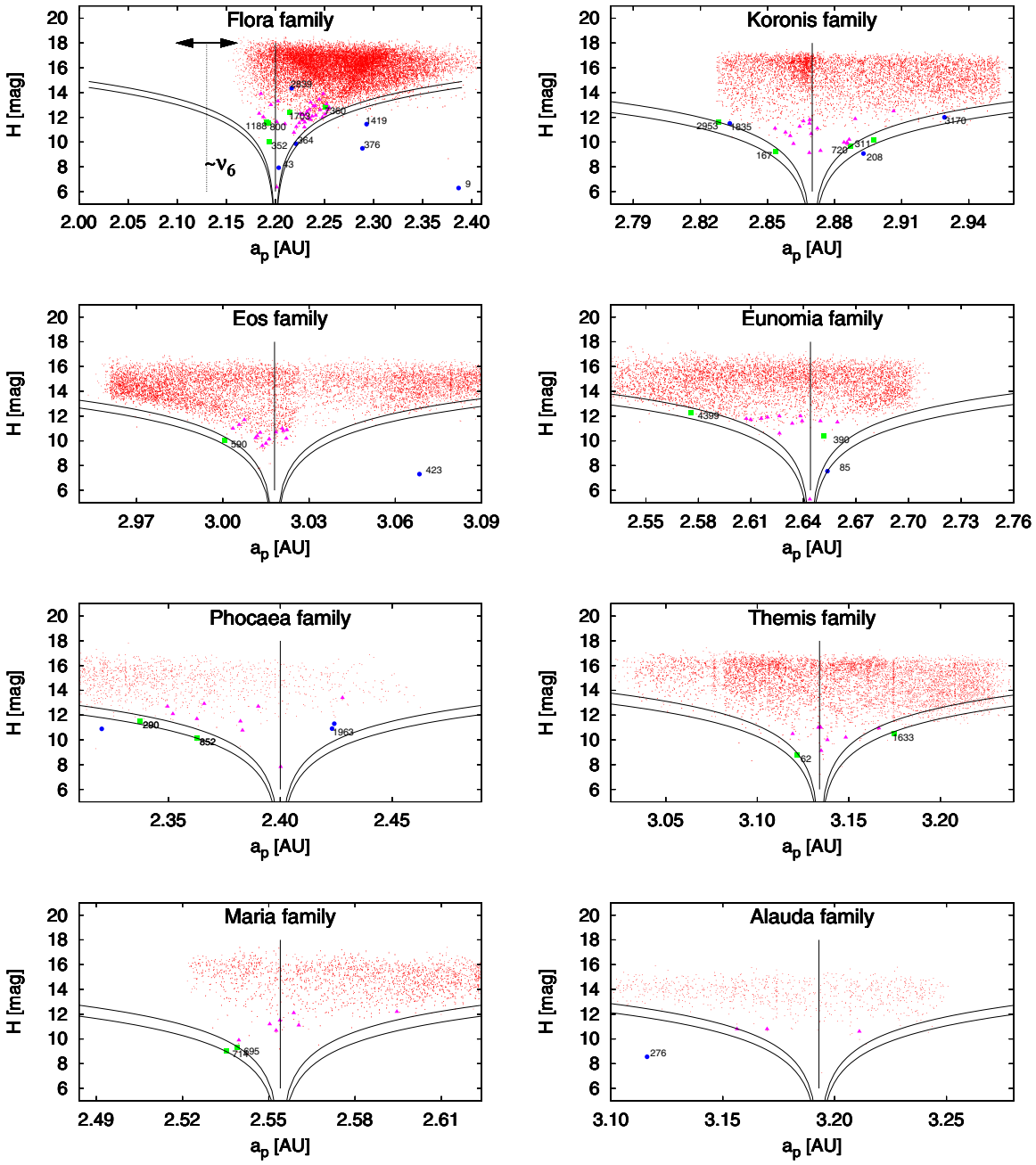


**Fig. 3.** Dependence of the absolute magnitude $H$ on the proper semi-major axis $a_p$ for the eight families: Flora, Koronis, Eos, Eunomia, Phocaea, Themis, Maria and Alauda with the likely positions of the family centers (vertical lines). We also plot the possible range of the ($a_p$, $H$) borders (two thick lines) of each family for values of the parameter $C$ from Brož et al. (2013) (different values correspond to a different initial extent of the family or different age and magnitude of the Yarkovsky semi-major axis drift.). The pink triangles represent the members from our sample (M), green circles borderline cases (B) and blue circles interlopers (I). Borderline cases and interlopers are identified by several methods including the position in the ($a_p$, $H$) diagram, and thus could also lie close to the center of the family (e.g., in the case of the Flora family).

diagrams for all eight studied families. We plotted the adopted ($a_p$, $H$) border (from Brož et al. 2013) and labeled the members, borderline cases, and interlopers by different colors.

Several asteroids in our sample belong to smaller and younger subclusters within the studied families (e.g., (832) Karin in the Koronis family, (1270) Datura in the Flora

family, or (2384) Schulhof in the Eunomia family). These subclusters were probably created by secondary collisions. As a result, the spin states of asteroids in these subclusters were randomly reoriented. Because our combined orbital- and spin-evolution model (see Sect. 4) includes secondary collisions (reorientations), using asteroids from subclusters in the study of the spin-vector distribution is thus essential: asteroids from subclusters correspond to reoriented asteroids in our synthetic population.

## 3. Observed spin vectors in families

There are eight asteroid families for which we find at least three members (together with borderline cases) in our data set of asteroid models (after the family membership revision, labeled by M or B in the last column of Table 5) – Flora (38 members), Koronis (23), Eos (16), Eunomia (14), Phocaea (11), Themis (9), Maria (9), and Alauda (3) families. Now that we have the models and membership, we can proceed to the discussion of the spin states in families in general (Sect. 3.1), and for families Flora and Koronis (Sects. 3.2, 3.3).

### 3.1. Spin-vector orientations in individual families

In Fig. 4, we show the dependence of asteroid's pole latitudes in ecliptic coordinates on the semi-major axes. If there are two possible pole solutions for an asteroid, we take the first one in Table 1, because it corresponds to a formally better solution, additionally, latitudes for both ambiguous models are usually similar. To determine the centers of families, we use all members of each family assigned by the HCM, see Figs. 1 and 3. The Eos family has an asymmetric V-shape (the ($a_p$, $H$) diagram), so we compute centers for both wings of the V-shape individually. For the Flora family, we use only the right wing of the V-shape to derive the center, while the left one is strongly affected by the $\nu_6$ secular resonance.

In the study of spin-vector properties in families, we simply use the ecliptic coordinates for the pole orientation: ecliptic longitude $\lambda$ and latitude $\beta$. A formally better approach would be to use the coordinates bound to the orbital plane of the asteroid: orbital longitude $\lambda_{orb}$ and latitude $\beta_{orb}$. The orbital latitude can then be easily transformed to obliquity, which directly tells us whether the asteroid rotates in a prograde or retrograde sense. However, for several reasons, we prefer the ecliptic coordinates: (i) most of the asteroids have low inclinations and thus the differences between their ecliptic and orbital latitudes are only a few degrees, and the maximum differences for the families with higher inclination (Eos, Eunomia, Phocaea, Maria) are 20–30°; (ii) the orbital coordinates of the pole direction cannot be computed for partial models, because we do not know the ecliptic longitude, these models represent about 20% of our studied sample; (iii) the positions of the asteroids in the ($a_p$, $\beta$) diagrams (i.e., to which quadrant they belong), namely if they have $\beta > 0°$ or $\beta < 0°$, are sufficient information. Because most of the asteroids have latitudes larger than 30°, their positions in the ($a_p$, $\beta_{orb}$) are similar (not true only for three asteroids out of 136); and (iv) we compare the ($a_p$, $\beta$) diagrams (numbers of objects in the quadrants) between the observed and synthetic populations for ecliptic latitudes, so the consistency is assured.

In general, we observe similar trends for all studied families: (i) larger asteroids are situated in the proximity of the center of the family; (ii) asteroids with $\beta > 0°$ are usually found to the right of the family center; (iii) asteroids with $\beta < 0°$ are to the left of the center; (iv) the majority of asteroids have large pole-ecliptic latitudes ($|\beta| \gtrsim 30°$); and finally (v) some families have a statistically significant excess of asteroids with $\beta > 0°$ or $\beta < 0°$.

Case (i) is evident for families Flora, Eunomia, Phocaea, Themis, or Maria. We have no large asteroids in the samples for the remaining families.

Cases (ii) and (iii) are present among all families with the exception of Eos, where all the asteroids are close to the (badly constrained) center. This phenomenon can be easily explained by the Yarkovsky drift, which can change asteroid's semi-major axes $a$; that is, it can increase $a$ of prograde rotators, and decrease $a$ of retrograde once. The magnitude of the Yarkovsky drift is dependent on the asteroid size, is negligible for asteroids with diameters $D \gtrsim 50$ km (the case of Eos), and increases with decreasing diameter. For the Flora, Eunomia, Phocaea, or Maria families, we can see that the smallest asteroids in the sample ($D \sim$ 5–10 km) can be situated far from the family center, and we can also notice a trend toward decreasing size with increasing distance from the center that probably corresponds to the magnitude of the Yarkovsky effect and the initial velocities $v_{ini}(D)$ that the objects gained after the break-up.

Observation (iv) is a result of the dynamical evolution of the asteroid's spin vector orientations dominated by the YORP effect, which increases the absolute value of the pole-ecliptic latitude. See papers Hanuš et al. (2011, 2013), where this effect is numerically investigated and compared with the observed anisotropic spin vector distribution of the sample of ~300 MBAs.

Case (v) concerns families Flora, Eunomia, Phocaea, Themis, and Maria. The different number of asteroids with $\beta > 0°$ and $\beta < 0°$ among these families is statistically significant and cannot be coincidental. The obvious choice for an explanation are mean-motion or secular resonances. Indeed, the $\nu_6$ secular resonance removed many objects with $\beta > 0°$ from the Flora family (see Sect. 3.2 for a more thorough discussion). The 8:3 resonance with Jupiter truncated the Eunomia family, which resulted in there being no objects with $a_p > 2.70$ AU; similarly, the 3:1 resonance with Jupiter affected the Maria family, for which we do not observe objects with smaller $a_p$ than 2.52 AU. The 3:1 resonance with Jupiter is situated near the Phocaea family at $a = 2.50$ AU. Due to the high inclination of objects in the Phocaea family ($I \sim 24°$), the resonance affects asteroids with $a_p > 2.40$ AU, which corresponds to the probable center of the family. The resonance removed a significant number of objects between 2.40 AU and 2.45 AU, and all objects with larger $a_p$.

The asymmetry of asteroids with $\beta > 0°$ and $\beta < 0°$ in the Themis family is caused by a selection effect: in the family, there are no objects with absolute magnitude $H < 12$ mag (i.e., large asteroids) and $a_p < 3.10$ AU. On the other hand, with $a_p > 3.10$ AU, there are more than a hundred such asteroids (see Fig. 1a). Our sample of asteroid models derived by the lightcurve inversion method is dominated by larger asteroids, so it is not surprising that we did not derive models for the Themis family asteroids with $a_p < 3.10$ AU. The Flora and Koronis families are also interesting for other aspects, and thus are discussed in more detail in Sects. 3.2 and 3.3.

### 3.2. The Flora family

The Flora cluster is situated in the inner part of the main belt between 2.17–2.40 AU, and its left part (with respect to the ($a_p$, $H$) diagram) is strongly affected by the secular $\nu_6$ resonance with Saturn, which is demonstrated in Fig. 1b. The probable center of the family matches the position of asteroid (8) Flora at $a = 2.202$ AU. Because of the relative proximity to the Earth,

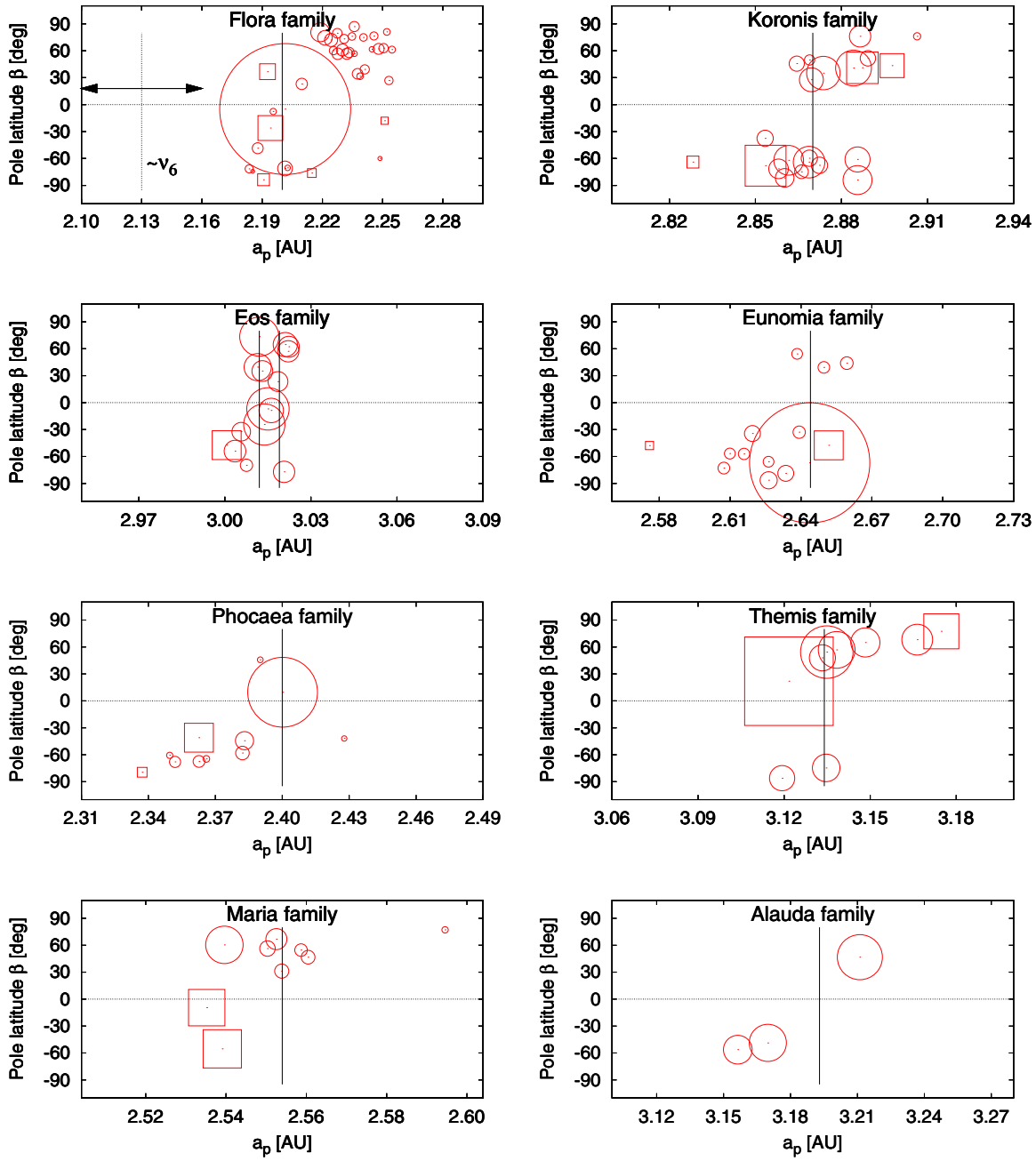


**Fig. 4.** Dependence of the pole latitude $\beta$ on the proper semi-major axis $a_p$ for eight studied asteroid families: Flora, Koronis, Eos, Eunomia, Phocaea, Themis, Maria, and Alauda. Family members are marked by circles and borderline cases by squares, whose sizes are scaled proportionally to diameters. Only the scale for (15) Eunomia was decreased by half to fit the figure. The vertical lines correspond to the likely centers of the asteroid families, whose uncertainties are usually <0.01 AU. The Eos family has an asymmetric V-shape (the ($a_p$, $H$) border is asymmetric), which makes the center determination harder, so we marked two possible positions. One corresponds to the right ($a_p$, $H$) border, the second to the left border. The uncertainties in $\beta$ are usually 5–20°. In most cases, the value of $|\beta| \gtrsim 30°$, hence the quadrant to which the asteroid belongs (defined by the center of the family and the value $\beta = 0°$), is *not* changed.

more photometric measurements of smaller asteroids are available than for more distant families, and thus more models were derived. So far, we identified 38 models of asteroids that belong to the Flora family (together with borderline cases).

The majority of asteroids within this family have $\beta > 0°$ (~68%; due to small inclinations of the family members, the majority of the objects with $\beta > 0°$ are definitely prograde rotators, because their obliquities are between 0° and 90°) and lie to the right of the center of the family, confirming the presence of the Yarkovsky drift. Nine out of twelve asteroids with $\beta < 0°$ can be found in Fig. 4 near to or to the left of the center of the family. The exceptions are the borderline asteroids (1703) Barry and (7360) Moberg, and asteroid (7169) Linda with $a_p$ close to 2.25 AU (see Fig. 4). The borderline category already suggests that the two asteroids could be possible interlopers, and their rotational state seems to support this statement. However, it is also possible that these asteroids have been reoriented by noncatastrophic collisions. The rotational state of another borderline asteroid (800) Kressmannia also does not agree with the Yarkovsky/YORP predictions, so it could be an interloper (or reoriented). The asteroid (7169) Linda classified as a member could still be an interloper, which was not detected by our methods for interloper removal, or could have recently been reoriented by a noncatastrophic collision. The typical timescale for a reorientation (Farinella et al. 1998, see Eq. (5)) of this 4km-sized asteroid with rotational period $P = 27.9$ h is $\tau_{reor} \sim 500$ Myr, which is comparable to the age of the family. The depopulation of poles close to the ecliptic plane is also clearly visible.

The $\nu_6$ resonance to the left of the center of the family creates an excess of retrograde rotators not only among the family, but also among the whole main belt population if we use the currently available sample of asteroid models (there are ~300 asteroid models in the DAMIT database). In the Flora family, there are 14 more asteroids with $\beta > 0°$ than with $\beta < 0°$ (i.e, we have a prograde excess), which corresponds to about 6% of the whole sample. This bias needs to be taken into consideration, for example, in the study of rotational properties among MBAs.

The missing asteroids with $\beta < 0°$ were delivered by this resonance to the orbits crossing the orbits of terrestrial planets and are responsible, for example, for the retrograde excess of the NEAs (La Spina et al. 2004). The $\nu_6$ resonance contributes to the NEA population only by retrograde rotators, and other major mean-motion resonances, such as the 3:1 resonance with Jupiter, deliver both prograde and retrograde rotators in a similar amount.

We did not observe a prograde group of asteroids with similar pole-ecliptic longitudes in the Flora family (i.e., a direct analog of the Slivan state in the Koronis family) that was proposed by Kryszczyńska (2013). Although Kryszczyńska (2013) claims that Slivan states are likely to be observed in the Flora family, no corresponding clustering of poles of the prograde rotators is shown, particularly for ecliptic longitudes. We believe that the term *Slivan state* was used incorrectly there.

### 3.3. The Koronis family

The Koronis family is located in the middle main belt between 2.83–2.95 AU with the center at $a = 2.874$ AU. We identified 23 members (together with borderline cases) with determined shape models. The concept given by the Yarkovsky and YORP predictions also work among the Koronis family (asteroids with $\beta < 0°$ lie to the left from the family center, asteroids with $\beta > 0°$ to the right, see Fig. 4). In addition to that, Slivan (2002) and Slivan et al. (2003) noticed that prograde rotators have also clustered pole longitudes. These asteroids were trapped in a secular spin-orbital resonance $s_6$ and are referred to as being in Slivan states (Vokrouhlický et al. 2003). Several asteroids were later recognized as being incompatible with the Slivan states, such as (832) Karin and (263) Dresda by Slivan & Molnar (2012). Asteroid (832) Karin is the largest member of a young (~5.8 Myr, Nesvorný & Bottke 2004) collisional family that is confined within the larger Koronis family. The spin state of (832) Karin was thus probably affected during this catastrophic event and changed to a random state. Asteroid (263) Dresda could be randomly reoriented by a noncatastrophic collision that is likely to happen for at least a few of 27 asteroids in the Koronis cluster with known spin state solutions, or its initial rotational state and shape did not allow a capture in the resonance. All four borderline asteroids have rotational states that agree with the Yarkovsky/YORP concept, which may support their membership in the Koronis cluster. On the other hand, rotational states of asteroids (277) Elvira and (321) Florentina do not match the expected values, and thus could again be interlopers or be affected by reorientations.

Being trapped in the spin-orbital resonance does not necessarily mean that the asteroid is a member of the Koronis family. It rather indicates that its initial orbital position, the rotational state, and the shape were favorable to being trapped in the resonance. For example, asteroids (311) Claudia, (720) Bohlinia, (1835) Gajdariya, and (3170) Dzhanibekov have expected rotational states but are either rejected from the Koronis family or classified as borderline cases by our membership revision.

## 4. Long-term evolution of spin vectors in asteroid families

Here we present a comparison of the observed spin-vector orientations in several asteroid families with a numerical model of the temporal spin-vector evolutions. We used a *combined* orbital- and spin-evolution model, which was described in detail in Brož et al. (2011). We need to account for the fact that the Yarkovsky semi-major axis drift is sensitive to the orientation of the spin axis, which is in turn affected by the YORP effect and nondisruptive collisions. This model includes the following processes, which are briefly described in the text: (i) impact disruption; (ii) gravitational perturbations of planets; (iii) the Yarkovsky effect; (iv) the YORP effect; (v) collisions and spin-axis reorientations; and (vi) mass shedding.

Impact disruption. To obtain initial conditions for the family just after the breakup event, we used a very simple model of an isotropic ejection of fragments from the work of Farinella et al. (1994). The distribution of velocities "at infinity" follows the function

$$\mathrm{d}N(v)\mathrm{d}v = C' v \left(v^2 + v_{\mathrm{esc}}^2\right)^{-(\alpha+1)/2} \mathrm{d}v, \tag{1}$$

with the exponent $\alpha$ as a free parameter, $C'$ a normalization constant and $v_{\mathrm{esc}}$ the escape velocity from the parent body, which is determined by its size $D_{\mathrm{PB}}$ and mean density $\rho_{\mathrm{PB}}$ as $v_{\mathrm{esc}} = \sqrt{(2/3)\pi G \rho_{\mathrm{PB}}}\, D_{\mathrm{PB}}$. The distribution is usually cut at a selected maximum-allowed velocity $v_{\mathrm{max}}$ to prevent outliers. The initial velocities $|v|$ of individual bodies are generated by a straightforward Monte-Carlo code, and the orientations of the velocity vectors $\boldsymbol{v}$ in space are assigned randomly. We also assume that the velocity of fragments is independent of their size.

We must also select initial osculating eccentricity $e_{\mathrm{i}}$ of the parent body, initial inclination $i_{\mathrm{i}}$, as well as true anomaly $f_{\mathrm{imp}}$ and argument of perihelion $\omega_{\mathrm{imp}}$ at the time of impact disruption, which determine the initial shape of the synthetic family just after the disruption of the parent body.

Gravitational perturbations of planets. Orbital integrations were performed using the SWIFT package (Levison & Duncan 1994), slightly modified to include necessary online digital filters and a second-order symplectic integrator (Laskar & Robutel 2001). The second-order symplectic scheme allows us to use a timestep up to $\Delta t = 91$ d.

Our simulations included perturbations by four outer planets, with their masses, initial positions and velocities taken from the JPL DE405 ephemeris (Standish et al. 1997). We modified the initial conditions of the planets and asteroids by a barycentric correction to partially account for the influence of the terrestrial planets. The absence of the terrestrial planets as perturbers is a reasonable approximation in the middle and outer parts of the main belt (for orbits with $a > 2.5$ AU and $e < 0.6$)[8].

Synthetic proper elements are computed as follows. We first apply a Fourier filter to the (nonsingular) orbital elements in a moving window of 0.7 Myr (with steps of 0.1 Myr) to eliminate all periods smaller than some threshold (1.5 kyr in our case). We use a sequence of Kaiser windows as in Quinn et al. (1991).

The filtered signal, which are mean orbital elements, is then passed through a frequency analysis code adapted from Šidlichovský & Nesvorný (1996) to obtain (planetary) forced and free terms in Fourier representation of the orbital elements. The isolated free terms are what we use as the proper orbital elements.

Yarkovsky effect. Both diurnal and seasonal components of the Yarkovsky accelerations are computed directly in the $N$-body integrator. We used a theory of Vokrouhlický (1998) and Vokrouhlický & Farinella (1999) for spherical objects (but the magnitude of the acceleration does not differ substantially for nonspherical shapes Vokrouhlický & Farinella 1998). The implementation within the SWIFT integrator is described in detail by Brož (2006).

YORP effect. The evolution of the orientation of the spin axis and of the angular velocity is given by

$$\frac{\mathrm{d}\omega}{\mathrm{d}t} = c f_i(\epsilon), \qquad i = 1 \ldots 200, \tag{2}$$

$$\frac{\mathrm{d}\epsilon}{\mathrm{d}t} = c\frac{g_i(\epsilon)}{\omega}, \tag{3}$$

where $f$- and $g$-functions describing the YORP effect for a set of 200 shapes were calculated numerically by Čapek & Vokrouhlický (2004) with the effective radius $R_0 = 1$ km and the bulk density $\rho_0 = 2500\,\mathrm{kg/m^3}$, located on a circular orbit with the semi-major axis $a_0 = 2.5$ AU. We assigned one of the artificial shapes (denoted by the index $i$) to each individual asteroid from our sample. The $f$- and $g$-functions were then scaled by the factor

$$c = c_{\mathrm{YORP}}\left(\frac{a}{a_0}\right)^{-2}\left(\frac{R}{R_0}\right)^{-2}\left(\frac{\rho_{\mathrm{bulk}}}{\rho_0}\right)^{-1}, \tag{4}$$

where $a$, $R$, and $\rho_{\mathrm{bulk}}$ denote the semi-major axis, the radius, and the density of the simulated body, respectively, and $c_{\mathrm{YORP}}$ is a free scaling parameter reflecting our uncertainty in the shape models and the magnitude of the YORP torque, which depends on small-sized surface features (even boulders, Statler 2009) and other simplifications in the modeling of the YORP torque. In Hanuš et al. (2013), we constrained this parameter and find $c_{\mathrm{YORP}} = 0.2$ to be the optimal value when comparing the results of the simulation with the observed latitude distribution of main belt asteroids. In our simulation, we used this value for $c_{\mathrm{YORP}}$.

The differential Eqs. (2) and (3) are integrated numerically by a simple Euler integrator. The usual time step is $\Delta t = 1000$ yr.

Collisions and spin-axis reorientations. We neglected the effect of disruptive collisions because we do not want to lose objects during the simulation, but we included spin axis reorientations caused by collisions. We use an estimate of the timescale by Farinella et al. (1998).

$$\tau_{\mathrm{reor}} = B\left(\frac{\omega}{\omega_0}\right)^{\beta_1}\left(\frac{D}{D_0}\right)^{\beta_2}, \tag{5}$$

where $B = 84.5$ kyr, $\beta_1 = 5/6$, $\beta_2 = 4/3$, $D_0 = 2$ m, and $\omega_0$ corresponds to period $P = 5$ h. These values are characteristic of the main belt.

Mass shedding. If the angular velocity approaches a critical value

$$\omega_{\mathrm{crit}} = \sqrt{\frac{4}{3}\pi G\rho_{\mathrm{bulk}}}, \tag{6}$$

we assume a mass shedding event, so we keep the orientation of the spin axis and the sense of rotation, but we reset the orbital period $P = 2\pi/\omega$ to a random value from the interval $(2.5, 9)$ h. We also change the assigned shape to a different one, since any change in shape may result in a different YORP effect.

Synthetic Flora, Koronis, and Eos families. In Fig. 5 (top panel), we show a long-term evolution of the synthetic Flora family in the proper semi-major axis $a_{\mathrm{p}}$ vs. the pole latitude $\beta$ plane for objects larger and smaller than 30 km. The values of the model parameters are listed in the figure caption. Larger asteroids do not evolve significantly and remain close to their initial positions. On the other hand, smaller asteroids ($D < 30$ km) are strongly affected by the Yarkovsky and YORP effects: They drift in the semi-major axis, differently for prograde and retrograde rotators, and their pole orientations become mostly perpendicular to their orbits (corresponding to the proximity of the ecliptic plane for small inclinations). After the simulation at $t = 1$ Gyr, we observe a deficiency of asteroids with $\beta > 0°$ to the left of the family center and a deficiency of asteroids with $\beta < 0°$ to the right of the family center.

The asymmetry of the synthetic Flora family with respect to its center (Fig. 5) caused by the secular $\nu_6$ resonance is obvious. The own-right hand quadrant ($\beta < 0°$, $a_{\mathrm{p}} > 2.202$ AU) still contains many objects for $t = 1$ Gyr, because for some of them the evolution in $\beta$ and $a_{\mathrm{p}}$ is rather small, and others were delivered to this quadrant by collisional reorientations.

The appearance of the evolved proper semi-major axis $a_{\mathrm{p}}$ vs. the pole latitude $\beta$ diagrams for Koronis and Eos families are qualitatively similar to the one of the Flora family. Because the asteroid samples for Koronis and Eos families are dominated by intermediate-sized asteroids ($D \sim 20$–$50$ km), the evolution in $a_{\mathrm{p}}$ and $\beta$ is on average slower than in the Flora family. We show the state of the simulation for Koronis family in 4 Gyr and

[8] For the Flora family located in the inner belt, we should account for terrestrial planets directly, because of mean-motion resonances with Mars, but we decided not do so to speed the computation up. Anyway, the major perturbation we need to account for is the $\nu_6$ secular resonance, which is indeed present in our model.

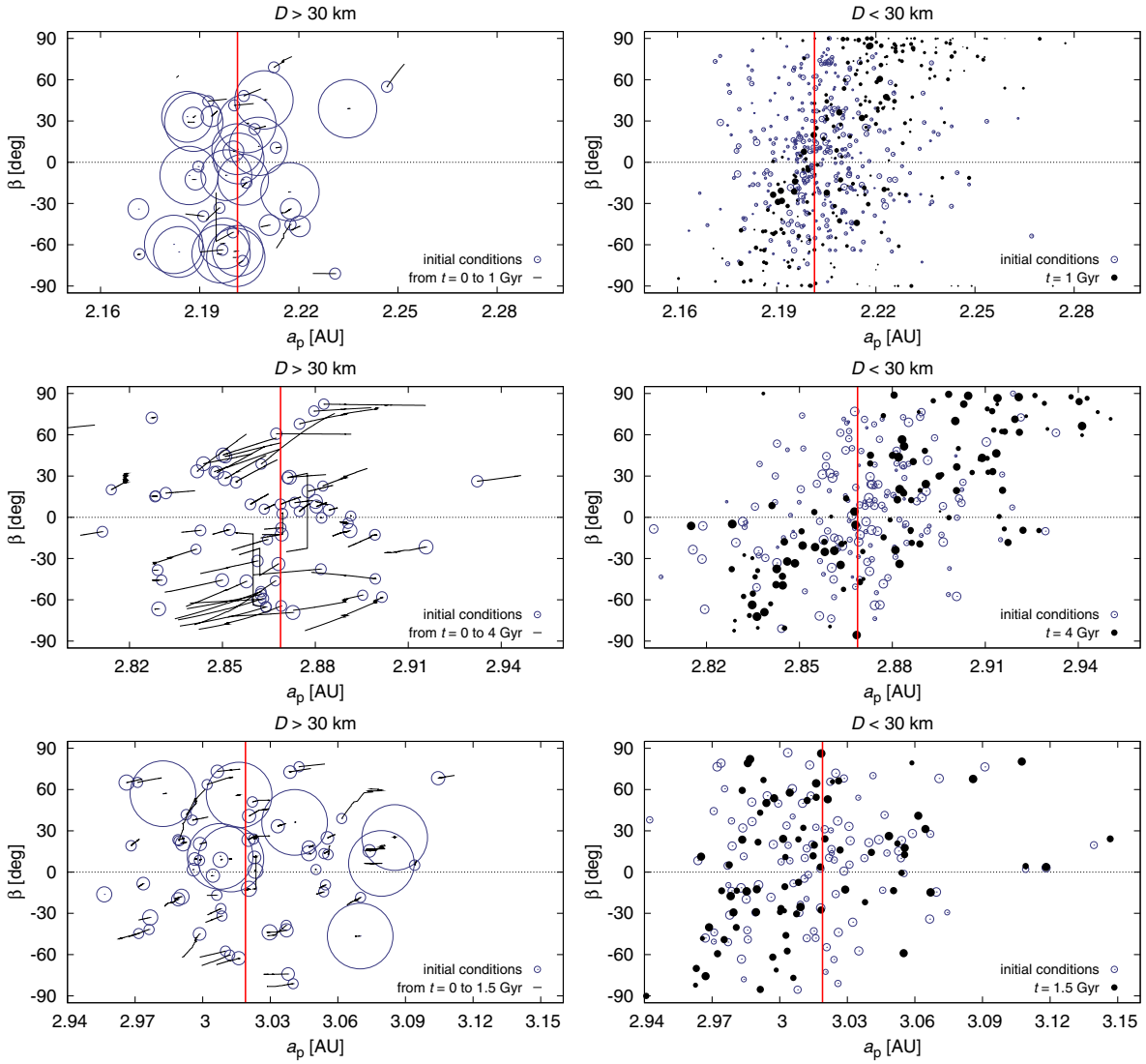


**Fig. 5.** A simulation of the long-term evolution of the synthetic Flora (*top*), Koronis (*middle*) and Eos (*bottom*) families in the proper semi-major axis $a_p$ vs. the pole latitude $\beta$ plane. *Left*: objects larger than $D > 30$ km, which almost do not evolve in $\beta$. *Right*: objects with $D \leq 30$ km, with the initial conditions denoted by empty circles and an evolved state at 1 Gyr denoted by full circles. The sizes of symbols correspond to the actual diameters $D$. The initial conditions for Flora correspond to an isotropic size-independent velocity field with $\alpha = 3.25$ and $v_{esc} = 95\,\mathrm{m\,s^{-1}}$, and a uniform distribution of poles (i.e. $\sin\beta$). We increase the number of objects 10 times compared to the observed members of the Flora (Koronis and Eos as well) family to improve statistics. We retain their size distribution, of course. The objects in Flora family are discarded from these plots when they left the family region (eccentricity $e_p = 0.1$ to 0.18, inclination $\sin I_p = 0.05$ to 0.13), because they are affected by strong mean-motion or secular resonances ($\nu_6$ in this case). Thermal parameters were set as follows: the bulk density $\rho_{bulk} = 2500\,\mathrm{kg\,m^{-3}}$, the surface density $\rho_{surf} = 1500\,\mathrm{kg\,m^{-3}}$, the thermal conductivity $K = 0.001\,\mathrm{W\,m^{-1}\,K^{-1}}$, the thermal capacity $C_t = 680\,\mathrm{J\,kg^{-1}}$, the Bond albedo $A = 0.1$, and the infrared emissivity $\epsilon = 0.9$. The time step for the orbital integration is $dt = 91$ days and $dt_{spin} = 10^3$ yr for the (parallel) spin integration. The parameters for Koronis and Eos are chosen similarly, only for Koronis do we use $v_{esc} = 100\,\mathrm{m\,s^{-1}}$, and $v_{esc} = 225\,\mathrm{m\,s^{-1}}$ and $\rho_{surf} = 2500\,\mathrm{kg\,m^{-3}}$ for Eos.

for Eos in 1.5 Gyr (based on the expected ages). The Eos family thus seems less evolved than the Koronis family.

We also checked the distributions of the proper eccentricities and inclinations of the synthetic Flora/Koronis/Eos objects for whether they (at least roughly) correspond to the observed family. However, the number of objects to compare is fairly low and seems insufficient for any detailed comparison of distributions in 3D space of proper elements ($a_p$, $e_p$, $\sin I_p$).

**Ages of the Flora, Koronis, and Eos families.** To quantitatively compare the simulation of the long-term evolution of the synthetic families in the proper semi-major axis $a_p$ vs. the pole latitude $\beta$ plane with the observation, we constructed the following metric: we divide the $(a_p, \beta)$ plane into four quadrants defined by the center of the family and value $\beta = 0°$ and compute the ratio $(k_2 + k_4)/(k_1 + k_3)$, where $k_i$ correspond to the numbers of synthetic objects in quadrants $i$ ($i = 1, 2, 3, 4$). In Fig. 6, we show the

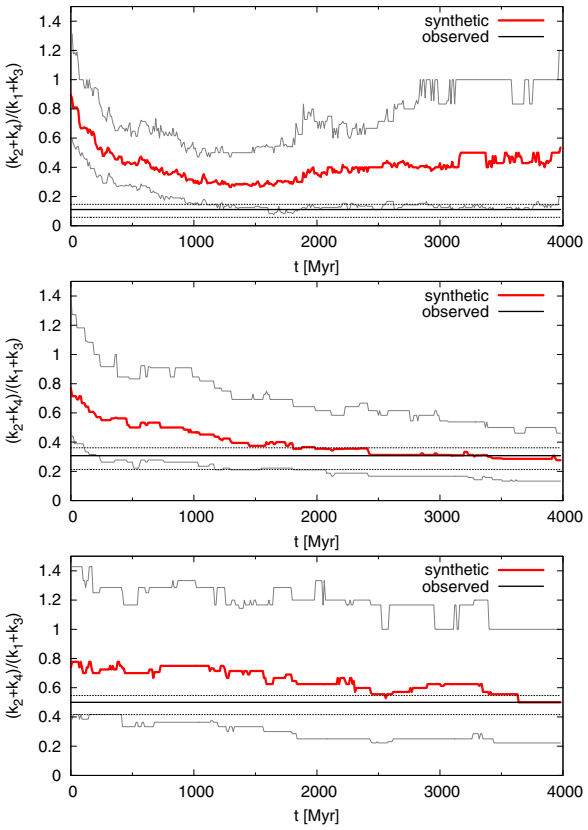


**Fig. 6.** Time evolution of the metric $(k_2 + k_4)/(k_1 + k_3)$, where $k_i$ correspond to the numbers of synthetic objects in quadrants $i$ ($i = 1, 2, 3, 4$) that are defined by the center of the family and value $\beta = 0°$, for synthetic Flora, Koronis, and Eos families (red lines). The spread corresponds to 100 different selections of objects (we simulate 10 times more objects to reach a better statistics). the upper curve denotes the 90% quantile and the bottom 10%. Thick horizontal line is the observed ratio $(k_2 + k_4)/(k_1 + k_3)$ with the uncertainty interval.

evolution of the metric $(k_2 + k_4)/(k_1 + k_3)$ during the simulation of families Flora, Koronis, and Eos for all synthetic objects with $D < 30$ km, and the value of the same metric for the observed population for comparison.

For the Koronis family (middle panel), the synthetic ratio reaches the observed one after $t = 2.5$ Gyr and remains similar until the end of the simulation at $t = 4$ Gyr. Bottke et al. (2001) published the age $t = (2.5 \pm 1.0)$ Gyr for the Koronis family. Unfortunately, we cannot constrain the age of the Eos family from this simulation owing to objects with the relatively small evolution in $a_p$ and $\beta$. The fit for the Flora family is not ideal, and the reason could be differences in the initial velocity field or the true anomaly $f_{imp}$ of the impact. The best agreement is for the age $t = (1.0 \pm 0.5)$ Gyr, which is approximately in agreement with the dynamical age in Nesvorný et al. (2005): $(1.5 \pm 0.5)$ Gyr.

## 5. Conclusions

We have identified 152 asteroids for which we have convex shape models, and simultaneously the HCM identifies them as members of ten collisional families. Owing to a large number of expected interlopers in families Vesta and Nysa/Polana, we excluded these families from the study of the rotational properties. In the remaining sample of asteroids from eight families, we identified ~20% of objects that are interlopers or borderline cases (see Table 4). We used several methods, described in Sect. 2.1, for their identification. The borderline cases are still possible members of the families and thus were included in our study of the spin-vector distribution.

From the dependence of the asteroid's pole latitudes on the semi-major axes, plotted in Fig. 4, we can see fingerprints of families spreading in $a$ and spin axis evolution due to Yarkovsky and YORP effects: Asteroids with $\beta < 0°$ lie on the left side of the center of the family, and asteroids with $\beta > 0°$ on the right side. The asymmetry with respect to the family centers is in most cases caused by various resonances that cut the families, and in the case of Themis family, a selection effect is responsible.

However, we did not observe *perfect* agreement with the Yarkovsky and YORP effects predictions. A few individual objects (eight) that have incompatible rotational states could (i) be incorrectly determined; (ii) be interlopers; (iii) have initial rotational states that only cause a small evolution in the $(a_p, \beta)$ space (i.e., they are close to their initial positions after the break-up); or (iv) be recently reoriented by collisional events.

In the case of the Flora family, significantly fewer asteroids with $\beta < 0°$ (~32%) than with $\beta > 0°$ (~68%) are present. The secular $\nu_6$ resonance is responsible for this strong deficit, because objects with $\beta < 0°$ are drifting towards this resonance and are subsequently removed from the family. They become part of the NEAs population where they create an excess of retrograde rotators. We did not find any analog of the Slivan states (observed in the Koronis family) among any other of the studied families.

We simulated a long-term evolution of the synthetic Flora, Koronis, and Eos families (Fig. 5) in the proper semi-major axis $a_p$ vs the pole latitude $\beta$ plane and compared the results with the properties of observed asteroid families. We obtained a good qualitative agreement between the observed and synthetic spin-vector distributions. For all three families, we computed evolution of the number of objects in the four quadrants of the families in the $(a_p, \beta)$ diagram, and we estimated ages for families Flora $(1.0 \pm 0.5)$ Gyr and Koronis (2.5 to 4 Gyr) that agree with previously published values. However, we did not estimate the age of the Eos family due to a small evolution of the objects in the $(a_p, \beta)$ diagram.

The uncertainties seem to be dominated by the observed quadrant ratios. We expect that increasing the sample size by a factor of 10 would decrease the relative uncertainty by a factor of about 3, which is a good motivation for further work on this subject.

*Acknowledgements.* The work of J.H. and J.D. has been supported by grants GACR P209/10/0537 and P209/12/0229 of the Czech Science Foundation, and the work of J.D. and M.B. by the Research Program MSM0021620860 of the Czech Ministry of Education. The work of M.B. has been also supported by grant GACR 13-013085 of the Czech Science Foundation.

## References

Binzel, R. P., Slivan, S. M., Magnusson, P., et al. 1993, Icarus, 105, 310
Bottke, W. F., Vokrouhlický, D., Brož, M., Nesvorný, D., & Morbidelli, A. 2001, Science, 294, 1693
Bottke, J. W. F., Vokrouhlický, D., Rubincam, D. P., & Nesvorný, D. 2006, Ann. Rev. Earth Planet. Sci., 34, 157
Brinsfield, J. W. 2008a, Minor Planet Bulletin, 35, 179
Brinsfield, J. W. 2008b, Minor Planet Bulletin, 35, 119
Brinsfield, J. W. 2009, Minor Planet Bulletin, 36, 127

Brož, M. 2006, Ph.D. Thesis, Charles University in Prague
Brož, M., Vokrouhlický, D., Morbidelli, A., Nesvorný, D., & Bottke, W. F. 2011, MNRAS, 414, 2716
Brož, M., Morbidelli, A., Bottke, W. F., et al. 2013, A&A, 551, A117
Bus, S. J., & Binzel, R. P. 2002, Icarus, 158, 146
Čapek, D., & Vokrouhlický, D. 2004, Icarus, 172, 526
Davies, M. E., Colvin, T. R., Belton, M. J. S., et al. 1994a, in AAS/Division for Planetary Sciences Meeting Abstracts #26, BAAS, 26, 1154
Davies, M. E., Colvin, T. R., Belton, M. J. S., Veverka, J., & Thomas, P. C. 1994b, Icarus, 107, 18
Drummond, J., Eckart, A., & Hege, E. K. 1988, Icarus, 73, 1
Ďurech, J., Scheirich, P., Kaasalainen, M., et al. 2007, in IAU Symp. 236, eds. G. B. Valsecchi, D. Vokrouhlický, & A. Milani, 191
Ďurech, J., Kaasalainen, M., Warner, B. D., et al. 2009, A&A, 493, 291
Ďurech, J., Sidorin, V., & Kaasalainen, M. 2010, A&A, 513, A46
Ďurech, J., Kaasalainen, M., Herald, D., et al. 2011, Icarus, 214, 652
Durkee, R. I. 2010, Minor Planet Bulletin, 37, 125
Farinella, P., Froeschlé, C., & Gonczi, R. 1994, in Asteroids, Comets, Meteors 1993, eds. A. Milani, M. di Martino, & A. Cellino, IAU Symp., 160, 205
Farinella, P., Vokrouhlický, D., & Hartmann, W. K. 1998, Icarus, 132, 378
Giblin, I., Martelli, G., Farinella, P., et al. 1998, Icarus, 134, 77
Hanuš, J., Ďurech, J., Brož, M., et al. 2011, A&A, 530, A134
Hanuš, J., Ďurech, J., Brož, M., et al. 2013, A&A, 551, A67
Higgins, D. 2011, Minor Planet Bulletin, 38, 41
Higgins, D., & Goncalves, R. M. D. 2007, Minor Planet Bulletin, 34, 16
Johansen, A., & Lacerda, P. 2010, MNRAS, 404, 475
Kaasalainen, M., & Torppa, J. 2001, Icarus, 153, 24
Kaasalainen, M., Torppa, J., & Muinonen, K. 2001, Icarus, 153, 37
Kaasalainen, M., Torppa, J., & Piironen, J. 2002, Icarus, 159, 369
Koff, R. A., Brincat, S. M., Stephens, R. D., & Pravec, P. 2001, Minor Planet Bulletin, 28, 46
Kryszczyńska, A. 2013, A&A, 551, A102
Kryszczyńska, A., La Spina, A., Paolicchi, P., et al. 2007, Icarus, 192, 223
La Spina, A., Paolicchi, P., Kryszczyńska, A., & Pravec, P. 2004, Nature, 428, 400
Lagerkvist, C., Barucci, M. A., Capria, M. T., et al. 1987, Asteroid photometric catalogue (Roma: CNR)
Larson, S., Beshore, E., Hill, R., et al. 2003, in AAS/Division for Planetary Sciences Meeting Abstracts #35, BAAS, 35, 982
Laskar, J., & Robutel, P. 2001, Celest. Mech. Dyn. Astron., 80, 39
Levison, H. F., & Duncan, M. J. 1994, Icarus, 108, 18
Magnusson, P. 1986, Icarus, 68, 1
Marchis, F., Kaasalainen, M., Hom, E. F. Y., et al. 2006, Icarus, 185, 39
Marciniak, A., Michałowski, T., Kaasalainen, M., et al. 2007, A&A, 473, 633
Masiero, J. R., Mainzer, A. K., Grav, T., et al. 2011, ApJ, 741, 68
Michel, P., Jutzi, M., Richardson, D. C., & Benz, W. 2011, Icarus, 211, 535
Nesvorný, D. 2012, in NASA Planetary Data System, 189
Nesvorný, D., & Bottke, W. F. 2004, Icarus, 170, 324
Nesvorný, D., & Morbidelli, A. 1998, AJ, 116, 3029
Nesvorný, D., Jedicke, R., Whiteley, R. J., & Ž. Ivezić. 2005, Icarus, 173, 132
Oey, J. 2006, Minor Planet Bulletin, 33, 96
Paolicchi, P., & Kryszczyńska, A. 2012, Planet. Space Sci., 73, 70
Parker, A., Ž. Ivezić, Jurić, M., et al. 2008, Icarus, 198, 138
Piironen, J., Lagerkvist, C., Torppa, J., Kaasalainen, M., & Warner, B. 2001, BAAS, 33, 1562
Polishook, D., Ofek, E. O., Waszczak, A., et al. 2012, MNRAS, 421, 2094
Pravec, P., Harris, A. W., Kušnirák, P., Galád, A., & Hornoch, K. 2012, Icarus, 221, 365
Pravec, P., Harris, A. W., & Michałowski, T. 2002, Asteroids III, 113
Quinn, T. R., Tremaine, S., & Duncan, M. 1991, AJ, 101, 2287
Rau, A., Kulkarni, S. R., Law, N. M., et al. 2009, PASP, 121, 1334
Rubincam, D. P. 2000, Icarus, 148, 2
Šidlichovský, M., & Nesvorný, D. 1996, Celest. Mech. Dyn. Astron., 65, 137
Skoglöv, E., & Erikson, A. 2002, Icarus, 160, 24
Slivan, S. M. 2002, Nature, 419, 49
Slivan, S. M., & Molnar, L. A. 2012, Icarus, 220, 1097
Slivan, S. M., Binzel, R. P., Crespo da Silva, L. D., et al. 2003, Icarus, 162, 285
Slivan, S. M., Binzel, R. P., Kaasalainen, M., et al. 2009, Icarus, 200, 514
Standish, E. M., Newhall, X. X., Williams, J. G., & Folkner, W. M. 1997, JPL Planetary and Lunar Ephemerides, CD-ROM published by Willmann-Bell, Inc., Richmond, Virginia
Statler, T. S. 2009, Icarus, 202, 502
Stephens, R. D. 2003, Minor Planet Bulletin, 30, 1
Stephens, R. D. 2005, Minor Planet Bulletin, 32, 66
Stephens, R. D. 2007a, Minor Planet Bulletin, 34, 31
Stephens, R. D. 2007b, Minor Planet Bulletin, 34, 102
Stephens, R. D. 2007c, Minor Planet Bulletin, 34, 64
Stephens, R. D. 2011a, Minor Planet Bulletin, 38, 211
Stephens, R. D. 2011b, Minor Planet Bulletin, 38, 23
Strabla, L., Quadri, U., Girelli, R., & Pilcher, F. 2012, Minor Planet Bulletin, 39, 154
Tholen, D. J. 1984, Ph.D. Thesis, Tucson: Arizona Univ.
Tholen, D. J. 1989, in Asteroids II, ed. R. P. Binzel, T. Gehrels, & M. S. Matthews, 1139
Torppa, J., Kaasalainen, M., Michałowski, T., et al. 2003, Icarus, 164, 346
Vokrouhlický, D. 1998, A&A, 335, 1093
Vokrouhlický, D., & Farinella, P. 1998, AJ, 116, 2032
Vokrouhlický, D., & Farinella, P. 1999, AJ, 118, 3049
Vokrouhlický, D., Nesvorný, D., & Bottke, W. F. 2003, Nature, 425, 147
Vokrouhlický, D., Brož, M., Michałowski, T., et al. 2006a, Icarus, 180, 217
Vokrouhlický, D., Nesvorný, D., & Bottke, W. F. 2006b, Icarus, 184, 1
Vokrouhlický, D., Durech, J., Michałowski, T., et al. 2009, A&A, 507, 495
Warner, B. 2001, Minor Planet Bulletin, 28, 40
Warner, B. D. 2004, Minor Planet Bulletin, 31, 19
Warner, B. D. 2005, Minor Planet Bulletin, 32, 29
Warner, B. D. 2006, Minor Planet Bulletin, 33, 82
Warner, B. D. 2009, Minor Planet Bulletin, 36, 172
Warner, B. D. 2010, Minor Planet Bulletin, 37, 112
Warner, B. D. 2011, Minor Planet Bulletin, 38, 63
Warner, B. D., & Pray, D. P. 2009, Minor Planet Bulletin, 36, 166
Warner, B. D., Harris, A. W., & Pravec, P. 2009, Icarus, 202, 134
Zappalà, V., Cellino, A., Farinella, P., & Knežević, Z. 1990, AJ, 100, 2030
Zappalà, V., Cellino, A., Farinella, P., & Milani, A. 1994, AJ, 107, 772

Pages 14 to 19 are available in the electronic edition of the journal at http://www.aanda.org

**Table 3.** Observations not included in the UAPC used for successful model determinations.

| Asteroid | | Date | Observer | Observatory (MPC code) |
|---|---|---|---|---|
| 364 | Isara | 2009 5–2009 05 | Warner (2009) | Palmer Divide Observatory (716) |
| 391 | Ingeborg | 2000 8–2000 12 | Koff et al. (2001) | Antelope Hills Observatory, Bennett (H09) |
| 502 | Sigune | 2007 6 – 2007 6 | Stephens (2007b) | Goat Mountain Astronomical Research Station (G79) |
| 553 | Kundry | 2004 12–2005 1 | Stephens (2005) | Goat Mountain Astronomical Research Station (G79) |
| 616 | Elly | 2010 1–2010 1 | Warner (2010) | Palmer Divide Observatory (716) |
| | | 2010 2–2010 2 | Durkee (2010) | Shed of Science Observatory, USA (H39) |
| 621 | Werdandi | 2012 1 22.9 | Strabla et al. (2012) | Bassano Bresciano Observatory (565) |
| | | 2012 1–2012 2 | Strabla et al. (2012) | Organ Mesa Observatory (G50) |
| 1307 | Chimmeria | 2004 9–2004 9 | Warner (2005) | Palmer Divide Observatory (716) |
| 1396 | Outeniqua | 2006 3–2006 3 | Warner (2006) | Palmer Divide Observatory (716) |
| 1446 | Sillanpaa | 2009 3–2009 3 | Higgins[1] | Hunters Hill Observatory, Ngunnawal (E14) |
| 1464 | Armisticia | 2008 1–2008 1 | Brinsfield (2008b) | Via Capote Sky Observatory, Thousand Oaks (G69) |
| 1619 | Ueta | 2010 9–2010 10 | Higgins (2011) | Hunters Hill Observatory, Ngunnawal (E14) |
| | | 2010 9–2010 9 | Stephens (2011b) | Goat Mountain Astronomical Research Station (G79) |
| 1633 | Chimay | 2008 4–2008 4 | Brinsfield (2008a) | Via Capote Sky Observatory, Thousand Oaks (G69) |
| 1987 | Kaplan | 2000 10–2000 10 | Warner (2001, 2011) | Palmer Divide Observatory (716) |
| | | 2011 12–2011 12 | Warner | Palmer Divide Observatory (716) |
| 2086 | Newell | 2007 1–2007 2 | Stephens (2007c) | Goat Mountain Astronomical Research Station (G79) |
| 2403 | Bruce Helin | 2006 9–2006 9 | Higgins[1] | Hunters Hill Observatory, Ngunnawal (E14) |
| 3279 | Solon | 2006 11–2006 11 | Stephens (2007a) | Goat Mountain Astronomical Research Station (G79) |
| 3492 | Petra-Pepi | 2011 6–2011 7 | Stephens (2011a) | Goat Mountain Astronomical Research Station (G79) |
| 3786 | Yamada | 2002 7–2002 8 | Stephens (2003) | Goat Mountain Astronomical Research Station (G79) |
| 3896 | Pordenone | 2007 10–2007 10 | Higgins[1] | Hunters Hill Observatory, Ngunnawal (E14) |
| 4209 | Briggs | 2003 9–2003 9 | Warner (2004) | Palmer Divide Observatory (716) |
| 4399 | Ashizuri | 2008 6–2008 6 | Brinsfield (2008a) | Via Capote Sky Observatory, Thousand Oaks (G69) |
| 4606 | Saheki | 2009 1–2009 3 | Brinsfield (2009) | Via Capote Sky Observatory, Thousand Oaks (G69) |
| 6159 | 1991 YH | 2006 3–2006 3 | Warner (2006) | Palmer Divide Observatory (716) |
| 6179 | Brett | 2009 4–2009 4 | Warner & Pray (2009) | Palmer Divide Observatory (716) |
| 6262 | Javid | 2010 2–2010 2 | PTF[2] | |
| 6403 | Steverin | 2004 9–2004 9 | Warner (2005) | Palmer Divide Observatory (716) |
| 7043 | Godart | 2008 8–2008 8 | Durkee | Shed of Science Observatory, USA (H39) |
| | | 2008 8–2008 9 | Pravec et al. (2012) | Goat Mountain Astronomical Research Station (G79) |
| 7055 | 1989 KB | 2007 5–2007 5 | Stephens (2007b) | Goat Mountain Astronomical Research Station (G79) |
| | | 2007 5–2007 6 | Higgins[1] | Hunters Hill Observatory, Ngunnawal (E14) |
| 7169 | Linda | 2006 8–2006 8 | Higgins & Goncalves (2007) | Hunters Hill Observatory, Ngunnawal (E14) |
| 7360 | Moberg | 2006 4–2006 4 | Oey (2006) | Leura (E17) |

**Notes.** [(1)] On line at `http://www.david-higgins.com/Astronomy/asteroid/lightcurves.htm` [(2)] Palomar Transient Factory survey (Rau et al. 2009), data taken from Polishook et al. (2012).

**Table 4.** List of asteroids for which the HCM alone suggests membership in families Flora, Koronis, Eos, Eunomia, Phocaea, and Alauda.

| Asteroid | | Status | Reason |
|---|---|---|---|
| | | | Flora |
| 9 | Metis | Interloper | Far from the ($a_p$, $H$) border, peculiar SFD |
| 43 | Ariadne | Interloper | Associated at $v_{cutoff}$ = 70 m/s, peculiar SFD |
| 352 | Gisela | Borderline | Associated at $v_{cutoff}$ = 70 m/s, big object |
| 364 | Isara | Interloper | Big, peculiar SFD, close to ($a_p$, $H$) border |
| 376 | Geometria | Interloper | Far from the ($a_p$, $H$) border, peculiar SFD |
| 800 | Kressmannia | Borderline | Associated at $v_{cutoff}$ = 70 m/s, lower albedo |
| 1188 | Gothlandia | Borderline | Associated at $v_{cutoff}$ = 70 m/s |
| 1419 | Danzing | Interloper | Far from the ($a_p$, $H$) border |
| 1703 | Barry | Borderline | Associated at $v_{cutoff}$ = 70 m/s |
| 2839 | Annette | Interloper | Associated at $v_{cutoff}$ = 70 m/s, C type |
| 7360 | Moberg | Borderline | Redder (color from SDSS MOC4) |
| | | | Koronis |
| 167 | Urda | Borderline | Close to the ($a_p$, $H$) border |
| 208 | Lacrimosa | Interloper | Far from the ($a_p$, $H$) border, peculiar SFD |
| 311 | Claudia | Borderline | Close to the ($a_p$, $H$) border |
| 720 | Bohlinia | Borderline | Close to the ($a_p$, $H$) border |
| 1835 | Gajdariya | Interloper | Close to the ($a_p$, $H$) border, incompatible albedo |
| 2953 | Vysheslavia | Borderline | Close to the ($a_p$, $H$) border |
| 3170 | Dzhanibekov | Interloper | Behind the ($a_p$, $H$) border, incompatible albedo |
| | | | Eos |
| 423 | Diotima | Interloper | Far from the ($a_p$, $H$) border, big, C type |
| 590 | Tomyris | Borderline | Close to the ($a_p$, $H$) border |
| | | | Eunomia |
| 85 | Io | Interloper | Behind the ($a_p$, $H$) border, peculiar SFD, incompatible albedo |
| 390 | Alma | Borderline | Borderline albedo, borderline in ($a_p$, $e_p$, $I_p$) space |
| 4399 | Ashizuri | Borderline | Close to the ($a_p$, $H$) border |
| | | | Phocaea |
| 290 | Bruna | Borderline | Close to the ($a_p$, $H$) border |
| 391 | Ingeborg | Interloper | Clearly outside ($a_p$, $H$) |
| 852 | Wladilena | Borderline | Slightly outside ($a_p$, $H$) |
| 1963 | Bezovec | Interloper | C type, incompatible albedo ($p_V$ = 0.04) |
| 5647 | 1990 TZ | Interloper | Incompatible albedo ($p_V$ = 0.64) |
| | | | Themis |
| 62 | Erato | Borderline | Close to the ($a_p$, $H$) border |
| 1633 | Chimay | Borderline | Close to the ($a_p$, $H$) border |
| | | | Maria |
| 695 | Bella | Borderline | Close to the ($a_p$, $H$) border |
| 714 | Ulula | Borderline | Close to the ($a_p$, $H$) border |
| | | | Alauda |
| 276 | Adelheid | Interloper | Far from the ($a_p$, $H$) border, big |

**Notes.** By additional methods for determining family membership we identify them as interlopers or borderline cases. We also give the name of the asteroid, the family membership according the HCM, if it is an interloper or a borderline case and the reason. Peculiar SFD means a size frequency distribution that is incompatible with the SFD typically created by catastrophic collisions or cratering events (i.e., a large remnant, large fragment, and steep slope). Quantity $v_{cutoff}$ corresponds to the cutoff value of the HCM for a particular family.

**Table 5.** List of asteroids that (i) have been identified as members of the Flora, Koronis, Eos, Eunomia, Phocaea, Themis, Maria, Vesta, Nysa/Polana, and Alauda families by the HCM; and (ii) for which shape models from LI are available in the DAMIT database or are newly derived.

| Asteroid | $\lambda_1$ [deg] | $\beta_1$ [deg] | $\lambda_2$ [deg] | $\beta_2$ [deg] | $P$ [hours] | $a_p$ [AU] | $D$ [km] | Bus/DeMeo | Tholen | $p_V$ | M/I/B | Reference |
|---|---|---|---|---|---|---|---|---|---|---|---|---|
| Flora | | | | | | | | | | | | |
| 8 Flora | 335 | −5 | 155 | 6 | 12.8667 | 2.2014 | 141.0 | – | S | 0.26 ± 0.05 | M | Torppa et al. (2003) |
| 9 Metis | 180 | 22 | | | 5.079177 | 2.3864 | 169.0 | – | S | 0.13 ± 0.02 | I | Torppa et al. (2003) |
| 43 Ariadne | 253 | −15 | | | 5.761987 | 2.2034 | 72.1 | Sk | S | 0.23 ± 0.05 | I | Kaasalainen et al. (2002) |
| 281 Lucretia | 128 | −49 | 309 | −61 | 4.349711 | 2.1878 | 11.8 | S | SU | 0.20 ± 0.01 | M | Hanuš et al. (2013)/Kryszczyńska (2013) |
| 352 Gisela | 205 | −26 | 23 | −20 | 7.48008 | 2.1941 | 26.7 | Sl | S | 0.19 ± 0.02 | B | Hanuš et al. (2013) |
| 364 Isara | 282 | 44 | 86 | 42 | 9.15748 | 2.2208 | 35.2 | – | S | 0.16 ± 0.03 | I | this work |
| 376 Geometria | 239 | 45 | 63 | 53 | 7.71098 | 2.2886 | 39.0 | Sl | S | 0.19 ± 0.04 | I | Hanuš et al. (2011) |
| 540 Rosamunde | 301 | 81 | 127 | 62 | 9.34779 | 2.2189 | 20.3 | – | S | 0.22 ± 0.05 | M | this work |
| 553 Kundry | 197 | 73 | 359 | 64 | 12.6025 | 2.2308 | 9.6 | S | – | 0.25 ± 0.04 | M | this work |
| 685 Hermia | 197 | 87 | 29 | 79 | 50.387 | 2.2359 | 10.9 | – | – | 0.28 ± 0.05 | M | Hanuš et al. (2011) |
| 700 Auravictrix | 67 | 46 | 267 | 51 | 6.074836 | 2.2295 | 20.6 | – | – | 0.14 ± 0.05 | M | Kryszczyńska (2013) |
| 800 Kressmannia | 345 | 37 | 172 | 34 | 4.460964 | 2.1927 | 17.0 | – | S | 0.15 ± 0.02 | B | Hanuš et al. (2011) |
| 823 Sisigambis | 86 | 74 | | | 146.58 | 2.2213 | 15.8 | – | – | 0.23 ± 0.03 | M | Hanuš et al. (2011) |
| 915 Cosette | 350 | 56 | 189 | 61 | 4.46974 | 2.2277 | 12.3 | – | – | 0.23 ± 0.04 | M | Ďurech et al. (2009) |
| 951 Gaspra | 20 | 23 | 198 | 15 | 7.04203 | 2.2097 | 12.2 | S | S | 0.33 ± 0.13 | M | this work |
| | 19 | 21 | | | | | | | | | | Davies et al. (1994b)[1] |
| 1056 Azalea | 242 | 61 | 49 | 48 | 15.0276 | 2.2300 | 13.0 | S | – | 0.25 ± 0.04 | M | Hanuš et al. (2013) |
| 1088 Mitaka | 280 | −71 | | | 3.035378 | 2.2014 | 16.0 | S | S | 0.16 ± 0.02 | M | Hanuš et al. (2011) |
| 1185 Nikko | 359 | 34 | | | 3.786149 | 2.2375 | 11.3 | S | S | 0.20 | M | Hanuš et al. (2011)/Ďurech et al. (2009) |
| 1188 Gothlandia | 133 | −84 | 335 | −81 | 3.491820 | 2.1907 | 12.7 | S | – | 0.25 ± 0.02 | B | Hanuš et al. (2013)/Kryszczyńska (2013) |
| 1249 Rutherfordia | 204 | 72 | 31 | 74 | 18.2183 | 2.2243 | 14.1 | – | S | 0.22 ± 0.02 | M | Hanuš et al. (2013) |
| 1270 Datura | 60 | 76 | | | 3.358100 | 2.2347 | 8.2 | – | – | 0.24 | M | Vokrouhlický et al. (2009) |
| 1307 Cimmeria | | 63 | | | 2.820723 | 2.2505 | 10.1 | – | S | 0.22 ± 0.02 | B | this work |
| 1396 Outeniqua | | 62 | | | 3.08175 | 2.2480 | 11.7 | – | – | 0.21 ± 0.01 | M | this work |
| 1419 Danzig | 22 | 76 | 193 | 62 | 8.11957 | 2.2928 | 14.1 | – | – | 0.24 ± 0.05 | I | Hanuš et al. (2011) |
| 1446 Sillanpaa | 129 | 76 | 288 | 63 | 9.65855 | 2.2457 | 8.8 | – | – | 0.21 ± 0.01 | M | this work |
| 1514 Ricouxa | 251 | 75 | 68 | 69 | 10.42467 | 2.2404 | 8.1 | – | – | 0.18 ± 0.04 | M | Hanuš et al. (2011) |
| 1518 Rovaniemi | 62 | 60 | 265 | 45 | 5.25047 | 2.2255 | 9.0 | – | – | 0.26 ± 0.04 | M | Hanuš et al. (2013) |
| 1527 Malmquista | 274 | 80 | | | 14.0591 | 2.2274 | 10.3 | – | – | 0.22 ± 0.02 | M | this work |
| 1619 Ueta | | 39 | | | 2.717943 | 2.2411 | 9.9 | – | S | 0.25 ± 0.03 | M | this work |
| 1675 Simonida | 23 | 58 | 227 | 54 | 5.287962 | 2.2332 | 11.1 | – | – | 0.25 ± 0.03 | M | Kryszczyńska (2013) |
| 1682 Karel | 232 | 32 | 51 | 41 | 3.37486 | 2.2388 | 7.1 | – | – | 0.24 | M | Hanuš et al. (2011) |
| 1703 Barry | 46 | −76 | 221 | −71 | 107.04 | 2.2148 | 9.4 | – | – | 0.22 ± 0.03 | B | this work |
| 1738 Oosterhoff | | −72 | | | 4.44896 | 2.1835 | 8.7 | S | – | 0.28 ± 0.04 | M | this work |
| 1785 Wurm | 11 | 57 | 192 | 47 | 3.26934 | 2.2359 | 6.2 | S | – | 0.24 | M | Hanuš et al. (2013) |
| 2017 Wesson | 159 | 81 | 356 | 79 | 3.415579 | 2.2521 | 7.2 | – | – | 0.20 ± 0.05 | M | Kryszczyńska (2013) |
| 2094 Magnitka | 107 | 57 | 272 | 48 | 6.11219 | 2.2323 | 12.1 | – | – | 0.13 ± 0.01 | M | Hanuš et al. (2013) |
| 2112 Ulyanov | 151 | 61 | 331 | 61 | 3.04071 | 2.2547 | 7.5 | – | – | 0.24 | M | Hanuš et al. (2013) |
| 2510 Shandong | 256 | 27 | 71 | 27 | 5.94638 | 2.2531 | 9.0 | – | S | 0.20 | M | Hanuš et al. (2013) |
| 2709 Sagan | 308 | −8 | 124 | −16 | 5.25638 | 2.1954 | 6.8 | S | – | 0.24 | M | Hanuš et al. (2013) |
| 2839 Annette | 341 | −49 | 154 | −36 | 10.4609 | 2.2166 | 7.6 | – | – | 0.06 ± 0.01 | I | Hanuš et al. (2013) |

**Notes.** For each asteroid, the table gives the spin state solution (i.e., ecliptic coordinates $\lambda$ and $\beta$ of the spin axis and the sidereal rotational period $P$, usually for both ambiguous pole solutions), the proper semi-major axis $a_p$, the diameter $D$ and albedo $p_v$ based on WISE data (Masiero et al. 2011), the SMASS II taxonomy (Bus & Binzel 2002), the Tholen (Tholen 1984, 1989) taxonomical type, the information if the asteroid is, according to our membership revision, a member (M), an interloper (I) or a borderline case (B), and the reference to the convex model. [(1)] The spin vector solution of asteroid (951) Gaspra is based on Galileo images obtained during the October 1991 flyby. [(2)] The solution of asteroid (243) Ida is based on Galileo images and photometric data.

**Table 5.** continued.

| Asteroid | $\lambda_1$ [deg] | $\beta_1$ [deg] | $\lambda_2$ [deg] | $\beta_2$ [deg] | $P$ [hours] | $a_p$ [AU] | $D$ [km] | Bus/DeMeo | Tholen | $p_V$ | M/I/B | Reference |
|---|---|---|---|---|---|---|---|---|---|---|---|---|
| 3279 Solon | 268 | −70 | | | 8.1041 | 2.2027 | 5.9 | – | – | 0.24 | M | this work |
| 7043 Godart | 73 | 62 | 235 | 80 | 8.4518 | 2.2447 | 5.7 | – | – | 0.23 ± 0.04 | M | this work |
| 7169 Linda | 11 | −60 | 198 | −61 | 27.864 | 2.2487 | 4.5 | – | – | 0.24 | M | this work |
| 7360 Moberg | | −18 | | | 4.58533 | 2.2510 | 7.7 | – | – | 0.22 ± 0.04 | B | this work |
| | | | | | | | Flora | | | | | |
| 31383 1998 XJ$_9$4 | 110 | −74 | 279 | −63 | 4.16818 | 2.1853 | 4.1 | – | – | 0.29 ± 0.03 | M | Hanuš et al. (2013) |
| | | | | | | | Koronis | | | | | |
| 158 Koronis | 30 | −64 | | | 14.2057 | 2.8687 | 47.7 | S | S | 0.14 ± 0.01 | M | Ďurech et al. (2011) |
| | 220 | −68 | 35 | −65 | 14.20569 | | | | | | | Slivan et al. (2003) |
| 167 Urda | 249 | −68 | 107 | −69 | 13.06133 | 2.8535 | 44.0 | Sk | S | 0.16 ± 0.04 | B | Ďurech et al. (2011) |
| | 225 | −73 | 40 | −75 | 13.06135 | | | | | | | Slivan et al. (2003) |
| 208 Lacrimosa | 170 | −68 | 350 | −71 | 14.076919 | 2.8929 | 45.0 | Sk | S | 0.17 ± 0.06 | I | Slivan et al. (2003) |
| 243 Ida | 259 | −66 | 74 | −61 | 4.633632 | 2.8616 | 28.0 | S | S | 0.24 ± 0.07 | M | this work |
| | 263 | −67 | | | 4.633632 | | | | | | | Davies et al. (1994a); Binzel et al. (1993)[2] |
| 263 Dresda | 105 | 76 | 285 | 80 | 16.81387 | 2.8865 | 25.5 | S | – | 0.18 ± 0.02 | M | Slivan et al. (2009) |
| 277 Elvira | 121 | −84 | | | 29.69219 | 2.8856 | 31.2 | – | S | 0.20 ± 0.05 | M | Hanuš et al. (2011) |
| | 50 | −80 | 244 | −81 | 29.69218 | | | | | | | Slivan et al. (2009) |
| 311 Claudia | 214 | 43 | 30 | 40 | 7.5314 | 2.8976 | 25.8 | – | S | 0.24 ± 0.03 | B | Hanuš et al. (2011) |
| | 209 | 48 | 24 | 48 | 7.53139 | | | | | | | Slivan et al. (2003) |
| 321 Florentina | 264 | −63 | 91 | −60 | 2.870866 | 2.8856 | 34.0 | S | S | 0.14 ± 0.01 | M | Slivan et al. (2003) |
| 462 Eriphyla | 108 | 35 | 294 | 34 | 8.65890 | 2.8737 | 41.9 | S | S | 0.17 ± 0.02 | M | Slivan et al. (2009) |
| 534 Nassovia | 66 | 41 | 252 | 42 | 9.46889 | 2.8842 | 38.6 | Sq | S | 0.12 ± 0.02 | M | Hanuš et al. (2011) |
| | 58 | 50 | 244 | 50 | 9.46896 | | | | | | | Slivan et al. (2003) |
| 720 Bohlinia | 230 | 41 | 40 | 43 | 8.91862 | 2.8873 | 34.0 | Sq | S | 0.20 ± 0.02 | B | Slivan et al. (2003) |
| 832 Karin | 242 | 46 | 59 | 44 | 18.35123 | 2.8644 | 16.3 | – | – | 0.21 ± 0.05 | M | Hanuš et al. (2011) |
| | 230 | 42 | 52 | 42 | 18.352 | | | | | | | Slivan & Molnar (2012) |
| 1223 Neckar | 252 | 28 | 69 | 30 | 7.82401 | 2.8695 | 25.7 | – | S | 0.15 ± 0.03 | M | Hanuš et al. (2011) |
| | 259 | 41 | 73 | 40 | 7.82124 | | | | | | | Slivan et al. (2003) |
| 1289 Kutaissi | 158 | −79 | 338 | −74 | 3.624174 | 2.8605 | 22.6 | – | S | 0.16 ± 0.04 | M | Slivan et al. (2003) |
| 1350 Rosselia | 166 | −72 | | | 8.14011 | 2.8580 | 21.1 | Sa | S | 0.20 ± 0.05 | M | Hanuš et al. (2011) |
| 1389 Onnie | 183 | −75 | 360 | −79 | 23.0447 | 2.8661 | 14.7 | – | – | 0.17 ± 0.04 | M | Hanuš et al. (2013) |
| 1423 Jose | 78 | −82 | | | 12.3127 | 2.8602 | 20.0 | S | – | 0.28 ± 0.04 | M | this work |
| 1482 Sebastiana | 262 | −68 | 91 | −67 | 10.48966 | 2.8723 | 17.6 | – | – | 0.21 ± 0.05 | M | Hanuš et al. (2011) |
| 1618 Dawn | 39 | −60 | 215 | −51 | 43.219 | 2.8688 | 17.5 | S | – | 0.15 ± 0.04 | M | this work |
| 1635 Bohrmann | 5 | −38 | 185 | −36 | 5.86427 | 2.8534 | 17.5 | S | – | 0.21 ± 0.02 | M | Hanuš et al. (2011) |
| 1742 Schaifers | 56 | 52 | 247 | 68 | 8.53271 | 2.8892 | 16.6 | – | – | 0.11 ± 0.02 | M | Hanuš et al. (2011) |
| 1835 Gajdariya | 34 | 74 | 204 | 69 | 6.33768 | 2.8331 | 12.8 | – | – | 0.27 ± 0.04 | I | this work |
| 2953 Vysheslavia | 11 | −64 | 192 | −68 | 6.29453 | 2.8282 | 12.8 | S | – | 0.25 ± 0.07 | B | Vokrouhlický et al. (2006a) |
| 3170 Dzhanibekov | 216 | 62 | 30 | 63 | 6.07167 | 2.9291 | 9.6 | S | – | 0.30 ± 0.04 | I | Hanuš et al. (2013) |
| 4507 1990 FV | 137 | 50 | 307 | 51 | 6.57932 | 2.8689 | 11.0 | – | – | 0.28 ± 0.02 | M | Hanuš et al. (2013) |
| 6262 Javid | 93 | 76 | 275 | 69 | 8.02054 | 2.9063 | 7.8 | – | – | 0.29 ± 0.04 | M | this work |
| | | | | | | | Eos | | | | | |
| 423 Diotima | 351 | 4 | | | 4.775377 | 3.0684 | 177.3 | C | C | 0.07 ± 0.00 | I | Marchis et al. (2006) |
| 573 Recha | 74 | −24 | 252 | −48 | 7.16585 | 3.0138 | 44.4 | – | – | 0.13 ± 0.02 | M | Hanuš et al. (2011) |
| 590 Tomyris | 273 | −47 | 120 | −46 | 5.55247 | 3.0006 | 31.1 | – | – | 0.18 ± 0.03 | B | Hanuš et al. (2011) |
| 669 Kypria | 31 | 40 | 190 | 50 | 14.2789 | 3.0114 | 29.2 | – | S | 0.17 ± 0.02 | M | Hanuš et al. (2013) |
| 807 Ceraskia | 325 | 23 | 132 | 26 | 7.37390 | 3.0185 | 21.4 | – | S | 0.21 ± 0.05 | M | Hanuš et al. (2013) |

**Table 5.** continued.

| Asteroid | $\lambda_1$ [deg] | $\beta_1$ [deg] | $\lambda_2$ [deg] | $\beta_2$ [deg] | $P$ [hours] | $a_p$ [AU] | $D$ [km] | Bus/DeMeo | Tholen | $p_V$ | M/I/B | Reference |
|---|---|---|---|---|---|---|---|---|---|---|---|---|
| 1087 Arabis | 334 | −7 | 155 | 12 | 5.79499 | 3.0150 | 45.6 | – | S | 0.10 ± 0.01 | M | Hanuš et al. (2011) |
| 1148 Rarahu | 148 | −9 | 322 | −9 | 6.54448 | 3.0161 | 26.3 | K | S | 0.22 ± 0.06 | M | Hanuš et al. (2011) |
| 1207 Ostenia | 310 | −77 | 124 | −51 | 9.07129 | 3.0207 | 22.9 | – | – | 0.13 ± 0.02 | M | Hanuš et al. (2011) |
| 1286 Banachiewicza | 214 | 62 | 64 | 60 | 8.63041 | 3.0223 | 22.6 | – | S | 0.16 ± 0.03 | M | this work |
| 1291 Phryne | 106 | 35 | 277 | 59 | 5.58414 | 3.0130 | 22.4 | – | – | 0.19 ± 0.04 | M | Hanuš et al. (2011) |
| 1339 Desagneauxa | | 65 | | | 9.37510 | 3.0211 | 26.1 | – | S | 0.12 ± 0.02 | M | this work |
| 1353 Maartje | 266 | 73 | 92 | 57 | 22.9927 | 3.0120 | 42.2 | – | – | 0.07 ± 0.00 | M | this work |
| 1464 Armisticia | 194 | −54 | 35 | −69 | 7.46699 | 3.0035 | 23.3 | – | – | 0.13 ± 0.36 | M | this work |
| 2957 Tatsuo | 88 | 57 | 246 | 37 | 6.82042 | 3.0221 | 22.9 | K | – | 0.29 ± 0.02 | M | Hanuš et al. (2013) |
| 3896 Pordenone | | −32 | | | 4.00366 | 3.0057 | 20.0 | – | – | 0.13 ± 0.01 | M | this work |
| 5281 Lindstrom | 238 | −72 | 84 | −81 | 9.2511 | 3.0125 | 20.0 | – | – | | M | Hanuš et al. (2013) |
| 19848 Yeungchuchiu | 66 | −70 | 190 | −67 | 3.45103 | 3.0075 | 13.2 | – | – | 0.21 ± 0.03 | M | Hanuš et al. (2013) |
| Eunomia | | | | | | | | | | | | |
| 15 Eunomia | 363 | −67 | | | 6.082752 | 2.6437 | 259.0 | S | S | 0.21 ± 0.06 | M | Kaasalainen et al. (2002) |
| 85 Io | 95 | −65 | | | 6.87478 | 2.6537 | 161.0 | B | FC | 0.06 ± 0.03 | I | Ďurech et al. (2011) |
| 390 Alma | 54 | −48 | 263 | −73 | 3.74117 | 2.6517 | 31.2 | – | DT | 0.13 ± 0.02 | B | Hanuš et al. (2013) |
| 812 Adele | 301 | 44 | 154 | 69 | 5.85745 | 2.6594 | 13.6 | – | – | 0.24 ± 0.03 | M | Hanuš et al. (2013) |
| 1333 Cevenola | 8 | −79 | 201 | −40 | 4.87933 | 2.6336 | 17.1 | – | – | 0.17 ± 0.04 | M | Hanuš et al. (2011) |
| 1495 Helsinki | 356 | −33 | | | 5.33131 | 2.6392 | 13.3 | – | – | 0.23 ± 0.02 | M | Hanuš et al. (2013) |
| 1503 Kuopio | 170 | −86 | 27 | −61 | 9.9586 | 2.6263 | 18.4 | – | – | 0.30 ± 0.06 | M | this work |
| 1554 Yugoslavia | 281 | −34 | 78 | −64 | 3.88766 | 2.6194 | 17.2 | – | – | 0.10 ± 0.01 | M | Hanuš et al. (2013) |
| 1927 Suvanto | 90 | 39 | 277 | 6 | 8.16154 | 2.6497 | 12.5 | – | – | 0.26 ± 0.04 | M | Hanuš et al. (2013) |
| 2384 Schulhof | 194 | −57 | 46 | −36 | 3.29367 | 2.6099 | 11.7 | – | – | 0.27 ± 0.02 | M | Hanuš et al. (2013) |
| 3017 Petrovic | | −73 | | | 4.08037 | 2.6074 | 12.7 | – | – | 0.21 ± 0.02 | M | this work |
| 3492 Petra–Pepi | 9 | −57 | 202 | −16 | 46.570 | 2.6159 | 12.2 | – | – | 0.23 ± 0.03 | M | this work |
| 4399 Ashizuri | 266 | −48 | 45 | −61 | 2.830302 | 2.5759 | 8.8 | – | – | 0.28 ± 0.06 | B | this work |
| 4467 Kaidanovskij | | 54 | | | 19.1454 | 2.6383 | 11.6 | – | – | 0.21 | M | this work |
| 8132 Vitginzburg | 33 | −66 | 193 | −48 | 7.27529 | 2.6263 | 11.6 | – | – | 0.21 | M | Hanuš et al. (2013) |
| Phocaea | | | | | | | | | | | | |
| 25 Phocaea | 347 | 10 | | | 9.935397 | 2.4002 | 75.1 | S | S | 0.23 ± 0.02 | M | Hanuš et al. (2013) |
| 290 Bruna | 286 | −80 | 37 | −74 | 13.8055 | 2.3372 | 10.4 | – | – | 0.42 ± 0.08 | B | Hanuš et al. (2013) |
| 391 Ingeborg | | −60 | | | 26.4145 | 2.3202 | 19.6 | S | S | 0.20 | I | this work |
| 502 Sigune | | −44 | | | 10.92667 | 2.3831 | 19.5 | – | S | 0.23 ± 0.02 | M | this work |
| 852 Wladilena | 218 | −41 | 57 | −16 | 4.613301 | 2.3627 | 31.1 | – | – | 0.16 ± 0.02 | B | Hanuš et al. (2013) |
| 1192 Prisma | | −65 | | | 6.55836 | 2.3660 | 7.2 | – | – | 0.23 | M | this work |
| 1568 Aisleen | 109 | −68 | | | 6.67598 | 2.3520 | 12.0 | – | – | 0.18 ± 0.03 | M | Hanuš et al. (2011) |
| 1963 Bezovec | 218 | 16 | 50 | −49 | 18.1655 | 2.4231 | 45.0 | – | C | 0.04 ± 0.01 | I | Hanuš et al. (2013) |
| 1987 Kaplan | 357 | −58 | | | 9.45950 | 2.3822 | 14.6 | – | – | 0.21 ± 0.04 | M | this work |
| 2430 Bruce Helin | 177 | −68 | | | 129.75 | 2.3627 | 12.7 | Sl | S | 0.23 | M | this work |
| 5647 1990 TZ | 266 | 69 | | | 6.13868 | 2.4241 | 9.3 | S | – | 0.64 ± 0.07 | I | Hanuš et al. (2013) |
| 6179 Brett | | −42 | | | 9.4063 | 2.4278 | 5.8 | – | – | 0.23 | M | this work |
| 7055 1989 KB | | −61 | | | 4.16878 | 2.3496 | 6.7 | – | – | 0.33 ± 0.15 | M | this work |
| 10772 1990 YM | 16 | 46 | | | 68.82 | 2.3901 | 6.2 | – | – | 0.38 ± 0.06 | M | Hanuš et al. (2013) |
| Themis | | | | | | | | | | | | |
| 62 Erato | 87 | 22 | 269 | 23 | 9.21813 | 3.1217 | 95.4 | Ch | BU | 0.06 ± 0.00 | B | Hanuš et al. (2011) |
| 222 Lucia | 107 | 54 | 290 | 51 | 7.83671 | 3.1349 | 56.5 | – | BU | 0.12 ± 0.02 | M | Hanuš et al. (2013) |
| 621 Werdandi | 247 | −86 | 66 | −77 | 11.77456 | 3.1193 | 27.1 | – | FCX | 0.15 ± 0.02 | M | this work |
| 936 Kunigunde | 47 | 57 | 234 | 50 | 8.82653 | 3.1383 | 39.6 | – | – | 0.11 ± 0.01 | M | this work |

**Table 5.** continued.

| | Asteroid | $\lambda_1$ [deg] | $\beta_1$ [deg] | $\lambda_2$ [deg] | $\beta_2$ [deg] | $P$ [hours] | $a_p$ [AU] | $D$ [km] | Bus/DeMeo | Tholen | $p_V$ | M/I/B | Reference |
|---|---|---|---|---|---|---|---|---|---|---|---|---|---|
| 1003 | Lilofee | | 65 | | | 8.24991 | 3.1483 | 31.4 | – | – | 0.15 ± 0.04 | M | this work |
| 1623 | Vivian | | −75 | | | 20.5235 | 3.1347 | 29.6 | – | – | 0.08 | M | this work |
| 1633 | Chimay | 322 | 77 | 116 | 81 | 6.59064 | 3.1748 | 37.7 | – | – | 0.08 ± 0.01 | B | this work |
| 1691 | Oort | 45 | 68 | 223 | 58 | 10.2684 | 3.1664 | 33.2 | – | CU | 0.07 ± 0.01 | M | this work |
| 1805 | Dirikis | 364 | 48 | 188 | 61 | 23.4543 | 3.1333 | 28.1 | – | – | 0.09 ± 0.01 | M | this work |
| | | | | | | | Maria | | | | | | |
| 616 | Elly | | 67 | | | 5.29771 | 2.5526 | 22.6 | – | S | 0.19 ± 0.04 | M | this work |
| 695 | Bella | 87 | −55 | 314 | −56 | 14.21899 | 2.5391 | 41.2 | – | S | 0.24 ± 0.03 | B | Hanuš et al. (2011) |
| 714 | Ulula | 224 | −10 | 41 | −5 | 6.99838 | 2.5352 | 39.2 | – | S | 0.27 ± 0.04 | B | Hanuš et al. (2011) |
| 787 | Moskva | 330 | 60 | 122 | 19 | 6.05581 | 2.5396 | 40.3 | – | – | 0.12 ± 0.02 | M | Hanuš et al. (2013) |
| 875 | Nymphe | 42 | 31 | 196 | 42 | 12.6213 | 2.5539 | 15.2 | – | – | 0.19 ± 0.02 | M | Hanuš et al. (2013) |
| 1160 | Illyria | | 47 | | | 4.10295 | 2.5604 | 14.8 | – | – | 0.22 ± 0.04 | M | this work |
| 1996 | Adams | 107 | 55 | | | 3.31114 | 2.5587 | 13.5 | – | – | 0.14 ± 0.01 | M | Hanuš et al. (2013) |
| 3786 | Yamada | | 56 | | | 4.03294 | 2.5503 | 16.7 | – | – | 0.23 ± 0.04 | M | this work |
| 6403 | Steverin | 246 | 77 | 109 | 73 | 3.49119 | 2.5945 | 6.9 | – | – | 0.49 ± 0.05 | M | this work |
| | | | | | | | Vesta | | | | | | |
| 63 | Ausonia | 305 | −21 | 120 | −15 | 9.29759 | 2.3952 | 90.0 | Sa | S | 0.16 ± 0.03 | – | Torppa et al. (2003) |
| 306 | Unitas | 79 | −35 | | | 8.73874 | 2.3580 | 49.0 | S | S | 0.17 ± 0.06 | – | Ďurech et al. (2007) |
| 336 | Lacadiera | 194 | 39 | 37 | 54 | 13.69555 | 2.2518 | 69.0 | Xk | D | 0.05 ± 0.01 | – | Hanuš et al. (2011) |
| 556 | Phyllis | 34 | 54 | 209 | 41 | 4.292622 | 2.4654 | 38.5 | S | S | 0.18 ± 0.03 | – | Marciniak et al. (2007) |
| 1933 | Tinchen | 113 | 26 | 309 | 36 | 3.67062 | 2.3530 | 6.5 | – | – | 0.29 ± 0.06 | – | Hanuš et al. (2013) |
| 2086 | Newell | | −60 | | | 78.09 | 2.4014 | 9.8 | Xc | – | 0.20 | – | this work |
| 6159 | 1991 YH | 266 | 67 | 62 | 67 | 10.6589 | 2.2914 | 5.4 | – | – | 0.46 ± 0.13 | – | this work |
| 8359 | 1989 WD | 121 | −68 | 274 | −68 | 2.89103 | 2.3500 | 8.2 | – | – | 0.22 ± 0.03 | – | Hanuš et al. (2013) |
| | | | | | | | Nysa/Polana | | | | | | |
| 44 | Nysa | 99 | 58 | | | 6.421417 | 2.4227 | 70.6 | Xc | E | 0.55 ± 0.07 | – | Kaasalainen et al. (2002) |
| 135 | Hertha | 272 | 52 | | | 8.40060 | 2.4285 | 77.0 | Xk | M | 0.15 ± 0.05 | – | Torppa et al. (2003) |
| 1378 | Leonce | 210 | −67 | 46 | −77 | 4.32526 | 2.3748 | 22.5 | – | – | 0.03 ± 0.00 | – | this work |
| 1493 | Sigrid | | 78 | | | 43.179 | 2.4297 | 22.1 | Xc | F | 0.04 ± 0.00 | – | this work |
| 4606 | Saheki | 44 | 59 | 222 | 68 | 4.97347 | 2.2518 | 6.7 | – | – | 0.33 ± 0.02 | – | this work |
| | | | | | | | Alauda | | | | | | |
| 276 | Adelheid | 199 | −20 | 9 | −4 | 6.319200 | 3.1162 | 125.0 | – | X | 0.06 ± 0.01 | I | Marciniak et al. (2007) |
| 1276 | Ucclia | | −49 | | | 4.90748 | 3.1698 | 40.0 | – | – | 0.05 ± 0.01 | M | this work |
| 1838 | Ursa | | 47 | | | 16.1635 | 3.2111 | 48.6 | – | – | 0.04 ± 0.01 | M | this work |
| 4209 | Briggs | | −56 | | | 12.2530 | 3.1564 | 30.9 | – | – | 0.09 ± 0.03 | M | this work |

The Astronomical Journal, 139:2258–2268, 2010 June doi:10.1088/0004-6256/139/6/2258


# A UNIFIED SOLUTION FOR THE ORBIT AND LIGHT-TIME EFFECT IN THE V505 Sgr SYSTEM

M. Brož[1], P. Mayer[1], T. Pribulla[2,4], P. Zasche[1], D. Vokrouhlický[1], and R. Uhlář[3]
[1] Astronomical Institute, Charles University, Prague, V Holešovičkách 2, 18000 Prague 8, Czech Republic
[2] Astrophysikalisches Institut und Universitäts-Sternwarte, Schillergässchen 2-3, D-07740 Jena, Germany
[3] Private Observatory, Pohoří 71, 25401 Jílové u Prahy, Czech Republic
*Received 2010 February 4; accepted 2010 March 28; published 2010 April 19*

## ABSTRACT

The multiple system V505 Sagittarii is composed of at least three stars: a compact eclipsing pair and a distant component, whose orbit is measured directly using speckle interferometry. In order to explain the observed orbit of the third body in V505 Sagittarii and also other observable quantities, namely the minima timings of the eclipsing binary and three different radial velocities (RVs) detected in the spectrum, we thoroughly test a fourth-body hypothesis—a perturbation by a dim, yet-unobserved object. We use an *N*-body numerical integrator to simulate future and past orbital evolution of three or four components in this system. We construct a suitable $\chi^2$ metric from all available speckle-interferometry, minima-timings, and RV data and we scan a part of a parameter space to get at least some of the possible solutions. In principle, we are able to explain all observable quantities by the presence of a fourth body, but the resulting likelihood of this hypothesis is very low. We also discuss other theoretical explanations of the minima-timing variations. Further observations of the minima timings during the next decade or high-resolution spectroscopic data can significantly constrain the model.

*Key words:* binaries: close – stars: individual (V505 Sgr)

*Online-only material:* color figures

## 1. INTRODUCTION

The star V505 Sagittarii (HD 187949, HR 7571, HIP 97849, WDS 19531-1436) is known as an eclipsing binary with a variable period. Spectral types of its primary and secondary components are A2 V and G5 IV, orbital period is 1.183 days, and visual magnitude is maximum $6\overset{\mathrm{m}}{.}5$ (Chambliss et al. 1993). In 1985, the V505 Sgr was also resolved using speckle interferometry (McAlister et al. 1987b), and several measurements of the third component were published since that time. Mayer (1997) attempted to join the measured times of minima with visual orbit and determined a distance of the system 102 pc.

The third-body orbit with the period of about 40 years seemed well justified until about the year 2000. An abrupt change in more recent data, however, excludes this simple model—it is impossible to fit *both* light-time effect data and the interferometric trajectory assuming three bodies on stable orbits. We thus test a fourth-body hypothesis: a perturbation by a low-mass star (i.e., the fourth body), which has not been resolved spatially so far. Such a fourth body was suspected already by Chochol et al. (2006) due to conspicuous deviations of minimum times from those expected. While we consider the fourth-body model as the main working hypothesis in this paper, we also discuss other possible effects that can produce minima timing variations.

The data set we have for V505 Sgr is described in Section 2. We introduce our dynamical model, numerical method, free/dependent parameters, and $\chi^2$ metric in Section 3. The results of our simulations and conclusions are presented in Sections 4 and 5.

[4] On leave from Astronomical Institute, Slovak Academy of Sciences, 05960 Tatranská Lomnica, Slovakia.

## 2. OBSERVATIONAL DATA

### 2.1. Speckle Interferometry

The available speckle-interferometry data are summarized in Table 1. Most of them were extracted from the Fourth Catalog of Interferometric Measurements of Binary Stars (Hartkopf et al. 2009), but we also added two speckle measurements from the SAO BTA 6 m telescope by E. Malogolovets (using a speckle camera and a method described in Balega et al. 2002 and Maksimov et al. 2009) and one direct-imaging measurement, performed at CFHT by S. Rucinski (using a method described in Rucinski et al. 2007).

We estimated weight factors $w$ and corresponding uncertainties as $\sigma_{\mathrm{sky}} = 0.005\,\mathrm{arcsec}/w$. This uncertainty refers to the measured position on the plane of the sky $(X^2 + Y^2)$, which results from a combination of uncertainties in the measured angular separations and position angles. The values of $\sigma_{\mathrm{sky}}$ vary because different telescopes and techniques were used. Any non-monotonic changes in the measured position angles are simply due to observational uncertainties.

We are aware of a possible 180° ambiguity in the speckle measurements, but V505 Sgr is a lucky case: we have one direct measurement by *Hipparcos* prior to 2000 perihelion passage, and another direct-imaging datum after 2000. We thus can be sure about the shape of the orbit.

### 2.2. Minima Timings

We list recent $O-C$ data for the (1+2) binary in Table 2. Only measurements not presented in Chambliss et al. (1993) are included in the table, but we use all of them of course. An uncertainty of a minimum determination is estimated to be $\sigma_{\mathrm{lite}} = 1$ minute in most cases, only photographic minima and data from *Hipparcos* were considered worse. Epoch and $O-C$ were calculated using the ephemeris of Mayer (1997), with zero

**Table 1**
Speckle-interferometry Data for V505 Sgr, Mainly from the Fourth Interferometric Catalogue (Hartkopf et al. 2009)[a]

| Year | P.A. (deg) | $\rho$ (mas) | Weight | Source |
|---|---|---|---|---|
| 1985.5150 | 189.6 | 302 | 1 | 3.6 m |
| 1985.8425 | 189.8 | 311 | 1 | 3.8 m |
| 1989.3069 | 181.0 | 261 | 1 | 4.0 m |
| 1990.3445 | 176.9 | 246 | 1 | 4.0 m |
| 1991.2500 | 170 | 234 | 0.6 | *Hipparcos* |
| 1991.3903 | 173.4 | 234 | 1 | 4.0 m |
| 1991.5575 | 174 | 240 | 0.4 | 2.1 m |
| 1991.5602 | 174 | 260 | 0.4 | 2.1 m |
| 1991.7124 | 173.3 | 226 | 1 | 4.0 m |
| 1992.4497 | 171.7 | 214 | 1 | 4.0 m |
| 1992.6961 | 164 | 190 | 0.4 | 2.1 m |
| 1994.7079 | 159.9 | 192 | 1 | 3.8 m |
| 1995.4398 | 152.5 | 169 | 0.6 | 2.5 m |
| 1995.7675 | 154.2 | 177 | 0.3 | 2.5 m |
| 1996.5320 | 145.8 | 149 | 0.3 | 2.5 m |
| 2003.6365 | 236.3 | 152 | 1 | 3.5 m |
| 2005.7948 | 218 | 183 | 0.6 | Direct CFHT |
| 2006.1947 | 215.8 | 182 | 1 | 4.0 m |
| 2007.3306 | 212.4 | 210 | 1 | 3.5 m |
| 2007.4927 | 212.0 | 212 | 1 | 6.0 m |
| 2008.4901 | 207.8 | 231 | 1 | 6.0 m |
| 2009.2662 | 204.2 | 247.5 | 1 | 4.0 m |

**Notes.** [a] P.A. denotes the position angle and $\rho$ the angular distance between the central pair (1+2) and the third component. Estimated weight factors $w$ and uncertainties $\sigma_{\rm sky} = 0.005\,{\rm arcsec}/w$ correspond to the sizes of telescopes and techniques, which were used to acquire these measurements (1991.25 and 2005 measurements result from direct imaging).

point shifted by 6754 epochs:

$$\text{Pri.Min.} = 2433490.483 + 1^{\rm d}.1828688 \times E\,. \qquad (1)$$

In the analysis below, when we compare minima timings to our simulations, the period and base minimum are treated as adjustable variables and may therefore differ from the values presented here.

### 2.3. Radial Velocities

We use radial-velocity (RV) data from Tomkin (1992), Table 4, who measured sharp spectral lines in the 5580–5610 Å region and attributed them to the third component. The values of $v_{\rm rad3}$ range from $-13$ to $-9\,{\rm km\,s^{-1}}$. One more measurement exists (Worek 1996), which confirms the values given by Tomkin.

The uncertainties of the RV data $\sigma_{\rm rv} = 2\,{\rm km\,s^{-1}}$ were estimated from a scatter of the RV measurements close in time. We also checked for possible blends with nearby faint lines—we computed a synthetic spectrum with the same resolution as Tomkin (1992) and fitted the lines in question by a Gaussian function. The observed width of the sharp lines is $\Delta\lambda \simeq 1$ Å. If we fit them by a Gaussian function, assuming the broadening is mostly caused by a rotational Doppler effect, we can estimate rotational velocity about $v_{\rm rot3} = (20 \pm 5)\,{\rm km\,s^{-1}}$.

Wide lines in the V505 Sgr spectrum are attributed to the components of the eclipsing pair (1+2). The binary is tight and in all likelihood rotates synchronously; thus the corresponding rotational Doppler broadening is large ($v_{\rm rot1+2} = (100 \pm 10)\,{\rm km\,s^{-1}}$). The systemic RV of the (1+2) body is $v_{\rm rad1+2} = (1.9 \pm 1.4)\,{\rm km\,s^{-1}}$.

**Table 2**
Minima Timings for the Eclipsing Binary (1+2) in V505 Sgr[a]

| HJD − 2400000 | Epoch | $O-C$ (d) | $\sigma_{\rm lite}$ (d) | Source |
|---|---|---|---|---|
| 48432.4871 | 12632.0 | +0.0054 | 0.0007 | R.-L. |
| 48501.0981 | 12690.0 | +0.0100 | 0.0021 | Chochol |
| 48858.3253 | 12992.0 | +0.0109 | 0.0007 | Müyesseroglu |
| 51000.4948 | 14803.0 | +0.0049 | 0.0007 | Ibanoglu |
| 51051.3578 | 14846.0 | +0.0046 | 0.0007 | ” |
| 51057.2724 | 14851.0 | +0.0048 | 0.0007 | ” |
| 51064.3692 | 14857.0 | +0.0044 | 0.0007 | ” |
| 52754.6756 | 16286.0 | −0.0087 | 0.0007 | Chochol |
| 52843.3891 | 16361.0 | −0.0103 | 0.0007 | ” |
| 53263.3029 | 16716.0 | −0.0150 | 0.0007 | ” |
| 53525.8969 | 16938.0 | −0.0178 | 0.0007 | Cook |
| 53626.4399 | 17023.0 | −0.0187 | 0.0007 | Chochol |
| 54267.5469 | 17565.0 | −0.0266 | 0.0007 | Zasche |
| 54267.5472 | 17565.0 | −0.0263 | 0.0007 | ” |
| 54648.4260 | 17887.0 | −0.0313 | 0.0005 | ” |
| 54655.5233 | 17893.0 | −0.0312 | 0.0003 | ” |
| 54658.4817 | 17895.5 | −0.0299 | 0.0005 | ” |
| 54706.3869 | 17936.0 | −0.0309 | 0.0002 | ” |
| 55027.5302 | 18207.5 | −0.0365 | 0.0018 | Uhlář |
| 55049.4152 | 18226.0 | −0.0346 | 0.0002 | ” |
| 55062.4266 | 18237.0 | −0.0347 | 0.0011 | Šmelcer |
| 55068.3400 | 18242.0 | −0.0357 | 0.0011 | Uhlář |

**Notes.** [a] Epoch and $O-C$ were calculated using the ephemeris Pri.Min. $= 2433490.483 + 1^{\rm d}.1828688 \times E$. $\sigma_{\rm lite}$ denotes the assumed standard uncertainty of the minimum determination. Only newer minima after Chambliss et al. (1993) are listed. The last four measurements are new.
**References**. Rovithis-Livaniou & Rovithis 1992; Müyesseroglu et al. 1996; Ibanoglu et al. 2000; Cook et al. 2005; Chochol et al. 2006; and Zasche et al. 2009.

**Table 3**
Free Parameters of Our Dynamical Four-body Model

| No. | Parameter | Brief Description |
|---|---|---|
| 1. | $d$ | Distance between the Earth and V505 Sgr barycenter, in pc |
| 2. | $m_3$ | Mass of the third body, in $M_\odot$ |
| 3. | $z_{h3}$ | Position, (1+2)-centric, epoch $T_0$, in AU |
| 4. | $v_{xh3}$ | Velocities, (1+2)-centric, epoch $T_0$, in AU d$^{-1}$ |
| 5. | $v_{yh3}$ | |
| 6. | $v_{zh3}$ | |
| 7. | $m_4$ | Mass of the fourth body, in $M_\odot$ |
| 8. | $x_{h4}$ | Positions, (1+2)-centric, epoch $T_0$, in AU |
| 9. | $y_{h4}$ | |
| 10. | $z_{h4}$ | |
| 11. | $v_{xh4}$ | Velocities, (1+2)-centric, epoch $T_0$, AU d$^{-1}$ |
| 12. | $v_{yh4}$ | |
| 13. | $v_{zh4}$ | |

## 3. NUMERICAL INTEGRATOR AND $\chi^2$ METRIC

In order to model orbital evolution of the multiple-star system V505 Sgr, namely mutual gravitational interactions of all bodies, we use a Bulirsch–Stöer (BS) $N$-body numerical integrator from the SWIFT package (Levison & Duncan 1994).

Our method is quite general—we can model classical Keplerian orbits, of course, but also non-Keplerian ones (involving three-body interactions). We are able to search for both bound (elliptical) and unbound (hyperbolic) trajectories. Free parameters of our model are listed in Table 3. Hereinafter, we strictly denote individual bodies by numbers: 1, 2 (Algol-type pair), 3 (resolved third component), and 4 to avoid any confusion.

Fixed (assumed) parameters are listed in Table 4. Masses of the first three components are well constrained by photometry

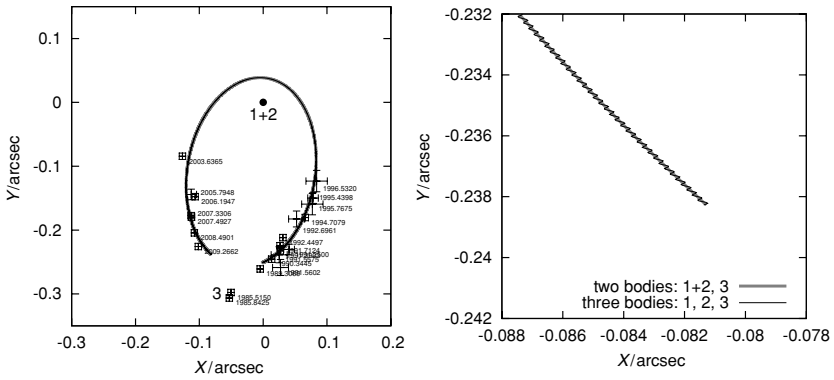


**Figure 1.** Comparison of two third-body trajectories, computed for three-body (1, 2, 3) and two-body (1+2, 3) configurations. Left: an overview of the trajectories in a 1-centric frame. Right: a detail of the small part of the trajectory, where the difference is visible. Error bars denote speckle-interferometry observations.

**Table 4**
Fixed (Assumed) Parameters of Our Model

| No. | Parameter | Brief Description |
|---|---|---|
| 14. | $m_{1+2} = 3.4\,M_\odot$ | Mass of the (1+2) body |
| 16. | $x_{h1+2} = 0$ AU | Positions of the (1+2) body, |
| 17. | $y_{h1+2} = 0$ | (1+2)-centric |
| 18. | $z_{h1+2} = 0$ | |
| 19. | $v_{xh1+2} = 0$ AU d$^{-1}$ | Velocities |
| 20. | $v_{yh1+2} = 0$ | |
| 21. | $v_{zh1+2} = 0$ | |
| 22. | $x_{h3}$ | Positions of the third body, |
| 23. | $y_{h3}$ | (1+2)-centric, in AU |
| 24. | $T_0 = 2446282.24375$ JD (or 2447607.5185) | UTC time corresponding to initial conditions |

and spectroscopy: $m_1 = (2.20 \pm 0.09)\,M_\odot$, $m_2 = (1.15 \pm 0.05)\,M_\odot$, $m_3 = (1.2 \pm 0.1)\,M_\odot$ (Chambliss et al. 1993; Tomkin 1992). We take $m_3$ as a free parameter, though, because of larger relative uncertainty. When we test three-body configurations, we have simply $m_4 = 0$.

First, it is often useful to adopt a simplification: first and second bodies can be regarded as a single (1+2) body in our dynamical model. The central pair (1+2) is so compact ($a = 0.033$ AU) and the distance of other components so large that it behaves like a single body; its equivalent $J_2$ gravitational moment is negligible. Indeed, at distance $r = 10$ AU,

$$J_2 \simeq \frac{1}{2}\left(\frac{a}{r}\right)^2 \frac{m_1 m_2}{(m_1+m_2)^2} \simeq 10^{-6}\,. \tag{2}$$

This can be confirmed easily by a direct numerical integration. The difference between trajectories computed for three-body (1, 2, 3) and two-body (1+2, 3) configurations is insignificant and always smaller than observational uncertainties (see Figure 1).

We also make use of the following two constraints: (1) initial positions $x_{h3}$, $y_{h3}$, and zero time $T_0$ of the third body correspond to a selected speckle-interferometry datum (e.g., the mean of the first two points, or to the third point) (2) third-body initial velocity components are almost tangent to the observed interferometric trajectory in the $(x, y)$ plane.

Initial conditions of the integration are specified in an arbitrary (usually 1+2-centric) frame. We then perform a transformation to a barycentric frame. The numerical integration runs in the barycentric Cartesian frame, where $x$, $y$ axes correspond to the sky plane, the $z$ axis is oriented from the observer toward the system. We use AU, AU day$^{-1}$ units for positions and velocities.

We integrate the system forward for 10,000 days and backward (i.e., with opposite sign of initial velocities) for 20,000 days in order to cover the observational time span. The time step used is $\Delta t = 10$ days and the precision parameter of the BS integrator is $\epsilon = 10^{-8}$. Finally, we transform the output back to the (1+2)-centric frame and linearly interpolate the output data to the exact times of observations.

In order to compare the observations to our model, we constructed a $\chi^2$ metric as follows:

$$\chi^2 = \chi^2_{\rm sky} + \chi^2_{\rm lite} + \chi^2_{\rm rv}\,, \tag{3}$$

where

$$\chi^2_{\rm sky} = \sum_{i=1}^{N_{\rm sky}} \frac{(x'_{h3} - x_{h3}[i])^2 + (y'_{h3} - y_{h3}[i])^2}{\sigma^2_{\rm sky}[i]}\,. \tag{4}$$

We denote $x'_{h3}$, $y'_{h3}$ (1+2)-centric coordinates of the third body calculated from our model, which were linearly interpolated to the times $t_{\rm sky}[i]$ of observations $x_{h3}[i]$, $y_{h3}[i]$. Distance $d$ is used to convert angular coordinates to AU. Second,

$$\chi^2_{\rm lite} = \sum_{i=1}^{N_{\rm lite}} \frac{(z'_{b1+2} - z_{b1+2}[i])^2}{\sigma^2_{\rm lite}[i]}\,, \tag{5}$$

where $z'_{b1+2}$ are barycentric coordinates of the (1+2) body computed from our model and interpolated to the times $t_{\rm lite}[i]$ of observations $z_{b1+2}[i]$. In order to convert $O-C$ values from Table 2 to AU, we use a simple formula: $z_{b1+2} = [O-C]_{\rm days} \cdot 86{,}400\,{\rm s} \cdot c$, where $c$ denotes the speed of light. Because of freedom in the period determination and freedom in the selection of initial velocities, we have to detrend the light-time effect data (by two least-square fits of $z'_{b1+2}(t)$ and $z_{b1+2}(t)$). Finally,

$$\chi^2_{\rm rv} = \sum_{i=1}^{N_{\rm rv}} \frac{(v'_{zh3} - v_{zh3}[i])^2}{\sigma^2_{\rm rv}[i]}\,, \tag{6}$$

where we again interpolate our model to the times $t_{\rm rv}[i]$. Note that in case of a four-body configuration we will attribute the velocities to the fourth body and change this metric correspondingly (see below).

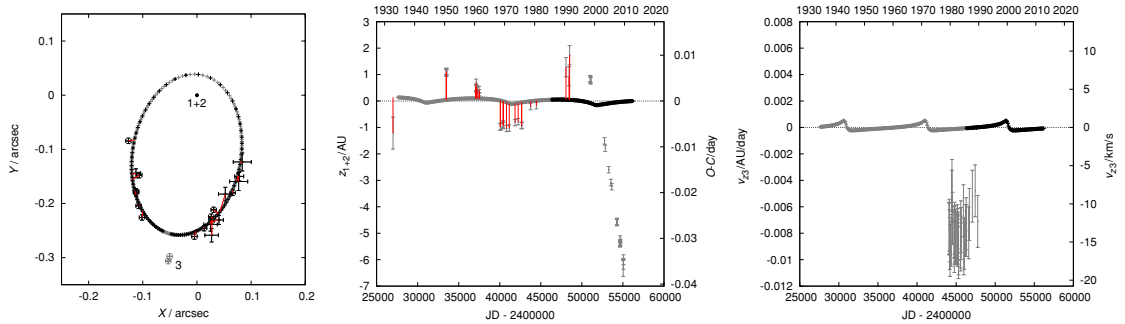


**Figure 2.** Best-fit solution for the trajectory of the third body, which corresponds to speckle-interferometry data (but excluding 1985 measurements). Neither light-time effect nor RVs were fitted in this case. Left panel: trajectory of the third body in the sky-plane angular coordinates $(X, Y)$, observations are denoted by error bars and our simulated data by small crosses, red lines represent the residuals. Middle panel: minima timings $(O-C)$ of the (1+2) eclipsing binary vs. time $(HJD)$. Right panel: RV $v_{zh3}$ of the third body vs. time. Parameters of the third body are $m_3 = 1.17\,M_\odot$, $x_{h3} = -0.15$ AU, $y_{h3} = -25.9$ AU, $z_{h3} = -0.63$ AU, $v_{xh3} = 0.0037\,\mathrm{AU\,d^{-1}}$, $v_{yh3} = 0.0017\,\mathrm{AU\,d^{-1}}$, $v_{zh3} = 0.0000\,\mathrm{AU\,d^{-1}}$ for $T_0 = 2447607.5185$ JD. The inclination of the orbit is very low in this case ($I = 1\overset{\circ}{.}5$). The resulting $\chi^2_{\rm sky} = 52$, with the number of data points $N_{\rm sky} = 20$. Note there is a strong disagreement of this Keplerian orbit with both $O-C$ data and RVs (total $\chi^2 = 1700$, $N = 90$).
(A color version of this figure is available in the online journal.)

Optionally, we can add an *artificial* function to $\chi^2$ in order to constrain the mass $m_4$ within reasonable limits, e.g.,

$$\chi^2_{m_4} = \left[\left(m_4 - \frac{m_{4\rm min} + m_{4\rm max}}{2}\right) \cdot \frac{2}{m_{4\rm max} - m_{4\rm min}}\right]^{100}, \quad (7)$$

with $m_{4\rm min} = 0.1\,M_\odot, m_{4\rm max} = 1.2\,M_\odot$. The upper limit follows from the fact that no other bright star is observed in the vicinity of V505 Sgr.

A similar expression can be used to constrain the absolute value of velocity $v_4$ (e.g., to be smaller than the escape velocity from the system, otherwise, we often obtain hyperbolic velocities).

Occasionally, we use a different metric instead of Equation (3):

$$\chi^2 = w_{\rm sky}\chi^2_{\rm sky} + w_{\rm lite}\chi^2_{\rm lite} + w_{\rm rv}\chi^2_{\rm rv}, \quad (8)$$

with weights $w_{\rm sky} \geqslant w_{\rm lite}, w_{\rm rv}$, in order to fit the interferometric trajectory better. There are only five points after the periastron passage, which would otherwise have too low statistical significance compared to a lot of light-time data.

What can we expect about the 13 dimensional function $\chi^2(d, m_3, z_{h3}, \ldots, v_{zh4})$? It will surely have many local minima, which would be statistically almost equivalent. (One can shoot the fourth body from a slightly different position with a slightly different velocity to get almost the same result.) The problem is degenerate in this sense. Clearly, there are strong correlations, e.g., between the mass $m_4$ and the minimal distance of a close encounter (and consequently initial positions/velocities of the fourth body). Minimization of the $\chi^2$ function is thus a difficult task.

We use a simplex algorithm (Press et al. 1997) to save computational resources and to find local minima. However, it is not our goal to find a global minimum of $\chi^2$, because of the degeneracy and the immense size of the parameter space. We anyway do not expect a deep, statistically significant global minimum. Instead, we will choose a set of starting points for the fourth body and look for a subset of *allowed* solutions.

On the other hand, in the case we test a three-body configuration only, the problem is much simpler: the six-dimensional $\chi^2(d, m_3, z_{h3}, v_{xh3}, v_{yh3}, v_{zh3})$ is well behaved and we may expect to find a unique solution (and its uncertainty).

## 4. RESULTS

In the following subsections, we consider and analyze several hypotheses about the nature of the V505 Sgr system.

1. There are three bodies only in V505 Sgr.
2. The third body directly perturbs the central pair.
3. A steady mass transfer causes minima timing variations.
4. There is modulation of mass transfer by the third body.
5. A sudden mass transfer occurred around 2000.
6. Appelgate's mechanism is operating.
7. A fourth body is present (either on a bound or hyperbolic orbit).

### 4.1. The Third Body Alone on a Keplerian Orbit

At first, let us test a standard "null" hypothesis, i.e., only a third body exists ($m_4 = 0$). It is possible to fit speckle data *alone* ($w_{\rm lite} = w_{\rm rv} = 0$) by an elliptical orbit with a $(29 \pm 1)$ year period, especially, if we assume the first two 1985 measurements are erroneous (offset by 50 mas; see Figure 2, left). The $\chi^2_{\rm sky} = 50$ for this fit and the respective number of data points is $N_{\rm sky} = 20$ (though ideally, $\chi^2$ should be comparable to $N$.).

Note the $\chi^2_{\rm sky}$ would be much higher, if we include the 1985 measurements: $\chi^2_{\rm sky} = 210$, $N_{\rm sky} = 22$. It means, if these two measurements are not systematic errors, the 29 year Keplerian orbit is essentially excluded! The two respective measurements were obtained by two *different* telescopes during two different nights (see McAlister et al. 1987a, 1987b). We checked measurements of another 34 stars in these publications, observed with the *same* telescope and during the same night as V505 Sgr, and we have found no indication of a wrong plate scale—all measurements lie on Keplerian ellipses within usual observational uncertainties (5 mas). We thus believe the 1985 measurements are *not* erroneous and they should be included in the $\chi^2$ metric.

Without additional (non-positional) data it is not possible to distinguish between different inclinations—there are equivalent low-$I$ and high-$I$ solutions with almost the same $\chi^2 \simeq 50$. Nevertheless, *every* inclined orbit of the third body has to cause a corresponding light-time effect, otherwise must be considered wrong! Even a slight $I \gtrsim 2^\circ$ inclination would easily be

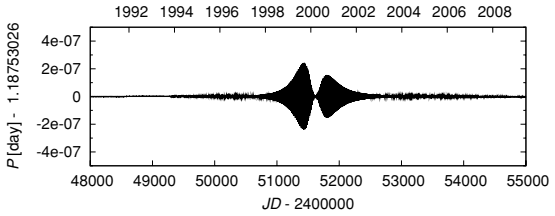


**Figure 3.** Simulated osculating orbital period $P$ of the central binary (bodies 1 and 2), perturbed by the third body. The periastron passage occurred in 2000 and the corresponding change of period is $\Delta P \lesssim 10^{-7}$ days. The observed values of $|\Delta P| \simeq 10^{-5}$ days are much larger than in this simulation.

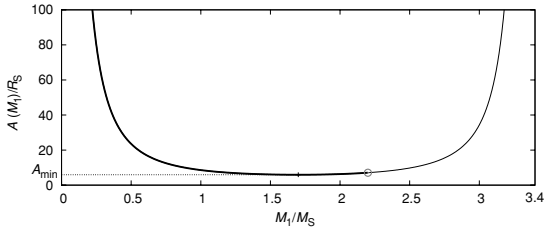


**Figure 4.** Dependence of separation $A$ of the eclipsing binary on the mass $M_1$ of the first body, resulting from the conservation of total mass and orbital angular momentum. The thick line denotes past evolution, the circle the current state $M_1 = 2.2\,M_\odot$, and the thin line the future evolution.

detectable in the light-time effect data (see Figure 2, middle). A period analysis of the $O-C$ data (with Period04 program; Lenz 2008) also does not show a prominent 29 year period. On the other hand, there is a clear signal at $P = 39$ years, with an amplitude of the peak $A = 0.0092$ days.

If we assume the $O-C$ data are indeed caused by a light-time effect, there is a strong disagreement of the 29 year Keplerian orbit with the light-time effect data (and also with RVs), even prior to 2000! If we try to fit the whole orbit and light-time effect data *together*, we would have $\chi^2_{\rm sky} = 107$ and $N_{\rm sky} = 20$, i.e., such an orbit is excluded with a high significance. There are also clear systematic departures between the observed interferometric data and calculated Keplerian orbit.

The only possibility is that the inclination of the third-body orbit is almost zero $I \lesssim 2^\circ$, so we do not see any light-time effect at all. The observed $O-C$ variations then must caused by an entirely different phenomenon (see Sections 4.2–4.6 for a detailed discussion).

Nevertheless, there still remains a strong disagreement with the observed high RVs $v_{\rm rad3} \simeq 10\,{\rm km\,s^{-1}}$, because a non-inclined orbit should have $v_{\rm rad3} \lesssim 1\,{\rm km\,s^{-1}}$. We have no solution for this problem (unless there is a fourth body present in the system; see Sections 4.7–4.9).

### 4.2. Direct Perturbation of the 1+2 Orbital Period by the Third Body

One may ask, if the observed variations in minima timings (Table 2), which correspond to the changes of the period of the order $|\Delta P| \simeq 10^{-5}$ days, could be caused by a *direct* gravitational perturbation of the tight central pair (1, 2) by the orbiting third body. In periastron, the minimum distance is of the order $\simeq$10 AU. So as to test this possibility, we use our dynamical model with three bodies 1, 2, and 3 taken separately. A detection of minute changes of the orbital period requires a smaller time step and higher precision of the BS integrator ($\Delta t = 0.01$ day, $\epsilon = 10^{-12}$). The resulting osculating orbital period changes during one periastron passage are shown in Figure 3. They are much smaller than $\Delta P \lesssim 10^{-7}$ days, if we compare values far from periastron, i.e., $\sim 2$ years before and after periastron passage. An extremely close encounter (within less than 0.1 AU, which corresponds to 0.001 arcsec) would be needed to change the orbital period of the tight Algol system substantially.

Moreover, *anything* directly connected with the third body should conform to the 39 year period of the minima timings and this, according to Section 4.1, is in conflict with any 29 year Keplerian orbit of the third body.

### 4.3. Effects of Mass Transfer Between 1 and 2

Past photometric and spectroscopic observations confirm that the central pair of V505 Sgr is a classical semi-detached Algol system, with a less-massive secondary filling its Roche lobe (Chambliss et al. 1993). In the case of a conservative mass transfer, the sum of masses is constant,

$$M_1(t) + M_2(t) = K\,, \tag{9}$$

as well as the orbital angular momentum

$$A(t) M_1^2(t) M_2^2(t) = C\,, \tag{10}$$

where $A(t)$ denotes the actual separation of the stars. We can substitute current masses and separation $A = 7.1\,R_\odot$ (Chambliss et al. 1993) into these equations, compute constants $K$, $C$, and consequently the dependence $A(M_1)$ (see also Figure 4),

$$A(M_1) = C\,M_1^{-2}(K - M_1)^{-2}\,. \tag{11}$$

A smooth conservative mass transfer should increase the orbital period steadily, since in the V505 Sgr case the mass ratio has been reversed already ($M_1 > M_2$). On the contrary, we observe an abrupt *decrease* of the period $\Delta P = -1.2 \times 10^{-5}$ days after 2000. We thus conclude a simple mass transfer cannot explain the observer minima timings.

### 4.4. Modulation of Mass Transfer Between 1 and 2 During the Third-body Encounter

In this section, we test if the third body is capable of changing the Roche potential of the central binary (bodies 1 and 2) in a such a way that the mass transfer rate $dM/dt$ (and consequently $dP/dt$) changes by a substantial amount. We add a third-body term to the Roche potential:

$$\Omega(x, y, z) = \frac{1}{r_1} + \frac{q}{r_2} + \frac{1}{2}(1+q)r_3^2 + \frac{q_{\rm 3rd}}{r_{\rm 3rd}}\,, \tag{12}$$

where $q = M_2/M_1$ denotes the mass ratio and similarly $q_{\rm 3rd} = M_3/M_1$. We see immediately, that relative change of the potential due to the third body at distance $r_{\rm 3rd} \simeq 10$ AU is $\delta\Omega/\Omega \simeq 10^{-13}$. We do not find it likely that such a minuscule perturbation of the potential, and thus the related tidal acceleration, could produce significant effects. Consequently, we cannot explain minima timing variations by the modulation of mass transfer. Finally, as in Section 4.2, this effect would also be in conflict with a 29 year Keplerian orbit of the third body.

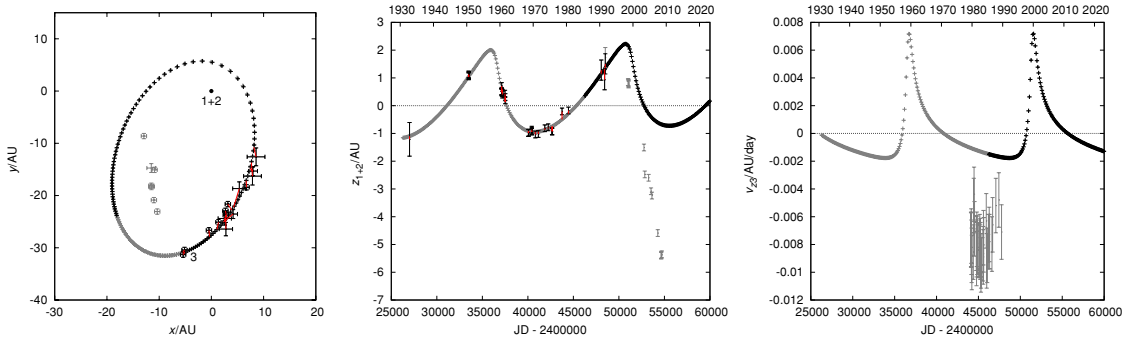


**Figure 5.** Best-fit solution for the orbit of the third body *and* the light-time effect before 2000: $d = 102$ pc, $m_3 = 1.2\,M_\odot$, $z_{h3} = 4.0$ AU, $v_{xh3} = 0.0036$ AU day$^{-1}$, $v_{yh3} = 0.0013$ AU day$^{-1}$, $v_{zh3} = -0.0015$ AU day$^{-1}$ for $T_0 = 2446282.24375$ JD. The resulting $\chi^2 = 88$, with the total number of data points $N = 46$. The red lines denote differences between observed and calculated data. Radial velocities were not fitted in this case; they are shown for comparison only.

(A color version of this figure is available in the online journal.)

### *4.5. A Sudden Mass Transfer of Biermann & Hall (1973)*

According to Biermann & Hall (1973) a sudden mass transfer between the Algol components may result in a *temporary* decrease of the orbital period, even though mass is flowing from the lighter component to the more massive one. In our case, we would need $dM/dt$ as high as $\simeq 10^{-6}\,M_\odot$ yr$^{-1}$ to explain period changes $|dP/dt| \simeq 10^{-6}$ days yr$^{-1}$. Such a mass transfer rate seems to be too large compared to theoretical models (Harmanec 1970), $dM/dt \gtrsim 10^{-6}\,M_\odot$ yr$^{-1}$ are reached only during a very short interval of time, before the reversal of mass ratio.

Another problem of this scenario is that we observe rather smooth periodic variations of the minima timings before 2000. These do not seem to be entirely compatible with this mechanism, which may be more irregular in time. This phenomenon is also rarely confirmed by independent observations. (It would require a very precise photometry on a long timescale or a spectroscopic confirmation of circumstellar matter.) Today, this mechanism is not generally accepted as a major cause of minima timing variations among Algol-type systems.

### *4.6. Applegate (1992) Magnetic Mechanism*

Applegate (1992) proposed that a gravitational quadrupole coupling of orbit and shape variations of a magnetically active subgiant (second component) can result in variations of the orbital period and hence minima timings. In this scenario, the observed 39 year period would correspond to the period of the magnetic dynamo.

The second (G5 IV) star rotates quickly (1.2 d); it has a convective envelope in this evolutionary stage and, presumably, there is a differential rotation and operating dynamo, which can result in a sufficiently strong magnetic field ($10^4$ G), necessary for Applegate's mechanism to work. Period changes of the order $\Delta P/P \simeq 10^{-5}$ should also correspond to changes of the luminosity $\Delta L_2/L_2 = 0.1$, in phase with minima timings. Unfortunately, we are not able to confirm this by our photometry (0.01 mag precision over tens of years would be required).

In principle, this mechanism can explain minima timing variations, but it is not clear, why there is an abrupt change after 2000. An independent confirmation is rare and difficult. One of the possibilities might be a spectroscopic observation of magnetically active lines (Ca II H and K or Mg II). This scenario also does not provide any solution for the observed large RVs.

### *4.7. Distance, Mass, and the Third-body Orbit (Prior to 2000)*

Hereinafter, we *assume* minima timing variations are caused mainly by the light-time effect due to the orbiting third body. Because the orbit of the third body prior the periastron passage in 2000 seems unperturbed, we first determine the optimal distance $d$ of the system, third-body mass $m_3$, and orbit ($z_3$, $v_{xh3}$, $v_{yh3}$, $v_{zh3}$). We use only the observational data older than 2000 for this purpose.

We compute $\chi^2$ values for the following set of initial conditions (we do not use a simplex here): $d \in (95, 105)$ pc, $\Delta d = 1$ pc, $m_3 \in (1.1, 1.3)\,M_\odot$, $\Delta m_3 = 0.1\,M_\odot$, $z_{h3} \in (2.0, 8.0)$ AU, $\Delta z_{h3} = 1.0$ AU, $v_{xh3} \in (0.0033, 0.0040)$ AU day$^{-1}$, $v_{yh3} \in (0.0008, 0.0016)$ AU day$^{-1}$, $v_{zh3} \in (-0.0018, 0.0012)$ AU day$^{-1}$, $\Delta v_{xh3} = \Delta v_{yh3} = \Delta v_{zh3} = 0.0001$ AU day$^{-1}$.

The best-fit solution is displayed in Figure 5. The orbital period of the third body is $P = (39 \pm 2)$ years. The resulting distance $d = (102 \pm 5)$ pc. This solution is very similar to that in Mayer (1997). The parallactic distance of V505 Sgr given by *Hipparcos* ($\pi = (8.40 \pm 0.57)$ mas, $d = 111$–$128$ pc, cf., van Leeuwen 2007) is offset and even the error intervals do not overlap.

Note that the RVs of the order $-10$ km s$^{-1}$ measured by Tomkin (1992) cannot be attributed to the third body, whose orbital velocity should be much smaller ($(-2.5 \pm 0.5)$ km s$^{-1}$) according to interferometric and light-time effect data. Consequently, we do not fit the velocities in this case ($w_{\rm rv} = 0$); we are going to attribute them to the fourth body (in Section 4.8).

Finally, it is important to mention that our solution does *not* depend on the two ("offset") 1985 speckle measurements at all! We can exclude them completely from our considerations and the result would be the same. Our only assumption was that minima timing variations are caused by the light-time effect and this enforces the orbital period of $P \simeq 39$ years. (But coincidentally, both 1985 measurements fit perfectly this longer-period orbit.)

### *4.8. Encounter with a Fourth Body (a $\chi^2$ Map)*

We next *fix* initial conditions of the third body according to the results in Section 4.7 and model a perturbation by a fourth body under different geometries.

The free parameters of the model are $m_4$, $x_{h4}$, $y_{h4}$, $z_{h4}$, $v_{xh4}$, $v_{yh4}$, $v_{zh4}$. We include RV data, but we assume the spectral lines (and corresponding velocities) belong to the fourth

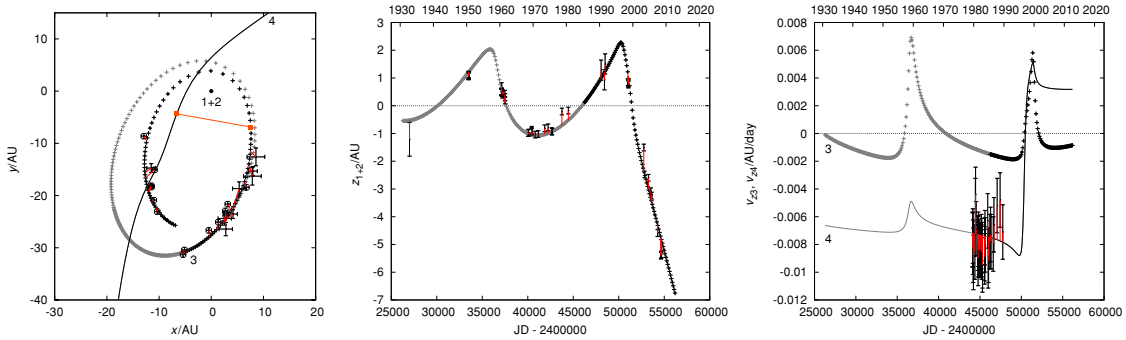


**Figure 6.** Best-fit solution for the trajectory of the fourth body, which best explains the observed trajectory of the third body, light-time effect, and RVs: $m_4 = 0.8\,M_\odot$, $x_{h4} = 45.0$ AU, $y_{h4} = 39.5$ AU, $z_{h4} = 28.0$ AU, $v_{xh4} = -0.0105$ AU day$^{-1}$, $v_{yh4} = -0.008$ AU day$^{-1}$, $v_{zh4} = -0.0075$ AU day$^{-1}$. The resulting $\chi^2 = 331$, with the total number of data points $N = 102$. The motion of the fourth body captured in the left panel spans from 1994 to 2003. The squares connected by a straight line indicate the closest encounter between the third and fourth bodies.

(A color version of this figure is available in the online journal.)

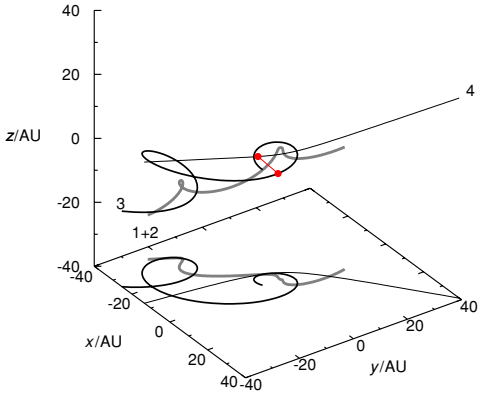


**Figure 7.** Orbits of bodies (1+2), 3, 4 in a barycentric frame and their projection to the plane ($z = -40$ AU).

(A color version of this figure is available in the online journal.)

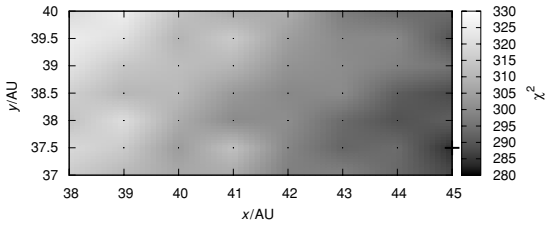


**Figure 8.** Minima of the seven-dimensional function $\chi^2(m_4, x_{h4}, y_{h4}, z_{h4}, v_{xh4}, v_{yh4}, v_{zh4})$ at given positions $(x_{h4}, y_{h4})$. The minimum is taken over remaining free parameters $m_4$, $z_{h4}$, $v_{xh4}$, $v_{yh4}$, $v_{zh4}$. Cross is an overall minimum and black dots represent computed points.

body. Note that there might be a problem with too low luminosity and thus too weak spectral lines of the fourth body, in case it has low mass. We discuss this possible inconsistency in detail in Section 4.11. We scan the following limited set of initial conditions (over 8 million trials): $m_4 \in (0.5, 0.8)\,M_\odot$, $\Delta m_4 = 0.05\,M_\odot$, $x_{h4} \in (38, 45)$ AU, $\Delta x_{h4} = 1.0$ AU, $y_{h4} \in (37, 40)$ AU, $\Delta y_{h4} = 0.5$ AU, $z_{h4} \in (20, 30)$ AU, $\Delta z_{h4} = 1.0$ AU, $v_{xh4} \in (-0.011, -0.005)$ AU day$^{-1}$, $v_{yh4} \in (-0.010, -0.005)$ AU day$^{-1}$, $v_{zh4} \in (-0.012, -0.006)$ AU day$^{-1}$, $\Delta v_{xh4} = \Delta v_{yh4} = \Delta v_{zh4} = 0.0005$ AU day$^{-1}$.

A comparison of the best-fit solution with observational data is displayed in Figure 6. We use a modified metric, Equation (8), with $w_{\rm sky} = 10$, $w_{\rm lite} = w_{\rm rv} = 1$. The respective trajectories of the bodies are shown in Figure 7. Note, however, that according to the $\chi^2$ map (Figure 8) there are many local minima, which cannot be distinguished from a statistical point of view, because the values of $\chi^2$ differ only little ($\chi^2 \in [284, 325]$). The corresponding $\chi^2$ probabilities $Q(\chi^2|N)$ that the observed value of $\chi^2 = 340$ (for a given number of degrees of freedom $N = 105$) is that large by chance even for a correct model are too low (essentially zero). It may also indicate that real uncertainties might be a bit larger (by a factor of 2) than the values estimated by us. Nevertheless, we will find better solutions using a simplex method (in Section 4.9).

### *4.9. Encounter with a Fourth Body (Different Geometry, Simplex)*

We selected a different set of initial conditions for the following modeling. They serve as starting points for the simplex algorithm: $m_4 = 0.5\,M_\odot$, $x_{h4} \in (-100, -10)$ AU, $y_{h4} \in (-50.1, -0.1)$ AU, $z_{h4} \in (0, 50)$ AU, $\Delta x_{h4} = \Delta y_{h4} = \Delta z_{h4} = 5.0$ AU, $v_{xh4} \in (0.005, 0.015)$ AU day$^{-1}$, $\Delta v_{xh4} = 0.001$ AU day$^{-1}$, $v_{yh4} \in (0, 0.01)$ AU day$^{-1}$, $\Delta v_{yh4} = 0.002$ AU day$^{-1}$, $v_{zh4} \in (-0.007, 0)$ AU day$^{-1}$, $\Delta v_{zh4} = 0.001$ AU day$^{-1}$. The total number of trials reaches $10^6$.

We reject RV constraints ($w_{\rm rv} = 0$), although we can find a lot of allowed solutions with velocities in the correct range ($v_{zh4} \doteq -0.008$ AU day$^{-1}$). On the other hand, we use a mass limit according to Equation (7). An example of a typical good fit is shown in Figure 9. We selected one with mass around $m_4 = 0.6\,M_\odot$; the corresponding $\chi^2 = 168$, $N = 73$, and probability $Q(\chi^2|N) \simeq 10^{-9}$, still too low. This solution can be further improved by a 15 dimensional simplex (i.e., with all parameters of the third-body free) to reach $\chi^2$ as low as 130 and $Q(\chi^2|N)$ as high as $10^{-5}$.

As before, there are many solutions, which are statistically equivalent. We present allowed solutions in Figure 10 as plots $\chi^2$ versus a free parameter, with each dot representing one local minimum found by simplex. Prominent concentrations of solutions in these plots can be regarded as an indication of more

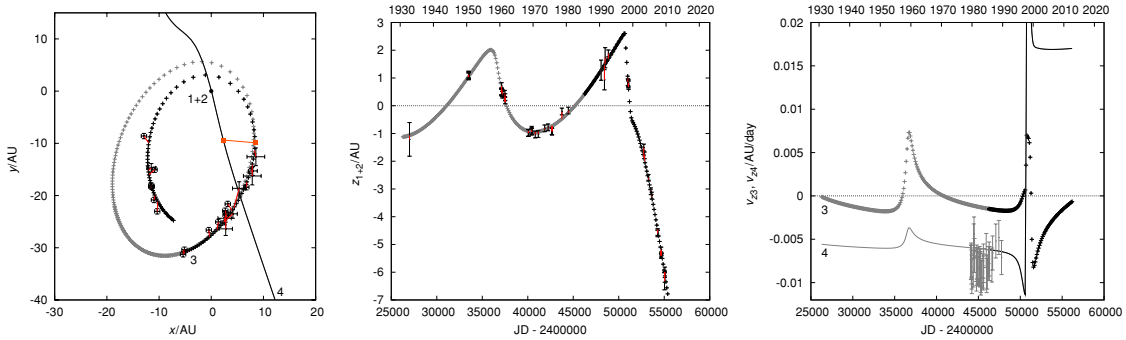


**Figure 9.** Typical solution (out of many) for the trajectory and light-time effect (without RVs): $m_4 = 0.576\,M_\odot$, $x_{h4} = 27.912$ AU, $y_{h4} = -84.809$ AU, $z_{h4} = 30.482$ AU, $v_{xh4} = -0.00584$ AU day$^{-1}$, $v_{yh4} = 0.01612$ AU day$^{-1}$, $v_{zh4} = -0.00620$ AU day$^{-1}$. The corresponding $\chi^2 = 168$, with the number of data points $N = 73$. This solution can be further improved by a 15 dimensional simplex to reach $\chi^2$ as low as 130.
(A color version of this figure is available in the online journal.)

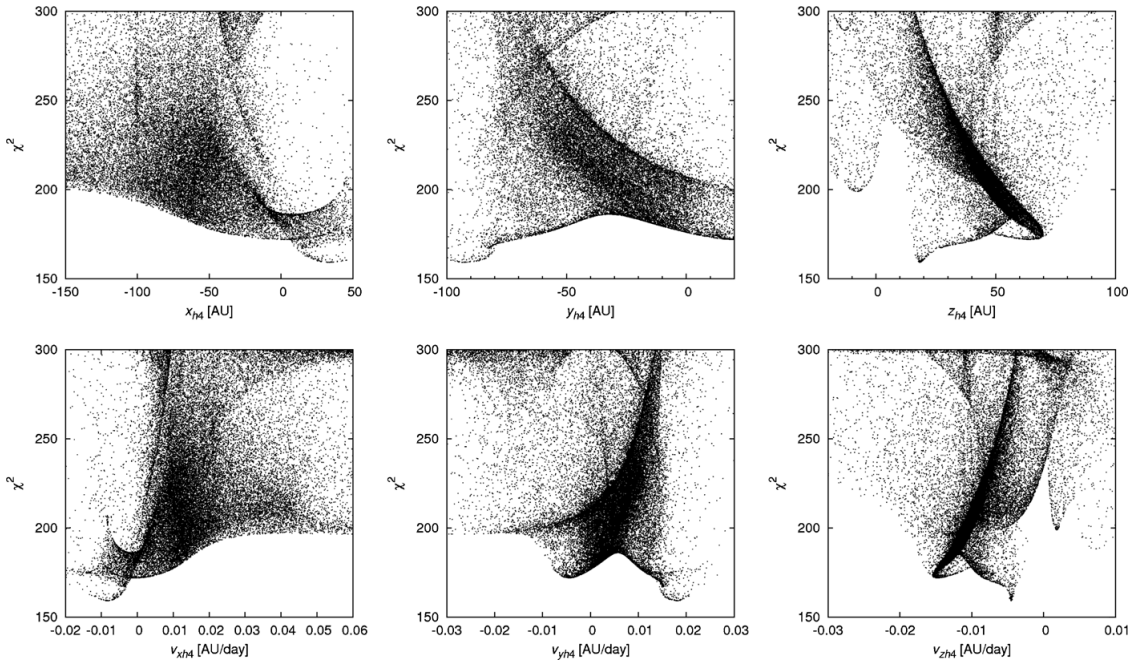


**Figure 10.** Distribution of good solutions ($\chi^2 < 300$) in the space of free parameters: $x_{h4}$, $y_{h4}$, $z_{h4}$, $v_{xh4}$, $v_{yh4}$, $v_{zh4}$.

probable solutions. Only minority of trials were successful. Most of them were stopped too early (at high $\chi^2$) due to numerous local minima.

According to the histogram of masses $m_4$ (Figure 11, left) the values $m_4 < 0.5\,M_\odot$ are less probable, and the histogram peaks around $m_4 = 0.9\,M_\odot$. Note the simplex sometimes tends to "drift" to zero or large masses, which leads to artificial peaks at the limits of the allowed interval. The same applies to velocity $v_4$.

Histogram of total energies $E_4$ of the fourth body (Figure 11, middle) shows a strong preference for hyperbolic orbits ($E_4 > 0$), but elliptic orbits ($E_4 < 0$) also exist (with a 1% probability and slightly larger best $\chi^2 = 199$). The reason for this preference stems from the fact that third-body orbit seems almost unperturbed prior to 2000, so one needs rather a higher-velocity encounter of the fourth body from larger initial distance.

Typical minimum distances between the fourth and third bodies during an encounter are around $d_{\min 3} \simeq 6$ AU and they are even smaller between the fourth body and the (1+2) body $d_{\min 1+2} \simeq 1.5$ AU (Figure 11, right). They are of comparable size and consequently a simple impulse approximation, i.e., an instantaneous change of orbital velocity, cannot be used to link the two elliptic orbits of the third body (before and after the perturbation). There are no good solutions (with $\chi^2 < 300$), which would lead to an escape of the third body.

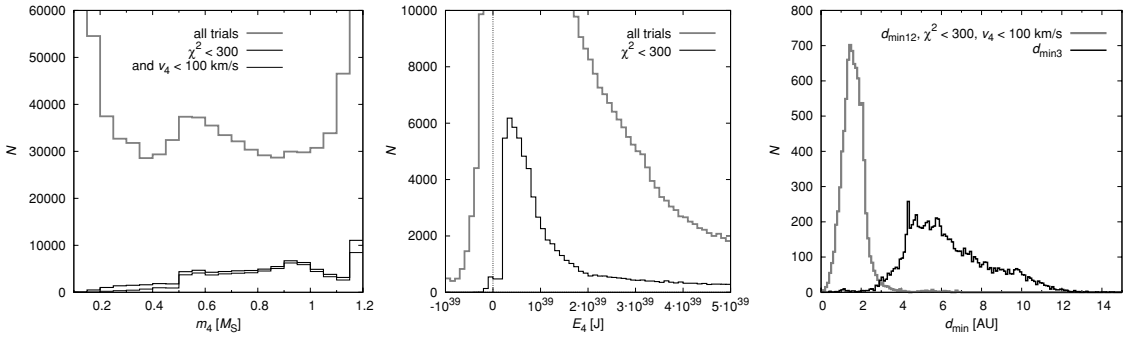


**Figure 11.** Left: histogram of masses $m_4$ of all trials and good ones (with $\chi^2 < 300$ and the lower absolute value of velocity $|v_4| < 100\,\mathrm{km\ s^{-1}}$). Middle: histogram of total energies $E_4$ of the fourth body at the epoch $T_0$. There is a strong preference for hyperbolic orbits ($E_4 > 0$), but one can find approximately 1% of orbits with negative energies. Right: histogram of minimum distances $d_{\mathrm{min1+2}}$, $d_{\mathrm{min3}}$ of the fourth body from the (1+2) and third body (only good trials are shown). According to these distributions, it is more likely that the fourth body approached the (1+2) body closer than the third body. Median values are $\tilde{d}_{\mathrm{min1+2}} = 1.6$ AU and $\tilde{d}_{\mathrm{min3}} = 5.9$ AU.

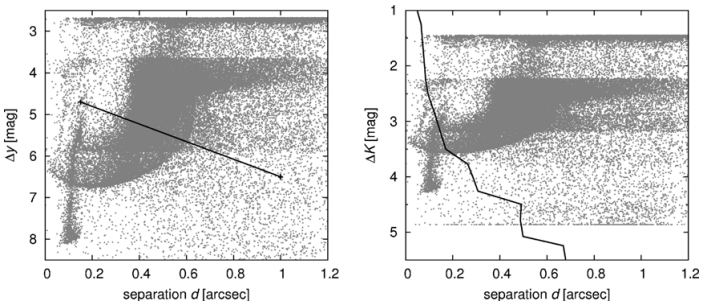


**Figure 12.** Observational limits (black lines) of interferometric measurements (left panel) and the CFHT imaging (right panel). Our solutions from Section 4.9 are plotted as dots. Many of them are well below the observational limits.

### *4.10. Observational Limits of Interferometry and CFHT Imaging*

Postulating an existence of a fourth body, inferred from its gravitational influence on the V505 Sgr system, we should check if this object could have been directly observed in the past.

According to A. Tokovinin (2009, private communication), the limit of recent interferometric measurements can be approximated by a linear dependence of brightness difference $\delta y$ in Strömgren $y$ magnitudes on angular separation $d$ of the components: $\Delta y = 4.7$ mag at $d = 0.15$ arcsec and $\Delta y = 6.5$ mag at $d = 1$ arcsec adaptive optics at CFHT can reach even fainter. The limit in the $K$ band is given by Rucinski et al. (2007), Figure 7, as a nonlinear dependence $\Delta K(d)$.

We can easily select solutions from Section 4.9, which fulfill *both* limits, albeit a lot of them is excluded by the CFHT limit (see Figure 12). Note that we are not able to predict exact magnitudes or positions of the fourth body, because there are still many solutions possible.

Note that there is an object in the USNO-A2.0 catalog, very close to V505 Sgr: 0750-19281506, R.A.$_{\mathrm{J2000}} = 298\overset{\circ}{.}277034$, decl.$_{\mathrm{J2000}} = -14\overset{\circ}{.}603839$. This corresponds to an angular separation of 2.6 arcsec and a position angle of 235° with respect to V505 Sgr, at the epoch of observation 1951.574. The magnitudes $R = 10.9$ mag and $B = 11.8$ mag are marked as uncertain (since the object is located in the area flooded by light of V505 Sgr). This is an interesting coincidence with "our" fourth body, but we doubt if the source is real. Moreover, if the brightness of the USNO source is correct within $\pm 1$ mag, it should be well above the observational limits of CFHT.

### *4.11. Constraints from Spectral Lines Radial-velocity Measurements*

In Section 4.8, we tried to attribute the observed high RVs to a hypothetic fourth component. We thus have to ask a question: could the low-mass fourth component be visible in the spectrum?

To this end, we used a grid of synthetic spectra based on Kurucz model atmospheres, which was calculated and provided for general use by J. Kubát (for details of the calculations, cf., e.g., Harmanec et al. 1997). We calculate synthetic spectra for three and four lights (stars) and compare them with the spectrum observed by Tomkin (1992), Figure 2. This spectrum was taken at HJD = 2444862.588, close to the primary eclipse of the central binary, which decreases the luminosity of the first component and thus weak narrow lines of the third (or fourth) component are more prominent.

Modeling of spectra (relative intensities) requires a number of parameters: luminosities, effective temperatures, surface gravity, rotational and RVs. Luminosities of the known components are $L_1 = 26\,L_\odot$, $L_2 = 3.8\,L_\odot$, $L_3 = 2.1\,L_\odot$, respectively. The amplitude of the light curve is $\Delta m = 1.1$ mag (Chambliss et al. 1993). The effective temperatures are approximately (Popper 1980) $T_{\mathrm{eff1}} \simeq 9000$ K (corresponding to A2 V spectral type), $T_{\mathrm{eff2}} \simeq 6000$ K (F8 IV to G6–8 IV), $T_{\mathrm{eff3}} \simeq 6000$ K (F8 V). We assume the following values of the surface gravitational

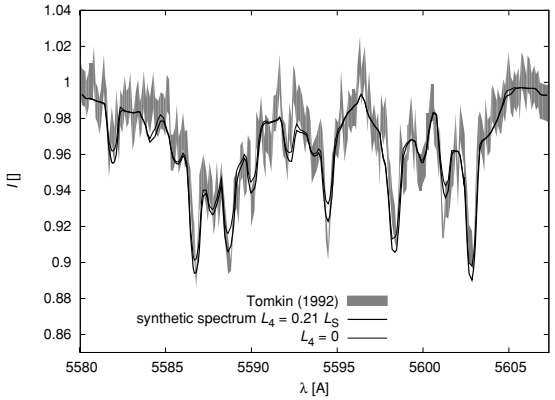


**Figure 13.** Synthetic spectrum with intensity normalized to the continuum for four and three lights (thick and thin lines) and for the temperature of the fourth body equal to 4000 K, compared with the observed spectrum (gray line, whose thickness corresponds to observational uncertainties), taken from Tomkin (1992). The wavelength range, which we fitted, was 5580–5607 Å. The best solution for the luminosity of the fourth body is $L_4 = 0.22\,L_\odot$ (with $\chi^2 = 465$, $N = 239$) The fit with three lights only is worse, with the $\chi^2$ value equal to 542. For $T_4 = 5700$ K, we would have $L_4 = 0.43\,L_\odot$ and $\chi^2 = 495$.

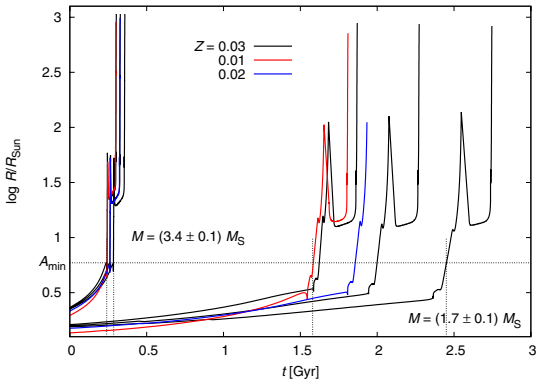


**Figure 14.** Evolution of radii for stars with different masses ($M = 1.6$, 1.7, 1.8, and 3.3, 3.4, 3.5 $M_\odot$, $Z = 0.03$) and metallicities ($M = 1.7$ and $3.4\,M_\odot$, $Z = 0.01$, 0.02). This computation was performed by the program EZ (Paxton 2004). The upper limit for the age of the second component is then 1.5–2.5 Gyr, while the lower limit is between 0.24 and 0.29 Gyr.

(A color version of this figure is available in the online journal.)

acceleration: $\log g_1 = \log g_2 = 4.0$ (cgs units), $\log g_3 = 4.5$ (valid for stars close to the main sequence). Rotational velocities of the first and second components, a semi-contact binary with an orbital period of 1.2 days, are synchronized by tidal lock and are of the order $v_{\rm rot1} \simeq v_{\rm rot2} \simeq 100\,{\rm km\,s^{-1}}$. These are in concert with the observed width of broad spectral lines $\Delta\lambda = 6$ Å. For the third component, we assume a lower velocity $v_{\rm rot3} = 20\,{\rm km\,s^{-1}}$, usual for late F-type main-sequence stars. This matches the width of sharp lines. Radial velocities of the first and second components are close to zero because of the eclipse proximity ($v_{\rm rad1} = v_{\rm rad2} \doteq 0$).

We assume the following reasonable parameters for the fourth component: $T_4 = 4000$ K or 5700 K, $\log g_4 = 4.0$, $v_{\rm rot4} = 20\,{\rm km\,s^{-1}}$. We construct a $\chi^2$ metric:

$$\chi^2 = \sum_{i=1}^{N_{\rm obs}} \frac{(I_{\rm obs}[i] - I')^2}{\sigma_{\rm obs}[i]^2}\,, \qquad (13)$$

where $I_{\rm obs}[i]$ denote observed relative intensities, $\sigma_{\rm obs}[i]$ associated uncertainties, and $I'$ is a sum of synthetic intensities weighted by luminosities:

$$I' = \frac{\sum_{j=1}^{4} I'(T_{{\rm eff}\,j}, \log g_j, v_{{\rm rot}\,j}) \cdot L_j}{\sum_{j=1}^{4} L_j} \qquad (14)$$

and of course Doppler shifted due to RVs ($\lambda' = \lambda_{\rm obs}[i](1 - v_{{\rm rad}\,j}/c)$) and interpolated to the required wavelengths $\lambda'$ using Hermite polynomials (Hill 1982). We use a simple eclipse modeling: we decrease $L_1$ according to the Pogson equation to get the observed total magnitude increase $\Delta m$. Errors $\sigma_{\rm obs}[i]$ were estimated from the scatter in small continua, $\sigma = 0.01$. Artificially small errors $\sigma = 0.003$ were assigned to the measurements in the cores of the narrow lines, in order to match precisely their depths.

We constructed a simplex algorithm (Press et al. 1997) with the following free parameters: $L_4$, $v_{\rm rad3}$, $v_{\rm rad4}$. Other luminosities and RVs remain fixed. This simplex is well behaved and converges to final values almost regardless of the starting point. There is no reasonable improvement, if we let all eight parameters ($L_j$, $v_{{\rm rad}\,j}$) to be free.

The result for a selected temperature $T_4 = 4000$ K is shown in Figure 13. The best fit is for $L_4 = 0.22\,L_\odot$, and it is marginally better that the fit with three lights only (i.e., with fixed $L_4 = 0$). The luminosity corresponds roughly to the mass $m_4/M_\odot \propto (L_4/L_\odot)^{1/4} = 0.68$, which seems reasonable with respect to the results in Section 4.9.

Note that we used $v_{\rm rot3} = 20\,{\rm km\,s^{-1}}$ for rotational velocity of the third body. No reasonable solution was found for $v_{\rm rot3}$ as high as $100\,{\rm km\,s^{-1}}$, which would cause a strong rotational broadening and almost a "disappearance" of spectral lines of the third body. It means that a low-mass fourth body *alone* cannot produce deep sharp lines. We thus suspect, there is a blend of lines in the spectrum observed by Tomkin (1992), which may originate on the third and fourth bodies, with low and high RVs. However, observations with high spectral resolution would be needed to resolve such blending.

### *4.12. Constraints from the Stellar Evolution of the Eclipsing Binary*

To assess the long-term evolution of V505 Sgr, we need some information about the age of the system. An *upper* limit for the age can be estimated easily from masses of stars. The semi-detached central binary (bodies 1 and 2) has a total mass $(3.4 \pm 0.1)\,M_\odot$. In order to evolve into the current stage, when the second *lighter* component fills its Roche lobe, the original mass of the second star had to be at least slightly larger than half of the total mass, i.e., $M_2 > 1.7\,M_\odot$. The evolution of radius is shown in Figure 14; we are mainly concerned with the large increase of radius, when the star leaves main sequence. Given the uncertainties of the masses and unknown metallicities, the upper limit for the age is $(2.0 \pm 0.5)$ Gyr.

In order to find a lower limit, we have to check a minimum separation of the components first (cf. Equation (11) and Figure 4). A minimum separation occurs when $M_1 = 0.5$ K, in our case $A_{\rm min} = (5.9 \pm 0.1)\,R_\odot$. This value is larger than the radius of a $3.4\,M_\odot$ star during the whole evolution on the main sequence. Thus, the mass transfer had to start later, in the red giant phase.

The maximum mass of the second star had to be slightly below the total mass, i.e., $M_2 < 3.4\,M_\odot$. According to the $R(t)$ dependence (Figure 14), the red giant phase starts at the age of $(0.26 \pm 0.03)$ Gyr, which could be considered as a *lower* limit for the age of the V505 Sgr system.

## 5. CONCLUSIONS

Generally speaking, we are able to explain the observed orbit of the third body together minima timings and RVs by a low-mass fourth body, which encounters the observed three bodies with a suitable geometry. There is no unique solution, but rather a set of allowed solutions for the trajectory of the hypothetic fourth body. It is quite difficult to find a solution for both speckle-interferometry and light-time effect data. There are a few systematic discrepancies at the $2\sigma$ level, which cause the likelihood of the hypothesis to be low. Possibly, realistic uncertainties $\sigma_{\rm sky}$ are slightly larger (by a factor of 1.5) than the errors estimated by us.

Of course, there are other hypotheses, which do not need a fourth body at all (a sudden mass transfer, Applegate's mechanism, etc.), but none of them provides a unified solution for *all* observational data we have for V505 Sgr.

Further observations of the light-time effect during the next decade can significantly constrain the model. A new determination of the systemic velocity of V505 Sgr may confirm, that the change in the $O-C$ data after 2000 resulted from an external perturbation. (Tomkin's (1992) value was $(1.9 \pm 1.4)$ km s$^{-1}$.) Spectroscopic measurements of the indicative sharp lines would also be very helpful to resolve the problem with radial velocities and relative intensity of spectral lines. These lines can be attributed neither to the third nor to the fourth body alone.

If we indeed observe the V505 Sgr system by chance during the phase of a close encounter with a fourth star, we can imagine several scenarios for its origin:

1. A random passing star approaching V505 Sgr on a hyperbolic orbit. The problem of this scenario is a very low number density of stars. If we take the value $n_\star \simeq 0.073\,{\rm pc}^{-3}$ from the solar vicinity (Fernández 2005), the mean velocity with respect to other stars of the order $v_{\rm rel} \simeq 10$ km s$^{-1}$ and the required minimum distance of the order $r_{\rm imp} \simeq 10^2$ AU, we end up with a mean time between two encounters $\tau \simeq 1/(n_\star v_{\rm rel} r_{\rm imp}^2) \simeq 10^{12}$ yr, thus an extremely unlikely event.
2. A loosely bound star on a highly eccentric orbit, with the same age as other three components of V505 Sgr. Unfortunately, there is a large number of revolutions and encounters ($10^2$–$10^5$) over the estimated age of V505 Sgr and the system practically cannot remain stable over this timescale (Valtonen & Mikkola 1991).
3. A more tightly bound star on a lower-eccentricity orbit, which experienced some sort of a late instability, induced by long-term evolution due to galactic tides, distant passing stars, which shifted an initially stable configuration into an unstable state, e.g., driven by mutual gravitational resonances between components. The problem in this case is that tightly bound orbits of the fourth body are very rare in our simulations, thus seem improbable.

None of the scenarios is satisfactory. Nevertheless, we find the fourth-body hypothesis, the only one which is able to explain all available observations. Clearly, more observations and theoretical effort is needed to better understand the V505 Sagittarii system.

This research has made use of the WDS Catalog maintained at the U.S. Naval Observatory and Aladin and Simbad services. We thank W. I. Hartkopf for sending us recent positional data of double stars, S.M. Rucinski, E.V. Malogolovets, and Y.Y. Balega for providing us with their measurements of the visual component of V505 Sgr (by CFHT and SAO BTA telescopes), and L. Šmelcer for his photometry of V505 Sgr. We acknowledge the use of a grid of synthetic spectra prepared by J. Kubát and we thank P. Harmanec for some advice on the construction of synthetic spectra for multiple systems. This work was supported by the Czech Science Foundation (grant no. P209/10/0715) and the Research Programme MSM0021620860 of the Czech Ministry of Education. T.P. acknowledges support from the EU in the FP6 MC ToK project MTKD-CT-2006-042514.

## REFERENCES

Applegate, J. H. 1992, ApJ, 385, 621
Balega, I. I., et al. 2002, A&A, 385, 87
Biermann, P., & Hall, D. S. 1973, A&A, 27, 249
Chambliss, C. R., et al. 1993, AJ, 106, 2058
Chochol, D., et al. 2006, Ap&SS, 304, 93
Cook, J. M., et al. 2005, IBVS, 5636, 1
Fernández, J. A. 2005, Comets (Dordrecht: Springer)
Harmanec, P. 1970, Bull. Astron. Inst. Czech., 21, 113
Harmanec, P., et al. 1997, A&A, 319, 867
Hartkopf, W. I., Mason, B. D., Wycoff, G. L., & McAlister, H. 2009, http://ad.usno.navy.mil/wds/int4.html
Hill, G. 1982, Publ. Dom. Astrophys. Obs. Victoria BC, 16, 67
Ibanoglu, C., et al. 2000, A&A, 354, 188
Lenz, P. 2008, http://www.astro.univie.ac.at/~dsn/dsn/Period04/
Levison, H. F., & Duncan, M. J. 1994, Icarus, 108, 18
Maksimov, A. F., et al. 2009, Astrophys. Bull., 64, 296
Mayer, P. 1997, A&A, 324, 988
McAlister, H., Hartkopf, W.I, Hutter, D., & Franz, O. 1987a, AJ, 93, 688
McAlister, H., Hutter, D., Shara, M., & Franz, O. 1987b, AJ, 92, 183
Müyesseroglu, Z., Gürol, B., & Selam, S. O. 1996, IBVS, 4380, 1
Paxton, B. 2004, PASP, 116, 699
Popper, D. M. 1980, ARA&A, 18, 115
Press, W. R., Teukolsky, S. A., Vetterling, W., & Flannery, B. P. 1997, Numerical Recipes: The Art of Scientific Computing (Cambridge: Cambridge Univ. Press)
Rovithis-Livaniou, H., & Rovithis, P. 1992, IBVS, 3803, 1
Rucinski, S. M., Pribulla, T., & van Kerkwijk, M. H. 2007, AJ, 134, 2353
Tomkin, J. 1992, ApJ, 387, 631
Valtonen, M., & Mikkola, S. 1991, ARA&A, 29, 9
van Leeuwen, F. 2007, A&A, 474, 653
Worek, T. F. 1996, PASP, 108, 962
Zasche, P., et al. 2009, AJ, 138, 664

A&A 531, A49 (2011)
DOI: 10.1051/0004-6361/201116610


Astronomy & Astrophysics

# V2368 Ophiuchi: an eclipsing and double-lined spectroscopic binary used as a photometric comparison star for U Ophiuchi⋆,⋆⋆,⋆⋆⋆

P. Harmanec[1], H. Božić[2], P. Mayer[1], P. Eenens[3], M. Brož[1], M. Wolf[1], S. Yang[4], M. Šlechta[5], D. Ruždjak[2], D. Sudar[2], and H. Ak[6]

[1] Astronomical Institute of the Charles University, Faculty of Mathematics and Physics, V Holešovičkách 2, 180 00 Praha 8, Czech Republic
e-mail: Petr.Harmanec@mff.cuni.cz
[2] Hvar Observatory, Faculty of Geodesy, University of Zagreb, 10000 Zagreb, Croatia
[3] Departamento de Astronomia, Universidad de Guanajuato, Apartado 144, 36000 Guanajuato, GTO, Mexico
[4] Physics & Astronomy Department, University of Victoria, PO Box 3055 STN CSC, Victoria, BC, V8W 3P6, Canada
[5] Astronomical Institute, Academy of Sciences of the Czech Republic, 251 65 Ondřejov, Czech Republic
[6] Department of Astronomy and Space Sciences, Faculty of Sciences, Erciyes University, 38039 Kayseri, Turkey

Received 31 January 2011 / Accepted 18 April 2011

**ABSTRACT**

The A-type star HR 6412 = V2368 Oph was used by several investigators as a photometric comparison star for the known eclipsing binary U Oph but was found to be variable by three independent groups, including us. By analysing series of new spectral and photometric observations and a critical compilation of available radial velocities, we were able to find the correct period of light and radial-velocity variations and demonstrate that the object is an eclipsing and double-lined spectroscopic binary moving in a highly eccentric orbit. We derived a linear ephemeris $T_{\rm min.I}$ = HJD (2 454 294.67 ± 0.01) + ($38\overset{\rm d}{.}32712 \pm 0\overset{\rm d}{.}00004$) × $E$ and estimated preliminary basic physical properties of the binary. The dereddened $UBV$ magnitudes and effective temperatures of the primary and secondary, based on our light- and velocity-curve solutions, led to distance estimates that agree with the Hipparcos distance within the errors. We find that the mass ratio must be close to one, but the limited number and wavelength range of our current spectra does not allow a truly precise determination of the binary masses. Nevertheless, our results show convincingly that both binary components are evolved away from the main sequence, which makes this system astrophysically very important. There are only a few similarly evolved A-type stars among known eclipsing binaries. Future systematic observations and careful analyses can provide very stringent tests for the stellar evolutionary theory.

**Key words.** stars: early-type – binaries: close – stars: individual: V2368 Oph – stars: individual: U Oph – binaries: spectroscopic

## 1. Introduction

HR 6412 = HD 156208 has often been used as the photometric comparison star for a well-known eclipsing binary U Oph, which exhibits apsidal motion (Huffer & Kopal 1951; Koch & Koegler 1977; Wolf et al. 2002; Vaz et al. 2007). McAlister et al. (1987) reported that HR 6412 is a speckle-interferometric binary with a separation of 0.″136 and estimated the orbital period to 72 years. However, McAlister et al. (1993) could not resolve this pair and concluded that the original detection had been spurious.

In Table 1, we summarize the various determinations of the yellow magnitude of V2368 Oph published by several authors. It seems to indicate that no secular variations in its brightness have been recorded, since the scatter of values of a few hundredths of a magnitude is quite normal for yellow magnitudes recorded in different photometric systems.

**Table 1.** Published yellow magnitudes of V2368 Oph.

| Mag. | Source | Photometric system |
|---|---|---|
| $6\overset{\rm m}{.}17$ | Eggen (1955) | $(P, V)_E$ system |
| $6\overset{\rm m}{.}19$ | Stokes (1972) | $uvby$ and H$\beta$ |
| $6\overset{\rm m}{.}16$ | Becker et al. (1975) | Cousins' values |
| $6\overset{\rm m}{.}178$ | Grønbech & Olsen (1976) | $uvby$; 1965–1970 |
| $6\overset{\rm m}{.}177$ | Sowell & Wilson (1993) | $uvby$; Nov. 1988 & Apr. 1991 |
| $6\overset{\rm m}{.}18$ | van Gent (1982) | $BVR$; 1970 |

During our 2001 observations of U Oph at San Pedro Mártir Observatory (SPM hereafter), HR 6412 was also used as the comparison star. We noticed large changes in this comparison on JD 2 452 071.71–1.85. Upon a literature search, we found that the variability of HR 6412 has been discovered by Perryman & ESA (1997), who classified it as an eclipsing binary with a period of $7\overset{\rm d}{.}70$. Kazarovets et al. (1999) then assigned it the variable-star name V2368 Oph. The variability has also been confirmed by Vaz et al. (2007), who mention that the period found by Perryman & ESA (1997) was incorrect but give no other details.

⋆ Based on new spectral and photometric observations from the following observatories: Dominion Astrophysical Observatory, Hvar, Ondřejov, San Pedro Mártir, Tubitak National Observatory, and ASAS service.
⋆⋆ Appendices are available in electronic form at http://www.aanda.org
⋆⋆⋆ Tables 2–4 are only available at the CDS via anonymous ftp to cdsarc.u-strasbg.fr (130.79.128.5) or via http://cdsarc.u-strasbg.fr/viz-bin/qcat?J/A+A/531/A49

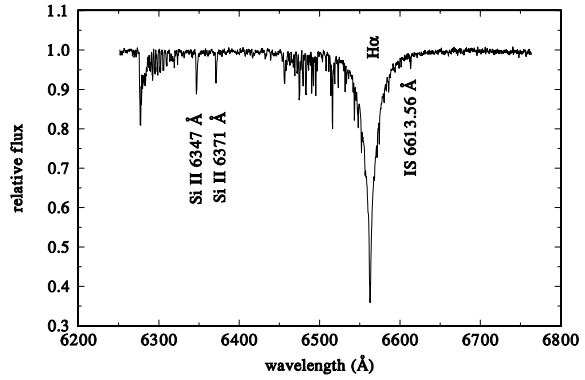


**Fig. 1.** One complete Ondřejov red spectrum of V2368 Oph, taken on HJD 2454357.2917, which shows that the only stronger lines, suitable for the RV measurements, are H$\alpha$ and the SiII 6347 and 6371 Å. The spectrum contains many water vapour and oxygen telluric lines and the interstellar line at 6613.56 Å.

The main goal of this study is to publish the first correct and accurate linear ephemeris of V2368 Oph, which can be used to correct earlier photometric observations of U Oph. We also derive preliminary orbital and light-curve solutions and show that they can lead to self-consistent basic physical properties of the binary. However, considering the limited amount and heterogeneity of our observational material, we do not aim to determine the final, accurate physical elements of the system.

## 2. Observational material used

### 2.1. Photometry

After realising that V2368 Oph is a variable star, we started systematic *UBV* observations of it at Hvar and SPM observatories. A limited set of *UBV* observations was also obtained by HA at the Turkish National Observatory. Besides, we compiled the Hipparcos $H_p$ observations and *V* photometry from the ASAS project (Pojmanski 2002). Details on data sets and their reduction are in Appendix A, and all individual *UBV* and *V* observations with their HJDs are provided in Table 2 (available at the CDS).

### 2.2. Spectroscopy

Simultaneously with photometric observations, we also begun to collect electronic spectra in Ondřejov, San Pedro Mártir, and Dominion Astrophysical Observatory (OND, SPM, and DAO hereafter). A detailed discussion of all spectra, their reduction, and a journal of observations can be found in Appendix B.

Here, we only want to add a few comments relevant to further analyses. The only spectral region that is available in the spectra from all three observatories is the red region containing only three strong enough spectral lines suitable for the RV measurements: the Balmer H$\alpha$ line and the doublet of SiII 6347 and 6371 Å lines (see Figs. 1 and 2). The SPM spectra also cover the region of MgII 4481 Å line, in which both components are clearly seen, so this line was also found suitable for the RV measurements. The RV measurements were carried out in three different ways. (1) We used the program SPEFO (Horn et al. 1996; Škoda 1996), which permits the RV measurements via sliding

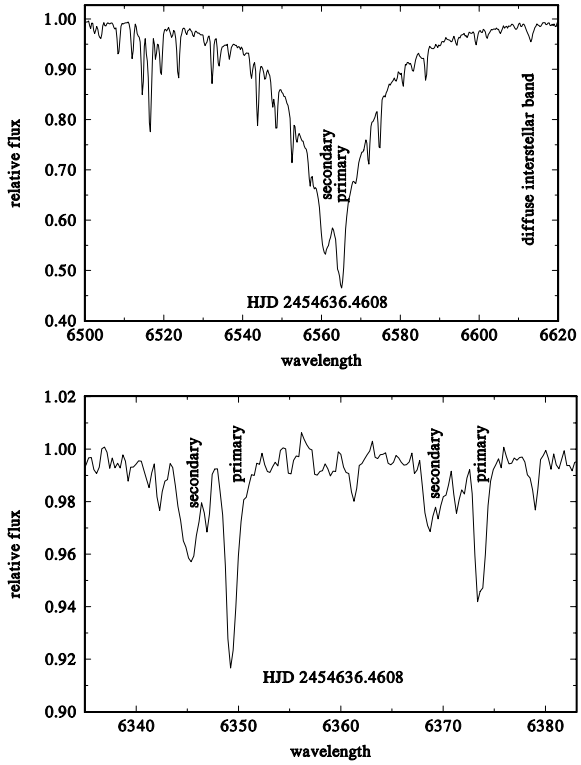


**Fig. 2.** The H$\alpha$ and SiII 6347 and 6371 Å line profiles from the Ondřejov spectrum taken near one periastron passage on HJD 2 454 636.4608. One can clearly see the lines of both binary components, separated by more than 200 km s$^{-1}$ in their radial velocity.

direct and flipped line profiles on the computer screen until a perfect match is obtained. (2) We fitted the observed line profiles by two Gaussians shifted in their positions in such a way as to obtain the best match of the observed, often blended line profiles of the primary and secondary. (3) We verified our RV values by an automated fitting of a combination of two synthetic spectra – selected from the Ondřejov library of synthetic spectra, prepared and freely distributed by Dr. J. Kubát – to each of the observed spectra using a simplex algorithm. The $\chi^2$ (defined in Brož et al. 2010) was calculated for the *entire* red spectrum in the wavelength range 6256 to 6768 Å, which includes all the individual lines analysed previously.

The second method is preferred as it returns the most likely velocity amplitudes. The results of the third method are statistically compatible. The first method (SPEFO RV measurements) usually underestimates the true semi-amplitudes of the orbital motion, because of the line blending, especially for the steep wings of H$\alpha$. We, therefore, used the SPEFO H$\alpha$ RVs only for the initial search of the orbital period, to combine them with older published RVs, measured in a standard way from the photographic spectra.

For all red spectra, we followed the procedure outlined in Horn et al. (1996) and measured RVs of a selection of unblended *telluric* lines in SPEFO. We then used the difference between the calculated heliocentric RV correction and the true mean RV of telluric lines to correct the zero point of the RV scale individually for each spectrogram. Regrettably, these corrections were

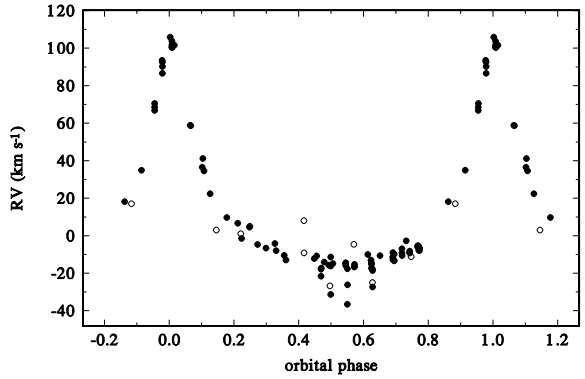


**Fig. 3.** The radial-velocity curve of the primary component of V2368 Oph based on H$\alpha$ RVs measured in SPEFO for our OND, DAO, and SPM spectra (filled circles) and published RVs (open circles) for the period of $38\overset{d}{.}3307$ from the FOTEL orbital solution with phase zero at periastron passage. See the text for details.

less reliable for the majority of the red SPM spectra, which only contain very weak telluric lines owing to the high altitude of that observatory. No such corrections were possible for the blue SPM spectra in the absence of telluric lines, of course.

Individual H$\alpha$, SiII, and MgII RVs, measured in a standard way in SPEFO and via Gaussian fits to line profiles with their HJDs of mid-exposures are in Table 3 (available at the CDS). The rectified and wavelength-calibrated spectra are in Table 4 (available at the CDS).

## 3. Preliminary analysis and search for a correct orbital period

As our observations progressed, it soon became obvious that the orbital period must be much longer than the $7\overset{d}{.}70$ period reported by Perryman & ESA (1997) and that the orbit had to have a high eccentricity, since we were observing a constant brightness and only small RV changes. When we finally succeeded in observing a decline into the minimum on the night JD 2 454 294.35-4.54, we were able to combine it with earlier minima recorded by Hipparcos, ASAS, and our discovery observation at SPM and to obtain the first guess that the period should be close to 38 days. Continuing spectroscopic observations then allowed us to cover parts of two periastron passages on JD 2 454 366-67, and JD 2 454 636 and an iterative analyses of the RV and light curves allowed us to estimate the value of the orbital period to $38\overset{d}{.}33$.

There are two limited sets of earlier RV measurements. Christie (1925) published five RVs covering the interval JD 2 423 233.8–995.8, and Palmer et al. (1968) published another five RVs from low-dispersion spectra covering JD 2 437 441.6-740.7. We combined these RVs with our own RV measurements in the program SPEFO (Horn et al. 1996; Škoda 1996) for the H$\alpha$ line and used the FOTEL program (Hadrava 1990, 2004a) to derive preliminary orbital elements and a more accurate value of the period. We obtained $P = 38\overset{d}{.}3302 \pm 0\overset{d}{.}0015$, $T_{\rm periast.}$ = HJD 54 290.894 ± 0.096, $T_{\rm min\,I}$ = HJD 54 294.417, $e = 0.551 \pm 0.010$, $\omega = 355.2 \pm 1.6$, $K_1 = 59.71 \pm 4.1$ km s$^{-1}$, $\gamma_{\rm old} = 17.0 \pm 3.4$, and $\gamma_{\rm new} = 10.07 \pm 0.50$, the rms errors of the model fit to the data per 1 observation being 10.3, and 4.1 km s$^{-1}$ for the old and new RVs.

Since the narrow and steep photometric eclipses are very sensitive to the phase shifts, we used an interactive computer program (written by HB), which allows the user to display the phase diagrams based on the observed data in the neighbourhood of the eclipses for various smoothly varied values of the orbital period. This way we found that the true orbital period must be very close to the value of $38\overset{d}{.}3272$.

## 4. Towards basic physical properties of the binary

To obtain self-consistent physical properties of the components and the binary system, we had to proceed in an iterative way. We selected several stronger lines seen in both binary components and derived their RVs via Gaussian fits to line profiles. In particular, we used the SiII 6347&6371 Å and H$\alpha$ lines, available in all spectra, and MgII 4481 Å, measurable in the SPM spectra. For H$\alpha$, the Gaussian profiles were not optimal so we tentatively disentangled the H$\alpha$ profiles, using the KOREL program (Hadrava 1995, 1997, 2004b, 2005) and used the disentangled profiles instead of Gaussians[1].

We alternatively used the programs PHOEBE (Prša & Zwitter 2005, 2006) based on the Wilson & Devinney (1971) program, and FOTEL, already used in the first step, to derive preliminary values of some critical parameters. To obtain the best possible estimate of the RV semi-amplitudes, we allowed for individual systemic velocities for each of the ions used. In particular, we found the systemic velocities of 2.97 ± 0.55, 0.14 ± 0.54, and 9.9 ± 6.0 for SiII, MgII, and H$\alpha$, respectively. The differences between these values are probably insignificant considering their errors and the inability to check the zero point of the RV scale for the blue spectra via measurements of the telluric lines. Since PHOEBE can treat only one joint systemic velocity, we subtracted the values of respective systemic velocities from the observed RVs and used these shifted RVs from all three ions as one dataset for the primary and another one for the secondary in PHOEBE. We then naturally kept the systemic velocity fixed at zero in PHOEBE solutions.

In the latest (development) version of PHOEBE that we are using, the convergence is governed by minimization of a cost function $\chi^2$ defined in the case of our datasets as

$$\chi^2 = \sum_p \frac{1}{\sigma_p^2} \sum_{i=1}^{N_p} w_i (f_i - s_i)^2, \qquad (1)$$

where index $p$ denotes the individual photometric passbands, $\sigma_p$ their standard deviations per 1 observation, $N_p$ is the number of individual observations for $p$th passband, $w_i$ are standard weights of individual observations, and $f_i$ and $s_i$ the observed and calculated fluxes, respectively. The value of the $\chi^2$ function is tabulated along with the solutions.

Although it should be possible to derive the effective temperatures of both binary components from calibrated *UBV* photometry (Prša & Zwitter 2006; Wilson 2008), the propagation of errors often leads to unreliable results. For that reason we restricted ourselves to the standard approach of estimating the effective temperature of the primary from the dereddened colours and observed spectra, then keeping its value fixed in the solutions.

[1] It would seem logical to derive the orbital solution directly with KOREL. However, due to heterogeneity of the available spectra, their different spectral resolutions and relatively limited number, this procedure was not satisfactory in the given case.

**Table 5.** Published *uvby* and H$\beta$ observations of V2368 Oph.

| $V$ | $b-y$ | $m_1$ | $c_1$ | $N_{uvby}$ | H$\beta$ | $N_{H\beta}$ | Source |
|---|---|---|---|---|---|---|---|
| – | $0^m.167$ | $0^m.090$ | $1^m.195$ | 5 | 2.850 | 4 | Crawford et al. (1972) |
| $6^m.19$ | $0^m.177$ | $0^m.095$ | $1^m.216$ | 3 | 2.860 | 3 | Stokes (1972) |
| $6^m.178(1)$ | $0^m.161(2)$ | $0^m.095(2)$ | $1^m.204(2)$ | 2 | – | | Grønbech & Olsen (1976) |
| – | – | – | – | | 2.870(2) | 3 | Gronbech et al. (1977) |
| $6^m.177(5)$ | $0^m.189(2)$ | $0^m.072(5)$ | $1^m.203(5)$ | 3 | – | | Sowell & Wilson (1993) |

**Table 6.** The final combined light-curve and RV-curve solutions obtained with PHOEBE.

| Element | | Primary | Binary | Secondary | Primary | Binary | Secondary |
|---|---|---|---|---|---|---|---|
| $P$ | (d) | | 38.327115(43) | | | 38.327118(43) | |
| $T_{\rm periastr.}$ | (RJD) | | 54291.039(11) | | | 54291.042(11) | |
| $T_{\rm min.I}$ | (RJD) | | 54294.670(17) | | | 54294.668(17) | |
| $T_{\rm min.II}$ | (RJD) | | 54287.498(17) | | | 54287.495(17) | |
| $e$ | | | 0.51527(14) | | | 0.51524(14) | |
| $\omega$ | (°) | | 359.33(20) | | | 359.41(20) | |
| $i$ | (°) | | 86.165(22) | | | 86.139(22) | |
| $r$ | | 0.0473 | | 0.0460 | 0.0477 | | 0.0464 |
| $\Omega$ | | 23.29(11) | | 24.75(12) | 23.05(11) | | 23.71(11) |
| $a$ | ($R_\odot$) | | 83.67(67) | | | 83.70(68) | |
| $K_{\rm j}$ | (km s$^{-1}$) | 65.7(8) | | 62.9(9) | 64.3(6) | | 64.3(6) |
| $K_2/K_1$ | | | 1.044(15) | | | 1.0 fixed | |
| $T_{\rm eff}$ | (K) | 9300 fixed | | 9500(200) | 9300 fixed | | 9500(200) |
| $M$ | ($M_\odot$) | 2.62(2) | | 2.74(7) | 2.68(8) | | 2.68(8) |
| $R$ | ($R_\odot$) | 3.96(2) | | 3.84(2) | 3.99(3) | | 3.87(2) |
| $M_{\rm bol}$ | (mag) | −0.31(9) | | −0.34(9) | −0.33(9) | | −0.36(9) |
| log g | [cgs] | 3.66(1) | | 3.71(1) | 3.66(3) | | 3.69(3) |
| $L_{\rm j}$ | $V$ band | 0.5029(30) | | 0.4971 | 0.5024(30) | | 0.4976 |
| $L_{\rm j}$ | $B$ band | 0.5004(32) | | 0.4996 | 0.4995(32) | | 0.5005 |
| $L_{\rm j}$ | $U$ band | 0.4942(37) | | 0.5058 | 0.4927(38) | | 0.5073 |
| $V$ | (mag) | 6.913(16) | 6.167(11) | 6.926(16) | 6.913(16) | 6.166(11) | 6.924(16) |
| $B$ | (mag) | 7.137(17) | 6.386(11) | 7.139(17) | 7.139(17) | 6.385(11) | 7.137(17) |
| $U$ | (mag) | 7.363(20) | 6.598(13) | 7.338(20) | 7.367(20) | 6.599(13) | 7.335(20) |
| $V_0$ | (mag) | 6.26(8) | | 6.29(8) | 6.26(8) | | 6.29(8) |
| $(B-V)_0$ | (mag) | 0.021(11) | | 0.014(11) | 0.021(11) | | 0.014(11) |
| $(U-B)_0$ | (mag) | 0.077(15) | | 0.054(15) | 0.078(15) | | 0.053(15) |
| No. of obs. | *UBV*/RV | | 1913 / 268 | | | 1913 /268 | |
| $\chi^2$ | | | 1726 | | | 1730 | |

**Notes.** Columns 2–4 contain a solution based on the free convergence; Cols 5–7 contain the solution for the fixed mass ratio of 1. All epochs are in RJD = HJD − 2 400 000. Probable elements and their formal error estimates are provided, where $\Omega$ is the value of the Roche-model potential used in the WD program, and $L_j$ ($j = 1, 2$) are the relative luminosities of the components in individual photometric passbands. They are normalized so that $L_1 + L_2 = 1$. The number of observations represents the sum of RVs of the primary and secondary and a sum of individual observations in all passbands.

There are four sets of *uvby* observations and three sets of H$\beta$ photometry of V2368 Oph – see Table 5. Using the program UVBYBETA written by T. T. Moon and modified by R. Napiwotzki, which is based on a calibration devised by Moon & Dworetsky (1985), we found that those sets of Strömgren photometry imply a mean effective temperature of the binary between 8900 K, and 9400 K and a mean log $g$ between 3.50 and 3.61.

Since both stars are detached well even near periastron, the light-curve solution basically does not depend on the exact value of the mass ratio. Considering this, a preliminary PHOEBE solution was used to derive relative luminosities of both components, *UBV* magnitudes of the binary at maximum light from the *UBV* observations transformed to the standard system and from them the *UBV* magnitudes of the primary and secondary in each passband. These were then dereddened in a standard way, assuming $A_V = 3.2\,E(B-V)$. The dereddened magnitudes and indices confirmed the spectral type of A2 for the primary. Using Flower (1996) calibration of $(B-V)_0$ indices vs. bolometric corrections and $T_{\rm eff}$, we estimated the effective temperature of the primary to (9300 ± 200) K. Keeping the value of 9300 K fixed, we derived a freely converged PHOEBE solution, which is presented in detail in Table 6. The rms errors of all converged parameters in PHOEBE are derived from a covariance matrix. For other, deduced parameters, we propagated the errors to obtain the estimates given in the Table. Since a realistic error of the effective temperature of the primary is about ±200 K, this must imply that the formal error of the effective temperature of the secondary, estimated from a covariance matrix in PHOEBE, is too low and must also be about ±200 K.

It is clear at first sight that this solution is not satisfactory since it leads to a model in which the more massive component is the less evolved of the two. We believe that the problem lies in the limited quality of our radial velocities. As a matter of fact, the solutions for RVs of individual ions oscillated between 0.95 and 1.05 in the resulting mass ratio. At the same time, since both binary components are well detached, the light curve solution is stable and basically does not depend on the mass ratio.

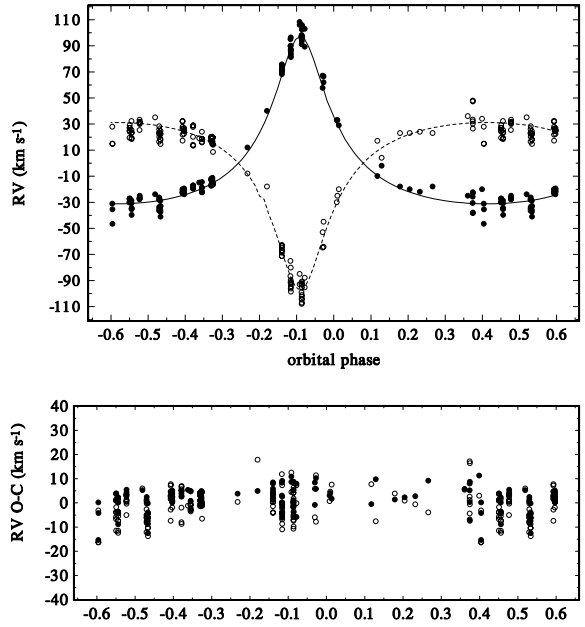


**Fig. 4.** The final radial-velocity curves of both binary components of V2368 Oph based on Gaussian fits (circles) and the theoretical RV curves based on our PHOEBE solution (lines). The lower panel shows the O−C residua from the solution. Typical observational uncertainties are 10 km s$^{-1}$. Orbital phases from ephemeris (2) are used.

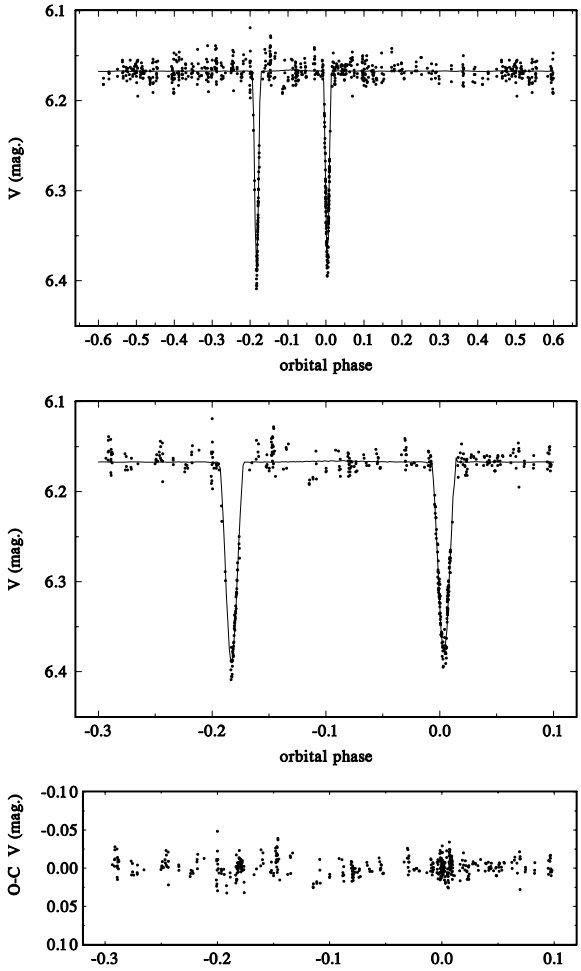


**Fig. 5.** The observed $V$-band light curve compared to the theoretical one, based on our PHOEBE solution. The lower panels show a zoom of the curves in the neighbourhood of both binary eclipses and the O−C residua from the model fit. Typical 1-$\sigma$ observational uncertainties are $^{\rm m}.01$. Orbital phases from ephemeris (2) are used.

Therefore, we derived another PHOEBE solution, this time with the mass ratio fixed to 1.0. This solution is also provided in the last three columns of Table 6 and we take it as the reference solution for the following discussion. The corresponding RV curves and the light curve in the $V$ band are shown in Figs. 4, and 5, respectively. It is seen that there is little difference in all parameters, which do not depend on the mass ratio between the two solutions. For completeness, we also derived another solution for the mass ratio of 0.95. This led to a slightly worse $\chi^2 = 1770$, but the photometric elements were again very similar to those two shown in Table 6.

The solutions led to the following linear ephemeris, which should enable correction of existing photometric observations of U Oph secured differentially relative to V2368 Oph:

$$T_{\rm min.I} = \text{HJD } 2\,454\,294.67 + 38^{\rm d}.32712 \times E. \quad (2)$$

It is encouraging to note that a separate dereddening of the *UBV* magnitudes of the primary and secondary led invariably to $E(B-V) = 0^{\rm m}.20$ and to distance moduli of 6.46(12), and 6.47(12) for the primary and secondary, respectively. The dereddened values of the secondary indicate a slightly earlier spectral type, in accordance with its higher effective temperature obtained from the PHOEBE solution. We note that $E(b-y)$ derived with the program UVBYBETA from the *uvby* values of Table 5 is $0^{\rm m}.15$, which agrees well with the $E(B-V)$ derived by us[2].

The parallax of V2368 Oph was obtained by the ESA Hipparcos mission, and its originally published value (Perryman & ESA 1997) is $0''.00554 \pm 0''.00086$, while an improved value obtained by van Leeuwen (2007a,b) reads as $0''.00455 \pm 0''.00048$. The distance modulus obtained from our photometric solution implies a parallax of $0''.00506$, in excellent agreement with the above values, deduced from the Hipparcos observations.

[2] Note that $E(b-y) = 0.74E(B-V)$.

## 5. Stellar evolution of the components

Since V2368 Oph is a detached binary with no evidence of mass transfer, one can use a one-dimensional program for stellar evolution to see whether the observed properties of the binary agree with the model prediction. To this end, we used the stellar-evolution module MESAstar by Paxton et al. (2011).

We first calculated the model evolution for the masses $M_1 = 2.62\,M_\odot$ and $M_2 = 2.74\,M_\odot$ which follow from the free PHOEBE solution with the lowest $\chi^2$ for the combined photometric and RV data (Table 6, left). We assumed the same metallicities of $Z = 0.02$ for both components, of course, the helium abundance $Y = 0.28$ and the mixing-length parameter $\alpha = 2.0$. The result is compared to the observed binary properties in the Hertzsprung–Russell diagram, and the $T_{\rm eff}$ vs. radius diagram

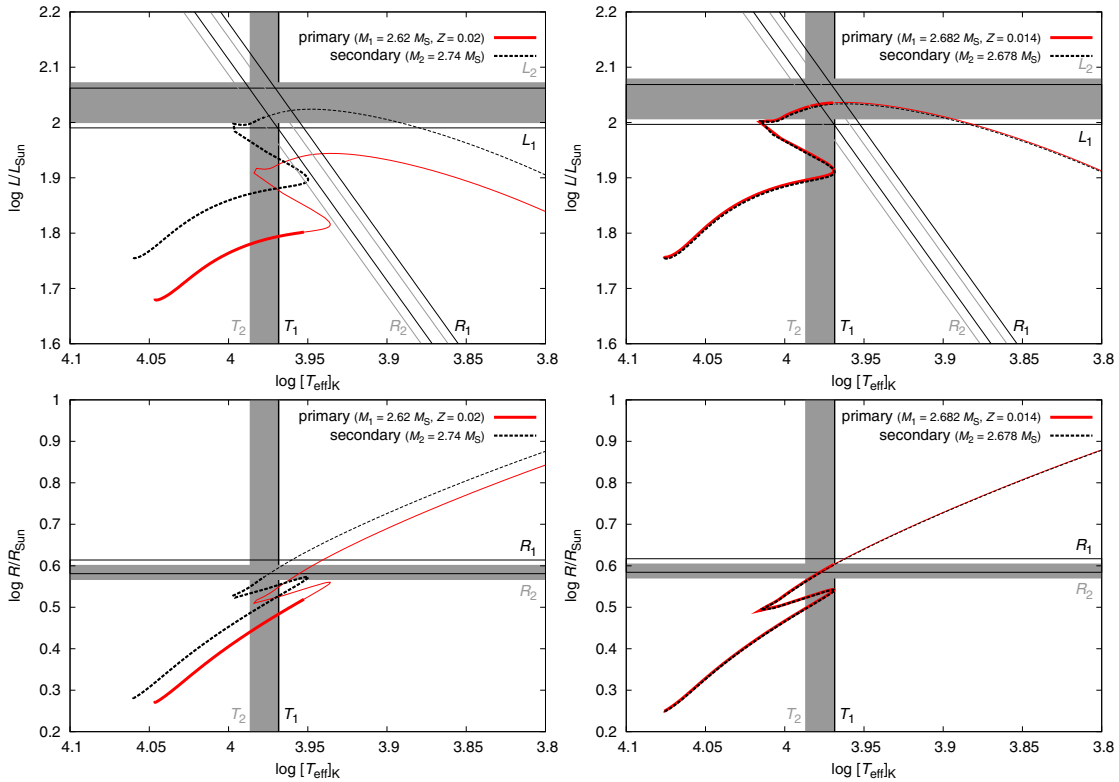


**Fig. 6.** *Left panels*: a Hertzsprung-Russel diagram (*top*), and the $T_{\rm eff}$ vs. radius diagram (*bottom*) showing the stellar evolution of the primary and secondary components of V2368 Oph. It was computed with the `MESAstar` module, for the masses $M_1 = 2.62\,M_\odot$, $M_2 = 2.74\,M_\odot$ and for the metallicity $Z = 0.02$. The evolutionary tracks are plotted by thick lines from ZAMS up to the age $3.877 \times 10^8$ y. The ranges in temperatures $T_1$, $T_2$, luminosities $L_1$, $L_2$ and radii $R_1$, $R_2$ inferred from photometry/spectroscopy are denoted by lines (refer to Table 6). There is a strong disagreement between the observations and the stellar evolution, especially for the primary. *Right panel*: same for the masses $M_1 = 2.682\,M_\odot$, $M_2 = 2.678\,M_\odot$ (i.e., the mass ratio very close to one), and a different value of the metallicity $Z = 0.014$. The thick lines are terminated at the age $3.938 \times 10^8$ y.

(Fig. 6, left panels). Even though there are uncertainties in temperatures, luminosities and masses of the individual components (refer to Table 6), their *differences* are established much more accurately; e.g., the difference in temperatures $T_2 - T_1 \simeq 200$ K is always present in `PHOEBE` solutions since this is enforced by the observed light curve and colour indices.

There is a clear disagreement between the photometric/spectroscopic observations and the predicted stellar evolution in this case. Since the mass ratio $q = M_1/M_2 \doteq 0.96$ differs significantly from 1, the calculated luminosities of the components are *always* very different owing to a strong dependence of the stellar evolution on the mass ($\log L_2/L_\odot$ reaches $\simeq$2.0 and $\log L_1/L_\odot \simeq 1.9$), while the observed luminosities are rather similar ($\log L_1/L_\odot \simeq \log L_2/L_\odot \simeq 2.03$). A change in neither metallicity nor in the mixing-length parameter could alter this result since a different value of $Z$ would shift both tracks in the same direction, and varying $\alpha$ from 1.5 to 2.5 does not alter evolutionary tracks significantly before the red giant branch is reached.

As a second test, we took the mass ratio $q$ close to 1, which is still compatible with the photometric/spectroscopic observations from a statistical point of view (Table 6, right). Because the stellar evolution is very sensitive to the stellar mass, we may actually use this approach to constrain the mass ratio of V2368 Oph. The most sensitive indicator seems to be the temperature – there is approximately a 200 K difference between $T_1$ and $T_2$, which corresponds to a 0.004 to 0.008 $M_\odot$ difference between $M_1$ and $M_2$, according to our tests. If we use $M_1 = 2.682\,M_\odot$ and $M_2 = 2.678\,M_\odot$ we also have to decrease the metallicity to $Z = 0.014$, which shifts both the evolutionary tracks towards higher $T$ and $L$, in order to match the observed state of V2368 Oph (Fig. 6, right panels). Another possibility would be to slightly increase the masses to $M_1 = 2.760\,M_\odot$ and $M_2 = 2.752\,M_\odot$ and to retain the $Z = 0.02$ value. To conclude, it is possible to find a consistent solution for the available photometry and spectroscopy and the stellar evolution, even though the parameters presented above cannot be considered as final, because the total mass of the system is not yet constrained precisely enough.

From the standpoint of stellar evolution, V2368 Oph is a very interesting evolved system with both components leaving the main sequence. It is in a rapid phase of evolution and consequently may serve as a very sensitive test case for the stellar-evolution programmes, provided new, accurate RVs and photometric observations are acquired. Considering the relatively short distance of the binary from us, its interferometry would also be of utmost importance, providing the angular separation of the components and orbital inclination, consequently a

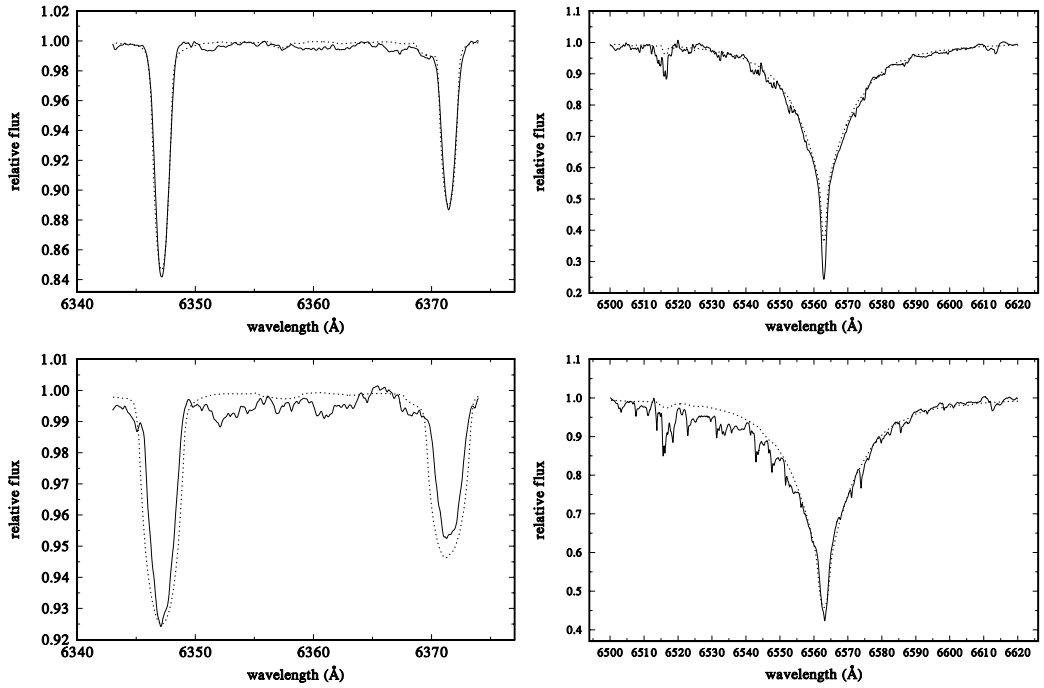


**Fig. 7.** A comparison of *disentangled* (solid lines) and synthetic (dotted lines) profiles of the SiII line (*left panels*) and H$\alpha$ line (*right*) for the primary (*top panels*) and secondary components (*bottom*). See the text for details.

much more precise parallax and the total mass of the system. Interferometry can also provide independent constraints on the component radii.

## 6. A comparison with synthetic spectra and the rotation of the binary components

As another consistency check, we disentangled the SiII and H$\alpha$ line profiles with the help of the KOREL program (Hadrava 1995, 1997, 2004b, 2005), keeping the orbital parameters from the second PHOEBE solution fixed, but using the mass ratio of 0.998 (considering the discussion above). In Fig. 7, the disentangled line profiles, normalized to their individual continua using the relative luminosities derived by PHOEBE, are compared with the synthetic line profiles from the Ondřejov library of synthetic spectra prepared and freely distributed by Dr. J. Kubát – see, e.g. Harmanec et al. (1997a) for details. We used the synthetic spectra for the parameters close to the PHOEBE results, namely $T_{\rm eff}$ = 9500 K and log $g$ = 3.5, rotationally broadened in SPEFO to 40 km s$^{-1}$ for the primary and to 90 km s$^{-1}$ for the secondary. Varying these values for more than ±5 km s$^{-1}$ would result in a significant disagreement in the depths and widths between the observed and synthetic line profiles.

The agreement between the observed and synthetic spectra is satisfactory, lending some credibility to our result. We warn, however, that the heterogeneity of our material means that there can still be rather large uncertainties in the derived masses, radii, and luminosities. Another study based on rich and homogeneous observational material is therefore desirable.

Taken at face value, the observed projected rotational velocities and the PHOEBE solution would imply the stellar rotational periods of $5\overset{\rm d}{.}0$ and $2\overset{\rm d}{.}2$ for the primary and secondary, respectively, while the spin-orbit synchronization in periastron would imply a rotational period of $10\overset{\rm d}{.}5$. It is notable that in their detailed study of another evolved A-type binary with eccentric orbit, $\theta^2$ Tau, Torres et al. (2011) also found the projected rotational velocity for the secondary roughly twice as high as for the primary.

In passing, we wish to mention that it is also possible to make a theoretical prediction of the internal structure constant based on the current evolutionary models of Claret (2004) with the standard chemical composition of $(X, Z) = (0.70, 0.02)$: $\log k_2 = -2.498$ for both binary components. Taking the values of the eccentricity and fractional radii from Table 6 into account, we can predict a very slow apsidal-motion rate of $\dot{\omega}_{\rm obs} = 0.00028$ deg/cycle, which is only 0.27 deg/century. The relativistic contribution to the apsidal motion is substantial: $\dot{\omega}_{\rm rel} = 0.00020$ deg/cycle or about 70% of the total apsidal-advance rate (Gimenez 1985). In other words, there is little chance of detecting a measurable apsidal motion for this binary in the foreseeable future.

*Acknowledgements.* We acknowledge the use of the latest version of the PHOEBE program, developed and freely distributed by Dr. A. Prša; of the latest publicly available versions of programs FOTEL and KOREL written and distributed by Dr. P. Hadrava; of the freely distributed MESAstar module for stellar evolution by Dr. B. Paxton and collaborators; and of the program UVBYBETA written by Dr. T. T. Moon and modified by Dr. R. Napiwotzki. We also profited from the use of the library of synthetic spectra prepared and provided by Dr. J. Kubát. The constructive criticism of an anonymous referee helped us improve the presentation of the results. The research of the Czech authors was supported by the grants 205/06/0304, 205/08/H005, and P209/10/0715 of the Czech Science Foundation and also from the Research Program MSM0021620860 *Physical study of objects and processes in the solar system and in astrophysics* of the Ministry of Education of the Czech Republic. We acknowledge the use of the electronic database from the CDS Strasbourg and the electronic bibliography maintained by the NASA/ADS system.

## References


Becker, G. A., Chambliss, C. R., & Kiasat, A. 1975, Inf. Bull. Var. Stars, 1067, 1
Brož, M., Mayer, P., Pribulla, T., et al. 2010, AJ, 139, 2258
Christie, W. H. 1925, Publ. Dominion Astrophys. Obs. Victoria, 3, 209
Claret, A. 2004, A&A, 424, 919
Crawford, D. L., Barnes, J. V., Gibson, J., et al. 1972, A&AS, 5, 109
Eggen, O. J. 1955, AJ, 60, 65
Flower, P. J. 1996, ApJ, 469, 355
Gimenez, A. 1985, ApJ, 297, 405
Grønbech, B., & Olsen, E. H. 1976, A&AS, 25, 213
Gronbech, B., Gyldenkerne, K., & Jorgensen, H. E. 1977, A&A, 55, 401
Hadrava, P. 1990, Contr. Astron. Obs. Skalnaté Pleso, 20, 23
Hadrava, P. 1995, A&AS, 114, 393
Hadrava, P. 1997, A&AS, 122, 581
Hadrava, P. 2004a, Publ. Astron. Inst. Acad. Sci. Czech Rep., 92, 1
Hadrava, P. 2004b, Publ. Astron. Inst. Acad. Sci. Czech Rep., 92, 15
Hadrava, P. 2005, Ap&SS, 296, 239
Harmanec, P. 1998, A&A, 334, 558
Harmanec, P., & Horn, J. 1998, J. Astron. Data, 4, 5
Harmanec, P., Horn, J., & Koubský, P. 1982, in Be Stars, ed. M. Jaschek, & H.-G. Groth, IAU Symp., 98, 269
Harmanec, P., Horn, J., & Juza, K. 1994, A&AS, 104, 121
Harmanec, P., Hadrava, P., Yang, S., et al. 1997a, A&A, 319, 867
Harmanec, P., Pavlovski, K., Božić, H., et al. 1997b, J. Astron. Data, 3, 5
Horn, J., Kubát, J., Harmanec, P., et al. 1996, A&A, 309, 521
Huffer, C. M., & Kopal, Z. 1951, ApJ, 114, 297
Kazarovets, A. V., Samus, N. N., Durlevich, O. V., et al. 1999, Inf. Bull. Var. Stars, 4659, 1
Koch, R. H., & Koegler, C. A. 1977, ApJ, 214, 423
Kuschnig, R., Paunzen, E., & Weiss, W. W. 1994, Inf. Bull. Var. Stars, 4070, 1
McAlister, H. A., Hartkopf, W. I., Hutter, D. J., Shara, M. M., & Franz, O. G. 1987, AJ, 93, 183
McAlister, H. A., Mason, B. D., Hartkopf, W. I., & Shara, M. 1993, AJ, 106, 1639
Moon, T. T., & Dworetsky, M. M. 1985, MNRAS, 217, 305
Palmer, D. R., Walker, E. N., Jones, D. H. P., & Wallis, R. E. 1968, Roy. Obs. Bull., 135, 385
Pavlovski, K., Harmanec, P., Božić, H., et al. 1997, A&AS, 125, 75
Paxton, B., Bildsten, L., Dotter, A., et al. 2011, ApJS, 192, 3
Perryman, M. A. C., & ESA 1997, The HIPPARCOS and TYCHO catalogues, Astrometric and photometric star catalogues derived from the ESA Hipparcos Space Astrometry Mission (Noordwijk, Netherlands: ESA Publications Division), ESA SP Ser., 1200
Pojmanski, G. 2002, Acta Astron., 52, 397
Prša, A., & Zwitter, T. 2005, ApJ, 628, 426
Prša, A., & Zwitter, T. 2006, Ap&SS, 304, 347
Škoda, P. 1996, in Astron. Data Anal. Soft. Syst. V, ASP Conf. Ser., 101, 187
Sowell, J. R., & Wilson, J. W. 1993, PASP, 105, 36
Stokes, N. R. 1972, MNRAS, 160, 155
Torres, K. B. V., Lampens, P., Frémat, Y., et al. 2011, A&A, 525, A50
van Gent, R. H. 1982, Inf. Bull. Var. Stars, 2140, 1
van Leeuwen, F. 2007a, in Astrophys. Space Sci. Lib. 350, ed. F. van Leeuwen, (Germany: Springer)
van Leeuwen, F. 2007b, A&A, 474, 653
Vaz, L. P. R., Andersen, J., & Claret, A. 2007, A&A, 469, 285
Wilson, R. E. 2008, ApJ, 672, 575
Wilson, R. E., & Devinney, E. J. 1971, ApJ, 166, 605
Wolf, M., Harmanec, P., Diethelm, R., Hornoch, K., & Eenens, P. 2002, A&A, 383, 533


Pages 9 to 10 are available in the electronic edition of the journal at http://www.aanda.org

## Appendix A: Photometry

Here we provide detailed comments on the photometric observations used in this study and the way we treated them.

1. Hvar observations were secured in 2007, 2008, and 2009 and reduced and transformed into the standard *UBV* system with the HEC22 release 16.1 reduction program via nonlinear transformation formulæ (Harmanec et al. 1994; Harmanec & Horn 1998). This recent version of the program allows modelling of variable extinction during the observing night, which significantly improves the accuracy of the observations. The typical rms errors of the multinight fit to all standard stars used to define the transformation formulæ in a given observating season are $0^{m}.008$ for $V$ and $B$, and $0^{m}.010$ for $U$. This is similar for observations from other observing stations reduced with the help of HEC22.
2. San Pedro Mártir observations were collected during the observational runs in 2001–2003 and 2007. Observations were reduced and transformed into the standard *UBV* system with the HEC22 release 14.1 reduction program via nonlinear transformation formulæ (Harmanec et al. 1994; Harmanec & Horn 1998). At that station V2368 Oph was used in 2001 as a recommended comparison star for the eclipsing binary U Oph and its magnitude difference relative to several comparison stars (HD 183324, HD 187458, HD 161132, HD 153808, and HD 144206) was derived. For all these stars, save HD 183324, the magnitudes and colours are well established from the calibrated Hvar all-sky photometry. HD 183324 = V1431 Aql was found to be a small-amplitude $\lambda$ Bootis variable (Kuschnig et al. 1994). It served for a long time as a comparison star for observations of V923 Aql and V1294 Aql in the Photometry of the Bright Northern Be Star Programme (Harmanec et al. 1982, 1994; Pavlovski et al. 1997; Harmanec et al. 1997b) and its variability on longer time scales is safely excluded by numerous Hvar observations. The mean all-sky *UBV* magnitudes of HD 183324 are accurately derived. It was actually used as a comparison for V2368 Oph only on the night JD 2 452 065, and we feel that its 2 mmag microvariability is not critical for the purpose of this study. For 13 observations secured on JD 2 452 071 (when we recorded the first eclipse of V2368 Oph), it was not possible to derive the differential values for it so we adopted its all-sky values instead, since enough standard stars had been observed during the night, and the nightly transformation coefficients (extinction and its variations and the zero points) could be derived. As soon as we realized that V2368 Oph is a variable, its subsequent observations in 2002 and 2003 were carried out differentially, relative to HD 154660 = HR 6361. This A9V star is a visual binary ADS 10347A with a close companion ADS 10347B at $20''.3$, which is some $3^{m}.35$ fainter than ADS 10347A. The 2007 observations were obtained with a larger diaphragm so that the light of the visual component ADS 10347B was recorded with the brighter component ADS 10347A = HD 6361. We carried out dedicated observations at Hvar to derive the total magnitude of both visual components and added this value to the magnitude differences var – comp. from this season. In all other instances, observations were carried out in such a way as to keep ADS 10347B outside the diaphragm.
3. Hipparcos all-sky $H_{\rm p}$ broad-band magnitudes secured between 1989 and 1993 (Perryman & ESA 1997) were transformed to the standard Johnson $V$ magnitude with the nonlinear transformation formula derived by Harmanec (1998). The rms error of the fit per 1 observations is $0^{m}.0067$. For the solutions, the transmission and the limb darkening coefficients for the $H_{\rm p}$ passband were considered, however. All data with error flags larger than 1 and one deviating point at HJD 2448661.4682 were omitted.
4. TNO (Tubitak National Observatory) observations were secured during two consecutive nights in 2003 and were reduced and transformed into the standard *UBV* system with the HEC22 release 14.1 reduction program via nonlinear transformation formulæ (Harmanec et al. 1994; Harmanec & Horn 1998).
5. ASAS $V$ magnitude observations were extracted from the public ASAS database (Pojmanski 2002); we used the data from the diaphragm, which gives the smallest rms errors and omitted a few clearly deviating data points.

The journal of all photometric observations is in Table A.1. Homogenized *UBV* magnitudes of all comparison and check stars used can be found in Table A.2.

## Appendix B: Spectroscopy

The journal of all spectroscopic observations can be found in Table B.1. The individual data files are identified there by letters. Below, we provide a few comments on them.

- *File A*. CCD spectra of V2368 Oph covering the wavelength region 6260–6750 Å. They were secured with a SITe-005 800 × 2000 CCD detector attached to the medium 0.7-m camera of the coudé focus of the Ondřejov 2.0 m telescope (OND). The spectra were obtained between June 2007 and June 2008 and have a linear dispersion of 17.2 Å mm$^{-1}$ (red) and a 2-pixel resolving power of about 12600 (11–12 km s$^{-1}$ per pixel). Their $S/N$ ranges from 50 (1 spectrum) to 370, and the majority have $S/N$ over 200.
- *File B*. CCD spectra covering the wavelength region 6150–6750 Å with a resolution of 6.6 km s$^{-1}$ per pixel. They were obtained at the DAO 1.22-m telescope between August 2007 and September 2009 and have a reciprocal linear dispersion of 10 Å mm$^{-1}$. The detector used was a SITe-4 4096 × 2048 CCD, and the 3-pixel resolving power was about 15 000. Their $S/N$ ranges from 100 to 370.
- *File C*. CCD echelle spectra secured with the 2.14-m reflector of the SPM observatory in April 2003. The CCD detector has 1024 × 1024 pixels, and the setting used covered the wavelength region from 4000 to 6700 Å in grating orders 33 to 60. The nominal resolution of the spectrograph is 18 000 at 5000 Å, which translates into 2-pixel resolution of about 17 km s$^{-1}$.
- *File D*. Another set of echelle CCD spectra from SPM, secured in April 2007.
- *File E*. The third set of echelle CCD spectra from SPM, secured from May 30 to June 1, 2007. The $S/N$ of the SPM spectra ranges between 120 and 500 for the red, and 85 to 230 for the blue parts of the spectra.

The initial reductions of the DAO spectra (bias subtraction, flat-fielding and conversion to 1-D images) were carried out by SY in IRAF. The initial reduction of the SPM and OND spectra was carried out by PE and by Dr. M. Šlechta, respectively, including the wavelength calibration. The remaining reductions of all spectra (including wavelength calibration for the DAO spectra, continuum rectification, and removal of cosmics and flaws) was carried out with the program `SPEFO` (Horn et al. 1996; Škoda 1996).

**Table A.1.** Journal of available photometry of V2368 Oph.

| Station | Time interval (HJD−2 400 000) | No. of obs. | Passbands | HD of comparison /check star | Source |
|---|---|---|---|---|---|
| 1 | 542 73.4–550 61.4 | 423 | *UBV* | 154660/154895 | this paper |
| 30 | 520 65.8–542 76.8 | 152 | *UBV* | *) | this paper |
| 66 | 527 65.4–527 66.6 | 10 | *UBV* | 154660/154895, 154445 | this paper |
| 61 | 479 12.6–490 61.9 | 111 | *V* | all-sky | Perryman & ESA (1997) |
| 93 | 530 55.9–532 90.5 | 47 | *V* | all-sky | Pojmanski (2002) |

**Notes.** Individual observing stations are distinguished by running numbers they have in the Prague/Zagreb photometric archives – see column *"Station":* 01 … Hvar 0.65-m, Cassegrain reflector, EMI9789QB tube; 30 … San Pedro Mártir, 0.84-m reflector, Cuenta-pulsos photometer; 61 … Hipparcos all-sky $H_p$ photometry transformed to Johnson *V*; 66 … TNO 0.40-m Cassegrain reflector, SSP5A photometer; 93 … ASAS data archive (Pojmanski 2002). *) All-sky photometry or differential photometry relative to various comparisons during the first season when V2368 Oph was used as a comparison for observations of U Oph, then relative to HD 154660 – see the text for details.

**Table A.2.** Comparisons and check stars of V2368 Oph.

| HD/BD | Other ident. | *V* | *B*−*V* | *U*−*B* |
|---|---|---|---|---|
| 154660 | HR 6361 | 6.357 | 0.211 | 0.103 |
| −01° 3292B | ADS 10347B | 9.71 | 0.66 | 0.15 |
| | ADS 10347AB | 6.308 | 0.227 | 0.094 |
| 154895 | HR 6367 | 6.058 | 0.075 | 0.028 |
| 183324 | *V*1431 Aql | 5.801 | 0.086 | 0.067 |
| 187458 | HR 7550 | 6.660 | 0.426 | −0.056 |
| 162132 | HR 6641 | 6.494 | 0.085 | 0.075 |
| 153808 | $\epsilon$ Her | 3.916 | −0.024 | −0.088 |
| 144206 | $\upsilon$ Her | 4.739 | −0.096 | −0.326 |

**Notes.** Magnitude and colours of ADS 10347AB are values resulting from co-added flux of HR 6361 and BD −01° 3292B measured simultaneously though a larger diaphragm in the photometer.

**Table B.1.** Journal of spectroscopic data of V2368 Oph.

| Spg. no. | Time interval (HJD−2 400 000) | No. of spectra | Station, telescope and instrument |
|---|---|---|---|
| A | 542 66.4–546 38.4 | 11 | OND 2.0-m, grating spg. |
| B | 543 39.7–551 02.6 | 19 | DAO 1.22-m, grating spg. |
| C | 527 45.8–527 49.0 | 21 | SPM 2.1-m, echelle spg. |
| D | 541 93.9–542 00.0 | 21 | SPM 2.1-m, echelle spg. |
| E | 542 50.8–542 53.0 | 12 | SPM 2.1-m, echelle spg. |

A&A 546, A123 (2012)
DOI: 10.1051/0004-6361/201118567


Astronomy & Astrophysics

# Large distance of $\varepsilon$ Aurigae inferred from interstellar absorption and reddening⋆,⋆⋆

E. F. Guinan[1], P. Mayer[2], P. Harmanec[2], H. Božić[3], M. Brož[2], J. Nemravová[2], S. Engle[1], M. Šlechta[4], P. Zasche[2], M. Wolf[2], D. Korčáková[2], and C. Johnston[1]

[1] Dept. of Astronomy & Astrophysics, Villanova University, 800 E. Lancester Ave., Villanova, PA 19085, USA
e-mail: Edward.Guinan@villanova.edu
[2] Astronomical Institute of the Charles University, Faculty of Mathematics and Physics, V Holešovičkách 2, 18000 Praha 8, Czech Republic
[3] Hvar Observatory, Faculty of Geodesy, University of Zagreb, 10000 Zagreb, Croatia
[4] Astronomical Institute, Academy of Sciences of the Czech Republic, 25165 Ondřejov, Czech Republic

Received 2 December 2011 / Accepted 16 July 2012

**ABSTRACT**

The long-period ($P$ = 27.1 years) peculiar eclipsing binary $\varepsilon$ Aur, which has recently completed its two year-long primary eclipse, has perplexed astronomers for over a century. The eclipse arises from the transit of a huge, cool and opaque, disk across the face of the F0 Iab star. One of the principal problems with understanding this binary is that the very small parallax of $p = (1.53 \pm 1.29)$ mas, implying a distance range of $d \sim (0.4–4.0)$ kpc, returned by a revised reduction of the H satellite observations, is so uncertain that it precludes a trustworthy estimate of the luminosities and masses of the binary components. A reliable distance determination would help solve the nature of this binary and distinguish between competing models.

A new approach is discussed here: we estimate the distance to $\varepsilon$ Aur from the calibration of reddening and interstellar-medium gas absorption in the direction of the system. The distance to $\varepsilon$ Aur is estimated from its measured $E(B-V)$ and the strength of the diffuse interstellar band 6613.56 Å. Spectroscopy and $UBV$ photometry of several B- and A-type stars (<1° of $\varepsilon$ Aur) were carried out. The distances of the reference stars were estimated from either measured or spectroscopic parallaxes. The range in distances of the reference stars is from 0.2 to 3.0 kpc. We find reasonably tight relations among $E(B-V)$, EW, and $I_c$ (6613 Å feature) with distance. From these calibrations, a distance of $d = (1.5 \pm 0.5)$ kpc is indicated for $\varepsilon$ Aur. If $\varepsilon$ Aur is indeed at (or near) this distance, its inferred absolute visual magnitude of $M_V \simeq (-9.1 \pm 1.1)$ mag for the F-supergiant indicates that it is a very young, luminous and massive star. Noteworthy, the high luminosity inferred here is well above the maximum value of $M_V \simeq -6\overset{m}{.}2$ expected for (less-massive) post asymptotic giant branch supergiant stars. Thus, based on the circumstantial evidence, the higher-mass model appears to best explain the properties of this mysterious binary system.

As a by-product of this study, our spectroscopy led to the finding that two of the stars used in the distance calibrations, HD 31617 and HD 31894, are newly discovered spectroscopic binaries, and HD 32328 is a new radial-velocity variable.

**Key words.** binaries: eclipsing – stars: AGB and post-AGB – stars: distances – stars: massive – stars: individual: eps Aurigae

## 1. Introduction

$\varepsilon$ Aur (7 Aur, HR 1605, HD 31964) is a bright ($V \simeq 3\overset{m}{.}0$) single-line eclipsing binary with so far the longest known orbital period of 27.1 years ($9890\overset{d}{.}3$) (Ludendorff 1903; Stefanik et al. 2010; Chadima et al. 2010). The duration of the eclipse is almost 2 years and its last eclipse terminated by the end of August 2011. For the first time, interferometric observations carried out during the recent eclipse (see Kloppenborg et al. 2010) "imaged" the dark, flattened disk component transiting the F-supergiant star.

Two principal models of the system have been considered, often referred to as the high- and low-mass models (Guinan & DeWarf 2002, and references therein). Although they differ quite substantially from each other, the distances that follow from the rather uncertain H parallax quoted in Table 1 do not allow to distinguish between the models from mainly luminosity considerations. In Table 1 we also summarize several other attempts to derive the parallax of $\varepsilon$ Aur. The true nature of this unusual eclipsing binary remains a puzzle in spite of many attempts to explain its properties. As noted previously, one of the principal problems is that the very small parallax returned by the H satellite is so uncertain that it precludes a trustworthy estimate of the luminosities and thus masses of the binary components. A reliable distance determination would help solve the nature of this binary and distinguish between the competing models that explain this extraordinary binary system.

According to the high-mass model, first considered by Kuiper et al. (1937) and later developed by Carroll et al. (1991), the F-supergiant component is a normal high mass/high luminosity Pop. I supergiant and its mysterious cool disk (+ star) companion is either a very young, high mass object that has accreted gas from the F-supergiant or a pre-Main Sequence star with circumstellar material.

In the low mass model, first suggested by Eggleton & Pringle (1985) and by Lambert & Sawyer (1986) and recently advocated by Hoard et al. (2010), the F-supergiant is a post-asymptotic giant branch (AGB) star, of low to moderate mass (initial mass

⋆ Based on new spectral and photometric observations from the Hvar, Ondřejov and Tautenburg Observatories, the Four College Automatic Photoelectric Telescope and from the ESA H satellite.
⋆⋆ Appendices are available in electronic form at http://www.aanda.org

**Table 1.** Various determinations of the parallax of $\varepsilon$ Aur.

| Source | $p$ (mas) | Notes |
|---|---|---|
| Adams & Joy (1917) | 11–22 | 1 |
| Adams & Joy (1917) | 60 | 2 |
| Strand (1959) | $6 \pm 4$ | 3 |
| Strand (1959) | 1 | 4 |
| van de Kamp & Lippincott (1968) | $4 \pm 2$ | 5 |
| van de Kamp (1978) | $1.72 \pm 0.08$ | 4 |
| Heintz & Cantor (1994) | $3 \pm 2$ | 6 |
| Heintz & Cantor (1994) | $1.65 \pm 0.15$ | 4 |
| Perryman & ESA (1997) | $1.60 \pm 1.16$ | 7 |
| van Leeuwen (2007a,b) | $1.53 \pm 1.29$ | 8 |

**Notes.** Trigonometric parallaxes are quoted unless specified otherwise. 1... spectroscopic parallax; 2... by Jewdokimow at Yerkes; 3... 59 nights, Yerkes 1926–58; 4... comparing the semi-major axis from the astrometric and spectroscopic solutions; 5... 174 obs. at Sproul in 1938–56; 6... an extended series of the Sproul 363 night means over 44 years; 7... original H parallax; 8... revised reduction of H parallaxes.

**Table 2.** Equatorial coordinates and spectral types of $\varepsilon$ Aur and the calibration stars in its neighbourhood.

| Star | $\alpha$ (J2000.0) | $\delta$ (J2000.0) | Sp. type | Note |
|---|---|---|---|---|
| $\varepsilon$ Aur | $5^h01^m58\overset{s}{.}13245$ | $43°49'23\overset{''}{.}9059$ | F0Ia | |
| HD 31617 | $4^h59^m21\overset{s}{.}24899$ | $43°19'24\overset{''}{.}1690$ | B2IV | 1 |
| HD 31894 | $5^h01^m34\overset{s}{.}29127$ | $43°26'08\overset{''}{.}6252$ | B2IV-V | 2 |
| HD 32328 | $5^h04^m32\overset{s}{.}73112$ | $43°43'39\overset{''}{.}5641$ | B8V | 1 |
| HD 277197 | $5^h01^m11\overset{s}{.}5460$ | $43°34'41\overset{''}{.}915$ | B3V | 3 |
| BD+43°1168 | $5^h02^m12\overset{s}{.}374$ | $43°51'42\overset{''}{.}35$ | B9Iab | |

**Notes.** 1... newly discovered SB1; 2... newly discovered SB2; 3... the spectral class estimated by us.

$\approx$1–7 $M_\odot$; final (current) mass <1.0 $M_\odot$). In this model, the large, cool disk binary component resulted from the recent capture of gas from a prior large mass-loss/transfer phase from the F-supergiant.

## 2. A methodology of the distance calibration

We initially selected three stars close in the sky to $\varepsilon$ Aur, HD 31617, HD 31894, and HD 277197, because they all have similarly small space motions and reddening values as $\varepsilon$ Aur itself. We thought that these stars, together with $\varepsilon$ Aur, could be the brighter members of a young stellar association. Even though this could be the case, the errors in their proper motions and spectroscopic distance estimates preclude drawing definite connection. But if this were the case, this would imply a distance to $\varepsilon$ Aur of about 1.1 kpc (see Table 10).

We decided to try an alternative approach to the problem. On the premise that the interstellar medium in the direction of $\varepsilon$ Aur has similar properties as in the surrounding directions (within a few degrees around $\varepsilon$ Aur) as projected onto the sky, we selected several stars closer than 1° to $\varepsilon$ Aur in the sky (and accessible to the telescopes available to us) and obtained their spectra and *UBV* photometry. The list of these stars is in Table 2.

Infrared data from DIRBE/COBE (Schlegel et al. 1998) confirm that our assumption is valid – the calibration stars are located at positions, where the dust thermal emission (summed along the line of sight) is indeed comparable (see Fig. 1).

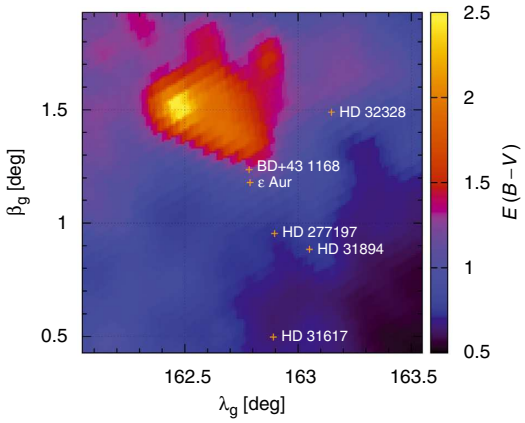


**Fig. 1.** Reddening $E(B-V)$ computed from IR emission for *extragalactic* sources as a function of galactic coordinates. The data were taken from Schlegel et al. (1998). Our calibration stars and $\varepsilon$ Aur are denoted by crosses. The values of $E(B-V)$ range from 0.65 to 1.22 for the positions of the calibration stars (note that these are *not* $E(B-V)$ for the stars themselves). The cloud visible in the north-east direction is the nebular region TGU H1105 (Dobashi et al. 2005).

**Table 3.** Comparison of the $E(B-V)$ and $E(V-K)$ reddening for our calibration stars in the neighbourhood of $\varepsilon$ Aur.

| Star | $E(B-V)$ | $E(V-K)$ | $E(V-K)/E(B-V)$ |
|---|---|---|---|
| HD 31617 | 0.25 | 0.63 | 2.52 |
| HD 31894 | 0.27 | 0.74 | 2.74 |
| HD 32328 | 0.06 | 0.19 | 3.17 |
| HD 277197 | 0.26 | 0.73 | 2.82 |
| BD+43°1168 | 0.90 | 2.46 | 2.74 |

**Notes.** See the text for details.

Using the data from the 2MASS catalogue, it is possible to calculate the ratio $E(V-K)/E(B-V)$ for all calibration stars (see Table 3). Comparison of these data with the values derived by Koornneef (1983) also clearly shows that the extinction of these stars is normal (cf. Table 4 of Johnson 1965).

Using the measured parallaxes or spectroscopically estimated distances to these stars, we attempted to derive two independent *calibration relations*: (1) the distance $d$ as a function of the strength of the diffuse interstellar band (DIB) at 6613.56 Å, and (2) the distance $d$ as a function of the $E(B-V)$ reddening. The idea is to use these calibrations for a new estimate of the distance to $\varepsilon$ Aur. It is worth noting that a smooth dependence of the reddening on the distance in the region near $\varepsilon$ Aur has already been found by McCuskey (1949), based on photographic spectra and magnitudes. There are several studies of the strength and shape of the DIB at 6613 Å in the recent literature (cf., e.g. Jenniskens & Desert 1994; Galazutdinov et al. 2008; Hobbs et al. 2009; McCall et al. 2010) but we were unable to find any published calibration of this feature vs. distance. Munari et al. (2008) found a tight relation between the EW of another DIB at 8620.4 Å and $E(B-V)$ and another, though a less perfect such relation was also published for the DIB at 5780.5 Å by McCall et al. (2010). The latter authors also found a very good correlation between the EWs of 6613.6 and 6196.0 DIBs. Unfortunately, none of these additional DIBs are covered by our spectra. The limited spectral resolution of our spectra may imply that our EWs only represent a lower limit to the true EW

of the 6613 DIB but in the light of the above-mentioned studies we do believe that with a homogeneous series of the spectra taken with the same instrument a calibration of the 6613 DIB vs. distance within a limited area in the sky should be feasible.

Details of all spectral observations, their reduction and radial-velocity (RV hereafter) measurements can be found in Appendix A, while the photoelectric *UBV* observations and their reductions are described in Appendix B.

For each of the calibration stars we proceed as follows: (i) using the observed spectra, we derive $T_{\rm eff}$, $\log g$ by matching the synthetic spectra; (ii) using a modern stellar-evolution code, we determine the corresponding mass $m_\star$ and luminosity $L$ which enables us to compute the distance. We now describe the procedure in more details.

One of us, JN, has developed a program, which derives the optimal values of the effective temperature $T_{\rm eff}$, logarithm of the gravitational acceleration $\log g$, projected rotational velocity $v \sin i$ and RV via interpolation in a grid of synthetic spectra and minimalization of the sum of squares of O−C between the observed and interpolated synthetic spectrum. For multiple systems of $N$ components, it also derives the relative luminosities of the components, preserving the constraint that $\sum_{j=1}^{N} L_i = 1$[1]. For practical applications, we used the grid of recent elaborated synthetic spectra published by Lanz & Hubeny (2007) (Bstar grid hereafter). We assumed a (fixed) value of metallicity $Z = 0.04$ corresponding to massive and consequently young stars.

Realistic uncertainties of the best-fit effective temperatures are of the order $\Delta T_{\rm eff} \simeq 1000$ K for hot stars (with $T_{\rm eff} \gtrsim 20\,000$ K) and down to 100 K for cooler stars ($T_{\rm eff} \lesssim 10\,000$ K). For $\log g$ we typically have an uncertainty of about $\Delta \log g \simeq 0.5$.

We also adopted Lanz & Hubeny (2007) bolometric corrections BC, interpolating for the optimal values of $T_{\rm eff}$ and $\log g$. Their BCs have a zero point defined by adopting the $\mathrm{BC}_\odot = -0\overset{\mathrm{m}}{.}07$. Following Torres (2010), we therefore adopted the observed Johnson $V$ magnitude of the Sun, $V_\odot = -26\overset{\mathrm{m}}{.}76 \pm 0\overset{\mathrm{m}}{.}03$ and the distance modulus $V_\odot - M_{V\odot} = -31\overset{\mathrm{m}}{.}572$. For a comparison with evolutionary models, it is therefore necessary to adopt $M_{\rm bol\odot} = M_{V\odot} + \mathrm{BC}_\odot = 4\overset{\mathrm{m}}{.}742$.

To obtain reasonable estimates of the masses and bolometric magnitudes of the calibration stars, we used the stellar-evolution module `MESAstar` by Paxton et al. (2011)[2]. We took the optimal values of $T_{\rm eff}$ and $\log g$ (with their uncertainties) from the modelling of synthetic spectra and we searched for the corresponding initial mass $m_\star$ (range of masses) of the star for which evolutionary tracks are compatible with the parameters ($\log T_{\rm eff}$, $\log g$) inferred above. We assumed initial helium abundance $Y = 0.320$, metallicity $Z = 0.040$, and the mixing-length parameter $\alpha = 2.0$.

As we shall see later, we usually obtain the values of $\log g = 4.0$ to 4.5 which correspond to stars located at the main sequence. Note that main-sequence stars are neither very sensitive to the value of $\alpha$ nor to the selected wind scheme. The major source of uncertainty in $m_\star$ is thus the uncertainty of the effective temperature $T_{\rm eff}$.

Given the values of $m_\star$ and evolutionary tracks in the HR diagram ($T_{\rm eff}$, $\log L$) for all calibration stars, we can easily take the luminosities $\log L$ or bolometric magnitudes $M_{\rm bol} = M_{\rm bol\odot} - 2.5 \log L$ and determine the (spectroscopic) distances and their uncertainties.

[1] By the relative luminosity we understand as usually the ratio $L_j / \sum_{j=1}^{N} L_j$ ($j = 1...N$) of the luminosities of individual components measured in physical units (outside the eclipses for the eclipsing systems).

[2] The latest release 3918 from April 2012.

In case the calibration star is a binary (as HD 31894) we can use the secondary as an independent check, with the mass ratio inferred from the RV curve being a strong additional constraint.

For the B9 Iab supegiant BD+43°1168, we adopted the unreddened $(B-V)_0$ index from the Johnson (1958) study. To obtain the dereddened $V_0$ magnitudes of all considered stars, we adopted the formula from Chap. 15 of Cox (2000)

$$V_0 = V - E(B-V) \cdot (3.30 + 0.28(B-V)_0 + 0.04E(B-V)) \,. \quad (1)$$

This way, our distance scale can contain a small systematic error but it should be internally consistent for all considered stars.

In the following sections, we first discuss the new observations and our detailed analyses of the individual calibration stars, then we establish the $d(EW)$, $d(I_c)$ and $d(E(B-V))$ calibrations, we derive appropriate 6613 Å line strengths and a range of $E(B-V)$ values for $\varepsilon$ Aur and finally apply them to $\varepsilon$ Aur.

## 3. The B type binary HD 31894

HD 31894 (BD+43°1164, HIP 23375) was classified B2IV-V by Walborn (1971). Danziger et al. (1967) included HD 31894 in their study of stars in the neighbourhood of the hydrogen-poor star HD 30353 in an effort to derive the distance to it. They studied the RVs and equivalent widths of the interstellar Na and also interstellar polarization as a function of the distance. For HD 31894, they obtained $E(B-V) = 0\overset{\mathrm{m}}{.}27$ and adopted the distance modulus $m - M = 10.8$, but from their mean curve through the dependence of interstellar polarization on the distance modulus, the modulus of HD 31894 should be less than 9, while from their mean curve distance vs. equivalent width of the sodium $D_1$ and $D_2$ lines, the modulus should be about 9.3.

The absolute visual magnitude of HD 31894 was estimated from the measured equivalent width of the H$\gamma$ line in two studies: Petrie & Lee (1966) obtained $M_{\rm V} = -1\overset{\mathrm{m}}{.}7$ while Walborn (1971) found $M_{\rm V} = -2\overset{\mathrm{m}}{.}9$. Carnochan (1986) studied the interstellar 2200 Å feature for a number of stars including HD 31894, adopting the following *UBV* values from Deutschman et al. (1976):

$$V = 8\overset{\mathrm{m}}{.}41,\ B-V = 0\overset{\mathrm{m}}{.}04,\ U-B = -0\overset{\mathrm{m}}{.}66, \text{ and } E(B-V) = 0\overset{\mathrm{m}}{.}28.$$

To derive the fundamental properties of HD 31894 more precisely, we began observing the star spectroscopically with the Ondřejov 2-m telescope and photometrically with the 0.65-m reflector at Hvar and later also with the 0.75-m Four-College Automatic Photoelectric Telescope (APT). One echelle spectrogram was kindly obtained and preliminarily reduced for us by Dr. Holger Lehmann with the Tautenburg Observatory 2-m reflector on JD 2 455 670.3.

To our surprise, already the first spectrum showed that the object is *a double-lined spectroscopic binary* and the second spectrum revealed a RV separation of 300 km s$^{-1}$ between the B2 primary and a secondary of some later B spectral subclass.

### 3.1. The orbital period and orbital solution

After accumulating some 12 spectra, we were able to find out that the correct orbital period must be slightly longer than 11 days. It also turned out that the orbit has a high eccentricity. We then used the program `PHOEBE` (Prša & Zwitter 2005, 2006) to derive the orbital solution which is presented in Table 4.

Dr. Alan H. Batten kindly found and communicated to us the mid-exposure times of the old DAO spectrograms, for which

**Table 4.** Orbital solution for HD 31894 derived in PHOEBE.

| Element | Unit | Value with error |
|---|---|---|
| $P$ | (d) | $11.0459 \pm 0.0051$ |
| $T_{\rm periastr.}$ | (RJD) | $55\,601.864 \pm 0.022$ |
| $T_{\rm super.c.}$ | (RJD) | $55\,601.431 \pm 0.022$ |
| $e$ | | $0.6183 \pm 0.0089$ |
| $\omega$ | (°) | $154.10 \pm 0.73$ |
| $a \sin i$ | ($R_\odot$) | $39.68 \pm 0.39$ |
| $\gamma$ | (km s$^{-1}$) | $-1.82 \pm 0.47$ |
| $K_1$ | (km s$^{-1}$) | $85.6 \pm 1.5$ |
| $K_1/K_2$ | | $0.5879 \pm 0.0093$ |
| $K_2$ | (km s$^{-1}$) | $145.6 \pm 2.6$ |
| $M_1 \sin^3 i$ | ($M_\odot$) | $4.33 \pm 0.13$ |
| $M_2 \sin^3 i$ | ($M_\odot$) | $2.55 \pm 0.08$ |
| $\chi^2$ | | 37.60 |
| No. of RVs | | 19+19 |

**Notes.** The epochs are in RJD = HJD – 2 400 000.

**Table 5.** Orbital solution for the old DAO spectra of HD 31894 derived in PHOEBE.

| Element | Unit | Value with error |
|---|---|---|
| $P$ | (d) | 11.0459 fixed |
| $T_{\rm periatr.}$ | (RJD) | $31\,743.29 \pm 0.10$ |
| $\gamma$ | (km s$^{-1}$) | $-8.8 \pm 3.9$ |
| $\chi^2$ | | 1.842 |
| No. of RVs | | 4 |

**Notes.** All elements, besides the epoch and systemic velocity, were kept fixed from the solution for the new data – see Table 4. The epochs are in RJD = HJD – 2 400 000.

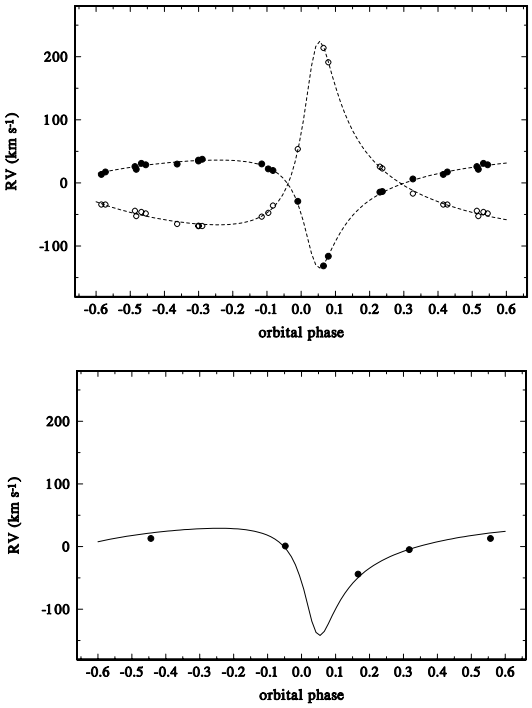


**Fig. 2.** Orbital radial-velocity curves of HD 31894 for the orbital period of 11$^{\rm d}$.0459. Phase zero corresponds to the superior conjunction. *Upper panel*: RV curves of the primary (filled circles) and secondary (open circles) and the PHOEBE solution calculated curves. *Bottom panel*: the RV curve based on the old DAO RVs.

the RVs were derived by Petrie & Pearce (1961). We calculated the corresponding heliocentric Julian dates and reproduce these RVs also in Table A.2.

Keeping the orbital elements fixed from the solution for our new RVs, we derived a separate solution for the old RVs, deriving only the epoch of periastron and the systemic velocity. The result is in Table 5 and the corresponding RV curve is shown in the lower panel of Fig. 2. Assuming that 2159, 2160 or 2161 orbital cycles elapsed between the old and new periastron epoch, we obtain the following possible values of the orbital period: 11$^{\rm d}$.0508, 11$^{\rm d}$.0456, and 11$^{\rm d}$.0405, respectively[3]. It is seen that after another season of observations, the accuracy of the orbital period derived from the new data would be sufficient to discriminate safely between the above three possible values of the orbital period. It is not clear, however, how significant the difference in the systemic velocity between the old and new RVs is. It is conceivable that some of the old RVs are actually slightly affected by the blending of the spectral lines of the primary and secondary. For the purpose of this study, we *have not* combined the old and new RVs to obtain a joint orbital solution. All subsequent discussion will be based on the orbital elements derived from the new spectra only – cf. Table 4 – and on the following ephemeris

$$T_{\rm super.conj.} = \text{HJD } 2\,455\,601.431 + 11^{\rm d}.0459 \times E. \quad (2)$$

### 3.2. Properties of the binary system and its components

Our photometric observations safely excluded the possibility of binary eclipses. This means that we are not able to obtain a unique solution and that some assumptions must be made. Nevertheless, the observational data we accumulated allow us to obtain reasonable estimates.

In spite of a limited number of available spectra, we tentatively disentangled them, using the KOREL program (Hadrava 1995, 1997, 2004b, 2005). It converged to a solution closely similar to that of Table 4 and provided the disentangled spectra of both binary components. For the final disentangling, we kept the orbital elements of Table 4 fixed and obtained the disentangled spectra in the following three spectral regions: 6327–6422 Å, 6422–6645 Å, and 6630–6750 Å. For the second region containing H$\alpha$, we also allowed KOREL to disentagle and remove the telluric lines.

Comparing the disentagled spectra of the primary and secondary normalized to the joint continuum of both stars with synthetic spectra from the Bstar grid using the program by JN, discussed above, we obtained the *formally* best fit for the following values:

$T_{\rm eff}$ = 23 490 K, log $g$ = 4.30, $v \sin i$ = 74.4 km s$^{-1}$, $L_1$ = 0.809,

and

$T_{\rm eff}$ = 17 810 K, log $g$ = 4.52, $v \sin i$ = 26.9 km s$^{-1}$, $L_2$ = 0.191

for the primary and secondary, respectively. A comparison of the disentangled spectra with the interpolated synthetic ones is shown in Fig. 3 for the primary and in Fig. 4 for the secondary. The value of log $g$ of 4.5 [cgs] is too high even for the zero-age main sequences stars. We verified that fixing log $g$ = 4.25 for both stars increases the $\chi^2$ of the fit by only 2 per cent, leading

[3] Note that propagating the errors of both epochs does alter the quoted period values only on the fourth decimal digit.

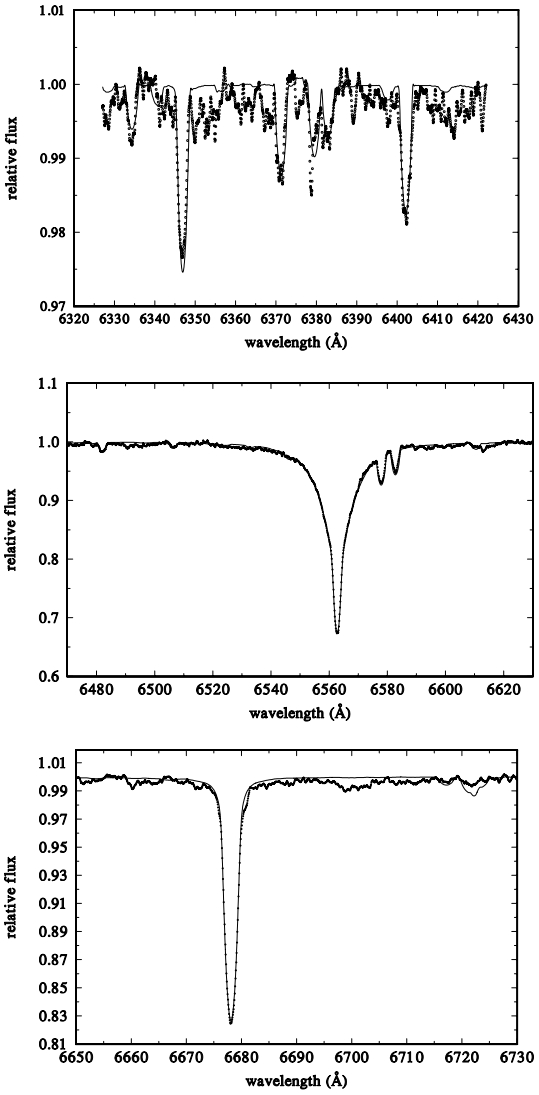


**Fig. 3.** A comparison of the disentangled line spectrum of the HD 31894 primary with a synthetic spectrum interpolated from the Bstar grid for $T_{\rm eff}$ = 23 490 K, log $g$ = 4.30 [cgs] and $v$ sin $i$ = 74.4 km s$^{-1}$ in three spectral segments containing stronger stellar lines. In all cases, dots denote the observed spectrum, while the synthetic spectra, shifted for the systemic velocity of −2 km s$^{-1}$, are shown as thin lines. A relative luminosity of the primary of $L_1$ = 0.809 was adopted for the comparison.

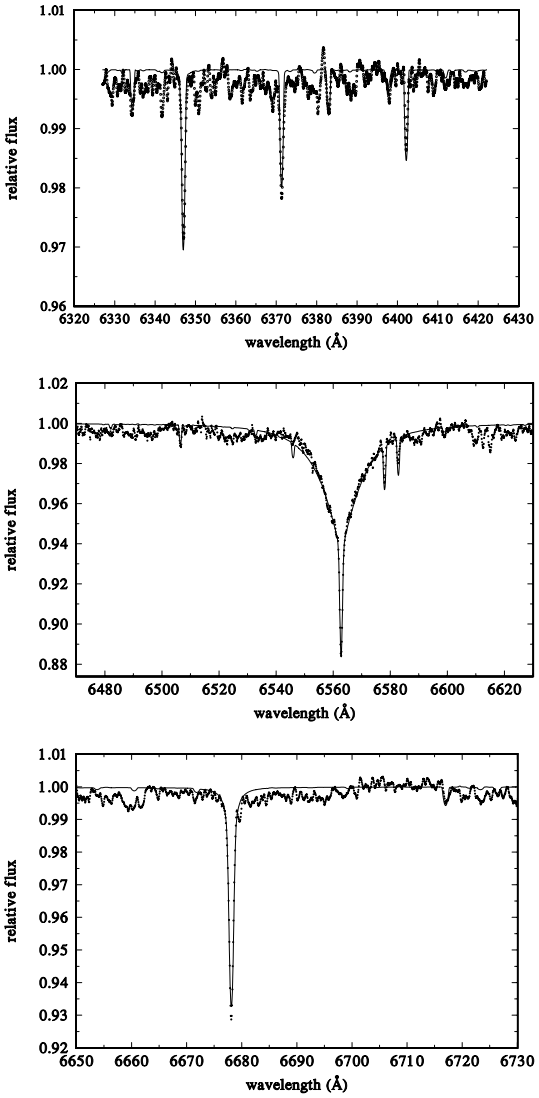


**Fig. 4.** A comparison of the disentangled line spectrum of the HD 31894 secondary with a synthetic spectrum interpolated from the Bstar grid for $T_{\rm eff}$ = 17 810 K, log $g$ = 4.52 [cgs] and $v$ sin $i$ = 26.9 km s$^{-1}$ in three spectral segments containing stronger stellar lines. In all cases, dots denote the observed spectrum, while the synthetic spectra, shifted for the systemic velocity of −2 km s$^{-1}$, are shown as thin lines. A relative luminosity of the secondary of $L_2$ = 0.191 was adopted for the comparison.

to lower $T_{\rm eff}$ of 22 800 and 17 000 K for the binary components. This confirms our estimate of typical uncertainties mentioned earlier.

In the next step we used the stellar-evolution module `MESAstar` by Paxton et al. (2011) to reproduce the observed $T_{\rm eff}$ and log $g$ of the HD 31894 primary. Using the mass ratio from our orbital solution, we then estimated the range of masses for the secondary and calculated also its evolution to see how consistent the model and observed properties of the secondary will be for the same evolutionary age as for the primary. The evolutionary tracks are shown in Fig. 5.

We again used `PHOEBE` and, keeping the orbital elements fixed at the values of Table 4 but setting $i$ = 50.°0, we included our *UBV* photometry and tuned the radii within reasonable limits to obtain the relative luminosity of the primary $L_1$ = 0.81 in the $V$ band. The fit with `PHOEBE` led to the following *UBV* magnitudes at maximum light

$V_{1+2} = 8.^{\rm m}499$, $B_{1+2} = 8.^{\rm m}543$, and $U_{1+2} = 7.^{\rm m}898$.

Using these values and the relative luminosities in all three passbands derived with `PHOEBE` (0.81, 0.82, and 0.84 in $V$, $B$, and $U$, respectively), we obtained the *UBV* magnitudes of both stars, and their standard dereddening led to the values presented in

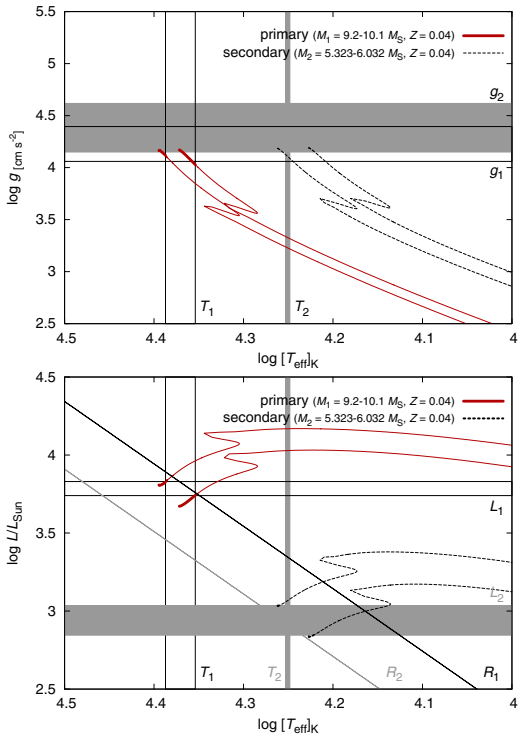


**Fig. 5.** Computed evolutionary tracks of both binary components of HD 31894 in a log $g$ vs. $T_{\rm eff}$ diagram and in the HR diagram. See the text for details.

**Table 6.** Dereddened magnitudes of both binary components based on the PHOEBE fit.

| Star | $E(B-V)$ | $E(U-B)$ | $V_0$ | $(B-V)_0$ | $(U-B)_0$ |
|---|---|---|---|---|---|
| prim. | 0.268 | 0.196 | 7.854 | –0.233 | –0.874 |
| sec. | 0.270 | 0.198 | 9.443 | –0.183 | –0.685 |

**Notes.** See the text for details.

Table 6. For illustration, the $V$-band light curve is shown in Fig. 6.

For the adopted range of effective temperatures of the primary from 23 000 to 24 000 K and of the secondary: 17 000–18 000 K, and estimating the range of bolometric magnitudes from the evolutionary calculations, one gets the ranges of the absolute visual magnitudes from $-2\overset{\rm m}{.}23$ to $-2\overset{\rm m}{.}55$ for the primary, and from $-0\overset{\rm m}{.}70$ to $-1\overset{\rm m}{.}32$ for the secondary. Combined with the dereddened $V_0$ magnitudes from Table 6 this gives the range of distances 1037–1202 pc for the primary, and 1066–1420 pc for the secondary. Weighting more the values for the primary, we adopt $d = 1150 \pm 150$ pc for the distance of the HD 31894 binary.

The radii we used in PHOEBE to fit the relative luminosities in the $V$ band are

$R_1 = 5.14\,R_\odot$ and $R_2 = 3.12\,R_\odot$.

## 4. The B star HD 31617

A relatively little studied B star HD 31617 (BD+43°1147, HIP 23186) is another object close to $\varepsilon$ Aur in the sky. It was

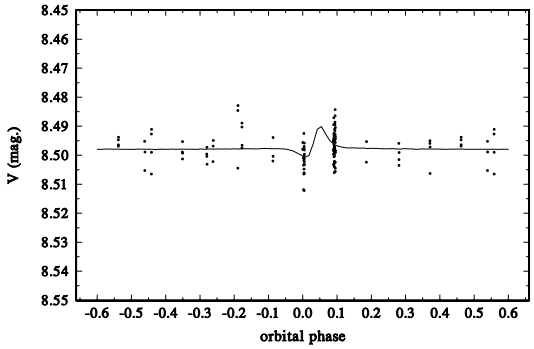


**Fig. 6.** Orbital $V$-band light curve of HD 31894 for the orbital period of $11\overset{\rm d}{.}0459$, based on a slightly more accurate APT individual observations. Phase zero corresponds to the superior conjunction. The PHOEBE solution, shown as a solid line, clearly exhibits the proximity effects near the periastron passage.

classified as B2IV by Hiltner (1956), who also obtained the following *UBV* values

$V = 7\overset{\rm m}{.}42$, $B-V = 0\overset{\rm m}{.}00$, $U-B = -0\overset{\rm m}{.}77$,

while Bouigue (1959) obtained

$V = 7\overset{\rm m}{.}35$, and $B-V = 0\overset{\rm m}{.}00$

as a mean of 3 individual observations. Plaskett & Pearce (1931) obtained 4 RVs at the Dominion Astrophysical Observatory (DAO) in 1924–1929 with a mean value of +3.5 km s$^{-1}$ and a range over 10 km s$^{-1}$. The new reduction of the H data by van Leeuwen (2007a,b) resulted in a negative value of the parallax. Therefore, no reliable trigonometrically measured distance to HD 31617 is available. However, Danziger et al. (1967) studied several stars near the hydrogen-poor star HD 30353 in an effort to derive its distance modulus via polarization mesurements by Hiltner and via the strength of the Na interstellar line. For HD 31617, they obtained a modulus of 9.6 mag from polarimetry, and 10.0 mag from the strength of the interstellar lines, which implies distances of 832 and 1000 pc, respectively. Savage et al. (1985) investigated excess ultraviolet extinction for a number of B stars and did not find any for HD 31617.

We obtained 13 individual standard *UBV* observations at Hvar. The star was also used as a check star for observations of HD 31894 at Villanova and 34 *UBV* observations were secured. There are also 97 $H_{\rm p}$ observations secured by the H satellite (Perryman & ESA 1997). None of these datasets show any significant light variability of this star. The mean standard Hvar values are in Table 9.

We succeded to secure 10 red Ondřejov spectra. The RV measurements of four good and sharp lines in SPEFO soon showed that the object is another single-line spectroscopic binary, for which we tentatively estimate an orbital period of about 60 d and a highly eccentric orbit. We use the inverse square of the rms errors of the mean RV of the four measured lines (H$\alpha$, He 6678 Å and the C doublet at 6578 & 6582 Å) for each measured spectrum to derive the weights of individual mean RVs. Our RV measurements, together with the low rms errors (mostly below 0.5 km s$^{-1}$) are reproduced in detail in Table A.3. We also tabulate there the old DAO RVs, for which we derived the heliocentric Julian dates. Regrettably, their phase distribution does not allow to improve the value of the orbital

**Table 7.** Orbital solution for HD 31617 derived in FOTEL.

| Element | Unit | Value with error |
|---|---|---|
| $P$ | (d) | $59.2 \pm 2.5$ |
| $T_{\rm periastr.}$ | (RJD) | $56\,015.39 \pm 0.50$ |
| $T_{\rm super.c.}$ | (RJD) | 56 028.45 |
| $e$ | | $0.759 \pm 0.043$ |
| $\omega$ | (°) | $295 \pm 12$ |
| $\gamma$ | (km s$^{-1}$) | $-4.79 \pm 0.81$ |
| $K_1$ | (km s$^{-1}$) | $16.9 \pm 4.9$ |
| $f(M)$ | ($M_\odot$) | 0.00815 |
| rms | (km s$^{-1}$) | 0.680 |
| No. of RVs | | 10 |

**Notes.** The epochs are in RJD = HJD – 2 400 000 and the rms is the standard error of 1 observation of unit weight.

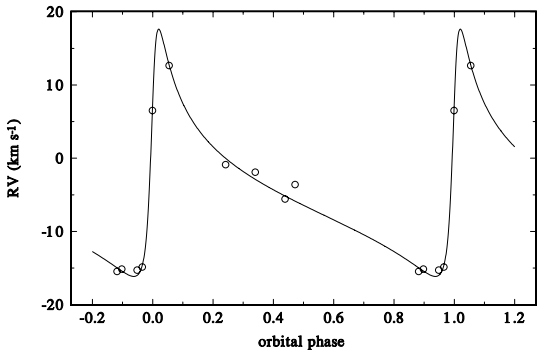


**Fig. 7.** Orbital radial-velocity curves of HD 31617 for the orbital period of $59\overset{\rm d}{.}2$. Phase zero corresponds to the superior conjunction.

period. A preliminary orbital solution derived with the program FOTEL (Hadrava 1990, 2004a) are presented in Table 7.

We disentangled the spectrum of the primary with KOREL and the comparison with the Bstar grid returned the following values:

$$T_{\rm eff} = 24\,519\,{\rm K},\ \log g = 3.863\,[{\rm cgs}],\ \text{and}\ v\,\sin i = 32.3\,{\rm km\,s^{-1}}.$$

A comparison of the disentangled spectrum with the synthetic one is in Fig. C.1 in Appendix C. Evolutionary tracks bracketing the above values are shown in Fig. C.4 in Appendix C. They imply the mass of the HD 31617 primary in the range of 9.5 to 15 $M_\odot$, the bolometric magnitude between $-4\overset{\rm m}{.}36$ and $-7\overset{\rm m}{.}36$ and the absolute visual magnitude between $-2\overset{\rm m}{.}06$ and $-4\overset{\rm m}{.}88$. Together with $V_0 = 6\overset{\rm m}{.}61$ (see Table 9) this implies a distance in the range from 540 to 1990 pc.

## 5. The B star HD 32328

Also rather neglected, HD 32328 (BD+43°1177, HIP 23603) is another object close to $\varepsilon$ Aur in the sky. It was classified as B8V in an objective prism survey by Duflot et al. (1957) and its only measured RV = +21 km s$^{-1}$ also comes from such a survey (Fehrenbach et al. 1996). It has a rather accurate parallax of $0\overset{''}{.}00612 \pm 0\overset{''}{.}00159$ from the H mission (van Leeuwen 2007a,b). Deutschman et al. (1976) obtained the following standard *UBV* values

$$V = 7\overset{\rm m}{.}57,\quad B-V = -0\overset{\rm m}{.}04,\quad U-B = -0\overset{\rm m}{.}35,$$

**Table 8.** Radiative parameters and projected rotational velocity of HD 32328 resulting from the fit of the three Ondřejov spectra with the highest S/N by interpolated synthetic spectra.

| RJD | $T_{\rm eff}$ (K) | $\log g$ [cgs] | $v \sin i$ (km s$^{-1}$) |
|---|---|---|---|
| 56 011.4508 | 12 891 | 4.426 | 44.2 |
| 56 013.4003 | 12 882 | 4.349 | 43.8 |
| 56 015.2794 | 12 861 | 4.278 | 43.4 |

**Notes.** Individual spectra are identified by their reduced Julian dates.

derived $E(B-V) = 0\overset{\rm m}{.}10$ and estimated a distance of 336 pc. For comparison, the measured H parallax implies a range of distances from 130 to 207 pc.

We obtained 10 red Ondřejov spectra and 10 individual *UBV* observations at Hvar. The Hvar photometry agrees well with that by Deutschman et al. (1976, see Table 9) and our value of the reddening is $E(B-V) = 0\overset{\rm m}{.}056$. The dereddened colours indicate a normal main-sequence object between B7 and B8.

Radial-velocity measurements of the sharp H$\alpha$ absorption core in our spectra (see Table A.4) show small variations with a full range of 8 km s$^{-1}$ and a possible timescale of 6.8 days. This means that also this object could be a single-line spectroscopic binary seen nearly pole-on (unless the component masses are strongly peculiar), but it is also conceivable that it is a rotating star with uneven brightness distribution or even an unusual pulsating star. The time distribution of our spectral, as well as photometric, observations is unsufficient to test such hypotheses, however. We can only state that no trace of a secondary spectrum is visible, therefore a comparison of the observed and synthetic spectra seems justified.

Since HD 32328 is cooler than the lower $T_{\rm eff}$ limit of the B star grid of synthetic spectra by Lanz & Hubeny (2007), we had to interpolate in the grid of synthetic spectra from the POLLUX database (Palacios et al. 2010), based on Kurucz's models. For the comparison we selected three spectra with the highest signal-to-noise ratios (S/N). The results are summarized in Table 8 and characterize the uncertainty of the fit. The comparison of model fits with these three spectra is shown in Fig. C.2 in Appendix C. Note that without being able to apply KOREL in this case, we could not remove the telluric lines from the observed spectra.

The corresponding evolutionary tracks are shown in Fig. C.5 in Appendix C. They imply a mass between 3.4 and 4.5 $M_\odot$, $M_{\rm bol} = -0\overset{\rm m}{.}49$ to $-1\overset{\rm m}{.}98$, $M_{\rm V} = 0\overset{\rm m}{.}31$ to $-1\overset{\rm m}{.}18$, which with $V_0 = 7\overset{\rm m}{.}475$ (Table 9) implies a distance between 270 and 540 pc. In contrast to it, the range of the distance following directly from the H parallax is $(175 \pm 45)$ pc. The question is whether HD 32328 is not indeed a binary composed from two similarly bright stars observed pole-on. In any case, we use the lower limit of the H measurements and the upper limit of the spectroscopic distance as the range of possible distances to HD 32328.

## 6. The B star HD 277197

HD 277197 (BD+43°1161; $V = 9\overset{\rm m}{.}5$) is a little studied B star. It is classified as B1 IV by Bouigue (1959) and B5 by McCuskey (1959) but no MKK classification was published. The only $B-V$ photometry was published by Bouigue (1959), who obtained

$$V = 9\overset{\rm m}{.}51,\quad \text{and}\quad B-V = +0\overset{\rm m}{.}06.$$

**Table 9.** *UBV* photometry of calibration stars and their dereddened values.

| Star | $V$ (mag) | $B-V$ (mag) | $U-B$ (mag) | $V_0$ (mag) | $(B-V)_0$ (mag) | $(U-B)_0$ (mag) |
|---|---|---|---|---|---|---|
| HD 31617 | $7.429 \pm 0.004$ | $+0.003 \pm 0.002$ | $-0.748 \pm 0.002$ | 6.612 | −0.249 | −0.933 |
| HD 32328 | $7.657 \pm 0.004$ | $-0.047 \pm 0.003$ | $-0.343 \pm 0.002$ | 7.475 | −0.103 | −0.383 |
| HD 277197 | $9.495 \pm 0.003$ | $+0.063 \pm 0.002$ | $-0.547 \pm 0.003$ | 8.649 | −0.197 | −0.737 |
| BD+43°1168 | $9.395 \pm 0.006$ | $+0.918 \pm 0.007$ | $+0.276 \pm 0.004$ | 6.425 | +0.02 | −0.56 |

We secured three red spectra of it with the Onřejov 2-m reflector and 31 individual *UBV* observations during 2011 and 2012 at Hvar.

Since the clouds interrupted the exposure of the first spectrum, it has a $S/N = 42$ only. However, the remaining two are well exposed and permit a comparison with the synthetic spectra. The mean RV of the H$\alpha$ and He 6678 Å lines from all three spectra is $-3.4 \pm 0.7$ km s$^{-1}$, rather similar to both $\varepsilon$ Aur and the HD 31894 binary. When comparing the second and third spectra to the synthetic spectra from the B star grid of Lanz & Hubeny (2007, see Fig. C.3 in Appendix C), we found that the best fit is obtained for

$$T_{\rm eff} = 17\,750\,{\rm K},\ \log g = 4.459\,[{\rm cgs}],\ \text{and}\ v \sin s = 44.7\,{\rm km\,s^{-1}}.$$

The differential Hvar *UBV* photometry did not reveal any variability during two seasons. We therefore derived robust mean values from all 31 individual observations to obtain $V = 9\overset{\rm m}{.}495 \pm 0.003$, $B-V = 0\overset{\rm m}{.}063 \pm 0.002$, and $U-B = -0\overset{\rm m}{.}547 \pm 0.003$.

A standard dereddening gives

$$(B-V)_0 = -0\overset{\rm m}{.}197,\ (U-B)_0 = -0\overset{\rm m}{.}737,\ \text{and}\ E(B-V) = 0\overset{\rm m}{.}260.$$

Both the derredened magnitudes and the $T_{\rm eff}$ deduced from the observed spectra agree with a spectral type near B3.

Evolutionary tracks modelling the results of the comparison of the observed and synthetic spectra are shown in Fig. C.6 in Appendix C and imply a mass of 5.5 to 6.7 $M_\odot$, $M_{\rm bol}$ between $-2\overset{\rm m}{.}49$ and $-3\overset{\rm m}{.}50$, $M_{\rm V}$ between $-0\overset{\rm m}{.}92$ and $-1\overset{\rm m}{.}81$ and for $V_0 = 8\overset{\rm m}{.}649$ the spectroscopic distance from 820 to 1230 pc.

## 7. The field star BD+43°1168

The B9 Iab supergiant BD+43°1168 (ADS 3605E) is the closest to $\varepsilon$ Aur in the sky from the stars considered here. The spectral classification was derived by Morgan et al. (1955), while its RV = −22 km s$^{-1}$ was measured by Münch (1957). The *UBV* photometry was derived by Hiltner (1956) as

$$V = 9\overset{\rm m}{.}39,\ \ B-V = 0\overset{\rm m}{.}92,\ \ U-B = 0\overset{\rm m}{.}20,$$

while Fernie (1983) obtained

$$V = 9\overset{\rm m}{.}48,\ \ B-V = 0\overset{\rm m}{.}95,\ \ U-B = 0\overset{\rm m}{.}12$$

as a mean of 3 individual observations.

The mean of 9 *UBV* observations secured at Hvar is

$$V = 9\overset{\rm m}{.}395 \pm 0\overset{\rm m}{.}006,$$

$$B-V = 0\overset{\rm m}{.}918 \pm 0\overset{\rm m}{.}007,$$

$$U-B = 0\overset{\rm m}{.}276 \pm 0\overset{\rm m}{.}004.$$

The above three determinations of *UBV* magnitudes differ a bit more than what one would expect. In Fig. 8 we reproduce a part of the better exposed spectrum of the star. From a comparison with a spectrum of another B9Iab star $\sigma$ Cyg taken with the same instrumentation, one can suspect the presence of a weak emission in the H$\alpha$ line of BD+43°1168. From analogy with other emission-line stars, a slight secular variability of BD+43°1168 cannot therefore be excluded.

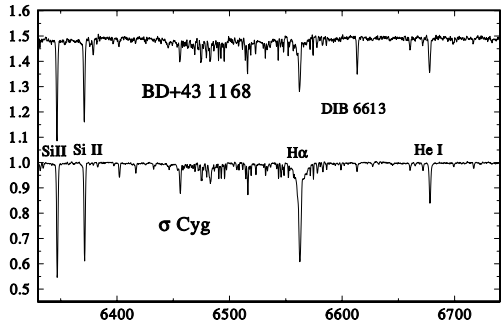


**Fig. 8.** A comparison of the Ondřejov red spectrum of BD+43°1168 taken on HJD 2 456 008.3159 with a spectrum of another B9Iab star $\sigma$ Cyg, taken with the same instrumentation and kindly put at our disposal by Dr. M. Kraus. Note the strong 6613.56 Å interstellar line in the spectrum of BD+43°1168 and its faint H$\alpha$ profile, obviously partly filled by emission.

According to Johnson (1958), the intrinsic colours of a B9Iab supergiant are $B-V = +0\overset{\rm m}{.}02$ and $U-B = -0\overset{\rm m}{.}52$. This implies $E(B-V) = 0\overset{\rm m}{.}90$ for Hiltner's and our Hvar values, and $E(B-V) = 0\overset{\rm m}{.}93$ for the values published by Fernie. From this, one then obtains the derredened $V_0$ magnitude from formula (1) to be $6\overset{\rm m}{.}39$ and $6\overset{\rm m}{.}37$, repectively. The absolute visual magnitude of a B9Iab supergiant is expected to be $-6\overset{\rm m}{.}2$ (Cox 2000) to $-6\overset{\rm m}{.}4$ (Straizys & Kuriliene 1981), which with the above estimated $V_0$ range implies a distance to BD+43°1168 between 3.27 and 3.61 kpc.

Our measured value of $EW(6613) = 0.230 \pm 0.020$ Å is in good agreement with a published value of 0.20 Å (Bromage & Nandy 1973).

## 8. Inferred calibration relations

We plot the distance calibrations based on the data for calibration stars in the neighbourhood of $\varepsilon$ Aur in the sky (see Table 10) in Fig. 9. One can see that all three calibrations $d$(EW), $d(I_{\rm c})$, $d(E(B-V))$ are well-defined and they are consistent with each other:

$$d({\rm EW}) = (1.474 \pm 0.028) \times 10^4\,{\rm EW}, \quad (3)$$

$$d\,(I_{\rm c}) = (-2.027 \pm 0.171) \times 10^4\ (1 - I_{\rm c})\,, \quad (4)$$

$$d(E(B-V)) = (3.888 \pm 0.089) \times 10^3\,E(B-V). \quad (5)$$

Also note that these calibrations are *not* dependent on any outliers. For example, if we drop the most distant star (BD+43 1168) and extrapolate linearly from the remaining data

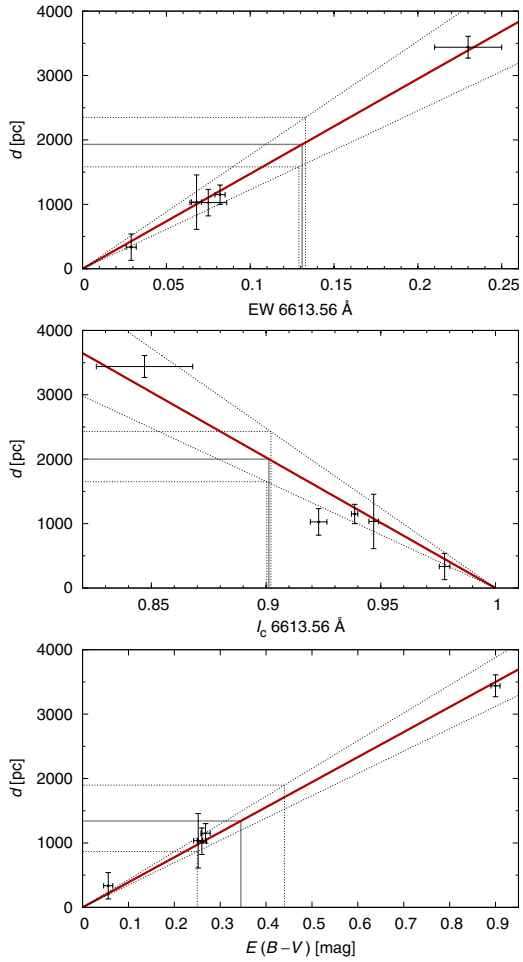


**Fig. 9.** Calibrations of the distance and a function of the strength of the diffuse interstellar 6613.56 Å line and of the $E(B-V)$ reddening. The solid gray lines show the mean EW, $I_c$, and $E(B-V)$ values of $\varepsilon$ Aur and the corresponding distance, the dotted lines indicate the range of uncertainties.

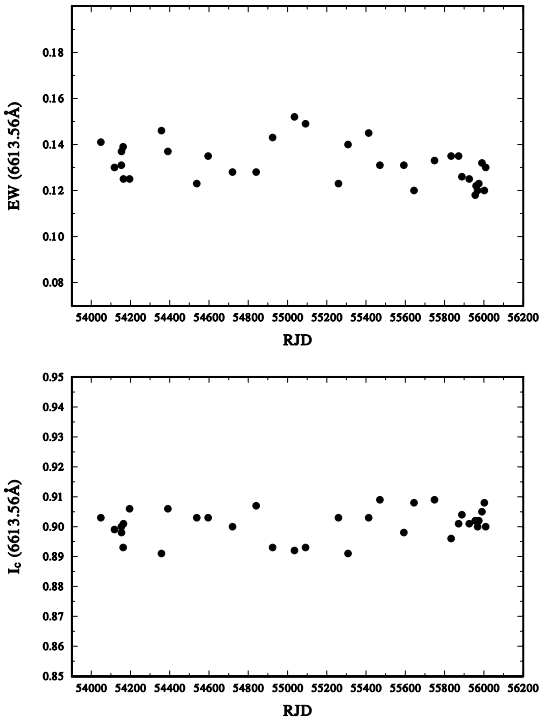


**Fig. 10.** Time plots of the equivalent width (EW) and central intensity ($I_c$) of the 6613.56 Å diffuse interstellar line measured on a representative sample of the Ondřejov CCD spectra over the time interval from 2006 to 2012. No significant change during the 2009−2011 primary eclipse (RJD 55 050 to 55 800) is observed, which corroborates the conclusion that the line is of a truly interstellar (not partly cirmcumstellar) origin.

we would obtain equivalent results for the distances in the 1000 to 2000 pc range.

## 9. Measured and deduced properties of $\varepsilon$ Aur

It is not quite straightforward to derive a reliable reddening of $\varepsilon$ Aur since its brightness and colours undergo cyclic physical variations on a time scale of some 50 to 120 days (cf., e.g. Chadima et al. 2011). An inspection of the existing 107 individual Hvar standard *UBV* observations secured prior and after the recent eclipse of $\varepsilon$ Aur shows that the observed $B-V$ is in the range between $0\overset{m}{.}51$ and $0\overset{m}{.}57$. Since the true nature of the physical variations is not known, we consider the mean value of $B-V = 0\overset{m}{.}54$ as well as both extremes. There is also some uncertainty regarding the effective temperature of the $\varepsilon$ Aur F primary. From a rather detailed line-profile modelling, Bennett et al. (2005) derived 7000 K, while Sadakane et al. (2010) and Chadima et al. (2011) arrived at 8000 K. Modelling the energy distribution, Hoard et al. (2010) used 7750 K for the F primary. Using again the calibration between the effective temperature and intrinsic $B-V$ colour, one arrives at $(B-V)_0$ between $+0\overset{m}{.}16$ and $+0\overset{m}{.}30$ for the calibration by Flower (1996), while Johnson (1958) gives $(B-V)_0 = +0.23$ for F0I stars. So the total range of $E(B-V)$ to be considered as appropriate for $\varepsilon$ Aur is $0\overset{m}{.}25$ to $0\overset{m}{.}44$. It should be noted that a small contribution to the observed reddening could arise from circumbinary dust. However, the large grain size indicated by the models (cf., e.g. Budaj 2011) and lack of variations in the diffuse interstellar band indicate that this contribution is probably insignificant.

We measured the equivalent width (EW) and central intensity ($I_c$) of the 6613.56 Å diffuse interstellar line in a representative selection of the Ondřejov spectra secured from 2006 to 2012, including the spectra taken during the 2009−2011 eclipse. Both these measured quantities are plotted vs. time in Fig. 10. One can see that there is no noticeable difference in the strength of the line between the eclipse and out-of-eclipse data. This indicates in our opinion that the line is of truly interstellar, not partly circumstellar origin and can be used as a distance indicator.

In Fig. 9 we can see that all three distance calibrations are consistent and put $\varepsilon$ Aur very clearly at a distance larger than about 900 pc. Considering the calibration results, we estimate the most probable distance to $\varepsilon$ Aur to be about (1500 ± 500) pc. Its uncertainty is mostly caused by the dispersion of $I_c$ and $E(B-V)$ observed for $\varepsilon$ Aur.

**Table 10.** Estimated distances, strength of the 6613.56 Å interstellar line and the $E(B-V)$ reddening for all calibration stars.

| Distance (pc) | $EW$ 6613 Å | $I_c$ 6613 Å | $E(B-V)$ | Object |
|---|---|---|---|---|
| 0 | 0 | 1 | 0 | zero distance |
| 335 ± 205 | 0.029 ± 0.003 | 0.9778 ± 0.0023 | 0.056 | HD 32328 |
| 1030 ± 210 | 0.075 ± 0.011 | 0.9229 ± 0.0036 | 0.260 | HD 277197 |
| 1035 ± 420 | 0.068 ± 0.003 | 0.9469 ± 0.0021 | 0.252 | HD 31617 |
| 1150 ± 150 | 0.082 ± 0.003 | 0.9386 ± 0.0014 | 0.268 | HD 31894 |
| ? | 0.131 ± 0.002 | 0.9012 ± 0.0009 | 0.25–0.44 | $\varepsilon$ Aur |
| 3440 ± 170 | 0.230 ± 0.020 | 0.847 ± 0.021 | 0.90 | BD+43 1168 |

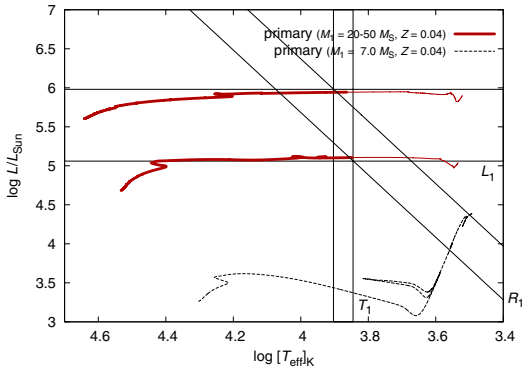


**Fig. 11.** Evolutionary tracks computed for $\varepsilon$ Aur in the HR diagram. We show the evolution from the zero-age main sequence. The thin lines correspond to the observed effective temperatures, radii and luminosities of $\varepsilon$ Aur. The range of masses are indicated in the legend. We also plot the evolutionary track for a lower-mass star ($m_{ini}$ = 7 $M_\odot$) for comparison as a dotted line. It never reaches the observed luminosity, even in the post-AGB phase. The post-AGB evolution track (not shown in the plot) is nearly horizontal (at nearly a constant log $L/L_\odot \sim 4.4$) as the star moves to the hotter (left) in the diagram.

Stencel et al. (2008) derived the angular diameter of the F primary of $\varepsilon$ Aur out of eclipse to be between 2.16 and 2.38 mas. For the distance of (1500 ± 500) pc this implies the F star radius of 232 to 512 $R_\odot$. The corresponding range of absolute visual magnitudes of $\varepsilon$ Aur is then $M_V = -7\overset{m}{.}9$ to $-10\overset{m}{.}2$ mag. This seems to speak in favour of the high-mass model for $\varepsilon$ Aur and identifies its primary as a relatively young object.

Indeed, the evolutionary tracks computed by the `MESAstar` module show that the allowed range of masses is 20 to 50 $M_\odot$ (see Fig. 11). We assumed initial helium abundance $Y = 0.320$ and metallicity $Z = 0.040$, the mixing-length parameter $\alpha = 2.0$, scheme for the wind by Reimers (1975) in the red giant branch (RGB) and by Blöcker (1995) in the AGB phase, respectively, with the efficiencies $\eta = 1.0$. We used $Z = 0.04$ for consistency with all investigated calibration (supposedly young) stars since the true evolutionary stage of $\varepsilon$ Aur is still not clear. We have verified, however, that the inferred mass range *is not sensitive* to the selected value of metallicity. Even with solar-like values $Z = 0.016$–$0.020$ and $Y = 0.28$, the evolutionary tracks are not significantly different, only the timescale is prolonged by approximately 6%. In this model, the star has evolved away from the main sequence and is in the evolutionary stage when the central hydrogen abundance dropped to zero and the star consequently moves to lower effective temperatures. For the 20 $M_\odot$ star, the star has already ignited the helium in the core so that the change in $T_{eff}$ is much slower than for the 50 $M_\odot$ model. For this reason, we consider the lower mass of 20 $M_\odot$ as more probable than the higher one. Note that the total mass loss is not important yet (less than 1% of the initial mass) and the selected wind parametrisation thus does not affect results significantly.

This is to be compared to the previous results of van Winckel (2003) who estimated the maximum luminosity for post-AGB supergiants, i.e. stars with *initial* masses lower than ∼7 $M_\odot$, to be log $L/L_\odot \approx 4.4$ ($M_{bol} = -6\overset{m}{.}2$ mag) which is well below the value estimated in this work. We thus conclude that the lower-mass model of $\varepsilon$ Aur does not fulfill observational constraints.

Formally, it is also possible to reproduce the observed properties of $\varepsilon$ Aur assuming that it is a pre-main sequence star with mass from 30 to 70 $M_\odot$ but this interpretation seems improbable since the evolution is so fast that the changes should be seen in the recorded history of the star, which is not the case (cf., e.g. Johnston et al. 2012).

If the high-mass model is confirmed, the future works should clarify whether the dark disk around the secondary could be formed by a strong wind from the F-supergiant primary. Since the current wind of the F supergiant appears too weak to sustain such a disk, one viable possibility is that prior to becoming an F supergiant, the star could have undergone a luminous blue variable (LBV) phase, in which a carbon rich super-wind was accreted by the secondary star. Note that the revision of the $\varepsilon$ Aur distance can have far reaching consequences also on some other results. For instance, the energy distributions derived by Hoard et al. (2010) and Hoard et al. (2012) need to be reconsidered (as also pointed to us by Bennett 2012, priv. comm.).

## 10. Prospects for future work

Note also that $\varepsilon$ Aur is catalogued as a little studied multiple star system (ADS 3605 ABCDE). The components ADS 3605B, C, and D are relatively faint and are located at 23, 45, and 47 arcsec from ADS 3605A = $\varepsilon$ Aur and have the $V$ magnitudes of $+14\overset{m}{.}0$, $+11\overset{m}{.}26$, and $+12\overset{m}{.}0$, respectively (Aitken & Doolittle 1932). Because $\varepsilon$ Aur lies very close to the galactic plane ($b = +1.18°$), it is possible that at least one or all of these putative faint components are field stars. For example ADS 3605C = BD+43°1166C has a published $B-V = +1\overset{m}{.}83$ (Lutz & Lutz 1977), which indicates that it may be a dM foreground star[4]. It would be important to secure spectroscopy and *UBV* photometry of these companions to determine if any of them is a physical companion to $\varepsilon$ Aur. This would provide a more definite distance check. No doubt the observations of these close companions

[4] The differential *UBV* observations of this star secured at Hvar (12 individual observations in 5 nights) give $V = (10\overset{m}{.}927 \pm 0\overset{m}{.}090)$, $B-V = 0\overset{m}{.}714 \pm 0\overset{m}{.}021$, and $U-B = 0\overset{m}{.}319 \pm 0\overset{m}{.}012$. However, these observations were challenging and strongly require independent verification.

to $\varepsilon$ Aur will be challenging due to the brightness of $\varepsilon$ Aur itself ($V \simeq +3\overset{m}{.}0$). (In the field of the 2-m telescope, these stars have always been outshone by $\varepsilon$ Aur itself and obtaining their spectra there is out of the question.) But their observations could readily be accomplished with current equipment using adaptive optics, coronagraph-equipped telescopes or interferometric nulling methods used for exoplanets. It would be worth the effort to learn more about the distance to $\varepsilon$ Aur and, consequently about its true nature.

In conclusion, the present study offers strong (but circumstantial) evidence that $\varepsilon$ Aur is at a distance of 1.0–2.0 kpc. This favours a high luminosity and radius for the F-supergiant and therefore supports $\varepsilon$ Aur as being a massive binary system, younger than about $7 \times 10^6$ yr. Note that additional arguments supporting this interpretation were recently provided by Johnston et al. (2012). But nothing seems to come easy in the study of $\varepsilon$ Aur. And as the concluding remarks of many previous papers on $\varepsilon$ Aur typically state: *More work is needed to finally unravel numerous mysteries and puzzles of this fascinating and intriguing eclipsing binary.*

*Acknowledgements.* We are grateful to Dr. H. Lehmann, who kindly obtained and reduced one echelle spectrum of HD 31894 for us, to Dr. A. H. Batten, who communicated to us the exact mid-exposure times of the four older DAO photographic spectra of HD 31894, and to Dr. Michaela Kraus for her permission to show here a plot of 1 Ondřejov spectrogram of $\sigma$ Cyg, which she obtained. We acknowledge the use of the public version of the programs FOTEL and KOREL written by Dr. P. Hadrava and the grid of synthetic spectra of B stars made publicly available by Hubeny and Lanz. We thank an anonymous referee for the tough but justified, fair and constructive criticism of the first version of this study and additonal useful suggestions to the second version, which led us to re-do the whole paper and hopefully strengthen the arguments in favour of a larger distance to $\varepsilon$ Aur. Useful discussions on the subject with Dr. S. S. Shore are also gratefully acknowledged. We profitted from the use of the bibliography maintained by the NASA/ADS system and the CDS in Strasbourg. The Czech authors were supported by the grant P209/10/0715 of the Czech Science Foundation and also from the research programs AV0Z10030501 and MSM0021620860. The US authors are very grateful for support of this work from NASA Grants NNX09AAH28G + GO-12302.01 and NSF/RUI Grants AST-0507542 + AST-1009903.

## References

Adams, W. S., & Joy, A. H. 1917, ApJ, 46, 313
Aitken, R. G., & Doolittle, E. 1932, New general catalogue of double stars within 120 of the North pole, Carnegie institution of Washington, Washington, D.C.
Bennett, P. D., Ake, T. B., & Harper, G. M. 2005, BAAS, 37, 495
Blöcker, T. 1995, A&A, 297, 727
Bouigue, R. 1959, Annales de l'Observatoire Astron. et Meteo. de Toulouse, 27, 47
Bromage, G. E., & Nandy, K. 1973, A&A, 26, 17
Budaj, J. 2011, A&A, 532, L12
Carnochan, D. J. 1986, MNRAS, 219, 903
Carroll, S. M., Guinan, E. F., McCook, G. P., & Donahue, R. A. 1991, ApJ, 367, 278
Chadima, P., Harmanec, P., Yang, S., et al. 2010, IBVS, 5937, 1
Chadima, P., Harmanec, P., Bennett, P. D., et al. 2011, A&A, 530, A146
Cox, A. N. 2000, Allen's Astrophysical Quantities, 4th edition, ed. by A. N. Cox (New York: AIP Press and Springer)
Danziger, I. J., Wallerstein, G., & Böhm-Vitense, E. 1967, ApJ, 150, 239
Deutschman, W. A., Davis, R. J., & Schild, R. E. 1976, ApJS, 30, 97
Dobashi, K., Uehara, H., Kandori, R., et al. 2005, PASJ, 57, 1
Duflot, M., Fehrenbach, C., Guillaume, J., & Ray, G. 1957, Publications of the Observatoire Haute-Provence, 4, 11
Eggleton, P. P., & Pringle, J. E. 1985, ApJ, 288, 275
Fehrenbach, C., Duflot, M., Genty, V., & Amieux, G. 1996, Bulletin d'Information du Centre de Données Stellaires, 48, 11
Fernie, J. D. 1983, ApJS, 52, 7
Flower, P. J. 1996, ApJ, 469, 355
Galazutdinov, G. A., LoCurto, G., & Krełowski, J. 2008, ApJ, 682, 1076
Guinan, E. F., & DeWarf, L. E. 2002, in Exotic Stars as Challenges to Evolution, eds. C. A. Tout, & W. van Hamme, ASP Conf. Ser., 279, 121
Hadrava, P. 1990, Contributions of the Astronomical Observatory Skalnaté Pleso, 20, 23
Hadrava, P. 1995, A&AS, 114, 393
Hadrava, P. 1997, A&AS, 122, 581
Hadrava, P. 2004a, Publ. Astron. Inst. Acad. Sci. Czech Rep., 92, 1
Hadrava, P. 2004b, Publ. Astron. Inst. Acad. Sci. Czech Rep., 92, 15
Hadrava, P. 2005, Ap&SS, 296, 239
Harmanec, P., Horn, J., & Juza, K. 1994, A&AS, 104, 121
Heintz, W. D., & Cantor, B. A. 1994, PASP, 106, 363
Hiltner, W. A. 1956, ApJS, 2, 389
Hoard, D. W., Howell, S. B., & Stencel, R. E. 2010, ApJ, 714, 549
Hoard, D. W., Ladjal, D., Stencel, R. E., & Howell, S. B. 2012, ApJ, 748, L28
Hobbs, L. M., York, D. G., Thorburn, J. A., et al. 2009, ApJ, 705, 32
Horn, J., Kubát, J., Harmanec, P., et al. 1996, A&A, 309, 521
Jenniskens, P., & Desert, F.-X. 1994, A&AS, 106, 39
Johnson, H. L. 1958, Lowell Observatory Bulletin, 4, 37
Johnson, H. L. 1965, ApJ, 141, 923
Johnston, C., Guinan, E. F., Harmanec, P., & Mayer, P. 2012, in AAS Meeting Abstracts, 219, 153.34
Koornneef, J. 1983, A&A, 128, 84
Kuiper, G. P., Struve, O., & Strömgren, B. 1937, ApJ, 86, 570
Lambert, D. L., & Sawyer, S. R. 1986, PASP, 98, 389
Lanz, T., & Hubeny, I. 2007, ApJS, 169, 83
Ludendorff, H. 1903, AN, 164, 81
Lutz, T. E., & Lutz, J. H. 1977, AJ, 82, 431
McCall, B. J., Drosback, M. M., Thorburn, J. A., et al. 2010, ApJ, 708, 1628
McCuskey, S. W. 1949, ApJ, 109, 414
McCuskey, S. W. 1959, ApJS, 4, 1
Morgan, W. W., Code, A. D., & Whitford, A. E. 1955, ApJS, 2, 41
Munari, U., Tomasella, L., Fiorucci, M., et al. 2008, A&A, 488, 969
Münch, G. 1957, ApJ, 125, 42
Palacios, A., Gebran, M., Josselin, E., et al. 2010, A&A, 516, A13
Paxton, B., Bildsten, L., Dotter, A., et al. 2011, ApJS, 192, 3
Perryman, M. A. C., & ESA. 1997, The H and TYCHO catalogues (Noordwijk, Netherlands: ESA Publications Division), ESA SP Ser., 1200
Petrie, R. M., & Lee, E. K. 1966, Publ. Dom. Astrophys. Obs. Victoria, 12, 435
Petrie, R. M., & Pearce, J. A. 1961, Publ. Dom. Astrophys. Obs. Victoria, 12, 1
Plaskett, J. S., & Pearce, J. A. 1931, Publ. Dom. Astrophys. Obs. Victoria, 5, 1
Prša, A., & Zwitter, T. 2005, ApJ, 628, 426
Prša, A., & Zwitter, T. 2006, Ap&SS, 304, 347
Reimers, D. 1975, Mem. Soc. Roy. Sci. Liege, 8, 369
Sadakane, K., Kambe, E., Sato, B., Honda, S., & Hashimoto, O. 2010, PASJ, 62, 1381
Savage, B. D., Massa, D., Meade, M., & Wesselius, P. R. 1985, ApJS, 59, 397
Schlegel, D. J., Finkbeiner, D. P., & Davis, M. 1998, ApJ, 500, 525
Škoda, P. 1996, in Astronomical Data Analysis Software and Systems V, ASP Conf. Ser. 101, 187
Stefanik, R. P., Torres, G., Lovegrove, J., et al. 2010, AJ, 139, 1254
Stencel, R. E., Creech-Eakman, M., Hart, A., et al. 2008, ApJ, 689, L137
Straizys, V., & Kuriliene, G. 1981, Ap&SS, 80, 353
Strand, K. A. 1959, AJ, 64, 346
Torres, G. 2010, AJ, 140, 1158
van de Kamp, P. 1978, AJ, 83, 975
van de Kamp, P., & Lippincott, S. L. 1968, AJ, 73, 781
van Leeuwen, F. 2007a, in Astrophysics and Space Science Library (Springer), 350
van Leeuwen, F. 2007b, A&A, 474, 653
van Winckel, H. 2003, ARA&A, 41, 391
Walborn, N. R. 1971, ApJS, 23, 257

Pages 12 to 15 are available in the electronic edition of the journal at http://www.aanda.org

## Appendix A: Details of spectroscopic observations and their analyses

With one exception, all spectra used in this study were secured in the coudé focus of the Ondřejov 2.0-m reflector and a 702-mm focal length camera with a SITe-005 800 × 2000 CCD detector covering the wavelength region 6260−6760 Å. The spectra have a linear dispersion 17.2 Å mm$^{-1}$ and a 2-pixel resolution $R \sim 12\,600$ ($\sim$11−12 km s$^{-1}$ per pixel). With one exception, their S/N is at least 100 or better. The journal of observations of all stars is in Table A.1.

**Table A.1.** Journal of spectral observations of $\varepsilon$ Aur and the calibration stars in its neighbourhood.

| Star | No. of. spectra | Time interval (RJD) |
|---|---|---|
| $\varepsilon$ Aur | 280 | 54 049.4–55 913.3 |
| HD 31617 | 10 | 55 959.4–56 043.3 |
| HD 31894 | 19 | 55 578.4–55 692.3 |
| HD 32328 | 10 | 55 960.3–56 043.3 |
| HD 277197 | 3 | 55 821.4–55 837.5 |
| BD+43°1168 | 2 | 55 976.4–56 008.3 |

**Table A.2.** Individual RVs of HD 31894 for the primary from the old photographic spectra and the RVs of the primary and secondary from the new electronic spectra measured via Gaussian fits.

| RJD | $RV_1$ (km s$^{-1}$) | $RV_2$ (km s$^{-1}$) | Obs. |
|---|---|---|---|
| 26 276.9788 | –44.0 | – | DAO |
| 31 749.0048 | 13.0 | – | DAO |
| 34 297.9639 | –5.0 | – | DAO |
| 34 735.7704 | 1.0 | – | DAO |
| 55 578.4268 | 19.6 | –35.9 | OND |
| 55 602.3073 | –116.2 | 191.4 | OND |
| 55 618.3613 | 31.1 | –46.1 | OND |
| 55 618.4995 | 28.7 | –48.4 | OND |
| 55 619.5146 | 29.8 | –65.1 | OND |
| 55 622.4573 | 22.3 | –47.5 | OND |
| 55 623.4108 | –29.2 | 53.6 | OND |
| 55 631.2495 | 36.1 | –68.0 | OND |
| 55 635.2864 | –131.6 | 213.9 | OND |
| 55 642.2977 | 34.7 | –68.5 | OND |
| 55 642.4187 | 37.5 | –68.4 | OND |
| 55 644.3406 | 30.1 | –53.6 | OND |
| 55 651.2891 | 26.0 | –44.3 | OND |
| 55 661.3810 | 17.3 | –34.3 | OND |
| 55 662.3785 | 21.4 | –52.7 | OND |
| 55 670.3250 | –13.8 | 22.9 | TLS |
| 55 671.3145 | +6.3 | –16.9 | OND |
| 55 672.2947 | +13.4 | –34.2 | OND |
| 55 692.3364 | –14.7 | 25.7 | OND |

**Notes.** The reduced heliocentric Julian dates RJD = HJD – 2 400 000 are tabulated.

For HD 31894, one echelle spectrogram (4700−7085 Å, 2-pixel resolution of 63 000) was kindly obtained for us by Dr. Holger Lehmann with the Tautenburg Observatory 2-m reflector on JD 2 455 670.3. Dr. Lehmann also kindly carried out the initial reductions of that spectrogram (bias subtraction, flat-fielding, order merging and wavelength calibration) in IRAF. Similar initial reductions of all Ondřejov spectrograms were carried out by MŠ, also in IRAF. The final reductions and RV measurements were carried out by PH in the program SPEFO, written by the late Dr. J. Horn and further developed by Dr. P. Škoda and Mr. J. Krpata (Horn et al. 1996; Škoda 1996). In SPEFO, one derives the RVs via sliding the direct and flipped image of a line profile until a perfect match is obtained. We also measured a selection of good telluric lines to use them to a fine correction of the RV zero point for each spectrogram. After these corrections, the final RVs for HD 31894 were derived via a Gaussian fit of the He 6678 Å line profile by PM. All individual RVs of HD 31894 are in Table A.2.

**Table A.3.** Individual DAO and Ondřejov RVs of HD 31617.

| RJD | RV (km s$^{-1}$) | rms (km s$^{-1}$) |
|---|---|---|
| 24 064.9953 | 4.80 | – |
| 25 614.8008 | 3.40 | – |
| 25 621.6945 | 8.30 | – |
| 25 642.7182 | –2.40 | – |
| 55 959.4293 | 12.64 | 0.23 |
| 55 970.5035 | –0.88 | 0.34 |
| 55 976.3167 | –1.91 | 0.31 |
| 56 008.3733 | –15.47 | 0.21 |
| 56 009.3183 | –15.14 | 0.47 |
| 56 012.3213 | –15.29 | 0.30 |
| 56 013.3368 | –14.86 | 0.19 |
| 56 015.3163 | 6.50 | 0.42 |
| 56 041.3434 | –5.57 | 0.12 |
| 56 043.3126 | –3.60 | 0.33 |

**Notes.** The RVs on the Ondřejov CCD spectra were measured in SPEFO and each value is the mean of the RVs of the following four lines: H$\alpha$ 6562.817 Å, He 6678.151 Å, C 6578.052 Å, and C 6582.882 Å. The reduced heliocentric Julian dates RJD = HJD – 2 400 000 are tabulated.

**Table A.4.** Individual Ondřejov RVs of HD 32328 measured in SPEFO on the sharp core of H$\alpha$.

| RJD | RV (km s$^{-1}$) |
|---|---|
| 55 960.3317 | 10.68 |
| 55 970.2849 | 7.73 |
| 56 008.4007 | 12.02 |
| 56 009.2846 | 9.18 |
| 56 011.4508 | 12.24 |
| 56 012.4020 | 14.91 |
| 56 013.4003 | 14.28 |
| 56 015.2794 | 10.85 |
| 56 041.3848 | 13.05 |
| 56 043.3463 | 13.54 |

**Notes.** The reduced heliocentric Julian dates RJD = HJD – 2 400 000 are tabulated.

## Appendix B: Photometry

The calibrated Hvar *UBV* observations of $\varepsilon$ Aur and all calibration stars were obtained differentially relative to the comparison star $\lambda$ Aur, used as the primary comparison by most observers of $\varepsilon$ Aur. HR 1644 served as the check star. All observations

**Table B.1.** Journal of *UBV* observations of $\varepsilon$ Aur and the calibration stars in its neighbourhood.

| Star | No. of. obs. | Time interval (RJD) | Note |
|---|---|---|---|
| $\varepsilon$ Aur | 334 | 45 307.5–56 015.3 | 1 |
| HD 31617 | 13 | 56 001.3–56 015.3 | 1 |
| HD 31894 | 87 | 55 574.3–55 858.7 | 1 |
| | 120 | 55 629.7–55 665.6 | 2 |
| HD 32328 | 10 | 56 001.3–56 015.3 | 1 |
| HD 277197 | 31 | 55 791.6–56 015.3 | 1 |
| BD+43°1168 | 9 | 56 001.3–56 013.3 | 1 |

**Notes.** 1... Hvar; 2... Villanova APT.

were carefully reduced to the standard Johnson system via non-linear transformation formulae (Harmanec et al. 1994) using the latest rel.17 of the program HEC22[5]. The more recent versions of HEC22 allow monitoring and modelling the variations of the atmospheric extinction during observing nights. The following mean Hvar all-sky values for $\lambda$ Aur were added to the respective magnitude differences var-comp and check-comp:

$V = 4\overset{\mathrm{m}}{.}706,\ \ B-V = 0\overset{\mathrm{m}}{.}619,\ \ U-B = 0\overset{\mathrm{m}}{.}143.$

The Villanova APT differential *UBV* observations of HD 31894 were secured relative to HR 1644 and reduced via a standard APT pipeline. The standard Hvar all-sky values for HR 1644

$V = 6\overset{\mathrm{m}}{.}224,\ \ B-V = 0\overset{\mathrm{m}}{.}451,\ \ U-B = 0\overset{\mathrm{m}}{.}334.$

were added to the magnitude differences var-comp. The journal of photometric observations is in Table B.1.

## Appendix C: Model fits

Here, we present a comparison of the disentangled spectrum of HD 31617 and the observed spectra of HD 32328 and HD 277197 with the best-fit interpolated synthetic spectra in Figs. C.1–C.3, respectively. For the same stars, we also show the evolutionary tracks calculated in such a way to fit the $T_{\rm eff}$ and log $g$ deduced from the observed spectra – see Figs. C.4–C.6, respectively.

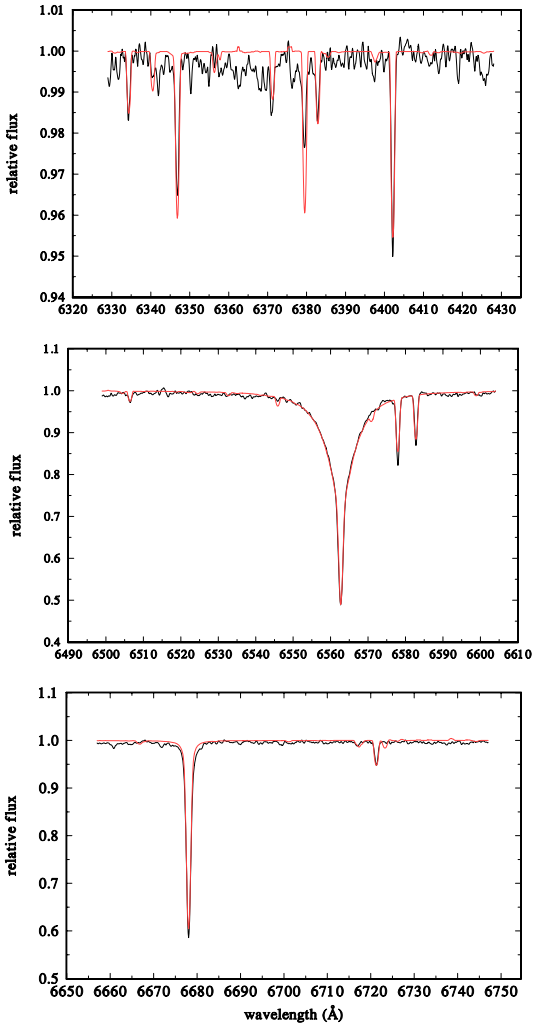


**Fig. C.1.** A comparison of the disentangled red spectrum of HD 31617 (black lines) with the model spectrum (red lines).

[5] The whole package containing the program HEC22 and other programs for complete photometric reductions, sorting and archiving the data, together with a very detailed User manual, is freely available at http://astro.troja.mff.cuni.cz/ftp/hec/PHOT.

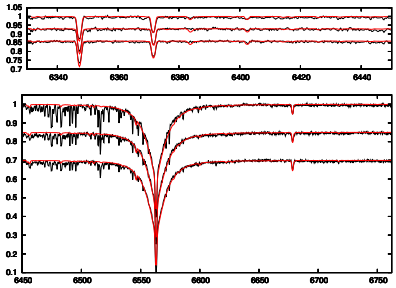

**Fig. C.2.** A comparison of three individual Ondřejov spectra of HD 32328 (black lines) having the highest S/N with the model spectra (red lines). From top to bottom, the spectra were taken on RJD 56 011.4508, 56 013.4003, and 56 015.2794, respectively. Note that we could not remove the telluric lines from the observed spectra in this case.

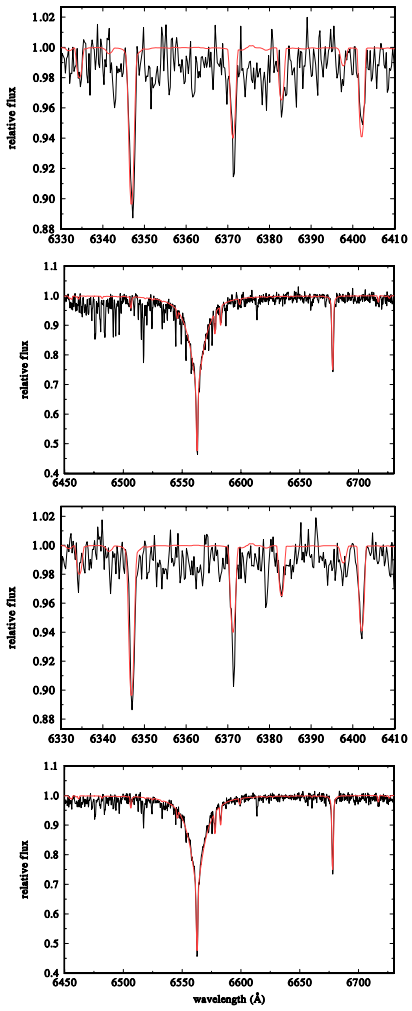


**Fig. C.3.** A comparison of two individual Ondřejov spectra of HD 277197 (black lines) with the model spectra (red lines). From top to bottom, the spectra were taken on RJD 55 833.4303 (*top* two plots) and RJD 55 837.4985 (*bottom* two plots). Note that the telluric and interstellar lines were not removed from the observed spectra in this case.

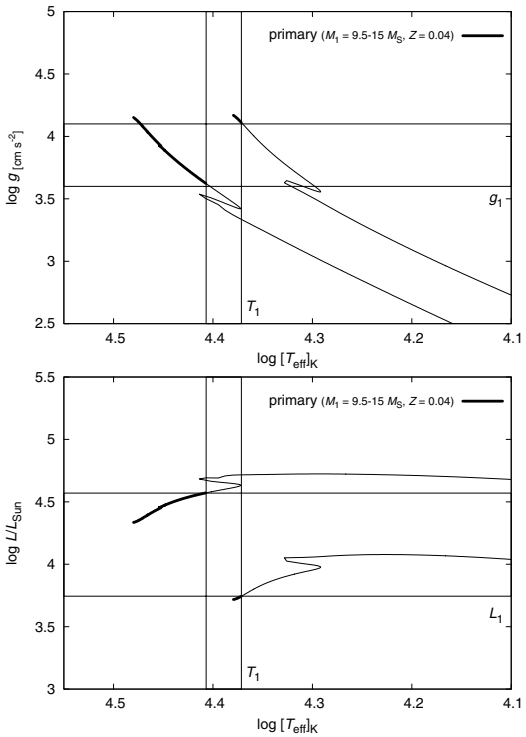


**Fig. C.4.** Computed evolutionary tracks of the primary of HD 31617 in a log $g$ vs. $T_{\rm eff}$ diagram and in the HR diagram. See the text for details.

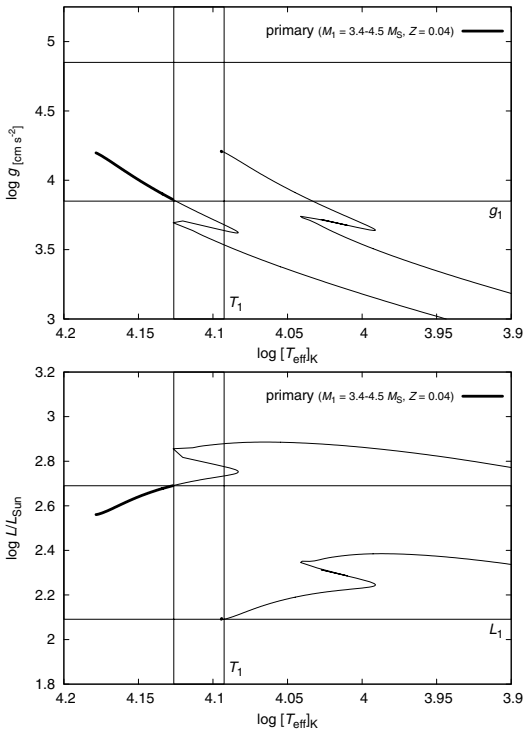


**Fig. C.5.** Computed evolutionary tracks of HD 32328 in a log $g$ vs. $T_{\rm eff}$ diagram and in the HR diagram. See the text for details.

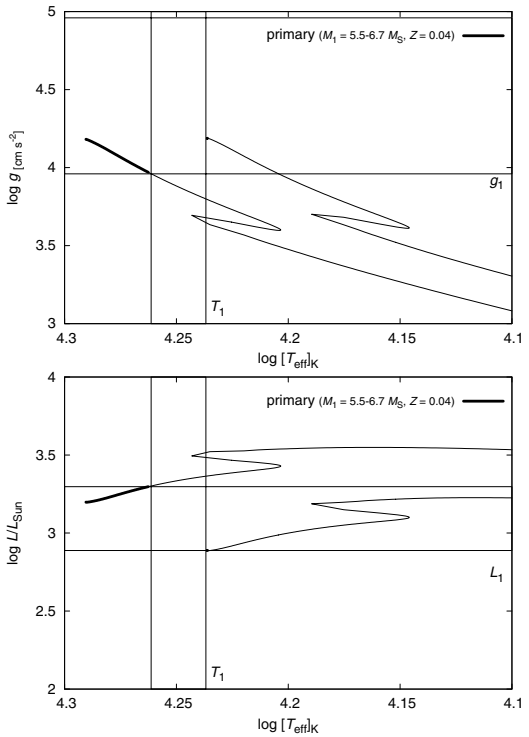


**Fig. C.6.** Computed evolutionary tracks of HD 277197 in a log $g$ vs. $T_{\rm eff}$ diagram and in the HR diagram. See the text for details.

# B Abstracts of bachelor and diploma theses

Abstracts of bachelor and diploma theses serve as a more detailed information on topics which were discussed with students in *some* depth. We list them in temporal order here:

1. Rozehnal, J.: Pozdní fáze formování velkých planet sluneční soustavy (Late phases of the formation of the giant planets in the Solar System), Bachelor thesis, Charles University, Praha, 2009.

   Abstract: In this work we study the processes in the Solar System, namely during the phases, which occurred after dissolution of the gaseous protoplanetary disk. At first we describe a standard accretion model of giant planets, which is not able to explain formation of Uranus and Neptune at large heliocentric distances. Secondly, we discuss migration of planets, which seems to be an inevitable process, both to explain current orbits of planets and distribution of small-body populations, like Plutinos. Last part of the thesis is devoted to our numerical simulations, which aim to explain some of the aspects of planetary migration.

2. Trojanová, L.: Spektrální vlastnosti rodin planetek podle přehlídky Sloan Digital Sky Survey (Spectral properties of asteroid families based on the Sloan Digital Sky Survey), Bachelor thesis, Hradec Králové University, Hradec Králové, 2010.

   Abstract: In this work we apply a principal component analysis (PCA) to photometric data of asteroids. The basic input for this work is a general mathematical PCA method and a catalogue of photometric data for 471,569 asteroids, which were observed by the Sloan Digital Sky Survey. We describe the calculation of pricipal components and we prepare algorithms, which enable practical computations. According to our results, we recommend to use three principle components, for which we inferred a specific physical interpretation, in studies of asteroids. We finally display principal components in the space of orbital elements of asteroids (most importantly semimajor axis, eccentricity and inclination) and verified a close relation between orbital and photometric data.

3. Cibulková, H.: Vývoj hvězd různých hmotností (The evolution of stars with various masses), Bachelor thesis, Charles University, Praha, 2011.

   Abstract: In the present work we study changes of the structure of a star that occur during stellar evolution and the dependence of these changes on the initial mass of the star. Internal changes affect also characteristics of the star which are observable from the outside like the effective temperature or luminosity. At first we briefly derive basic equations of the stellar structure which describe the most important processes inside the star. We assume the star is nonrotating and spherically symmetric. For a detailed description of the stellar evolution, we plot individual quantities for different initial masses (from 0,1 to 100 $M_\odot$). We use the program EZ2 for numerical calculations which enables to model the stellar evolution as long as the condition of the hydrostatistic equilibrium is satisfied. Finally, we use the theory of the stellar evolution to determine the ages of two open clusters NGC 188 and M 45 using the method of isochrones.

4. Řehák, M.: Dynamické procesy v prstencích Jupiteru a Saturnu (Dynamical processes in Jupiter's and Saturn's ring systems), Bachelor thesis, Charles University, Praha, 2011.

   Abstract: The main subject of this thesis is a review of dynamical processes acting in Jupiter's and Saturn's rings. The thesis is divided into three chapters. Observed orbital and physical characteristics of the rings are described in the first one. In Chapter 2, we discuss physical processes forming the rings. Tidal disruptions, mutual collisions of ring particles, meteoroid bombardment and ballistic transport are among them. Various electromagnetic effects are analyzed too e.g. the Poynting–Robertson effect, the Lorentz resonaces, plasma drag and radiation pressure. Yet another types of phenomena are resonant gravitational influence of satellites, shepherding moons and also collective dynamics of ring particles which results in formation of spiral waves. Finally, there is a review of theories concerning the origin of Saturn's rings in Chapter 3. We can distinguish three types of models a disruption of a moon, a disruption of an external body and a formation from protolunar matter. At present, a tidal disruption of large differentiated moon seems to be the most probable theory.

5. Pohl, L.: Heat diffusion equation in the physics of asteroids and meteoroids, Bachelor thesis, Charles University, Praha, 2011.

   Abstract: Non-gravitational forces caused by thermal emission of photons can significantly change orbits and spin states of asteroids in the long term. A solution of the Heat Conduction Equation

(HCE) in an asteroid is necessary to evaluate the forces. Finite Difference Methods (FDMs) are implemented in a Fortran numerical HCE solver to calculate a temperature distribution within a system of 1-dimensional slabs which approximate the asteroid. We compare the methods w.r.t. convergence, accuracy and computational efficiency. The numerical results are compared with a simplified steady-state analytical solution. We calculate the non-gravitational accelerations and resulting semimajor axis drift from the numerical results. The implemented FDMs are shown to be convergent with denser grids and the best method has been selected. The analytical solution provides a good first-guess estimate of the temperature amplitude. The drift in semimajor axis of the tested asteroids, which is due to the non-gravitational forces, is in order-of-magnitude agreement with more accurate models and observational data.

6. Zajaček, M.: The Late Heavy Bombardment at various places of the Solar System, Bachelor thesis, Charles University, Praha, 2012.

   Abstract: In this work, we study the Late Heavy Bombardment (LHB) in the Solar System which took place from 4.1 to 3.8 billion years ago, and represents a period of intense collisions whose traces are observed on the Moon and other bodies mainly in the form of craters or impact melts. The first part of the thesis is a review on the LHB with the focus on observational evidence and recent dynamical models. In the second part, we test a particular dynamical model of the LHB using the observed cratering records on various Solar-System bodies, which was not done previously to such an extent. For this purpose, we use the symplectic integrator SyMBA, the collisional code Boulder, and various projectile–crater scaling laws. We discuss the sources of uncertainties of the observations as well as that of the models. Furthermore, we use our results to constrain the size-frequency distribution of the primordial cometary population.

7. Rozehnal, J.: Rodiny planetek a jejich vztah k migraci planet (Asteroid families and their relation to the planetary migration), Diploma thesis, Charles University, Praha, 2012.

   Abstract: In this thesis, we study how the planetary migration acts asteroid families. We identify the families among the Trojans of Jupiter by analysing their properties in the space of resonant elements, the size-frequency distribution and the colour indices. The previously reported number of families (10) seems to be overestimated, our analysis indicates that there is only one collisional family among Trojans with the parent-body size DPB ¿ 100 km. We also performed a simulation of the long-term orbital evolution of the Trojan families. We used a modified version of the SWIFT symplectic integrator where the migration is set analytically. We found that the families are unstable even in the late stages of the migration, when Jupiter and Saturn recede from their mutual 1:2 resonance. Hence, the families observed today must have been created after the planetary migration ended. In the last part of the work, we study a formation of asteroid families in the Main Belt during the Late Heavy Bombardement. We simulate perturbations induced by migrating planets in the "jumping Jupiter" scenario (Morbidelli et al., 2010) and we conclude that big families (DPB ¿ 200 km) created during the bombardement should be observable today.

8. Cibulková, H.: Kolizní vývoj hlavního pásu asteroidů po dobu čtyř miliard let (Collisional evolution of the main asteroid belt over 4 billion years), Diploma thesis, Charles University, Praha, 2013.

   Abstract: In this work, we constructed a new model for the collisional evolution of the Main Asteroid Belt. Our goals are to test the scaling law from the work of Benz & Asphaug (1999) and ascertain if it can be used for the whole belt. We want to find initial size-frequency distributions (SFDs) for the considered six parts of the belt, and to verify if the number of asteroid families created during the simulation matches the number of observed families as well. We used new observational data from the WISE satellite (Masiero et al., 2011) to construct the observed SFDs. We simulated mutual collisions of asteroids with a modified Boulder code (Morbidelli et al., 2009), in which the results of hydrodynamic (SPH) simulations from the work of Durda et al. (2007) are included. Because material characteristics can act breakups, we created two models — for monolithic asteroids and for rubble-piles (Benavidez et al., 2012). The results for monolithic and rubble-pile asteroids are comparable and in both cases the number of created families is, within uncertainties, consistent with the observations. A disagreement of the SFDs for a limited size range D ' 1 to 5 km a is a good motivation to conduct new SPH simulations with relatively small targets.

9. Chrenko, O.: Původ asteroidů ve 2:1 rezonanci středního pohybu s Jupiterem (Origin of asteroids in the 2:1 mean-motion resonance with Jupiter), Bachelor thesis, Charles University, Praha, 2013.

Abstract: Asteroids located in the 2:1 mean-motion resonance with Jupiter are classified as stable (called Zhongguos), marginally stable (called Griquas) and unstable (called Zulus) according to their dynamical lifetime. The stable asteroids reside in two separate stable islands in the pseudo-proper element space. In this thesis, we update the resonant population on the basis of up-to-date observational data and we determine orbital and physical properties of the resonant population. Using collisional models, we demonstrate that the observed Zhongguos and Griquas might be up to 4 Gyr old, thus their origin might be related to the planetary migration. Performing dynamical N-body simulations, we test two hypotheses of the origin of the long-lived population: the primordial population scenario, and the asteroidal capture scenario. Our results imply that the resonant population is not primordial but it was rather formed by the asteroids captured from an asteroidal family located in outer main belt.

10. Sváda, P.: Aplikace dalekohledu LSST ve fyzice malých těles sluneční soustavy (Applications of the LSST telescope in physics of small solar-system bodies), Bachelor thesis, Charles University, Praha, 2013.

    Abstract: This thesis is devoted to the description of the Large Synoptics Survey Telescope (LSST) and its use in the physics of small solar-system bodies. Based on the telescope optics parameters and the theory of signal and noise we calculate limiting magnitude of the LSST $(24.9 \pm 0.4)$ mag (in the V band). This value, together with data from MPC and WISE databases, serve as an input parameter for the calculation of the minimum diameter $(273 \pm 55)$ m of a main-belt asteroid, that LSST will be able to observe. We also estimated that $(160 \pm 118)$ million asteroids could be observable by the LSST. Taking into account the planned observational strategy and cadence, we calculated that a sufficiently bright asteroid will be observed approximately 370 times. Finally, the possible applications of the LSST are discussed: e.g. a development of collisional models, explanation of orbital and rotational dynamics of sub- kilometer objects.

11. Ševeček, P.: Vliv tepelné emise topografických útvarů na rotační dynamiku planetek (Rotational dynamics of asteroids affected by thermal emission from topographic features), Bachelor thesis, Charles University, Praha, 2014.

    Abstract: Infrared radiation emitted from an asteroid surface causes a torque that can significantly affect rotational state of the asteroid. The influence of small topographic features on this phenomenon, called the YORP effect, hasn't been studied yet in detail. In this work, we show that lateral heat diffusion in surface features of suitable sizes leads to the emergence of a local YORP effect which magnitude is comparable to the YORP effect due to the global shape. We solve a three-dimensional heat diffusion equation in a boulder and its surroundings by the finite element method using the FreeFem++ code. The contribution to the total torque is then inferred from the computed temperature distribution. We compare the torque for various boulder shapes and material properties. For an idealized boulder our result is consistent with an existing one-dimensional model. Topographic features may cause a spherical asteroid of radius 1 km on a circular orbit at 2.5 AU to undergo a rotational acceleration of about $(2.2 \pm 1.1) \cdot 10^{-9}\,\mathrm{rad/day^2}$, which corresponds to the spin-up timescale of the order $\tau = (32 \pm 16)$ Myr. We estimated a size distribution of boulders based on close-up images of (25143) Itokawa surface. Finally, we realized that topographic features of Itokawa can induce a rotational acceleration of the order $10^{-7}\,\mathrm{rad/day^2}$ and can therefore explain the observed phase shift in light curves.

12. Řehák, M.: Asteroidální rodiny versus velké pozdní bombardování (Asteroid families versus the Late Heavy Bombardment), Diploma thesis, Charles University, Praha, 2014.

    Abstract: The aim of this thesis is to ascertain if main-belt asteroid families are compatible with the existence of the Late Heavy Bombardment (LHB), which occurred in the Solar System approximately 4.1 to 3.8 billion years ago (Hartmann et al., 2000). At rst, we have newly identied families in the pristine zone between 2.83 and 2.96 AU, using data from catalogues AstDyS and WISE. We found clumps of bodies (19 in total) in the orbital data and calculated their statistical signicance by a MonteCarlo method. We selected members of 918 Itha, 709 Fringilla and 15477 families using the hierarchical clustering method. These three families form a representative sample in the proper element space and with respect to their taxonomic type.

    We performed simulations of the long-term orbital evolution using the numerical integrator Swift (Levison and Duncan, 2013). We used the KolmogorovSmirnov test to compare the distributions of proper elements of the simulated and observed families. We also compared the numbers of bodies

scattered by gravitational resonances to determine likely ages of the families: Itha $t > 2.5\,\mathrm{Gyr}$, Fringilla $t > 3.0\,\mathrm{Gyr}$ and 15477 $t \simeq 0.8\,\mathrm{Gyr}$.

We simulated also their collisional evolution using the Boulder code (Morbidelli et al., 2009). The initial size-frequency distributions were selected according to the results of SPH simulations of disruptions (Durda et al., 2007). By comparing the simulated distributions with the observed ones we obtained independent estimates of the ages: Itha $t > 2.3\,\mathrm{Gyr}$, Fringilla $t > 3.3\,\mathrm{Gyr}$ and 15477 approximately $t \in [0.47, 0.61]\,\mathrm{Gyr}$. The results of our simulations indicate that the Itha and Fringilla families are indeed very old and their origin during the LHB is still possible.